

ACTA TECHNICA

**Volume 56 (2011)
Supplement to Topical Issue**

ISSN 0001-7043



Institute of Thermomechanics AS CR, v.v.i.

Topical issue containing selected papers
presented at the 24th Symposium
on Plasma Physics and Technology

Guest Editors

KAROL BUJAČEK

YULIYA KLENKO

JAN NEUŽIL

JAN SLÁMA

The Symposium on Plasma Physics and Technology has a long tradition and is usually held biennially. It was originally founded for the presentation of results of the Institute of Plasma Physics of the Czechoslovak Academy of Sciences in 1967. Since 1969 it has gradually become a Czechoslovak forum in this branch, and many famous foreign scientists presented there their contributions. Since 1993 the Symposium has been held in co-operation with the Department of Physics, Faculty of Electrical Engineering of the Czech Technical University in Prague.

About 200 participants, particularly from European countries, take usually part in symposium activities. In recent years, the participation of young scientists has been supported with the financial grant of the European Physical Society.

The symposium topics cover almost the complete field of the plasma physics, namely

- tokamaks and other magnetic confinement devices,
- short lived plasmas (plasma focus, z-pinch, particle beam plasma interaction, X-ray sources),
- laser plasma,
- non-equilibrium low temperature plasma,
- thermal plasmas,
- plasma technology,
- fundamental plasma physics,
- plasma theory and simulation.

The next (25th) symposium will be held on June 18–21, 2012. Details are presented at <http://spt.aldebaran.cz/>.

Spatial-temporal behavior of individual microdischarges in dielectric barrier discharge¹

YURI AKISHEV², GREGORY APONIN², ANTON BALAKIREV²,
MIKHAIL GRUSHIN², VLADIMIR KARALNIK²,
ALEXANDER PETRYAKOV², NIKOLAY TRUSHKIN²

Abstract. Results of experimental study on a spatial-time behavior of microdischarges (MDs) in steady-state dielectric barrier discharge (DBD) are presented. It was revealed that MDs of DBD have a spatial “memory”, i.e., every subsequent MD does not jump in arbitrary point of the barrier surface but appears exactly at the same place that was occupied by the preceding MD. This memory is derived from slow recombination of plasma in the MDs channels for a period between two neighbor half-periods (HPs). In such a case, there is no necessity in newly local avalanche volume breakdowns at every HP. MDs in steady-state DBD have a great scattering with time of their appearance over every HP. This scattering is attributed to the local surface breakdowns around every MD.

Key words. Dielectric barrier discharge, microdischarge, electron avalanche breakdown, alternating voltage, chaotic behavior, gas flow.

1. Introduction

Dielectric barrier discharge (DBD) is widely used at present in various practical applications: the ozone generation, pumping of gas discharge lasers and excimer lamps, plasma displays, surface modification, biomedicine, etc. [1]–[5]. Each application field presents its own specific requirements to the DBD as the composition of plasma forming gas and on the discharge regime. For this reason dielectric barrier discharge have been widely studied over last few decades. As it is known, the plane-to-plane DBD exhibits three different current modes:

¹This work is partly supported by the RFBR (project No. 09-02-00994a).

²State Research Center of Russian Federation, Troitsk Institute for Innovation and Fusion Research, Troitsk, Moscow region, Russia

- 1) the transverse uniform mode with a single current pick [6] and many regular current picks [7],
- 2) the regularly patterned mode [8], [9], and
- 3) the regime with numerous microdischarges (MD) showing a spatial-time chaotic behavior [10]. Namely this regime of steady-state DBD is the subject of our investigation.

There is a wide-spread opinion that the MDs are randomly distributed in time and space, i.e., the MDs have no spatial “memory”, and they appear by each half-period (HP) always at new points which have no any relation to the former places occupied by the MDs in previous HP. According to such a view, every MD is newly formed once an electric field in the gap gets up to the critical value. The formation of alone MD was studied numerically in many publications [11]–[14]. This formation can be roughly divided, by these publications, into two sequential stages:

- 1) electron avalanche gas breakdown of the gap between barriers, and
- 2) electron avalanche breakdown over the dielectric surfaces.

The first stage (volume breakdown) results in local shunting the gap by plasma. The second stage (partial surface breakdown around the MD ends) results in a quick increasing the local barrier capacity which enables increasing drastically the magnitude of electric current passing through the MD.

Numerical calculations of a steady-state DBD with the repeating transient MDs are absent in literature. Using the models based on the idea of a new gap breakdown in every HP meets with a difficulty to explain the peculiarities of real steady-state DBD. For instance, according to these models, the MDs have to arise by every HP at well-defined moments correlated with an appearance of the critical electric field in the gap. In reality, the MDs exhibit a chaotic behavior in time. Another difficulty for the models assuming the gap breakdown at fixed voltage by every HP is the conclusion that a DBD can be sustained only by applying an alternating voltage the amplitude U of which exceeds so-called inception voltage U_1 (the inception voltage corresponds to the appearance of the MD due to the avalanche gap breakdown). However, it is well known that a steady-state DBD can exist not only under higher voltages $U \geq U_1$ but under lower voltages $U_1 > U > U_2$ as well. Here, U_2 is the extinction voltage which correlates with a full disappearance of a discharge in the gap ($U_2 < U_1$ such that U_2 can be as low as $0.6 U_1$ [15]).

This work was motivated by the aspiration to answer the two main questions:

- 1) Is there a spatial “memory” for MDs in steady-state DBD?
- 2) What are the reasons for the MD chaotic behavior in time and space?

For this purpose we have done a detailed search on spatial-time behavior of MDs in a steady-state DBD.

2. Experimental set-up

The sketch of the experimental set-up is shown in Fig. 1. A gas discharge was activated between transparent plane electrodes connected to a power supply with a sinusoidal voltage of variable frequency and amplitude (two-dimensional DBD). The spatial-time behavior of great number of MDs was observed through transparent plane electrodes ($35 \times 35 \text{ mm}^2$) fabricated of very thin metallic mesh with the high degree of geometrical transparence of 92 % or vacuum-evaporated Au layer with optical transparence of 35 %. The dielectric barrier discharge was activated with a sinusoidal voltage of variable frequency (from 50 Hz to 100 kHz) and amplitude (up to 20 kV). The inter-electrode gap was varied from 1.2 to 2 mm. The plasma forming gas was ambient air and nitrogen of a high purity (99.999 %) at atmospheric pressure. To prevent the gas heating in the gap, experiments with steady-state DBD were performed either in gas flow or in gas at rest but under DBD excitation limited with time of $1 \div 2 \text{ s}$ that is much longer compared to HP. The discharge current and voltage waveforms covering many periods were recorded by digital oscilloscope Tektronix TDS-520. These waveforms can be synchronized with a sequence of four DBD pictures taken with a high-speed electron camera at short exposure time (up to 50 ns) and/or with the shots of DBD taken by video-camera Panasonic NV-GS 500 or digital camera Canon EOS 40D. The duration of video film was up to 2 s. Two optical signals of the light collected by two optical fibers from different small discharge areas were recorded by two photomultipliers. The optical signals correlate with the appearance of individual MDs at the fixed local areas of diameter of $80 \text{ }\mu\text{m}$.

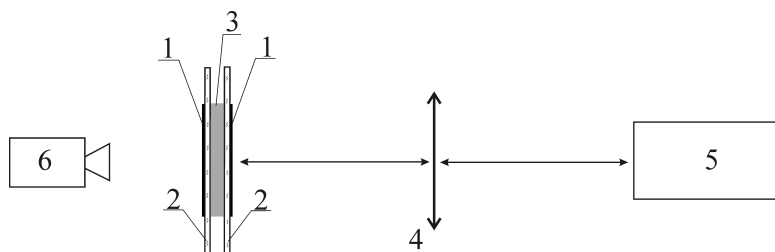


Fig. 1. Schematic of the experimental set-up; 1—transparent metallic plate, 2—glass barriers, 3—discharge gap varied from 1.2 to 2 mm, 4—quartz lens, 5—photomultipliers equipped with optical fibers or high-speed electronic camera with high image intensifying, 6—video-camera Panasonic NV-GS 500 or digital camera Canon EOS 40D

3. Results and discussion

In accordance with the opinion mentioned above, the MDs in a two-dimensional DBD (plane-to-plane electrode geometry) have to be distributed randomly in space and time. We recorded the optical signals of the light collected by two thin fibers from two different but fixed and very small regions of DBD. The diameter of each area was $80\ \mu\text{m}$, which is smaller compared to a typical diameter of the MD (about $100 \div 200\ \mu\text{m}$ [10]). It means that the acquisition system of each photomultiplier would collect only the light emitted from a single MD. The optical signals of two photomultipliers recorded by the oscilloscope Tektronix TDS 520 are presented in Fig. 2.

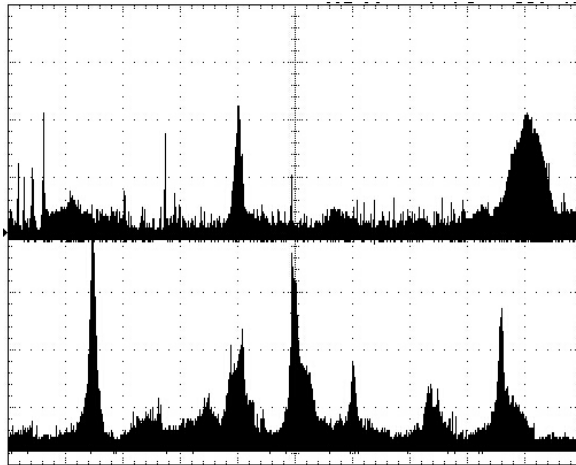


Fig. 2. Optical signals recorded by two photomultipliers from different small areas of DBD; diameter of each small area is $80\ \mu\text{m}$, distance between two points of observation is $10\ \text{mm}$, time scale is $5\ \text{ms/div}$, the gap is $1.2\ \text{mm}$, ambient air at rest, average current per HP is $10\ \text{mA}$

One can see, indeed, that MDs appear not always at a fixed place. However, if such event happens, the MDs “stay” at this place over many periods—up to 300 HPs at the frequency of $100\ \text{kHz}$ (more precisely, MDs slowly move through the fixed area). It means that the displacement of MD during one HP of an alternating voltage is smaller than $0.25\ \mu\text{m}$ —this value is negligible compared to the MD diameter. Hence, this experiment proves unambiguously that MDs in a steady-state DBD have a spatial “memory”, i.e., every subsequent MD does not jump at an arbitrary point of the barrier surface but appears exactly at the same place that was occupied by the preceding MD. To answer the question of how many breakdowns can occur at the same local place over a single HP, we recorded the light signal with a high time resolution that allowed us to find out

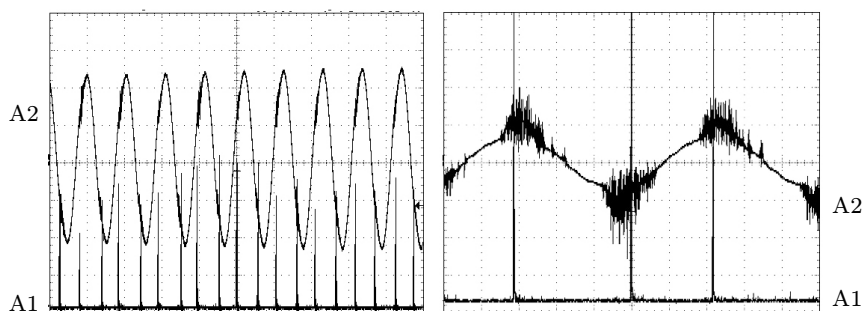


Fig. 3. Correlation of photomultiplier signal from a single MD with applied voltage (*left*) and discharge current (*right*); the gap is 1.2 mm, gas is ambient air at rest; *left*: A1—photomultiplier signal, A2—applied voltage waveform; time scale is $10\ \mu\text{s}/\text{div}$, voltage scale $2.6\ \text{kV}/\text{div}$; *right*: A1—photomultiplier signal, A2—discharge current signal; time scale is $2\ \mu\text{s}/\text{div}$, current scale $100\ \text{mA}/\text{div}$

the time behavior of MDs at the fixed small place ($80\ \mu\text{m}$) during the single HP. The results are shown in Fig. 3.

On closer examination it proved that MD appears at the fixed place every half-period but in most cases (more than 95 %) only once during the single HP. This conclusion is fair for the whole frequency and voltage region investigated. Frequency and voltage amplitudes varied from 50 Hz to 100 kHz, and up to 20 kV, respectively (i.e., maximum voltage amplitude was much higher than the inception voltage $U_1 \approx 10.4\ \text{kV}$).

The instant images of DBD at different average currents per HP are presented in Fig. 4.

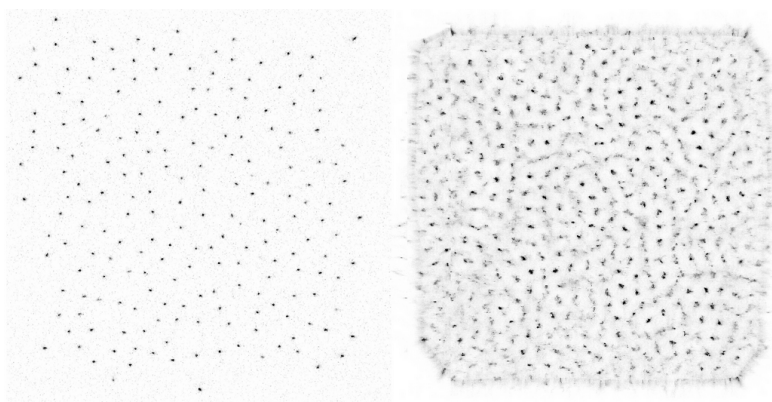


Fig. 4. Instant images of DBD in ambient air at rest under different average currents per HP; the pictures were taken with camera Canon EOS 40D; voltage frequency is 100 kHz, discharge gap is 1.2 mm; *left*: average current per HP is 5.6 mA, exposure time is 1 ms; *right*: average current per HP is 35 mA, exposure time is 40 ms

Figure 4 was taken under short exposure time $t = 1$ ms, that is smaller or comparable to characteristic time $\tau = \Delta/V \leq 1$ ms, where Δ is the transverse size of the spot formed by MDs and $V \leq 1$ m/s is the average velocity of this spot. This means that the displacement of the spot during the exposure time is smaller compared to its transverse size. It is evident that under such conditions the number of the spots is equal to the number of MDs appearing in the gap during a single HP (if operating conditions are fixed, the number of MDs does not change from one HP to another because DBD average current per whole period is equal to zero). The images show that the location regularity of the spots in the gap increases with increase of the average current per HP. Indeed, the image in Fig. 4-right (DBD at high current) was taken under much longer exposure time, nevertheless there is only low blurring of the spot image. Moreover, under high current the clear location regularity can be observed even by the naked eye.

The images in Fig. 4 demonstrate that number of spots in a steady-state DBD increases with increase of the average current per HP. The minimal distance between neighbor spots is close to the length of inter-electrode gap. It means that there is the highest possible amount of the spots for a concrete DBD, which is determined by the electrode square and does not depend on frequency of the applied voltage. It seems plausible that further increase in DBD current can result in transition of non-regular DBD to the patterned DBD and further to the transverse homogeneous regime.

Both the time spent by alone spot to cross the fixed area and the time between two visits in this area by different spots vary chaotically. The characteristic time of these variations ranges over $2 \div 20$ ms (see Fig. 2) that is much higher than the applied voltage period. It means that DBD spots travel slowly and chaotically in the gap. In such a case, it is possible to catch slow movement of the spots by a normal digital video-camera and trace the trajectories (or paths) of many spots during a long time. Such experiments were performed with DBD sustained in gas at rest and in gas flow.

We used a power supply that was able to generate sinusoidal voltage the amplitude of which could vary with time by pre-set manner: the amplitude exceeds the breakdown voltage U_1 during the first 30 ms, thereafter the amplitude drops down to the preset voltage U . It was found out that

- 1) DBD is a steady-state discharge if the amplitude U is equal to or exceeds some critical value $U^* < U_1$, and
- 2) DBD decays very slowly (the characteristic time about 1 s) if the amplitude ranges within the limits $U^* > U > U_2$ (remind that extinction voltage U_2 corresponds to the momentary extinction of MDs all over the gap, i.e., to the instant DBD switching off).

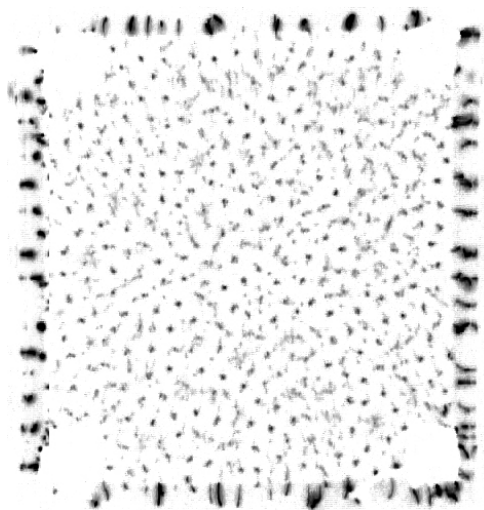


Fig. 5. Image of steady-state DBD in ambient air at rest under average current of 30 mA per HP; the picture was taken by camera Panasonic NV-GS 500 at exposure time 10 ms; voltage frequency is 100 kHz, the gap is 1.2 mm; metallic plate is vacuum-evaporated Au layer with optical transparency of 35 %; the MDs located along perimeter of the gold plate (more precisely, outside the area covered by Au) look brightly compared to those in the middle of discharge area

At our experimental conditions we found out the magnitudes U_1 , U^* , U_2 for DBD supported by frequency of 100 kHz: $U_1 = (10.4 \pm 0.3)$ kV, $U^* = (6.5 \pm 0.3)$ kV, $U_2 = (5.0 \pm 0.3)$ kV. Within the scattering pointed, these values are the same for air and nitrogen.

A closer examination of the discharge shots (see Fig. 5) showed that the magnitude U^* correlates with appearance of many steady-state MDs having stable positions along the whole length of a discharge area perimeter (remind that the discharge area is determined by square of the metallic plates). A reason for appearance of the stable MDs is the following. Due to boundary conditions at the sharp edges of metallic plates, the local electric field at the perimeter is higher compared to that in the middle of discharge area. This boundary effect provides local breakdowns at the periphery (i.e., new permanent formation of MDs) even under voltage lower than U_1 corresponding to the breakdown over the whole discharge area.

The results related to the long-time behavior of MDs in the slowly decaying DBD under voltage amplitude $U^* > U > U_2$ are presented in Figs. 6 and 7, which correspond to the decaying DBD in ambient air at rest and under airflow, respectively. Each picture in this figure is a superposition of several shots from different pieces of video-film. Due to such procedure, we revealed that

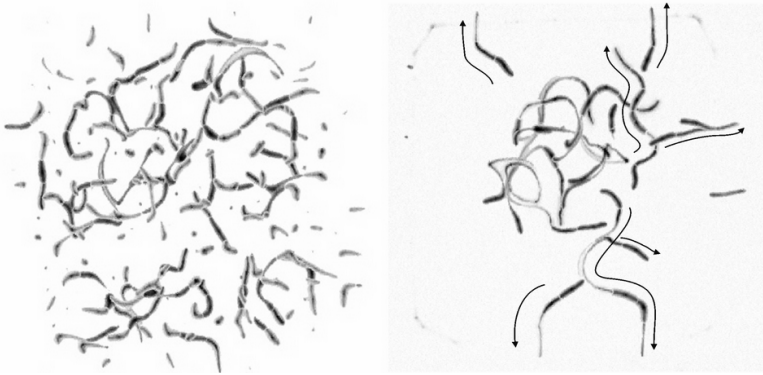


Fig. 6. Images of decaying DBD in ambient air at rest; the shots are taken with camera Panasonic NV-GS 500; the gap is 1.2 mm, voltage frequency 100 kHz, the averaged current per HP 6 mA; *left*: superposition of 3 shots; exposure time of each shot is 40 ms and the first shot was taken with delay of 40 ms after DBD breakdown; *right*: superposition of 7 shots; exposure time of each shot is 40 ms; the first shot was taken with delay of 200 ms after DBD breakdown; the arrowed lines show the motion direction of some points

- 1) every spot is not fixed in the gap but slowly and chaotically moves on the barrier surface and draws its own trajectory,
- 2) there is a general tendency that there are no steady-state spots along the perimeter of the discharge area, and, therefore, other spots slowly and chaotically (similarly to the Brown movement) drift from the center to the periphery and disappear after crossing the perimeter of DBD.

Hence, the total number of the spots in DBD slowly decreases with time down to zero (Fig. 6). This process leads to a very slow (about 1 s) decay of DBD. Such behavior of MDs is typical for the decaying DBD in air and nitrogen but in the latter case a decay of DBD takes much longer time. The gas flow blown through the gap does not change the amplitudes U_1 , U^* , and U_2 , but accelerates the DBD decay because of fast convective removal of the spots from the gap (Fig. 7).

In the case of a steady-state DBD ($U > U^*$) the spots also move chaotically but because of great number of spots the length of their trajectories is shorter and restricted by space of the order of inter-electrode distance. The spots from the discharge area do not cross the perimeter because the perimeter is occupied closely with MDs formed by local high strength electric field (figuratively speaking, the MDs at the perimeter serve as a guard prohibiting the transition through perimeter for MDs from central area). In such a case, the number of spots does not change with time, and steady-state DBD is established.

The existence of the steady-state DBD under lower voltage $U_1 > U > U^*$ (i.e., without avalanche breakdowns of the gap inside the discharge area) is

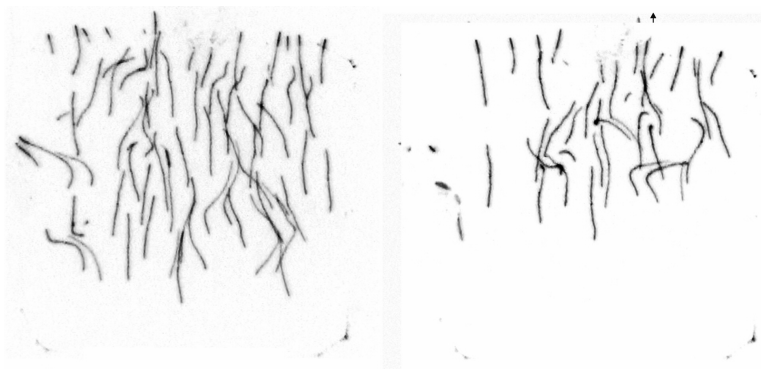


Fig. 7. Images of decaying DBD in ambient air under airflow; the shots are taken with camera Panasonic NV-GS 500; the gap is 1.2 mm, voltage frequency 100 kHz, the averaged current per HP 6 mA; airflow direction is upward and gas flow velocity is 0.2 m/s; *left*: a single shot, exposure time being 40 ms; this shot was taken with delay of 40 ms after DBD breakdown; *right*: a single shot, exposure time being 40 ms; this shot was taken with delay of 80 ms after DBD breakdown.

directly related to spatial “memory” of MDs. This memory is derived from slow recombination of plasma in the MDs channels for a period between two neighbor HPs. It means that in steady-state DBD, there are always many plasma channels shunting the gap. In such a case, there is no need of new local avalanche volume breakdowns at every HP—it is sufficient to create the plasma only one time in the very first (initial) breakdown of the gap under $U \geq U_1$. After that the decaying plasma of the MD channels can be supported periodically by the lower applied voltage due to partial surface breakdowns around the ends of plasma channels. The surface breakdown around every MD leads to a quick and short-term increasing of local barrier capacity providing the transfer of current through the barrier. The increase in local capacity results in a sharp current pulse raising the plasma density in the transient MD to the former level. In such an event, the avalanche volume breakdown in steady-state DBD is of no importance. Because of that, the first current pulse by HP appears at maximum voltage (if $U = U_1$) but the pulses by the second and other HPs appear at lower voltage.

This statement is illustrated by Fig. 8 presenting the current and voltage waveforms of DBD at 50 Hz and 100 kHz. Note that in the case of 50 Hz the displacement current is negligible, and the current waveform looks like a set of the pulses corresponding to the conductivity current. Oppositely, in the case of 100 kHz the displacement current is high, and the current waveform looks like a superposition of a sinusoidal curve (displacement current) and pulses (conductivity current).

Hence, due to both existence of a “spatial” memory and the MDs confinement within the discharge area, the number of MDs in steady-state DBD is

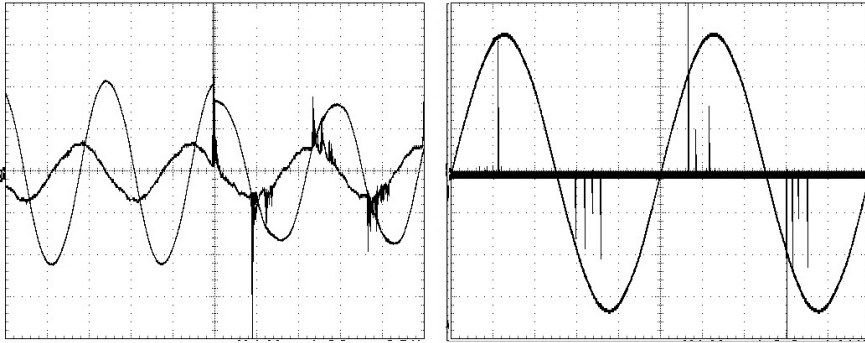


Fig. 8. Current vs. voltage oscillograms showing the first breakdown current pulse and others pulses under lower gap voltage corresponding to steady-state DBD in ambient air at rest; gas gap is 1.2 mm; *left*: voltage frequency is 100 kHz, time scale is 4 μ s/div, voltage and current scales are 5.2 kV/div and 100 mA/div; *right*: voltage frequency is 50 Hz, time scale is 4 ms/div, voltage and current scales are 3.2 kV/div and 40 mA/div

the same at every HP. However, there is a strong scattering in time over HP for an appearance of every MD at the spot corresponding to this MD. Namely, this scattering results in the well-known chaotic behavior of the DBD current pulses the order and amplitude of which are not reproducible from HP to HP. This scattering is illustrated by Fig. 9.

One can see in Fig. 9 that MDs appear at their own places not simultaneously but irregularly with time and predominantly by several groups with a different amount of MDs in each group, i.e., each current pulse consists, in fact, of many MDs distributed at different places of the barrier surface. The experiment revealed a great scattering in time for appearance of the surface breakdown over the HP.

4. Conclusion

Our study on a spatial-time behavior of MDs in steady-state DBD revealed the following.

1. MDs have a spatial “memory”, i.e., every subsequent MD does not jump in arbitrary point of the barrier surface but appears exactly at the same place that was occupied by the preceding MD. This memory is derived from slow recombination of plasma in the MDs channels for a period between two neighbor HPs. It means that in steady-state DBD there are always many plasma channels shunting the gap. In such a case, there is no need of new local avalanche volume breakdowns at every HP—it is sufficient to create the plasma only one time in the very first (initial) breakdown of the gap under $U \geq U_1$. After that the decaying plasma of the MD channels can be supported periodically by the

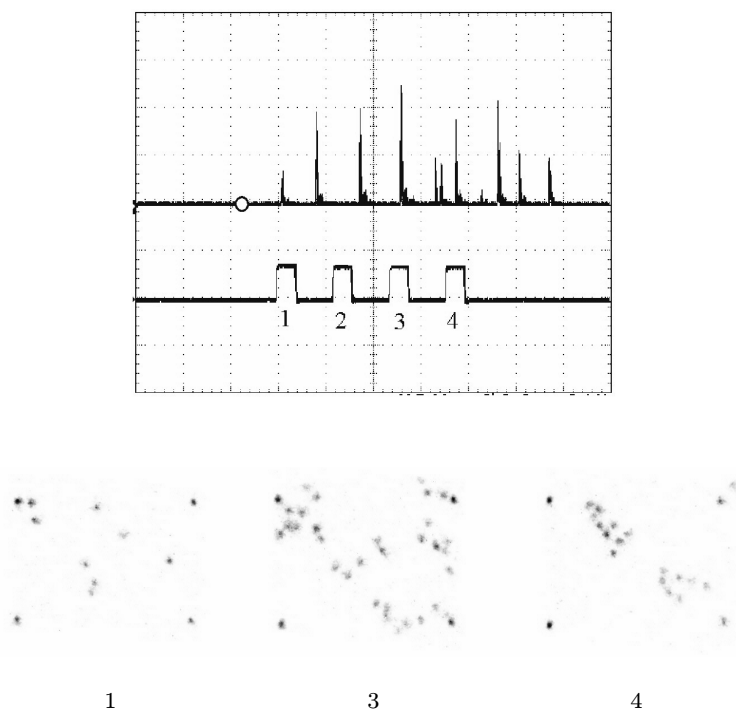


Fig. 9. Scattering in time over a single HP for the case of appearance of MDs at their places formed by previous MDs; the DBD in ambient air at rest; voltage frequency is 8 kHz, gas gap is 1.2 mm; *upper picture*: upper line—the train of current pulses of steady-state DBD over a single HP; the circle correlates with the moment $U(t) = 0$; lower line—the moments when the shots 1, 3, 4 were taken; time scale is $2.5 \mu\text{s}/\text{div}$, current scale is $100 \text{ mA}/\text{div}$; *lower picture*: DBD surface shots taken at the moments 1, 3, 4 with exposure time $1 \mu\text{s}$; four bright points at the corners of each shot represent frame borders

lower applied voltage due to partial surface breakdowns around the ends of plasma channels. Every current pulse correlated with the surface breakdown raises the plasma density in the transient MD to former level.

2. In most cases (more than 95 %), each MD appears at a fixed place by every half-period only once during the HP. It may well be true that more essential increase in the amplitude of the applied voltage can lead to an appearance of the repeated MD breakdown at the same MDS over a single HP but we did not perform such experiments.

3. For the plane-to-plane DBD with restricted electrode area there is a threshold amplitude U^* of the applied voltage. If the applied voltage amplitude exceeds U^* , then DBD exists in steady-state regime with constant number of microdischarges in each HP. If the applied voltage amplitude is less than U^* , DBD decays slowly because the number of MDs inside the gap decreases due to

their Brown motion from the central region to the outside of discharge area. At the applied voltage amplitude below U^* , blowing the gap by gas flow can provide a fast convective removal of MDs and, therefore, a quick decaying of DBD.

4. The MDs in steady-state DBD have a great scattering with time of their appearance over every HP. This scattering is attributed to the surface breakdowns which occur in every HP.

References

- [1] U. KOGELSCHATZ: *Industrial innovation based on fundamental physics*. Plasma Sources Sci. Technol. *11* (2002), A1–A6.
- [2] U. KOGELSCHATZ: *Dielectric-barrier discharges: Their history, discharge physics, and industrial applications*. Plasma Chem. Plasma Process. *23* (2003), 1–46.
- [3] R. MORENT, N. DE GEYTER, L. GENGEMBRE, C. LEYS, E. PAYEN, S. VAN VLIERBERGHE, E. SCHACHT: *Surface treatment of a polypropylene film with a nitrogen DBD at medium pressure*. Eur. Phys. J. Appl. Phys. *43* (2008), 289–294.
- [4] H. YASUDA, M. HASHIMOTO, M. RAHMAN, K. TAKASHIMA, A. MIZUNO: *States of biological components in bacteria and bacteriophages during inactivation by atmospheric dielectric barrier discharges*. Plasma Process. Polym. *5* (2008), 615–621.
- [5] J. R. ROTH, J. RAHEL, X. DAI, D. M. SHERMAN: *The physics and phenomenology of One Atmospheric Uniform Glow Discharge Plasma (OAUGDP) reactors for surface treatment applications*. J. Phys. D: Appl. Phys. *38* (2005), 555–567.
- [6] F. MASSINES, A. RABEHI, P. DECOMPS, R. B. GADRI, P. SEGUR, C. MAYOUX: *Experimental and theoretical study of a glow discharge at atmospheric pressure controlled by dielectric barrier*. J. Appl. Phys. *83* (1998), 2950–2957.
- [7] YU. AKISHEV, A. DEMYANOV, V. KARALNIK, M. PANKIN, N. TRUSHKIN: *Pulsed regime of diffusive mode of barrier discharge in helium*. Plasma Phys. Rep. *27* (2001), 164–171.
- [8] I. MULLER, C. PUNSET, E. AMMELT, H.-G. PURWINS, J. P. BOEUF: *Self-organized filaments in dielectric barrier glow discharges*. IEEE Trans. Plasma Sci. *27* (1999), 20–21.
- [9] I. MULLER, E. AMMELT, H.-G. PURWINS: *Self-organized quasiparticles: Breathing filaments in a gas discharge system*. Phys. Rev. Lett. *82* (1999), 3428–3431.
- [10] B. ELIASSON, U. KOGELSHATZ: *Modeling and applications of silent discharge plasmas*. IEEE Trans. Plasma Sci. *19* (1991), 309–323.
- [11] D. BRAUN, V. GIBALOV, G. PIETSCH: *Two-dimensional modelling of the dielectric barrier discharge in air*. Plasma Sources Sci. Technol. *1* (1992), 166–174.
- [12] J. MEUNIER, PH. BELENGUER, J. P. BOEUF: *Numerical model of an ac plasma display panel in neon-xenon mixtures*. J. Appl. Phys. *78* (1995), 731–745.
- [13] C. PUNSET, J. P. BOEUF, L. C. PITCHFORD: *Two-dimensional simulation of an alternating current matrix plasma display cell: Cross-talk and other geometric effects*. J. Appl. Phys. *83* (1998), 1884–1897.
- [14] I. RADU, R. BARTNIKAS, M. R. WERTHEIMER: *Dielectric barrier discharges in helium at atmospheric pressure: experiments and model in the needle-plane geometry*. J. Phys. D: Appl. Phys. *36* (2003), 1284–1291.
- [15] V. G. SAMOILOVICH, V. I. GIBALOV, K. V. KOZLOV: *Physical chemistry of the barrier discharge*. DVS-Verlag, Düsseldorf 1997.

Transitions between space charge limited and temperature limited emission of electrons from a planar collector immersed in a plasma that contains an electron beam¹

TOMAŽ GYERGYEK^{2,3,4}, JERNEJ KOVAČIČ^{2,3},
MILAN ČERČEK^{3,4,5}

Abstract. Potential formation in front of a negative electron emitting electrode immersed in a plasma that contains a mono-energetic electron beam is studied by a one-dimensional fluid model. Dependence of the floating potential of the electrode and of the potential where transition from space charge limited into temperature limited emission occurs on electron emission are calculated. The current voltage characteristics of the electrode is then calculated and the “saturation” of the collector floating potential with respect to increasing electron emission is explained quantitatively. The plasma parameters are selected in such a way, that they are suitable for later comparison with emissive probe data in low pressure discharge plasma devices.

Key words. Plasma, sheath, electron emission, electron beam, Bohm criterion.

1. Introduction

Plasmas that in addition to the basic, usually Maxwellian, electron population contain also an energetic electron population are very important in technological and fusion applications. Energetic electron populations are often

¹This work has been carried out within the Association EURATOM-MHEST. The content of the publication is the sole responsibility of its authors and it does not necessarily represent the view of the Commission or its services. This work has been partially supported by the grants J2-9160, L2-0858 and P2-0073 of the Slovenian research agency.

²University of Ljubljana, Faculty of Electrical Engineering, Tržaška 25, 1000 Ljubljana, Slovenia

³Association EURATOM-MHEST

⁴Jožef Stefan Institute, Jamova 39, 1000 Ljubljana, Slovenia

⁵University of Maribor, Faculty of Civil Engineering, Smetanova 17, 2000 Maribor, Slovenia

created in fusion devices during electron cyclotron and lower hybrid resonance heating and at the rf current drive. Because of the great practical interest numerous studies of the sheath formation in front of a negative electrode immersed in this type of plasmas can be found in the literature. We mention only very few [1]–[8].

On the other hand, sheath formation in front of electron emitting electrodes is also a very important topic for understanding emissive probe behavior. Emissive probes are, as it is well known, very important plasma diagnostic tool [9]. Attempts to study effects of energetic and emitted electrons simultaneously are relatively rare [10]. In this area also our group has been active in recent years [11]–[15]. We have studied the problem of the sheath formation in front of an electron emitting electrode that immersed in a plasma that contains a two-temperature Maxwellian distributed electrons by a one-dimensional fluid model. This means that the energetic electrons were modeled as Maxwellian distributed, but with considerably higher temperature as the “basic” electron population. Because of that the electrons of the basic population are called the “cool” electrons and the energetic electrons are called the “hot” electrons. In this work the hot electrons are replaced by a mono-energetic electron beam. All the beam electrons have the same speed but the directions of their velocities are uniformly distributed in space. Such “water-bag” electron velocity distribution function is usually a very good approximation for the primary electrons in low pressure DC hot cathode discharges. We study the dependence of the floating potential of an electron emitting electrode on electron emission for the case, when the electron emitting electrode is immersed in a plasma that contains an isotropic mono-energetic electron beam.

In the next section the mathematical model is presented. In section 3 we show some results and in the last section conclusions are given.

2. Model

An infinitely large planar electrode (collector) has its surface perpendicular to the x -axis and is located at $x = 0$. This electrode absorbs all the particles that hit it. On the other hand, it may also emit electrons. This electron emission can be thermal or secondary. The details of the emission mechanism are not essential for the model and will not be specified in this work. When the collector is floating or biased negatively with respect to the plasma potential, it reflects negative electrons and attracts positive ions. The potential profile in the sheath is determined by the one-dimensional Poisson equation

$$\frac{d^2\Phi}{dx^2} = -\frac{e_0}{\varepsilon_0} (n_i(x) - n_{e1}(x) - n_{e2}(x) - n_{e3}(x)) . \quad (1)$$

definition of plasma the dimensions of the plasma system must be much larger than the Debye length: $L \gg d \gg \lambda_D$. The limit when $\lambda_D/L \rightarrow 0$ is called the asymptotic two-scale limit [16]. Our model is done in this limit on the sheath scale. On the sheath scale the electric field at the sheath edge vanishes so that the boundary conditions for the Poisson equation (1) are:

$$\Phi(x)|_{x=d} = \Phi_S, \quad \left. \frac{d\Phi(x)}{dx} \right|_{x=d} = 0. \quad (2)$$

Note that in Fig. 1 d and L are not plotted in scale. Because of that also the potential profile in Fig. 1 does not have a vanishing electric field at $x = d$, as stated by the boundary condition (2).

The singly charged positive ions are assumed to be all at rest at a large ($x > L$) distance from the collector. Through the potential drop in the pre-sheath they are accelerated towards the collector. Riemann [16] has shown that in the pre-sheath the following relation is true:

$$\frac{d}{dx} \left(\frac{1}{2} m_i v_i^2(x) + e_0 \Phi(x) \right) < \frac{k T_e^*}{j_i} \frac{dj_i}{dx}. \quad (3)$$

Here k is the Boltzmann constant, T_e^* is the screening temperature [16] to be defined in (24) below, m_i is the ion mass, $v_i(x)$ is the ion velocity in the pre-sheath (at $d < x < L$) and $j_i(x)$ is the ion flux in the pre-sheath. This means that in the pre-sheath either (i) the ion flux j_i increases as one approaches to the collector or (ii) the total ion energy decreases due to a retarding force acting on ions, or both. In a planar geometry with no magnetic field the first effect can be caused only by ionization collisions, while the second effect is a consequence of elastic collisions of the ions with other particle species. In this work we shall assume that only the second effect has to be taken into account. The energy that the ions lose in the pre-sheath because of elastic collisions with other particle species is A_c . The total ion energy at the sheath edge is therefore

$$\frac{1}{2} m_i v_S^2 + e_0 \Phi_S + A_c = 0. \quad (4)$$

Here v_S is the ion velocity at the sheath edge. In the sheath the ion flux and the total ion energy are conserved, because the sheath is assumed to be thin enough for collisions inside it to be negligible; thus,

$$n_i(x) v_i(x) = n_S v_S, \quad (5)$$

$$\frac{1}{2} m_i v_i^2 + e_0 \Phi_S + A_c = \frac{1}{2} m_i v_i^2(x) + e_0 \Phi(x), \quad (6)$$

where n_S is the ion density at the sheath edge and x refers to a position in the sheath, $x < d$. From (4)–(6) one gets

$$n_i(x) = n_S \sqrt{\frac{e_0 \Phi_S + A_c}{e_0 \Phi(x)}} \quad (7)$$

and

$$v_S = \sqrt{-\frac{2(e_0\Phi_S + A_c)}{m_i}}. \quad (8)$$

The emitted electrons are assumed to be mono-energetic, and they all leave the collector with the same initial velocity v_C , which is assumed to be non-zero. The flux j_{e3} of emitted electrons is one-dimensional and perpendicular to the collector surface. In the sheath the flux j_{e3} is conserved,

$$j_{e3} = n_{e3}(x)v_{e3}(x). \quad (9)$$

The energy of the emitted electrons in the sheath is also conserved,

$$\frac{1}{2}m_e v_{e3}^2(x) - e_0\Phi(x) = \frac{1}{2}m_e v_C^2 - e_0\Phi_C. \quad (10)$$

From (9) and (10) one gets

$$n_{e3}(x) = \frac{j_{e3}}{\sqrt{v_C^2 - \frac{2e_0(\Phi_C - \Phi(x))}{m_e}}}. \quad (11)$$

The main electron population has a Maxwellian velocity distribution. In the sheath the density of these electrons obeys the Boltzmann law

$$n_{e1}(x) = n_1 \exp\left(\frac{e_0\Phi(x)}{kT}\right). \quad (12)$$

Here T is the electron temperature and n_1 is the density of the bulk electron population at a large distance from the collector, where the potential is zero.

The beam electrons are assumed to be mono-energetic. At a large distance ($x > L$) from the collector their density is n_{e2} and they have all the same speed v_2 . The directions of their velocities, however, are uniformly distributed in space. The velocity distribution is given by

$$f_{e2}(v) = \frac{n_{e2}}{4\pi v_2^2} \delta(v - v_2). \quad (13)$$

The density of the beam electrons at the distance x from the collector is found by integration of the distribution (13) over the velocity space:

$$\begin{aligned} n_{e2}(x) &= \int_v f_2(v) d^3v = \frac{n_{e2}}{4\pi v_2^2} \int_0^\infty v^2 \delta(v - v_2) dv \int_0^{2\pi} d\varphi \int_0^{\Theta_c} \sin\theta d\theta = \\ &= \frac{1}{2}n_{e2} (1 - \cos\Theta_c) = \frac{1}{2}n_{e2} \left(1 - \sqrt{-\frac{2e_0\Phi(x)}{m_e v_2^2}}\right). \end{aligned} \quad (14)$$

Here m_e is the electron mass and Θ_c is the critical (maximum) angle between the x -axis and the velocity of an electron at which this electron can still reach the point x , where the potential is $\Phi(x)$ (see Fig. 1). This angle is determined by the conditions

$$\frac{1}{2}m_e v_2^2 \cos^2 \Theta_c = -e_0 \Phi(x), \quad \cos \Theta_c = \sqrt{-\frac{2e_0 \Phi(x)}{m_e v_2^2}}. \quad (15)$$

Note that for the beam electrons any collisions in the pre-sheath are neglected in order to keep the model as simple as possible.

The flux of the beam electrons in the direction towards the collector is

$$\begin{aligned} j_{e2}(x) &= \int_v v \cos \Theta f_2(v) d^3 v = \\ &= \frac{n_{e2}}{4\pi v_2^2} \int_0^\infty v^3 \delta(v - v_2) dv \int_0^{2\pi} d\varphi \int_0^{\Theta_c} \cos \Theta \sin \Theta d\Theta = \\ &= \frac{1}{4} n_{e2} v_2 \left(1 + \frac{2e_0 \Phi(x)}{m_e v_2^2} \right). \end{aligned} \quad (16)$$

The contribution of the beam electrons to the electric current density to the collector with the potential Φ_C is then given by

$$j_{2e} = \frac{1}{4} e_0 n_{e2} v_2 \left(1 + \frac{2e_0 \Phi_C}{m_e v_2^2} \right) H \left(1 + \frac{2e_0 \Phi_C}{m_e v_2^2} \right), \quad (17)$$

where H is the Heaviside unit step function. With such formulation of j_{2e} it is ensured that j_{2e} is zero if the repulsive potential Φ_C of the collector is larger in absolute value than the kinetic energy of the beam electrons. The flux of the beam electrons $j_{2e}(\Phi_C)$ decreases linearly with the potential Φ_C —formula (17), while their density $n_2(\Phi(x))$ decreases with the square root of the potential—formula (14). In a recent paper [15] a similar problem was investigated, only the velocity of all the beam electrons was perpendicular to the collector. In that case the flux of the beam electrons is independent of the collector potential as long as the kinetic energy of the beam is larger than the collector potential. When the collector potential exceeds the kinetic energy of the beam, the flux drops to zero. The density of the beam electrons, on the other hand, is inversely proportional to the square root of the potential.

Combining (1), (7), (11) and (14), the Poisson equation is written as

$$\begin{aligned} -\frac{d^2 \Phi}{dx^2} &= \frac{\rho(\Phi(x))}{\varepsilon_0} = \frac{e_0}{\varepsilon_0} \left[n_S \sqrt{\frac{e_0 \Phi_S + A_c}{e_0 \Phi(x)}} - n_1 \exp\left(\frac{e_0 \Phi(x)}{kT}\right) - \right. \\ &\quad \left. - \frac{1}{2} n_{e2} \left(1 - \sqrt{-\frac{2e_0 \Phi(x)}{m_e v_2^2}} \right) - \frac{j_{e3}}{\sqrt{v_C^2 - \frac{2e_0 (\Phi_C - \Phi(x))}{m_e}}} \right]. \end{aligned} \quad (18)$$

At the sheath edge the quasi-neutrality is valid so that the space charge density $\rho(\Phi_S)$ defined in (18) is zero:

$$n_S \sqrt{\frac{e_0 \Phi_S + A_c}{e_0 \Phi(x)}} - n_1 \exp\left(\frac{e_0 \Phi(x)}{kT}\right) - \frac{1}{2} n_{e2} \left(1 - \sqrt{-\frac{2e_0 \Phi(x)}{m_e v_2^2}}\right) - \frac{j_{e3}}{\sqrt{v_C^2 - \frac{2e_0(\Phi_C - \Phi(x))}{m_e}}} = 0. \quad (19)$$

From (19) the ion density at the sheath edge n_S is eliminated and inserted into (18). The following Poisson equation is obtained:

$$-\frac{d^2 \Phi}{dx^2} = \frac{e_0}{\varepsilon_0} \left[\sqrt{\frac{\Phi_S}{\Phi(x)}} \times \left(n_1 \exp\left(\frac{e_0 \Phi_S}{kT}\right) + \frac{1}{2} n_{e2} \left(1 - \sqrt{-\frac{2e_0 \Phi_S}{m_e v_2^2}}\right) + \frac{j_{e3}}{\sqrt{v_C^2 - \frac{2e_0(\Phi_C - \Phi_S)}{m_e}}} \right) - n_1 \exp\left(\frac{e_0 \Phi(x)}{kT}\right) - \frac{1}{2} n_{e2} \left(1 - \sqrt{-\frac{2e_0 \Phi(x)}{m_e v_2^2}}\right) - \frac{j_{e3}}{\sqrt{v_C^2 - \frac{2e_0(\Phi_C - \Phi(x))}{m_e}}} \right]. \quad (20)$$

A similar method for eliminating the positive ion density at the sheath edge was used by Amemiya [3].

The total electric current density to the collector j_{et} is the sum of four contributions. In order to define the direction of the current in technical sense, the contributions of the main electron population and of the electron beam are taken with the positive sign, while the contributions of the positive ions and of the emitted electrons are taken with the negative sign:

$$j_{et}(\Phi_C) = e_0 n_1 \sqrt{\frac{kT}{2\pi m_e}} \exp\left(\frac{e_0 \Phi_C}{kT}\right) + \frac{1}{4} e_0 n_{e2} v_2 \left(1 + \frac{2e_0 \Phi_C}{m_e v_2^2}\right) H\left(1 + \frac{2e_0 \Phi_C}{m_e v_2^2}\right) - e_0 \sqrt{-\frac{2(e_0 \Phi_S + A_c)}{m_i}} \left(n_1 \exp\left(\frac{e_0 \Phi_S}{kT}\right) + \frac{1}{2} n_{e2} \left(1 - \sqrt{-\frac{2e_0 \Phi_S}{m_e v_2^2}}\right) + \frac{j_{e3}}{\sqrt{v_C^2 - \frac{2e_0(\Phi_C - \Phi_S)}{m_e}}} \right) - j_{e3} e_0. \quad (21)$$

If a stable sheath with a monotonically decreasing potential profile is to be formed in front of a negative collector, the ions must enter in the sheath with a velocity that is equal to or greater than the ion sound velocity c_s so that

$$v_S \geq c_s . \quad (22)$$

This is a very well known Bohm criterion [17]. In planar geometry, like in our case, the Bohm criterion is fulfilled in marginal form, i.e. with equality sign. Following Riemann [16], the Bohm criterion (22) is written as

$$v_S = \sqrt{-\frac{2(e_0\Phi_S + A_c)}{m_i}} = \sqrt{\frac{k(T_e^* + \kappa T_i)}{m_i}} \Big|_{x=d} . \quad (23)$$

Here κ is the polytropic coefficient and T_e^* is the electron screening temperature, defined as [16]

$$T_e^* = \frac{e_0 n_e(\Phi)}{k \frac{dn_e}{d\Phi}} \Big|_{\Phi=\Phi_S} , \quad (24)$$

where $n_e(\Phi)$ can be read from the Poisson equation (20)

$$n_e(\Phi(x)) = n_1 \exp\left(\frac{e_0\Phi(x)}{kT}\right) + \frac{1}{2}n_{e2} \left(1 - \sqrt{-\frac{2e_0\Phi(x)}{m_e v_2^2}}\right) + \frac{j_{e3}}{\sqrt{v_C^2 - \frac{2e_0(\Phi_C - \Phi(x))}{m_e}}} . \quad (25)$$

Combining (23)—(25) with $T_i = 0$, one derives the Bohm criterion in the form of a transcendental equation for the sheath edge potential Φ_S

$$\Phi_S = -\frac{A_c}{e_0} + \left(-\frac{1}{2e_0}\right) \times \left[\frac{n_1 \exp\left(\frac{e_0\Phi_S}{kT}\right) + \frac{1}{2}n_{e2} \left(1 - \sqrt{-\frac{2e_0\Phi_S}{m_e v_2^2}}\right) + \frac{j_{e3}}{\sqrt{v_C^2 - \frac{2e_0(\Phi_C - \Phi_S)}{m_e}}}}{\frac{n_1}{kT} \exp\left(\frac{e_0\Phi_S}{kT}\right) + \frac{n_{e2}}{2m_e v_2^2} \sqrt{-\frac{m_e v_2^2}{2e_0\Phi_S}} - \frac{j_{e3}}{m_e} \left(v_C^2 - \frac{2e_0(\Phi_C - \Phi_S)}{m_e}\right)^{-3/2}} \right] . \quad (26)$$

The following variables are introduced:

$$\begin{aligned}\Psi &= \frac{e_0\Phi(x)}{kT}, & \Psi_C &= \frac{e_0\Phi_C}{kT}, & \Psi_S &= \frac{e_0\Phi_S}{kT}, & \varphi &= \frac{A_c}{kT}, \\ \mu &= \frac{m_e}{m_i}, & J_3 &= \frac{j_{e3}}{n_1\sqrt{\frac{kT}{m_e}}}, & J_t &= \frac{j_{et}}{e_0n_1\sqrt{\frac{kT}{m_e}}}, & \beta &= \frac{n_{e2}}{n_1}, \\ v_C &= \Omega\sqrt{\frac{kT}{m_e}}, & v_2 &= \theta\sqrt{\frac{kT}{m_e}}, & z &= \frac{x}{\lambda_D}, & \lambda_D &= \sqrt{\frac{\varepsilon_0kT}{n_1e_0^2}}.\end{aligned}\quad (27)$$

The potential is normalized to the electron temperature divided by the elementary charge kT/e_0 , and the velocities v_C and v_2 are normalized to the electron thermal velocity $\sqrt{kT/m_e}$. The normalized initial velocity of the emitted electrons is labeled by Ω , and θ gives the normalized velocity of the electron beam at a large distance from the collector. The distance x from the collector is normalized to the Debye length λ_D that is defined with the density and temperature of the basic electron population.

With these variables the Bohm criterion (26) is written in the form

$$\Psi_S = -\varphi + \left(-\frac{1}{2}\right) \frac{\exp(\Psi_S) + \frac{\beta}{2} \left(1 - \sqrt{-\frac{2\Psi_S}{\theta^2}}\right) + J_3(\Omega^2 - 2(\Psi_C - \Psi_S))^{-1/2}}{\exp(\Psi_S) + \frac{\beta}{2\theta\sqrt{-2\Psi_S}} - J_3(\Omega^2 - 2(\Psi_C - \Psi_S))^{-3/2}}, \quad (28)$$

the total electric current density to the collector (21) becomes

$$\begin{aligned}J_t &= \frac{1}{\sqrt{2\pi}} \exp(\Psi_C) + \frac{1}{4}\beta\theta \left(1 + \frac{2\Psi_C}{\theta^2}\right) H\left(1 + \frac{2\Psi_C}{\theta^2}\right) - J_3 - \\ &- \sqrt{-2\mu(\Psi_S + \varphi)} \left(\exp(\Psi_S) + \frac{\beta}{2} \left(1 - \sqrt{-\frac{2\Psi_S}{\theta^2}}\right) + J_3(\Omega^2 - 2(\Psi_C - \Psi_S))^{-1/2}\right),\end{aligned}\quad (29)$$

the Poisson equation (20) reads

$$\begin{aligned}\frac{d^2\Psi}{dz^2} &= \exp(\Psi(z)) + \frac{\beta}{2} \left(1 - \sqrt{-\frac{2\Psi(z)}{\theta^2}}\right) + J_3(\Omega^2 - 2(\Psi_C - \Psi(z)))^{-1/2} - \\ &- \sqrt{\frac{\Psi_S}{\Psi(z)}} \left(\exp(\Psi_S) + \frac{\beta}{2} \left(1 - \sqrt{-\frac{2\Psi_S}{\theta^2}}\right) + J_3(\Omega^2 - 2(\Psi_C - \Psi_S))^{-1/2}\right),\end{aligned}\quad (30)$$

and the boundary conditions (2) are transformed into

$$\Psi(z)|_{z=d/\lambda_D} = \Psi_S, \quad \left.\frac{d\Psi(z)}{dz}\right|_{z=d/\lambda_D} = 0. \quad (31)$$

The Poisson equation (30) is multiplied by $d\Psi/dz$. Taking the relation

$$\frac{1}{2} \frac{d}{dz} \left(\frac{d\Psi}{dz} \right)^2 = \frac{d\Psi}{dz} \frac{d^2\Psi}{dz^2} \quad (32)$$

into account, the equation (30) is integrated once over Ψ from $\Psi = \Psi_S$ at the sheath edge to arbitrary Ψ inside the sheath. The following expression is obtained:

$$\begin{aligned} \frac{1}{2} \left(\frac{d\Psi}{dz} \right)_{\Psi}^2 - \frac{1}{2} \left(\frac{d\Psi}{dz} \right)_{\Psi=\Psi_S}^2 &= \frac{1}{2} \left(\frac{d\Psi}{dz} \right)_{\Psi}^2 = \\ &= \exp(\Psi) - \exp(\Psi_S) + J_3 \left(\sqrt{\Omega^2 - 2(\Psi_C - \Psi)} - \sqrt{\Omega^2 - 2(\Psi_C - \Psi_S)} \right) + \\ &\quad + \frac{\beta}{6\theta} \left(2\sqrt{2} \left(\Psi_S \sqrt{-\Psi_S} + (-\Psi)^{-3/2} \right) - 3\theta(\Psi_S - \Psi) \right) + \\ &\quad + \left(\Psi_S + \sqrt{\Psi\Psi_S} \right) (\beta + 2\exp(\Psi_S)) + \\ &+ \left(\frac{\beta\sqrt{2}}{\theta} \Psi_S + 2J_3(\Omega^2 - 2(\Psi_C - \Psi_S))^{-1/2} \right) (\sqrt{-\Psi} - \sqrt{-\Psi_S}) = g(\Psi). \quad (33) \end{aligned}$$

The function $g(\Psi)$ defined in (33) gives one half of the square of electric field in the sheath as a function of the potential Ψ . If the upper integration boundary in (33) is shifted to the collector potential Ψ_C , the value $g(\Psi)|_{\Psi=\Psi_C}$ gives one half of the square of electric field at the collector. If the electron emission J_3 from the collector increases for any reason, the absolute value of the electric field at the collector decreases and eventually becomes equal to zero. The emission becomes space charge limited or critical. The corresponding current density of the emitted electrons is called critical emission and is labeled $J_{3\text{cr}}$. The zero electric field condition at the collector is given by

$$g(\Psi)|_{\Psi=\Psi_C} = 0. \quad (34)$$

3. Results

It is known (e.g. [18]) that when electron emission from an emitting electrode is increased, the floating potential of such an electrode increases and the absolute value of electric field in front of the electrode surface decreases. Eventually the electric field becomes equal to zero and the emission becomes space charge limited or critical. If emission is increased even further a potential well (virtual cathode) can form in front of the collector. In many experimental situations the main reason for the electron emission from the collector is the

heating of the electrode, and the emission current density j_R in such a case is given by the Richardson formula

$$j_R = A_R T_C^2 \exp\left(\frac{-e_0 \Phi_w}{k T_C}\right), \quad (35)$$

where A_R is the Richardson constant, T_C is the absolute temperature of the collector, Φ_w is the work function of the collector and e_0 is the elementary charge. The theoretical value of the Richardson constant is $A_R = 4\pi m_e e_0 k^2 / h^3 = 120 \text{ A}/(\text{cm}^2 \text{K}^2)$. Actual values for various metals are different. For example, for tungsten the value is approximately $60 \text{ A}/(\text{cm}^2 \text{K}^2)$. The value of the work function for tungsten $e_0 \Phi_w$ is approximately 4.5 eV. The electron emission, which is below the space charge limit is often called temperature limited emission (see Fig. 1), or subcritical emission, because the emission current density is determined (limited) by the temperature of the collector. In our model the physical mechanism of the emission is not specified. The emission may be thermal or secondary, but we shall nevertheless use the expression temperature limited and space charge limited (or also critical) emission.

We shall now use the model presented in the previous section to determine the transition between the space charge limited and temperature limited electron emission for given sets of parameters μ , θ , β , Ω and J_3 or Ψ_C . We select such parameters that could be relevant for the linear magnetized discharge plasma device at the Jožef Stefan Institute. If μ , θ , β , Ω and J_3 are selected, the collector potential Ψ_{C0} where the transition from the space charge limited into temperature limited electron emission occurs. One simply solves the system of equations (28) and (34) for Ψ_S and the transition collector potential Ψ_{C0} . On the other hand, the system (28) and (29) (with $J_t = 0$) can also be solved with the same parameters in order to find Ψ_S and the floating potential Ψ_{Cf} .

In Fig. 2 we show the dependence of the transition potential Ψ_{C0} and the floating potential Ψ_{Cf} on the electron emission J_3 for the following parameters: $\mu = 1.36166 \times 10^{-5}$ (Ar⁺ ions), $\beta = 0.01$, $\Omega = 0.001$, and $\theta = 6$ (left hand figure) while for the right hand figure the same parameters are selected with $\beta = 0$. The emission current density J_3 is gradually increased from 0 to 0.1 in steps of 0.001. For each set of parameters the systems (28) and (34), and (28) and (29) (with $J_t = 0$) are solved for Ψ_S , Ψ_{C0} and Ψ_{Cf} . When J_3 increases, the transition potential Ψ_{C0} decreases, while the floating potential Ψ_{Cf} increases. At certain J_3 they become equal. If J_3 is increased even further, Ψ_{Cf} becomes larger than Ψ_{C0} .

This result gives a clear instruction of how the current voltage characteristics of an electron emitting electrode should be calculated using the model presented in the previous section. For given values of μ , θ , β , Ω and J_3 first the transition potential Ψ_{C0} and the corresponding sheath edge potential Ψ_S must be found from the system (28) and (34). Next J_t is found as a function of Ψ_C

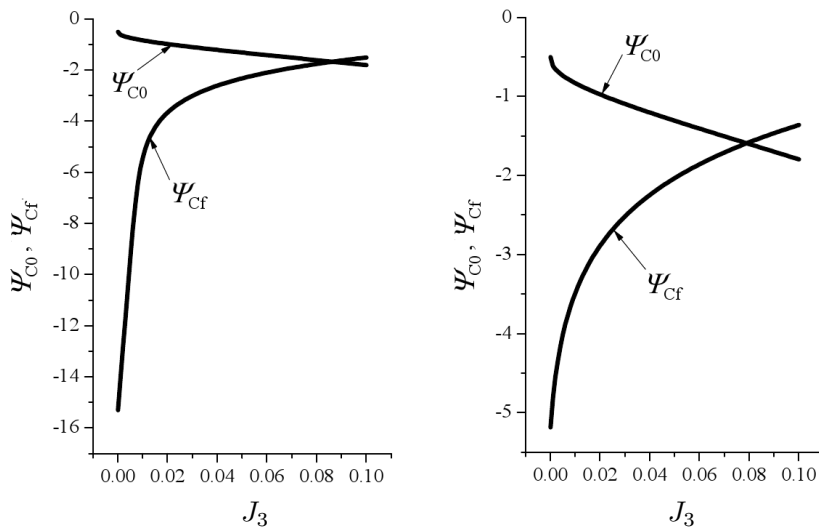


Fig. 2. Dependence of the transition potential Ψ_{C0} and the floating potential Ψ_{Cf} on the electron emission J_3 ; *left*: for the parameters $\mu = 1.36166 \times 10^{-5}$ (Ar⁺ ions), $\beta = 0.01$, $\Omega = 0.001$, and $\theta = 6$, *right*: for the same parameters except β —here $\beta = 0$

in a two-step procedure. For $\Psi_C < \Psi_{C0}$, J_t is found from (29). For every Ψ_C the corresponding Ψ_S must first be found from (28) and then inserted into (29). For $\Psi_C > \Psi_{C0}$, J_t is also found from (29), but for every Ψ_C the corresponding Ψ_S and J_3 must first be found from the system (28) and (34) and then inserted into (29).

In Fig. 3 we show a few examples of the current voltage characteristics of the collector for the following parameters: $\mu = 1.36166 \times 10^{-5}$, $\beta = 0.01$, $\Omega = 0.001$, $\theta = 8$ and 7 different values of J_3 indicated in the figure. As J_3 is increased, the floating potential Ψ_{Cf} also increases. The intersection between the J_t curve and the zero line moves towards the actual plasma potential, which is set to zero. A more careful examination shows that the floating potentials of the J_t curves that correspond to $J_3 = 0.10$ and to $J_3 = 0.12$ are equal. One says that the floating potential of the collector gets “saturated”: above certain J_3 the floating potential Ψ_{Cf} stops increasing, even if J_3 is increased further. This obviously occurs at J_3 , where the floating and the transition potentials become equal. Such “saturation” of the floating potential with respect to the increasing electron emission is known from emissive probe applications [9]. Our model therefore offers a quantitative explanation of this phenomenon.

Emissive probes are a standard plasma diagnostic tool for determination of the plasma potential, because its floating potential is usually very close to the plasma potential, provided that the electron emission is sufficiently high to make the probe operate in the saturated floating potential mode. Generally an

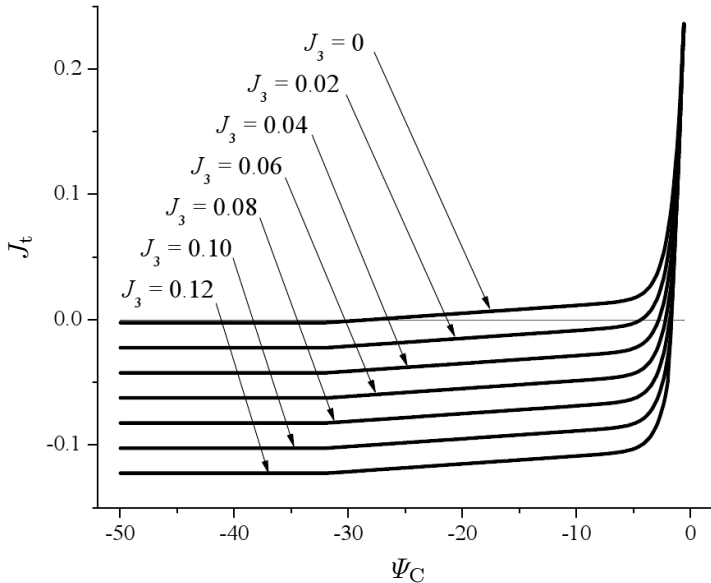


Fig. 3. Some examples of the current voltage characteristics of the collector for the following parameters: $\mu = 1.36166 \times 10^{-5}$, $\beta = 0.01$, $\Omega = 0.001$, $\theta = 8$ and 7 different values of J_3 .

emission current that is equal to the electron saturation current is considered as sufficiently high. The result shown in Fig. 3 indicates that already about by 50 % lower emission current is sufficient. A great advantage of the emissive probe is that it shows the plasma potential even in the presence of an electron beam in the plasma. In Fig. 4 we show a few examples of the current voltage characteristics of the collector for the following parameters: $\mu = 1.36166 \times 10^{-5}$, $\Omega = 0.001$, $J_3 = 0.2$ and several values of β and θ . The result is very instructive. When either the density (β) or the energy (θ) of the electron beam are changed, this can be very well observed on the current voltage characteristics of the collector, but the floating potential remains unchanged. Thus, the floating potential of an electron emitting electrode is a good indication of the plasma potential even in the presence of an electron beam in the plasma.

4. Conclusions

We have presented a simple one-dimensional fluid model of the sheath formation in front of an electron emitting electrode that is immersed in a plasma that contains a mono-energetic electron beam with the uniformly distributed directions of the electron velocities. The model reproduces two phenomena well known from experiments with emissive probes, which are the increase of the floating potential with increasing electron emission from the collector and

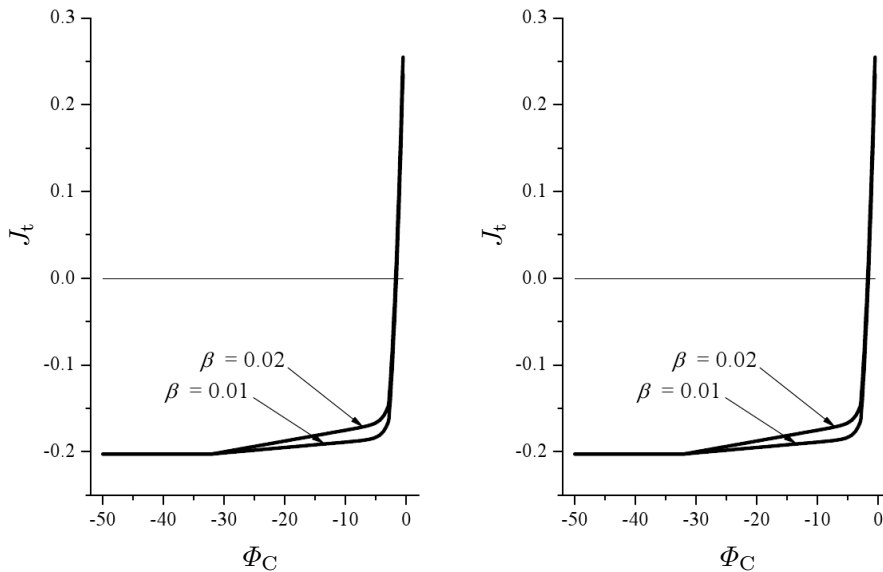


Fig. 4. Examples of current voltage characteristics of the collector for the parameters $\mu = 1.36166 \times 10^{-5}$, $\Omega = 0.001$, $J_3 = 0.2$ and several values of β and θ ;
left: $\theta = 8$, the corresponding values of β are indicated in the figure,
right: $\beta = 0.01$, the corresponding values of θ are indicated in the figure

saturation of the floating potential above certain electron emission. Our model offers a quantitative explanation of the saturation of the floating potential. As the electron emission is increased, the transition potential between the space charge limited and temperature limited emission decreases, while the floating potential increases. When the transition potential drops below the floating potential, the floating potential cannot change anymore with increasing emission and this results in the saturation of the floating potential with respect to increased electron emission. The presence of an electron beam in the plasma affects the shape of the current voltage characteristics of an electron emitting electrode, but the floating potential remains the same if the electron emission is sufficiently high. This means that the floating potential of an emissive probe is a very good indication of the plasma potential also in a plasma that contains an electron beam.

References

- [1] L. SCHOTT: *Plasma boundary layer in the presence of fast primary electrons*. Phys. Fluids *30* (1987), 1795–1800.
- [2] N. JELIĆ, M. ČERČEK, M. STANOJEVIĆ, T. GYERGYEK: *An investigation of the collisionless discharge in the presence of an electron beam*. J. Phys. D: Appl. Phys. *27* (1994), 2487–2498.

- [3] H. AMEMIYA: *Criterion for sheath formation in negative ion plasma with electron beam*. J. Phys. Soc. Jap. *64* (1995), 2444–2454.
- [4] J. W. BRADLEY: *The plasma boundary containing fast isotropic electrons: a comparison between kinetic and fluid ion models*. J. Phys. D: Appl. Phys. (*34*) (2001), 3241–3246.
- [5] S. TAKAMURA: *Sheath formation in a plasma with energetic electrons*. Phys. Lett. A *133* (1988), 312–314.
- [6] M. TATANOVA, G. THIEME, R. BASNER, M. HANNEMANN, YU. B. GOLUBOVSKII, H. KERSTEN: *About the EDF formation in a capacitively coupled argon plasma*. Plasma Sources Sci. Technol. *15* (2006), 507–516.
- [7] K. SATO, F. MIYAWAKI: *Formation of presheath and current-free double layer in a two-electron-temperature plasma*. Phys. Fluids B *4* (1992), 1247–1254.
- [8] M. ČERČEK, T. GYERGYEK, M. STANOJEVIĆ: *Effects of energetic electrons on collector and source potentials in a finite ion temperature plasma*. Contrib. Plasma Phys. *39* (1999), 541–556.
- [9] R. SCHRITTWIESER, C. IONITA, P. BALAN, R. GSTREIN, O. GRULKE, T. WINDISCH, C. BRANDT, T. KLINGER, R. MADANI, G. AMARANDEI, ARUN K. SARMA: *Laser-heated emissive plasma probe*. Rev. Sci. Instrum. *79* (2008), 083508.
- [10] D. TSKHAKAYA, S. KUHN, V. PETRŽILKA, R. KHANAL: *Effects of energetic electrons on magnetized electrostatic plasma sheaths*. Phys. Plasmas *9* (2002), 2486–2496.
- [11] T. GYERGYEK, M. ČERČEK: *Fluid model of a sheath formed in front of an electron emitting electrode immersed in a plasma with two electron temperatures*. Contrib. Plasma Phys. *45* (2005), 89–110.
- [12] T. GYERGYEK, M. ČERČEK: *Sheath in front of a negatively biased collector that emits electrons and is immersed in a two electron temperature plasma*. Contrib. Plasma Phys. *45* (2005), 568–581.
- [13] T. GYERGYEK, M. ČERČEK: *A fluid model of the current-voltage characteristics of an electron emitting electrode immersed in a two electron temperature plasma*. Eur. Phys. J. D *42* (2007), 441–454.
- [14] T. GYERGYEK, B. JURČIČ-ZLOBEC, M. ČERČEK, J. KOVAČIČ: *Sheath structure in front of an electron emitting electrode immersed in a two-electron temperature plasma: a fluid model and numerical solutions of the Poisson equation*. Plasma Sources Sci. Technol. *18* (2009), 035001.
- [15] T. GYERGYEK, J. KOVAČIČ, M. ČERČEK: *A fluid model of the sheath formation in front of an electron emitting electrode with space charge limited emission immersed in a plasma that contains a one-dimensional mono-energetic electron beam*. Contrib. Plasma Phys. *50* (2010), 121–134.
- [16] K. U. RIEMANN: *Theory of the plasma-sheath transition*. J. Tech. Phys. *41* (2000), Special Issue, 89–121.
- [17] D. BOHM: *Minimum ionic kinetic energy for a stable sheath*. The characteristics of electrical discharges in magnetic fields (A. Guthrie, R. K. Wakerling, eds.), McGraw-Hill, New York 1949, Chap. 3, 77–86.
- [18] N. HERSHKOWITZ: *How does the potential get from A to B in a plasma?* IEEE Trans. Plasma Sci. *22* (1994), 11–21.

First results of the COMPASS tokamak

RADOMÍR PÁNEK¹, MILAN AFTANAS¹, PETRA BÍLKOVÁ¹,
PETR BOHM¹, JOSEF HAVLÍČEK¹, JAN HORÁČEK¹,
MARTIN HRON¹, FILIP JANKY¹, DIANA NAYDENKOVA¹,
JAN STOCKEL¹, JAKUB URBAN¹, VLADIMÍR WEINZETTL¹,
JAROMÍR ZAJAC¹, FRANTIŠEK ŽÁČEK¹, THE COMPASS TEAM¹

Abstract. The present status of the COMPASS tokamak, diagnostics and additional systems as well as the first results are described. The COMPASS tokamak has recently started its new operation in the Institute of Plasma Physics of the Academy of Sciences of the Czech Republic in Prague, Czech Republic. COMPASS will be able to operate in a clear H-mode in ITER-relevant geometry and will be equipped by a comprehensive set of diagnostics focused mainly on edge plasma region. High plasma performance will be achieved by two neutral beam injection systems.

Key words. Tokamak COMPASS, power supply, plasma breakdown, plasma diagnostics.

1. Introduction

The COMPASS tokamak is a small fusion device, which was originally operated in UKAEA Culham. Recently it has been re-installed in the Institute of Plasma Physics (IPP) of the Academy of Sciences of the Czech Republic in Prague, Czech Republic, and several of its systems were significantly upgraded [1]. The test operation of this device started in February 2009. The full performance is expected at the autumn 2010. Afterwards, COMPASS tokamak will be able to work in a clear H-mode and ITER-relevant geometry (Fig. 1) [2]. Its parameters are summarized in Table 1. ITER-relevant plasma conditions will be achieved by installation of two new neutral beam injection systems (2×300 kW), enabling co-injections and balanced injections. Installation of Lower Hybrid Wave system (3.7 GHz, $1 \div 1.5$ MW) is also considered. The existing unique fully configurable set of copper saddle coils makes COMPASS an ideal device for resonant perturbation technique studies. As the edge plasma

¹Institute of Plasma Physics AS CR, v.v.i., Association EURATOM/IPP.CR, Za Slovankou 3, 182 00 Praha 8, Czech Republic

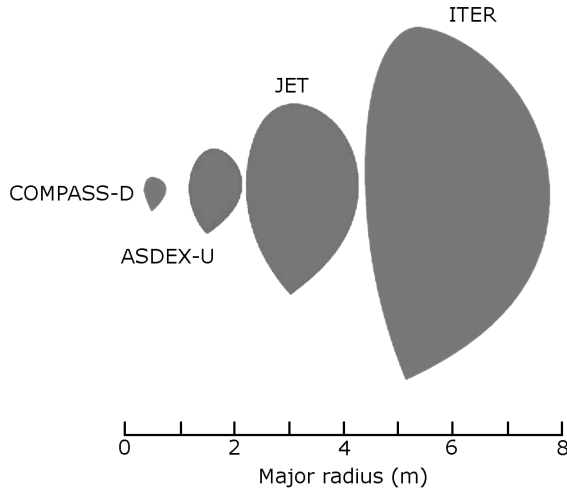


Fig. 1. Comparison of plasma cross-section of tokamaks with ITER-like plasma shape

physics forms the main part of the envisaged COMPASS scientific program, a comprehensive set of diagnostics focused mainly on the edge plasma is being installed.

2. Status of COMPASS

The COMPASS tokamak has been transported to IPP Prague and installed into a new tokamak building during period 2006–2008. The vacuum chamber, magnetic field coils and tokamak support structure were used from the COMPASS-D; however, all the auxiliary systems (power supplies, cooling, vacuum, Control, Data Acquisition and Communication system (CODAC), etc.)

Table 1. Main parameters of the COMPASS tokamak in IPP Prague

Major radius	0.56 m
Minor radius	0.2 m
Plasma current	< 350 kA
Magnetic field	0.8 ÷ 2.1 T
Triangularity	0.5
Elongation	1.6
Pulse length	< 1 s
NBI system	2 × 0.3 MW
LHW system (3.7 GHz)	1 MW

were developed completely new. These new systems were developed, manufactured and commissioned by end of 2008. During the test operation started in February 2009 the optimization of the plasma discharge is being performed and parameters are gradually increased to the maximum performance. In this paper, we summarize and describe the present status of the tokamak and its main systems. We also briefly describe the obtained plasma parameters and performance.

3. Power supply system

Magnetic field coils systems and additional heating systems are generally the main consumers of the electrical power. The COMPASS tokamak requires electrical input power of 50 MW for flat-top duration about 0.5 s for the full performance at the maximum magnetic field 2.1 T. Such a power was accessible in Culham Laboratory directly from the 33 kV grid. However, only 1 MW power is available from the 22 kV grid at the campus of the Academy of Sciences in Prague. Therefore, an installation of two fly-wheel generators (Fig. 2) was chosen [3], [4] as a proved solution used at several larger tokamaks. The fly-wheel generators were developed by CKD Group company in Czech Republic, and they provide the necessary power (70 MW, 100 MJ) as well as a reasonable redundancy in case of a failure of one of them. The system then enables easy reconnection of the power supplies to power the tokamak only from one of the generators and operate with a reduced plasma performance. The power supply system is controlled by a control system based on SIEMENS SIMATIC standards. The power supply control system communicates with the CODAC (Control, Data Acquisition and Communication) via a communication unit in a real time (every 0.5 ms). CODAC is the main control system for tokamak operation. It sends every 0.5 ms values of currents in AC/DC convertors supplying the magnetic coils required according to pre-programmed wave forms or feedback algorithms.

4. Diagnostics

A new set of diagnostics focused mainly on the edge plasma and pedestal region is being developed for the COMPASS tokamak. Due to the region of interest, the challenging spatial resolution in the range of $1 \div 3$ mm is required for most of these diagnostics (e.g. [5]). The other limitation is a relatively small size of diagnostic ports and their limited accessibility due to compactness of the COMPASS tokamak. The development is ongoing and below one can see the list of the diagnostics according to the year of installation:

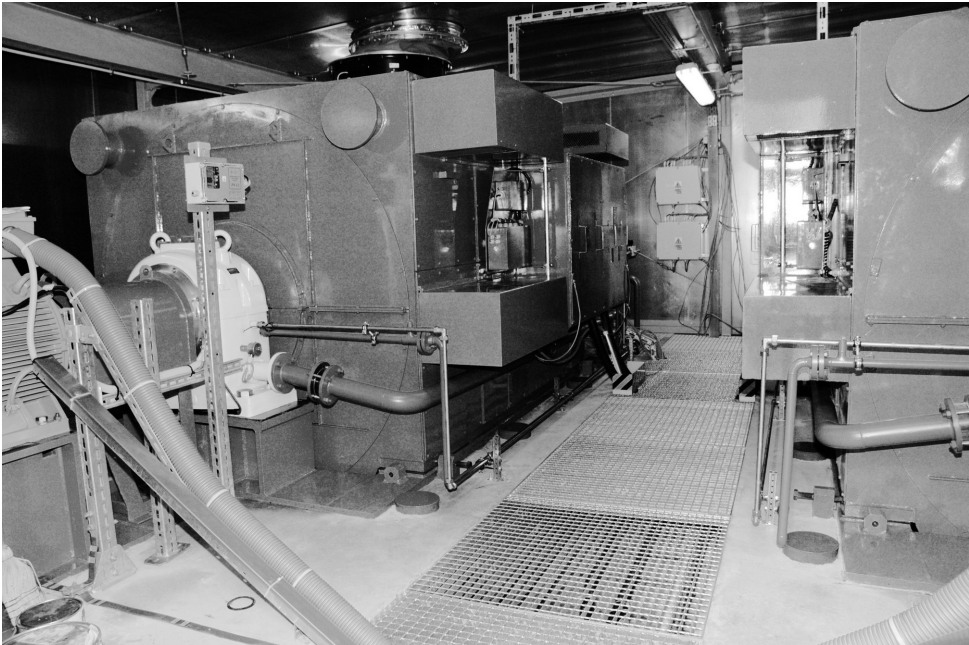


Fig. 2. Two fly-wheel generators for the COMPASS tokamak (2×35 MW)

Diagnostics in operation:

- Magnetics (400 magnetic coils)
- Single channel interferometer
- Multichord spectroscopy (2D) D_α , SXR, radiation losses
- Divertor probes
- Fast Visible Camera EDICAM (Event Detection Intelligent Camera)

Diagnostics being installed during 2010:

- Second Fast Visible Camera EDICAM
- Li (Na, He) beam diagnostics
- HR Thomson scattering core + edge
- Edge reflectometry
- Advanced electrical probes (Tunnel probe, Ball-pen probe, etc)
- Electron Cyclotron Emission/Electron Bernstein Wave Radiometry
- Neutral Particle Analyzer
- Atomic beam probe (edge current density measurement)

In more details we will describe the two new advanced diagnostics High resolution Thomson scattering system (HRTS) for measurement of electron temperature and density with high spatial resolution and a microwave reflectometer for fast measurement of edge plasma density and its fluctuation.

4.1. Thomson scattering system

A set of two multi-point High Resolution Thomson scattering diagnostics focused on core plasma and edge plasma is being developed on the COMPASS tokamak. HRTS on COMPASS is based on a set of two Nd:YAG lasers, two objectives collecting the light from both the core and edge plasma regions and number of polychromators equipped by APD and spectral filters (see Fig. 3).

A high energy laser source is needed for Thomson scattering (TS) since the TS effect has a very small scattering cross-section. Calculations of necessary laser energy for sufficient collected scattered photons resulted in laser pulse energy value approx 3 J for desired performance. This will be achieved by using two Nd:YAG lasers, each laser with 1.5 J pulses (polarized) at wavelength of 1064 nm and a repetition rate of 30 Hz.

Two separate collective objectives have been designed to focus scattered light from both the core and the edge plasma regions (core and edge objective) onto the inputs of optical fibre bundles. The optical design is considerably influenced by the size and position of ports, especially in case of edge objective. The optical fibres guide the light into a five channel polychromator, which serves as spectral analyzer of the scattered light. The polychromators of the fourth generation were developed at Culham Centre for Fusion Energy (CCFE), UK. The light is then analyzed by a set of five spectral filters and detected by Avalanche photodiodes.

Signals from all 28 polychromators, where 5 spectral filters are used for the core region and 4 spectral filters for edge region (in total 120 spectral channels), are synchronously digitalized by fast and slow Analog Digital Convertors (ADC). The fast ADCs convert data with high throughput of 1 GSample/s, 8-bit resolution and inter-channel skew < 300 ps. These ADC cards (2 channels in each ADC card) have 8 MB/channel onboard memory and are housed in 4 chassis.

First tests of the individual parts of the system have been successfully performed and the whole system will be in full operation by the end of 2010.

4.2. Microwave reflectometer

The reflectometry systems for the COMPASS tokamak will allow the fast measurement (~ 1 ms) of plasma density profiles as well as the correlation properties of plasma turbulence. It will be equipped with channels covering the K, Ka, U and E frequency bands. The whole frequency range is $18 \div 90$ GHz. Due to relatively small diagnostic port, the channels, in fact the separate reflectometers, will be combined in a quasi-optical band combiner. The combined wave will be transmitted to the plasma by a wideband quasi-optical transmitting antenna. The identical antenna and band-combiner will be used in the receiving path. The quasi-optical part of the reflectometry system (i.e. band combiners and antennas) is being developed in collaboration with the Institute

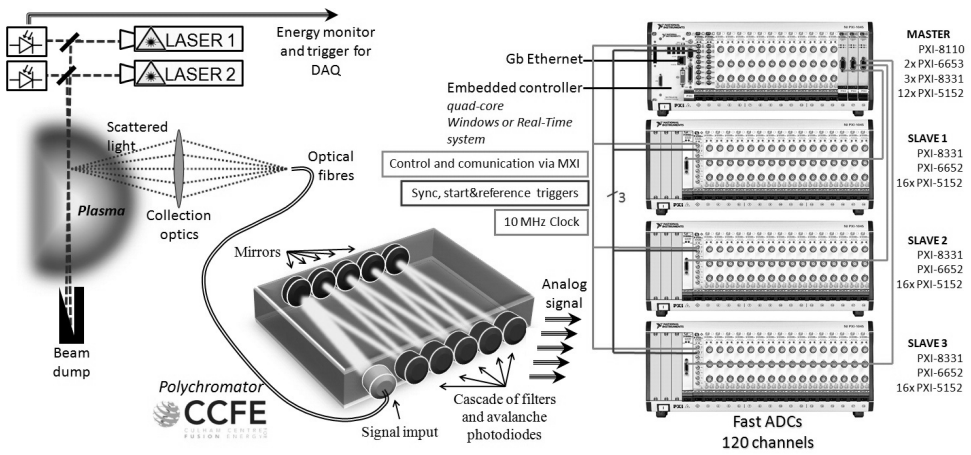


Fig. 3. Scheme of the Thomson scattering system in the COMPASS tokamak

of Radioelectronics (IRE) Kharkov, Ukraine. The microwave electronics and software equipment is provided by Instituto Superior Técnico Lisbon, Portugal. The schematic layout is shown in Fig. 4. The full system will be in a routine operation by end of 2010.

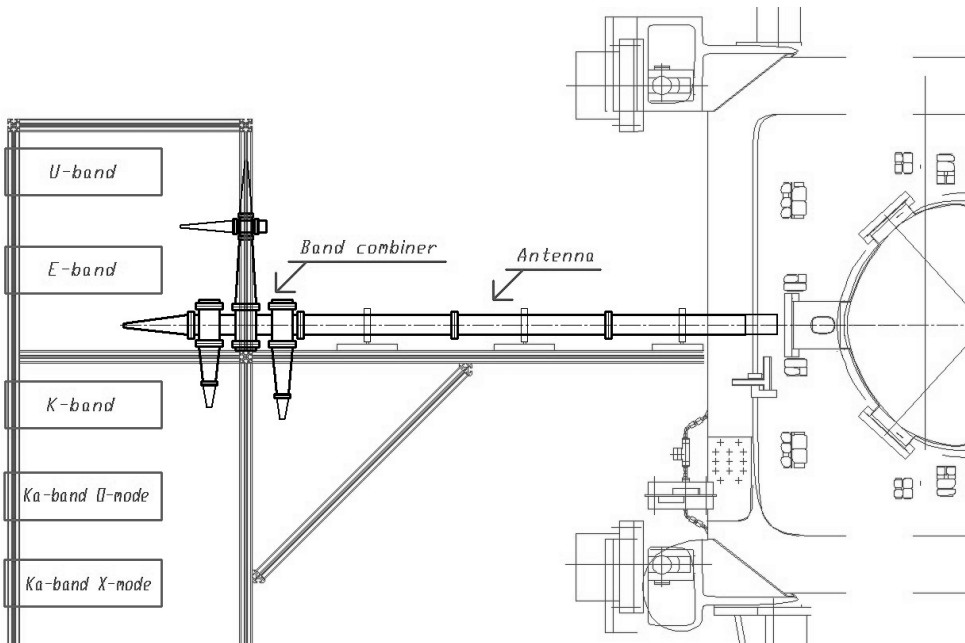


Fig. 4. Scheme of the microwave reflectometer installation at the COMPASS tokamak

5. Neutral beam injection heating system

A new Neutral Beam Injection (NBI) system for additional heating and current drive is being developed by Budker Institute for Nuclear Physics in Novosibirsk, Russian federation. The system will be installed and commissioned at the COMPASS tokamak in autumn 2010. As COMPASS is a compact tokamak the trajectory of interaction between neutrals and plasma is relatively short, the NBI power, energy and geometry is chosen carefully. In addition, the NBI system has to be designed to provide also a flexible heating and current drive system. Therefore, it will consist of two injectors with particle energy 40 keV and 300 kW output power each in deuterium, delivering approximately 600 kW of total power to the plasma. The geometry of injection will be flexible and easy to change between co-injection and balanced injection. These configurations are shown in Fig. 5-*left* is optimized for plasma heating.

If both beams are aimed in co-direction with respect to the plasma current, the system is optimized for plasma heating and the orbit losses are minimized [6].

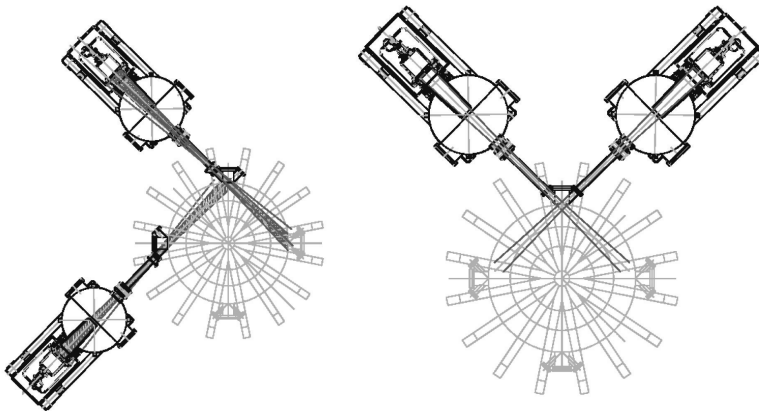


Fig. 5. Top view on the NBI system layout;
left: co-injection, *right*: balanced injection

In case of the balanced injection both injectors will be located at the same port, aiming in co- and counter-current directions as shown in Fig. 5-*right*. With proper power modulation to compensate different orbit losses for co- and counter-beams, one can obtain NBI scenario with minimum momentum input. Such a plasma conditions are highly relevant to ITER where low plasma rotation is expected.

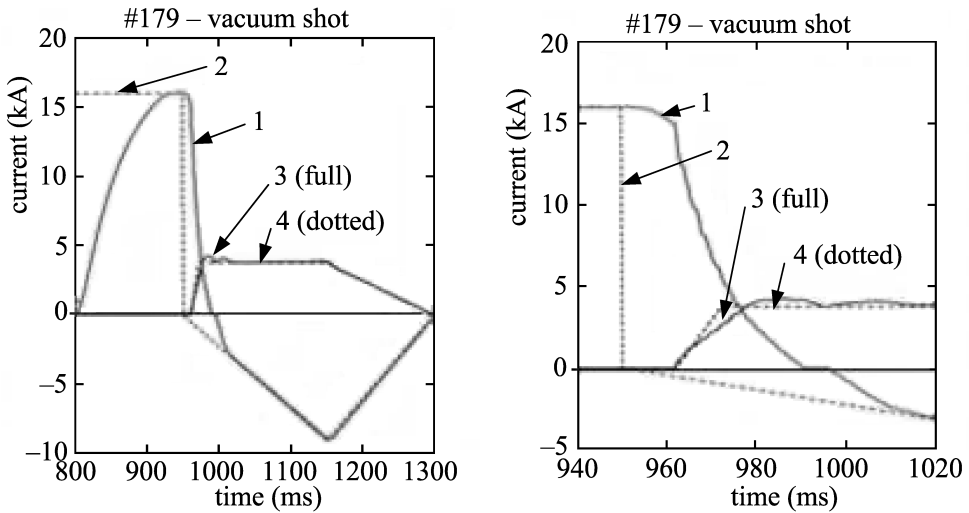


Fig. 6. Measured temporal evolution of the MFPS (line 1) and EFPS (line 3) currents in poloidal field coils and their comparison to the requested waveforms (dotted lines 2 and 4). *Left panel:* Evolution of the MFPS and EFPS currents in poloidal field coils during the whole plasma discharge. *Right panel:* Zoom of the time interval corresponding to the start up phase of the discharge. The loop voltage required for breakdown is generated during the fast ramp-down of I_{MFPS} current at the time ~ 963 ms.

6. First plasma performance in COMPASS

The COMPASS tokamak is in a test operation regime in 2010, when the individual operational and diagnostic systems are tested and their parameters are gradually increased. The tokamak operates presently with the toroidal magnetic field up to 1.8 T. The further increase to the maximum value 2.1 T will be possible after completion of work on the vertical preload system for compensation of the electromagnetic forces acting on the toroidal field coils.

The temporal evolutions of the toroidal, magnetizing and equilibrium fields are pre-programmed and controlled by the CODAC system. A novel design has been used for the magnetizing circuit, where interruption of the current in the circuit to generate high loop voltage for plasma breakdown is based on a system of thyristors and high power resistors. Generally, this system consists of vacuum breakers, which, however, have only a limited lifetime and lower reliability.

Typical current waveforms of the magnetizing field power supply (MFPS) and equilibrium field power supply (EFPS) are shown in Fig. 6.

It is seen that the currents in the poloidal field coils follow the requested waveforms and, specially, the magnetizing circuit is capable to generate sufficient loop voltage for plasma breakdown.

During the test period, a study of the plasma breakdown was performed in order to minimize the necessary loop voltage (Uloop). An efficient breakdown and a reproducible ramp-up of plasma current require an optimization. An example of such attempt is shown in Fig. 7, where the pressure of working gas is changed on a shot-to-shot basis for several values of magnetizing current $I_{\text{MFPS}}^{\text{max}}$. The aim of this scan is to find an optimum pressure region, in which the loop voltage is low but still sufficient for breakdown (to save voltseconds and reduce the production of runaway electrons during the breakdown phase). Simultaneously, we search conditions at which the discharge is sufficiently long and the plasma current high enough ($> 30 \div 50$ kA). This optimization has been done with feedback of the plasma position not in operation. The equilibrium current is pre-programmed to start at $t_{\text{EFPS}} = 961$ ms and ramps up with $dI_{\text{EFPS}}/dt = 310$ A/ms to its maximum value $I_{\text{EFPS}} = 4.8$ kA.

It is seen that, the loop voltage at the breakdown (the top panel) is predominantly determined by the maximum value I_{MFPS} , and its consequent fast ramp-down. The Uloop versus pressure dependence for each value of $I_{\text{MFPS}}^{\text{max}}$ resembles the Paschen curve. It is seen that the Uloop can be reduced down to 10 V at $I_{\text{MFPS}}^{\text{max}} = 8$ kA, which is noticeably lower than the breakdown voltage achieved routinely on COMPASS-D at Culham ($\sim 15 \div 18$ V). However, the discharge duration is less than 10 ms and the maximum plasma current $I_p < 30$ kA at these conditions.

The optimum pressure window ($40 \times 10^{-6} \div 90 \times 10^{-6}$ mbar of H_2) is marked in the figure by shadowing. We see that the discharge duration is long enough (> 30 ms) to ramp-up the plasma current up to ~ 90 kA in this range of filling pressures.

Figure 8 presents an example of the discharge evolution. This 70 ms discharge, stopped by a disruption, was stable with a flat top phase at $I_p \sim 120$ kA and the line average density $\sim 10^{19} \text{m}^{-3}$. Figure 9 shows the plasma behavior during this discharge observed by the Fast Visible Camera EDICAM in visible spectral range during different phases of the plasma shot—flat top phase, contact with vacuum vessel wall and shot termination by a disruption.

Commissioning of the fast feedback for plasma position is presently ongoing. The full performance including the elongated diverted plasma, maximum plasma current and H-mode discharges is planned to autumn 2010.

7. Conclusion

The COMPASS tokamak has been installed and put in operation in IPP Prague. Presently, COMPASS is in a test operation and the first obtained results were presented in the paper. The full plasma performance and an H-mode regime will be reached in Autumn 2010.

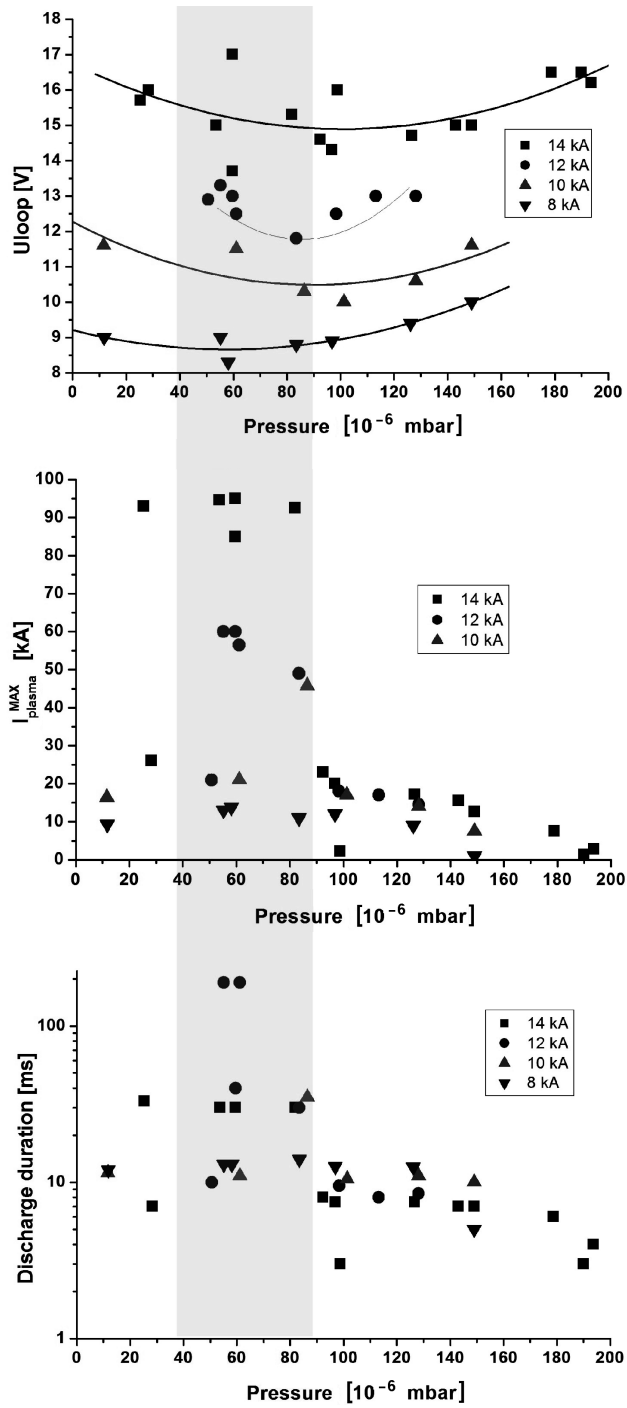


Fig. 7. Dependence of the loop voltage at the breakdown, the duration of the discharge and the maximum plasma current on the filling pressure at different values of $I_{\text{MFPs}}^{\text{max}}$ (# 473-515)

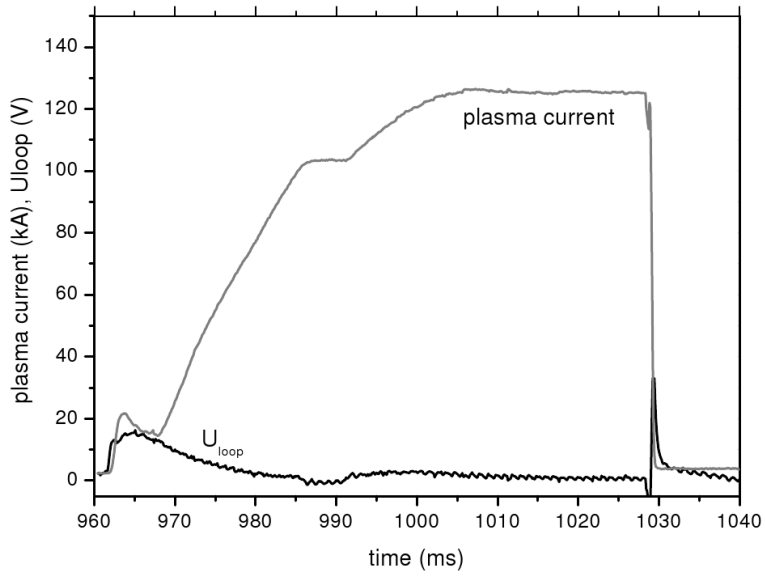


Fig. 8. Temporal evolution of the loop voltage and plasma current

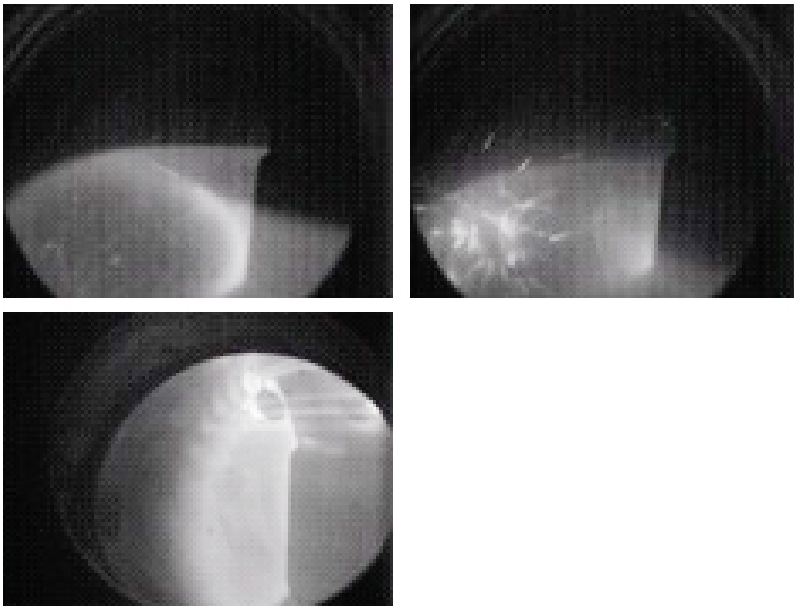


Fig. 9. Images of the plasma discharge by the fast camera in the visible range

After the installation of the NBI system, the COMPASS tokamak will be—together with JET and ASDEX-U—one of few tokamaks with highly ITER relevant plasmas. COMPASS will allow fast and low-cost implementation of technical modifications and programmatic adaptations if needed to optimize ITER relevant results.

References

- [1] R. PANEK, O. BILYKOVA, V. FUCHS, M. HRON, P. CHRASKA, P. PAVLO, J. STOCKEL, J. URBAN, V. WEINZETTL, J. ZAJAC, F. ZACEK: *Reinstallation of the COMPASS-D tokamak in IPP ASCR*. Czechoslovak J. Phys. *56* (2006), B125–B137.
- [2] O. HRONOVA-BILYKOVA, V. FUCHS, R. PANEK, J. URBAN, F. ZACEK, J. STOCKEL, I. VOITSEKHOVITCH, M. VALOVIC, M. FITZGERALD: *COMPASS-D magnetic equilibria with LH and NBI current drive*. Czechoslovak J. Phys. *56* (2006), B24–B30.
- [3] J. ZAJAC, R. PANEK, F. ZACEK, J. VLCEK, M. HRON, A. KRIVSKA, R. HAUPTMANN, M. DANEK, J. SIMEK, J. PROSEK: *Power supply system for COMPASS tokamak re-installed at the IPP Prague*. Fusion Eng. Design *84* (2009), 2020–2024.
- [4] J. ZAJAC, F. ZACEK, Z. BRETTSCHEIDER, V. LEJSEK: *Short-term power sources for tokamaks and other physical experiments*. Fusion Eng. Design *82* (2007), 369–379.
- [5] D. SESTAK, V. WEINZETTL, P. BILKOVA, P. BOHM, M. AFTANAS, D. NAYDENKOVA, J. STOCKEL, I. DURAN, M. J. WALSH: *Design and engineering of optical diagnostics for COMPASS*. Fusion Eng. Design *84* (2009), 1755–1758.
- [6] J. URBAN, V. FUCHS, R. PANEK, J. PREINHAELTER, J. STOCKEL, F. ZACEK, V. I. DAVYDENKO, V. V. MISHAGIN: *NBI system for reinstalled COMPASS-D tokamak*. Czechoslovak J. Phys. *56* (2006), B176–B181.

Received March 31, 2010

An experimental and modelling study of acetaldehyde oxidation by an atmospheric non-thermal plasma discharge¹

CHARLES KLETT², SYLVAIN TOUCHARD², ARLETTE VEGA²,
MICHAEL REDOLFI², XAVIER DUTEN², KHALED HASSOUNI²

Abstract. The results obtained for the degradation of acetaldehyde by an atmospheric plasma corona discharge in a wire to cylinder (WTC) configuration are reported. The process efficiency is characterized in terms of acetaldehyde removal efficiency as a function of the input energy. Main degradation products CO, CO₂, CH₃OH are identified and quantified. A homogenous 0D chemical model allows us to simulate the studied experimental conditions. Simulation results are in a quite good accuracy with experiments.

Key words. Plasma modelling, pulsed corona discharge, acetaldehyde removal, atmospheric plasma.

1. General

Acetaldehyde (CH₃CHO) is a well known atmospheric and indoor pollutant, coming from natural emissions or human activities. But recent development of agrofuels, for which incomplete combustion produces great amounts of aldehydes, has strengthened the necessity of new abatement researches on this type of molecules [1]–[7].

Among the air and industrial exhaust gas possible treatments, atmospheric plasma processes have raised a particular interest and demonstrated a quite good efficiency [6], [7] particularly for acetaldehyde removal with [8]–[10] or without [11]–[13] a catalyst.

¹This work has been financially supported by Agence Nationale de la Recherche (JCJC BIOPAC).

²Laboratoire d'Ingénierie des Matériaux et des Hautes Pressions, CNRS-UPR1311, Université Paris 13, 99 Avenue J. B. Clément, 93430 Villetaneuse, France

This work is an experimental and modelling study of acetaldehyde degradation by an atmospheric pulsed plasma reactor device in a wire to cylinder (WTC) configuration.

2. Experimental part

The reactor used in the present work consists in a 100 μm diameter tungsten wire anode placed in a 20 mm diameter cylindrical steel cell (Fig. 1).

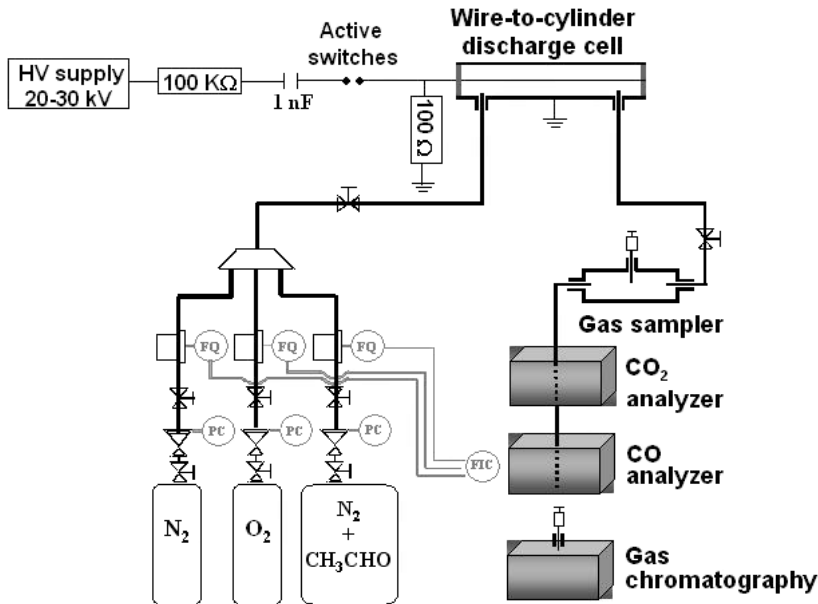


Fig. 1. Experimental setup for investigation of oxidation of acetaldehyde in WTC corona discharge

The atmospheric pressure pulsed corona discharge is generated with the help of a one-stage Marx generator. A capacitance is charged with an input voltage ranging between 10 kV and 25 kV, and discharged by means of active switches. The Marx generator makes use of a capacitor charging device (model Alimtronic CCR70P300 that delivers up to 70 kV at 8.65 mA). It produces voltage pulses with durations in the range 50 ÷ 350 ns. The rate of the voltage increase is of the order of 1 ÷ 2 kV per ns, while the peak values achieved may be as high as 25 kV. The discharge repetition rate can be varied between 1 and 100 pulses per second.

The discharge voltage is measured using a 100 MHz bandwidth high-voltage probe that allows monitoring voltage pulses with amplitude as high as 40 kV. The discharge current is acquired with a Pearson current monitor (model 287)

with a typical rise time of 5 ns. The signals delivered by the voltage and current probes are processed with a Lecroy model LC584AM oscilloscope, the bandwidth and sampling rate of which are 1 GHz and 8 GS/s, respectively.

The feed gas consists of N₂/O₂ mixtures with a small amount of CH₃CHO. The base values of oxygen and acetaldehyde concentrations in the feed gas are 5 % and 500 ppm, respectively. The oxygen contents in the feed gas was varied in the ranges 0 ÷ 20 %. The flow rate entering the discharge cell is monitored with three digital BRONKHORST HI-TEC mass flow-meters the full range of which are 5, 100 and 200 sccm, respectively. The relative experimental error on the flow measurements is 1 % of the full scale.

Acetaldehyde removal efficiency has been evaluated by measuring the pollutant residual concentration as well as the CO and CO₂ one in the cell outlet. Residual acetaldehyde measurements and oxidation by-products identification and quantification are achieved via a Shimadzu GC-2110 Gas chromatography device. The continuous monitoring of CO, CO₂ and H₂O concentrations is realised with a multi gas-analyser (Environnement S. A.), and ozone amounts are monitored by a UV analyser (IN USA).

The energy deposition of the investigated discharge was evaluated through the specific input energy, SIE. This parameter corresponds to the energy deposited per unit volume of inlet gas mixture in the discharge cell. It is obtained from the discharge pulse frequency, the energy deposited per pulse and the inlet gas flow rate using the following expression:

$$\text{SIE} = \frac{\text{Pulse energy} \times \text{Frequency} \times 60}{\text{Flow rate}} . \quad (1)$$

When the residual fraction of acetaldehyde varies exponentially with the specific input energy SIE, the discharge efficiency for VOC's conversion may be evaluated through the energy cost β as follows:

$$\ln \frac{[\text{CH}_3\text{CHO}]_{\text{in}}}{[\text{CH}_3\text{CHO}]_{\text{out}}} = -\frac{\text{SIE}}{\beta} ; \quad (2)$$

$[\text{CH}_3\text{CHO}]_{\text{in}}$ and $[\text{CH}_3\text{CHO}]_{\text{out}}$ are the concentrations of acetaldehyde in the feed gas and in the gas flow leaving the discharge cell, respectively.

The energy deposited during one discharge pulse is estimated from the measured current and voltage. Figure 2 shows typical voltage and current waveforms associated to the pulsed corona discharge. In the example shown here, the discharge current reaches a maximum of 60 A and is equal to 0 A after 200 ns. The energy absorbed by the discharge during a single pulse was evaluated by integrating the product of voltage and current over the discharge duration. The typical value for the energy deposited in the discharge ranges between 20 and 60 mJ per pulse, which corresponds to an average power of 1 W for a frequency of 1 kHz.

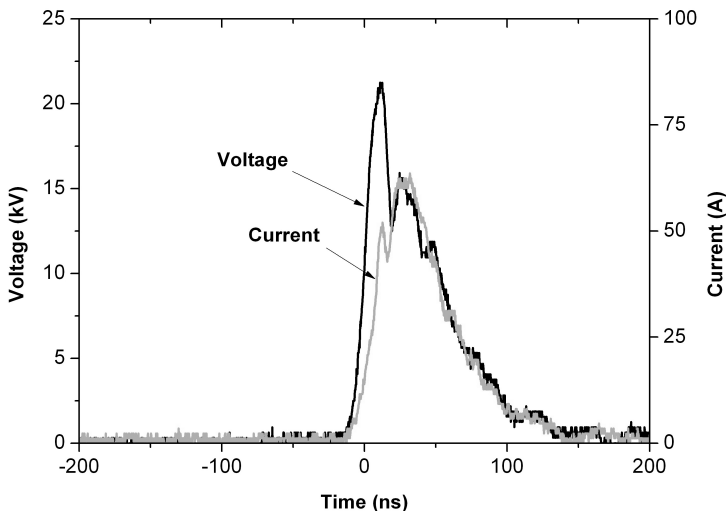


Fig. 2. Typical voltage and current temporal profile during one pulse

3. Experimental results

Experimentally, the acetaldehyde removal efficiency has been evaluated by studying the following parameters:

- Residual acetaldehyde as a function of the SIE.
- Detection and quantification of by-products.
- Carbon balance and CO_2/CO yields ratio.

Pollutant removal efficiency

Concerning the acetaldehyde removal efficiency, the results reported on Fig. 3 lead to two main observations:

One of them is a change of energetic cost between low and high SIE values. Indeed, for SIE values under 100 J/L, the energetic cost β is around 103 J/L, whereas for SIE values over 100 J/L, β decreases to 50 J/L. Considering that, in our conditions, higher SIE values are correlated to higher values of pulse frequency, one explanation could be the higher influence of pulse chemistry in acetaldehyde conversion at high SIE values comparing to post-discharge chemistry which is predominant at low SIE values.

The other observation is that our process is more efficient for an initial gas mixture containing O_2 than for a pure N_2 plasma.

In pure N_2 mixture, the removal efficiency reaches 80 % at 200 J/L. This efficiency largely increases when adding a small amount of oxygen in the mixture. Using N_2 and 5 % O_2 , more than 90 % of degradation of acetaldehyde

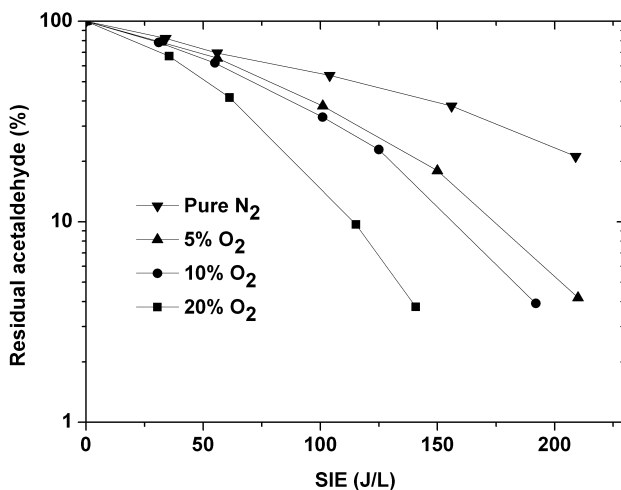


Fig. 3. Residual acetaldehyde as a function of SIE for various O₂ concentration in the inlet gas mixture

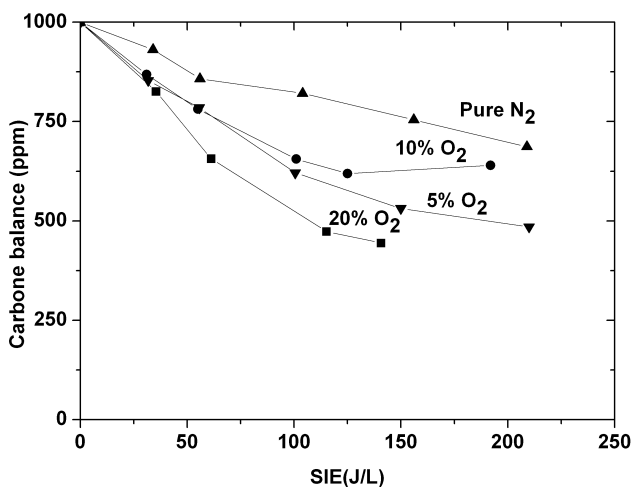


Fig. 4. Carbon balance as a function of SIE

is obtained with a SIE lower than 200 J/L. Adding more oxygen has a real benefit on the acetaldehyde conversion, but mainly for the highest value of SIE. Indeed, on the one hand, for a specific input energy equal to 35 J L^{-1} the conversion of acetaldehyde increases only by 10 % when the percentage of O₂ increases from 5 to 20 %, whereas, on the other hand, at 150 J/L, acetaldehyde is almost totally converted with 20 % of O₂, 20 % of the initial acetaldehyde staying in the gas outlet for 5 % of O₂.

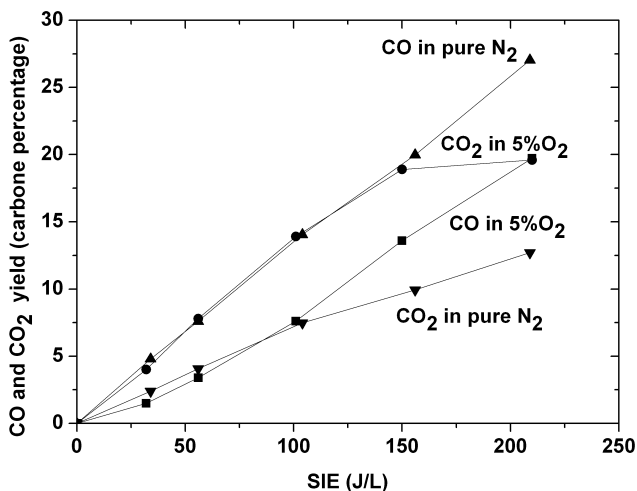


Fig. 5. CO and CO₂ yields in percentage of initial C as a function of SIE

Main detected by-products

The second part of this experimental work deals with the identification and quantification of the acetaldehyde decomposition by-products. In addition to CO and CO₂, methanol, methane, formaldehyde and acetic acid have been identified by gas chromatography, but only methanol and acetaldehyde have been precisely quantified.

Despite this fact, computed carbon balance including CO, CO₂, methanol, residual acetaldehyde and acetone gives a satisfactory result at low SIE with a variation between 70 % and 90 % of the initial carbon converted carbon (see Fig. 4). Results are less good at high SIE certainly due to a larger by-product distribution at those energies.

CO and CO₂ production

Concerning the CO and CO₂ production ratio after conversion of acetaldehyde, it has been estimated by following their yields in initial carbon percentage as a function of SIE. This yield is computed by the following expression:

$$\text{Yield of CO (\% C)} = \frac{[\text{CO}]}{2 \times [\text{CH}_3\text{CHO}]_{\text{initial}}} \times 100. \quad (3)$$

Figure 5 illustrates the evolution of CO and CO₂ yields as a function of the specific input energy for two experimental conditions, without or with 5 % of O₂ in the N₂/acetaldehyde inlet mixture.

CO and CO₂ production results show clearly a difference between plasma with O₂ and plasma without O₂ for the CO/CO₂ ratio. In a first analysis, it is not surprising that addition of O₂ leads to an inversion in the CO/CO₂ ratio, CO₂ concentration being predominant on CO one in oxygenated plasma, whereas in pure N₂ plasma, CO amounts are greater than CO₂ ones with factor 2.5. The interesting point is in the relatively great amount of CO₂ formed in pure N₂ conditions, whereas the only source of O atom is in the C=O bond and the C=O bond energy is around 10 eV. We could consider two possible pathways of C=O bond breaking. Whereas the mean electron energy in the plasma is around 3 ÷ 4 eV, a small part of the electron corresponding to the tail of the electron distribution function, can be involved in the C=O bond breaking. Metastable states of nitrogen (N₂ (A, B, C,)) may also be involved in the bond breaking of C=O. We are still working on that point. An analysis on possible other pathways of formation of O or OH active species is still in progress.

Methanol and acetone production

Concerning methanol formation its production seems to be independent of the amount of O₂ in the initial mixture, but decreased by the factor 2 in absence of oxygen, as shown in Figs. 6 and 7.

This is certainly due the production of a great amount of atomic O radicals in the N₂/O₂ discharge, which react with the CH₃ radicals (directly produced by acetaldehyde decomposition) to form CH₃O radicals. Then, CH₃O radicals react with other CH₃O radicals to form formaldehyde and methanol. This main way of methanol production is cut in N₂ plasma due to the low quantity of O generated in this type of plasma.

Concerning acetone production, Fig. 7 clearly shows that this molecule is formed in small amount in both conditions, even if its formation is enhanced in pure N₂. This is probably due to the fact that acetone is formed by recombination between methyl and acetyl radical, this pathway being certainly of minor importance in oxygen rich conditions because of the high reactivity between acetyl radical and oxygenated species O and O₂. Another explanation could be that CH₃CO is mainly produced in O₂ containing plasma by H abstraction by O and OH active species and this pathway begins very minor or disappears in pure N₂ plasma.

4. Modelling part

Description of the model

To understand the chemistry and to confirm suspected pathways of decomposition of acetaldehyde as well as to identify other minor by-products, a 0D model of the discharge cell has been developed for this work.

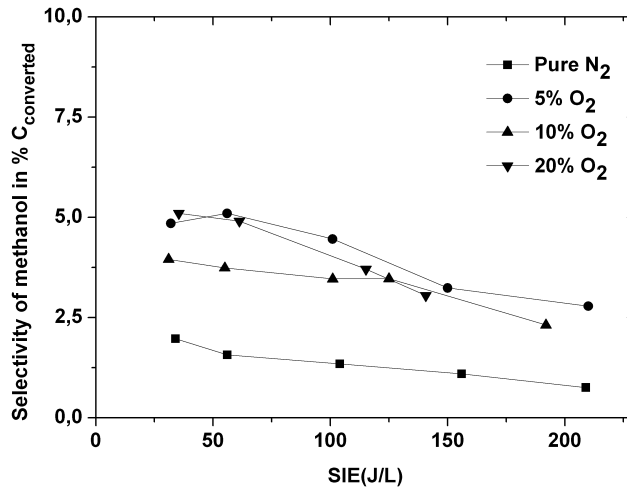


Fig. 6. Selectivity in methanol as a function of SIE for different percentage of O₂ in the inlet gas mixture

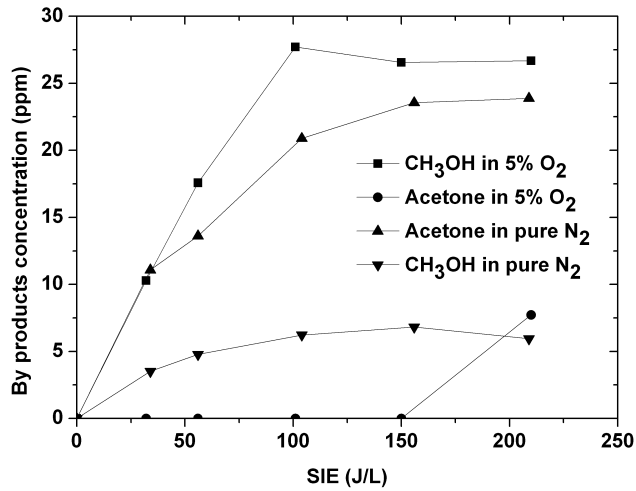


Fig. 7. Comparison between methanol and acetone production as a function of SIE with and without 5% of O₂ in the initial mixture

It consists in a quasi homogeneous model which is a adaptation of a former model developed for the study of acetylene discharge in a pin to plane configuration [14].

A major problem encountered in the present wire to cylinder configuration was to estimate the medium number of streamers appearing between the cathode and the anode during one pulse. First investigations lead us to a medium number of 400 streamers appearing during a discharge pulse on the 200 mm wire electrode.

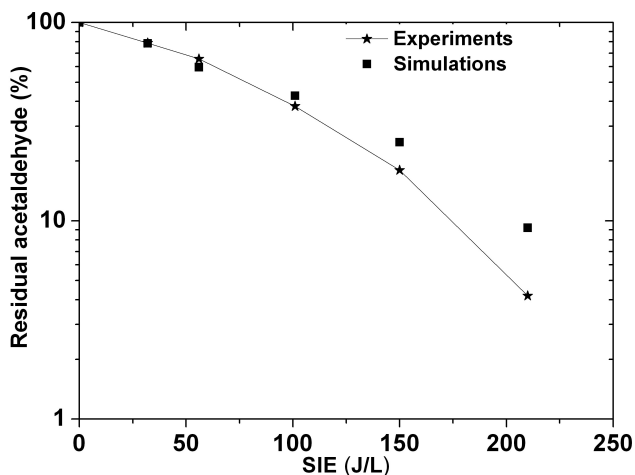


Fig. 8. Residual acetaldehyde as a function of SIE for 500 ppm of acetaldehyde and 5 % of O₂

Concerning the chemical scheme, our model includes 90 species reacting in 450 elementary processes. In this chemical scheme some essential reactions often reported in the literature for acetaldehyde decomposition at atmospheric pressure [8]–[11] have been introduced:

- Electronic impacts for CH₃CHO decomposition, even if the 200 ns discharge time is quite small comparing the post discharge time (100 to 1000 ms).
- Collision of acetaldehyde with N₂ molecules at the first electronic excited state, (mainly N₂(A³Σ_U⁺) and N₂(a¹Σ_u⁻); even if these species have a short life-time in the post-discharge, they seem to play a great role in the pollutant removal when the pulse frequency is high enough.
- Metathesis CH₃CHO decomposition reactions by main active species (O, OH, H, CH₃O), which play the major role in the pollutant removal due to their long lifetime in the post-discharge.

Comparison between model and experiments

Simulated results for conversion of acetaldehyde are shown in Fig. 8. Quite a good accordance between results and simulation for acetaldehyde conversion can be noticed.

The selected model has allowed us to reproduce the change of energetic cost β observed experimentally for an SIE exceeding 100 J L⁻¹.

Concerning the simulation results obtained for main byproduct concentrations, comparison between experiments and simulations has shown a very good accordance for O₃ (see Fig. 9) and CH₃OH (see Fig. 10). This globally means that chemistry of active species like O and O₂ is well described by the model.

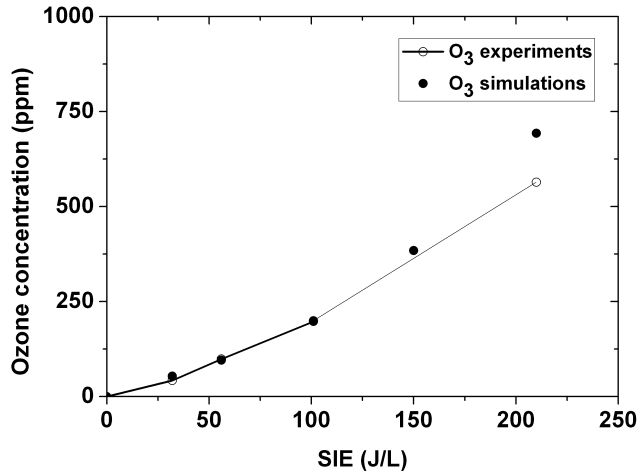


Fig. 9. Evolution of ozone concentration as a function of SIE for a 5 % O₂ inlet mixture

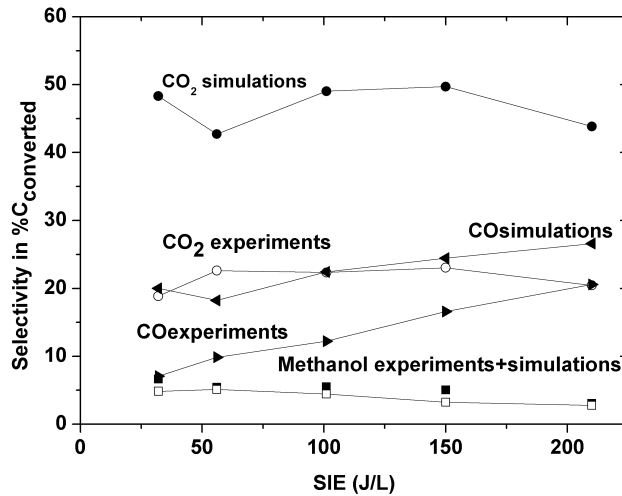


Fig. 10. Selectivity of main by-products as a function of SIE in percentage of converted carbon

Nevertheless, the simulated results obtained for CO₂ and CO concentrations represents twice as much than those experimentally obtained (see Fig. 9). This difference can be explained by the simplifications introduced in the model for the decomposition of active radical like CH₃CO, CH₃ or CHO.

This hypothesis is confirmed by the flow analysis achieved for CO₂ and CO main pathways of formation illustrated respectively by Figs. 11 and 12. Both species are products coming from acetyl radical (CH₃CO) decomposition

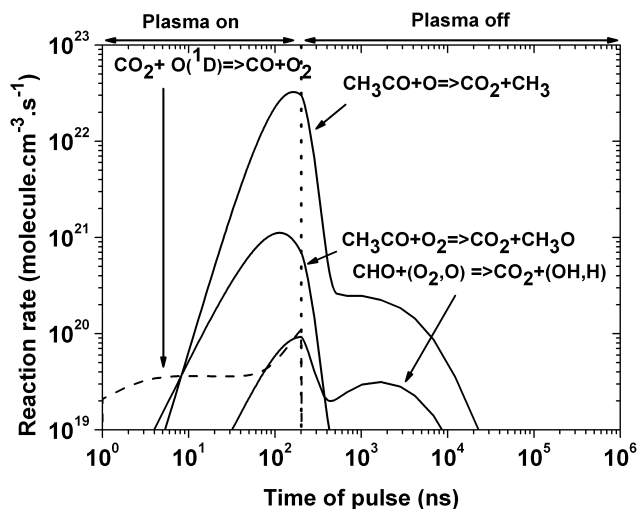


Fig. 11. Analysis of the main CO_2 production flow during one pulse in the discharge at 210 J/L

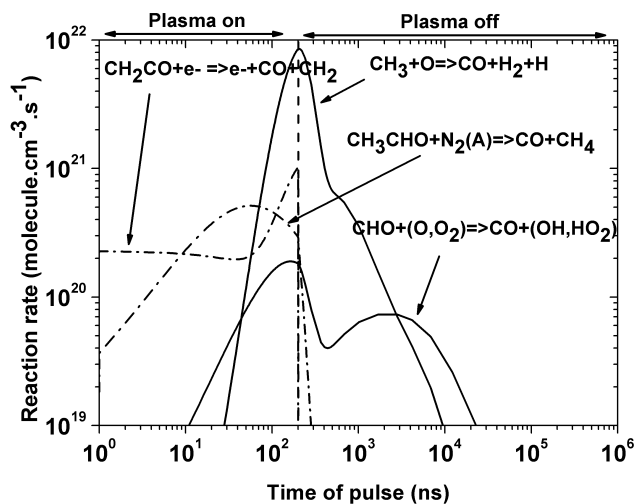


Fig. 12. Analysis of the main CO production flow during one pulse in the discharge at 210 J/L

which is directly produced from acetaldehyde decomposition. Then 90 % of computed consumption flow of CH_3CO is converted in CO_2 and CH_3 by O and O_2 addition.

Concerning CO pathways of formation, simulations give two major ways of formation implying addition of O or O_2 on CH_3 methyl radical and CHO formyl radical, two species directly formed by acetaldehyde decomposition and for CH_3 by CH_3CO decomposition.

Simplifying the reaction scheme by neglecting other pathways of consumption of CH_3CO radical (such as CH_3CO self-recombination or recombination with HO_2 or CH_3O) leads logically to higher computed concentrations for CO_2 and CO than measured ones.

As a conclusion it can be noticed that the quasi-homogeneous model used in this study reproduces in a good scale the reactivity of the plasma discharge, but some decomposition pathways of acetaldehyde by-products have to be re-investigated.

5. Conclusion

The combined experimental and modelling studies presented in this paper has allowed us to have a first picture of the performance of a pulsed corona discharge working in the nanosecond regime in a wire to cylinder configuration for acetaldehyde removal.

It has been demonstrated that our WTC configuration allows a quantitative oxidation of acetaldehyde (more than 90 % conversion) for a specific input energy around 200 J L^{-1} at ambient temperature and at low oxygen concentration (5 %) in the inlet gas mixture. This efficiency can reach a total removal of the 1000 ppmc of acetaldehyde introduced initially, if they are mixed with 20 % of O_2 . and with only a 150 J L^{-1} specific input energy.

The quasi-homogeneous model proposed in this study has permitted to have a first approach of the reactivity of acetaldehyde and has allowed us to reproduce with a quite good accordance the main by-products concentration for CO , CO_2 , O_3 and CH_3OH .

References

- [1] H. DESTAILLATS, R. L. MADDALENA, B. C. SINGER, A. T. HODGSON, T. E. MCKONE: *Indoor pollutants emitted by office equipment: A review of reported data and information needs*. Atmosph. Environ. *42* (2008), 1371–1388.
- [2] L. A. GRAHAM, S. L. BELISLE, CARA-LYNN BAAS: *Emissions from light duty gasoline vehicles operating on low blend ethanol gasoline and E85*. Atmosph. Environ. *42* (2008), 4498–4516.
- [3] YAGE DI, C. S. CHEUNG, ZUOHUA HUANG: *Comparison of the effect of biodiesel-diesel and ethanol-diesel on the gaseous emission of a direct-injection diesel engine*. Atmosph. Environ. *43* (2009), 2721–2730.
- [4] BANG-QUAN HE, SHI-JIN SHUAI, JIAN-XIN WANG, HONG HE: *The effect of ethanol blended diesel fuels on emissions from a diesel engine*. Atmosph. Environ. *37* (2003), 4965–4971.
- [5] G. KARAVLAKIS, S. STOURNAS, E. BAKEAS: *Light vehicle regulated and unregulated emissions from different biodiesels*. Sci. Total Environ. *407* (2009), 3338–3346.

- [6] HSIN LIANG CHEN, HOW MING LEE, SHIAW HUEI CHEN, MOO BEEN CHANG, SHENG JEN YU, SHOU NAN LI: *Removal of volatile organic compounds by single-stage and two-stage plasma catalysis systems: A review of the performance enhancement mechanisms, current status, and suitable applications*. *Environ. Sci. Technol.* *43* (2009), 2216–2227.
- [7] HYUN-HA KIM: *Nonthermal plasma processing for air-pollution control: A historical review, current issues, and future prospects*. *Plasma Process. Polymer.* *1* (2004), 91–110.
- [8] N. SANO, T. NAGAMOTO, H. TAMON, T. SUZUKI, M. OKAZAKI: *Removal of acetaldehyde and skatole in gas by corona-discharge*. *Ind. Eng. Chem. Res.* *36* (1997), 3783–3791.
- [9] A. S. CHIPER, N. BLIN-SIMIAND, F. JORAND, S. PASQUIERS, G. POPA, C. POSTEL: *Influence of water vapour on acetaldehyde removal efficiency by DBD*. *J. Optoelectron. Advanced Mater.* *8* (2006), 208–211.
- [10] L. MAGNE, S. PASQUIER, V. EDON, F. JORAND, C. POSTEL, J. AMORIM: *Production of hydroxyl radicals and removal of acetaldehyde in a photo-triggered discharge in $N_2/O_2/CH_3CHO$ mixtures*. *J. Phys. D: Appl. Phys.* *38* (2005), 3446–3450.
- [11] HOW MING LEE, MOO BEEN CHANG: *Gas-phase removal of acetaldehyde via packed-bed dielectric barrier discharge reactor*. *Plasma Chem. Plasma Process.* *21* (2001), 329–343.
- [12] J. CHAICHANAWONG, W. TANTHAPANICHAKOON, T. CHARINPANITKUL, A. EIAD-UA, N. SANO, H. TAMON: *High-temperature simultaneous removal of acetaldehyde and ammonia gases using corona discharge*. *Sci. Technol. Advanced Mater.* *6* (2005), 319–324.
- [13] J. VAN DURME, J. DEWULF, K. DEMEESTERE, C. LEYS, H. VAN LANGENHOVE: *Post-plasma catalytic technology for the removal of toluene from indoor air: effect of humidity*. *Appl. Catal. B: Environ.* *87* (2009), 78–83.
- [14] M. REDOLFI, N. AGGADI, X. DUTEN, S. TOUCHARD, S. PASQUIERS, K. HASSOUNI: *Oxidation of acetylene in atmospheric pressure pulsed corona discharge cell working in the nanosecond regime*. *Plasma Chem. Plasma Process.* *29* (2009), 173–195.

Received April 29, 2010

Laser–plasma coupling in the shock-ignition intensity regime¹

LUCA ANTONELLI², DIMITRI BATANI², ANDREA PATRIA²,
ORLANDO CIRICOSTA³, CARLO A. CECCHETTI³,
PETRA KOESTER³, LUCA LABATE³, ANTONIO GIULIETTI³,
LEONIDA A. GIZZI³, ALESSANDRO MORETTI⁴, MARIA RICHETTA⁴,
LORENZO GIUFFRIDA⁵, LORENZO TORRISI⁵, MICHAELA KOZLOVÁ⁶,
JAROSLAV NEJDL⁶, MAGDA SAWICKA⁶, DANIELE MARGARONE⁶,
BEDŘICH RUS⁶, GUY SCHURTZ⁷, XAVIER RIBEYRE⁷,
MARION LAFON⁷, CHRIS SPINDLOE⁸, TIM O'DELL⁸

Abstract. A novel approach to ICF called shock ignition, that relies on delivery of a very strong shock created by a laser pulse at intensities around 10^{16} Wcm⁻², is investigated. In this context, an experiment using two beams from the Prague Asterix Laser System with time duration of 300 ps was performed at the PALS laboratory. The first beam at low intensity was used to create extended preformed plasma, and the second one to create a strong shock. Several diagnostics were used to characterize the preformed plasma and the interaction of the main pulse with the target.

Key words. Inertial confinement fusion, Laser-driven shock, parametric instabilities, X-ray deflectometry.

¹The present experiment was performed in the framework of the HiPER European project and supported by LASERLAB. The authors warmly acknowledge the contribution of the PALS laser and technical team. Targets were supplied by Scitech Precision and the Rutherford Appleton Laboratory Target Fabrication Group.

²Dipartimento di Fisica, Università di Milano Bicocca, Piazza della Scienza 3, 20134 Milano, Italy

³INO—Istituto Nazionale di Ottica, Area della Ricerca del CNR, Via Moruzzi, 1, 56124 Pisa, Italy

⁴Università di Roma “Tor Vergata”, Via del Politecnico, 1, 00100 Roma, Italy

⁵University of Messina and INFN Catania, Ctr. Papardo Sperone, 31, 98166 S. Agata, Messina, Italy

⁶PALS Laboratory, Na Slovance 2, 182 21 Praha 8, Czech Republic

⁷CELIA, Université de Bordeaux 1, 351 Cours de la Liberation, 33405 Talence, France

⁸Scitech Precision Limited, Rutherford Appleton Laboratory, Didcot, Oxfordshire OX11 0QX

Introduction

Shock ignition is a novel approach to Inertial Confinement Fusion (ICF) [1], which, like fast ignition, is based on the separation of the compression and ignition phases. The first phase implies “normal” compression of a thermonuclear DT pellet with nanosecond laser beams at intensity $I \approx 10^{14} \text{ Wcm}^{-2}$. Several experiments in the past have already shown that compression to a regime of interest for ICF is possible [2] while they failed to achieve ignition using the classical central hot spot isobaric approach [3]. The second phase relies on delivery of a very strong shock (pressure P about several hundred Mbar), created by a laser pulse at intensities $I \approx 10^{15} \div 10^{16} \text{ Wcm}^{-2}$, which heats the central part of the compressed fuel and creates the conditions for ignition. This scheme could also allow to get ignition using a smaller laser energy for compression (a few hundred kJ plus about 100 kJ for ignition); of course this implies that higher gains are achievable.

One of the main problems with the shock ignition approach is that such intensity regime has not been studied much in the past in the framework of ICF studies because parametric instabilities may easily develop and reflect a substantial amount of the incident laser light. Also the final driving pulse should propagate through a well-extended plasma corona, which may act to decouple the pulse from the compressed core.

In this context, we have recently performed an experiment at the PALS laboratory using two beams from the Prague Asterix Laser System. The first beam at low intensity was used to create extended preformed plasma, and the second one to create a strong shock. Goals of the experiment were:

1. To study the effect of laser–plasma instabilities at $I \approx 10^{16} \text{ Wcm}^{-2}$. Do they develop? How much light do they reflect? Do they create many hot electrons and at what energy?
2. To study the coupling of the high-intensity laser beam to the payload through an extended plasma corona. Is it really possible, under such conditions, to create a strong shock?

The experiment concluded in April 2010. Here we just present a preliminary analysis of the results.

Experimental set-up

The experiment was divided into two phases. Phase 1 was dedicated to the creation of the extended preplasma and its characterization with:

1. X-ray deflectometry, using the PALS X-ray laser to get density profiles.
2. X-ray spectroscopy, to obtain plasma temperature.
3. X-ray pin-hole cameras, to obtain the transversal size of preplasma.

Phase 2 addressed the characterization of shock formation and laser-plasma interaction. The interaction of the main pulse has been studied using:

1. Energy encoded X-ray pin-hole camera (EEPHC) to measure plasma extension and characterize its emission.
2. Ion diagnostics (ion collectors).
3. Shock chronometry (measuring the self emission from the target rear side with a streak camera).
4. Optical imaging, spectroscopy, and calorimetry of back reflected radiation to evaluate the onset and amount of back reflected light from parametric instabilities: Stimulated Raman Scattering, Stimulated Brillouin Scattering, and Two Plasmon Decay (SRS, SBS, TPD).

The PALS system is an Iodine Laser delivering a pulse at $\lambda = 1.3 \mu\text{m}$, duration = 300 ps, and maximum energy $E = 1 \text{ kJ}$ in the fundamental frequency. Such a beam was linearly focused and used in Phase 1 to create the XRL beam for diagnostics [4]. To create the strong shock in Phase 2, we converted the beam to the third harmonic (getting $\lambda = 438 \text{ nm}$ and $E \leq 500 \text{ J}$). Such a beam was used in Phase 1 to create the XRL beam for diagnostics, and in Phase 2 to create the strong shock. In this case it was focused to a spot of diameter $100 \mu\text{m}$ to get the intensity $I = 10^{16} \text{ Wcm}^{-2}$.

Using the scaling law reported in [3] and measuring I in Wcm^{-2} and λ in μm , one gets

$$P = 8.6 \cdot \left(\frac{I}{10^{14} \lambda} \right)^{2/3} \cdot \left(\frac{A}{2Z} \right)^{1/3} \approx 320 \text{ Mbar} \quad (1)$$

where A and Z are the atomic weight and atomic number of the target material, respectively.

The auxiliary beam creating extended plasma was operating at the fundamental with $E = 30 \text{ J}$, $\lambda = 1.3 \mu\text{m}$, pulse duration = 300 ps. This was focused to an extended spot (diameter $\leq 1 \text{ mm}$), in order to create an approximately 1D expanding plasma, providing an intensity $I \leq 2 \times 10^{13} \text{ Wcm}^{-2}$.

The use of the fundamental wavelength was important because it allows getting a relatively high temperature at the critical surface despite of the low intensity, which allows a better simulation of the conditions of the plasma corona in an ICF target. With the same scaling as above one gets

$$T_e = 10^{-6} \cdot [I \cdot \lambda^2]^{2/3} \approx 750 \text{ eV} . \quad (2)$$

The principle of the experiment is shown in Fig 1. We used stepped targets allowing to deduce pressure from shock breakout chronometry [5].

There are of course several constraints on the target. We used two layers. The first CH layer simulated the low- Z material of a pellet shell. The second

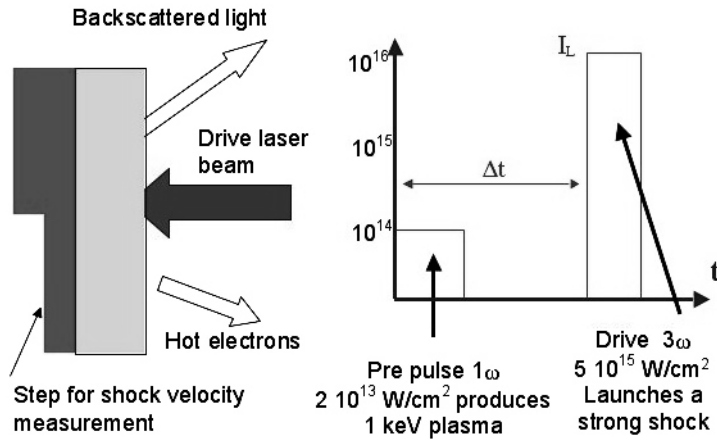


Fig. 1. Scheme of the experimental set-up used at PALS. Both the prepulse and the drive beam impinges on target front side. On target rear side, the step allows for shock velocity measurements. Time delay Δt between prepulse and drive is changed in the experiment.

Al layer was used because Al is a standard material for shock measurements. In principle the CH thickness must allow for the second shock to catch up the first shock in CH. The choice of the Al thickness is a compromise: with thin Al, the pressure measurement occurs before the end of the main pulse (before the rarefaction wave launched at the end of the pulse catches up with the shock); on the other side, thick Al increases the time resolution. The final target configuration included a $25 \mu\text{m}$ CH layer (containing Cl to allow for X-ray spectroscopy) and a $25 \mu\text{m}$ Al layer (plus $10 \mu\text{m}$ Al step on some targets). Targets were produced at the target preparation facility at the Rutherford Appleton Laboratory (UK).

Experimental results: Phase 1

The density measurements were performed using XRL deflectometry, a technique based on the deformation of Talbot pattern of 2D grating caused by gradients of index of refraction (electron density) of the plasma [6]. Assuming cylindrical symmetry allows resolving the electron density profile via inverse Abel transform. The scheme is shown in Fig. 2. The basic principle relies on the fact that each “ray” selected by the grid arrives onto the detector with an angle which is dependent on the deviation accumulated while travelling through the plasma, which in each position bends the ray according to the local refraction index.

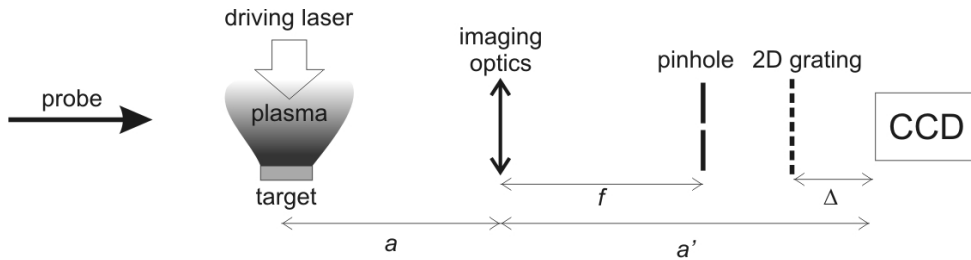


Fig. 2. Experimental scheme for XRL deflectometry. The focal length of the imaging element is f , the distance between the 2D grating and the CCD is Δ . The object and image distances are labelled as a and a' , respectively.

A Ne-like zinc X-ray laser was used, emitting at 21.2 nm, operated in single pass providing 150 ps pulses of 200 μJ . A Mo-Si multilayered spherical mirror with focal length $f = 250$ mm was used to image the plasma on back-illuminated X-ray CCD with magnification $M = 8.2$. A 0.5 mm diameter pinhole was put to the image of the XRL source (2800 mm from the imaging mirror), to reduce the signal from plasma self-emission. The 100 μm period laser-drilled grid made of 5 μm thick steel was at 1275 mm from CCD. Figure 3 shows both the deviation pattern and the obtained 2D density profiles 0.3 ns and 0.9 ns after the arrival driving pulse.

From such images we see that the plasma with electron density $n_e > 10^{20} \text{ cm}^{-3}$ extends over 200 μm (perpendicularly to target surface) and over 800 μm radially (comparable to the expected spot size ≈ 1 mm). These numbers are also confirmed by X-ray pin-hole camera (PHC) images. The X-ray keV spectrometer used a flat ADP (ammonium dihydrogen phosphate) crystal with the crystal interplanar spacing $2d \approx 10.659 \text{ \AA}$ placed at about 20 cm from the source and with a Bragg angle of about 19° . It was used to characterize the X-ray spectra from pre-plasma with an observed range from 2600 to 3600 eV. We detected X-ray lines from Li-, He- and H-like Cl ions. However the spectral resolution was poor due to large source size (about 1 mm implying a line width $\Delta E \approx 40$ eV). We used RATION [7] to simulate the obtained Cl spectra and we got a qualitative agreement for a plasma $T_e \approx 300$ eV which makes the He and Li lines are comparable, as it happens in the experimental spectrum. This temperature is lower than expected, but detailed analysis is in progress.

The spectrometer was also used in Phase 2 but there were no significant changes in spectrum although with the main laser T_e should drastically increase. We suspect that this is due to volume effect (the heated preplasma is substantially smaller than the preplasma due to the different focal spot size).

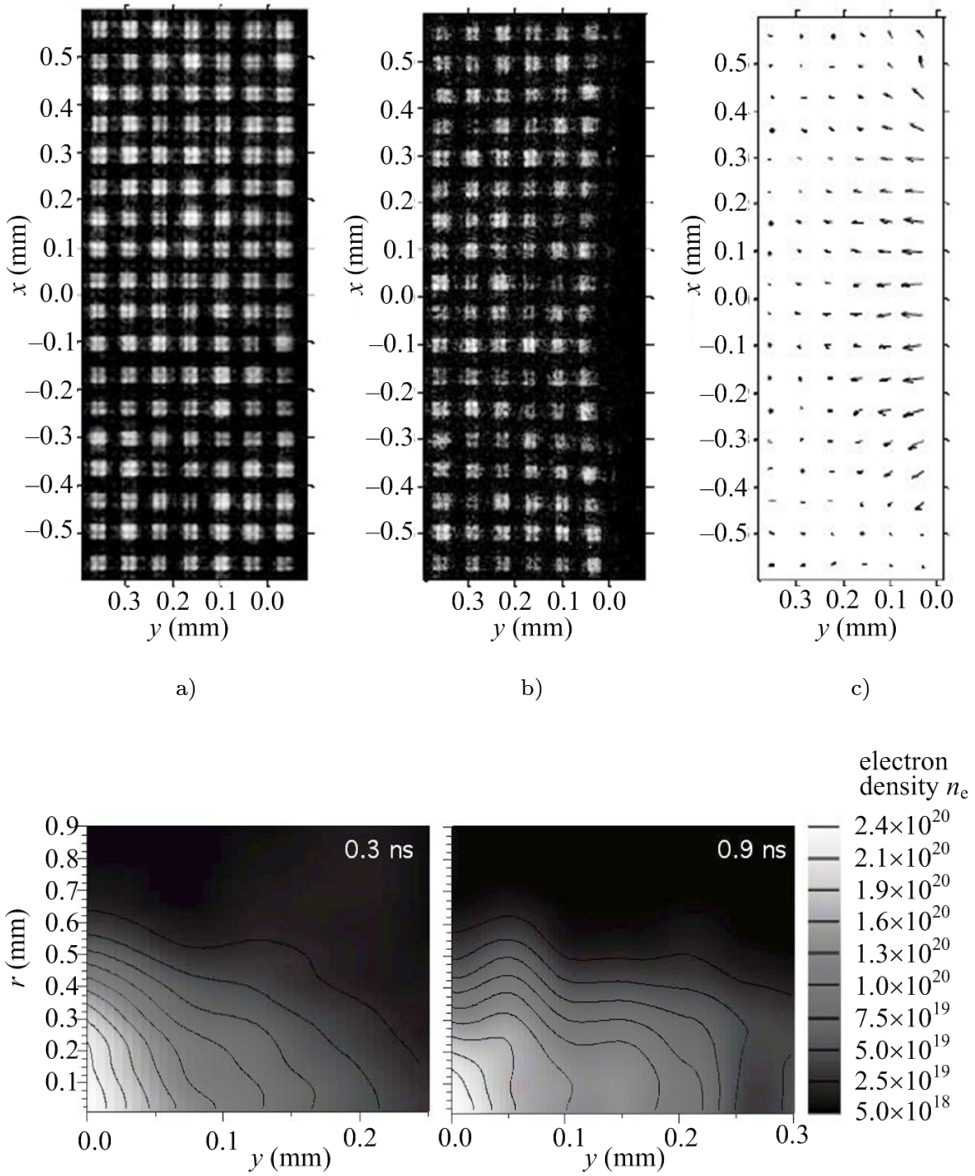


Fig. 3. Experimental results from XRL deflectometry. *Up*: probing of CH plasma by XRL beam 0.3 ns after driving pulse arrival; a) reference pattern without plasma, b) signal recorded when probing the plasma, c) field of pattern deformation; *down*: 2D electron density profiles (in cm^{-3}) at 0.3 ns and 0.9 ns after the arrival driving pulse.

Experimental results: Phase 2

In phase 2, we used the Energy encoded X-ray PHC [8], [9] to get a characterization of the plasma size (heated by the main pulse) as well as its spectroscopic characterization and a possible signature from hot electrons. When using such a diagnostics we added a thin ($1\ \mu\text{m}$) Cu layer between Al and CH. We also used Ti/Cu targets (no exploitable result was obtained without main beam, i.e. in Phase 1). Figure 4 shows a result obtained with a Al/Cu/CHCl target shooting with both the main drive beam and the prepulse (creation beam). It shows a focal spot diameter FWHM $\approx 100\ \mu\text{m}$, and it also implies the presence of K- α photons from the Cu layer.

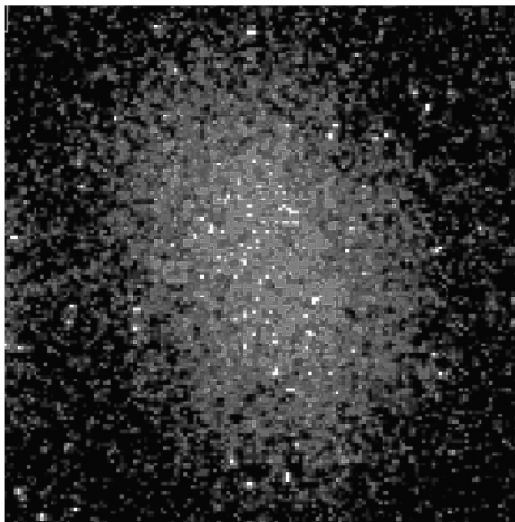


Fig. 4. Typical image obtained with Energy encoded PHC.

For fast electrons at intensity $10^{16}\ \text{Wcm}^{-2}$, from the scaling shown in [10] one expects

$$T_e = 100 \cdot [I \cdot \lambda^2 \cdot 10^{-17}]^{1/3} \leq 50\ \text{keV} \quad (3)$$

(although higher energies may be produced by SRS). The typical penetration range of hot electrons with such energy is less than $7\ \mu\text{m}$ in Cu, and $40\ \mu\text{m}$ in CH. Images like that in Fig. 4 were obtained at energies corresponding to the K- α lines of both Cu and Ti, thereby confirming the presence of fast electrons (the work is in progress to try retrieving the exact hot electron energy). The source size did not exceed $100\ \mu\text{m}$, which can be assumed to characterize the focal spot of the main beam (due to the low penetration range of such hot

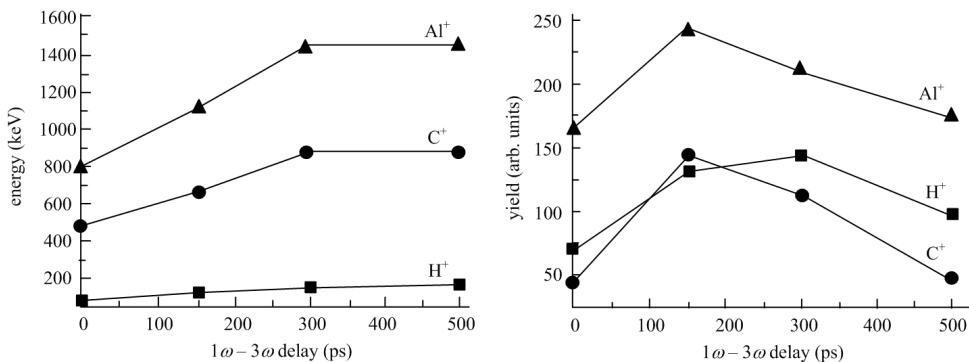


Fig. 5. Results from the ion diagnostics; *left*: ion energy vs. prepulse delay, *right*: ion yield vs. prepulse delay

electrons). The results for spectroscopy obtained by EEPHC showed the presence of Cu K- α and K- β lines as well as of a bremsstrahlung tail corresponding to a temperature of 600 eV (much lower than expected; however, a detailed analysis is still in progress).

The ion emission diagnostics used an ion collector on the target front side [11]. In order to interpret the obtained ion spectra we used a Maxwell–Boltzmann–Coulomb shifted function [12]

$$F(t) = A \cdot \left(\frac{m}{2\pi kT}\right)^{2/3} \cdot \left(\frac{L^4}{t^5}\right) \cdot \exp\left(-\left(\frac{m}{2\pi kT}\right) \left(\frac{L}{t} - \sqrt{\frac{\gamma kT}{m}} - \sqrt{\frac{2zeV_0}{m}}\right)^2\right), \quad (4)$$

where m is the ion mass, kT the equivalent temperature, L is the target–detector distance, γ the adiabatic coefficient, ze the ion charge and V_0 the equivalent voltage developed in the non-equilibrium plasma. Analysis of the ion spectra also allows obtaining the plasma temperature, which in this case was of about 1500 eV. Again, this is quite low when considering that in this case the laser intensity on target was much higher ($I = 10^{16}$ Wcm⁻²). Ion spectra were also measured with both the main beam and the prepulse beam changing the delay between the two. Figure 5 shows the typical ion energy and the ion yield vs. prepulse delay and presents a typical “bell shape” behaviour.

As for shock chronometry, a typical result is shown in Fig. 6. The measurement of shock velocity provides the value of shock pressure using an EOS (equation of state) model (we used the Sesame tables [13]). With stepped targets, we got two independent measurements per shot, i.e. the Δt between irradiation and first shock breakout on the base of the target, and the Δt between breakout on base and on step.

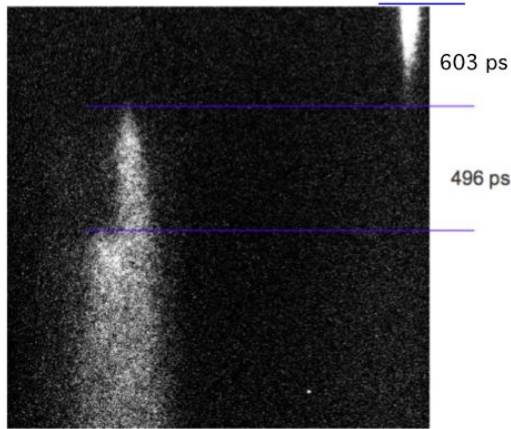


Fig. 6. Shock chronometry for a stepped target with $E(3\omega) = 245$ J, E prepulse = 29 J, and delay between prepulse and main of 500 ps

The shot in Fig. 6 provides a shock velocity (measured in the step) of 20.2 km s^{-1} , corresponding to the pressure $P = 6.3$ Mbar. Although this measured value of P is very low, it may not be in contradiction with expectations. Indeed, we must notice how in our experimental configuration the shock pressure undergoes a rapid decrease due to

- i) 2D effects during shock propagation,
- ii) the relaxation waves originating from front side when the laser turns off.

To check this, we performed some preliminary simulations using the hydro code MULTI 2D [14], which for an irradiation $I \approx 2 \times 10^{15} \text{ W cm}^{-2}$ (corresponding to a generated pressure on the target front side of $P \approx 100$ Mbar) leads to a delay of shock breakout of $\Delta t \approx 600$ ps (as in experimental results), and measured an average shock pressure in the step $P \approx 10$ Mbar.

Another interesting feature of shock chronometry is that if we plot the time of first shock breakout (delay between irradiation time and breakout on the base of the target) (see Fig. 7), we get the same “bell shape” behaviour of ion measurements, i.e., the values of shock breakout time for $\Delta t = 500$ ps are very close to those without prepulse.

Let us finally come to the backscattering diagnostics. A beam splitter (reflectivity 1%) was installed before the main focusing lens to collect back reflected light. This was further split into different beam lines performing, respectively, imaging of the focal spot region at ω (438 nm), imaging at $\omega/2$, spectrometry and calorimetry. The whole system included three lenses: the main focusing lens ($f = 60$ cm), a lens with $f = 170$ cm after the beam splitter

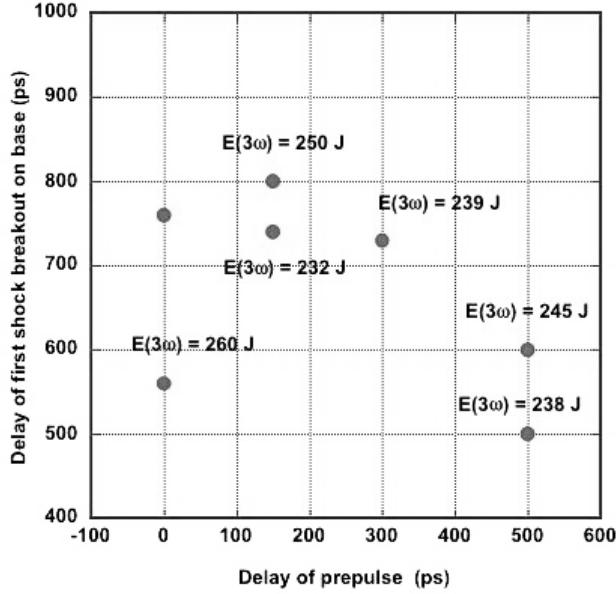


Fig. 7. Shock chronometry: breakout on base vs. prepulse time delay

and (for the imaging systems only) a microscope objective with $10 \times$ magnification placed before the CCDs.

The spectroscopic diagnostics allowed measuring TPD (with typical emission at $3\omega/2$) and SRS (with emission between ω , corresponding to the low density regions of the plasma corona, $n_e \approx 0$, and $\omega/2$, corresponding to $n_e \approx n_c/4$, where n_c is the critical density of the laser). However, SRS was not detectable because the spectral shift in this case was too low compared to the spectral resolution of the used spectrometer so that SRS could not be distinguished from the scattered light at the fundamental wavelength. Figure 8 shows some examples of SRS spectra. We notice that the spectral shape does not seem to be affected by the prepulse to main pulse time delay.

We remind that SRS spectra are characterized by the emission wavelength

$$\lambda_{\text{SRS}} = \lambda_0 \cdot \left[1 - \left(\frac{n_e}{n_c} \right)^{1/2} \cdot (1 + 3k^2 \lambda_D^2)^{1/2} \right]^{-1} \quad (5)$$

where λ_D is the plasma (local) Debye length. We then see that all our spectra are characterized by a blue cut-off due to Landau damping ($k\lambda_D \approx 0.2$) while no emission from the plasma region with electron density $n_c/4$ was observed. It may imply depletion of the laser pump due to strong delocalised collisional absorption in the plasma corona (again, the work is in progress).

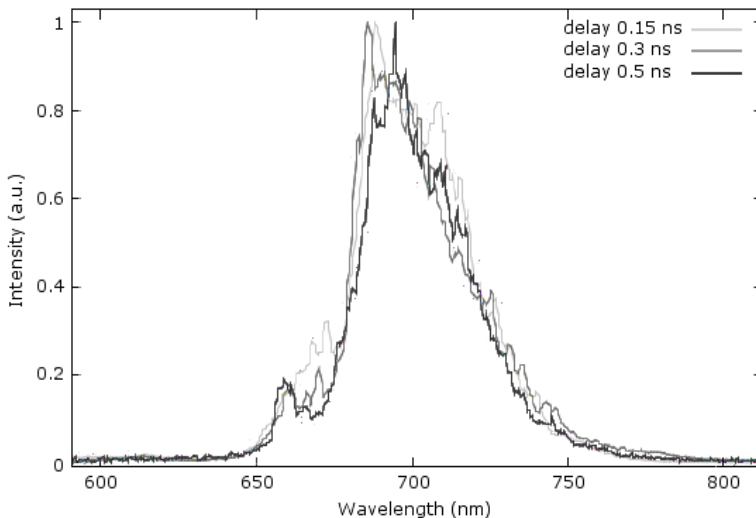


Fig. 8. Backreflected Raman spectra at different prepulse time delays

As for the back scattering calorimetry, we found that a surprisingly small fraction of light (less than 5 % in all cases) was backscattered in our experimental conditions ($I \approx 10^{15} \div 10^{16} \text{ Wcm}^{-2}$, $\lambda = 438 \text{ nm}$). This appears to be in contrast with the results obtained at the Omega facility [15] which gave 33% back reflection at $I \approx 8 \times 10^{15} \text{ Wcm}^{-2}$, and also with results from numerical simulations [16] which also predict large SRS. Although this could be a good news for shock ignition, the detailed reasons for this result still remain to be investigated and understood.

Conclusions

The feasibility of the shock ignition approach to ICF critically relies on the ability to produce a strong shock by coupling an intense laser beam to a payload through an extended plasma corona. In turn it critically depends on the amount of light, which is reflected by parametric instabilities, and the amount and energy of the hot electrons generated in the process. The analysis of our results is still preliminary. However we are confident that the detailed characterization of the preplasma and the plasma conditions will finally allow a precise comparison with numerical simulations.

At the moment our data show a comparatively negligible amount of back-reflected light and seem to confirm that a strong shock may, indeed, be generated. On the other side, the “bell shape” behaviour of shock chronometry and ion diagnostics data seem to suggest that the plasma is dispersed in about

500 ps (data without a preplasma are, indeed, comparable to those obtained with a prepulse to main pulse delay of 500 ps). However, this conclusion does not seem to be supported by XRL deflectometry data (which show that the plasma is still present as late as 900 ps after irradiation with the auxiliary beam) nor by SRS data, which show similar spectra for all delays.

References

- [1] L. J. PERKINS, R. BETTI, K. N. LAFORTUNE, W. H. WILLIAMS: *Shock ignition: a new approach to high gain inertial confinement fusion on the National Ignition Facility*. Phys. Rev. Lett. *103* (2009), 045004.
- [2] H. AZECHI, M. D. CABLE, R. O. STAPF: *Review of secondary and tertiary reactions, and neutron scattering as diagnostic techniques for inertial confinement fusion targets*. Laser and Particle Beams *9* (1991), 119–134.
- [3] J. LINDL: *Development of the indirect-drive approach to inertial confinement fusion and the target physics basis for ignition and gain*. Phys. Plasmas *2* (1995), 3933–4024.
- [4] B. RUS, T. MOCEK, A. R. PRÄG, M. KOZLOVÁ, G. JAMELOT, A. CARILLON, D. ROS, D. JOYEUX, D. PHALIPPOU: *Multimillijoule, highly coherent X-ray laser at 21 nm operating in deep saturation through double-pass amplification*. Phys. Rev. A *66* (2002), 063806.
- [5] M. KOENIG, B. FARAL, J. M. BOUDENNE, D. BATANI, S. BOSSI, A. BENUZZI, C. REMOND, J. PERRINE, M. TEMPORAL, S. ATZENI: *Relative consistency of equation of state by laser driven shock waves*. Phys. Rev. Lett. *74* (1995), 2260–2263.
- [6] J. NEJDL, M. KOZLOVÁ: *Plasma density-gradient measurement using X-ray laser wavefront distortion*. Soft X-Ray Lasers and Applications VIII (J. Dunn, G. J. Tallents, eds.), Proc. SPIE *7451* (2009), 745117.
- [7] R. W. LEE: *User Manual for RATION*. Lawrence Livermore National Laboratory, Livermore 1990.
- [8] T. LEVATO, L. LABATE, N. C. PATHAK, C. CECCHETTI, P. KOESTER, E. DI FABRIZIO, P. DELOGU, A. GIULIETTI, D. GIULIETTI, L. A. GIZZI: *Pin-hole array production and detailed data analysis for advanced single-shot X-ray imaging of laboratory plasmas*. Nucl. Instrum. Meth. Phys. Res. A *623* (2010), 842–844.
- [9] L. A. GIZZI, A. GIULIETTI, D. GIULIETTI, P. KÖSTER, L. LABATE, T. LEVATO, F. ZAMPONI, A. LÜBCKE, T. KÄMPFER, I. USCHMANN, E. FÖRSTER, A. ANTONICCI, D. BATANI: *Observation of electron transport dynamics in high intensity laser interactions using multi-energy monochromatic X-ray imaging*. Plasma Phys. Control. Fusion *49* (2007), B211–B221.
- [10] F. N. BEG, A. R. BELL, A. E. DANGOR, C. N. DANSON, A. P. FEWS, M. E. GLINSKY, B. A. HAMMEL, P. LEE, P. A. NORREYS, M. TATARAKIS: *A study of picosecond laser-solid interactions up to 10^{19} Wcm⁻²*. Phys. Plasmas *4* (1997), 447–457.
- [11] E. WORYNA, P. PARYS, J. WOŁOWSKI, M. MROZ: *Corpuscular diagnostics and processing methods applied in investigations of laser-produced plasma as a source of highly ionized ions*. Laser and Particle Beams *14* (1996), 293–321.
- [12] A. PICCIOTTO, J. KRÁSA, L. LÁSKA, K. ROHLENA, L. TORRISI, S. GAMMINO, A. M. MEZZASALMA, F. CARIDI: *Plasma temperature and ion current analysis of gold ablation at different laser power rates*. Nucl. Instrum. Meth. Phys. Res. B *247* (2006), 261–267.
- [13] *SESAME tables 3712 and 3717 for Al*. SESAME report on the Los Alamos Equation of State Library, Report No. LALP-83-4, T4 Group LANL, Los Alamos 1983.

- [14] R. RAMIS, J. MEYER-TER-VEHN, J. RAMÍREZ: *MULTI2D—a computer code for two-dimensional radiation hydrodynamics*. *Computer Phys. Commun.* *180* (2009) 977–994.
- [15] W. THEOBALD, R. BETTI, C. STOECKL, K. S. ANDERSON, J. A. DELETTREZ, V. YU. GLEBOV, V. N. GONCHAROV, F. J. MARSHALL, D. N. MAYWAR, R. L. MCCRORY, D. D. MEYERHOFER, P. B. RADHA, T. C. SANGSTER, W. SEKA, D. SHVARTS, V. A. SMALYUK, A. A. SOLODOV, B. YAAKOBI, C. D. ZHOU, J. A. FRENJE, C. K. LI, F. H. SÉGUIN, R. D. PETRASSO, L. J. PERKINS: *Initial experiments on the shock-ignition inertial confinement fusion concept*. *Phys. Plasmas* *15* (2008), 056306.
- [16] O. KLIMO, S. WEBER, V. T. TIKHONCHUK, J. LIMPOUCH: *Particle-in-cell simulations of laser–plasma interaction for the shock ignition scenario*. *Plasma Phys. Control. Fusion* *52* (2010), 055013.

Received April 30, 2010

Precise evaluation of the plasma potential in COMPASS tokamak divertor area¹

PAVLINA IVANOVA^{2,3}, TSVIATKO POPOV²,
MIGLENA DIMITROVA³, EVGENIA BENOVA²,
TODOR BOGDANOV², JAN STÖCKEL⁴, REUNARD DEJARNAC⁴

Abstract. In this paper we report results of the precise evaluation of the plasma potential, the electron temperatures and the electron densities during the current shot in He and H in the COMPASS tokamak (IPP.CR, Prague, Czech Republic). The results obtained from processing the data measured by divertor probes confirmed the applicability of the technique proposed. The accuracy of the values evaluated is discussed. The comparison with results from model calculations based on an extended formula for the electron probe current, as well as from a classical method, shows a satisfactory agreement. The results presented demonstrate that the procedure proposed allows one to acquire additional plasma parameters using the electron part of the current–voltage Langmuir probe characteristics in tokamak edge plasma probe measurements in comparison with the classical method, which uses the ion part of the IV characteristics.

Key Words. Plasma potential, electron energy distribution function (EEDF), Langmuir probe, tokamak edge plasma, first derivative probe method.

¹The results presented were obtained in implementation of task P4 of Work Plan 2010 of the Association EURATOM/INRNE.BG in collaboration with the Association EURATOM/IPP.CR, Prague, Czech Republic.

²Faculty of Physics, St. Kl. Ohridski University of Sofia, 5, J. Bourchier Blvd., 1164 Sofia, Bulgaria; e-mail: tpopov@phys.uni-sofia.bg

³Emil Djakov Institute of Electronics, Bulgarian Academy of Sciences, 72, Tzarigradsko Chaussee, 1784 Sofia, Bulgaria

⁴Institute of Plasma Physics, Academy of Sciences of the Czech Republic v.v.i., Za Slovankou 3, 182 00 Prague 8, Czech Republic

1. Introduction

Among the contact methods of plasma diagnostics, the electric probes are the most reliable diagnostic tools allowing one to measure edge plasma parameters with a sufficiently high temporal and spatial resolution. In non-magnetized low-density plasmas Langmuir probes (LP) allow local measurements of the plasma potential, the charged particles density and the electron energy distribution functions, $f(\varepsilon)$, (EEDF) [1]–[7].

In magnetized plasma, the interpretation of the electron part of current–voltage (IV) characteristics above the floating potential, U_{fl} , still remains difficult [8] because the electron part of the IV characteristics is distorted due to the influence of the magnetic field. For this reason, in the strongly magnetized tokamak plasmas, the ion saturation branch of the IV and the part around the floating potential are usually used when retrieving the plasma parameters [9]. This classical method assumes a Maxwellian EDF for the electrons only, but in fact does not measure the real one. The approximation for the probe current around the floating potential, U_{fl} , and ion saturation current, I_{s}^{i} , is [10]

$$I(U) = I_{\text{s}}^{\text{i}} \left\{ 1 - \exp \left[-\frac{e(U_{\text{fl}} - U)}{kT_{\text{e}}} \right] \right\}, \quad (1)$$

where $I_{\text{s}}^{\text{i}} \approx 0.5n_{\text{e}}c_{\text{s}}A_{\text{pr}}e$; n_{e} and e are the electron density and charge; $c_{\text{s}} = [k(T_{\text{e}} + T_{\text{i}})/m_{\text{i}}]^{1/2}$ is the (isothermal) ion acoustic velocity; and A_{pr} is the probe area. The difference between the floating potential and the plasma potential is given by [10]

$$U_{\text{sf}} = \frac{kT_{\text{e}}}{2e} \ln \left[2\pi \frac{m_{\text{e}}}{m_{\text{i}}} \left(1 + \frac{T_{\text{i}}}{T_{\text{e}}} \right) (1 - \delta)^{-2} \right]. \quad (2)$$

For example, for H^{+} ions, $T_{\text{i}} = T_{\text{e}}$ and the secondary electron emission coefficient $\delta = 0$, one obtains $U_{\text{sf}} \approx -2.5kT_{\text{e}}/e$. In [11] the value $U_{\text{sf}} \approx -3.4kT_{\text{e}}/e$ is calculated for a large probe in isothermal plasma. In general this is in agreement with the commonly stated approximation that “the plasma potential is $\approx 3T_{\text{e}}$ above U_{fl} ”.

It is clear that the small uncertainties in the measured ion saturation branch of the IV can lead to a significant error in the evaluation of the plasma potential. On the other hand, the precise evaluation of the plasma potential and the real EEDF is of great importance in understanding the underlying physics of the processes occurring at the plasma edge in tokamaks, such as the formation of transport barriers, plasma-wall interactions, edge plasma turbulence, etc.

We recently proposed a first-derivative probe method [8] for precise evaluation of the plasma potential and the EEDF from the first derivative of the

electron current of the IV characteristics. The method was successfully applied in the investigation in the old Czech CASTOR tokamak. In this paper we report results of the evaluation of the plasma potential, the electron temperatures and the electron densities during the current shot in He and H in the new COMPASS tokamak (IPP.CR, Prague, the Czech Republic). The results obtained from the data measured by divertor probes confirmed the applicability of the technique proposed.

2. First derivative Langmuir probe method

The first-derivative probe method for evaluating the plasma parameters in tokamak edge plasma was published and discussed in details in [8]. The theory for magnetized plasmas was developed for LPs in a non-local approach when the electrons reach the probe in a diffusion regime [12]. The tokamak plasma is usually considered as non-collisional plasma. The edge plasma is strongly turbulent plasma. In the turbulence, the electric field vector changes its orientation in arbitrary directions. This causes changes in the direction of the electrons motion but does not change their kinetic energy. The result is similar to the case of elastic collisions [13], so that to evaluate the EEDF for turbulent edge plasma we can use the method presented in [12]. It was shown there that the electron current flowing to a cylindrical probe negatively biased by potential U_p is given by

$$I_e(U) = -\frac{8\pi eS}{3m^2} \int_{eU}^{\infty} \frac{(W - eU)f(W) dW}{\gamma(W) \left[1 + \frac{(W - eU)}{W} \psi(W)\right]}, \quad (3)$$

where W is the electron energy; e , m and n are the electron charge, mass and density; S is the probe area; U is the probe potential with respect to the plasma potential U_{pl} ($U = U_p - U_{pl}$). The geometric factor $\gamma = \gamma(R/\lambda)$ assumes values in the range $0.71 \leq \gamma \leq 4/3$ (R being the probe radius) [12]. Here $f(W)$ is the isotropic EEDF normalized by

$$\frac{4\pi\sqrt{2}}{m^{3/2}} \int_0^{\infty} f(W) \sqrt{W} dW = \int_0^{\infty} f(\varepsilon) \sqrt{\varepsilon} d\varepsilon = n \quad (4)$$

and the diffusion parameter $\psi(W)$ is given by

$$\psi(W) = \frac{1}{\gamma\lambda(W)} \int_R^{\infty} \frac{D(W) dr}{(r/R)D(W - e\varphi(r))}. \quad (5)$$

Here $D = v\lambda(W)/3$ is the diffusion coefficient, where $\lambda(W)$ is the free path of the electrons with velocity v and energy W ; R is the probe radius and $\varphi(r)$ is the potential variation introduced by the probe. As it was shown in [8] for probes oriented perpendicular to the magnetic field, the diffusion parameter is

$$\psi_{\perp}(W) = \frac{R \ln\left(\frac{\pi L'}{4R}\right)}{16\gamma R_L(W, B)}. \quad (6)$$

For probes oriented parallel with respect to the magnetic field, the area disturbed by the probe is assumed to be an oblate ellipsoid of revolution and the diffusion parameter can be written as

$$\psi_{\parallel}(W) = \frac{\pi L'}{64\gamma R_L(W, B)}. \quad (7)$$

Here L' and $R_L(W, B)$ are the characteristic length of the turbulences and the electron Larmor radius.

It was shown in [8] that at strong magnetic fields, i.e., for high values of the diffusion parameter $\psi(W) = \psi_0/\sqrt{W} \gg 1$, the minimum of the first derivative of the IV characteristics is shifted negatively by a value of $1.5T_e$ with respect to the plasma potential. The model calculations of the electron probe current for a Maxwellian EEDF ($T_e = 10$ eV) using equation (3) are presented in Fig. 1. Figure 2 shows its first derivatives for different values of ψ_0 .

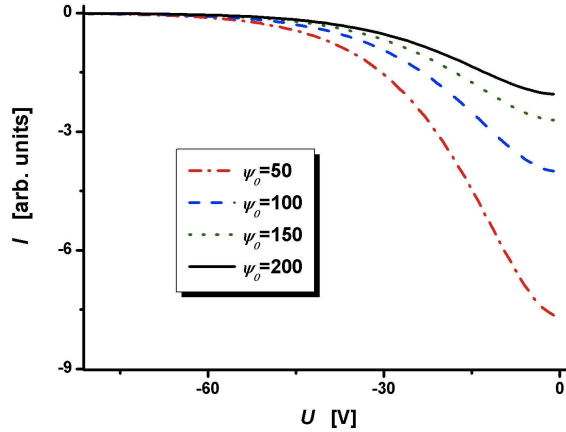


Fig. 1. Model calculations for a Maxwellian EEDF ($T_e = 10$ eV) of the IV characteristics (Eq. (3)) at different values of ψ_0 in the diffusion parameter $\psi(W) = \psi_0/\sqrt{W}$

In this case, and in order to evaluate accurately U_{p1} , we propose the following procedure: the electron temperature is evaluated from the slope in logarithmic scale of the first derivative of the non-distorted part of the experimental IV characteristics. Using this temperature, a model curve of the first derivative (derivative of equation (3)) is calculated. Then the best fit with the experimental first derivative provides the value of the plasma potential.

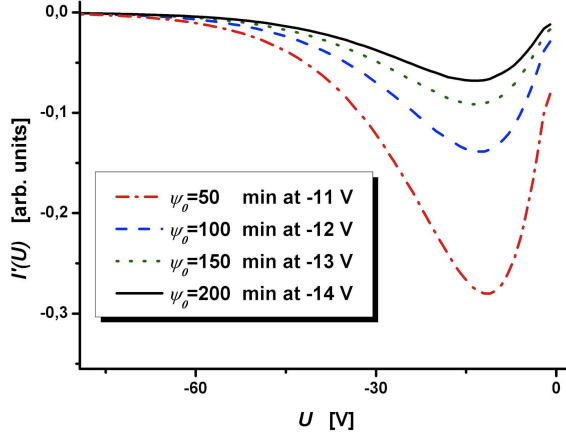


Fig. 2. Model calculations for a Maxwellian EEDF ($T_e = 10 \text{ eV}$) of the first derivative of the IV characteristics at different values of ψ_0 in the diffusion parameter equation $\psi(W) = \psi_0/\sqrt{W}$

As it was shown [8], the EEDF is not represented by the second derivative of the electron probe current (Druyvesteyn formula) but rather by its first derivative.

$$I_e'(U) = -\text{const} \frac{eU\sqrt{eU}}{\psi_0} f(eU) \quad (8)$$

Taking into account equation (6) for the EEDF measured by a cylindrical probe perpendicular to the magnetic field, we obtain

$$f(\varepsilon) = -\frac{3\sqrt{2m}R \ln\left(\frac{\pi L'}{4R}\right) dI}{32e^3 S R_L(\varepsilon, B) U dU}. \quad (9)$$

The EEDF measured by a cylindrical probe parallel to the magnetic field is expressed as

$$f(\varepsilon) = -\frac{3\pi\sqrt{2m}L' dI}{128e^3 S R_L(\varepsilon, B) U dU}. \quad (10)$$

3. Langmuir probe measurements in COMPASS divertor area

The divertor probe system on COMPASS consists of 39 graphite single Langmuir probes embedded in the divertor target, providing profiles with typical spatial resolution in the poloidal direction down to 5 mm. The probe area exposed in the plasma is $S = 112.5 \times 10^{-6} \text{ m}^2$.

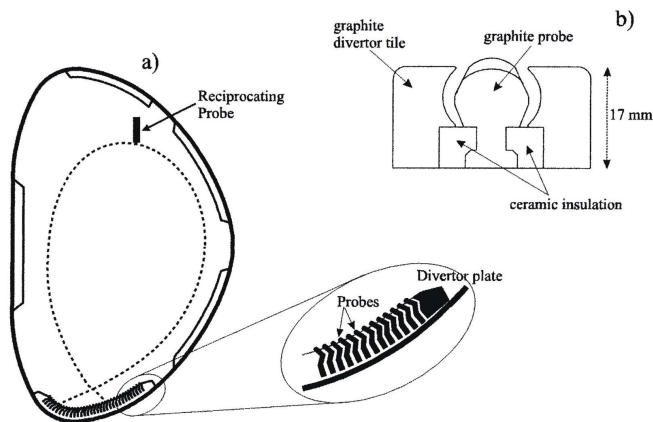


Fig. 3. a—Poloidal cross-section of COMPASS with the position of the divertor probe system; b—toroidal cross-section through the divertor target showing a Langmuir probe

During the starting campaign of the new Czech COMPASS, IPP tokamak, probe measurements were performed in H_2 and He plasma. As it was found, the signals on the divertor probes appeared at the end of the discharge, when the plasma column moved downward. The duration of the measurable signal was about 5 ms. The signal varied in time so that we did not observe any quasi-stationary phase, which is required to measure the IV characteristics in a standard way, when the sweeping voltage should have a triangular shape and the ramp-up/ramp-down phases should be as short as possible (0.5 ms).

The record of the sweeping probe bias U_p (a) from Kepco 100-4M and the probe current I (b) during shot 889 in probe #4 (working gas He) is presented in Fig. 4.

We processed the probe IV characteristics #2, #7 and #8 as indicated in Fig. 4b. The IV #1, #3, #4, #5 and #6 are too noisy. The data measured was processed by the classical method [10], which makes use of the ion saturation part and the part around floating potential of the IV characteristics, as well as by the first derivative probe method [8].

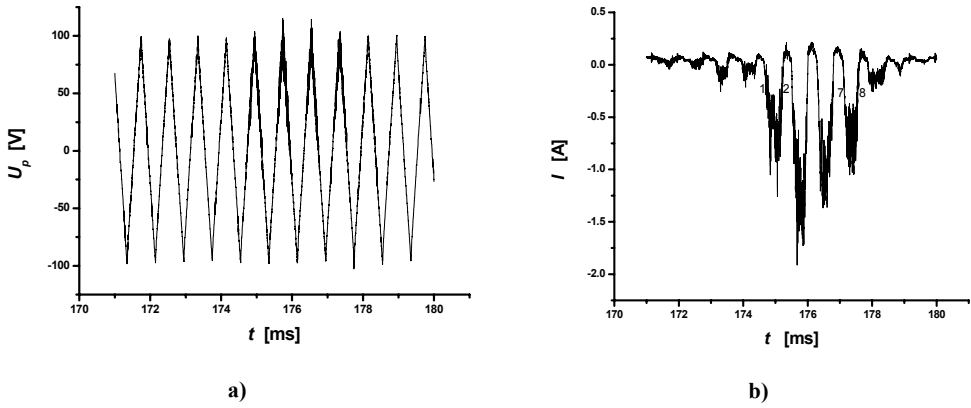


Fig. 4. a—Probe bias U_p ; b—probe current $I(U_p)$ as a function of the time t during shot 889 for probe #4

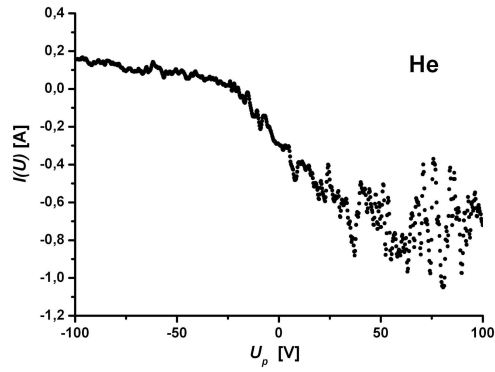


Fig. 5. Single IV characteristic, shot 889 for probe #4, IV7; working gas He

To demonstrate the procedure of evaluating U_{p1} , $f(\varepsilon)$ and n , we will analyze a single IV characteristics, shot 889 for probe #4; working gas He, presented in Fig. 5.

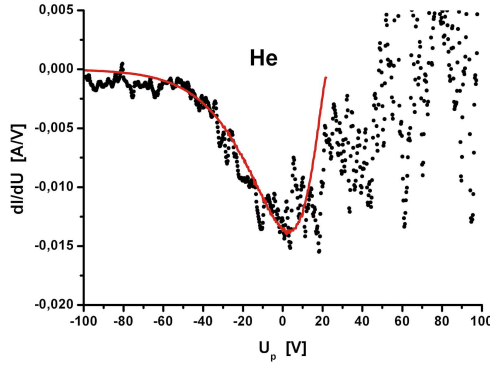


Fig. 6. First derivative of the smoothed experimental IV curve (dots), shot 889 for probe #4, IV7; model curve – solid line

Figure 6 presents the first derivative of the smoothed IV curve. In the same figure the fit with the model curve (first derivative of equation (3)) is presented. Using this comparison one can evaluate the plasma potential $U_{pl} = 21$ V. One can also observe there a more or less pronounced bend in the experimental curve. In practice, even a small increment of $I(U)$ at a probe potential U positive with respect to plasma potential leads to $I'(U)$ deviating from zero at U_{pl} . Additional reasons for this feature come are the plasma potential fluctuations due to the plasma turbulence and the smoothing of the experimental IV characteristics.

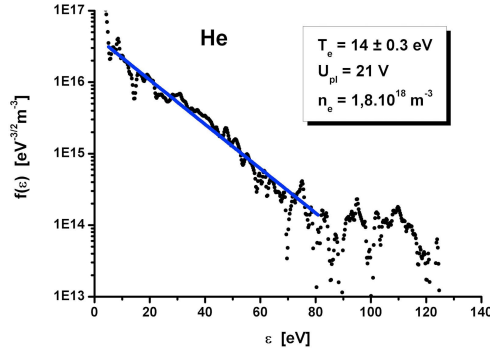


Fig. 7. The EEDF obtained by the first derivative probe method

Figure 7 presents the EEDF obtained for perpendicular probe #4, shot 889, by using equation (10) (dots). The EEDF may be approximated by a Maxwellian with electron temperature $T = 14$ eV (solid line). The electron density is calculated by using equation (4).

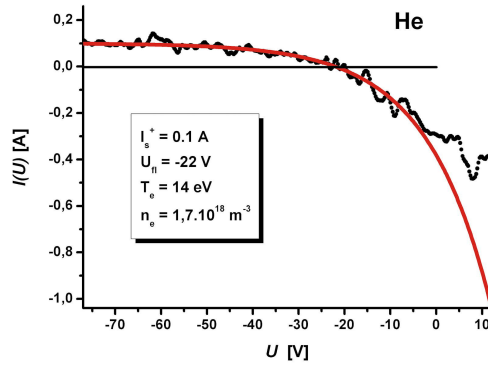


Fig. 8. Single IV characteristics, shot 889 for probe #4, IV7 and calculated by the classical method (solid line) using equation (1)

For comparison, Fig. 8 presents the results for the electron temperature and density obtained by the classical method. As one can see, the agreement is satisfactory.

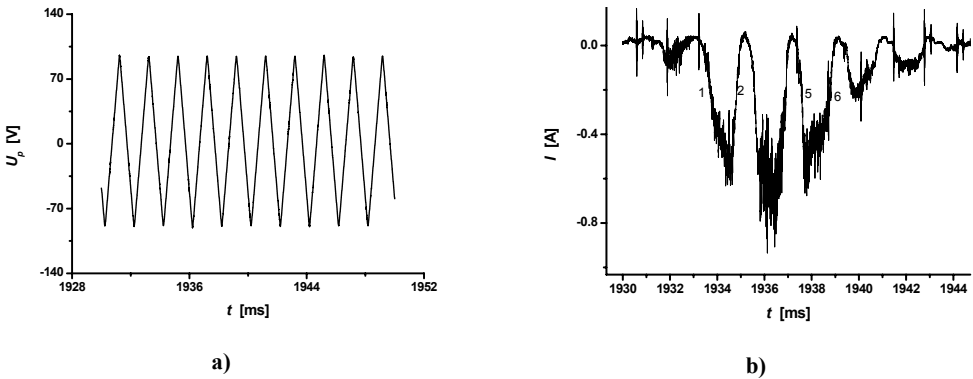


Fig. 9. a—Probe bias U_p ; b—probe current $I(U_p)$ as a function of the time t during the shot 976 for probe #4

Similar results were acquired from shot 976 with working gas H_2 . Examples are presented in Figs. 9–13.

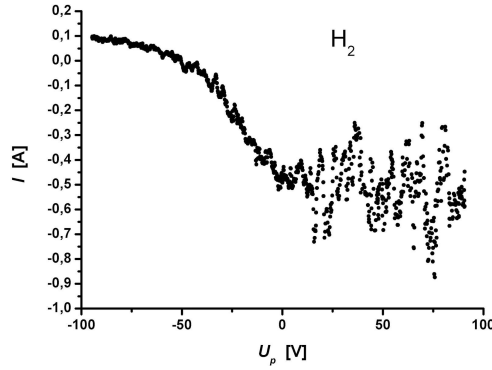


Fig. 10. Single IV characteristics, shot 976 for probe #4, IV3 working gas H₂

Examples of the results obtained are presented in Table 1. The uncertainties in the values are calculated by regression analysis. The best fit of the plasma potential values has accuracy of about 10%. For comparison, the last table row presents the values intervals obtained by the classical method. The lower limit was estimated by using equation (2). The difference between the floating and the plasma potential is $U_{sf} \approx -2.5kT_e/e$ for H⁺ and $U_{sf} \approx -2.8kT_e/e$ for He⁺ (here the electron temperature is in units of K). The divertor probes are of a relatively high size, which is why we used as an upper limit the expressions $U_{sf} \approx -3.4kT_e/e$ for H⁺ and $U_{sf} \approx -4.1kT_e/e$ for He⁺ [11]. One can see that our estimates agree well with the intervals yielded by the classical method and are closer to the upper limits. This confirms the assumption of large probe approach.

Table 1. Results

	He, shot 889 probe #4			H ₂ , shot 976 probe # 4		
	IV2	IV7	IV8	IV2	IV3	IV6
T_e , eV	15 ± 0.5	14 ± 0.3	14 ± 0.4	14 ± 0.9	15 ± 0.8	10 ± 0.9
n_e , m ⁻³	(2.2 ± 0.4) $\times 10^{18}$	(1.8 ± 0.3) $\times 10^{18}$	(1.9 ± 0.4) $\times 10^{18}$	(1.2 ± 0.2) $\times 10^{18}$	(1.5 ± 0.3) $\times 10^{18}$	(1.0 ± 0.2) $\times 10^{18}$
U_{pl} , V	29 ± 3	21 ± 2	23 ± 2	-1 ± 2	-3 ± 2	-8 ± 3
U_{pl} , V (classical method)	$19 \div 37$	$18 \div 35$	$11 \div 28$	$-20 \div 0$	$-12 \div 1$	$-22 \div 11$

Finally, using the values obtained by the first derivative probe method we performed model calculations for the IV characteristics (eq. (3)). Examples of the comparison with the experimental IV curves are presented in Fig. 14. The good agreement between the model and experimental curves can be seen.

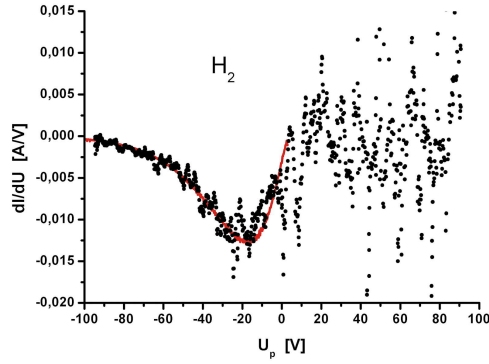


Fig. 11. First derivative of the smoothed experimental IV curve (dots), shot 976 for probe #4, IV3; model curve – solid line

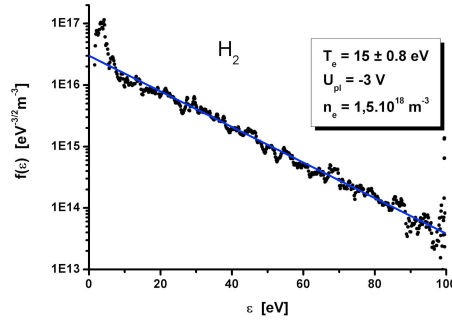


Fig. 12. The EEDF obtained by using the first derivative probe method

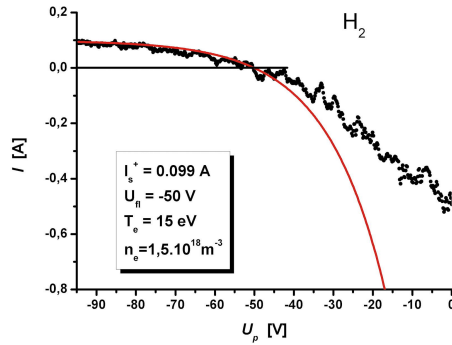


Fig. 13. Single IV characteristics, shot 976, for probe #4, IV3 and calculated by the classical method (solid line) using equation (1)

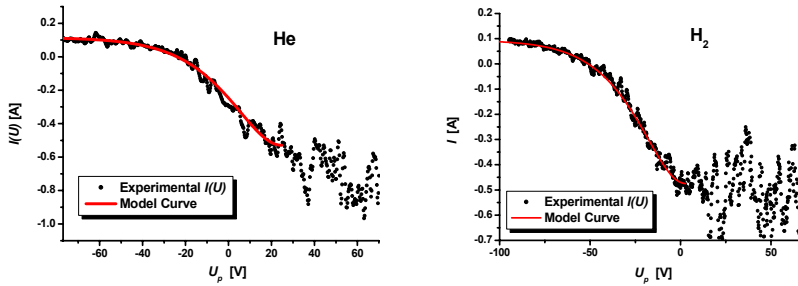


Fig. 14. Comparison between model calculations (solid lines) and IV7 for He and IV3 for H_2 (dots)

4. Conclusions

The first derivative probe method was used for precise evaluation of the plasma potential, the EEDF (or, respectively, the electron temperature) and the electron density during the current shots in the COMPASS tokamak, (IPP.CR, Prague, Czech Republic).

- The results obtained after processing the data measured by divertor probes in H_2 and He plasma are reported.
- The accuracy of the values evaluated is discussed.
- The comparisons with model calculations based on an extended formula for the electron probe current, as well as with results obtained by a classical method, show a satisfactory agreement.

The results presented demonstrate that the procedure proposed allows one to acquire plasma parameters and, in particular, the plasma potential with high accuracy using the electron part of the current–voltage LP characteristics in tokamak edge plasma probe measurements in comparison with the classical method, which uses the ion part of the IV characteristics.

References

- [1] M. J. DRUYVESTSEYN: *Der Niedervoltbogen*. Zeitschrier für Physic a Hadrons and Nuclei, *64* (1930), 781–798.
- [2] Y. M. KAGAN, V. I. PEREL: *Probe methods in plasma research*. Soviet Physics Uspekhi, *6* (1964), 767–791.
- [3] F. F. CHEN: *Plasma Diagnostic Techniques*. Academic Press, New York 1965.
- [4] J. D. SWIFT, M. J. R. SCHWAR: *Electrical probes for plasma diagnostics*. Elsevier, New York 1969.
- [5] N. HERSHKOWITZ: *Plasma Diagnostics*. Academic Press, Boston 1989.
- [6] V. I. DEMIDOV, N. B. KOLOKOLOV, A. A. KUDRYAVTSEV: *Probe methods for low-temperature plasma investigations*. Energoatomizdat, Moscow 1996.
- [7] TSV. K. POPOV, M. DIMITROVA, F. M. DIAS, V. N. TSANEVA, N. A. STELMASHENKO, M. G. BLAMIRE, Z. H. BARBER: *Second derivative Langmuir probe diagnostics of gas discharge plasma at intermediate pressures (review article)*. Journal of Physics: Conference series, *44* (2006), 60–69.
- [8] TSV. K. POPOV, P. IVANOVA, J. STÖCKEL, R. DEJARNAC: *Electron energy distribution function, plasma potential and electron density measured by Langmuir probe in tokamak edge plasma*. Plasma Physics and Controlled Fusion, *51* (2009), 065014.
- [9] J. A. TAGLE, P. C. STANGEBY, S. K. ERENTS: *Errors in measuring electron temperatures using a single Langmuir probe in a magnetic field*. Plasma Physics and Controlled Fusion, *29* (1987), 297–301.
- [10] P. C. STANGEBY, G. M. MCCRACKEN: *Plasma boundary phenomena in tokamaks*. Nuclear Fusion, *30* (1990), 1225–1238.
- [11] O. V. KOZLOV: *Electric probe in plasma*. Atomizdat, Moscow 1969.
- [12] R. R. ARSLANBEKOV, N. A. KHROMOV, A. A. KUDRYAVTSEV: *Probe measurements of electron energy distribution function at intermediate and high pressures and in a magnetic field*. Plasma Sources Science Technology, *3* (1994), 528–538.
- [13] V. E. GOLANT, A. P. ZHILINSKI, I. E. SAKHAROV: *Fundamentals of Plasma Physics*. Wiley, New York 1980.

Diamond detectors for diagnostic of fast alpha particles escaping from the tokamak plasma¹

IWONA WODNIAK^{2,3}, KRZYSZTOF DROZDOWICZ²,
JAN DANKOWSKI², BARBARA GABAŃSKA², ANDRZEJ IGIELSKI²,
ARKADIUSZ KUROWSKI², BARBARA MARCZEWSKA²,
TOMASZ NOWAK², URSZULA WOŹNICKA²

Abstract. Spectrometric properties of the diamond detectors have been investigated. Synthetic high-purity CVD (Chemical Vapour Deposition) monocrystalline diamond detectors have been used, fabricated for this dedicated application by the Diamond Detector, Ltd. The diamond plates have been 0.05 mm and 0.5 mm thick with the active area diameter equal to 1.9 mm. The energy calibration and the study of energy resolution of the detectors have been carried out using a triple alpha particle isotope source, ²³⁹Pu, ²⁴¹Am, ²⁴⁴Cm (AMR33). Very good results have been obtained comparing to the classical silicon detector. Spectrometric properties of the detectors have been investigated using a Van de Graaff accelerator. Accelerated helium ions have been scattered on the Au thin foil (100 μg cm⁻²) and the back-scattered ions (alphas) have been measured at a well defined angle which assured a well defined monoenergetic beam, changed between 0.4 and 2 MeV. A very good linearity of the energy measurement has been found, including also results obtained with the AMR33 source which emits alpha particles with the energies around 5.5 MeV. This result is very promising in aspect of potential application of diamond detectors for spectrometric diagnostic of the lost alphas which maximum energy from the thermonuclear reaction is equal to 3.5 MeV.

Key Words. Fast alpha particles, diamond detector, tokamak, ITER.

¹This research has been supported by the EFDA (European Fusion Development Agreement) WP08-09-DIAG-01-02. Task Agreement “Escaping Fast Alpha Diagnostics” and the Association EURATOM–IPPLM (Poland). We are indebted to Prof. Marian Jaskóła and Dr. Andrzej Korman for preparation of the experiment at the Van de Graaff accelerator in the Soltan Institute of Nuclear Studies (Warsaw, Poland) and for their assistance at the measurements and for valuable discussions. I. W. has been partly supported by the EU Human Capital Operation Program, Polish Project No. POKL.04.0101-00-434/08-00.

²The Henryk Niewodniczański Institute of Nuclear Physics Polish Academy of Sciences, Radzikowskiego 152 Str., PL-31-342 Kraków, Poland

³Interdisciplinary Doctoral Studies, AGH Univ. of Science and Technology, Mickiewicza 30 Av., Kraków, Poland

1. Introduction

International Thermonuclear Experimental Reactor (ITER), the next fusion device after Joint European Torus is built in Cadarache in France. This tokamak installation will be operating with the deuterium-tritium fuel. In a fusion reaction between deuterium and tritium will be created a neutron, α particle and energy. Some fraction of the created α particles instead of transmitting their energy to deuterium and/or helium ions, can take some part of energy outside. This is the reason why detection of so-called ‘escaping α particles’ is very important to get information on the energetic balance in tokamak [1], [2]. The flux of neutrons and α particles will be large in tokamak and the detection will be carried at harsh environment, so damage resistant detectors will be required. High flux of particles and high temperature restrict the use of common semiconductors, e. g. silicon detectors. Diamond has some of the most extreme physical properties of any materials. Such properties as its large band gap, high breakdown, high electron and hole mobility, large saturated carrier velocity, radiation and corrosion resistance, optical transparency, fast response, low noise arising from leakage current make it an attractive semiconductor detector used for spectrometric α measurement [3]–[5]. These parameters ensure its usage especially in extremely hard conditions. Comparison of properties of diamond and silicon is presented in Table 1. The diamond detector can detect every kind of electromagnetic radiation with energy greater than the width band gap including: UV, X-rays and γ -rays and high energy particles, e. g. α particles, neutrons, electrons and others. A lower atomic number of diamond than of silicon causes lower sensitivity for electromagnetic radiation [7].

Operating principle of a diamond detector is simple. The diamond detector is a semiconductor detector. An external electric field is supplied to the electrodes of the diamond detector from a power supply unit. The radiation due to the interaction with diamond can carry electrons from the valence band to the conduction band and in this way create free carriers: electrons and holes in diamond. The external applied electric field separates the pairs of electrons and holes before they recombine. Electrons drift towards the anode, holes to the cathode, and the charge is collected by the electrodes (charge collection). The motion of the free carriers in the applied electric field across detector causes an electrical current in an external circuit. A schematic figure of the semiconductor detector is presented in Fig. 1.

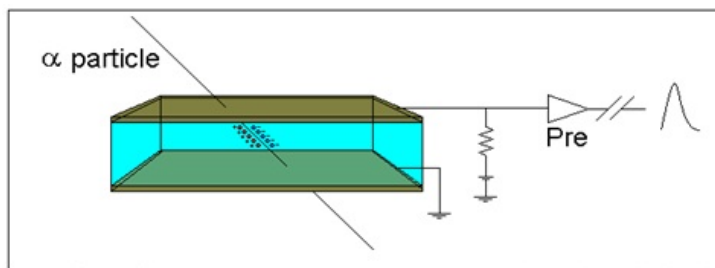
Fig. 1. Principle of α detection by a semiconductor detector

Table 1. The physical properties of diamond and silicon

Property	Diamond	Silicon
Mass density [g cm^3]	3.5	2.33
Atomic number	6	14
Band gap [eV]	5.5	1.12
Energy to create e-h pair [eV]	13	3.6
Breakdown field [V m^{-1}]	10^7	3×10^5
Intrinsic carrier density [cm^{-3}]	$< 10^3$	1.5×10^{10}
Resistivity [$\Omega \text{ cm}$]	$> 10^{11}$	2.3×10^5
Electron mobility [$\text{cm}^2 (\text{Vs})^{-1}$]	1800	1350
Hole mobility [$\text{cm}^2 (\text{Vs})^{-1}$]	1200	480
Saturation velocity [km s^{-1}]	220	82

2. Measurements of alpha particles by the diamond detector

The synthetic high-purity CVD (Chemical Vapour Deposition) monocrystalline diamond has been used in the experiment. The diamond detector⁴ is a single crystal plate that has a thickness $0.05 (+0.01, -0.02)$ mm, size of $2.5 \text{ mm} \times 2.5 \text{ mm} (\pm 0.01 \text{ mm})$ and gold contacts of the thickness of 20 nm. The diameter of the detector together with housing is 27 mm and the active diameter of the diamond detector on which the irradiation is fallen equals 1.9 mm. The energy calibration and the study of energy resolution of the diamond and silicon detectors have been carried out using a triple alpha particle isotopic source, ^{239}Pu , ^{241}Am , ^{244}Cm (AMR33). The energy resolution of the diamond detector has been evaluated using the detection line consisting of the diamond

⁴Diamond Detector, Ltd.

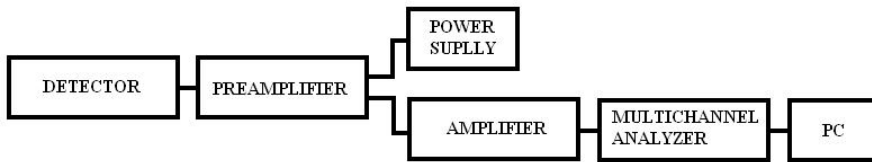


Fig. 2. Block diagram of the detection line

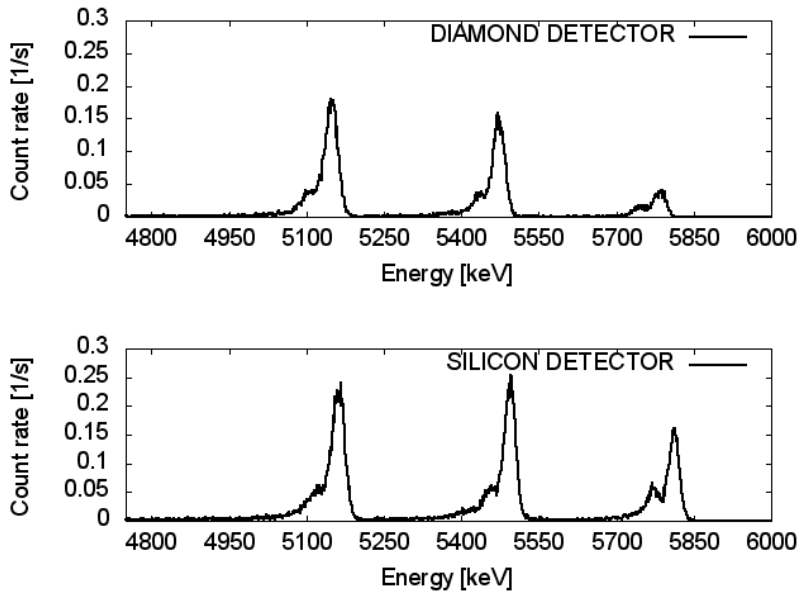


Fig. 3. Energy spectra of the AMR33 source recorded with the diamond and silicon detectors

detector with the SMA connector and the charge preamplifier ORTEC 142A, the spectroscopy amplifier ORTEC 672, the multichannel analyzer ORTEC 927 and a computer. A schematic block diagram of the detection line is presented in Fig. 2.

The diamond detector has always been operated and stored at the room temperature. The time of data collection has been equal 1800 s. The α spectra acquired by the diamond and silicon detectors are shown in Fig. 3.

The AMR33 source emits α particles with three main energies, therefore three corresponding peaks are clearly visible in the spectra. There are other small peaks that appear at the left hand side of the main peaks due to small contributions of α particles emitted by the AMR33 source with lower energies.

Energies of α particles emitted by the AMR33 source, energies of the α peaks returned from the calibration lines and full width at half maximum of the peaks are presented in Table 2. The differences between energies of α particles emitted by the AMR33 source and these returned values of energy are small and do not exceed the half-width of the peaks. Comparison of energy resolution of these detectors shows that the diamond detector has as good energy resolution as the silicon detector.

Table 2. Alpha particle energies returned from the calibration lines and energy resolutions of the detectors

E_t [keV]	Diamond detector				Silicon detector			
	E_m [keV]	$E_t - E_m$ [keV]	ΔE [keV]	$\frac{\Delta E}{E_m}$ [%]	E_m [keV]	$E_t - E_m$ [keV]	ΔE [keV]	$\frac{\Delta E}{E_m}$ [%]
5156.65	5146	11	23	0.45	5166	-10	24	0.46
5485.68	5469	17	26	0.48	5496	-10	20	0.36
5804.86	5784	21	21	0.36	5813	-8	19	0.33

E_t is energy of α particles emitted by the AMR33 source, E_m is determined peak energy of α particles and ΔE is full width at half maximum of the peak (FWHM).

3. Measurements of the monoenergetic helium ion beams

Spectrometric properties of the diamond detector have been investigated using a Van de Graaff accelerator that is placed in a laboratory of the Institute of Nuclear Studies (Świerk/Otwock, Warsaw Branch, Poland). The Van de Graaff accelerator has accelerated the once-ionized helium ions (${}^4_2\text{He}^+$) to obtain finally monoenergetic beam of the α particles. The whole arrangement has been placed in a vacuum chamber (Fig. 4) which has been connected with the accelerator through the pipe 1. The accelerated ion beam has passed along the pipe 1 which has been introduced into the vacuum chamber and then has fallen on a scattering foil. The thin gold foil of superficial mass $100 \mu\text{g cm}^{-2}$ has been held by two handles. The diamond detector has been placed under the β (45°) angle with respect to the beam of the ions and 4 cm from the scattering foil. Only the ions scattered back under the angles β have been detected. The position of the diamond detector was not changed in all measurements. Two collimators have been set within the pipe 1 that have had the diameter 2 mm and 1 mm respectively. These collimators have been placed at the distance of 170 mm from each other. The Faraday's box has collected the ions which have undergone through the foil. The electronic line has been the same as in the calibration measurements.

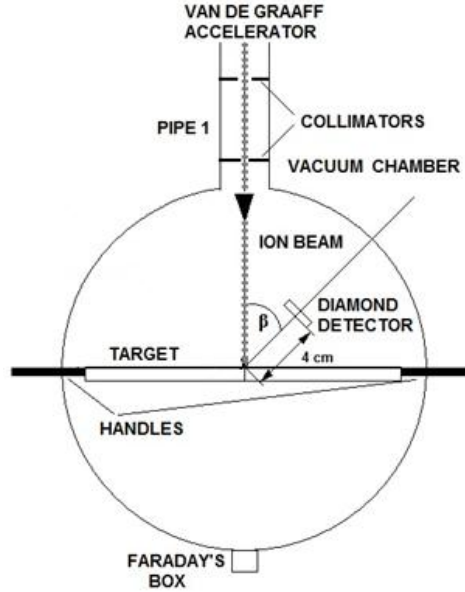


Fig. 4. Geometry of the detection of the backscattered ions

The incident beam of helium ion ${}^4_2\text{He}^+$ (energy E_0) has bombarded the thin gold foil. The accelerated ion of mass M has penetrated the foil and has interacted via either elastic collision with atoms of gold of mass M_1 or inelastic collision with electrons. The final energy E_1 of ions scattered under the angle $\Theta = 180^\circ - \beta$ can be calculated from the relation [8]

$$K = \frac{E_1}{E_2} = \left[\frac{(M_1^2 - M^2 \sin^2 \Theta)^{1/2} + M \cos \Theta}{M_1 + M} \right]^2. \quad (1)$$

The following energies E_0 of the incident helium ions have been used: 400 keV, 1000 keV, 1500 keV and 2000 keV. The scattered ion energies have been found from Eq. (1). This calculation is insufficiently precise because Eq. (1) is exactly fulfilled for one-atomic layer of the gold. The maximum loss of energy of helium ions has been estimated in gold layer of a finite thickness on the base of superficial mass and stopping power [9]. After subtracting from initial energy of helium ions E_0 this estimated maximum loss energy, the energy E_3 has been obtained. The results of the calculation and the values of the measured energies of the helium ions are collected in Table 3. The calibration made with the AMR33 source has been used. The energy spectra of helium ions acquired by the diamond detector are presented in Fig. 5.

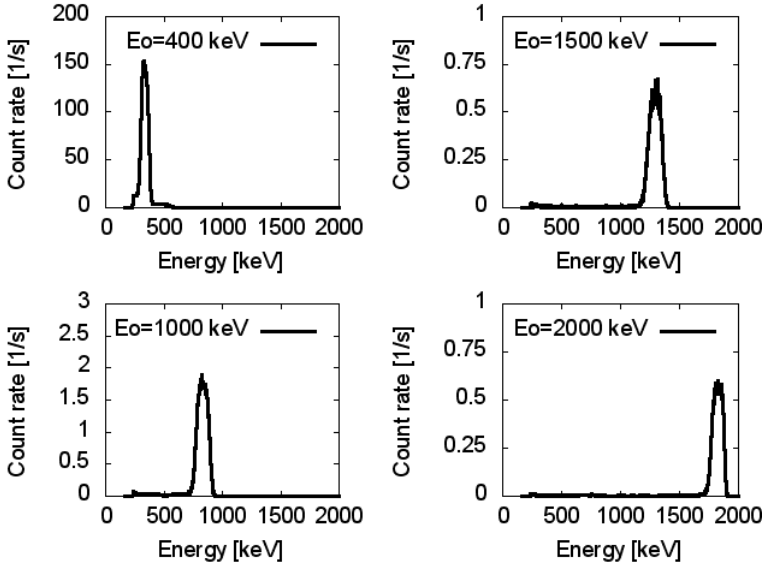


Fig. 5. Energy spectra of helium ions scattered on gold foil of $100 \mu\text{g cm}^{-2}$ recorded with the diamond detector

Table 3. Calculated (E_1 and E_3) and measured (E_m) energies of the helium ions

E_0 [keV]	E_1 [keV]	$\sigma(E_1)$ [keV]	E_3 [keV]	$\sigma(E_3)$ [keV]	E_m [keV]	ΔE [keV]
400	373	11	324	44	330	50
1000	933	27	908	54	826	110
1500	1399	40	1411	52	1350	130
2000	1866	54	1917	48	1836	96

Linearity of the amplitude signal has been investigated as well. The measured peak energy values E_m as a function of the known values of the scattered helium ion energy E_1 and peak positions E_t of the AMR33 source are plotted in Fig. 6. All the points lie perfectly on the same calibration line which has been obtained from measurements with the monoenergetic beams only.

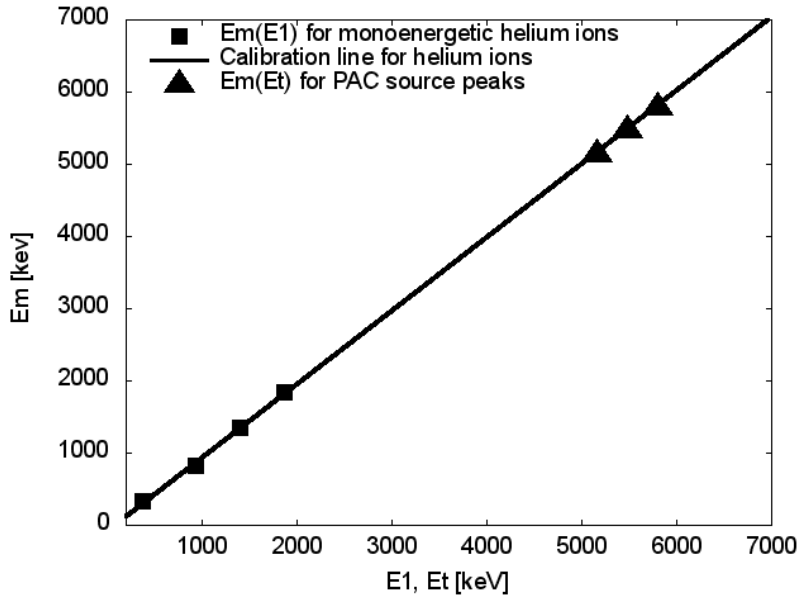


Fig. 6. E_m vs. reference (beam E_1 or source E_t) α energy

4. Conclusion

The performed measurements of energy resolution point out that the diamond detector has the energy resolution comparable with the silicon detector. The experiment relying on the measurements of the well defined helium ion energies shows that the determined energies of helium ions differ only about a half width of the peak from their calculated or estimated energies. A very good linearity of the detector signal vs. the helium ion energy has been received, including also the results obtained with the AMR33 source that emits α particles with the energies about 5.5 MeV. The maximum energies of α particles from the thermonuclear reaction will be equal 3.5 MeV, so the obtained results are very promising in the aspect of the application of the diamond detector for the spectrometric detection of α particles.

References

- [1] C. LLEWELLYN SMITH: *The path to fusion power*. Eur. Phys. J. Special Topics., 176 (2009), 167–178.
- [2] D. S. DARROW, S. J. ZWEBEN, H. W. HERRMANN: *Alpha particle loss diagnostics in TFTR and tokamak reactors*. Fusion Eng. Design, 34–35 (1997), 53–58.
- [3] M. ANGELONE, D. LATTANZI, M. PILLON: *Development of single crystal diamond neutron detectors and test at JET tokamak*. Nucl. Instrum. Meth. A, 595 (2008), 616–622.
- [4] A. GALBIATI, S. LYNN, K. OLIVER: *Performance of monocrystalline diamond radiation detectors fabricated using TiW, Cr/Au and a novel ohmic DLC/Pt/Au electrical contact*. IEEE Trans. Nucl. Sci., 56 (2009), 1863–1874.
- [5] F. FOULONA, P. BERGONZOA, V. N. AMOSOV: *Characterisation of CVD diamond detectors used for fast neutron flux monitoring*. Nucl. Instrum. Meth. A, 47 (2002), 495–499.
- [6] W. DULINSKI, K. K. GAN, S. HAN, J. HASSARD, A. HOWARD, H. KAGAN, S. KANDA, D. R. KANIA, R. KASS, S. K. KIM, R. L. MALCHOW, E. NYGÅRD, L. S. PAN, S. ROE, J. STRAVER, S. R. SCHNETZER, R. STONE, Y. SUGIMOTO, R. J. TESAREK, W. TRISCHUK, G. B. THOMSON, R. TURCHETTA, R. WAGNER, P. WEILHAMMER, C. WHITE, S. ZHAO: *Diamond detectors for future particle physics experiments*. 27th International Conference on High-energy Physics (P. J. Bussey, I. G. Knowles). Institute of Physics, Glasgow 1994, CERN-PPE-94-222.
- [7] A. MAINWOOD: *CVD diamond particle detectors*. Diamond Rel. Mater., 7 (1998), 504–509.
- [8] F. BASSANI, G. L. LIELD, P. WYDER: *Encyclopedia of Condensed Matter Physics*. Elsevier Ltd., 2005.
- [9] <http://www.nucleonica.net>, NUCLEONICA – a new nuclear science web portal from the European Commission’s Joint Research Centre containing the compiled base of data., April 22, 2010.

Received May 13, 2010

The optical system for visible plasma radiation measurements in the COMPASS tokamak – design and testing¹

DIANA NAYDENKOVA^{2,3}, VLADIMÍR WEINZETTL³,
JAN STÖCKEL³, DAVID ŠESTÁK³, FILIP JANKY^{2,3}

Abstract. The COMPASS tokamak will be equipped with a tomographic system for visible plasma radiation measurements with both high temporal and spatial resolutions. The system was already designed and manufactured. Nowadays the components of the system are under tests. The detection part tests are described in article. Spectroscopic measurements were done on the COMPASS tokamak during the first phase of experiments.

Key Words. COMPASS tokamak, visible plasma radiation tomography, visible plasma radiation spectroscopy.

Introduction

The COMPASS tokamak, a divertor device with a clear H-mode and ITER-relevant geometry ($R = 0.56$ m, $a = 0.23 \times 0.38$ m, $I_p = 200 \div 400$ kA, $B_T = 1.2 \div 2.1$ T and pulse length up to 1 s), was reinstalled to IPP Prague from Culham in U.K. [1]. Many new diagnostic tools, among them multichannel multirange spectroscopic diagnostics, have been built to address aims of the new scientific program of COMPASS presently focused on H-mode physics and pedestal investigations. The main aim of spectroscopic measurements there is to study the visible and near ultraviolet radiation of excited neutral atoms and ions from the plasma periphery, in particular to monitor hydrogen recycling and impurity influx. These parameters but in another discharge regimes have

¹This work was performed in the frame of the grant No. 202/08/H057 and the grant GA CR No. 202/09/1467.

²Charles University in Prague, Faculty of Mathematics and Physics, V Holešovičkách 2, 180 00, Prague, Czech Republic

³Institute of Plasma Physics AS CR, v.v.i., Association EURATOM/IPP.CR, Za Slovankou 3, 182 00 Prague, Czech Republic

been already studied on other toroidal devices [2], [3] using analogical diagnostics. The applied principles can be also be used for the ITER tokamak [4]. It is the only in-situ temporally resolved method to study impurity transport in small-scale tokamaks. The advantage of our system is very high time resolution, comparing with other systems (usually CCD based), and at the same time quite good spatial resolution (~ 1 cm). The disadvantage included in the system design is a strong space limitation given by size and positions of diagnostic ports on COMPASS and the fact that only two observation points located at the same toroidal position are available for tomographic measurements. Nowadays the complex of spectroscopic diagnostics is under construction. However, some parts of the system like two minispectrometers have been already in operation in temporal set-up.

The high-speed miniature Czerny–Turner type spectrometers (HR2000+) provide measurements of hydrogen and the most intensive impurity spectral lines in the ranges $247 \div 472$ nm and $460 \div 663$ nm with time resolution ~ 10 ms and spatial resolution ~ 0.17 nm and ~ 0.15 nm respectively.

The tomographic system for visible plasma radiation measurement consists of two parts, which will be installed at the same toroidal position. Both parts are designed in the same manner, but viewing the plasma cross-section from two different poloidal angles. Wide observation angle of the system allows collecting radiation from whole plasma cross section. Visible light detectors with detection range $400 \div 1000$ nm are located outside of tokamak hall to be shielded against X-ray radiation from the plasma. Optical cables with transmittance $\sim 95\%$ in range of interest are used to connect the objective with the detectors.

Design and construction of the multi-channel optical system for visible plasma radiation measurements will be described in the second section. The recorded temporal evolutions of spectra during discharges will be given to show the emission of visible and near ultraviolet radiation of excited neutral atoms and ions of impurities from the plasma edge. In future it will give a possibility to estimate roughly the impurity influx and hydrogen recycling during the discharge.

Tomographic system

The aim of the first phase of operation of the tomographic system is monitoring of the integral plasma radiation in a visible spectral range both from the plasma core and from the plasma edge. The tomographic reconstructions with the temporal resolution in the range of a few microseconds and the spatial resolution of about $\gg 1$ cm can be reached by the system [5]. Determination of the effective ionic charge Z_{eff} from the line free region is planned in the next phase by using the interference filter ~ 523 nm. The required radial profiles

of plasma density and temperature will be measured by the Thomson scattering diagnostic, which is now under construction. The physical base of such studies connected with basic questions concerning mechanisms of anomalous transport, the role of plasma impurities, the particle confinement and tokamak performance etc. is well described in [6], [8].

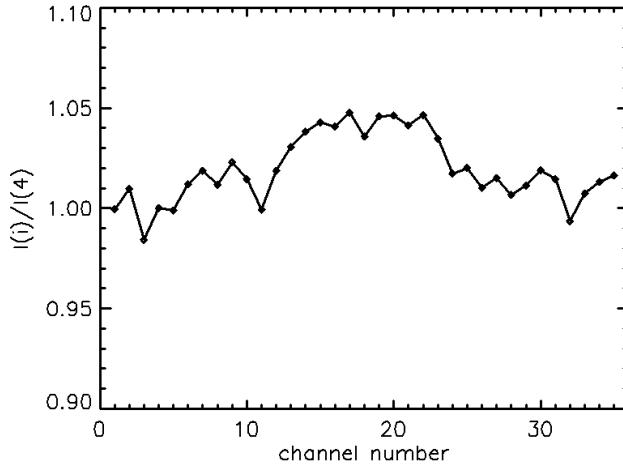


Fig. 1. Ratio of light intensities of i -th and 4-th channel dependent on channel's number for homogeneous light source

The two identical visible light diagnostic systems will be set at the poloidal cross-section 6/7. Each system consists of the focusing lens-based objective located inside the radially viewing diagnostic port and detection part. The design of “sandwich” structure plug for the angular ports was described in details in [7]. The NW35 vacuum window was made from Spectrosil 2000 by Vacom and is used as a part of optical system for visible light transfer to separate vacuum and atmospheric pressure parts of the system. The objective consisting of three parts was described in [8]. An interference filter can be set as a part of optical system depending on an aim of experiments. The observation angle of the collimation optical system is 110° . The optical part of the system is under tests in the Department of Optical Diagnostics of IPP in Turnov now. One silica/silica fiber with 200 mm core represents each spatial channel. The system of fibres, which realises connection of collimation and light detection parts of the system, is quite flexible. It was reached using exchangeable endpieces that allow fibre reconnection with only few per cent loss of light at the ends. Each fibre represents one spatial point in the plasma. Two types of optical fibres end-connectors were designed to fulfil our requirements for a light transfer. The “tokamak side” 37-channels optical fibre connectors were designed to be mounted directly into the objectives. The “detector side”

35-channels optical fibre connectors were designed to transmit light between optical cables and detectors with negligible overlap of channels. Twenty-meter long optical cables can lead, depending on purpose of the experiment, either to a 35-channel detector S4114-35Q by Hamamatsu, or to minispectrometers HR2000+.

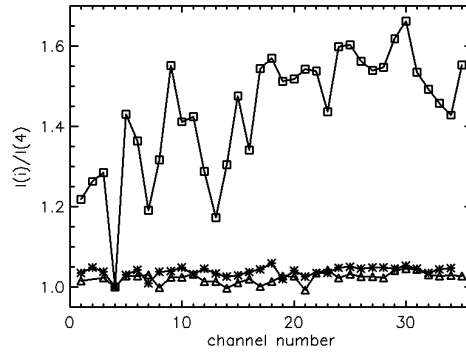


Fig. 2. Ratio of light intensities of i -th and 4-th channel dependent on channel's number; curve marked as 'x' is signal from the testing channel, '◇' one is overlapping signal from the right neighbouring channel and '△' one is overlapping signal from the left one; the 4-th channel was chosen as a reference channel

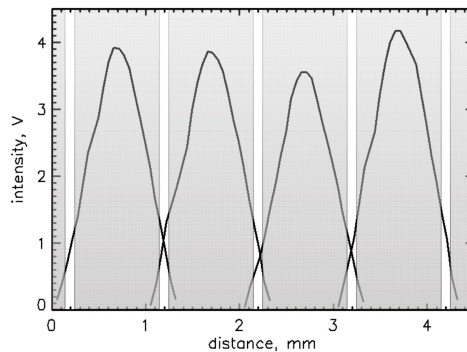


Fig. 3. Evolution of light intensity for four neighbouring channels with fibre position shift along detection surface

The system provides line-integrated measurements along spatially stepped lines of sight with resolution about 1 cm. Two stage 70-channels amplifier with amplification ratio $\sim 5 \times 10^5$ was designed and manufactured in our laboratory for signal registration in the range of $0 \div 5$ V. Level of noise after amplification

was registered as 2 mV. Temporal resolution of the amplifier is limited approximately to 1 MHz. The connectors between the optical cables and the detectors were designed as a part of the amplifier's box with a possibility to optimize the fibres endpiece position relatively to detectors in the arrays.

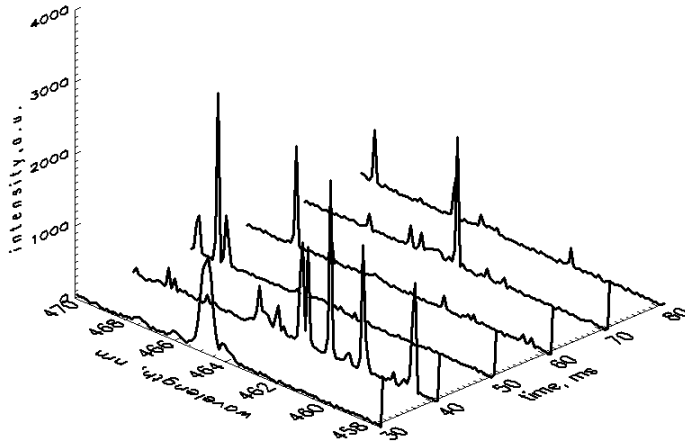


Fig. 4. The part of spectrum for a short (~ 200 ms) discharge #862 measured by means of the HR 2000+ spectrometer; the time resolution is 10 ms

Two sets of measurements were provided to check detection part alignment of the system. The tests of light registration non-uniformity by the detector array were done as a reference measurement (Fig. 1). The level of this non-uniformity was estimated as approximately 5%. Tests of channels overlapping were done to estimate precision of fibre end-connector spacing to array detection surface and to evaluate level of signal overlapping for neighbour channels. In these tests, the fibre array was moved along the detector array. Distribution of light intensity depending on fibre position shift to detection surface was received. Initial position of fibres is set to zero at the Fig. 2, where the distribution of light for 2-nd up to 5-th channels is shown. It is possible to see that the channels are not equal in transmittance of light. It can be connected with precision of end-connectors and fibres production. The overlapping of the light for neighbouring channels can take place for our system, when fibres are not close enough to the detector. The ratio of light intensities of i -th and reference channel dependent on channel's number is possible to see in Fig. 3. The

overlapping measured on the neighbouring channels is also demonstrated. It is possible to see quite strong difference between channels. The level of overlapping was different for each channel but not more than 20 % for less than 1 mm distance between the fibre and detection surface. This tests show it will be required to introduce of calibration constants for each channel, which include difference in light transmittance and overlapping. This constant should be calculated for assembled system for each channel separately and used during data procession.

Spectroscopic measurements

The two mini-spectrometers HR 2000+ manufactured by Ocean Optics are used for spectral measurements in our experiments. In the first sets of experiments it was used toroidal view to vacuum volume for measurements of time-integrated spectra or with temporal resolution 7 ms. At second step it is used poloidal view at sector 12/13. At this stage of tokamak operation it is not possible to make temporally resolved measurements because the tokamak discharges are quite short ($\gg 10$ ms) and the photosensitivity of the spectrometer's detector is not high enough to make measurements with temporal integration less then 7 ms. Therefore only temporally integrated measurements were done for this case. Finally the spectrometers will used poloidal view and will be spaced at sector 6/7 of the COMPASS tokamak.

Figure 4 shows the time resolved spectrum of one of long discharges, which was received from toroidal view. The most intensive line (H_α) belongs to hydrogen, which is used as the working gas. We also observe several lines of impurity ions, mostly single and double ionized carbon and wall material elements [4], [9]. The carbon lines appear because of the plasma interaction with graphite tiles, which serve as limiters and cover the bottom of the vessel (divertor tiles) and the central column (see [9]). The carbon lines could appear also because of sputtering of dust particles, which are present in the vessel. It is possible to see break down phase at the beginning of discharge and two highly populated spectra because of strong plasma-wall interaction during instabilities. Such spectra were measured in poloidal direction and can be used to make rough estimation of particles or ions flux coefficients. Atomic hydrogen fluxes are commonly determined via the intensity measurements of the Balmer lines in the visible part of the spectrum. The conversion of the photon intensities I_a into particle fluxes Γ_a is conventionally performed via the relation: $\Gamma_a = S/XB \times I_a$ [$s^{-1} m^2$] [10], where the factor S/XB (ionisation rate/branching ratio \times excitation rate) can be determined using a collisional radiative model (CRM). It can be calculated, for example, by means of FLYCHK code [11] using measured value of electron density and electron temperature. Similarly as in the atomic case the molecular flux Γ_m is then given by $\Gamma_m = D/XB \times I_m$. In this case S is replaced by

the total molecular decay rate D including ionisation and dissociation. However, optical resolution of our spectrometers is too poor to measure molecular spectra. It means only atomic hydrogen flux can be estimated in our case. The ratio of atomic flux of the hydrogen and carbon or any other impurities flux gives an influx of this impurity to plasma volume.

At the current phase of COMPASS operation, the spectrum in the wavelength range of $247 \div 472$ nm, integrated over the whole discharge duration, was measured from poloidal view. It was decided to use this wavelength range to observe radiation of high-ionized ions, C V line for example. But our plasma conditions at current stage of our experiments do not allow such a state. All presented lines correspond mainly to low ionised carbon states.

Conclusions

The existing optical system for visible plasma radiation measurements at COMPASS tokamak includes two spectrometers HR2000+ measuring in a spectral range of $247 \div 472$ nm and $457 \div 653$ nm with optical resolution 0.17 nm and 0.15 nm. It is sufficient for registration of plasma composition in different discharge regimes. The triggering of the spectrometers allows measuring spectra with a temporal resolution limited by photosensitivity of the spectrometer detector. It is $\sim 7 \div 10$ ms in a range of interest. In future such measurements will allow making rough estimation of impurities influx and hydrogen atomic recycling using electron density and electron temperature (Thomson scattering, interferometry, reflectometry) measurements. It will be also possible to receive these values with quite high temporal resolution but only for chosen spectral lines using interference filters by means of photomultipliers.

The multichannel tomographic system at a few microseconds temporal and with spatial resolution ~ 1 cm was developed and all components of the system were produced. In combination with other diagnostics on the COMPASS tokamak it will be used for studying of anomalous transport, namely in H-mode. In future, the parameters of the optical system will be slightly modified according to the first observations of plasma in the COMPASS tokamak and correspondingly to emergent physical needs.

References

- [1] R. PANEK, O. BILKOVA, V. FUCHS, J. URBAN, F. ZACEK, J. STOCKEL, I. VOITSEKHOVITCH, M. VALOVIC, M. FITZGERALD: *COMPASS-D magnetic equilibria with LH and NBI current drive*. Czechoslovak Journal of Physics, *56* (2006), 125–137.
- [2] D. P. SCHISSEL, R. E. STOCKDALE, H. ST. JOHN, W. M. TANG: *Measurements and implications of Z_{eff} profiles on the DIII-D tokamak*. Phys. Fluids, *31* (1988), 3738–3743.
- [3] H. YAMAZAKI, S. MORITA, M. GOTO, K. TANAKA, R. SAKAMOTO: *Application of visible bremsstrahlung to a density monitor in steady state fusion reactor*. Fusion Engineering and Design, *81* (2006), 2817–2821.
- [4] T. SUGIE, A. COSTLEY, A. MALAQUIAS, C. WALKER: *Spectroscopic diagnostics for ITER*. Journal of Plasma and Fusion Research, *79* (2003), 100–104.
- [5] D. I. NAYDENKOVA, V. WEINZETTL, J. STOCKEL, D. SESTAK, M. AFTANAS: *Design of new optical system for visible plasma radiation measurements at COMPASS tokamak*. WDS'08 Proceedings of Contributed Papers (Jana Safrankova, Jiri Pavlu). Matfyzpress, Prague 2008, 100–104.
- [6] L. C. INGESSON, J. J. KONING, A. J. H. DON, D. C. SCHRAM: *Visible light tomography using an optical imaging system*. Rev. Sci. Instrum., *83* (1992), 5185–5187.
- [7] D. SESTAK, V. WEINZETTL V., P. BILKOVA, P. BOHM, M. AFTANAS, D. I. NAYDENKOVA, J. STOCKEL, I. DURAN, M. J. WALSH: *Design and engineering of optical diagnostics for COMPASS*. Fusion Engineering and Design, *84* (2009), 1755–1758.
- [8] V. WEINZETTL, D. I. NAYDENKOVA, D. SESTAK, J. VLCEK, J. MLYNAR, R. MELICH, D. JARES, J. MALOT, D. SARYCHEV, V. IGOCHINE: *Design of multi-range tomographic system for transport studies in tokamak plasmas*. Nuclear Instruments and Methods in Physics Research Section A, *623* (2010), 806–808.
- [9] D. I. NAYDENKOVA, J. STOCKEL, V. WEINZETTL, D. SESTAK, J. HAVLICEK: *First Spectroscopic Measurements on the COMPASS Tokamak*. WDS'09 Proceedings of Contributed Papers (Jana Safrankova, Jiri Pavlu). Part II – Physics of Plasmas and Ionized Media, Matfyzpress, Prague 2009, 158–162.
- [10] A. POSPIESZCZYK, S. BREZINSEK, PH. MERTENS, G. SERGIENKO: *The role of hydrogen atoms and molecules in the plasma boundary*. Contribution to Plasma Physics, *42* (2002), 663–667.
- [11] H.-K. CHUNG, M. H. CHEN, W. L. MORGAN, Y. RALCHENKO, R. W. LEE: *FLYCHK: Generalized population kinetics and spectral model for rapid spectroscopic analysis for all elements*. High Energy Density Physics, *1* (2005), 3–12.

Received May 13, 2010

Plasma accumulation and confinement in a multislit electromagnetic trap “Jupiter F”¹

NATALYIA A. KRUTKO², OLEG A. LAVRENT'EV²,
VOLODYMYR A. MASLOV², V. P. OBOZNYJ²

Abstract. Experimental results of plasma confinement in multislit electromagnetic trap are presented in this paper. The efficiency of ferromagnetic materials application in the electromagnetic trap are shown. Plasma density in the central region of the trap is $0.8 \times 10^{12} \text{ cm}^{-3}$ with a current in a magnetic system is 200 A (the maximal values of magnetic field in the central ring slit 2000 Gs). The possibility to realize of Brillouin electron injection in electromagnetic trap with ferromagnetic cores are shown.

Key Words. Electromagnetic trap, plasma, plasma density, accumulation, confinement, Brillouin injection.

Introduction

The first experimental researches of plasma accumulation and confinement in a multislit electromagnetic trap “Jupiter F” [1] are presented in this paper.

The plasma in the electromagnetic trap is created by the neutral gas ionisation with electrons which are injected through axial aperture. For realization of Brillouin injection electronic guns are placed in the region of low magnetic field in axial concentrators. In this case the electronic beam is injected in the central region of the trap where the magnetic field is absent.

Power of the magnetic system in these experiments was carried out by constant current source, which allows to change the current in the magnetic coils from 0 to 200 A. Power supply system of the constant current operated during three seconds. Electron injection was carried out at the end of the third second. The duration of the pulse injection was 12 ms.

¹This work is supported by company “Concord” under project No. 3.

²Institute of Plasma Physics of the National Science Center “Kharkov Institute of Physics and Technology”

The plasma density was measured by microwave interferometer. Measurement of the average plasma density in the cross section of the microwave sensing interferometer based on phase change passing through the plasma wave due to changes in the dielectric constant of the medium is uniquely associated with change in plasma concentration. Probing was carried out in a diagonal direction at an angle of 45° . The system for collecting, processing and storage of experimental data based on digital conversion board SDI-AD12-128H is able to simultaneously register 64 differential signal with a temporary interchange 1.5 ms, and specially designed programs allow to display results of processing these signals.

Experimental results

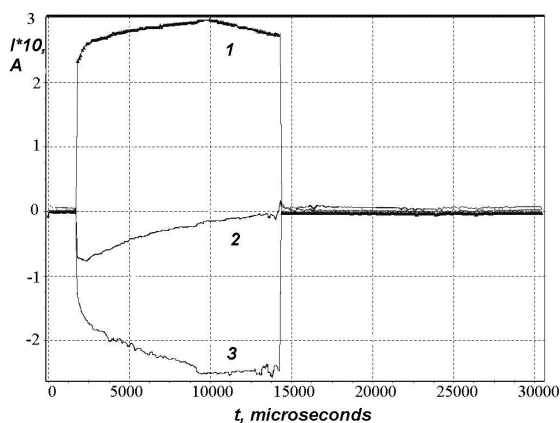


Fig. 1. The waveform of the injection current of electrons in the trap 1, the current injected electrons emerging from the trap on locking electrodes 2 and limiting the accumulation region of the plasma anode aperture 3, with injection into an unlocked trap

The figure shows that the balance sheet included in the trap and out of the electrons observed. With increasing magnetic field strength fraction of electrons arriving at the locking electrodes increases and decreases in the anode aperture.

When a negative potential is on the locking electrodes – loss of electrons along the magnetic lines of force are eliminated. Electrons can leave the trap only by diffusion through a magnetic field to the limiting aperture, the time of their lives in the trap greatly increased. As a result of ionization of neutral gas there is an accumulation of plasma and plasma gets negative potential. Ions in a trap are confined by space charge of electrons. They can leave the trap only

through the magnetic slits, where the potential barrier for them is reduced due to slack capacity in the slit. The negative potential of the side locking electrodes was less than central to the secondary electron emission from the central electrode could fall into the trap through the central magnetic slits.

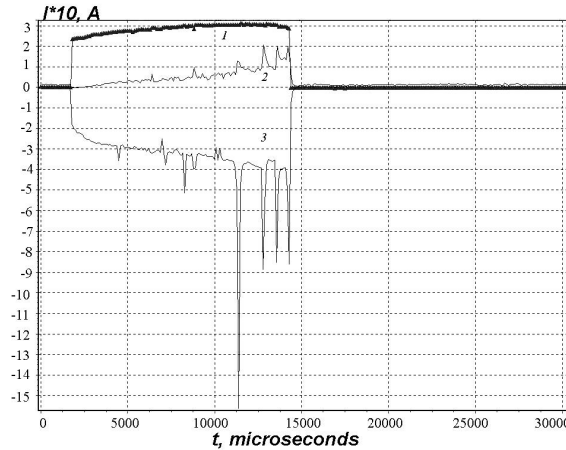


Fig. 2. The oscillograms of the injection current of electrons 1, the ion current to the electrodes in a magnetic locking slits 2 and the current diffusion of electrons to the anode diaphragm 3 bounding the region of accumulation of plasma current in the magnetic coils 100 A

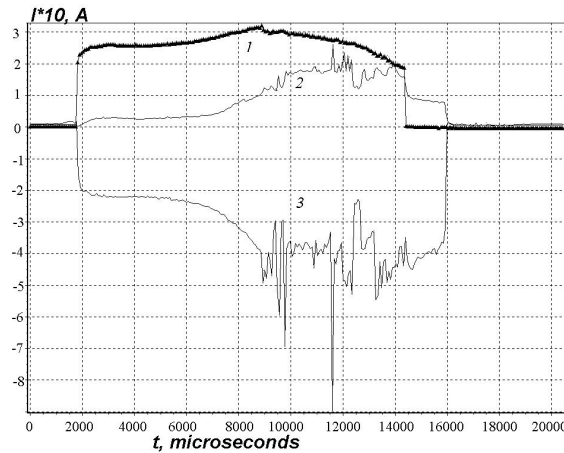


Fig. 3. The oscillograms of the injection current of electrons 1, the ion current to the electrodes in a magnetic locking slits 2 and the current diffusion of electrons to the anode diaphragm 3 bounding the region of accumulation of plasma current in the magnetic coils 200 A

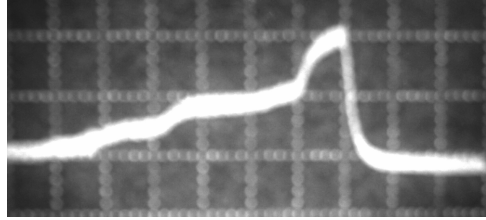


Fig. 4. The oscillograms of the phase shift passes through the plasma wave, proportional change in the linear plasma density nL in section sensing which correspond to the oscillograms balance of currents presented in Fig. 2

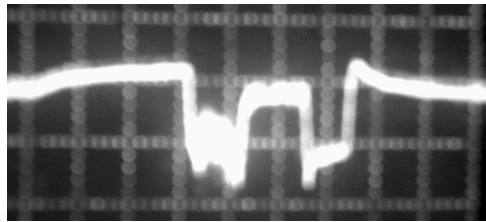


Fig. 5. The oscillograms of the phase shift passes through the plasma wave, proportional change in the linear plasma density nL in section sensing which correspond to the oscillograms balance of currents presented in Fig. 3

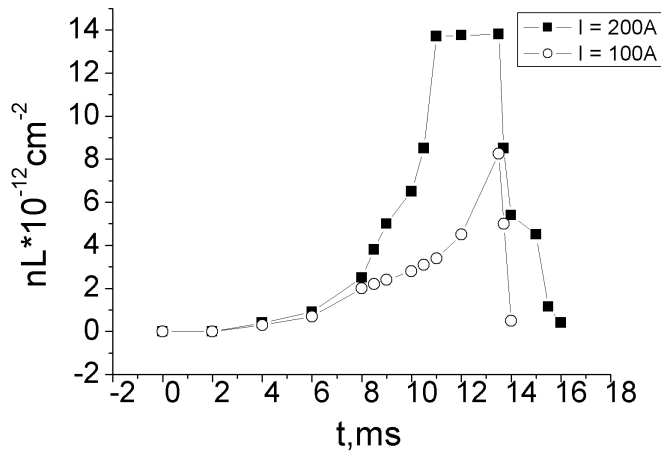


Fig. 6. The dependence of the linear plasma density along the section of the sensing time for the current in the magnet system $I = 100 \text{ A}$ and $I = 200 \text{ A}$

Dependencies are obtained by processing the oscillograms of the phase shift passes through the plasma wave (Figs. 3 and 5) from the expression

$$nL = 7.75 \times 10^{10} \arccos\left(1 - \frac{2I}{I_0}\right), \quad (1)$$

where I – amplitude of the signal, and I_0 – amplitude of the corresponding change in signal phase shift in 180° .

The above figures show that when applying a negative potential to the central electrode is blocking the injected electrons and the accumulation of plasma in the trap due to ionization of neutral gas, resulting in a phase shift of the microwave interferometer and yield of the central electrodes (Figs. 2, 3). The increase of current in the coils of the magnetic system leads to an increase of ion current on the central electrode and the phase shift of the microwave interferometer is proportional to the linear plasma density along the section nL sensing (Figs. 4, 5). Figure 6 shows that the linear density of the plasma nL when changing the current in the coils from 100 to 200 A is increasing from $8 \times 10^{12} \text{ cm}^{-2}$ to $14 \times 10^{12} \text{ cm}^{-2}$. The plasma density in the center of the trap in this case is $4.5 \times 10^{11} \text{ cm}^{-3}$ and $8 \times 10^{11} \text{ cm}^{-3}$, respectively.

With increasing current in the magnetic coils observed continued accumulation of plasma after the injection pulse (Fig. 3). This is due to increase of ion current with increasing plasma density, resulting in secondary emission from the central electrode is sufficient to produce the accumulation of plasma in the trap after the end of the injection current. Lack of high frequency oscillations in the oscillograms of currents indicates that by the Brillouin injection as the injected electrons from the electron guns through the axial holes, and secondary electrons through the annular gap. With increasing plasma density and ion current to the central electrode, apparently, can be carried accumulation of plasma due to secondary emission from the central electrode. Electronic injection through the axial holes of the electron guns will be required only for the initial establishment of the plasma in the trap.

Conclusion

The first experiments of the research of plasma accumulation and confinement in a multislit electromagnetic trap “Jupiter F” allow to do following conclusions:

- Application of the ferromagnetic screen led to increase of intensity of a magnetic field more than twice. It means that expenses for creation of a keeping magnetic field decrease more, than four times.
- The plasma with density of $0.8 \times 10^{12} \text{ cm}^{-3}$ in the central region of the trap at a current in a magnetic system 200 A. In the trap

Jupiter 2M3 [2] of a similar configuration, but without the ferromagnetic core, the plasma density $2 \times 10^{12} \text{ cm}^{-3}$ has been received at current in the magnetic system 2000 A.

- Realisation possibility Brillouin electron injection through ring magnetic slits at the expense of secondary electronic issue from the central electrodes of an electromagnetic trap with ferromagnetic cores.

References

- [1] O. A. LAVRENT'EV, V. A. MASLOV, N. A. KRUTKO, V. P. OBOZNYJ: *Multislit electromagnetic trap "Jupiter F"*. Problems of atomic science and technology, 6 (2008), 40–42.
- [2] O. A. LAVRENT'EV, V. A. MASLOV, M. G. NOZDRACHOV, V. P. OBOZNYJ, S. A. GOLYUK, N. A. KRUTKO: *Multislit electromagnetic trap "Jupiter 2M3"*. Problems of atomic science and technology, 1 (2007), 27–29.

Received May 5, 2010

Optical spectroscopy of plasma beam interaction with tungsten target and temporal characteristic of spectral line emission in PF-1000¹

KATARZYNA JAKUBOWSKA², MONIKA KUBKOWSKA²,
ELZBIETA SKLADNIK-SADOWSKA³, KAROL MALINOWSKI³,
MARIAN PADUCH², MAREK JAN SADOWSKI^{2,3},
MAREK SCHOLZ², MARINA LADYGINA⁴

Abstract. The optical emission in the visible range was applied for studies of dense pulsed plasma-ion streams and their interactions with tungsten targets were studied in order to define plasma characteristics. Preliminary results, obtained in PF-1000 experiments with the new installed isolator, showed a distinct decay of the electron density as a function of the time after the discharge current peculiarity. The electron density was estimated on the basis of the observed Stark broadening of the D_β and D_γ lines. Spectroscopic measurements were also performed with the tungsten targets. The obtained spectra contained, beside impurity lines (Cu, Fe), W I and W II lines. A relatively low resolution of the applied spectrometer made impossible a quantitative analysis of the recorded tungsten lines. The results of the described studies might be of interest for fusion technology because tungsten is one of the materials designed for plasma facing components in the International Thermonuclear Experimental Reactor (ITER).

Key Words. Optical spectroscopy, free plasma stream, plasma-focus, plasma interaction with tungsten, Balmer lines, tungsten lines.

¹This work was realized within a frame of the Agreement about Scientific Collaboration between Poland and Ukraine, and it was supported by a grant (No. 584/N-Ukraine/2009/0) from the Ministry of Science and Higher Education, Poland

²Institute of Plasma Physics and Laser Microfusion (IPPLM), Warsaw, Poland

³The Andrzej Soltan Institute for Nuclear Studies (IPJ), Otwock-Swierk, Poland

⁴Institute of Plasma Physics, NSC KIPT, 61-108 Kharkov, Ukraine

Introduction

Characterization of tungsten properties and studies of its erosion are presently of primary importance because of possibility of its application as in-vessel components in future thermonuclear reactors. The paper presents an investigation of plasma generated by high-current discharges in the Plasma-Focus, PF-1000 facility [1], operated at IPPLM in Warsaw, Poland. The main attention was given to spectroscopic measurements of free-propagating plasma streams and their interactions with pure tungsten targets. Similar studies were performed in the past within the RPI-IBIS facility [2], [3] and in experiments on the interaction of laser beams with a tungsten target [3]–[5]. Preliminary spectroscopic studies of the plasma interaction with a solid target (C+W) were also performed at the PF-1000 facility but in different experimental condition [6].

Experimental setup

The described experiment was performed within the PF-1000 facility operated with deuterium as a working gas. The Mather-type device was equipped with coaxial electrodes of 460 mm in length. The inner electrode of 230 mm in diameter was made of copper (Cu) and the outer one of 400 mm in diameter – consisted of 12 stainless-steel (mainly Fe) tubes of 80 mm in diameter each. The experiment was carried out within a vacuum chamber pumped out to the basic pressure of 2×10^{-5} hPa and filled up with the pure deuterium gas (D_2) under pressure of $P_0 = 2.8$ and 2.9 hPa.

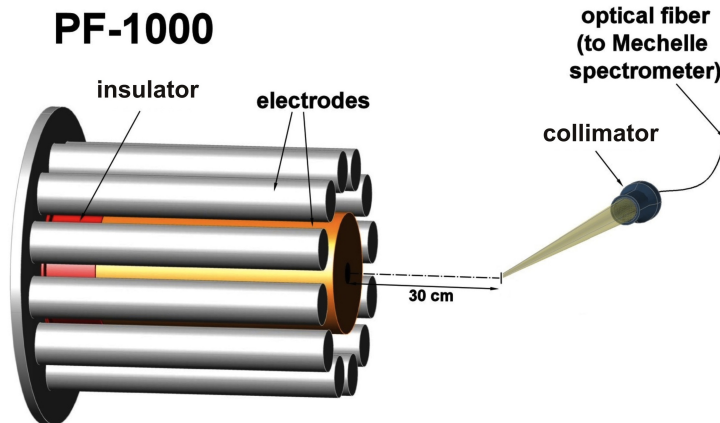


Fig. 1. Geometry of the setup at the PF-1000 facility

The visible radiation was collected from a spot of 10 mm in diameter, on the z -axis, at a distance of 30 cm from the electrode ends, by means a quartz collimator placed side-on the vacuum chamber and oriented perpendicular to the discharge axis, as shown in Fig. 1. Such a geometry of the setup was chosen in order to minimize an influence of impurities on the measured optical spectrum. Optical signals were sent through a 10 m long fibre cable (made of MgF_2) to a Mechelle-900 spectrometer equipped with a PCO SensiCam camera. Exposure time was varied within the range from 0.1 μs to 20 μs (the smallest value determined by the camera operation). Optical spectra were measured in a wavelength range from 300 nm to 1100 nm.

Experimental results

The described experimental campaign was divided into two parts. The first one was related to study of the pure deuterium (D_2) plasma, while the second one was devoted to observations connected with interactions of the pulsed plasma-ion beams with a tungsten target. In both cases the recorded spectra were wavelength- and intensity-calibrated using an ArHg lamp and DW lamp, respectively. Several series of experiments were performed with the exposure time $t_{\text{exp}} = 0.1 \mu\text{s}$ and different delay times (from $-2 \mu\text{s}$ to $7 \mu\text{s}$) in relation to the discharge current peculiarity (so-called DIP), as shown in Fig. 2. The measurements were performed at the deuterium pressure of 2.9 hPa and charging voltage on the condenser bank equal to 22 kV. In that case, beside deuterium Balmer lines, only single impurity lines (e.g. Cu I 465.11 nm, Cu I 515.32 nm) were observed.

Since in most of the investigated cases the Balmer- α line ($n' = 3 \rightarrow n = 2$, $\lambda_{\text{D}\alpha} = 656.1 \text{ nm}$) was strongly reabsorbed, the electron density was evaluated on basis of Balmer- β ($n' = 4 \rightarrow n = 2$, $\lambda_{\text{D}\beta} = 486.029 \text{ nm}$) and Balmer- γ ($n' = 5 \rightarrow n = 2$, $\lambda_{\text{D}\gamma} = 433.298 \text{ nm}$) lines of the deuterium-plasma emission. In order to determine the electron density (n_e) detailed analysis of the shapes of D_β and D_γ lines was performed.

Assuming a quasistatic approximation the use was made of the following equation [7]

$$n_e = \left(\frac{\Delta\lambda_S \times 10^9}{2.5\alpha_{1/2}} \right)^{3/2}, \quad (1)$$

where $\Delta\lambda_S$ is a Stark width and $\alpha_{1/2}$ is a fractional semi-half-width parameter taken from [8].

Taking into account the width of the central peak of D_β and D_γ line, a dependence of the electron density (n_e) on a time delay before and after the DIP was determined. Figure 3 shows a relatively good agreement between n_e values calculated from the Stark broadening of the D_β and D_γ lines for instants

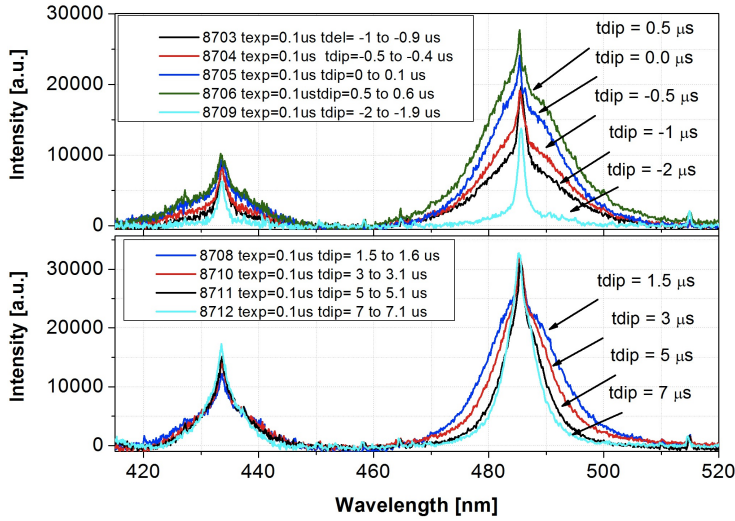


Fig. 2. Dependence of a chosen part of the recorded spectra on a time delay before (top) and after (bottom) the current peculiarity

before and more than $2 \mu\text{s}$ after the DIP. Most probably the increased plasma density during and just after the DIP was induced by the interaction of fast ions escaping from the pinch. A discrepancy between data obtained from D_β and D_γ , as observed for times close to the DIP, could suggest that in that period the applied quasistatic approximation was invalid.

The second part of the experimental campaign was concentrated on interactions of the pulsed plasma-ion streams with a tungsten (W) target. In that case the applied experimental conditions were as follows: the initial pressure of the deuterium filling gas of 2.8 hPa and the charging voltage on the condenser bank was 27 kV.

The observed spectral lines were identified on the basis of the data from the NIST Atomic Spectral Database.

An example of a part of the recorded spectrum (in the wavelength range from 350 to 380 nm) in a comparison with the spectrum obtain in the earlier laser-experiment performed also with the pure tungsten target [4], [5], is presented in Fig. 4. In the spectra presented in Fig. 4 common tungsten lines are marked by the dashed lines. Because of the rich spectral database of tungsten as well as the appearance of some impurity (e.g. Fe) lines, further measurements with a higher resolution spectrometer are needed. Some lines may also correspond to W III or higher ionized tungsten ions, but information about such species is missing in the available databases. A relatively low resolution of applied

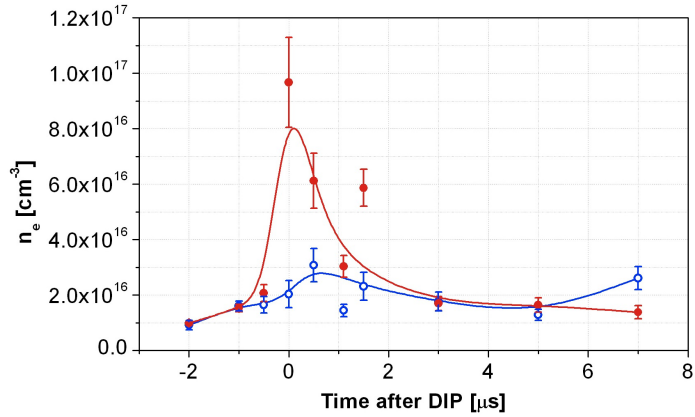


Fig. 3. Electron density as a function of time before ($t < 0$) and after ($t > 0$) the DIP, as calculated from the Stark broadening of the D_{β} (closed circles, upper trace) and D_{γ} lines (open circles, bottom trace)

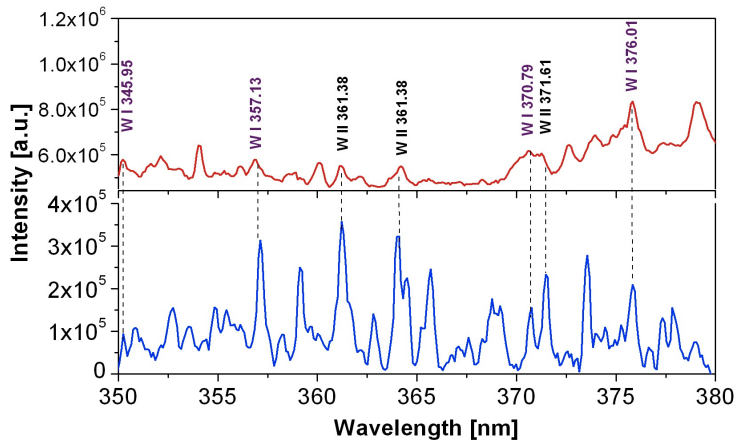


Fig. 4. Comparison of the chosen part of the spectrum, as obtained from the plasma stream-target experiment in the PF-1000 facility (top trace) and from the earlier laser-target experiment (bottom trace)

spectrometer ($\Delta\lambda/\lambda \simeq 900$) made impossible a quantitative analysis of the recorded tungsten lines.

Summary and conclusions

It can be concluded that the optical spectroscopy in the visible range can provide valuable information about parameters of plasma streams propagating through a low-density gas, as well as about interactions of such streams with solid targets (including tungsten ones). The values of the plasma density, as estimated on basis of the Balmer lines of deuterium, remain in agreement with the previous results. Due to a low resolution of the spectroscopic measurements of plasma produced from the the wolfram target none quantitative analysis was possible, but one could identify some tungsten lines and estimate dynamics of such plasma.

References

- [1] M. SCHOLZ, B. BIENKOWSKA, M. BOROWIECKI, I. IVANOWA-STANIK, L. KARPINSKI, W. STEPNIEWSKI, M. PADUCH, K. TOMASZEWSKI, M. J. SADOWSKI, A. SZYDLOWSKI, P. KUBES, J. KRAVARIK: *Status of a mega-joule scale plasma-focus experiments*. Nukleonika, *51* (2006), 79–84.
- [2] E. SKLADNIK-SADOWSKA, K. MALINOWSKI, M. J. SADOWSKI, K. CZAUS, M. KUBKOWSKA, M. S. LADYGINA, B. SARTOWSKA: *Study of deuterium plasma interaction with a tungsten target within RPI-IBIS facility*. Problems Atomic Science and Technology. Series: Plasma Physics, *14* (2008), 95–97.
- [3] E. SKLADNIK-SADOWSKA, K. MALINOWSKI, M. J. SADOWSKI, J. WOLOWSKI, P. GASIOR, M. KUBKOWSKA, M. ROSINSKI, A. K. MARCHENKO, B. SARTOWSKA: *Spectroscopy of the tungsten plasma produced by pulsed plasma-ion streams or laser beams*. Journal of Nuclear Materials, *390391* (2009), 847–851.
- [4] M. J. SADOWSKI, E. SKLADNIK-SADOWSKA, K. MALINOWSKI, J. WOLOWSKI, A. CZARNECKA, P. GASIOR, P. PARYS, M. ROSINSKI, A. MARCHENKO, A. TSARENKO: *Observation of tungsten spectral lines during interaction of laser beam with tungsten target*. Czech. J. Phys. Suppl. B, *56* (2006), B550–B556.
- [5] M. KUBKOWSKA, P. GASIOR, M. ROSINSKI, J. WOLOWSKI, M. J. SADOWSKI, K. MALINOWSKI, E. SKLADNIK-SADOWSKA: *Characterisation of laser-produced tungsten plasma using optical spectroscopy method*. Eur. Phys. J. D, *54* (2009), 463–466.
- [6] E. SKLADNIK-SADOWSKA, K. MALINOWSKI, M. J. SADOWSKI, L. KARPINSKI, R. MIKLASZEWSKI, M. PADUCH, M. SCHOLZ, A. MARCHENKO, A. V. TSARENKO, V. GARKUSHA, V. TERESHIN, A. V. DUBROVSKY, V. A. GRIBKOV, V. N. PIMENOV, S. MASLJAEV: *Optical spectroscopy of pulsed plasma-ion streams and their interactions with W + C target at PF-1000 facility*. AIP CP, *993* (2008), 365–368.
- [7] P. KEPPLER, H. R. GRIEM: *Improved stark profile calculations for the hydrogen lines H alpha, H beta, H gamma, and H delta*. Phys. Rev., *173* (1968), 317–325.
- [8] H. R. GRIEM: *Spectral Line Broadening by Plasmas*. Academic Press, New York and London 1974.

Features of plasma focus formation in different operation modes of gas-discharge magnetoplasma compressor

ANNA MARCHENKO¹, IGOR GARKUSHA¹,
VLADIMIR CHEBOTAREV¹, MARINA LADYGINA¹,
YURIJ PETROV¹, DMITRIJ SOLYAKOV¹, VLADIMIR TERESHIN¹,
VALERIJ STALTSOV¹, AHMED HASSANEIN²,
ELZBETA SKLADNIK-SADOWSKA³

Abstract. The paper presents investigations of dense plasma streams generated by the magneto-plasma compressor (MPC) of compact geometry. Distributions of electrical currents in plasma stream are carefully measured for different operation regimes by sets of magnetic probes. Output currents achieve (25 ÷ 35) % of I_d . Development of electric current vortices in plasma resulting in formation of compact plasma toroid is discussed. Maximum plasma stream density was about 10^{18} cm^{-3} , average electron temperature along a line of view $\sim 5 \div 7 \text{ eV}$ and plasma stream velocity at the MPC output 10^7 cm/s . EUV (extreme ultraviolet) radiation measurements from the compression region show that radiation power of Xe plasma in $12.2 \div 15.8 \text{ nm}$ wavelength band achieves 18 kW. The obtained results are in importance for lithography-oriented applications of MPCs, for development of hot plasma generators and efficient fuelling techniques (plasmoids) as well as Xe plasma injectors for disruption mitigation and other fusion applications.

Key Words. Magnetoplasma compressor, gas-discharge plasma, spectroscopy diagnostic, EUV radiation, outlet currents, plasma electron density.

¹NSC “Kharkov Institute of Physics and Technology”, Institute of Plasma Physics, Kharkov, Ukraine

²Purdue University, USA

³The Andrzej Soltan Institute for Nuclear Studies, 05-400 Otwock-Swierk, Poland

Introduction

Extreme ultraviolet (EUV) sources at $\lambda = 13.5$ nm basing on gas discharge Xe plasma are considered to be most promising candidates for next generation lithography [1], [2]. One of the perspective systems for generation of powerful EUV radiation by dense magnetized plasma is magneto-plasma compressor (MPC). Studies of high-energy plasma dynamics are in importance also for other fundamental problems: development of new technologies of materials modification, fusion researches, plasma propulsion and thrusters and powerful radiation sources of broad spectrum.

For these tasks, development of diagnostics for dense magnetized plasma of different ions, including heavy noble gases is necessary to estimate efficiency of plasma systems. Spectral analysis of high-ionized plasma composition and studies of plasma dynamics important for understanding of acceleration and compression processes. In particular, plasma compression zone is also interesting object for investigations of different nonlinear effects occurred in dense magnetized plasmas, for example, hot spots [3].

This paper presents investigations of dense plasma streams generated by the magneto-plasma compressor (MPC) of compact geometry [4], which is able to operate with different gases and their mixtures and, thus, to provide variation of operation regimes in wide range for different applications. Different modes of MPC operation were investigated and compared: helium discharge, pure xenon discharges with pulsed gas supply and discharges in helium under various residual pressures with additional pulsed injection of xenon directly into the compression zone [5].

Experimental setup and diagnostic equipment

Figure 1 shows general view of MPC experimental device and plasma source itself. The both electrodes of magnetoplasma compressor was made from copper. Outer electrode (anode) consists of solid cylindrical part ($\varnothing_{\text{cyl}} = 130$ mm) and output rod structure including 12 copper rods with diameter of 10 mm and of 147 mm in length ($\varnothing_{\text{out}} = 92$ mm). Inner electrode (cathode) has diameter of 60 mm in cylindrical part and out diameter is 30 mm in conical part. MPC is equipped with electrodynamic valve to provide the required amount of gas supply either for operation under the varied residual pressure or for pulsed gas supply to the inter-electrodes area. The discharge is powered from the condenser bank ($C_v = 90 \mu\text{F}$) charged up to 25 kV, discharge current can achieved 500 kA, duration is equal to $8 \div 10 \mu\text{s}$ and corresponds to half-period of discharge current.

Spectral diagnostics included EUV and X-ray spectrometer, visible spectrometer, electron-optical converter, which was synchronized with discharge

ignition, monochromators, PEMS (photomultiplier), high-speed imaging using CMOS camera PCO AG and fast photo recorder with $1 \mu\text{s}$ temporal resolution. EUV radiation intensity was analyzed by registration system consisting of absolutely calibrated AXUV diodes with thin-films filters for different wavelength ranges ($5 \div 13 \text{ nm}$, $12.2 \div 15.8 \text{ nm}$ and $17 \div 80 \text{ nm}$) and multi-layered MoSi mirrors. Moveable calorimeters, electric and magnetic probes, Rogovski coils, high-voltage dividers etc. were applied also.



Fig. 1. Experimental device

Dynamics of outlet plasma currents.

Spatial distributions measurements of magnetic field in MPC plasma stream were carried out with local movable magnetic probes. Reconstruction of electrical current distributions has been performed from measurements of azimuthal magnetic field using Maxwell equations. Lines of equal electrical current value in plasma stream for different modes of MPC operation are presented in Fig. 2.

Performed measurements show that total value of electric current flowing outside accelerating channel is about $25 \div 30 \%$ of discharge current I_d . Electrical current propagated to distance up to $25 \div 30 \text{ cm}$ from MPC output during first half period of discharge current for both modes of operation with buffering gas and pulsed gas supply. It is found correlation between configuration of output current and dynamics of compression plasma focus region. The current vortexes appearance is attributed to the inclined shock wave formation in compression zone that affects on plasma dynamics outside the source. Shock wave is observed by high-speed imaging (Fig. 3), shock wave existence can also be recognized from electric current peculiarities as shown in (Fig. 2b). High-speed imaging can also provide about plasma pinch evolution with temporal resolution $1 \mu\text{s}$, from these images it was possible to estimate the plasma stream

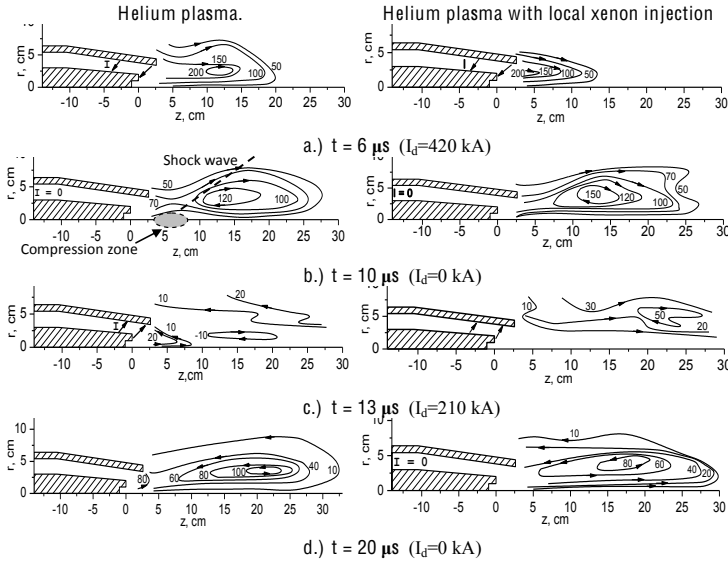


Fig. 2. Time evolution of outlet currents in helium and helium-xenon plasma stream; values of outlet currents are in kA, direction is marked by arrow

average velocity which is equal to $(2 \div 4) \times 10^6$ cm/s. In some regimes the current displacement from the compression region was observed. In conditions when currents are pulsed out and compression region became current free, the magnetic and gas dynamical pressure balance at the boundary of compression zone is achieved at the B -field energy of $10 \div 15$ J/cm³. For measured by Stark broadening electron density in compression region $N_e = (5 \div 7) \times 10^{17}$ cm⁻³ the plasma temperature can be estimated as $(T_e + T_i) \sim 50 \div 100$ eV.

EUV radiation measurements.

EUV radiation in $5 \div 80$ nm wave range was detected by registration system consisting on absolutely calibrated AXUV diodes with thin-films filters for different wavelength ranges and multi-layered MoSi mirrors. Measurement scheme is presented in Fig. 4. Set of different AXUV diodes was placed into duralumin corps. Connection tube with diaphragms determined spatial resolution which was typically below 1 cm. Permanent magnets was installed to produce magnetic field of 0.5 T inside the tube to avoid plasma contact with registration elements. Multilayer Mo/Si mirror was used for selection of different parts of EUV radiation spectrum. Thus, visible radiation and particles made no influence on EUV radiation measurements. Typical waveforms of discharge

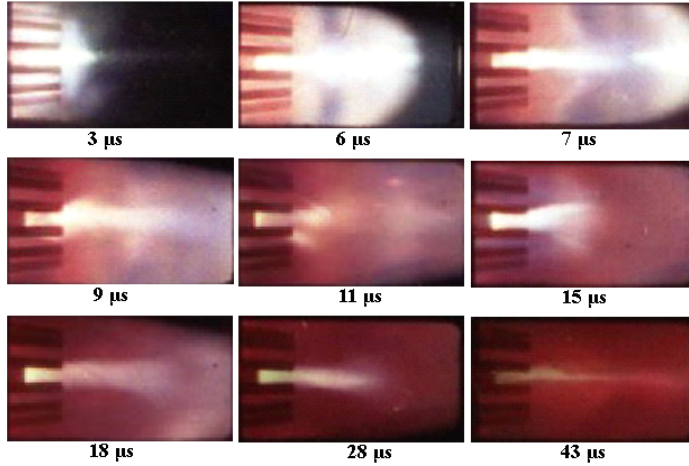


Fig. 3. High-speed imaging of plasma compression with frame exposition $1\mu\text{s}$

current and signal from AXUV 20 Mo/Si in $12.2 \div 15.8\text{ nm}$ wave range are presented in Fig. 5 for discharge current $I_d = 400\text{ kA}$ and helium filling pressure of 5 Torr. Experiments show that radiation energy increases with increasing discharge current and it strongly depends on MPC operation regime. For pure Xe discharges EUV radiation from compression zone is strongly absorbed in surrounding peripheral area by neutral and low ionized xenon atoms. Xe injection applied directly into the compression zone and optimization of operation regimes allowed essential increase of EUV energy in $12.2 \div 15.8\text{ nm}$ wavelength range achieving 10^{-1} J ($P_{\text{max}} = 18\text{ kW}$). In this regime, Xe V spectral lines were registered by spectroscopy in plasma focus area and its appearance correlate with significant increase of EUV radiation detected.

Spectroscopy measurements

In spectral observations of temporal behavior of Xe spectral lines emission, EOC (electro-optical converter) operation was synchronized with plasma discharges with varied time of exposition start. Xenon spectral lines are recorded with short enough exposition (in a comparison with the discharge duration) and with different delays in the relation to the discharge beginning. In visible wavelength spectroscopy studies, particular attention was paid to the temporal and spatial behavior of Xe spectral lines and impurities. Xe II–V species

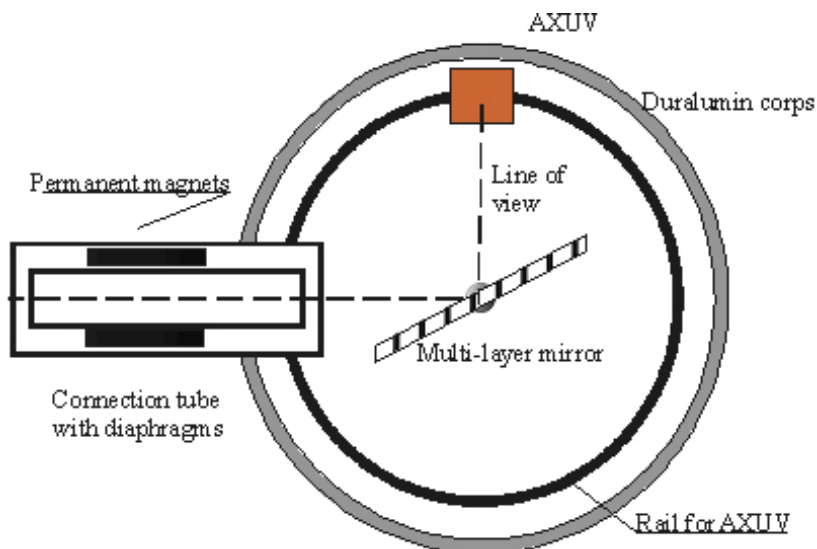


Fig. 4. Scheme of EUV radiation measurements

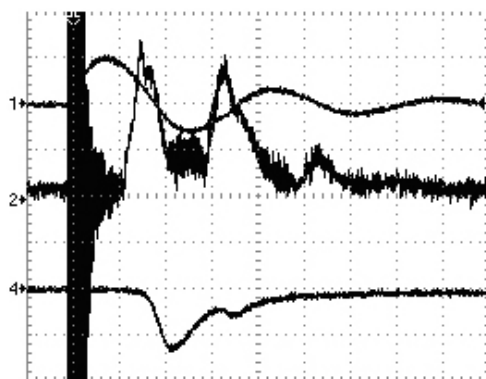


Fig. 5. Wave forms of discharge current (1), AXUV signal in wave range of 12.2 ÷ 15.8 nm (2) and signal from photodiode in visible range (4) for local xenon injection into compression zone; maximum discharge current is 400 kA, buffering He gas pressure 5 Torr

were identified, however high-ionized Xe ions are recorded only for MPC operation with local injection of Xe into compression region and achievement of maximal plasma parameters in compression zone. Thus, radiation of Xe V spectral lines is attributed to the plasma focus formation and it decreases with Xe II species appearance. Temporal dependence of Stark widths for Xe V

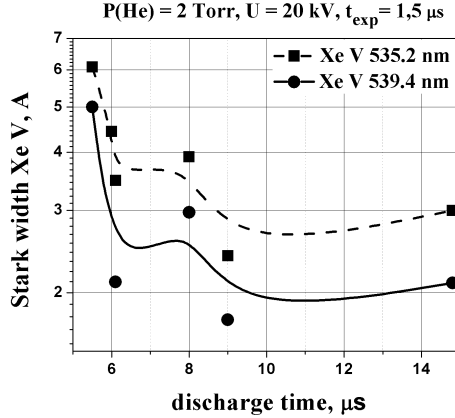


Fig. 6. Temporal distributions of XeV Stark widths

spectral lines (Fig. 6) illustrates the dynamics of plasma compression and it corresponds to hot and high-energy part of plasma stream with duration of generation $\sim 1.5 \div 2 \mu\text{s}$.

Electron density was measured using Stark broadening of Xe II and Xe III lines. Temporal dependence of N_e obtained for buffering gas pressure 2 and 10 Torr with local Xe injection into compression zone is presented in Fig. 7 with different temporal resolution. Electron density distribution for operation mode when buffering gas filled whole accelerating channel (10 Torr) has only one peak with maximum value $N_e = 7 \times 10^{17} \text{ cm}^{-3}$. Operation with smaller pressures (2 Torr) is characterized by two peaks on N_e dependence, which correspond to the first and second half-periods of discharge current respectively. Radiation intensity of Xe II, III lines in the second half-period of discharge current for high residual pressure (10 Torr) is considerably smaller. Therefore plasma density estimations were not performed in this case. Impurities (Cu, C) are appeared in plasma column after 10 μs from the discharge ignition, but even in late stage the impurity spectral lines are not dominant in whole spectrum and they do not influence on plasma focus formation.

Measurements of temporal behavior of N_e were supplemented with spatial ones. Abel inversion procedure was applied for determination of radial distributions of plasma density in near axis region. Example of space-time distributions of electron density at distance 6 cm from central electrode is presented in Fig. 8. For MPC operation at buffering gas pressure of 2 Torr and Xe local injection maximum plasma stream density achieves 10^{18} cm^{-3} , average electron temperature along the line of view $\sim 5 \div 7 \text{ eV}$ and plasma stream velocity at the MPC output $\sim 10^7 \text{ cm/s}$.

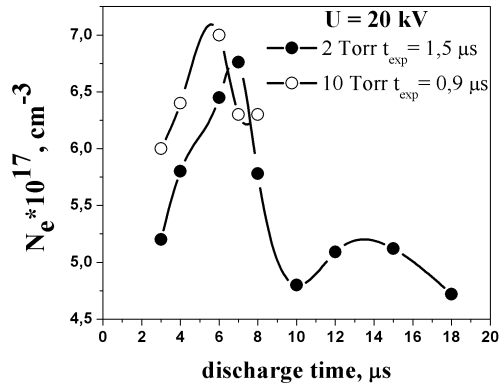


Fig. 7. Temporal plasma electron density for different MPC operating modes

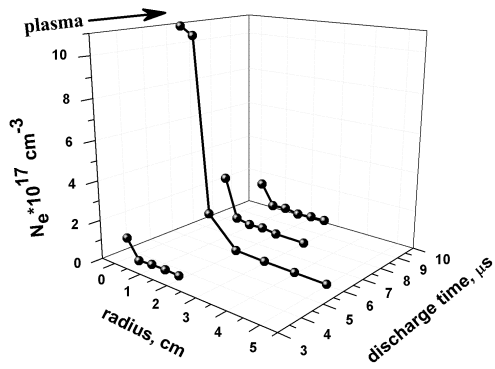


Fig. 8. Space-time electron density distribution at distance of 6 cm from central electrode obtained for MPC operation at buffering He pressure of 2 Torr and local Xe injection

Conclusions

Features of plasma compression zone formation in different modes of MPC operation have been investigated. Spectroscopic analysis of Xe II–Xe V lines identified in visible wavelength range was performed. Electron density was measured with high resolution ($\sim 0.5 \mu\text{s}$) using Stark broadening of Xe II and Xe III lines. Corresponding values of electron density achieved 10^{18} cm^{-3} in operation mode with buffering He gas and local Xe injection into compression region.

Spatial distributions electrical currents in plasma stream have been studied. Output currents achieve $25 \div 30\%$ of I_d . Development of electric current vortexes in plasma was found. Current loops promote the formation of compact plasma toroid. The current vortexes appearance is attributed to the inclined shock wave formation in compression zone which affects on plasma dynamics outside the source. In some regimes the current displacement from the compression region was observed. Pressure balance at the boundary achieved at the B -field energy of $10 \div 15 \text{ J/cm}^3$. For $N_e = (5 \div 10) \times 10^{17} \text{ cm}^{-3}$ the $(T_e + T_i) \sim 50 \div 100 \text{ eV}$.

Observation of compression zone dynamics with high speed imaging well correlate with temporal dependencies of N_e and spatial distributions of output current for different time moments.

Analysis of EUV radiation from compression region shows that radiation energy increases with increasing discharge current and it strongly depends on MPC operation regime. For pure Xe discharges EUV radiation from compression zone is strongly absorbed in surrounding peripheral area by neutral and low ionized xenon atoms. Xe injection applied directly into the compression zone and optimization of operation regimes allowed essential increase of EUV energy in $12.2 \div 15.8 \text{ nm}$ wavelength range achieving 10^{-1} J ($P_{\text{max}} = 18 \text{ kW}$). In this regime, Xe V spectral lines were registered by spectroscopy in plasma focus area and its appearance correlate with significant increase of EUV radiation detected.

References

- [1] G. SCHRIEVER, U. STAMM, K. GÄBEL, M. DARSCHT, V. BORISOV, O. KHRISTOFOROV, A. VINOKHOV: *High power EUV sources based on gas discharge plasmas and laser produced plasmas*. *Microelectronic Engineering*, 61–62 (2002), 83–88.
- [2] S. R. MOHANTY, E. ROBERT, R. DUSSART, R. VILADROSA, J.-M. POUVESLE, C. FLEURIER, C. CACHONCINLLE: *A novel fast capillary discharge system emitting intense EUV radiation: possible source for EUV lithography*. *Microelectronic Engineering*, 65 (2003), 47–59.
- [3] L. JAKUBOWSKI, M. J. SADOWSKI: *Hot-spots in plasma-focus discharges as intense sources of different radiation pulses*. *Brazilian Journal of Physics*, 32 (2002), 187–192.

- [4] V. V. CHEBOTAREV, I. E. GARKUSHA, M. S. LADYGINA, A. K. MARCHENKO, YU. V. PETROV, D. G. SOLYAKOV, V. I. TERESHIN, S. A. TRUBCHANINOV, A. V. TSARENKO, A. HASSANEIN: *Investigation of pinching discharges in MPC device operating with nitrogen and xenon gases*. Czechoslovak J. of Phys., 56 (2006), 335–341.
- [5] I. E. GARKUSHA, V. V. CHEBOTAREV, M. S. LADYGINA, A. K. MARCHENKO, YU. V. PETROV, D. G. SOLYAKOV, V. I. TERESHIN, D. V. YELISEEV, A. HASSANEIN: *Dynamics of dense Xe plasma generated by MPC and features of EUV radiation from compression zone*. VI International Conference “Plasma Physics and Plasma Technology” (PPPT-6) Minsk, Belarus, *Contributed papers* (2009), 178–185.

Received May 10, 2010

Measuring the EUV pulse shape of the fs laser¹

VERONIKA PICKOVÁ², LIBOR ŠVÉDA², ONDŘEJ KLIMO²,
ADAM DAREBNÍČEK², MICHAL DRAHOKOUPIL²

Abstract. The paper describes an experiment in which X-ray radiation was generated by a femtosecond laser focused onto the target. AXUV5 high speed photodiode [4] was used to measure the pulse shape. There were several filters to protect the photodiode from visible radiation and solid particles flying from the target. At the same time we have measured the spectrum via X-ray spectrometer. We have initially controlled the spark on the target as a function of laser beam power to find the optimal focus. For measuring the X-ray itself we have used several filters in rotating holder, enabling to change the filters without opening the vacuum chamber. The problem with visible light going through the filters covering the diode appeared during the measurements. Therefore we have finally chosen the polymer opaque filter with the thickness 25 μm to prevent the incidence of stray visible light on the diode. Experimental setup is presented. The experiment will be modified to measure with the other filters and pinhole in near future.

Key Words. High speed photodiode, femtosecond laser, X-ray radiation pulse shape.

Femtosecond laser

The Titanium-Sapphire femtosecond laser [1], based on the so-called *Chirped Pulse Amplification*, is operated at the Czech Technical University. It consists of a fully integrated Ti:Sapphire oscillator, a stretcher, a regenerative amplifier and a multipass one and finally a compressor. Ti:Sapphire laser delivers 60 fs pulse of energy up to 10 mJ with repetition 10 Hz.

¹We acknowledge the support of Ministry of education, youth and sports of the Czech Republic, grant “Laser systems, radiation and modern optical applications”, grant number MSM6840770022

²Czech Technical University in Prague, Faculty of Nuclear Sciences and Physical Engineering

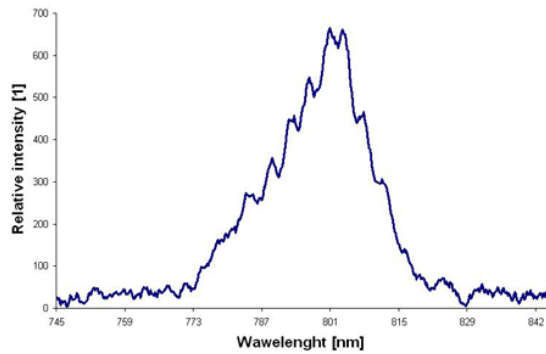


Fig. 1. Spectrum of the laser beam

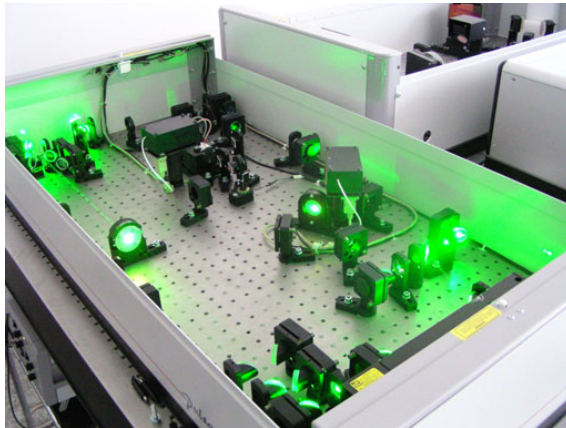


Fig. 2. Titanium-Sapphire femtosecond laser

Experiment goals

Our motivation was to take an initial step toward understanding the plasma radiation generated in our experimental setup. EUV radiation was expected to be produced by the plasma, hence we have decided to perform the following measurements:

- Measure visible light via photodiode, while protecting the photodiode only by transparent foil with the thickness 0.5 mm to verify the status of the used photodiode.

- Find the optimal laser focus by moving the target and optimize the plasma temperature.
- In the focused position measure the signal on the photodiode shielded by the aluminium filter with the thickness $0.8\ \mu\text{m}$ (initial estimate). At the same time measure the spectrum via X-ray spectrometer.
- Change the filters using the motorized filter wheel placed in front of the photodiode. At the same time measure the spectrum via X-ray spectrometer.

Experimental setup

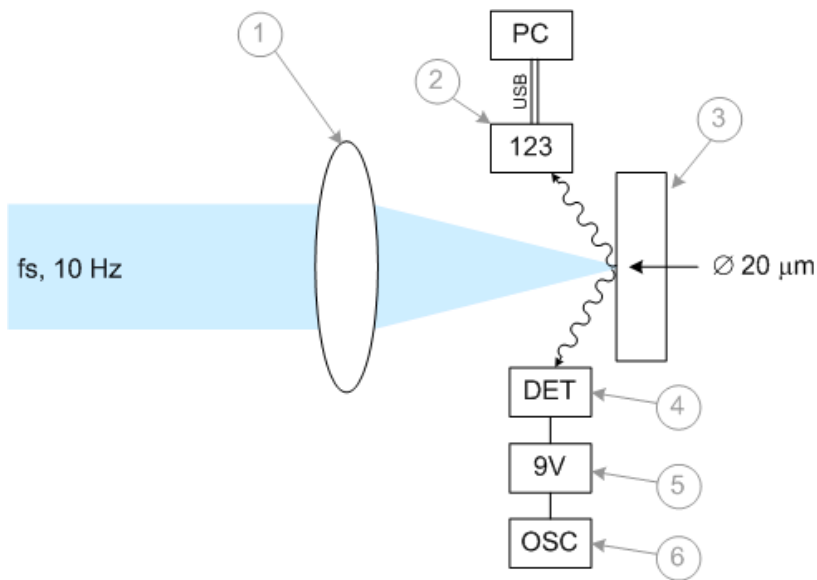


Fig. 3. Experimental setup (1—focusing lens, 2—Amptek X-ray detector, 3—target (brass, aluminium), 4—high speed AXUV photodiode, 5—power supply of 9 V, 6—oscilloscope)

Filter wheel

Photodiode itself was protected by the filter (aluminium filter with the thickness $0.8\ \mu\text{m}$ at first, later on by the polymer opaque filter $25\ \mu\text{m}$) to prevent the visible light detection. Additionally there was the rotating filter wheel (see Fig. 4) enabling to change the filter without the necessity to open the vacuum chamber.



Fig. 4. Filter wheel

Laser focustation

Laser power was set to the maximum of the energy. The spark changes its intensity when moving the target along the laser beam. It is very bright when the focus is behind the target surface, while much lower when in front of it. Optimal focus is therefore near the intensity step. Thus, the process of finding the optimum was in several steps. In each step, the laser beam energy was decreased by additional gray filter and the intensity step was found having the position of the intensity step from previous step as an initial estimate. Finally we have removed the filter and measure with the maximum of the laser beam energy.

Experimental results – photodiode

Originally, we supposed that there is only EUV radiation going from the laser plasma. Following the hypothesis, we have chosen these filters (see Fig. 5):

- aluminium filter with the thickness $0.8 \mu\text{m}$
- nickel filter with the thickness $1 \mu\text{m}$
- zirconium filter with the thickness $1 \mu\text{m}$

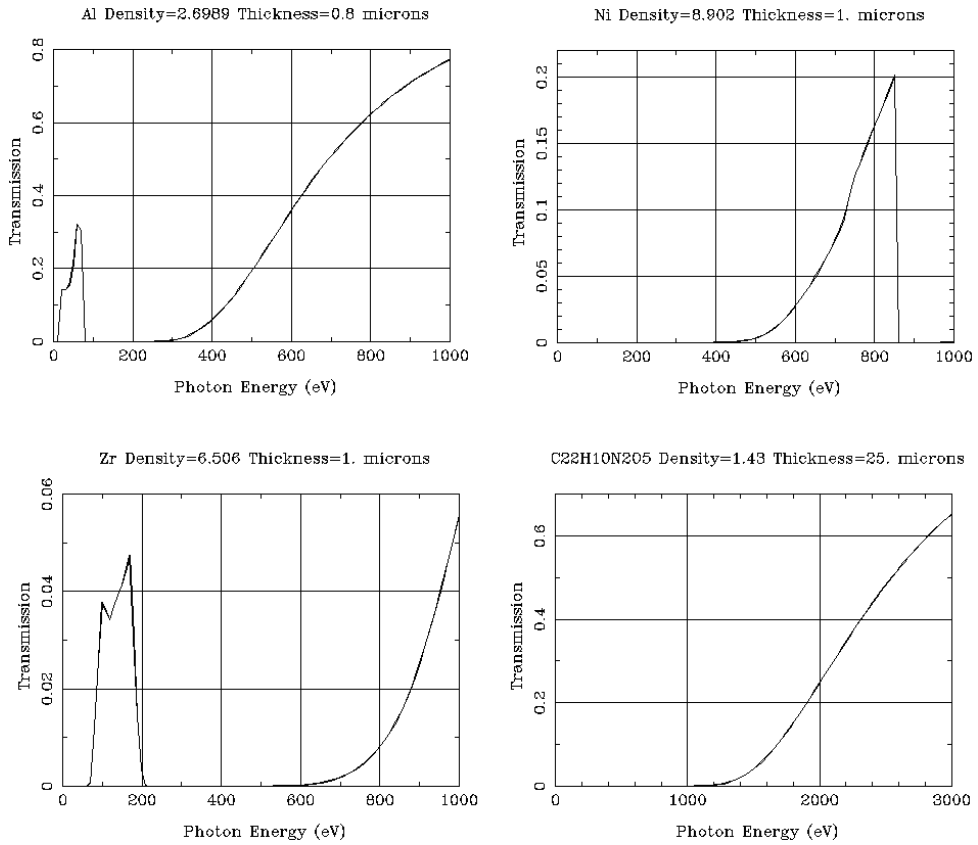


Fig. 5. Transmission filters used

It turned out that the filters were too thin and both visible light and X-rays passed through. Signal on the diode was almost identical (see Figs. 6–9) for all these filter combinations:

- aluminium filter
- aluminium + aluminium filter
- aluminium + nickel filter
- aluminium + zirconium filter

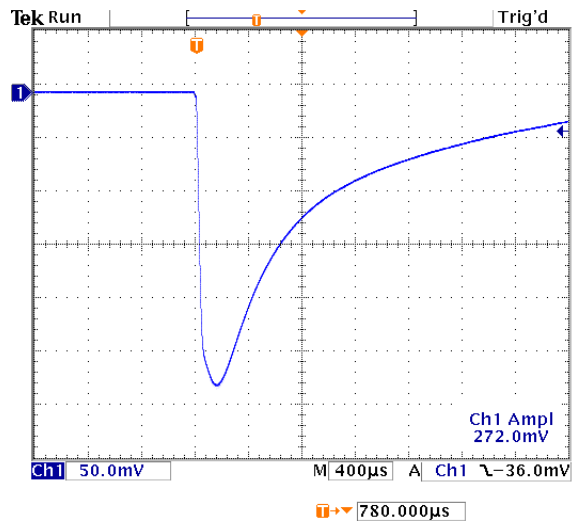


Fig. 6. Signal on the diode with aluminium filter

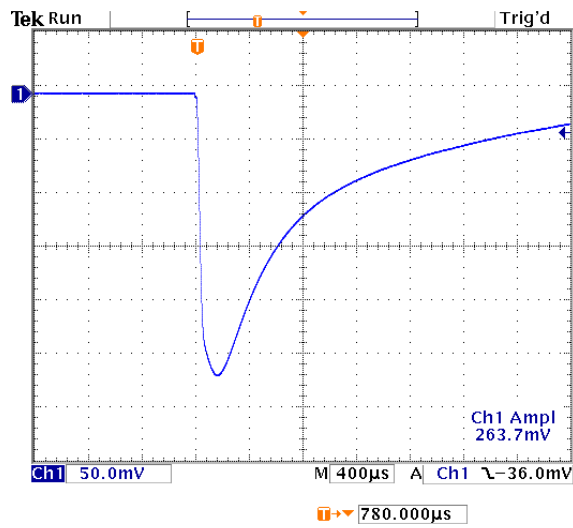


Fig. 7. Signal on the diode with aluminium + aluminium filter

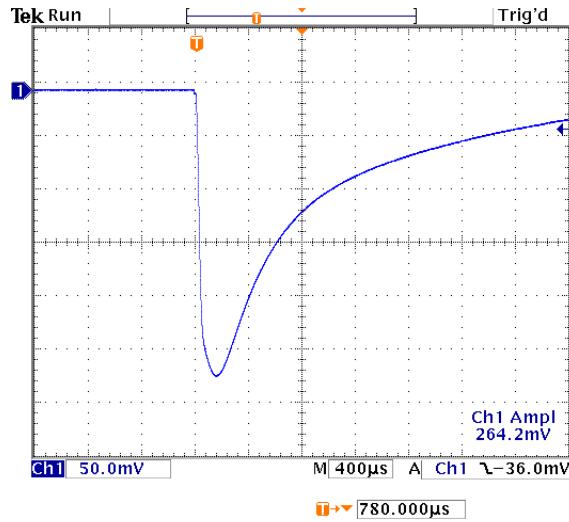


Fig. 8. Signal on the diode with aluminium + nickel filter

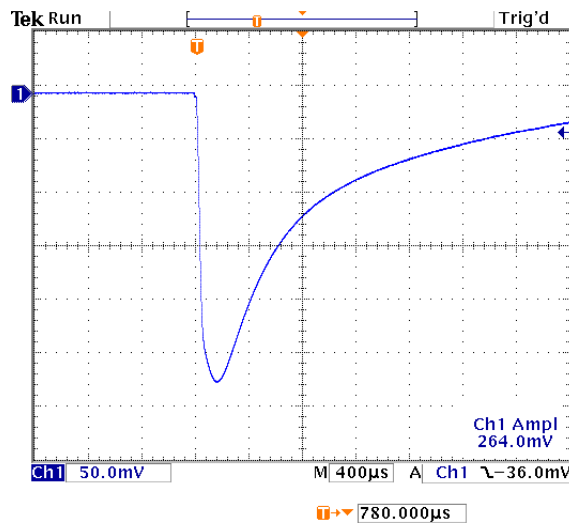


Fig. 9. Signal on the diode with aluminium + zirconium filter

Our selected filters were replaced by the polymer opaque filter with the thickness $25\ \mu\text{m}$ (see Fig. 5). There was no visible light on the photodiode in experimental setup with this polymer filter along with better shielding the whole setup excluding this polymer window by light-tight foil. The verification was made using the piece of lead glass. When we placed the piece of lead glass

in front of the photodiode setup, there was no signal (only electric signal noise, which weakened gradually). Without lead glass we obtained periodic signal with the much greater intensity than the electric signal noise (see Figs. 10, 11).

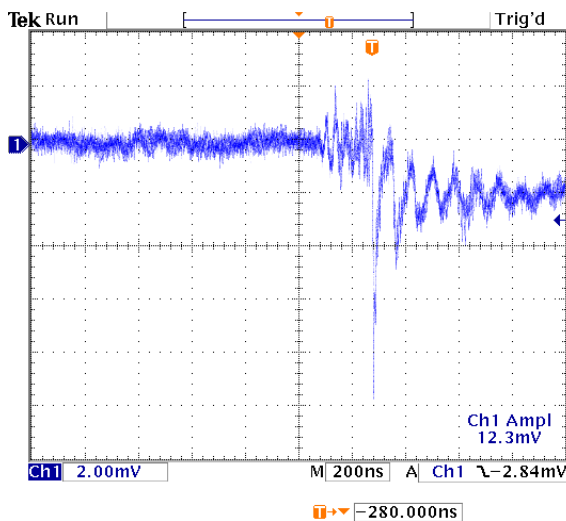


Fig. 10. Signal on the diode with lead glass
(electric signalnoise)

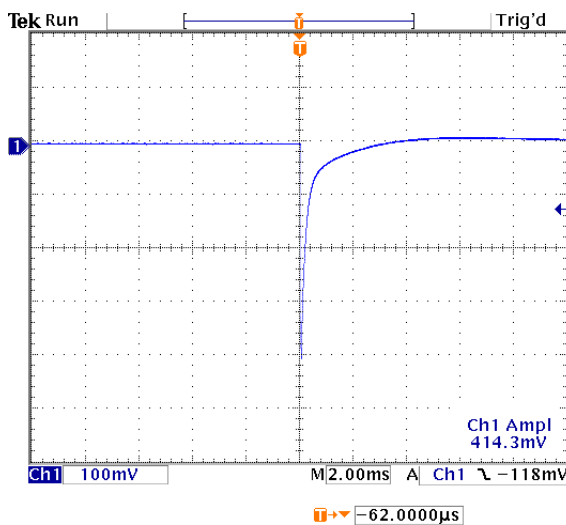


Fig. 11. Signal on the diode without lead glass

Experimental results – spectrometer

The X-ray spectrum measurements passed off at the same time and have been performed in the same configuration like the experiment with the photodiode. The Amptek X-123SDD X-ray spectrometer was used to record the spectrum at an angle of about 45 deg from the target normal at the target front side. The 1 mil (25 μm) thick beryllium window at the entrance of the spectrometer prevents accurate detection of sub keV photons, while it does not significantly influence the detection efficiency at higher photon energies. The thick solid targets used in this experiment were composed of Brass and Copper and they were attached to the micro-positioning equipment with three linear displacements. This enabled us to shoot on the fresh target surface with 10 Hz repetition rate and record the X-ray spectrum at different positions of the target with respect to the best focus.

The spectra recorded with the Brass target and various target displacements are plotted in Fig. 12. They approximately consist of two exponential curves, which can be associated with bremsstrahlung emission due cold and hot electrons. The cold and hot electron temperatures estimated from the spectra recorded at the best focal position are 0.19 and 2.61 keV respectively. The dependence of the X-ray spectra with respect to the target position is clearly observed. This dependence is almost symmetrical for the same displacement of the target in both direction (positive and negative with respect to the best focus) and therefore we present just the results for the positive displacement. While the bremsstrahlung spectra extend up to about 10 keV energies, no X-ray line emission has been observed during this experiment.

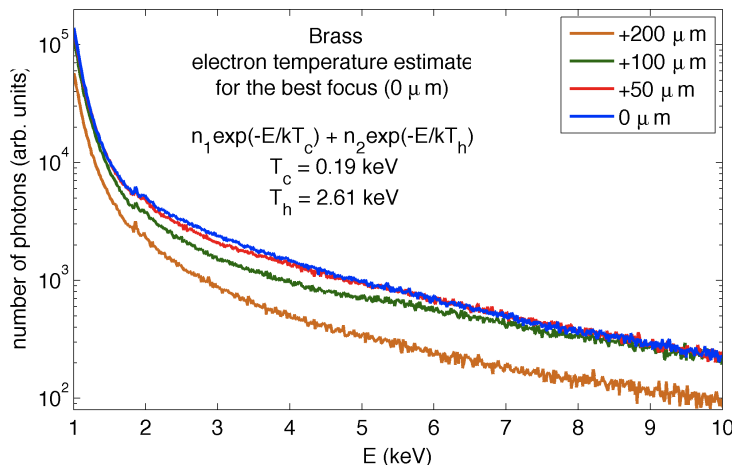


Fig. 12. The spectra recorded with the Brass target and various target displacements

The same measurements have been performed also for the pure Copper target. The X-ray spectra we have recorded are almost the same as for the Brass up to normalization constant. These spectra are compared in Fig. 13 for the minimum and the maximum target displacement form the best focus.

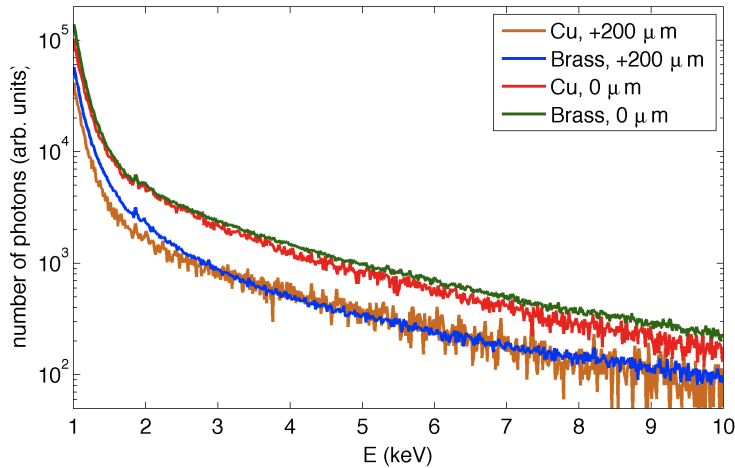


Fig. 13. Comparison the spectra for the Brass and Copper target

Next period of measuring

As was proved, there is more radiation with higher photon energies than we supposed. On account of this it will be needed to use the thicker filters to measure the pulse shape of the fs laser via photodiode at different photon energies. This knowledge will also help us in the next period of the experiment – measuring the pulse shape via pinhole, where the sensitive CCD camera [2] will be used. In this setup will be necessary to protect the CCD camera and prevent the camera saturation.

We keep at disposition several pinholes including the top hat pinhole which we normally use for X-ray metrology.

References

- [1] J. LIMPOUCH, M. DRAHOKOUPIL, D. KLIR, V. KUBECEK, M. TAMAS: *Femtosecond laser-target interaction experiments at FNSPE CTU*. Programme & Abstract Book of the 23rd Symposium on Plasma Physics and Technology (J. Khun, V. Kříha, J. Píchal, M. Píchal). CTU in Prague, FEE & IPP AS, Prague 2008, 53–53.

- [2] V. PICKOVA: Study of focusing EUV radiation from the capillary discharge, diploma thesis. FNSPE CTU, Prague 2007.
- [3] http://henke.lbl.gov/optical_constants/, CXRO X-ray Interactions With Matter, March 2010.
- [4] http://www.ird-inc.com/packages/uvg_axuv_sxuv_5.htm, TO5, March 2010.

Received May 10, 2010

Production of multiple charged and high energy ions by moderate energy laser facilities¹

YURIY V. KOROBKIN², VICTOR L. PAPERNY³,
IGOR V. ROMANOV², ANDREI V. BRANTOV²,
ALEKSANDR A. RUPASOV², ANDREY S. SHIKANOV²

Abstract. A brief survey of studies of sources of the multiple charged and high energy metallic ions based on moderate energy laser facilities are presented. There are applied two designs of the facilities. The first one provides production of the ion flow from a plasma flame produced by irradiation of Al target by pulse of a Nd:glass laser of moderate light energy (90 mJ) and intensity (4.2×10^{12} W/cm²) and of 27 ps pulse duration. It is established that ions of the target material up to Al¹¹⁺ are emitted from the laser produced plasma with maximum ion energy approaches 7 keV/Z. The second type of ion source presents a low voltage (about 2.5 kV) vacuum discharge that is initiated by a laser pulse of low energy. Al ions of the charge states up to +9 are observed and their maximum energies fit the scaling $E = 12$ keV/Z. The ions are produced from the micropinch that is formed within cathode plasma jet expanding into the vacuum ambient.

Key Words. Laser produced plasma, multiple charged ions, accelerated ions, vacuum discharge micropinch.

1. Introduction

The recent time they carry on the intensive activity aiming the elaboration of sources of the multiple charge ions for searches in nuclear physics, medicine, modifying material properties etc. [1]–[3]. As a rule, production of the ions by

¹The work was supported by the Russian Foundation for Basic Researches under projects # 09-02-01084 and # 09-08-01114 as well as by the Ministry for Education and Science under project # 2.1.1/473.

²Lebedev Physical Institute, Moscow, Russia

³Irkutsk State University, Irkutsk, Russia; e-mail: paperny@math.isu.runnet.ru

the elaborated sources occurs in the plasma flame arising as a result of irradiation of a solid target with a high power laser beam as well as in plasma of high current sparks. The main disadvantages of these sources are the high energy consumption required for production of the heated plasma, low efficiency and high cost. For instance, to produce ions with energies of a few tens of MeV, they should apply a laser pulse of the femtosecond length and of the power density exceeding of 10^{19} W/cm².

At the same time, the recent studies revealed that they can obtain ions beams with the high energy content at the rather moderate characteristics of the apparatus applied [4], [5]. The results were based on the revealed effect of pinching of cathode plasma jet produced at a low inductance and low voltage vacuum spark with the high current rise rate, exceeding of 10^{10} A/s. Micropinches with the electron temperature of a few hundreds of eV were produced there at the discharge current just about of a kiloampere that is near two orders of value less than these at conventional high-current vacuum sparks. The micropinch provides both the additional ionization of a cathode material and acceleration of the produced multiple charged ions by the space charge of the ejected electrons. Therewith, the ion energies per a charge unit yielded when acceleration can exceeded significantly the interelectrode voltage applied.

Earlier, the authors had studied both experimentally and theoretically the features of running of the fast laser-induced vacuum discharges [6]–[8]. It was established that features of the laser produced pre-plasma play a key role in the pinch formation. It was shown that through optimization of characteristics of the laser pulse initiating the discharge it is possible to stabilize the instant of the neck formation and enhance the plasma constriction degree. Otherwise, the process of micropinch formation at the cathode plasma jet occurring at a low inductance vacuum spark differs significantly from plasma pinching of at the “classical” high current spark. Namely, the principal parameter that govern the process in our case is the discharge current rise rate, while it is the current maximum that controls the process at the latter case.

The paper presents results of the experimental studies of ion emission from the laser-produced plasma and plasma of the laser-induced low voltage vacuum discharge. In both cases a low-energy laser facilities is applied.

2. Experimental set-up and results

The investigations are performed with a two types of the experimental facility. In both cases is comprises a Nd:glass laser with wavelength of $1.06\ \mu\text{m}$ operating at the mode-locked regime with a pulse energy that is varied at the range of $W = 8 \div 500$ mJ and a duration $\tau = 27$ ps, and the ion emission diagnostics. The first set of studies is performed with the laser-produced plasma. In the second set of studies we used a vacuum diode that is initiated with the

laser beam that is focused at surface of the target that serves as a cathode as well. A diameter of the focal spot in both sets of experiments is of $300\ \mu\text{m}$ so that the irradiation intensity is $I_L = 4 \times 10^{11} \div 2 \times 10^{13}\ \text{W}/\text{cm}^2$. As a target (cathode) we use a plate of super pure Al of 99.99% content that is placed in a vacuum chamber where the pressure of residual gases is less than $10^{-4}\ \text{Pa}$ (see Fig. 1). The target is irradiated with the laser beam at 45° with respect to the surface normal. In the first set of experiments a voltage is applied between the target as cathode and an anode, so that the laser pulse initiate a vacuum discharge therewith the discharge current is sustained with a capacitor ($C = 0.22\ \mu\text{F}$) with a storage voltage is of $-2.3\ \text{kV}$ that is connected to the cathode. As the anode we use a grounded stain-steel anode of the design presented in Fig. 1. The anode length is of $1.5\ \text{cm}$ and its inner surface is a semi-sphere of $2.2\ \text{cm}$ in diameter. To provide the ions travelling into the drift area placed beyond the discharge gap, a hole is made in the anode of $0.6\ \text{cm}$ in diameter. Due to the presented electrode array design, the minimum inter-electrode gap is of $0.6\ \text{cm}$ and it can be enlarged up to $3\ \text{cm}$. After 3–4 shots the electrode array is displaced with a special device so that the laser beam is focused at a fresh area at the cathode surface. The current is measured by a Rogowski coil immediately in the cathode circuit. The total inductance of the discharge circuit is as much as $63\ \text{nH}$ and semi-period of the discharge is about of $360\ \text{ns}$.

The energy and charge state distributions of ions are measured by the time-of-flight method with the help of an ion electrostatic analyzer (IEA) of the “plane capacitor” type with the energy resolution $\Delta\varepsilon/\varepsilon \approx 2 \cdot 10^{-2}$ and the maximum ion energy per a charge unit to be measured is about $28\ \text{keV}/Z$. A microchannel plate is used as a detector of ions in the analyzer. The gain of the plate is adjusted for different ion charge states and impact energies using the data obtained in [9]. The entrance orifice of the analyzer is oriented perpendicular to the target surface and with the aim to enhance sensitivity of the detector we apply the relatively short pass of flight of ions from the target to the analyzer that was of $77\ \text{cm}$. The signals in the experiments are acquired with a *Tektronix* of $500\ \text{MHz}$ wideband.

Let us consider now results with the first set of experiments that are performed with the laser-produced plasma at energy of the laser pulse is $W = 90\ \text{mJ}$, hence the irradiation intensity is $I_L = 4.2 \times 10^{12}\ \text{W}/\text{cm}^2$. Figure 2 presents a typical wave form, where a charge state spectrum of Al ions for $E_i/Z = 3.9\ \text{keV}$ obtained at a single shot is depicted. It can be seen from the figure that a set of peaks corresponding to different charge states of Al ions up to ions Al^{+11} were observed. Signals corresponding to ions Al^{+12} were recorded in a few shots near the threshold of sensitivity of the detector, hence we can make principally just a qualitative conclusion that these ions are present in the plasma plume. The significant peak of ions H^+ was also registered in addition to the peaks attributed to ions of the target material. One can see that ions

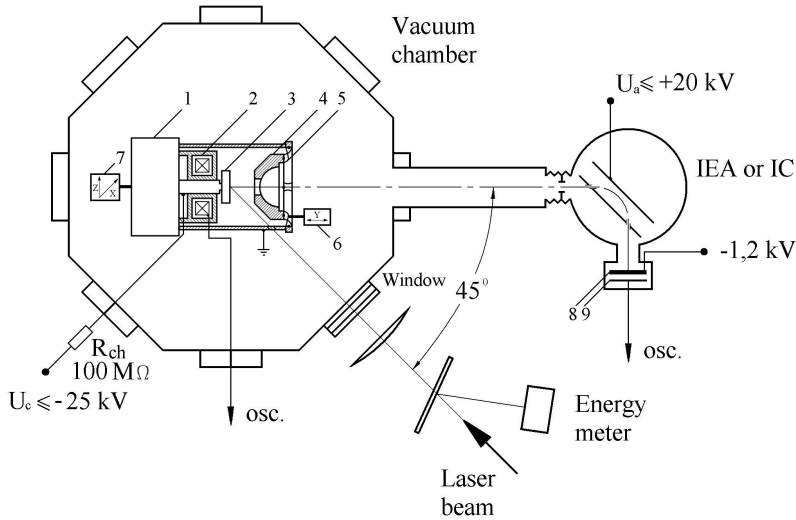


Fig. 1. Schematic diagram of the experimental set-up: 1—capacitor 0.22 μF , 2—Rogowski coil, 3—planar Al target – cathode, 4—steel anode, 5—flexible conductive line, 6, 7—coordinate – moving devices, 8—detector: microchannel plate, 9—electron collector

of other light impurities desorbed from the surface of the cathode, namely, O^{4+} , O^{5+} , O^{6+} , C^{3+} , C^{4+} , C^{5+} are present in the signal as well. Moreover, the light impurities ions having ratio of μ/Z that is close or equal to this for corresponding Al ions may contribute to the spectrum and we can not separate this contribution, for example, in case of ions Al^{+9} and C^{+4} .

Ion signals detected in various shots had a considerable scatter in amplitude; for this reason, these signals were averaged over a series of shots for subsequent processing. The averaged amplitudes of the signals corresponding to ions of a given charge state and measured for various values of E/Z were used for constructing of energy spectrum of these ions. Figure 3 shows the ion spectra obtained in this way for a few selected ionization states of ions Al^{n+} . The figure shows, in fact, the significant scatter in the data, so the energy spectra are presented as the trends that are built up from the experimental data for the corresponding ion charge states. Figure 3 exhibits that a typical spectrum of a bulk of ion is of a near Maxwellian shape with a slightly pronounced “tail” of accelerated ions whose energy can be, approximately, as high as 65 keV.

The ranges of kinetic energies for all ion species Al^{n+} , which are measured with the use of the IEA, are presented in Fig. 4. This figure exhibit that the peak energy of each ion species E_p grow nearly linearly with the ion charge state up to $Z = +9$ and it fits the relation $E_p = 7.5 \text{ keV}/Z$ therewith the

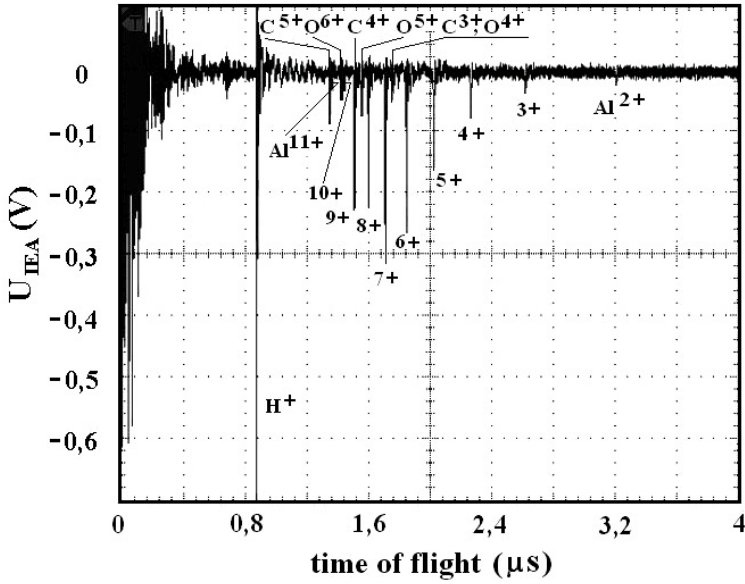


Fig. 2. Charge state spectrum of Al ions from laser produced plasma for $E/Z = 3.9$ keV

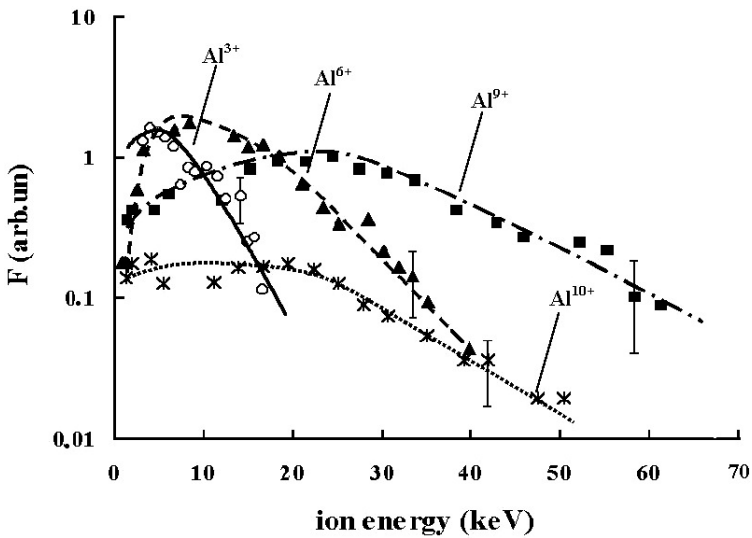


Fig. 3. Energy distributions for selected ion charge states from the laser produced plasma

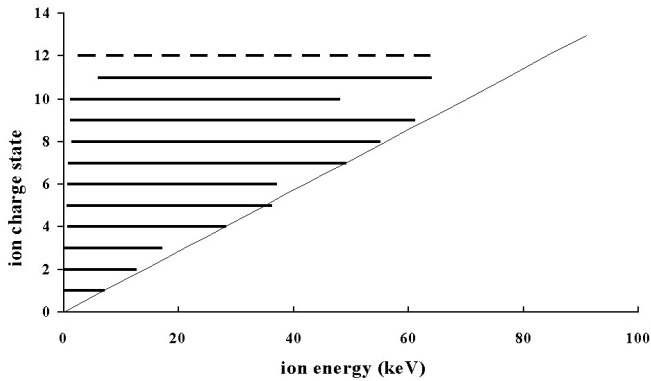


Fig. 4. Ranges of kinetic energy of Al^{n+} ions from the laser produced plasma, which are measured with the IEA; the linear fit corresponds to the relation $E_{max} = kZ$ with coefficient $k = 7.5 \text{ keV}/Z$

energies drop for Al^{10+} and Al^{11+} species. We suppose that it is the low level of the analyzer signal for these species, especially for ions of the high energy tail (see Fig. 3), as was mentioned above, which results in this drop.

By integrating of the energy spectra, we obtained the charge states distribution of ion beam for the given intensity of the laser pulse that is presented in Fig. 5. As it was mentioned above, ions of the light impurities can contribute to abundance of ions with the same ratio μ/Z , so we suggest that just C^{+4} ions are responsible for the burst observed at abundance of Al^{+9} . This contribution scarcely can be accounted with a relevant accuracy, hence the average charge state of the ion beam may be estimated from the distribution presented in Fig. 5 as lying in the range of $+(4.6 \div 4.8)$.

Let us consider now results of the second set of experiments that are performed with the laser-initiated vacuum discharge. According to results of [7], [8], for a discharge with the parameters as storage energy, inductance of the discharge circuit etc., hold constant, there is a range of optimum values of the laser pulse energies and inter-electrode gaps wherein the maximum single pinching of the cathode plasma jet is approached. Note, that at the enlarged gap the pinching can occur once more. Hence, the optimization of characteristics of both the discharge and the laser pulse is performed that permits us to attain a regular and reproducible plasma pinching at the capacitor voltage of 2.3 kV, the inter-electrode gap of 7.2 mm and the laser pulse energy of $8 \div 10 \text{ mJ}$ (i.e. the power density is about $I_L = 5 \times 10^{11} \text{ W}/\text{cm}^2$).

Figure 7 depicts wave forms of the discharge current, its derivative and charge state spectrum obtained with the IEA for the specified energy per a charge unit $E/Z = 3.14 \text{ keV}$ of the ions recorded. It can be seen from the

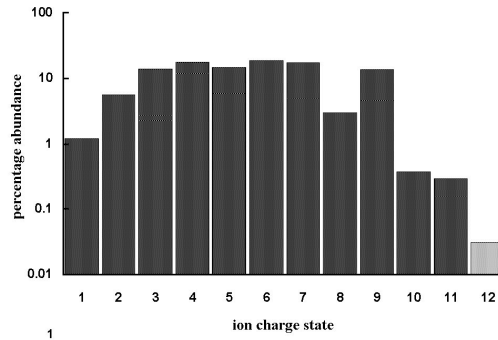


Fig. 5. The abundances of a variety of the Al ion species from the laser produced plasma

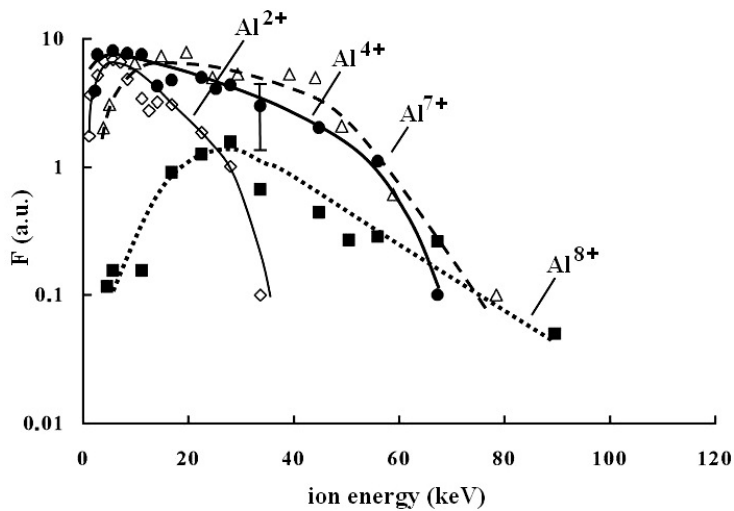


Fig. 6. Energy distributions for selected ion charge states from the discharge plasma

figure that, approximately, after 80 ns after the discharge onset, a short-run (less than of 100 ns length) peculiarities at both the discharge current and its derivative wave-forms are observed. It was a presence of these peculiarities that corresponded to bursts of the soft X-ray radiation, that permitted us to conclude in [6]–[8] that a micropinch was formed at plasma of a laser-initiated discharge. Specification of peaks at wave-form in Fig. 7 is performed by the time-of-flight method with the same procedure as that described above.

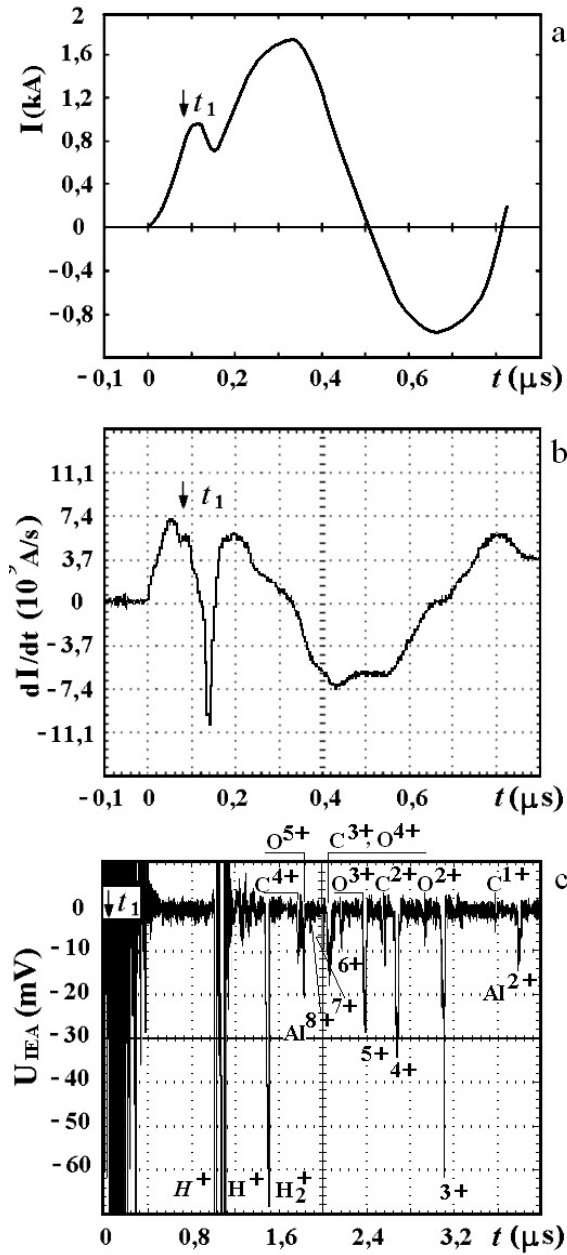


Fig. 7. Wave forms of the discharge current (a) and its derivative (b) at the storage voltage of 2.3 kV and energy of the initiating laser pulse $W = 8$ mJ ($I_p = 5 \times 10^{11}$ W/cm²); charge state spectrum of ions from the discharge plasma at energy $E/Z = 3.14$ keV (c); the arrow points the instant of generation of all ion species from the plasma

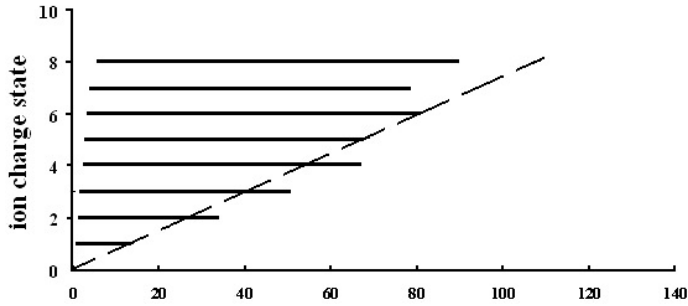


Fig. 8. Ranges of kinetic energy of Al^{n+} ions from the discharge plasma, which are measured with the IEA; the linear fit corresponds to the theoretical model, $E_{\max} = kZ$ with coefficient $k = 12 \text{ keV}/Z$

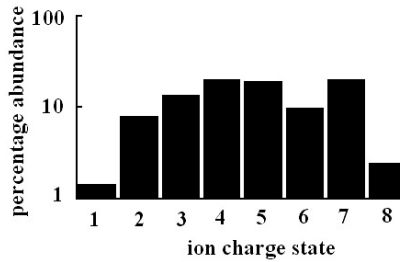


Fig. 9. The abundances of a variety of the Al ion species from the discharge plasma

Also, by means of the similar procedure, we build up energy distribution for a few ion species. These distributions are presented in Fig. 6. One can see from the figure that the distributions are of the non-Maxwellial shape with the pronounced tails of the accelerated ions, with energies exceeding of 80 keV. Like it was performed above, the ranges of kinetic energies for all ion species Al^{n+} , which are measured with the use of the IEA, are presented in Fig. 8. This figure exhibit that the peak energy of each ion species E_p grow nearly linearly with the ion charge state up to $Z = +8$ and it fits, approximately, the relation $E_p = 12 \text{ keV}/Z$.

By integrating of the energy spectra, like in this way as it was performed above, one can obtain the charge states distribution of ion beam for the given intensity of the initiating laser pulse and the given discharge voltage. This distribution is presented in Fig. 9. One can see that ion species at the charge states up to +8 are present in the given plasma jet.

3. Discussion and conclusion

The results presented exhibit that both the laser-produced plasma and plasma of the laser-induced low voltage discharge are sources of the highly charged and accelerated ions of a cathode material. Let us compare now characteristics of the ions beams produced with these sources. One can see that energies of the discharge-produced ions exceed those of the laser-produced ions. Intensity of ion beams from the first source is lower that of the latter as well. If one takes in mind that energy of the initiating laser beam near an order of value less than that of the laser sources and moderate value of the storage energy in the discharge, then a conclusion can be done that the discharge plasma is more effective sources than the laser-produced one.

These ions are produced at a micropinch that is formed within the cathode plasma flow. One can see that energy distributions of the plasma produced ions are of the Maxwellian shape, hence mechanism of their acceleration is due to capture by the ambipolar electric field arising as a consequence of expanding of the thermal electrons from the laser produced plasma. Nevertheless, the non-Maxwellian tails observable at energy distributions of the discharge-produced ions shows that there is an additional acceleration mechanism of these ions. Note that the similar effect has been observed earlier at experiments with plasma of a low-voltage vacuum spark [4]. Therewith, the voltage applied to the discharge gap was lower than 500 V, so one could not explain these energies by action of the voltage. We suggest that mechanism of the additional ion acceleration at the discharge plasma is similar to that described in papers [10] by which they explain ion acceleration in the spark stage of a vacuum discharge.

So, we conclude that the laser-initiated low-voltage discharge is a promising source of the accelerated and highly charged metallic ions for a variety of applications.

References

- [1] H. HASEROTH, E. HILL: *Multicharged ion sources for pulsed accelerators Laser and Particle Beams*. Review of Scientific Instruments, *67* (1996), 945–949.
- [2] F. P. BOODY, R. HÖPFL, H. HORA, J. KELLY: *Laser-driven ion source for reduced-cost implantation of metal ions for strong reduction of dry friction and increased durability*. Laser and Particle Beams, *14* (1996), 443–448.
- [3] T. E. COWAN, T. DIMITRE, J. ZWEIBACK, V. P. YANOVSKY: *Nuclear fusion from explosions of femtosecond laser-heated deuterium clusters*. Nature, *398* (1999), 489–495.
- [4] E. A. ZVEREV, V. I. KRASOV, I. A. KRINBERG, V. L. PAPERNY: *Formation of a micropinch and generation of multiply charged ions at the front of a current-carrying plasma jet*. Plasma Physics Reports, *31* (2005), 843–854.

- [5] M. F. ARTAMONOV, V. I. KRASOV, V. L. PAPERNY: *Vacuum discharge as an effective source of multiply charged ions*. Technical Physics Letters, *27* (2005), 1018–1020.
- [6] YU. V. KOROBKIN, I. V. ROMANOV, A. A. RUPASOV, A. S. SHIKANOV: *Hard X-ray emission in laser-induced vacuum discharge*. Laser and Particle Beams, *23* (2005), 333–339.
- [7] YU. V. KOROBKIN, V. L. PAPERNY, I. V. ROMANOV, A. A. RUPASOV, A. S. SHIKANOV: *Micropinches in laser induced moderate power vacuum discharge*. Plasma Physics and Controlled Fusion, *50* (2008), 065002.
- [8] YU. V. KOROBKIN, V. L. PAPERNY, I. V. ROMANOV, A. A. RUPASOV, A. S. SHIKANOV: *Control of parameters of micropinches formed in current-carrying plasma jet*. Physics Letters A, *372* (2008), 1292–1296.
- [9] M. P. STOCKLI, D. FRY: *Analog gain of microchannel plates for 1.5–154 keV/q Ar^{q+} ($3 \leq q \leq 16$)*. Review of Scientific Instruments, *68* (1997), 3053–3059.
- [10] D. L. SHMELEV, S. A. BARENGOLTS: *Model of Collective Acceleration of Ions in Spark Stage of Vacuum Discharge*. IEEE Transaction on Plasma Science, *37* (2009), 1375–1381.

Received May 17, 2010

Post-acceleration of ions produced by laser-generated plasma

LORENZO TORRISI^{1, 2}, LORENZO GIUFFRIDA^{1, 2}

Abstract. A Nd:Yag laser, 1064 nm wavelength, 9 ns pulse width, 900 mJ maximum pulse energy, 1 ÷ 30 Hz repetition rate, is focused, at an intensity of about 10^{10} W/cm², on different targets placed in high vacuum. The ion emission is characterized by high directionality, current and charge states up to 10^+ . Laser-generated plasma occurs inside an extraction chamber placed, together to the target, to +30 kV potential with respect to the chamber ground. The post acceleration field is applied along the normal to the target surface. Its effect is that to accelerate the ions proportionally to their charge state. Time-of-flight technique is employed to analyze the post ion acceleration, to measure the ion species, charge states, current and their energies. Multi-energetic ion beams (H, C, Ti and Ge), multiply of 30 keV, can be produced with an ion beam spot diameter of about 8 mm². Generally a dose of the order of 10^{14} ions/cm² is obtained in 1 hour of laser irradiation at 10 Hz repetition rate. This laser ion source can be employed with success in the field of the ion implantation, in order to modify the chemical and physical surface layer properties of many material substrates.

Key Words. Post-ion acceleration, laser-generated plasma, time-of-flight technique, ion implantation.

1. Introduction

Pulsed laser-generated plasmas are useful to generate high ion stream emissions with high directionality, high kinetic energy and high charge states. At high laser intensities, of the order of 10^{16} W/cm², the ion emission yield is of the order of 10^{19} ions/laser pulse, the kinetic ion energy is of the order of 10 keV/amu and the charge states of the order of 40^+ [1]. At low laser intensities, of the order of 10^{11} W/cm², the ion emission yield is about 10^{16} ions/laser pulse, the kinetic ion energy is of the order of 100 eV/amu and the maximum charge states of about 10^+ [2].

¹Dip.to di Fisica, Università di Messina, Ctr. Papardo 31, 98166 S. Agata, Messina, Italy

²INFN-Laboratori Nazionali del Sud, Via S. Sofia 44, 98123 Catania, Italy

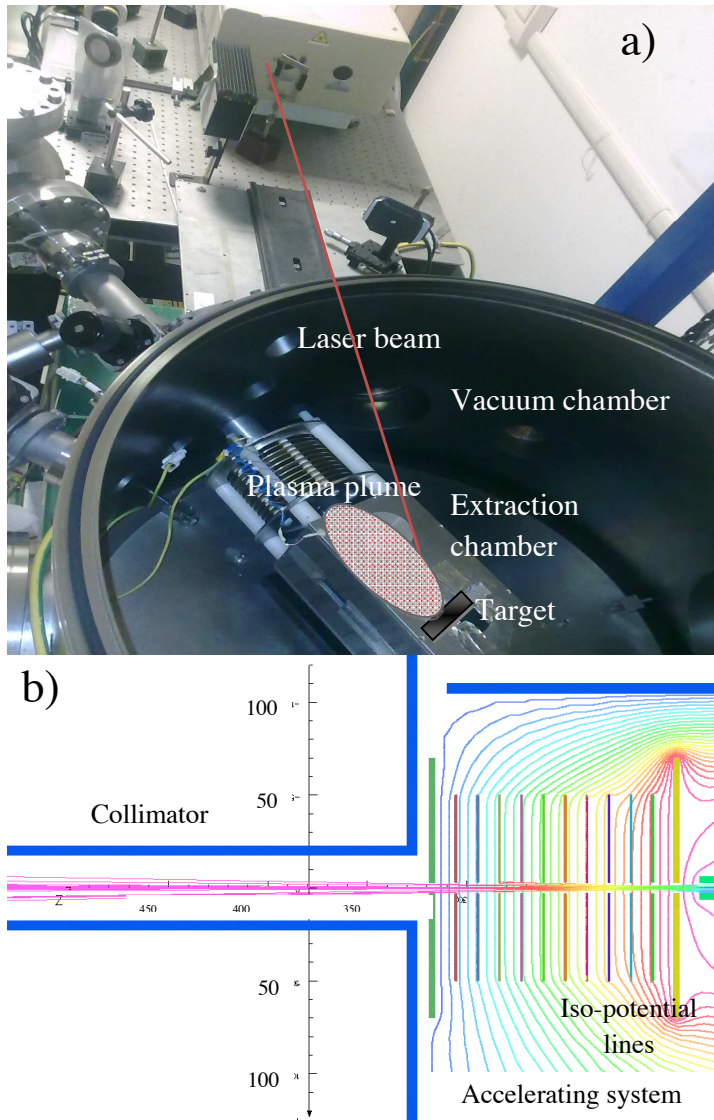


Fig. 1. a—photo of the set-up apparatus, b—Opera 3D simulations of the iso-potential lines and of the Ti ion trajectories inside and outside the extraction chamber placed at 30 kV acceleration voltage

The high intensity lasers are useful to accelerate ions at energies above the MeV and to use these ions to penetrate deeply in different material substrates exposed to the ion plasma emission. The main disadvantage of these lasers consists in their low pulse repetition rate and high cost. The low intensity

lasers, more available because less expensive, confer low kinetic energy to the emitted ions but they have the advantage to use high repetition rates and to generate a high current emission from a thick laser irradiated target [3]. The technique to generate ions from a laser ion source (LIS) using both methods, at high or at low laser intensity, is interesting not only to characterize the non-equilibrium plasma and understand the base physical generation mechanisms but also to prepare ion beams useful for many applications.

The advantage to use a post-ion acceleration method to increase the ion kinetic energy of the emitted charges, generated at low laser intensity, permits to prepare a high current multi-energetic ion beam using not expensive lasers. These beams, easy to obtain, find applications in the field of the ion implantation, ion sputtering, surface treatments, radiation damage, ion sources, pulse laser deposition, etc. [4].

In this article the technique of the post-ion acceleration using 30 kV potential is presented and discussed.

2. Experimental section

A Nd:Yag laser, with 9 ns pulse width, maximum pulse energy of 0.9 J, operating at 1064 nm fundamental wavelength with a repetition rate between 1 and 30 Hz, has been used for this experiment at INFN-LNS of Catania. The laser beam was focused, through a glass window, on different targets (CH_2 , Ti and Ge) placed inside a vacuum chamber at $10 \div 6$ mbar pressure. The incidence angle of the laser beam was 30° and the ion diagnostic has been placed along the normal to the target surface.

The post-accelerating set-up consists in a parallelepiped expansion chamber (26 cm long with a 11 cm quadric side) as reported in Fig. 1a. The target is placed at the centre of the extraction chamber. A lateral hole permits to the laser to enter and to hit the target. Target and extraction chamber were connected together to the same positive electrical potential, settable between 0 and +30 kV by using a high voltage power supply (Heinzinger, 30 kV–, 200 mA). The frontal base of the extraction chamber is open and, in front of it, 12 metallic discs with 2 mm thickness and 10 cm diameter, are aligned (parallel along the normal to the target surface) to the axe of the extraction chamber, maintaining 5 mm distance one for the other. Each disc has a central hole with 8 mm diameter. All discs are connected one with the other through a 1 M Ω resistor; in this way the 1st disc is connected to the high voltage and the last is connected to the ground.

The distance between the 1st and the last disc was 6 cm and the corresponding maximum electric field was 5 kV/cm.

The discs were used in order to obtain an uniform accelerating electric field, in agreement to the simulations carried out with Opera 3D code [5] (see

Fig. 1b), that permits to plot the electrical field lines, the iso-potential lines and the trajectories of all ions emitted from the target and travel toward the extraction zone.

The target was fixed inside the extraction chamber through a target holder that can be moved both in vertical and in rotation, in order to change the spot position and the incidence angle, respectively. All the targets were pure sheets $2\text{ cm} \times 2\text{ cm}$ surface and 1 mm thickness.

Generally the used pulse energy was 340 mJ, corresponding to a laser intensity of $3.8 \times 10^9\text{ W/cm}^2$, and the laser spot at 30° was 1 mm^2 . Some times higher laser energies up to 800 mJ were employed. A ring ion collector (ICR), with an inner diameter hole of 15 mm, an external diameter of 25 mm and a surface of about 314 mm^2 , was placed along the normal to the target surface at 100 cm distance from the target. Time of flight (TOF) technique was employed for the ion detection [6].

An electrostatic Ion Energy Analyzer (IEA) was used to measure the energy-to-charge ratio of the detected particles emitted from the plasma and post-accelerated along the normal to the target surface [6]. The IEA spectrometer deflects electro-statically the ions of 90° with respect to the target normal direction, so that they are detected by a windowless electron multiplier (WEM). The distance between target and WEM was 160 cm. By varying the bias voltages of the deflection plates was possible to measure different ion energies and to plot the ion energy distributions vs. the ion charge states.

The ion signals were recorded by using a fast Tektronics storage oscilloscope with 500 MHz frequency, 2 Gs/s sampling velocity and $50\ \Omega$ input resistance.

The ion implanted samples were analyzed by using the Rutherford Backscattering Spectroscopy (RBS) at 2.25 MeV alpha particles, in order to obtain information about the ion dose, the ion species and the ion range in the implanted substrates [7]. The backscattered alpha particles were collected at 170° and the RBS calibration factor was 2.57 energy/channel.

3. Results

Figure 2 reports a comparison between three ICR spectra obtained detecting the ion emission from the laser irradiation of thick CH_2 (a, b), Ti (c, d) and Ge (e, f) targets without post acceleration (0 kV), at left, and with 30 kV post acceleration, at right. The TOF spectra peaks are relative to the global C, Ti and Ge ions detected for the three laser-irradiated targets, respectively.

Without post acceleration the peaks correspond approximately to a mean kinetic energy of about 620 eV, 625 eV and 760 eV for C, Ti and Ge ions, respectively. The proton emission obtained during the laser ablation of CH_2 target is not time-separable from that of carbon ions.

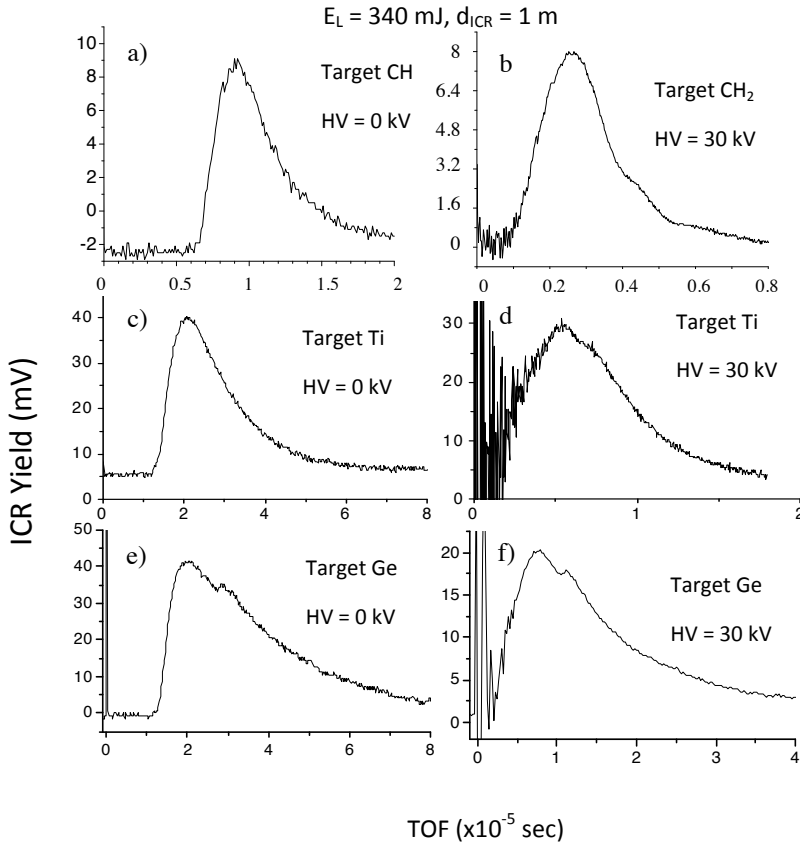


Fig. 2. Experimental TOF-ICR spectra at 100 cm distance from the target, for CH₂ (a and b), Ti (c and d) and Ge (e and f) without post-acceleration (left) and at +30 kV post acceleration (right)

With the 30 kV post acceleration the peaks are shifted towards low TOF values demonstrating that the mean kinetic ion energy increases significantly. The calculation of the velocity of the post-accelerated ions considers the ions travelling the extraction chamber (15 cm length) without acceleration, while they are accelerated at the extraction chamber output by the accelerating discs system (6 cm length). After the post acceleration ions move in free flight towards the detector placed at 85 cm from the extraction chamber.

The spectra at the right of Fig. 2 indicating a mean TOF of 2.6 μs, 5 μs and 6 μs, for post accelerated C, Ti and Ge ions, respectively, must be corrected by subtracting the drift times of 1.5 μs, 3 μs and 3.3 μs, respectively, in order to take in account the time that ions spend to go from the target surface to the output of the extraction chamber, before to be accelerated. This analysis permits to evaluate a mean ion energy of about 39 eV, 46 eV and 54 eV for C,

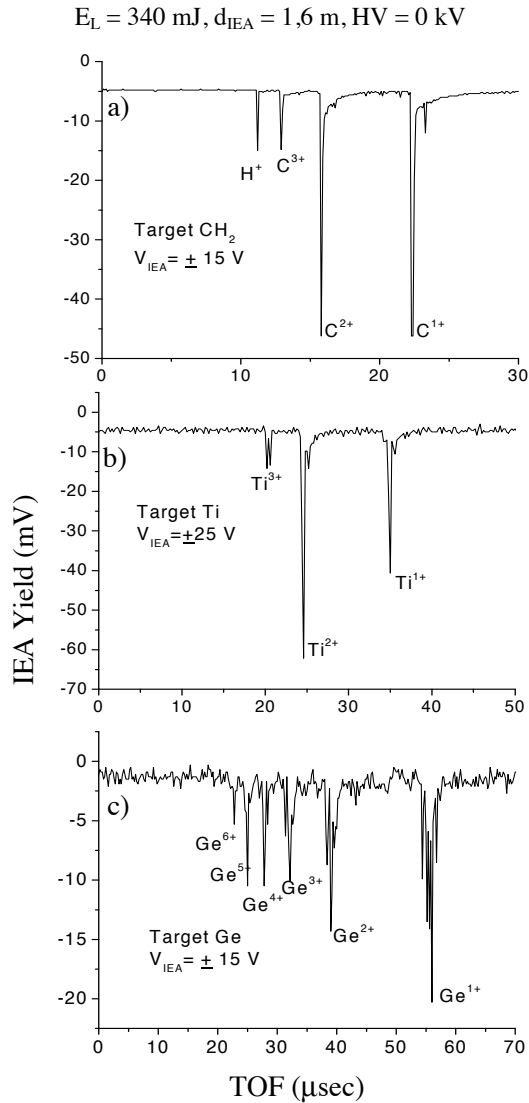


Fig. 3. Experimental TOF-IEA spectra at 1.6m distance from the target; in the case of CH_2 (a) there is the presence of three charge states of C and of hydrogen, in the case of Ti (b) there are three charge states, while in the case of Ge (c) there are six charge states

Ti and Ge ions, respectively, indicating that charge states are higher than 1^+ . The ICR peaks start at TOF times compatible with ion energies of the order of 90 eV, corresponding with the possibility to have up to 3 charge states of the post accelerated ions.

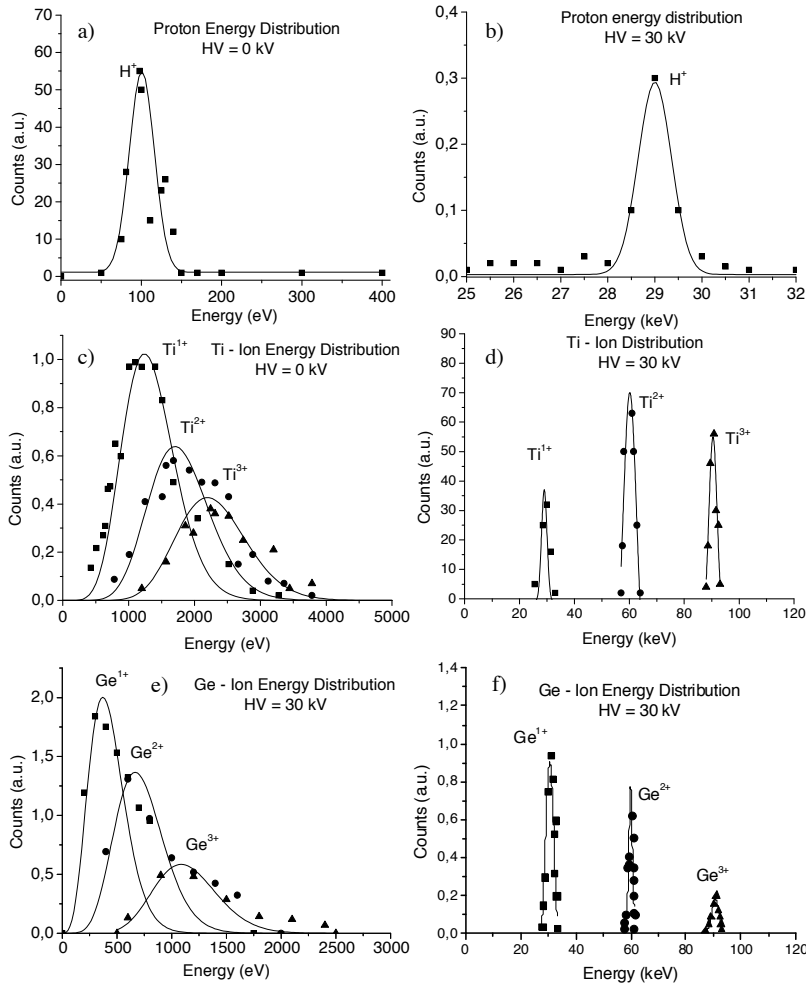


Fig. 4. Ion energy distributions of H (a and b), Ti (c and d) and Ge (e and f) without post-acceleration (left) and with +30 kV post acceleration (right)

The spectra shows also that the post-accelerated ion yield peaks are about 8 mV, 30 mV and 20 mV and the peak duration is about 40 μ s, 12 μ s, and 20 μ s for C, Ti and Ge ions, respectively. The analysis of these peaks indicates that the yields correspond to the detection of about 4×10^{10} C-ions/pulse, 5×10^9 Ti-ions/pulse and 5×10^{10} Ge-ions/pulse. Thus by using 10 Hz laser repetition rate, hitting a roto-translating thick target, the obtainable mean emitted current, assuming the mean charge state to be 2⁺, is of about 13 nA, 16 nA and 160 nA for C, Ti and Ge ion beams, respectively.

The use of the IEA permitted to evaluate more accurately the ion charge states of the plasma-generated particles. Figure 3 shows, as an example, three typical IEA ion spectra relative to the ion emission of H and C (a), Ti (b) and Ge (c) ions detected without post acceleration (0 kV). It is possible to observe that three charge states are detected for C and Ti ions while a charge state up to 6+ is detected for the Ge ions. Moreover, the ablation of CH₂ target shows clear protons emission.

The IEA analyses obtained by changing the electrostatic deflection bias permitted to evaluate the ion energy distributions as a function of ion charge state. Results confirm that the ion energy distributions follow the “Coulomb-Boltzmann-Shifted (CBS)” distribution presented in precedent articles [9]. Figure 4 shows the experimental ion energy distributions of the protons and of the three charge states of Ti and Ge ions, obtained by analyzing the IEA spectra of the H⁺ (a, b), Tiⁿ⁺ (c, d) and Geⁿ⁺ (e, f) ions obtained irradiating the CH₂, Ti and Ge targets, respectively, without (left) and with 30 kV (right) acceleration voltage. It is possible to observe that the ion energy distributions are peaked at 100 eV for protons, at about 500 eV for Ti and at about 700 eV for Ge. Such peaks are shifted at the energies of 30 eV, 60 eV and 90 eV, proportionally to their ion charge state, when 30 kV voltage are applied. The post accelerated ion energy distributions have an average energy resolution of the order of 3.4 % for protons, 10 %, 8 % and 4 % for Ti⁺, Ti²⁺ and Ti³⁺, respectively and 12 %, 3 % and 4 % for Ge⁺, Ge²⁺ and Ge³⁺, respectively. This resolution depends not only on the energy spread of the produced ion emission from plasma but also on the power supply stability and maximum extractable current. Using a power supply with a low current the risk to induce arc discharges during the plasma production increases and the high voltage may be little decreased with respect to the nominal value. This effect may induce energy decreasing of the particle with consequent loss of ion energy resolution.

The implant of the multi energetic post accelerated particles in different substrates can be analyzed though the Rutherford Backscattering Spectroscopy (RBS) of 2.25 MeV alpha particles in order to determine the ion dose and the ion penetration depth [7].

Figure 5 reports the RBS analysis of the 30 kV post accelerated Ge ion implantation in Si at a dose of $1 \times 10^{15}/\text{cm}^2$ (a) and the relative RBS X-RUMP simulation [8] (b). The spectra demonstrate that the Ge ions are implanted up to a depth of about 50 nm, corresponding to the range of Ge-ions with a kinetic energy of about 65 eV.

The same figure reports the RBS spectrum relative to the Ti ion implantation of C-substrate (c) and the relative RBS X-RUMP simulation (d) demonstrating that the Ti ion penetration is of about 40 nm, corresponding to the range of Ti-ions with a kinetic energy of about 50 eV.

The same figure reports the ion spot of Ti ions obtained by irradiating a GAF-Chromic detector film [9] (d, e). This polymer detector has high detection

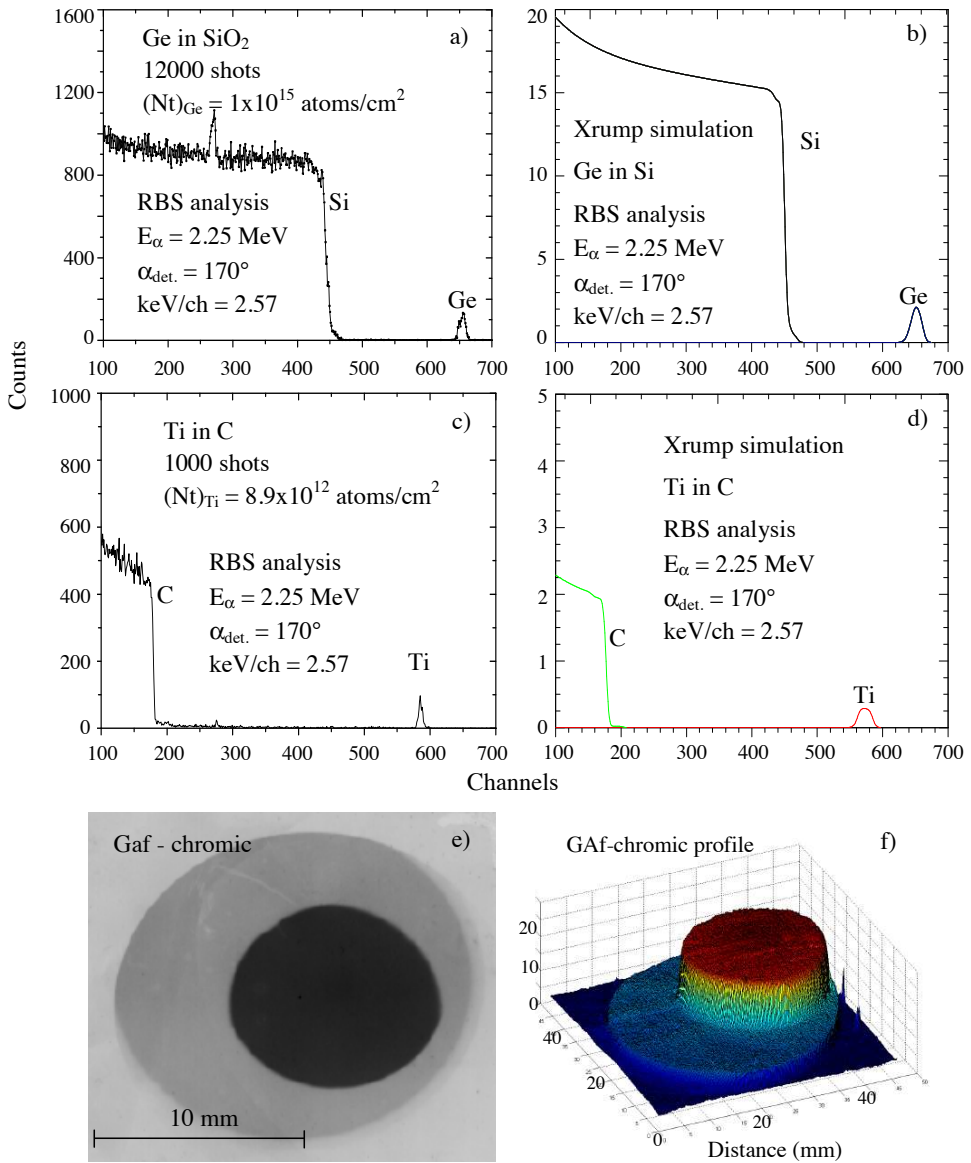


Fig. 5. RBS spectra of Ge implanted in SiO₂ substrate (a) and of Ti implanted in C substrate (c); for comparison the relative XRUMP simulations (b and d) are also reported (right); Ti implantation of a GAF chromic film (e), where is possible distinguish the black zone corresponding to the X-ray and ion irradiation and a light zone corresponding only to the ion implantation; the last figure (f) shows the GAF chromic profile

efficiency for ions and X-rays, also at very low implanted energies and doses. The polymer detector, placed at 100 cm distance from the extraction chamber, shows a large spot due to the ion implantation and a concentric spot, darker, due to the detection of X-rays, neutrals and ions. The ion dose used to obtain the dark spot on the polymer is 10^{11} ion/cm². The ion spot diameter is 10 cm and the corresponding total angular aperture of the post accelerated Ti ions is about 6°.

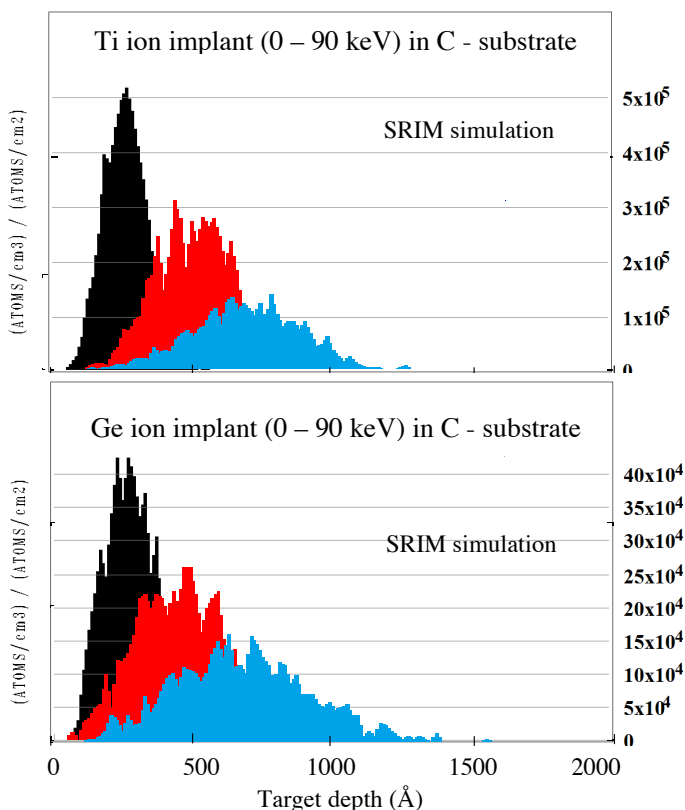


Fig. 6. SRIM simulations of Ti ions implanted in C substrates (a) and Ge ions implanted in Si substrates (b) with an energy range of $0 \div 90$ eV

The multi-energetic ion implantation in different materials can be followed by using the SRIM simulation program of Ziegler [10], which permits to determine the range straggling and the ion implanted depth profiles as a function of the ion energy. Two examples of SRIM simulations are reported in Fig. 6 relatively to the ion implantation of the Ti ions of 30 eV, 60 eV and 90 eV in Carbon (a) and to the ion implantation of Ge ions, of 30 eV, 60 eV and 90 keV

in Si-substrate. The amount of the Ti and Ge ions are proportional to the ionization cross section, i.e. are inversely proportional to the potential ionization of the electron sub-shells. Thus because the first three potential ionizations of titanium are 6.8 eV, 13.6 eV and 27.5 eV for Ti^+ , Ti^{2+} and Ti^{3+} , respectively, the relative amounts of Ti ions in the SRIM simulations, normalized to the first ionized specie, are maintained inversely proportional to these potentials. Similarly, because the first three potential ionizations of germanium are 7.9 eV, 15.9 eV and 34.2 eV for Ge^+ , Ge^{2+} and Ge^{3+} , respectively, the relative amounts of Ge ions in the SRIM simulations, normalized to the first ionized specie, are maintained inversely proportional to these potentials.

The SRIM depth profiles give a real representation of the multiple ion implantation in the substrate and permit to evaluate the surface layers that can endure chemical and physical modification due to the energy release of the implanted species. SRIM simulations are in good agreement with the experimental RBS analysis on the ion implanted substrates.

4. Discussion and Conclusions

Although high intensity laser, of the order of 10^{15} W/cm², can be employed to generate plasmas that accelerate ions at energies of the order of hundred keV and to induce direct ion implantation in different substrates [1], low laser intensities, of the order of 10^{10} W/cm², can be employed to reach the same aim coupling the laser-generate plasma system to a post-ion acceleration equipment.

In this case the main advantages consist in: the ion energy that can be controlled by the high voltage power supply used for the post acceleration; the high repetition rates of the laser pulse that can be employed in order to obtain a near constant ion current extracted from the plasma; in the high current densities that can be obtained irradiating thick roto-translating targets; in the low cost of the laser system.

A special attention to this problem is represented by the field of the ion implantation technique because the use of a laser ion source permits to accelerate any kind of ion and the use of multi-energetic ion beams is useful in the cases where the first surface layers can be modified by the implanted species as a function of their energy and their dose.

In polymers the chemical and physical properties, such as the thermal and electric conductivity, roughness, wetting ability, wear, chemical reactivity, hardness and mechanical resistance, can be modified at relatively low ion doses, such as 10^{13} ions/cm² [11]. In metals the chemical and physical properties can be modified at higher ion doses, of the order of 10^{16} ions/cm² [12].

Work is in progress in order to increase the kV post ion acceleration (up to 100 kV) and the implanted dose-rate, obtainable by increasing the extracted ion current.

References

- [1] L. LASKA, K. JUNGWIRTH, B. KRALILOVA, J. KRASA, M. PFEIFER, K. ROHLENA, J. SKALA, J. ULLSCHMIED, J. BADZIAK, P. PARYS, J. WOLOWSKI, E. WORYNA, S. GAMMINO, L. TORRISI, F. P. BOODY, H. HORA: *Generation of multiply charged ions at low and high laser-power densities*. Plasma Phys. Control. Fusion, *45* (2003), 585–599.
- [2] L. TORRISI, S. GAMMINO, L. ANDÒ, L. LASKA: *Tantalum ions production by 1064 nm pulsed laser irradiation*. J. Appl. Phys., *91*(5) (2002), 4685–4692.
- [3] S. GAMMINO, G. CIAVOLA, L. TORRISI, L. ANDÒ, M. PRESTI, L. LASKA, J. KRASA, J. WOLOWSKI: *Innovative ion sources for accelerators. The benefits of the plasma technology*. Czech. J. of Physics, *54 Suppl. C* (2004), C883–C888.
- [4] J. J. BELTRANO, L. TORRISI, D. MARGARONE: *Biocompatible film decomposition by using Nd:Yag pulsed laser*. Rad. Eff. & Def. in Solids, *160* (10–12) (2005), 545–552.
- [5] **Vector Field Software**, <http://www.vectorfields.com/content/view/26/49>, 2010.
- [6] E. WORYNA, P. PARYS, J. WOLOWSKI, M. MROZ: *Corpuscular diagnostics and processing methods applied in investigations of laser-produced plasma as a source of highly ionized ions*. Laser Part. Beams, *14*(3) (1996), 293–321.
- [7] L. C. FELDMAN, J. W. MAYER: *Fundamental of surface and thin film analysis*. North-Holland Ed., New York 1986.
- [8] **Genplot Software**, <http://www.genplot.com/>, 2010.
- [9] Y. YAMAMOTO, S. TAKAHASHI, A. KOMATSU, N. UCHIDA, H. KATO: *Evaluation of GAF Chromic Dosimetry and Its Application to PDD and OCR Curves*. Jpn. J. Radiol Technol 2001, *57*(11) (2000), 1357–1364.
- [10] J. F. Ziegler, **SRIM Software**, <http://www.srim.org/>, 2010.
- [11] A. VALENZA, A. M. VISCO, L. TORRISI AND N. CAMPO: *Characterization of ultra-high-molecular weight polyethylene (UHMWPE) modified by ion implantation*. Polymer J., *45* (2004), 1707–1715.
- [12] F. P. BOODY, R. HÖPFL, H. HORA, J. C. KELLY: *Laser-driven ion source for ion implantation of metal ions for strong reduction of dry friction*. Laser and Particle Beams, *14* (1996), 443–448.

Received May 14, 2010

Effect of gas type on pinch current and soft X-ray emission in Sahand plasma focus

MOHAMMAD A. MOHAMMADI^{1,2}, SAMAD SOBHANIAN^{1,2},
MASOMEH KIANTAJ¹

Abstract. The effect of Nitrogen, oxygen, neon and argon as a working gas in Sahand Filippov type plasma focus facility (90 kJ, 25 kV) on pinch current has been studied. In the first section of this paper, at 0.25 Torr pressure and 14 kV working voltage, the effect of gas type on comparative study of soft X-ray is investigated. We find experimentally that in argon and neon Sahand machine emits more X-ray than in nitrogen and oxygen case. Furthermore the result shows that in Sahand with nitrogen and oxygen as a working gas, the pinch occur in 14 kV at 0.25 Torr pressure but in neon and argon it occurs at 0.25 Torr for different voltages. Decrease in time difference between the maximum current and the pinch current with increase in atomic number is another result in our research. The results of this work can help us in choosing gas type to use plasma focus as an X-ray source.

Key Words. Filippov type, plasma focus, X-ray, pinch current.

1. Introduction

Dense magnetized plasma can be produced by different devices, such as plasma accelerators, dense plasma focus (DPF), pinch facilities, etc. Plasma focus device was developed in the former Soviet Union [1] and USA [2] independently in the early 1960s. The plasma focus (PF) is a kind of pinch discharge in which a high pulsed voltage is applied over a low-pressure gas using a coaxial cylindrical electrode system. The central electrode which is connected to the positive high voltage, is the anode and it is partially covered with a coaxial insulator. In the DPF, with self generated magnetic field a pulsed plasma column with high temperature ($\sim 1 \div 2$ keV) and high density ($\sim 10^{25} \div 10^{26} \text{ m}^{-3}$) is produced. In the PF with deuterium as a working gas, the plasma column

¹Department of Atomic and Molecular Physics, Faculty of physics, University of Tabriz, Tabriz, Iran

²Research Institute for Applied Physics and Astronomy, University of Tabriz, Tabriz, Iran

emits burst of neutron with energy ~ 2.45 MeV [3], [4]. DPF in addition belong a source of neutron, also produced energetic ions [5], high energy electrons [6] and is a powerful source of soft X-ray (SXR) and hard X-ray (HXR) [7]–[10]. An important part of the experimental studies on X-ray and particle emission from DPF is oriented to interesting applications such as a source of SXRs for medico-biological and industrial applications such as microscopy, radiography, activation of enzymes, defectoscopy, microlithography, pump source for lasers and micromachining [11]–[13]. In these applications, it is important to be able to accurately monitor and measure the SXR yield or dosage. In the present work, comparative study of soft X-ray emission from Sahand plasma focus with argon, neon, oxygen and nitrogen as working gases at the same condition (same pressures and voltages) is investigated. Special, attention is paid to estimate the relation between soft X-ray and pinch current with the gas atomic number.

2. Experimental Setup

Experiments were carried out in the Filippov-Type plasma focus called Sahand [14]. Sahand is a 90 kJ Filippov type machine whose various parts are shown in Fig. 1.

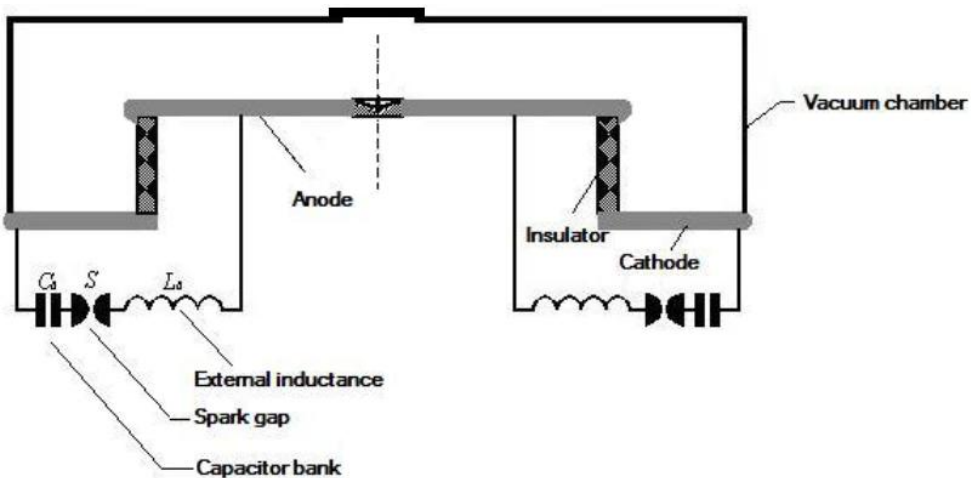


Fig. 1. Schematic view of Sahand plasma focus

The discharge chamber which serves also as the cathode is a stainless steel cylinder of 76 cm diameter and 26 cm height. Anode, which is a copper disc of 50 cm diameter, is placed on a ceramic cylinder of 48 cm diameter and 11 cm height. A replaceable anode insert is installed in the central part of the anode as it gets eroded after many focus shots. Anode is connected to the spark gap

via 24 copper rods. As the working gas, we used nitrogen, oxygen, argon and neon with the pressure of 0.25 Torr in our experiments. The required energy for the production of discharge and focusing is provided by a capacitor bank of 288 μF which consists of 24 capacitors. A triggered spark gap switch connected the inner electrode to the positively charged terminal of the capacitor. The maximum charging voltage and the maximum stored energy are 25 kV and 90 kJ respectively which induces a discharge current of ~ 1.1 MA. For the study of soft X-ray emission from the Sahand in a wide range of the spectrum the semiconductor detector, SPPD11-02 type (PIN-diode) has been used. An Al-filter, 7 μm thick, and a mesh with transparency 0.35, preventing the plasma effect on the detector and on the filter and attenuating the radiation flux, are installed in front of a sensitive element. As the PF emission power in a X-ray range is great, these measures are usually insufficient for providing linear operational mode of the detector. Therefore for decrease of the energy flux on the detector an additional diaphragm is used.

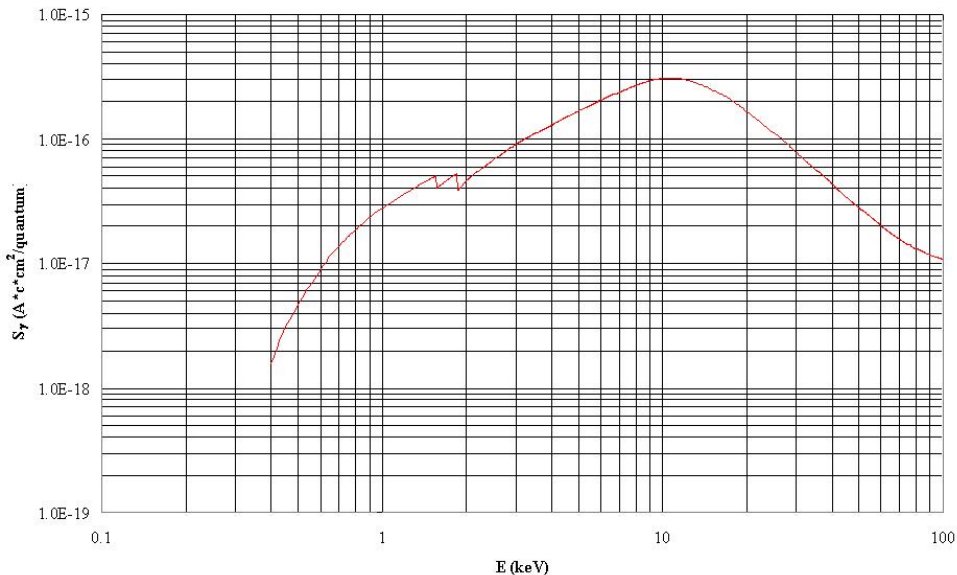


Fig. 2. quantum sensitivity of the SPPD detector

The spectral sensitivity of the detector, S_γ , is given in Fig. 2. An important specific feature of this detector is that it possesses of a rather high sensitivity in the quantum energy range 1 keV. Therefore this instrument is the main diagnostics element for registering the soft X-ray radiation in integral mode, as well as with a time resolution.

3. Results and Discussion

In this experiment, we used Sahand with 14kV working voltage and 0.25 Torr working pressure. With these conditions the total energy stored in DPF is 28.2 kJ. The typical current derivative signals from different gases are shown in Fig. 3. A dip in current derivative signal is associated with pinching, as “focusing”, of the plasma column. This is due to the rapid increase in inductance at pinching.

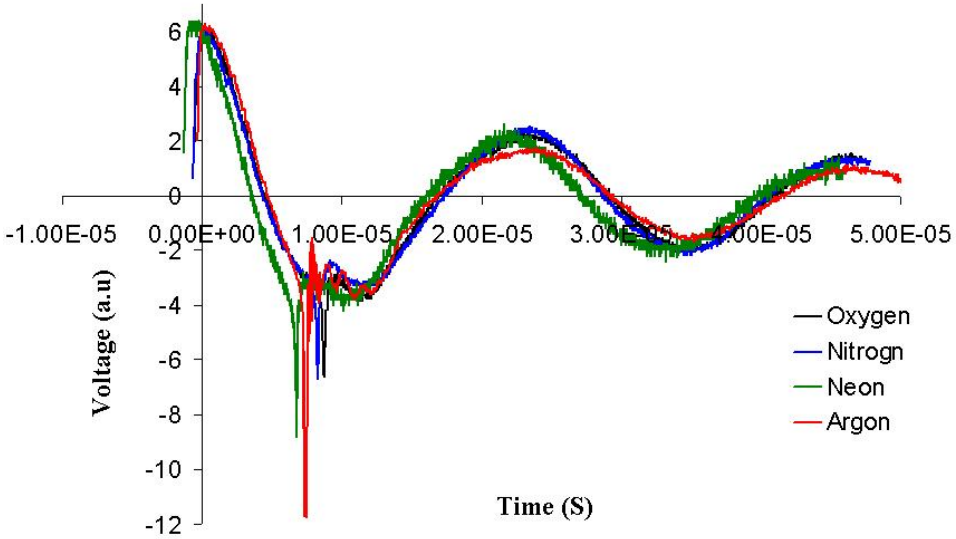


Fig. 3. A typical dI/dt trace for nitrogen, oxygen, neon and argon

Time differences between current derivative signals rising and pinch time for gases are different. This difference confirms that the energy delivered to the plasma is different. In Fig. 4 the time difference and pinch current are shown. In Fig. 4a the variation of time difference between maximum current and pinch current is shown. Minimum time difference is found for argon. This means that in gases with higher atomic number, more electron and ions are produced. In Fig. 4b shows that at higher atomic number the current derivative is also higher. In other words at higher atomic number more energy is converted into the plasma column. We expect that in working with argon and neon more X-ray will be produced. This result will be explained in next section of this paragraph.

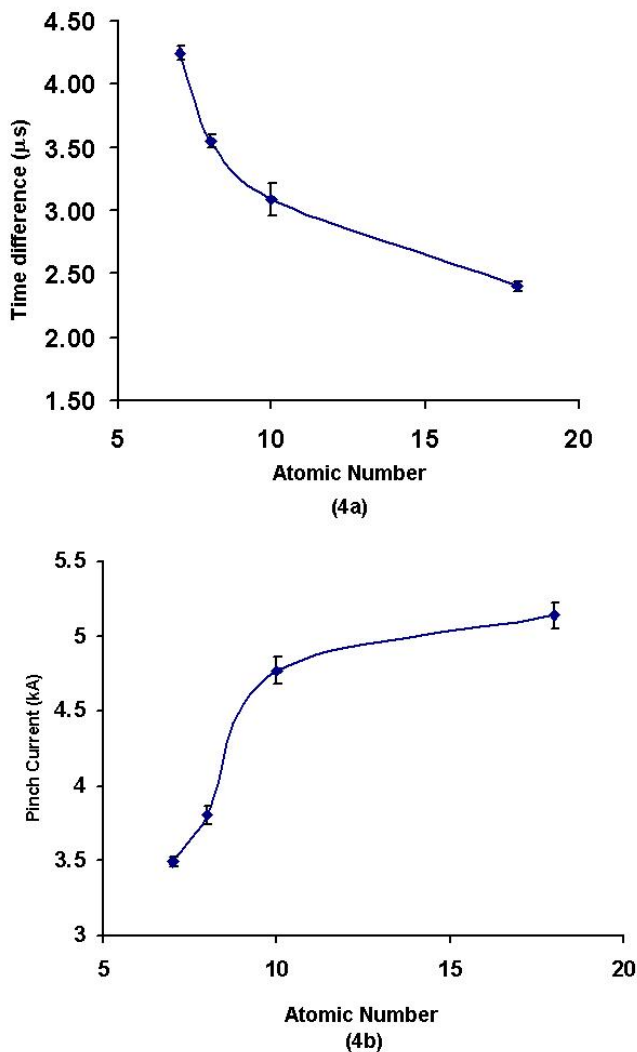


Fig. 4. (4a) time difference between pinch and maximum currents and (4b) pinch currents with atomic number

In Fig. 5 typical signal of X-ray from pin diodes with current and current derivative is shown.

Multiple dips were observed over at 0.25 Torr of filling pressure with nitrogen as a working gas, whereas in neon and argon and oxygen, these multiple dips are not observed at this not at high pressures (until 0.75 Torr).

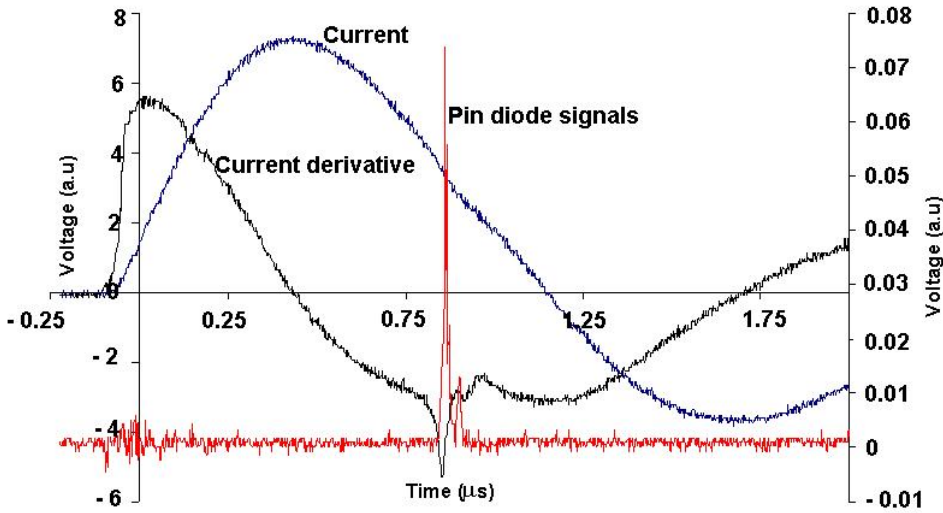


Fig. 5. Typical signals of current, current derivative and X-ray

In Fig. 6, time resolved signals of pin diode for different gases are shown. This result shows that for these gases with higher atomic number, the soft X-ray yield is increased. In plasma focus devices the main emissions of X-rays are due to bremsstrahlung, radiative recombination and de-excitation (line radiation) [15]. In all these mechanisms the radiation power is proportional to the charge number of ions. In Fig. 4b, the pinch current is increased with increasing of atomic number and this means that at higher atomic numbers more charges are produced so we conclude that the charge number of ions is increased. In Fig. 6 we see that the soft X-ray yield difference between neon and argon increases rapidly compared with other gases. With this result we conclude that in argon hot spots are produced which cause more X-rays emission.

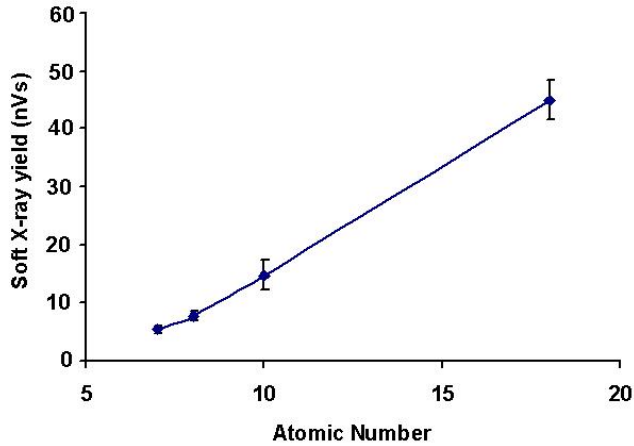


Fig. 6. Soft X-ray yield for different gases

4. Conclusion

In this paper the effect of nitrogen, oxygen, neon and argon as a working gas in Sahand Filippov type plasma focus facility (90 kJ, 25 kV) on pinch current is researched. We conclude that at higher atomic numbers the time difference between the pinch current and the maximum current is decreased. At higher atomic numbers more energy is delivered to plasma and this means that the charge number of ions is increased. The increasing of soft X-ray yield with atomic number is another result of this paper. In comparison with neon, oxygen and nitrogen, argon seems to be a good source for soft X-rays.

References

- [1] N. V. FILIPPOV, T. I. FILIPPOVA, V. P. VINOGRADOV: *Dense high temperature plasma in a non cylindrical Z-pinch compression*. Nuc. Fusion Suppl., 2 (1962), 577–583.
- [2] J. W. MATHER: *Investigation of high energy acceleration mode in the coaxial gun*. Physics Fluids Supplement, 7 (1964), 28–34.
- [3] S. V. SPRINGHAM, S. LEE, M. S. RAFIQUE: *Correlated deuteron energy spectra and neutron yield for a 3kJ plasma focus*. Plasma Physics and Controlled Fusion, 42 (2000), 1023–1032.
- [4] J. MORENO, L. BIRSTEIN, R. E. MAYER, P. SILVA, L. SOTO: *System for measurement of low yield neutron pulses from D–D fusion reactions based upon a ^3He proportional counter*. Measurement Science and Technology, 19 (2008), 87002.

- [5] C. S. WONG, P. CHOI, W. S. LEONG, J. SINGH: *Generation of high energy ion beams from a plasma focus modified for low pressure operation*. *Japanes Journal of Applied Physics*, *41* (2002), 3943–3946.
- [6] A. PATRAN, D. STOENESCU, R. S. RAWAT, S. V. SPRINGHAM, T. L. TAN, L. C. TAN, M. S. RAFIQUE, P. LEE, S. LEE: *A magnetic electron analyzer for plasma focus electron energy distribution studies*. *J. of Fusion Energy*, *25* (2006), 57–66.
- [7] M. A. MOHAMMADI, R. VERMA, S. SOBHANIAN, C. S. WONG, S. LEE, S. V. SPRINGHAM, T. L. TAN, P. LEE, R. S. RAWAT: *Neon soft X-ray emission studies from the UNU-ICTP plasma focus operated with longer than optimal anode length*. *Plasma Sources Science and Technology*, *16* (2007), 785–790.
- [8] M. ZAKAULLAH, A. ALAMGIR, M. SHAFIQ, M. SHARIF, A. WAHEED: *Scope of plasma focus with argon as a soft X-Ray source*. *IEEE Transactions on Plasma Science*, *30* (2002), 2089–2094.
- [9] H. BHUYAN, S. R. MOHANTY, N. K. NEAGY, S. BUJARBARUA, R. K. ROUT: *Comparative study of soft X-ray emission characteristics in a low energy dense plasma focus device*. *Journal of Applied Physics*, *95* (2004), 2975–2981.
- [10] M. SHAFIQ, S. HUSSAIN, A. WAHEED, M. ZAKAULLAH: *X-ray emission from a plasma focus with high-Z inserts at the anode tip*. *Plasma Sources Science and Technology*, *12* (2003), 199–204.
- [11] V. A. GRIBKOV, A. SRIVASTAVA, P. L. C. KEAT, V. KUDRYASHOV, S. LEE: *Operation of NX2 dense plasma focus device with argon filling as a possible radiation source for micro-machining*. *IEEE Transactions on Plasma Science*, *30* (2002), 1331–1338.
- [12] F. N. BEG, I. ROSS, A. LORENA, J. F. WORLEY, A. E. DANGER, M. G. HANIES: *Study of X-ray emission from a table top plasma focus and its application as an X-ray backlighter*. *Journal of Applied Physics*, *88* (2000), 3225–3230.
- [13] N. P. KOZLOV, V. A. ALEKSEV, Y. S. PROTISOV, A. B. RUBINOV: *High-power ultraviolet paraterphenyl-solution laser excited by the plasma focus of a magnetoplasma compressor*. *JEPT Letters*, *20* (1974), 331–332.
- [14] M. A. MOHAMMADI, S. SOBHANIAN, M. GHOMEISHI, E. GHARESHABANI, M. MOSLEHI-FARD, S. LEE, R. S. RAWAT: *Current sheath dynamics and its evolution studies in Sahand Filippov type plasma focus*. *Journal of fusion energy*, *28* (2009), 371–376.
- [15] M. H. LIU: *Soft X-rays from compact plasma focus*. Ph.D. theses, Nanyang technological university, 1996.

Received May 10, 2010

Ion collisions and deceleration in laser-produced plasma-jet interaction with walls¹

OLDŘICH RENNER², EDUARD KROUSKÝ², RICHARD LISKA³,
MICHAL ŠMÍD³, OLIVIER LARROCHE⁴, ELISABETH DALIMIER⁵

Abstract. Phenomena accompanying interaction of plasma jets with solid materials are systematically studied for their relevance to magnetic and inertial confinement fusion, primarily in the context of a development of future fusion reactors. We report results of experiments carried out on the PALS iodine laser system (one or two beams with pulse energy $5 \div 200$ J, wavelength $0.44/1.315$ μm , duration $0.25 \div 0.3$ ns, focused intensity $< 1 \times 10^{16}$ W/cm^2) with double-foil Al/Mg targets. The plasma jets produced at rear surface of laser-irradiated Al foils streamed towards Mg targets representing the walls preheated by the action of high-energy photons, particle and laser beams. The accelerated Al ions collided with the counter-propagating matter ejected from the wall, the environmental conditions in near-wall regions were analyzed using high-resolution X-ray spectroscopy and temporally resolved X-ray imaging. The deceleration profiles of the incident Al ions were quantitatively characterized via Doppler shifts of the optically thin J-satellite from the Al Ly α spectral group. The velocity oscillations at the double-side irradiated targets were revealed. The plasma evolution and interaction were modeled using the 2D arbitrary Lagrangian Eulerian hydrocode PALE and the multifluid code MULTIF. The interlocked experimental and theoretical methods demonstrate a potential of advanced X-ray diagnosis in investigation of the laser-produced plasma-wall interactions.

Key Words. Laser-produced plasma, plasma-wall interaction, plasma diagnostics, X-ray spectroscopy, fluid and kinetic plasma simulation.

¹This research is supported by the Czech Science Foundation Grant P205/10/0814, the CNRS PICS project No. 4343, and the Czech Ministry of Education, Youth, and Sports projects No. LC528 and 6840770022.

²Institute of Physics of the ASCR, v.v.i., Na Slovance 2, 182 21 Prague, Czech Republic

³Czech Technical University in Prague, FNSPE, 115 90 Prague, Czech Republic

⁴CEA DIF, Bruyères le Châtel, 91297 Arpajon Cedex, France

⁵Université Pierre et Marie Curie UPMC, LULI, UMR 7605, Paris, France

1. Introduction

Interaction of high-temperature plasmas with solid surfaces (generally known as plasma-wall interaction, PWI) is systematically studied for its relevance to numerous applications, starting from laboratory astrophysics and experiments modeling various stellar situations up to a research in the field of magnetic and inertial confinement fusion directed primarily to the development of future fusion reactors and to the design of sophisticated indirectly driven targets (see [1] and references therein). The investigation of transient processes occurring near surfaces of plasma-exposed materials contributes to an explanation of the PWI effects, provides experimental data for novel theoretical models and technological concepts needed to move from the scientific proof of the principle to a commercial reactor stage.

Energetic plasma jets formed at different conditions of laser-matter interaction represent a flexible and well-defined model environment for investigation of plasma interactions with solid surfaces (walls). By varying the parameters of laser-matter interaction (laser pulse energy, duration, target geometry and irradiance), plasma beams with tailored particle distribution, energy and degree of collimation can be produced [2].

The products of plasma-wall interactions are typically post-analyzed by microscopic and micro-spectroscopic methods (like X-ray fluorescence, Rutherford backscattering spectrometry, or electron probe microanalysis). In order to understand the mechanisms decisive for formation of these products, a detailed knowledge of environmental conditions in regions where the high-temperature plasma interacts with solids is extremely important. This information is typically obtained by optical (primarily infrared and visible) diagnosis, by laser interferometry, and by particle and X-ray diagnostic methods. Among the latter ones, applications of the high-resolution X-ray spectroscopy [3] are particularly useful, as the complex analysis of the intense spectral line emission accompanying the plasma impact is generally the most efficient tool for visualizing the phenomena of PWI in the densest plasma regions opaque for optical probing.

Previous experiments dedicated to laser-produced plasma-wall interaction (LPWI) defined the field of the processes investigated [4], [5]. The surface of the secondary target submitted to plasma jets or intense radiation fluxes is rapidly heated and partially ablated. The energetic ions approaching the obstacle interpenetrate the near-surface layer, collide with the counter-propagating matter and capture a large number of electrons to high-lying atomic levels. The macroscopic characteristics of the impinging plasma (density, temperature, charge and excited states distribution) are strongly modified, material mixing phenomena result in radiative or three-body recombination, charge exchange and formation of hollow atoms [6].

Due to a complexity of the problems studied, contemporary theoretical modeling of the LPWI phenomena based on fluid hydrodynamic models, kinetic simulations or their hybrids provides only qualitative predictions of the shock formation induced by the ion impact and the subsequent plasma evolution. The acquisition of complex information on processes involved in near-wall plasma collisions thus depends mostly on the realization of well characterized experiments. Most of the previous measurements directed at the X-ray investigation of LPWI were performed with low-resolution instrumentation and with limited knowledge of interaction conditions. Here we report precise, well-characterized test-bed experiments directed at investigation of PWI phenomena in colliding plasmas produced at single- or double-side laser-irradiated Al/Mg targets.

2. PALS experiment

In the pilot experiments carried out on the Prague PALS iodine laser system [7], the modification of macroscopic characteristics of the Al plasma formations generated at laser-irradiated double-foil Al/Mg targets was studied using high-resolution, high-dispersion X-ray spectroscopy and temporally resolved one-dimensional (1D) imaging. The scheme of the experiment is shown in Fig. 1.

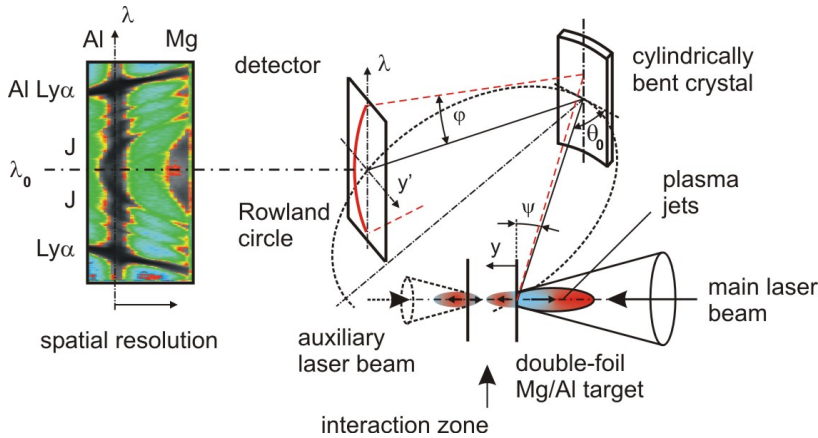


Fig. 1. Scheme of the experiment showing the plasma jet formation at double-foil Al/Mg targets and the spectra detection with the vertical-geometry Johann spectrometer

The targets consisting of two parallel foils of Al (thickness $0.8 \mu\text{m}$) and Mg (thickness $2 \mu\text{m}$) with a variable spacing were irradiated at normal incidence with one or two counter-propagating laser beams. The laser beams delivered pulses with variable energy ($5 \div 200 \text{ J}$), wavelength (0.44 or $1.315 \mu\text{m}$) and duration ($0.25 \div 0.3 \text{ ns}$). Being focused to a diameter of $80 \mu\text{m}$ (main beam) or

50 μm (auxiliary beam), they yielded a maximum intensity of $1 \times 10^{16} \text{ W/cm}^2$ on the target. Here we concentrate on the evaluation of two typical experimental configurations. In the first one, the data was obtained at foils separated by a distance of 550 μm and irradiated from the Al side only with the laser energy of 193 J at fundamental frequency (1.315 μm). In the second one, the foils were separated by a distance of 600 μm and double-side irradiated using frequency-tripled beams with energy of 115 J (Al foil) and 6 J (Mg foil).

The primary diagnostic data was recorded with a pinhole coupled to a low-magnification X-ray streak camera and a vertical dispersion Johann spectrometer (VJS) fitted with the cylindrically bent crystal of quartz (100). The VJS provides simultaneously two sets of mirror-symmetric spectra [8] characterized by high spectral (at the level of 8000) and 1D spatial resolution (8 μm) along the y -axis of the plasma jets expansion. By observing the plasma emission at a shallow angle of $\psi = 0.8^\circ$, the spectra integration over strong plasma gradients perpendicular to the foil surface was avoided.

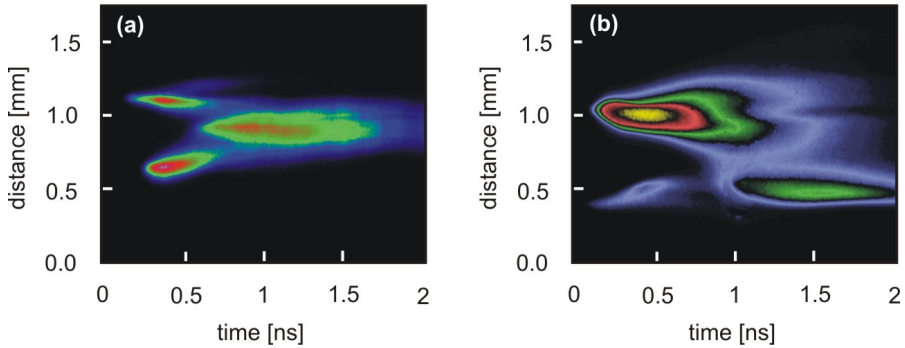


Fig. 2. X-ray streak records of the plasma evolution at the double-foil targets irradiated by the single laser beam at the fundamental frequency (a) and by two frequency-tripled beams (b); the main laser beam irradiates the Al foil from above thus forming the upper plasma plume; the prospective auxiliary beam strikes the Mg foil from below

The time-resolved streak images are presented in Fig. 2, where the vertical axis displays the distance measured along the normal to the target surfaces; the origin of the horizontal (temporal) axis vs. the laser pulse maximum was controlled by a delay line. These images demonstrate a diverse character of the plasma formation in the two experimental configurations discussed. At the Al/Mg target irradiated by the single laser beam at the fundamental frequency (a), the upper Al foil burns through well before the laser pulse maximum, thus the Al ions streaming towards Mg foil are not trapped by the cold secondary-target material but collide with the counter-propagating matter ejected from the wall. The strong X-ray emission from the interaction zone (close to the midplane between both foils) and insignificant interpenetration of

both ionic species towards opposite foils indicate a high collisionality [9] of the interacting plasma plumes. The streak camera record presented in Fig. 2b corresponds to the Al/Mg target irradiated with two counter-propagating, frequency-tripled laser beams. The streaked image of X-rays emitting Al and Mg plumes demonstrates the temporally synchronized evolution of the plasma jets at both foils and, after approximately 1 ns, their strong interaction resulting in an enhanced emission from the plasma region close to the Mg foil. The distribution of effective macroscopic plasma parameters following from interpretation of time-integrated, spatially resolved X-ray spectra will be discussed in the next section.

3. Results and discussion

The reconstructed high-resolution spectra used to derive the environmental conditions in the plasma interaction zone are presented in Fig. 3. The outer pair of the dominant spectral lines belongs to Ly α doublet of the hydrogenic Al, the inner pairs of lines are identified as dielectronic satellites 2l2l' - 1s2l' with the J-satellite closest to the axis of symmetry. A limited range of the Al Ly α group emission distinctly seen in single-side irradiated Al/Mg structure (Fig. 3a) indicates an efficient build-up of the stagnated plasma at the collision front between two counter-propagating plasmas. Within the interaction zone, the broadened resonance Ly α doublet was saturated, thus the plasma parameters were estimated from the satellite structure only. The comparison of the experimental data with the synthetic spectra produced by the collisional-radiative code PrismSPECT [10] indicates a thermalization of the colliding plasmas to temperatures of the order of several keV; the detailed interpretation of these spectra is being finalized.

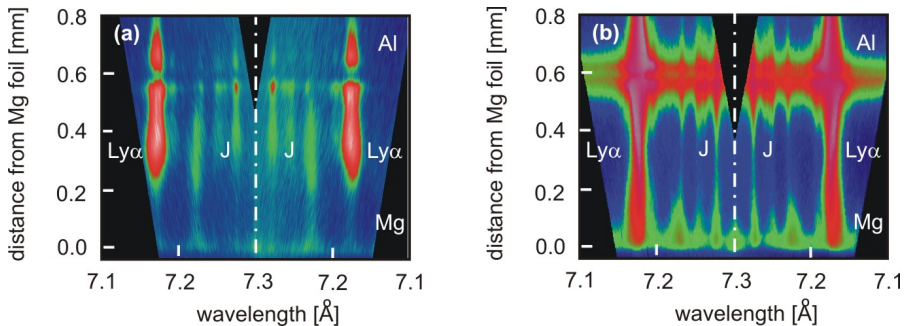


Fig. 3. Spatially resolved emission spectra of the Al Ly α spectral group observed at single-side (a) and two-side irradiated (b) Al/Mg double-foil targets

The character of the spectrum recorded in the case of two-side irradiated Al/Mg target (Fig. 3b) is distinctly different. The satellite-rich structure observed at the rear surface of the Al foil gradually reduces to the emission of the J-satellite only, the full satellite structure reappears near the Mg foil. This spectra behavior reflects the variable macroscopic parameters of the interpenetrating plasma jets. The analysis of the Al Ly α group emission [1] proved a formation of relatively cold dense plasma at the laser-exploded Al foil with the effective electron density $n_e = (3 \div 5) \times 10^{21} \text{ cm}^{-3}$, temperature $T_e = 300 \text{ eV}$, and the photon path length $L = 200 \mu\text{m}$. Close to the midplane, the density of the expanding plasma ($L = 350 \mu\text{m}$) drops to $n_e = 5 \times 10^{20} \text{ cm}^{-3}$ and its temperature increases to values $T_e > 700 \text{ eV}$, whereas subsequent deceleration, trapping, and thermalization of Al ions in the colliding plasma close to the Mg foil surface result in parameters $n_e \approx 3 \times 10^{21} \text{ cm}^{-3}$, $T_e \approx 220 \text{ eV}$, and $L \approx 500 \mu\text{m}$.

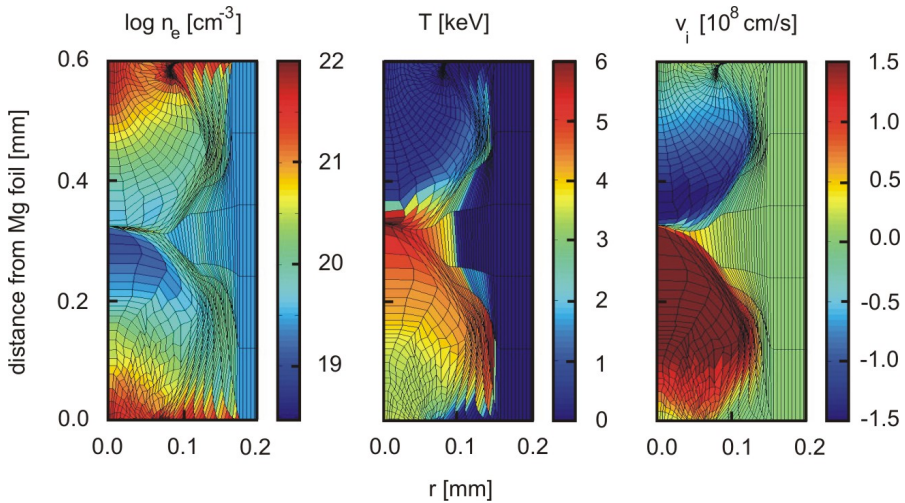


Fig. 4. PALE simulations of the electron density n_e , temperature T , and Al ion velocity v_i in colliding plasma jets at time $t = -50 \text{ ps}$ before the laser pulse maximum

The validity of this interpretation of the observed spectral profiles was supported by theoretical modeling. An early stage of the plasma evolution was simulated by the Prague Arbitrary Lagrangian Eulerian hydrocode PALE [11]. The code models plasma as a compressible gas by using hydrodynamic Euler equations for conservation of mass, momentum, and energy with heat conductivity and laser absorption terms. Here standard Spitzer–Harm heat conductivity with heat flux limiter and laser absorption on the critical surface is employed, whereas fast electrons and ions are not incorporated. After several steps of Lagrangian simulations, the deformed moving mesh is reconstructed

and the conservative quantities are remapped (Eulerian part) on to a smoother grid. An example of the simulations shown in Fig. 4 indicates that already at time $t = -150$ ps before the laser maximum, the upper Al foil burns through and the Al internal energy starts to decrease (mostly being transformed into the kinetic energy of expansion) despite a progressive laser absorption at the border of the hole in the Al foil. The lower Mg foil burns through slightly later at $t = -80$ ps; around this time, the compression of the counter-streaming plasmas attains its maximum and afterwards the plasmas between the foils start to expand in the radial direction r . After $t = -50$ ps, the axial kinetic energy of Al ions starts to decrease and the Al plasma expansion in the direction of the laser axis is gradually slowed down by the counter-propagating Mg plasma.

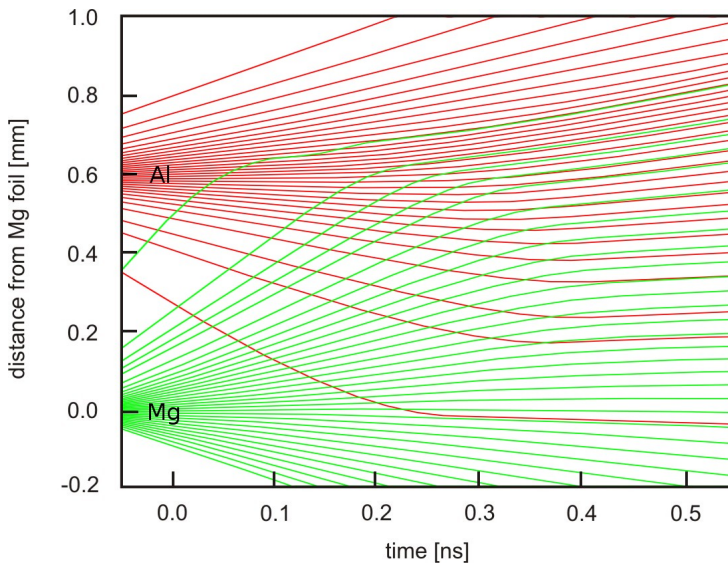


Fig. 5. MULTIF code modeling of the Al plasma jet interaction with the counter-propagating Mg plasma. The positions of the individual ion species are tracked by means of pseudo-Lagrangian markers

The interpenetration of the Al and Mg ions was simulated with the multifluid code MULTIF [12]. This code computes the hydrodynamics of an arbitrary number of the ion species on a common Eulerian grid in the presence of a neutralizing electron background, and takes into account the interactions among all ion and electron fluids due to Coulomb collisions through slowing-down and heating terms. The geometry is 1.5-dimensional, with the main spatial resolution axis along the inter-target distance and a self-similar expansion model in the transverse directions. Each individual ion species is tracked by means of pseudo-Lagrangian markers, whose motion for the case of the on-axis Al ions interaction with the Mg plasma is displayed in Fig. 5. The trajectories of

the fluid elements evidence regions and periods where the Al and Mg plasmas interpenetrate and/or stagnate with respect to each other.

The region close to the Mg foil is of particular interest for studying the effects of the ion–wall interaction and plasma interpenetration phenomena. In addition to the above demonstrated mapping of the macroscopic plasma parameters, the distinct frequency shifts of the optically thin Al J-satellite, which are clearly seen in Fig. 3b, provide an unique opportunity to measure the ion deceleration via Doppler effect.

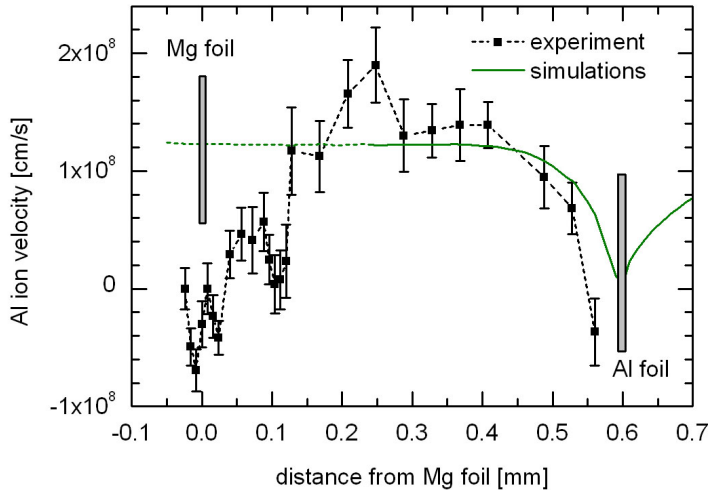


Fig. 6. Effective Al ions velocities (points with error bars) derived from Doppler shifts of the J-satellites; ion deceleration in the interaction zone is compared with theoretical predictions of the ion velocity distribution (solid and dashed line) at free-standing single-side irradiated foil

The previous experiments with single-side irradiated double-foil targets revealed almost monotonically decreasing red shifts of the Al J-satellite with the decreasing distance from the Mg foil [13]. This satellite behavior agrees with the expected stopping of the Al ions at the secondary target. The more complicated dependence of the ion deceleration close to the wall was found in plasmas produced at the double-side irradiated Al/Mg targets. Starting from the inner foil surface, the Al ions are accelerated until the zone of the intense plasma interaction; this results in the shift of the J-satellite to red. After passing a distance of about 250 μm from the Mg foil, the Al ion deceleration reveals in the decreasing Doppler shifts. The conversion of the observed shifts to ion velocities is shown in Fig. 6, where also the effective ion velocity profile simulated for the free-standing Al foil single-side irradiated by the same laser energy [1] is depicted for comparison. Assuming the gradual deceleration

and simple trapping of the Al ions at the Mg surface, the velocities should monotonically decrease to zero. In contrast, their detailed spatial distribution exhibits oscillations and even negative values which reflect the more complicated scenario of the ion deceleration including the ion reverse motion. The detailed interpretation of this phenomenon based on rigorous 2D description of the interpenetrating plasmas and post-processing of the hydrodynamic data is in progress.

4. Conclusion

The reported research proves a feasibility of the spectroscopic investigation of the laser-produced plasma–wall interactions. Modern methods of X-ray spectroscopy provide an unique opportunity to measure precisely the emission spectra with the complex satellite structure capable of characterizing the spatial distribution of the plasma parameters in the interaction zone. The deceleration and trapping of ions impinging on the walls are studied via Doppler shifts of the optically thin satellite transitions. The interlocked experimental and theoretical approaches enhance a potential of advanced X-ray diagnosis in investigation of the effects accompanying the plasma–wall interaction.

References

- [1] O. RENNER, R. LISKA, F. B. ROSMEJ: *Laser-produced plasma–wall interaction*. Laser Part. Beams, *27* (2009), 725–731.
- [2] T. PISARCZYK, A. KASPERCZUK, E. KROUSKY, K. MASEK, R. MIKLASZEWSKI, PH. NICOLAI, M. PFEIFER, P. PISARCZYK, K. ROHLENA, K. STENC, J. SKALA, V. TIKHONCHUK, J. ULLSCHMIED: *The PALS iodine laser-driven jets*. Plasma Phys. Control. Fusion, *49* (2007), B611–B619.
- [3] O. RENNER, I. USCHMANN, E. FÖRSTER: *Diagnostic potential of advanced X-ray spectroscopy for investigation of hot dense plasmas*. Laser Part. Beams, *22* (2004), 25–28.
- [4] I. L. BEIGMAN, P. YA. PIROGOVSKIY, L. P. PRESNYAKOV, A. P. SHEVELKO, D. B. USKOV: *Interaction of a laser-produced plasma with a solid surface: soft X-ray spectroscopy of high-Z ions in a cool dense plasma*. J. Phys. B: At. Mol. Phys., *22* (1989), 2493–2502.
- [5] A. P. SHEVELKO, L. V. KNIGHT, J. B. PEATROSS, Q. WANG: *Structure and intensity of X-ray radiation in a laser plasma–wall interaction*. Proc. SPIE, *4505* (2001), 171–178.
- [6] F. B. ROSMEJ, V. S. LISITSA, R. SCHOTT, E. DALIMIER, D. RILEY, A. DELSERIEYS, O. RENNER, E. KROUSKY: *Charge exchange driven X-ray emission from highly ionized plasma jets*. Europhys. Lett., *76* (2006), 815–821.

- [7] F. B. ROSMEJ, V. S. LISITSA, R. SCHOTT, E. DALIMIER, D. RILEY, A. DELSERIEYS, O. RENNER, E. KROUSKY: *Charge exchange driven X-ray emission from highly ionized plasma jets*. *Europhys. Lett.*, *76* (2006), 815–821.
- [8] O. RENNER, T. MISSALLA, P. SONDDHAUSS, E. KROUSKY, E. FÖRSTER, C. CHENAIS-POPOVICS, O. RANCU: *High-luminosity, high-resolution X-ray spectroscopy of laser-produced plasma by vertical-geometry Johann spectrometer*. *Rev. Sci. Instrum.*, *68* (1997), 2393–2403.
- [9] P. W. RAMBO, J. DENAVIT: *Interpenetration and ion separation in colliding plasmas*. *Phys. Plasmas*, *1* (1994), 4050–4060.
- [10] J. J. MACFARLANE, I. E. GOLOVKIN, O. WANG, P. R. WOODRUFF, N. A. PEREYRA: *SPECT3D – A multi-dimensional collisional-radiative code for generating diagnostic signatures based on hydrodynamics and PIC simulation output*. *High Energy Density Phys.*, *3* (2007), 181–190.
- [11] R. LISKA, J. LIMPOUCH, M. KUCHARIK, O. RENNER: *Selected laser plasma simulations by ALE method*. *J. Phys.: Conf. Series*, *112* (2008), –.
- [12] C. CHENAIS-POPOVICS, P. RENAUDIN, O. RANCU, F. GILLERON, J. C. GAUTHIER, O. LARROCHE, O. PEYRUSSE, M. DIRKSMÖLLER, P. SONDDHAUSS, T. MISSALLA, I. USCHMANN, E. FÖRSTER, O. RENNER, E. KROUSKY: *Kinetic to thermal energy transfer and interpenetration in the collision of laser-produced plasmas*. *Phys. Plasmas*, *4* (1997), 190–208.
- [13] O. RENNER, P. ADAMEK, E. DALIMIER, A. DELSERIEYS, E. KROUSKY, J. LIMPOUCH, R. LISKA, D. RILEY, F. B. ROSMEJ, R. SCHOTT: *Spectroscopic characterization of ion collisions and trapping at laser irradiated double-foil targets*. *High Energy Density Phys.*, *3* (2007), 211–217.

Received May 4, 2010

Brillouin back scattering in vertically magnetized plasmas

ALIREZA PAKNEZHAD¹, DAVOUD DORRANIAN²

Abstract. Brillouin scattering occurs in the interaction of picosecond laser pulse with a plasma which involves the coupling of large amplitude light wave into a scattered light wave plus an ion acoustic wave. Previous researches have shown that this scattering leads to instability with specific growth rate in a plasma. In this paper, we investigated Brillouin Back scattering instability growth rate in a magnetized plasma. As a research, plasma is imbedded in an uniform external vertically magnetic field. It is shown that this magnetic field alters the growth rate significantly.

Key Words. Brillouin scattering, Brillouin instability, ion acoustic wave, growth rate.

Introduction

Stimulated Brillouin scattering (SBS) plays an important role in laser–plasma interaction as it produces a backscattered light, and therefore this process is one of the real threat to the inertial confinement fusion research. After the invention of the ruby laser in 1960, Chiao et al. [7] was the first to observe SBS.

The control of the stimulated Brillouin scattering (SBS) instability remains one of the key issues for the success of laser fusion. In the context of laser–plasma interaction, incident laser wave couples to an ion-acoustic wave (IAW) to give rise to a scattered transverse wave, leading to a net energy loss in the case of backscattering [9].

Stimulated Brillouin scattering in a plasma is the decay of an incident (pump) light wave into a frequency downshifted (Stokes) light wave and an ion-acoustic (sound wave). It is important in direct and indirect inertial confinement fusion (ICF) experiments because it scatters the laser beams away

¹Islamic Azad University, Shabestar Branch, Iran; email: A.paknezhad@iaushab.ac.ir

²Laser Laboratory, Plasma Physics Research Center, Science and Research Branch, Islamic Azad University, Tehran, Iran

from the target, thereby reducing the energy available to drive the compressive heating of the nuclear fuel [1], [4].

Parametric Instabilities

Large amplitude waves encountered in plasma-based sources of coherent radiation are susceptible to parametric instabilities. In a parametric process a large amplitude pump wave couples to a low-frequency mode of the plasma to produce a sideband wave. The pump and the sideband wave exert a nonlinear force on the plasma particles to drive the low-frequency mode. In this process the amplitudes of the low-frequency mode and the sideband, called the daughter waves, grow with time once the pump power exceeds a threshold value, set by the linear damping or convective losses of the daughter waves. The parametric instability saturates via pump wave depletion or a downward cascade of energy from the sideband wave. In a plasma-based source of coherent radiation, parametric instabilities should lead to frequency broadening of the beam driven mode. Hence an in depth study of parametric instabilities in plasma-filled devices is of considerable importance. Parametric instabilities have been studied extensively in laser-produced plasmas where stimulated Raman and Brillouin scattering (SRS) and (SBS) are two dominant parametric processes.

In a SRS process an intense laser beam drives a Langmuir wave and an electromagnetic sideband wave. The instability occurs at densities below quarter critical. However, the density of the plasma should not be too small otherwise the Langmuir wave is strongly Landau-damped by the electrons. The growth rate peaks when the sideband wave propagates opposite to the pump wave. In the SBS process, the laser excites an ion acoustic wave and an electromagnetic sideband wave. The instability occurs over a wide range of electron density, up to the critical layer. Nevertheless, it requires nonisothermal plasma where the electron temperature is much larger than the ion temperature, otherwise the ion Landau damping will suppress the Brillouin instability.

Stenflo has developed an elegant theory of parametric instabilities including the effect of a magnetic field [10].

The Brillouin instability can be most simply characterized as the resonant decay of an incident photon with frequency ω_0 and wave number k_0 into a scattered photon with frequency ω_s and wave number k_s plus an ion acoustic phonon. The frequency and wave number matching conditions then are $(\omega_0 = \omega_s + \omega)$ and $(\mathbf{k}_0 = \mathbf{k}_s + \mathbf{k})$. Where now ω and \mathbf{k} are the frequency and wave number of the ion acoustic wave. Since the frequency of an ion acoustic wave is much less than ω_0 , it is clear that this instability can occur throughout the underdense plasma. Furthermore, nearly all the energy can be transferred to the scattered light wave.

Instability Analysis

To obtain the coupled equation describing the Brillouin instability, we consider the response of an initially uniform plasma driven by a large amplitude light wave. For clarity we consider an ordinary light wave propagating through a plasma with a uniform density and temperature. Plasma is imbedded in a constant magnetic field \mathbf{B}_0 in \hat{y} direction. Electric field of electromagnetic wave has the form of $\mathbf{E} = \hat{e}_x E(z, t) \cos(k_0 z - \omega_0 t)$ and its magnetic field \mathbf{B}_0 is in the \hat{y} direction. We can ignore the magnetic field of the light wave in comparison with strong external magnetic field. Thus, the wave equation and the force equation of electrons are respectively

$$\left[\nabla^2 - \frac{1}{c^2} \frac{\partial^2}{\partial t^2} \right] \mathbf{E} = \frac{4\pi}{c} \frac{\partial \mathbf{J}}{\partial t}, \quad (1)$$

$$\frac{d\mathbf{v}}{dt} = -\frac{e}{m} (\mathbf{E} + \mathbf{v} \times \mathbf{B}_0). \quad (2)$$

Equation (2) has two components,

$$\frac{\partial v_x}{\partial t} = -\frac{e}{m} E_x + \omega_c v_z, \quad (3)$$

$$\frac{\partial v_z}{\partial t} = -\omega_c v_x, \quad (4)$$

where $\omega_c = eB_0/m$, is the electron cyclotron frequency. We solve this equations to obtain (5) and (6) as below:

$$v_{\perp} = v_x = \frac{ca\omega^2}{(\omega^2 - \omega_c^2)} \sin(kz - \omega t), \quad (5)$$

$$v_z = -\frac{ca\omega\omega_c}{(\omega^2 - \omega_c^2)} \cos(kz - \omega t). \quad (6)$$

Thus we can write the current density of electrons as

$$J_x = -nev_{\perp} = -enca \left[\frac{\omega^2}{(\omega^2 - \omega_c^2)} \right] \sin(kz - \omega t). \quad (7)$$

Hence the equation (1) becomes

$$\left(\frac{\partial^2}{\partial t^2} - c^2 \nabla^2 \right) \mathbf{A} = -\frac{4\pi n_e e^2}{m_e} \left[\frac{\omega^2}{(\omega^2 - \omega_c^2)} \right] \mathbf{A}, \quad (8)$$

where \mathbf{A} is the vector potential of the light wave and $\mathbf{a} = e\mathbf{A}/mc^2$ is the normalized potential vector. To obtain the coupled equations describing the Brillouin instability, we consider the response of an initially uniform plasma driven by a large amplitude light wave. We can write equation for the generation of scattered light wave with vector potential $\tilde{\mathbf{A}}$ by the coupling of a large amplitude light wave with vector potential \mathbf{A}_1 with an electron fluctuation \tilde{n}_e . Hence current density can be taken as $\tilde{\mathbf{J}} = -ne\tilde{\mathbf{v}}_\perp - \tilde{n}_e\mathbf{v}_{\perp 0}$. Then equation (1) has the form of

$$\left(\frac{\partial^2}{\partial t^2} - c^2 \nabla^2 + \omega_{pe}^2 \left[\frac{\omega^2}{(\omega^2 - \omega_c^2)} \right] \right) \tilde{\mathbf{A}} = -\frac{4\pi\tilde{n}_e e^2}{m_e} \left[\frac{\omega_0^2}{\omega_0^2 - \omega_c^2} \right] \mathbf{A}_1, \quad (9)$$

where ω_{pe} is the electron plasma frequency and ω is the frequency of scattered light wave. Only the fluctuation in electron density appears in Eq. (9), since the ion response to the light frequency field of the light wave is less than the electron response by Zm/M , where Z is the charge state, m the electron mass, and M the ion mass. For the Brillouin instability, the density fluctuation \tilde{n}_e is the low frequency fluctuation associated with an ion acoustic wave. We describe the electrons as a warm fluid and separate the fluid velocity \mathbf{v}_e into longitudinal (u_1) and transverse components ($e\mathbf{A}/mc$). Then by the taken of continuity and force equations

$$\begin{aligned} \frac{\partial \tilde{n}_e}{\partial t} + n_0 \nabla \cdot \tilde{\mathbf{v}}_e &= 0, \\ \frac{\partial \tilde{\mathbf{v}}_e}{\partial t} + \mathbf{v}_e \cdot \nabla \tilde{\mathbf{v}}_e &= -\frac{e}{m} \left(\mathbf{E} + \frac{\mathbf{v}_e \times \mathbf{B}}{c} \right) - \frac{\nabla \tilde{p}}{n_e m_e}, \end{aligned}$$

we obtain

$$\frac{\partial \mathbf{u}_1}{\partial t} = \frac{e}{m} \nabla \varphi - \frac{1}{2} \nabla \left(\mathbf{u}_1 + \frac{e\mathbf{A}}{mc} \right)^2 - \frac{\nabla p_e}{n_e m_e}, \quad (10)$$

where φ is the electrostatic potential, p_e the electron pressure, and n_e the electron density. Since we are now considering a low frequency fluctuation, we neglect the electron inertia ($\partial u_1 / \partial t \rightarrow 0$) and use the isothermal equation of state ($p_e = n_e \theta_e$, where $\theta_e = T_e$ is the electron temperature). We then linearize Eq. (10) by letting $n_e = n_0 + \tilde{n}_e$, $\mathbf{A} = \mathbf{A}_1 + \tilde{\mathbf{A}}$ and $\varphi = \tilde{\varphi}$, which gives

$$\frac{e}{m} \nabla \tilde{\varphi} = \frac{e^2}{m^2 c^2} \nabla \left(\mathbf{A}_1 \cdot \tilde{\mathbf{A}} \right) + \frac{v_e^2}{n_0} \nabla \tilde{n}_e. \quad (11)$$

The electrical potential transmits the ponderomotive force to the ions. To treat the ion response, we describe the ions as a charged fluid with density n_i and velocity \mathbf{u}_i . The continuity and force equations of ions are

$$\frac{\partial n_i}{\partial t} + \nabla \cdot (n_i \mathbf{u}_i) = 0,$$

$$\frac{\partial \mathbf{u}_i}{\partial t} + \mathbf{u}_i \cdot \nabla \mathbf{u}_i = -\frac{Ze}{M} \nabla \varphi,$$

where we have neglect the ion pressure for simplicity. We next linearize these equations by taking $n_i = n_{0i} + \tilde{n}_i$, $u_i = \tilde{u}_i$ and $\varphi = \tilde{\varphi}$. Then

$$\frac{\partial \tilde{n}_i}{\partial t} + n_{0i} \nabla \cdot \tilde{\mathbf{u}}_i = 0, \quad (12)$$

$$\frac{\partial \tilde{u}_i}{\partial t} = -\frac{Ze}{M} \nabla \tilde{\varphi}. \quad (13)$$

Taking a time derivative of Eq. (13), a divergence of Eq. (12) and combining then gives

$$\frac{\partial^2 n_i}{\partial t^2} - \frac{n_{0i} Ze}{M} \nabla^2 \tilde{\varphi} = 0.$$

If we substitute for $\tilde{\varphi}$ using Eq. (11), we finally obtain an equation for the low frequency density fluctuation

$$\frac{\partial^2 \tilde{n}_e}{\partial t^2} - c_s^2 \nabla^2 \tilde{n}_e = \frac{Z n_0 e^2}{m M c^2} \nabla^2 (\mathbf{A}_1 \cdot \tilde{\mathbf{A}}). \quad (14)$$

Hence $A_1 = A_1 \cos(k_0 z - \omega_0 t)$ is the ion acoustic velocity. Eq. (9) describing the excitation of an ion acoustic wave by the interaction between the incident and scattered light waves.

Dispersion Relation

By taking the $A_1 = A_1 \cos(k_0 z - \omega_0 t)$ for incident light wave and using the Fourier-analyze Eq. (9) and (14), then we can obtain the dispersion relation from the coupled equations for \tilde{A} and \tilde{n}_e .

$$D(k, \omega) \tilde{A}(k, \omega) = \frac{4\pi e^2}{m_e} \left[\frac{\omega_0^2}{\omega_0^2 - \omega_c^2} \right] \frac{A_1}{2} \times \\ \times [\tilde{n}_e(k - k_0, \omega - \omega_0) + \tilde{n}_e(k + k_0, \omega + \omega_0)] \quad (15)$$

$$(\omega^2 - c_s^2 k^2) \tilde{n}_e = \frac{Z n_0 e^2 k^2}{m M c^2} \frac{1}{2} \mathbf{A}_1 \cdot [\tilde{A}(k - k_0, \omega - \omega_0) + \tilde{A}(k + k_0, \omega + \omega_0)] \quad (16)$$

where $D(k, \omega) = \omega^2 - c^2 k^2 - \omega_{pe}^2 \left(\frac{\omega^2}{\omega^2 - \omega_c^2} \right)$, $v_{os} = \frac{e A_1}{m c}$ and $\omega_{pi} = \omega_{pe} \left(\frac{Z m}{M} \right)^{\frac{1}{2}}$.

Now we use Eq. (15) to eliminate $\tilde{\mathbf{A}}(k - k_0, \omega - \omega_0)$ and $\tilde{\mathbf{A}}(k + k_0, \omega + \omega_0)$ from Eq. (16). considering lower plasma frequency ($\omega \ll \omega_0$) and neglecting the higher non-resonant terms, then gives dispersion relation

$$\omega^2 - c_s^2 k^2 = \frac{k^2 v_{os}^2}{4} \omega_{pi}^2 \left(\frac{\omega_0^2}{\omega_0^2 - \omega_c^2} \right) \times \left[\frac{1}{D(\omega - \omega_0, k - k_0)} + \frac{1}{D(\omega + \omega_0, k + k_0)} \right], \quad (17)$$

where the dispersion relation for incident light wave is

$$\omega_0^2 - c^2 k_0^2 - \omega_{pe}^2 \left(\frac{\omega_0^2}{\omega_0^2 - \omega_c^2} \right) = 0.$$

For Brillouin back scattering, only the downshifted light wave is resonant, [1] then

$$(\omega^2 - c_s^2 k^2) (\omega^2 - 2\omega\omega_0 + 2c^2 \mathbf{k} \cdot \mathbf{k}_0 - c^2 k^2) = \frac{k^2 v_{os}^2}{4} \omega_{pi}^2 \left(\frac{\omega_0^2}{\omega_0^2 - \omega_c^2} \right). \quad (18)$$

For founding the growth rate of Brillouin back scattering (BBS) instability (γ), we assume $\omega = kc_s + i\gamma$ where $\gamma \ll kc_s$, Eq. (9) becomes

$$2i\gamma kc_s (-2i\gamma\omega_0 - 2k\omega_0 c_s + 2kk_0 c^2 - c^2 k^2) = \frac{k^2 v_{os}^2}{4} \omega_{pi}^2 \left(\frac{\omega_0^2}{\omega_0^2 - \omega_c^2} \right)$$

and the we can obtain the growth rate for (BBS) as below,

$$\gamma = \frac{1}{2\sqrt{2}} \frac{k_0 v_{os} \omega_{pi}}{\sqrt{\omega_0 k_0 c_s}} \left(\frac{\omega_0^2}{\omega_0^2 - \omega_c^2} \right), \quad (19)$$

$$k_0 = \frac{1}{c} \left(\omega_0^2 - \frac{\omega_0^2 \omega_p^2}{\omega_0^2 - \omega_c^2} \right)^{\frac{1}{2}}, \quad (20)$$

where k_0 is the wave number of incident light. By combining the (19) and (20) we can find the growth rate of BBS as below,

$$\gamma = a \omega_{pi} \left(\frac{c}{8c_s} \right)^{\frac{1}{2}} \left[1 - \frac{\omega_{pe}^2}{\omega_0^2 - \omega_c^2} \right]^{\frac{1}{4}} \quad (21)$$

and

$$\frac{\gamma}{\omega_{pi}} = a \left(\frac{c}{8c_s} \right)^{\frac{1}{2}} \left[1 - \frac{(\omega_{pe}^2/\omega_c^2)}{(\omega_0^2/\omega_c^2) - 1} \right]^{\frac{1}{4}}. \quad (22)$$

Figure 1 represent the variation of BBS growth rate by variation in plasma frequency in both magnetized and unmagnetized plasma where $\omega_c/\omega_0 = 0.3$, $a = 0.1$, $c/8c_s = 10^4$.

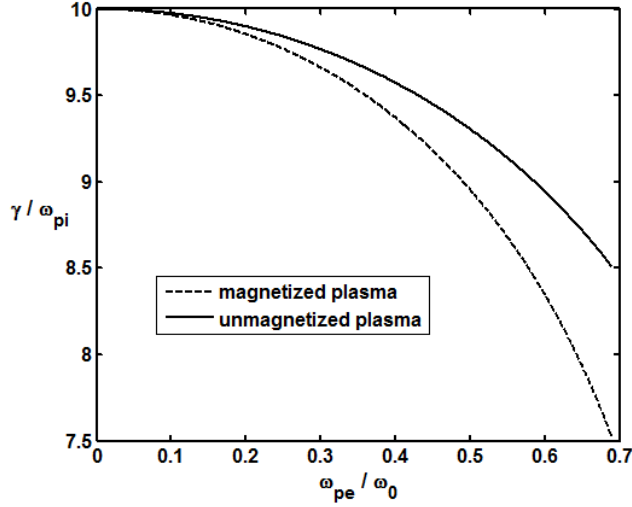


Fig. 1. Growth rate of BBS in magnetized and unmagnetized plasma

Figure 2 shows the variation of BBS growth rate by variation in electron cyclotron frequency in magnetized plasma where $\omega_p/\omega_0 = 0.3$, $c/8c_s = 10^4$, $a = 0.1$.

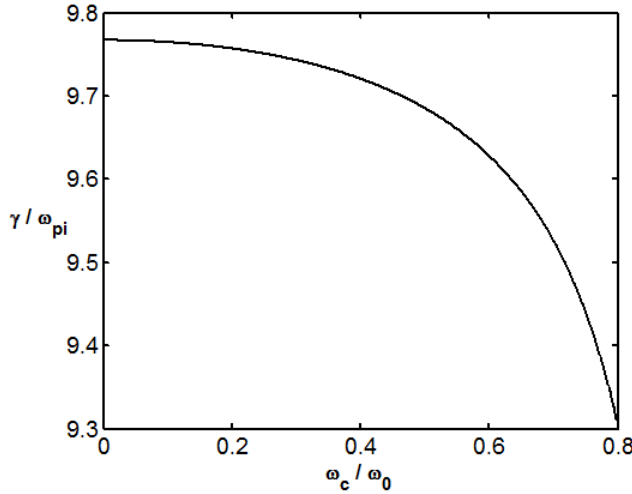


Fig. 2. Growth rate of BBS in magnetized plasma

Conclusions

About some other works associated with present work, Bawaaneh has investigated the problem of stimulated Brillouin scattering of an extraordinary light wave from a magnetized plasma[6]. He has shown that small values of static magnetic field increases the instability growth rate, while high magnetic fields reduce the instability bringing it to zero at a cut-off field. In our present work, we have considered the Brillouin scattering of an ordinary electromagnetic wave from a vertically magnetized plasma. The growth rate of Brillouin instability in the interaction of high power short laser pulse with an underdense plasma in the presence of external magnetic field ($\mathbf{B}_0 \perp \mathbf{k}_0$) is investigated. Results show a decreasing in the growth rate of Brillouin instability due to external magnetic field in comparison with unmagnetized plasma. Also growth rate is decreased when the external magnetic field is increased.

References

- [1] W. L. KRUER: The physics of laser plasma interaction. Addison-Wesley, London 1988.
- [2] F. F. CHEN: Introduction to plasma physics. Plenum Press, New York 1985.
- [3] P. A. BERNHARDT, C. A. SELCHER, R. H. LEHMBERG, S. P. RODRIGUEZ, J. F. THOMASON, K. M. GROVES, M. J. McCARRICK, G. J. FRAZER5: *Stimulated Brillouin Scatter in a Magnetized Ionospheric Plasma*. Phys.Rev.Lett, *104* (2010), 165001.
- [4] N. K. JAIMANA, V. K. TRIPATHI: *Stimulated Brillouin scattering of an electromagnetic wave in a strongly magnetized plasma*. Phys. Plasmas, *5* (1998), 222–226.
- [5] L. SHI-BING, C. SHI-GANG: *Brillouin instability in underdense plasma under an intense laser field*. Chinese Phys. Lett., *14* (1997), 861–864.
- [6] M. S. BAWA'ANEH: *Stimulated Brillouin scattering of X-waves in magnetized plasma*. J. Plasma Physics, *72* (2006), 687–697.
- [7] J. D. LINDL: *Development of the indirect-drive approach to inertial confinement fusion and the target physics basis for ignition and gain*. P. of Plasmas, *2* (1995), 3933–4024.
- [8] J. D. LINDL, P. AMENDT, R. L. BERGER, S. GLENDINNING, S. H. GLENZER, S. W. HAAN, R. L. KAUFFMAN, O. L. LANDEN, L. J. SUTER: *The physics basis for ignition using indirect-drive targets on the National Ignition Facility*. Physics of Plasmas, *11* (2004), 339–491.
- [9] L. YIN, B. J. ALBRIGHT, K. J. BOWERS, W. DAUGHTON, H. A. ROSE: *Saturation of Backward Stimulated Scattering of a Laser Beam in the Kinetic Regime*. Phys. Rev. Lett., *99* (2007), 265004.
- [10] G. BRODIN, L. STENFLO: *Parametric instabilities of finite amplitude alfvén waves*. Physica Scripta, *37* (1988), 89–92.

Generation of high energy electrons and ion acceleration in small structured targets¹

JAN PŠIKAL², JIŘÍ LIMPOUCH²,
ONDŘEJ KLIMO², VLADIMIR TIKHONCHUK³

Abstract. The employment of microstructured targets for efficient ion acceleration by short intense laser pulses is discussed. We further examine recently proposed targets, such as foil with hole or foil with slice joint to its front surface, by two dimensional PIC simulations. These targets enable to accelerate protons to higher maximum energies compared with simple thin foils due to additional acceleration of hot electrons during laser-target interaction. On the other hand, we found that the energy fluencies of protons accelerated in those specially designed targets are reduced compared with thin foils irradiated by obliquely incident laser pulses.

Key Words. Laser plasmas, femtosecond laser pulses, ion acceleration, microstructured targets, PIC simulations.

Introduction

Laser-driven ion acceleration has attracted much attention due to its potential in realizing compact ultrahigh-energy particle accelerators. The energetic ion beams generated in the interaction of ultrashort relativistic laser pulses with plasma could be useful in many important applications, which have various demands in terms of ion energy, flux, or monoenergeticity. The progress in laser-driven ion sources can be achieved not only through laser technology advancement but also via target design improvements.

Several ideas on the target design have been recently proposed to generate high-energy ions more efficiently by widely used target-normal sheath acceleration (TNSA) mechanism [1]. In the TNSA, ions are accelerated in the sheath

¹This work is partially supported by the Czech Ministry of Education, Youth and Sports (Projects LC528 and MSM6840770022).

²Czech Technical University in Prague, Faculty of Nuclear Sciences and Physical Engineering, Czech Republic

³Centre Lasers Intenses et Applications, University of Bordeaux 1 - CEA - CNRS. France

layer created by hot electrons which are generated during laser–target interaction by collisionless absorption. It has been already demonstrated experimentally that the maximum energy of accelerated ions and the laser-to-proton energy conversion efficiency increase by using conical targets [2] or foils of reduced surface [3]. PIC simulations have shown enhanced ion acceleration in multihole thin foil target with holes of subwavelength diameter [4], hole-target of the optimal hole diameter of about $2\ \mu\text{m}$ [5], and foil with a slice on its front side [6].

In our recent study [7], we have discussed efficient electron acceleration along the surface of an ionized foil when the target is irradiated by femtosecond laser pulse at large incidence angle (more than 60°). In this case, generated strong quasistatic magnetic and electric fields confine electrons in a potential well along the target surface and the electrons are resonantly accelerated by laser electric field inside the potential well. As a result, such electrons transported towards foil edges accelerate protons from the edges to a relatively high maximum energy. Similar phenomena of enhanced electron heating and ion acceleration (here, from the rear side of targets) have been observed in foils with a hole [5] or a slice [6].

In this contribution, we further examine these proposed foil targets [5], [6] by two-dimensional particle-in-cell (PIC) simulations. Up to now, ion acceleration in those targets has been compared with acceleration in thin foil by normally incident laser pulse only, although it is known that the acceleration is enhanced at oblique incidence. Thus, we perform simulation of the foil irradiated by laser pulse incident at 45° for comparison. We also propose and investigate foil target with a cone joint to its front surface.

Simulation method and parameters

Our relativistic collisionless PIC code with two spatial and three velocity components is described in Ref. [8]. Various targets employed in our numerical studies are sketched schematically in Fig. 1 (in 2D geometry). Optimal diameter of a hole in the target b) (about $2\ \mu\text{m}$) is chosen according to Ref. [5]. Opening angle of a cone in the target c) is set on 30° to obtain optimal incidence angle of the laser beam on the cone walls, which is about 75° [7], in order to generate ultrahigh energy electrons traveling along the walls. The height of a slice in the target d) is set to be the same as the height of the cone in the case c), the slice diameter is chosen in agreement with Ref. [6].

The targets have initial density of $20\ n_c$, hydrogen plasma is assumed for simplicity. The laser of wavelength $1\ \mu\text{m}$ has maximum intensity $3.5 \times 10^{19}\ \text{W}/\text{cm}^2$, the laser beam of the width $4\ \mu\text{m}$ (FWHM) has a super-gaussian shape ($n = 3$). The pulse duration is set to 100 fs, the temporal laser pulse profile has a trapezoidal shape of duration 70 fs and two linear ramps of 15 fs at the beginning

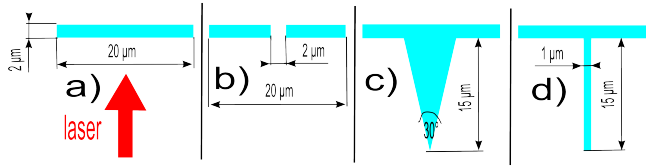


Fig. 1. Targets employed in our PIC simulations: a) thin foil; b) foil with hole; c) foil with cone; d) foil with slice

and at the end of the pulse. The simulation box size is $64 \mu\text{m} \times 60 \mu\text{m}$, outgoing electromagnetic waves are absorbed at the box boundaries and escaping electrons are frozen there. The cell size is set to 20 nm. Each simulation run is stopped 350 fs after the moment when laser pulse hits the foil.

To evaluate the efficiency of ion acceleration from those targets and to analyze the laser–target interaction, we are interested mainly in energy spectra of hot electrons located behind rear side of the targets at the end of laser–plasma interaction (when the energy of heated electrons is at maximum) and proton energy spectra at the end of simulations.

Results and discussion

Figure 2 shows fast electron energy spectra at the end of laser–target interaction (at time moment $t = 1.0\tau_L$, where τ_L is the laser pulse duration) and proton energy spectra at the end of simulations (at $t = 3.5\tau_L$). Only electrons and protons located behind the rear surface of targets are taken into account (as the acceleration of protons is most efficient there). In the case of foil both with normal and oblique incidence, electron energy distribution functions can be attributed to a single hot electron temperature. The temperature is about 0.5 MeV for normal incidence and about 1 MeV for oblique incidence. Note that the ponderomotive potential is $U_p \approx 2 \text{ MeV}$. In the case of microstructured targets, electron energy distribution function is modified and cannot be approximated by a single temperature. The number of electrons is lower in the energy range from 0 to $2 \div 4 \text{ MeV}$ and larger for higher energies than in the case of thin foils. This effect can be explained by additional acceleration of hot electrons to very high energies when the laser pulse is incident on the target surface at large incidence angles [7]. When ultraintense laser pulses irradiate solid targets at a large incident angle, quasistatic magnetic and electric fields are induced, electrons along the target surface are confined in a potential well created by those quasistatic fields and can be resonantly accelerated along the surface by oscillating laser field [9]. By this surface acceleration process,

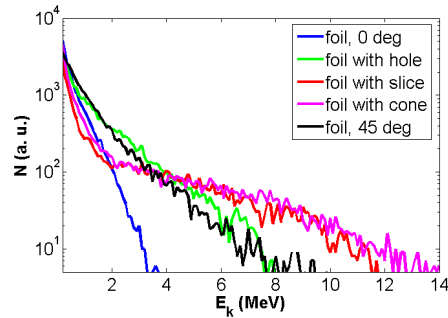


Fig. 2. Energy spectra of hot electrons at the end of laser-plasma interaction

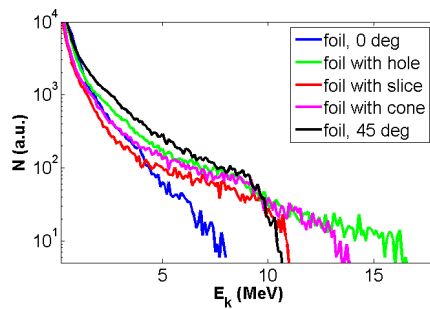


Fig. 3. Energy spectra of protons accelerated from the rear side of target at the end of simulation runs

high energy electrons are effectively generated with temperatures exceeding the ponderomotive energy significantly.

As the protons are accelerated by hot electrons, electron energy distribution affects the spectra of accelerated protons (in Fig. 3). Although the highest obtained proton energy fluence (calculated for protons with energy higher than 1 MeV), about 18 kJ/cm^2 , is found when the laser pulse is incident at 45° on a thin foil (black line), the highest maximum proton energy is observed for the foil with a hole (green line) where the fluence is only about 11 kJ/cm^2 . The energy fluencies for the foil irradiated at normal incidence (blue line) and for foils with cone (magenta line) and with slice (red line) joint to its front surface are about 4.5 kJ/cm^2 , 7.5 kJ/cm^2 , and 5 kJ/cm^2 , respectively. Thus, our numerical simulations have demonstrated that the employment of complex

targets (such as foil with cone or foil with slice) can enhance maximum energy of ions, but the number of accelerated protons is reduced compared with a simple foil irradiated by the same laser pulse at oblique incidence. Moreover, the complex targets, which require complicated manufacturing and has to be irradiated by laser very precisely onto their center, are less favorable to obtain higher maximum proton energy than foils with a hole.

As discussed in our previous paper [7], the maximum proton energy is approximately proportional to average hot electron energy (or hot electron temperature), while the total energy (thus, energy fluence) depends stronger on hot electron density. Moreover, electron energy spectra dominated by a relatively small number of fast electrons is not favorable for an efficient ion acceleration, because these most energetic electrons overcome the potential barrier created by the ions and by themselves, and are lost from the system (they are accumulated on the boundaries of the simulation box), whereas less energetic confined electrons participate in the acceleration, according to a theoretical model of Ref. [10]. The highest density of hot electrons is observed in the case of obliquely irradiated foil which corresponds to the highest proton energy fluence. On the other hand, a higher number of electrons with energies from 2 MeV to 6 MeV is generated due to the presence of a hole in the foil, which leads to a higher maximum proton energy. In the complex targets, even though more energetic electrons are generated, the number of less energetic electrons is lower, and a substantial part of the most energetic electrons escape from the target without significant energy transfer to protons.

The total absorption of laser pulse energy in ionized targets is 24 %, 34 %, 54 %, and 42 % in our simulations, for the target *a*, *b*, *c*, and *d* (see Fig. 1), respectively. These values are consistent with our discussion in previous paragraphs. A higher laser pulse absorption (the energy of laser is initially transferred to electrons and, then, from the electrons partly to ions) does not necessarily mean a higher total energy of accelerated ions (e.g., energy fluence). The key parameter is the electron energy distribution function.

Conclusions

Maximum energy of accelerated ions can be enhanced when the laser pulse is incident on a thin foil with a hole or on complex targets (foil with slice or cone joint on its front surface). However, we found that their number is reduced and the total energy of protons emitted from the target rear side is the highest when a simple thin foil is irradiated by the same laser pulse at oblique incidence. Differences in maximum proton energy and total energy (or energy fluence) for various types of targets are explained by energy distribution function of hot electrons at the beginning of proton acceleration. In the case of complex targets, a small number of very energetic hot electrons is generated

due to electron acceleration by laser field along the target surface, but these electrons mostly escape the target potential and only the rest of them can accelerate a small number protons on a high maximum energy. Less energetic electrons, which are more numerous after the laser pulse interaction with a thin foil, transfer their energy to protons more efficiently.

References

- [1] S. C. WILKS, A. B. LANGDON, T. E. COWAN, M. ROTH, M. SINGH, S. HATCHETT, M. H. KEY, D. PENNINGTON, A. MACKINNON, R. A. SNAVELY: *Energetic proton generation in ultra-intense laser–solid interactions*. P. of Plasmas, 8 (2001), 542–549.
- [2] K. A. FLIPPO, E. D’HUMIERES, S. A. GAILLARD, J. RASSUCHINE, D. C. GAUTIER, M. SCHOLLMEIER, F. NURNBERG, J. L. KLINE, J. ADAMS, B. ALBRIGHT, M. BAKEMAN, K. HARRES, R. P. JOHNSON, G. KORGAN, S. LETZRING, S. MALEKOS, N. RENARD-LEGALLOUDEC, Y. SENTOKU, T. SHIMADA, M. ROTH, T. E. COWAN, J. C. FERNANDEZ, B. M. HEGELICH: *Increased efficiency of short-pulse laser-generated proton beams from novel flat-top cone targets*. P. of Plasmas, 15 (2008), 056709.
- [3] S. BUFFECHOUX, J. PSIKAL, M. NAKATSUTSUMI, L. ROMAGNANI, A. ANDREEV, K. ZEIL, M. AMIN, P. ANTICI, T. BURRIS-MOG, A. COMPANT-LA-FONTAINE, E. D’HUMIERES, S. FOURMAUX, S. GAILLARD, F. GOBET, F. HANNACHI, S. KRAFT, A. MANCIC, C. PLAISIR, G. SARRI, M. TARISIEN, T. TONCIAN, U. SCHRAMM, M. TAMPO, P. AUDEBERT, O. WILLI, T. E. COWAN, H. PEPIN, V. TIKHONCHUK, M. BORGHESI, J. FUCHS: *Hot electrons transverse refluxing in ultra-intense laser–solid interactions*. Physical Review Letters, 105 (2010), 015005.
- [4] Y. NODERA, S. KAWATA, N. ONUMA, J. LIMPOUCH, O. KLIMO, T. KIKUCHI: *Improvement of energy-conversion efficiency from laser to proton beam in a laser–foil interaction*. Physical Review E, 78 (2008), 046401.
- [5] K. H. PAE, I. W. CHOI, S. J. HAHN, J. R. CARY, J. LEE: *Proposed hole-target for improving maximum proton energy driven by a short intense laser pulse*. Physics of Plasmas, 16 (2009), 073106.
- [6] F. WANG, B. SHEN, X. ZHANG, Z. JIN, M. WEN, L. JI, W. WANG, J. XU, M. Y. YU, J. CARY: *High-energy monoenergetic proton bunch from laser interaction with a complex target*. Physics of Plasmas, 16 (2009), 093112.
- [7] J. PSIKAL, V. T. TIKHONCHUK, J. LIMPOUCH, O. KLIMO: *Lateral hot electron transport and ion acceleration in femtosecond laser pulse interaction with thin foils*. Physics of Plasmas, 17 (2010), 013102.
- [8] J. PSIKAL, J. LIMPOUCH, S. KAWATA, A. A. ANDREEV: *PIC simulations of femtosecond interactions with mass-limited targets*. C. J. of Physics, 56 (2006), B515–B521.
- [9] T. NAKAMURA, K. MIMA, H. SAKAGAMI, T. JOHZAKI: *Electron surface acceleration on a solid capillary target inner wall irradiated with ultraintense laser pulses*. Physics of Plasmas, 14 (2007), 053112.
- [10] M. PASSONI, M. LONTANO: *Theory of light-ion acceleration driven by a strong charge separation*. Physical Review Letters, 101 (2008), 115001.

Effect of filler amount in the welding of plastics induced by visible laser irradiation¹

LORENZO TORRISI^{2,3}, FRANCESCO CARIDI⁴,
ANNA M. VISCO⁵, NINO CAMPO⁵

Abstract. Laser welding of plastics is based on the local energy release of the laser beam to the polymer joint. The process, known as Through Transmission Visible Laser Welding (TTVLW) technique, involves a ns pulsed laser beam of visible light, transmitted by the transparent polymeric part and absorbed at the surface of the other polymeric part. It promotes photo-thermal, photo-chemical and ion implantation processes locally, in the small regions of the irradiated polymer which enables the parts to be welded rapidly. In this work, the TTVLW is applied in order to induce the welding between different polyethylene films, pure and filled with carbon or iron nano-compounds. The mechanical resistance and the physical features of the welded joints are investigated by physical and static mechanical tests. Results proved the effectiveness of the TTVLW technique since high resistance joints are obtained. The joints are investigated as a function of some laser irradiation parameters and polymeric materials properties.

Key Words. Plastics welding, joints mechanical resistance, laser irradiation.

1. Introduction

Laser technology offers many advantages in the application of joining plastics. It is possible to weld seams near sensitive electronic components, to create invisible and aesthetic bonds with high-quality surfaces free from pores and debris after the welding process. A wide range of polymers can be joined by laser

¹This work is supported by University of Time under project No. 12345.

²Dipartimento di Fisica, Università di Messina, Ctr. Papardo 31, 98166 S. Agata, Messina, Italy

³INFN – Laboratori Nazionali del Sud, Via S. Sofia 44, 95124 Catania, Italy

⁴Facoltà di Scienze M.F.N., Università di Messina, Ctr. Papardo 31, 98166 S. Agata, Messina, Italy

⁵Dip.to di Chimica Ind. e Ingegneria dei Materiali, facoltà di Ingegneria, Università di Messina, Ctr. Di Dio, 98166 S. Agata, Messina, Italy

welding; the effect can be improved using special absorbers to the laser wavelength, such as nanocomposites, nanotubes and microstructures embedded on the polymeric materials or by using coverage absorbent thin films [1].

The laser polymer joining processes for optimized thermal management in combination with wavelength-adapted polymers and additives will provide to process at high speed the sample. Key innovations are the high laser intensity, the laser wavelength, the laser transmission in the first polymer and absorption in the second polymer, the mask and spot size and the scanning speed of the welding sample [2].

The Through Transmission Visible Laser Welding (TTVLW) process involves localized heating at the interface of two pieces of plastic to be joined to produce strong, hermetically sealed welds with minimal thermal and mechanical stress, without particulates production and very little flash, making it ideal for medical device applications. Only certain materials and combinations of materials are suitable for transmission laser welding. One of the plastics needs to be optically transparent to the laser with the other being absorbing. There are various methods of making the lower plastic absorb the laser energy, such as that to use nanostructures embedded in the polymer which have high absorption at the used laser wavelength. Additives such as carbon-nanotubes and Fe_2O_3 nanostructures, for example, can be used to colour black and red, respectively, the polymer sample and to increase the visible laser absorption in the first sample monolayers [3]. Also thin absorbent coating films can be sprayed for covering the absorbent polymer.

Application areas include medical devices such as filters, microfluidic devices, medical packaging (blood bags), catheters and prostheses. The use of a pulsed Nd:Yag laser presented in this article is innovative with respect to the traditional laser polymer welding based on continuum diode lasers, which induce only thermal effects. The laser here reported produces not only thermal effects but also a hot plasma, i.e. a ionized gas which accelerate particles at energies of the order of 1 keV [4] and which may promote photo-chemical reactions and ion implantation processes improving significantly the thermal adhesion of the welding area.

2. Experimental

A Nd:Yag laser, 3 ns pulse duration, was employed to irradiate in air the polymers (Physic laboratory, Messina University). The laser operated at 532 nm and 10 Hz repetition rate. The laser intensity was about 8×10^8 W/cm², with maximum pulse energy of 150 mJ and a laser spot of 6 mm² (no focusing lens were employed). The incident angle of the laser beam was 0°. Ultra High Molecular Weight Polyethylene (UHMWPE, Ticona GUR 1020) was prepared by compression molding (Polymer Laboratory of Messina University).

The crystalline degree of UHMWPE is 86 % and decreases to a value of 53 % after the compression molding [5]. The polymer powder was kept at 200 °C for 20 minutes at 20 MPa pressure to prepare UHMWPE sheets pure and mixed with 1, 5 and 10 weight % of Multi Wall Carbon NanoTubes (CNTs) or iron oxide (Fe_2O_3). The nanotubes were prepared by using the Chemical Vapor Deposition (CVD) method in the Catalysis Laboratories of Messina University. Iron Oxide was supplied by ACROSS and has a purity level of 99.999 %.

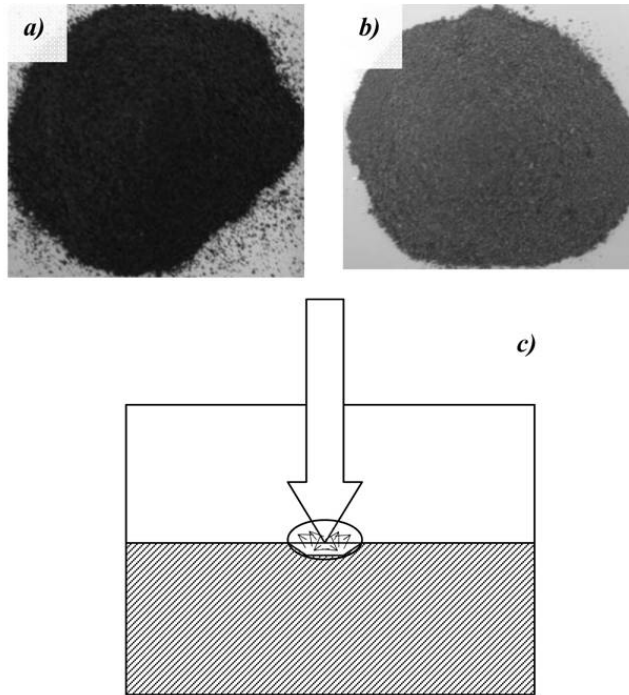


Fig. 1. Photos of the mixed powders made by: UH+10% CNT(a), UH+10% Fe_2O_3 (b) and scheme of laser irradiation (c)

The mixed powders were obtained by a ball milling (Fritsch, mod. MiniMill II of Messina University, Material Laboratory). It operates at 5 minutes and 250 rpm speed and repeats the dispersion cycle 100 times. Figure 1 shows the powders containing 1 wt % filler amount of CNTs (a) and of as Fe_2O_3 (b). The code of the polyethylene pristine sheet is “UHMWPE” while those of the filled sheets are “UH-CNT” or “UH- Fe_2O_3 ”. The geometry of all the sheets was 20×30 mm surface and 1 mm thickness. The welded joints were obtained by laser irradiating an UHMWPE transparent sheet coupled with an absorbent filled in the opposite face, as shown in the scheme of Fig. 1c. The two overlapped sheets were pressed between them with a pressure of about 200 kPa, by using mechanical clips pressing the two polymer faces. At the interface a

plasma is generated by the high energy released by the laser pulse. In this area photo-thermal, photo-chemical and ion implantation effects are localized and contribute to the final adhesion between the two polymer. Two joints were prepared and studied in this work: -UH/UH-CNT joint, made by irradiating the transparent UHMWPE film pressed against the absorbent UH-CNT; -UH/UH-Fe₂O₃ joint using as absorbent polymer the UHMWPE embedded into Fe₂O₃. Measurements of 532 nm light transmission demonstrated that the optical properties of UHMWPE are similar and that 1 mm thickness of polymer transmits about 55 % light. A little decrement of absorption, of the order of 5 ÷ 8 % is recorded for with respect to UHMWPE. The light transmission in 50 μm UH/CNT thickness is practically zero, demonstrating that the carbon filled polymer shows high light absorption also at nanotube carbon content below 1 %. The measured absorption coefficient μ value is 6.1 cm⁻¹ in the transparent UHMWPE. It increases up to 184 cm⁻¹ and 380 cm⁻¹ in the absorbent UH-Fe₂O₃ (1 wt %) and in the UH-CNT (1 wt %), respectively [6]. Thus the first polymer sheet, thank to its high crystalline content (50 %), is high transparent while the second polymer sheet is highly absorbent in the first superficial layers both for CNT than Fe₂O₃ embedded nanostructures. Morphologic analyses were performed by a JEOL JSM 5600 LU Scanning Electron Microscopy (SEM). The plastic materials were covered with a thin gold film in order to make them electrically conductive. The mechanical tests were performed by using a Lloyd Universal Testing Machine model LR10K, with a crosshead speed of 5 mm/min. The specimen geometry was made according to the ASTM 638 M-3 international protocols (60 mm total length, 10 mm useful length, 2.5 mm minimal width, 1 mm thickness) by using a manual DGT System sample cutting press. Sample dimension for the tensile and shear tests performed on the lap joints were of 10 mm × 20 mm. The shear tests permit to evaluate the shear strength (σ_S) for the joints.

3. Results

Figure 2a, b shows the laser imprinting induced by 2 min irradiation time (at 10 Hz repetitive laser pulse) on the UH/UH-Fe₂O₃ joint as laser entrance polymer (a) and opposite part (b) containing the 1 wt % of Fe₂O₃ (a, b), the 5 wt % of (c,d) and the 10 % of Fe₂O₃ (e, f). Fe₂O₃ (e, f) and the 10 % of Fe₂O₃ (i, l). The spots size increases with increasing the polymer filler content. This is clearly visible in both the opposit parts, especially in the white transmitting one. Besides, a more consistent darkened area surrounds the spots in the 10 wt % filled sheets, suggesting that this amount of filler increases the polymeric thermal conductivity.

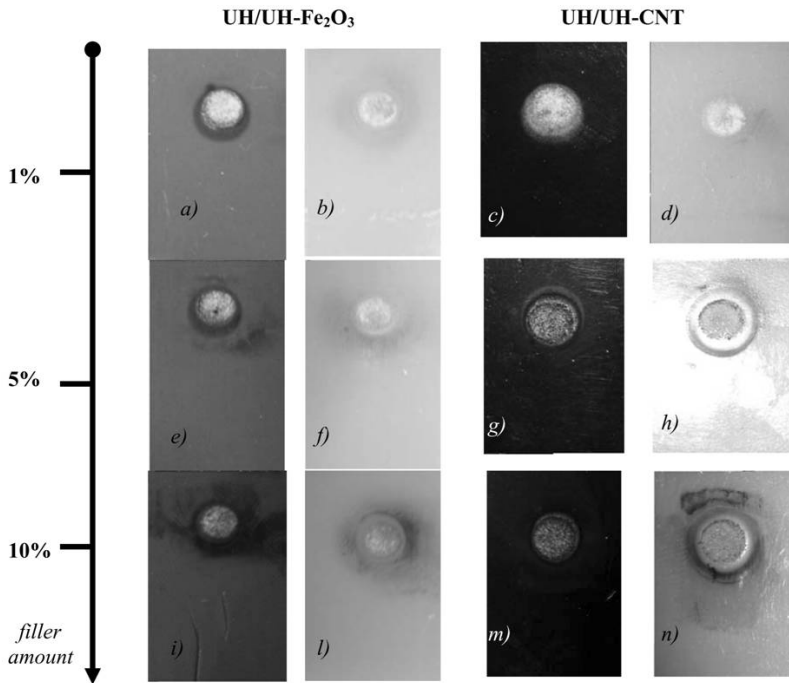


Fig. 2. Welding area induced by 2 minutes of laser exposition in the in the UH/UH-Fe₂O₃ joint (sx) and UH/UH-CNT joint (dx) parts containing 1 wt % (a,b,c,d), 5 wt % (e,f,g,h) and 10 % (i,l,m,n) of filler

Similar considerations concern the welding areas induced by an irradiation of 2 min of the UH/UH-CNT joint reported in Fig. 2 for the laser entrance polymer (c) and opposite part (d). Also in this case, the spot area increases with increasing the filler content and a higher damage is induced in the highest filler content joint. In particular the images show a ring of plasticized polymer around the spot of UH/UH+5% CNT and UH/UH+10% CNT joints. In this last joint appears the area of polymer carbonization.

Mechanical shear stress measurements of the joints vs. the laser irradiation time are plotted in Fig. 3. Generally, the shear stress decreases with increasing the percentage amount of the filler, as reported for the UH/UH-CNT (Fig. 3a) and UH/UH+Fe₂O₃ (Fig. 3c) joints. On the contrary, the welding area decreases with increasing percentage amount of the filler, as reported in Fig. 3b, d. This result can be explained by considering that the laser adhesion mechanism involves the pure polymer while the filler represents the photon absorbing media that transmits the heat at the interface of the two polymers, where the polymer smelts bonding each other the two opposite parts.

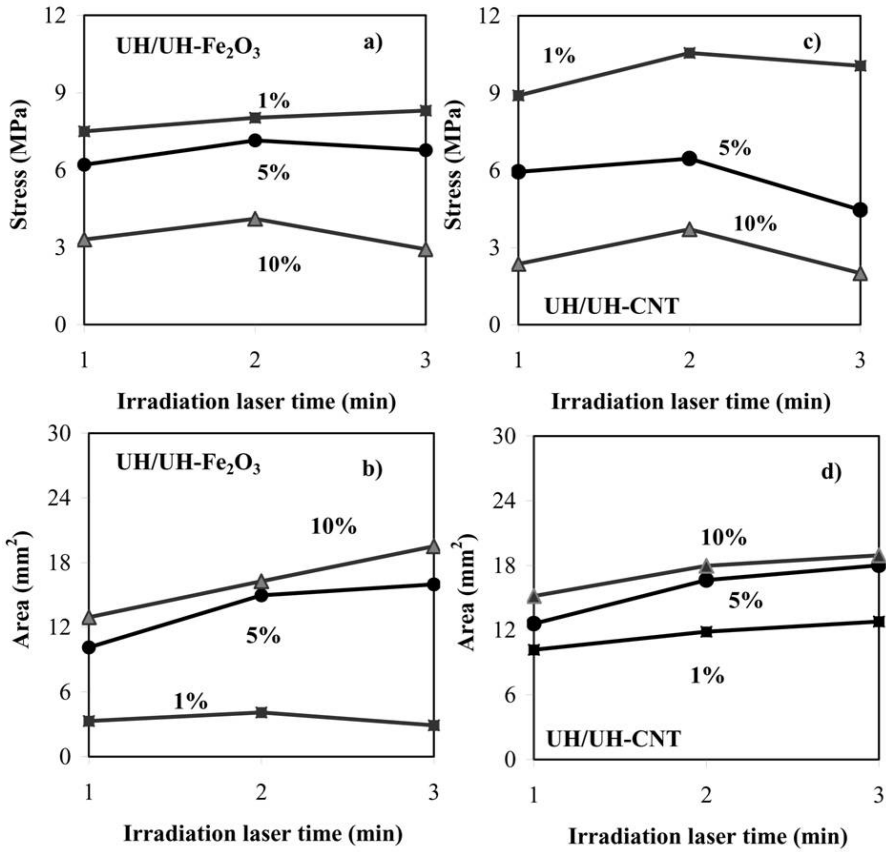


Fig. 3. Shear stress (a, c) and laser irradiated area (b, d) vs. the laser irradiation time of the UH/UH-CNT and UH/UH-Fe₂O₃ joints

With increasing the filler content, the base polymer content decreases so that a weaker adhesion occurs between the two polymeric sheets. Moreover this increment generates a higher heat development at the interface that increases the welding area up to a thermal degradation phenomena may occur. These last degradation effects are more developed in the UH/UH-CNT joints compared to the UH/UH+Fe₂O₃ ones. This can be observed in the images reported in Fig. 4, where the two opposite parts of the two joints typologies, containing the same filler amount (5% or 10%), are compared. The higher damage is present in the UH/UH-CNT joint, with respect to the UH/UH+Fe₂O₃ one, and it is due to the higher absorption coefficient of the carbon nanotubes.

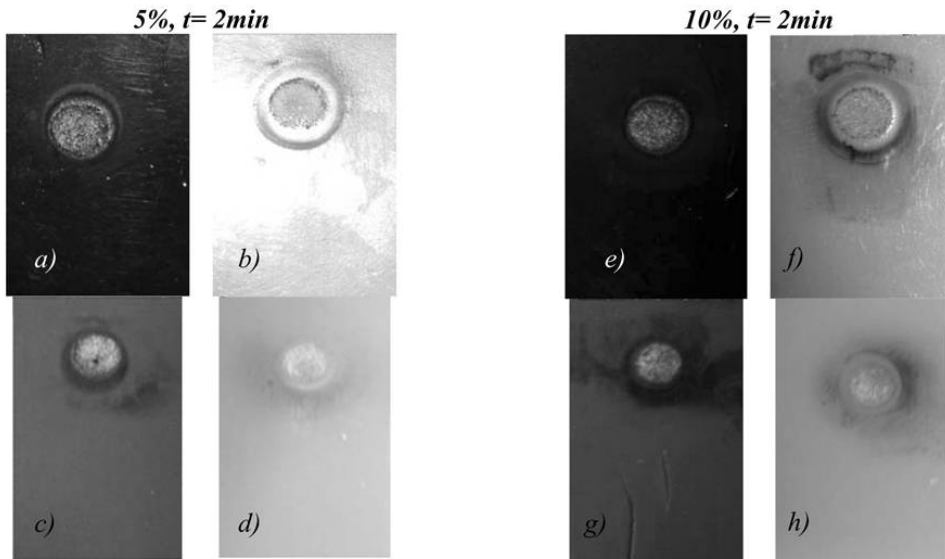


Fig. 4. Comparison of welding area induced by an irradiation of 2 minutes in the in the UH/UH-CNT and UH/UH-Fe₂O₃ joint opposite parts containing the 5 wt % (a, b, c, d) and 10 wt % of fillers (e, f, g, h)

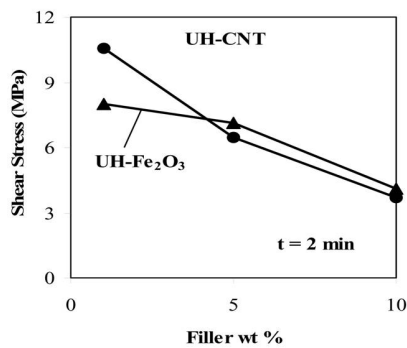


Fig. 5. Shear stress of the UH/UH-CNT and UH/UH-Fe₂O₃ joints containing different fillers percentages and laser irradiated for 2 minutes

In the plot of Fig. 5 the shear stress values are plotted as a function of the filler content (percentage of CNT or Fe₂O₃). The experimental results indicate the mechanical resistance of the joint decreases with the percentage of the filler and suggest that filler amount higher than 5 wt % is dangerous for the mechanical performance of the joint. At low filler amounts, the mechanical

performance of the joint is maintained high and an improvement is obtained using as polyethylene filler the carbon nanotubes instead of the iron oxide.

Finally, the SEM micrographs (Fig. 6) of the welding area induced in the UH-1% CNT and UH-1% Fe₂O₃ opposite parts show a similar morphology induced by the laser irradiation. The low magnification micrographs of Fig. 6a, b show the welding area of the two sheets. They appear melted and constituted by many isles with dimensions of the order of 100 microns. Moreover, their original colour, black or red for the UH-1% CNT and UH-1% Fe₂O₃, respectively, results whitened. The counterpart polymer, instead, show presence or black or red zones. This result suggests that the fillers are detached by the laser source contact and welded to the transparent polyethylene. The two magnifications at 100× of Fig. 6c, d evidence the melted areas of the polymer with formation of micro crakes and of isles with about 100 micron in diameter. The SEM images suggest that the joint efficiency of both welded areas is very high, according to the static mechanical test results.

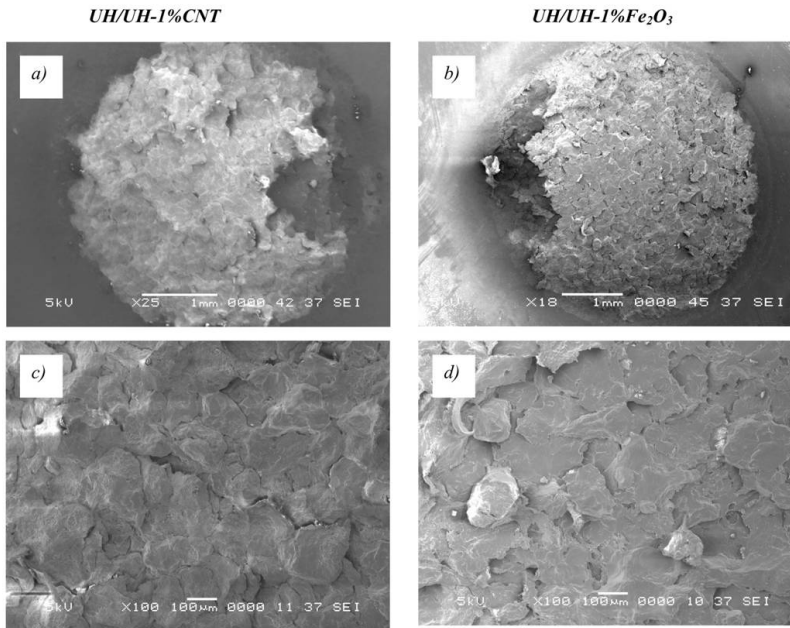


Fig. 6. SEM micrographs of the spot of UH-1%CNT (a, c) and UH-1%Fe₂O₃ (b, d) induced by 2 minutes of laser exposition at different magnifications (×25, ×18 and ×100)

4. Conclusions

The laser welding of two polymers can be made by coupling two polymeric sheets, polyethylene based, one of pure polyethylene, semi-crystalline material and transparent to the laser light radiation and the other of nanostructures embedded in polyethylene to confer high absorption to the laser light radiation.

The laser light energy, transmitted by the first polymer and absorbed in the first layers of the second one, is deposited at the interface where it generates a plasma with formation of heating and accelerated particles. The heating induces thermal-effects, while the accelerated particles induce photo-chemical effects and ion implantation processes. A good adhesion is obtained as demonstrated by the high measured shear stress of the order of 10 MPa. The effect of the filler amount percentage was also investigated in terms of shear stress resistance and welded area. In particular, the presence of a low amount of carbon nanotube (1 weight percent) improves the welding mechanical resistance compared to the iron oxide. Moreover, the increment of the filler content worsens the mechanical resistance of the joint. The joints should not have a high filler content because of the high heat diffusion through the materials and the consequent polymer degradation effects. In fact the mechanical resistance decreases in sheets containing a filler amount higher than 5 weight percent. Also the laser irradiation time, at 10 Hz repetition rate, worsens the mechanical resistance if it is maintained for times higher than about 6 ÷ 7 min [7].

The welding area is generally regular and easily predictable. So the laser welding of plastic materials, compared to the more traditional welding techniques (such as, for example, the simple heating or the electrical melting) represents a successful alternative way to induce welding with a pulsed Nd:Yag laser without the use of diode lasers.

Acknowledgments

The Authors gratefully thank prof. C. Milone of Engineering Faculty, Messina University, for the Carbon nanotube preparation.

References

- [1] S. T. AMANCIO-FILHO, J. F. DOS SANTOS: *Joining of polymers and polymer-metal hybrid structures: recent developments and trends*. Polymer Engineering and Science, *49* (2009), 1461–1476.
- [2] S. GLASER: *Joining Plastics 2006*. Rapra Technology Ltd., London 2006.
- [3] V. V. SEMAK, R. J. STEELE, P. W. FUERSCHBACH, B. K. DAMKROGER: *Role of beam absorption in plasma during laser welding*. Journal of Physics D: Applied Physics, *33* (2000), 1179–1185.

- [4] A. BORRIELLI, L. TORRISI, A. M. MEZZASALMA, J. BADZIAK, J. WOLOWSKI, L. LASKA, J. KRASA, J. ULLSCHMIED: *Ion energy enhancement in laser-generated plasma of metallic doped polymers*. Radiation Effects and Defects in Solids, *163* (2008), 339–348.
- [5] A. M. VISCO, L. TORRISI, N. CAMPO, U. EMANUELE, A. TRIFIRÒ, M. TRIMARCHI: *Mechanical performance of electron-beam-irradiated UHMWPE in vacuum and in air*. Journal of Biomedical Materials Research B, *89* (2009), 55–64.
- [6] L. TORRISI, F. CARIDI, A. M. VISCO, N. CAMPO, *Polyethylene welding induced by pulsed visible laser irradiation*, submitted to NIM B (2009).
- [7] A. M. VISCO, N. CAMPO, L. TORRISI, A. BORRIELLI: *Polyethylene film welding induced by 532 nm pulsed laser*. Rad. Eff. and Defects in Solids, *165* (2010), 601–608.

Received April 30, 2010

Emission of vacuum ultraviolet radiation by a micro atmospheric pressure plasma jet operated in helium–oxygen mixtures into ambient air¹

HENDRIK BAHRE², VOLKER SCHULZ-VON DER GATHEN²,
HARTMUT LANGE³, RÜDIGER FOEST³

Abstract. The VUV emission of a microscale atmospheric pressure plasma jet (μ -APPJ) operated at 13.56 MHz in He with small O₂ additions (< 0.7 %) is analysed between 115 nm and 230 nm. Two atomic emission lines at 115 nm (¹D - ¹Do) and 130 nm (³P - ³S^o) dominate the spectra. Absolutely calibrated measurements of the VUV radiance provide line integrated radiances of 15 and 27 $\mu\text{W mm}^{-2}\text{sr}^{-1}$ respectively for an oxygen admixture of 0.1 vol. % and at 4 mm distance from the nozzle. The axial dependence of the singlet line 115 nm can be described with a decay based on the absorption by atomic and molecular oxygen and ozone. The measurements demonstrate that VUV radiation with photons of 10 eV is transported through the afterglow of the plasma jet over the distance of > 1 cm.

Key Words. VUV emission, absolutely calibrated radiance, micro plasma jet.

1. Introduction

Non-equilibrium atmospheric pressure micro plasma devices are known to produce intense UV and VUV emissions. Radiation within this wavelength range along with chemical reactivity caused by high densities of free radicals while maintaining low gas temperatures plays an essential role for applications as e.g. the modification of temperature-sensitive surfaces or the interaction of the plasma with biological material [1]. Micro plasma jets introduce a new range of applicability by adding the possibility of localized treatment [2].

¹Support of this work by the DFG in the frame of the research group FOR1123 and project SCHU 2353/1 is gratefully acknowledged. The authors also would like to thank Mr. P. Holtz for technical support.

²Ruhr-University Bochum, Application Orientated Plasmaphysics, Bochum, Germany

³Leibniz Institute for Plasmascience and Technology e.V., Greifswald, Germany

The energy transport processes from the plasma core region into the chemically reactive effluent region are of particular interest as this region is targeted for technological exploitations. Means of energy transport are e.g. metastables or radiation transport by VUV photons with correspondingly high energy. The vacuum ultraviolet (VUV) emission in the wavelength range between 115 nm and 230 nm is analysed and the effect of varying the oxygen admixture to the helium flow is studied. The absolute VUV radiance is presented. The spectra presented in the current work originate from both the active discharge region and from the downstream afterglow region of the μ -APPJ. The intent of the VUV spectroscopy on the plasma jet is to characterize the spatially resolved and temporally averaged optical emission.

2. Experimental

Investigations on the plasma radiation are carried out at the so-called μ -APPJ, an especially designed micro scale version of the APPJ providing excellent access for optical diagnostics, in particular to the core plasma [3]. This core plasma is enclosed between two coplanar 1 mm wide stainless steel electrodes. The electrodes are located inside a quartz cuvette at 1 mm distance thus forming a 30 mm long discharge channel with a cross section of 1 mm². The electrodes extending out of the quartz cuvette form a nozzle of about 4 mm length. This μ -APPJ is operated with applied transceiver powers between 5 and 10 W at radio frequency (13.56 MHz) in pure He (around 1 slm) and mixtures with O₂ (around 0.5 vol. %) expanding in open atmosphere. The gas velocity of this effluent is at about 20 ms⁻¹. At these conditions the discharge operates in the α -mode characterised by a weak homogeneous emission. The optical spectra were obtained using a 0.5 m VUV scanning monochromator from Acton Research Corporation (VM 505) with a grating of 1200 G/mm blazed at 150 nm. A photomultiplier tube from Thorn/EMI (9635 QB) in combination with a sodium salicylate coated window was used as detector of the VUV radiation. The optical emission was measured end on by placing the quartz cuvette in the axis of the optical system. The system consists of a measuring aperture, imaging mirror and entrance slit, which are located in a vacuum chamber with a pressure of 2×10^{-6} mbar [4]. The plasma jet was positioned in open air at different distances axially to the MgF₂ window, which seals the vacuum chamber. This window is located in close proximity to the measuring aperture (diameter 0.6 mm) and couples the VUV radiation into the vacuum chamber. The mirror in the vacuum chamber images the area of the aperture on the entrance slit of the monochromator, to define the emitting area. The setup is also equipped with a deuterium lamp (Cathodeon, V03 with MgF₂ window) calibrated by the Physikalisch Technische Bundesanstalt (PTB) in units of radiance ($\mu\text{Wnm}^{-1}\text{mm}^{-2}\text{sr}^{-1}$, spectral bandwidth of 1.6 nm,

low cut off wavelength 115 nm). The emission of this lamp is transferred via the same optical components to the entrance slit of the monochromator alternatively, so that no geometric corrections are needed (to obtain absolute radiance values). The spectral response of the detection system is received by dividing the spectral scan obtained from the radiance data provided by the deuterium lamp. Dividing spectral scans measured from the plasma jet, by the response function described above, gives the absolute radiance end on from the jet. These output spectra correspond to the VUV radiation emitted from a 0.282 mm^2 area (defined by the aperture). The entrance slit of the monochromator was kept at 1.0 mm to ensure the same spectral bandwidth of 1.6 nm during the measurements of the radiance. Better resolved (0.2 nm bandwidth) uncalibrated spectral measurements were performed with a reduced entrance slit width, for line identifications.

3. Results

Figure 1 shows an uncalibrated VUV section of the μ -APPJ emission. The main contributions of VUV radiation are assigned to two oxygen atomic lines, the hydrogen Lyman- α line, and parts of the Schumann–Runge bands. The weak emission of the latter is not shown in Fig. 1. The spectrum is dominated by the O I (neutral atomic oxygen) resonance line ($^3\text{So}-^3\text{P}$) at 130 nm. The emission line at 115 nm ($^1\text{D}^o-^1\text{D}$) ends in the lowest metastable state of the singlet system. The emission feature at 121 nm is not identified without doubt due to the limited spectral resolution. It might be attributed to the hydrogen Lyman- α emission ($\lambda = 121.6 \text{ nm}$) from impurities in the working gases and water desorption from the walls. This is unlikely since the OH emission at 308 nm shows a different behaviour when observing an oxygen admixture variation. Therefore we attribute this emission to a O I ($^1\text{S } ^1\text{P}^o$, $l = 121.7 \text{ nm}$) transition ending in a metastable state at about 4 eV. The VUV emission can be observed for distances from the nozzle of the discharge up to several centimetres. This comparably far expansion is caused by the radiation propagating in the rare gas stream leaving the jet before it vanishes due to turbulence effects. The radial and axial dependences of the O I lines, in particular the resonance line at 130 nm, are investigated for oxygen admixtures around 0.5%. Different decay mechanisms of observed lines are discussed. By varying distance from the nozzle, total flow and composition i.e. oxygen admixture another series of measurements could be carried out. The absolute value of the radiation is an important information for modelling of the complex radiative processes of the system. Figure 2 shows the absolutely calibrated

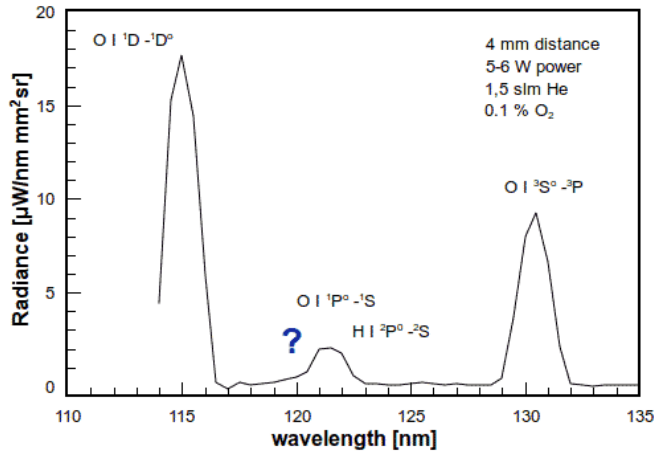


Fig. 1. Uncalibrated VUV spectrum of the μ -APPJ operated in a helium/oxygen mixture displaying atomic oxygen emission from low lying singlet and triplet states of atomic oxygen and eventually Hydrogne Lyman- α from gas impurities

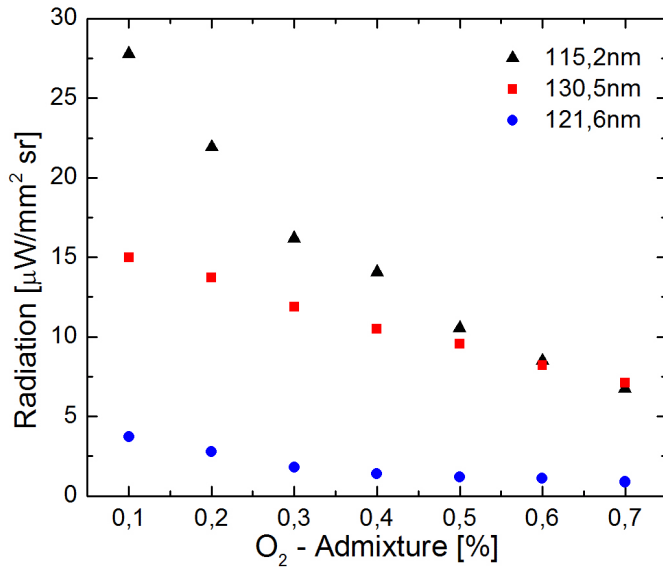


Fig. 2. Line integrated radiances of O ¹D (115 nm, black triangles), O ³P (130 nm, red squares) and Lyman- α (121.6 nm, blue dots) for increasing O₂ admixtures measured at a flow of 1.5 slm He at 4 mm distance from the discharge nozzle

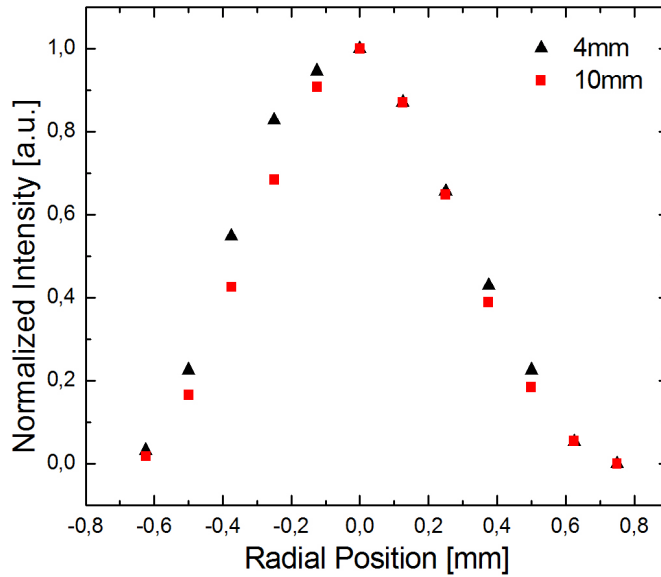


Fig. 3. Radial profiles of the 130 nm radiation measured at 4 (black triangles) and 10 mm (red squares) distance from the nozzle of the discharge

radiances of the 3 observed VUV lines in units of $\mu\text{W sr}^{-1} \text{mm}^{-2}$ in dependence on the oxygen admixture measured at a distance of 4 mm from the nozzle. The helium flow was kept constant at 3 slm for these measurements. As a first result it is found that the calibrated radiance ratio between the two oxygen lines is reversed. For low oxygen admixtures the singlet emission line at 115 nm is about a factor of 3 stronger than the 130 nm resonance line. Radiances of about $10 \mu\text{W sr}^{-1} \text{mm}^{-2}$ are measured for the resonance transition into the atomic oxygen ground state. This observation could be explained by the presence of a substantial amount of metastable ^1D oxygen atoms within the discharge core excited by electrons of relatively low energy. The radiance of the 120 nm emission feature is about one order of magnitude lower than the singlet emission. The maximum radiance for all three lines is observed for lowest O_2 admixtures. It decreases with increasing admixtures. The general decay of the lines could either be attributed to changes of the excitation function of the discharge or additional absorption due to molecular oxygen. The singlet line shows a much stronger decay than the resonance line. This corresponds very well with the known strong quenching of the metastable oxygen ^1D state by molecular oxygen [5]. One of the most important advantages of micro plasma jets is the possibility of localized treatment of sensitive surfaces. Prerequisite for this application is a collimated effluent. It was demonstrated by TALIF spectroscopy that the beam of oxygen atoms stays collimated after leaving the nozzle of the jet over distances of several centimetres [6]. This is confirmed

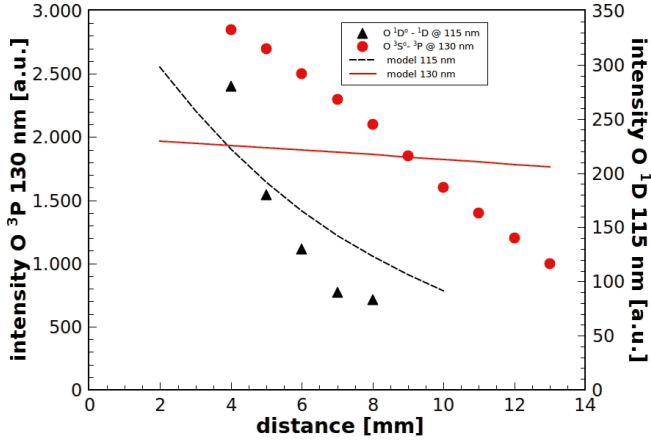


Fig. 4. Comparison of the fluorescence decay of the oxygen VUV lines (triangles: $l = 115$ nm, $^1D - ^1D^\circ$; dots: $l = 115$ nm, $^3P - ^3S$) to calculations based on absorption coefficients for atomic and molecular oxygen and ozone [8] indicated by solid and dashed lines in the respective sequence for a 0.7 vol. % oxygen admixture at a flow of 1.5 slm helium

here by measurements scanning the radial emission profiles transversely to the electrodes at various distances from the nozzle. For these measurements the nozzle of the μ -APPJ is displaced transversely towards the entrance aperture of the diagnostics system. Results are displayed in Fig. 3 for 4 and 10 mm distance from the nozzle for a gas flow of 1.5 slm helium and an admixture of 0.1 vol. % oxygen. A constant width of the beam of about 0.8 mm is observed at both distances. This value is very close to the diameter measured by TALIF spectroscopy. Small deviations might be explained by a small misalignment of the jet's axis towards the observation axis or an effect of the end-on measurement. Figure 4 shows the decay with distance of the singlet and triplet emission lines at 115 and 130 nm at a flow of 1.5 slm He with an admixture of 0.7 vol. % oxygen. The measurements were done starting at a distance of 4 mm from the discharge core defined by the glass cuvette up to 14 mm. It is obvious from Fig. 4 that the singlet line at 115 nm (triangles) is absorbed rapidly and shows an exponential decay within a distance of about 2 mm. Taking into account the flow velocity of about 20 ms^{-1} this corresponds to a decay time of 0.1 ms. The 130 nm triplet line (dots) shows a significantly different behaviour. The fluorescence decreases slowly to half maximum value over a distance of about 8 mm. Provided that absorption at this distance is mostly determined by the working gases the locally transmitted intensity can be calculated for both lines. For this estimation we assumed a constant molecular oxygen concentration of 0.7 vol. %. This is an acceptable approximation since outside the discharge core

the ozone and atomic oxygen ground state densities have been measured to be below 1 percent of the molecular oxygen concentration. The associated profiles, measured by UV absorption [7] and with TALIF [6] respectively, have also been incorporated into the estimate of the respective contributions to absorption. The absorption coefficients for molecular oxygen and ozone were taken from Okabe [8]. For atomic oxygen the values were calculated via the absorption oscillator strength. The resulting atomic absorption is about an order of magnitude smaller than the other ones. The respective theoretical decay behaviour for both lines is shown as red and black lines corresponding to the colour of the measured values. It appears that the absorption of the singlet line at 115 nm is well approximated by this coarse model. However, this is not the case for the triplet line at 130 nm. Here, additional contributions must be taken into account. One candidate could be metastable oxygen $O_2(a^1\Delta_g)$, yet its absorption coefficient at 130 nm is too low to provide a significant contribution [9].

4. Conclusions

Absolutely calibrated measurements of the VUV radiance of an RF micro plasma jet have been carried out and presented. Operated in helium with a vol. % admixture of molecular oxygen two atomic emission lines at 115 and 130 nm dominate the observed spectra. Radiance from other plasma components as molecular oxygen and hydrogen from impurities only constitute below 10 % of the total radiance in the wavelength region between 115 and 230 nm. The dominant transition observed at 115 nm is located in the singlet system of the atomic oxygen and ends in the lowest lying metastable state. (1D). The observed exponential decay of the radiance outside the discharge core allows an estimate of the radiance at the nozzle to be at about $500 \mu\text{W mm}^{-2}\text{sr}^{-1}$ for an oxygen admixture of 0.1 vol. %. This emission contributes significantly to the total radiation of the discharge and in consequence influences its energy balance. The population of the metastable ground state is rapidly quenched in the effluent of the discharge by collisions with oxygen molecules. This is confirmed by the rapid absorption of the 115 nm emission line and the decay of the emission with increasing oxygen admixture. The second important atomic oxygen VUV emission is a resonance line at 130 nm. The maximum radiance of this contribution is much less influenced by the amount of admixed oxygen. The radiation decay in the afterglow of the μ -APPJ cannot be explained solely from the absorption of oxygen constituents as atomic and molecular oxygen, ozone or metastable oxygen molecules. It is therefore assumed that at larger distances ambient air diffuses into the effluent and starts to determine the absorption. In summary the measurements demonstrate that VUV radiation with photons of beyond 10 eV is transported through the helium atmosphere of the plasma jet afterglow to distances of centimetres. This radiation is strictly

localized to a diameter corresponding to the cross section of the micro jet. The energy and radiance of these photons is sufficient to break molecular bonds and has therefore to be taken into account for applications of the micro jet.

References

- [1] A. SCHÜTZE, J. Y. JEONG, S. E. BABAYAN, J. PARK, G. S. SELWYN, R. F. HICKS: *The Atmospheric-Pressure Plasma Jet: A Review and Comparison to Other Plasma Sources*. IEEE Trans. Plasma Sci., 26 (1998), 1685–1693.
- [2] R. FÖEST, M. SCHMIDT, K. BECKER: *Microplasmas, an emerging field of low-temperature plasma science and technology*. Int. J. Mass Spectr., 248 (2006), 87–102.
- [3] V. SCHULZ-VON DER GATHEN, L. SCHAPER, N. KNAKE, S. REUTER, K. NIEMI, T. GANS, J. WINTER: *Spatially resolved diagnostics on a microscale atmospheric pressure plasma jet*. J. Phys. D: Appl. Phys., 41 (2008), 1–6.
- [4] H. LANGE, R. FOEST, J. SCHÄFER, K. D. WELTMANN: *Absolute vacuum UV emission from the effluent of an atmospheric pressure plasma jet with Ar/Xe and Ar/Kr mixtures in ambient air*. Acta Technica CSAV, 53 (2008), 323–331.
- [5] J. A. DAVIDSON, C. M. SADOWSKI, H. I. SCHIFF, G. E. STREIT, C. J. HOWARD, D. A. JENNINGS, A. L. SCHMELTEKOPF: *Absolute rate constant determinations for the deactivation of $O(^1D)$ by time resolved decay of $O(^1D) \rightarrow O(^3P)$ emission*. J. Chem. Phys., 64 (1976), 57–62.
- [6] N. KNAKE, K. NIEMI, S. REUTER, V. SCHULZ-VON DER GATHEN, J. WINTER: *Absolute atomic oxygen density profiles in the discharge core of a microscale atmospheric pressure plasma jet*. Appl. Phys. Lett., 93 (2008), 131503.
- [7] V. SCHULZ-VON DER GATHEN, V. BUCK, T. GANS, N. KNAKE, K. NIEMI, S. REUTER, L. SCHAPER, J. WINTER: *Optical diagnostics of micro discharge jets*. Contrib. Plasma Phys., 47 (2007), 510–519.
- [8] H. OKABE: Photochemistry of small molecules. Wiley-Interscience, New York 1987.
- [9] R. J. COLLINS, D. HUSAIN, R. J. DONOVAN: *Kinetic and spectroscopic studies of $O_2(a^1\Delta_g)$ by time-resolved absorption spectroscopy in the vacuum ultra-violet*. Faraday Trans., 2 (1973), 145–157.

Received April 22, 2010

Diagnosics of plasma at atmospheric pressure by optical emission spectroscopy using broadening of lines¹

DANA SKÁCELOVÁ², PAVEL SLAVÍČEK²

Abstract. We study one type of plasma jet with name “Plasma pencil” generated at atmospheric pressure by generator with frequency 13,56 MHz. Plasma pencil is a special type of the plasma nozzle working at atmospheric pressure, which is interesting for possible applications such as local treatment of surface, deposition of thin films, change surface energy, cutting in surgery, sterilization, etc. Through this nozzle, which is made from quartz tube with typical inner diameter 2 mm, flows working gas (typically argon). The powered electrode is connected through the matching unit to the rf generator. In this contribution, we present diagnostics of unipolar discharge channel generated by the Plasma pencil. For different conditions the parameters of the plasma channel were estimated from optical emission spectra in the spectral range 200 ÷ 900 nm, rotational temperature from OH rotational lines and first results of concentration of electrons from Stark broadening of hydrogen lines were estimated.

Key Words. Barrier discharge, plasma diagnostics.

Introduction

Low-temperature plasmas are extensively used for the plasma processing [1], light sources, various plasma technologies [2] etc. Therefore, the interest for plasma diagnostics is growing. The optical emission spectroscopy (OES) technique is of particular interest, especially if standard spectroscopic instrumentation is available in laboratory. Barrier discharges at atmospheric pressure are intensively studied for possible industrial applications [1], [8], [6]. In this paper diagnostics of radio frequency discharge by optical emission spectroscopy will be presented.

¹This research has been partially supported by the grant 202/09/2064 by the Czech Science Foundation and by the research intent MSM:0021622411 funding by the Ministry of Education of the Czech republic and by the contracts KAN101630651, KAN311610701 by Grant Agency of Academy of Science of Czech Republic.

² Masaryk University, Faculty of Science, Department of Physical Electronics

Experimental setup

The schematic diagram of the experimental arrangement is shown in Fig. 1 and photograph is shown in Fig. 2. The powered electrode is separated by the dielectric tube (nozzle with the inner diameter of about 2 mm) from plasma. In this experimental device a quartz tube with length 5 cm was used. Through the nozzle flows working gas. Working gas was argon with purity 99.996 %. Note, that the working gas flowing from the nozzle stabilizes the discharge. The detail description and discussion of several variants of the nozzle are also presented in [6], [7]. The electrode is connected through the matching unit to the rf generator Cesar – 1310 by Dressler driven at frequency 13.56 MHz. This type of discharge has a lot of applications [5], [6]. Plasma pencil is interesting for possible applications such as local treatment of surface, deposition of thin films, change surface energy, cutting in surgery, sterilisation etc.

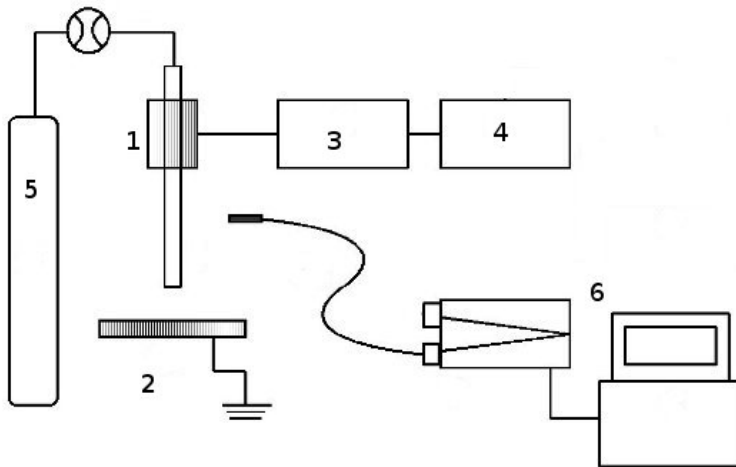


Fig. 1. Experimental setup: 1 – nozzle, 2 – ground electrode, 3 – matching unit, 4 – rf generator, 5 – working gas (argon), 6 – spectrometer

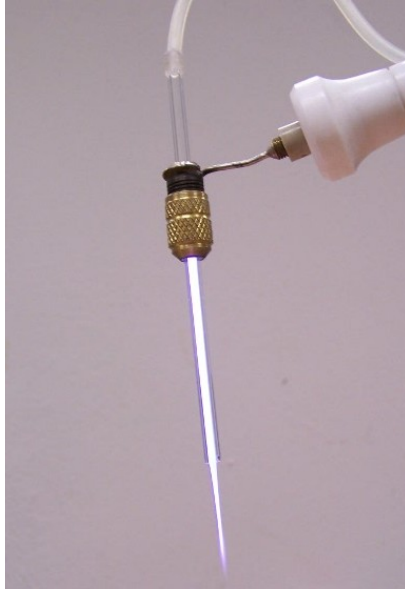


Fig. 2. Photo of plasma pencil

Optical emission spectroscopy of the plasma channel was realized by means of the spectrometer FHR1000 by Jobin–Yvon–Horiba (grid were 2400 gr/mm and 3600 gr/mm, CCD detector Symphony cooled by four stages Peltier cooler). The spectra were recorded perpendicularly to the plasma channel for different discharge parameters.

Rotational temperatures were calculated from rotational lines of OH from branch Q_1 . Rotational temperature were calculated from Boltzmann plot [3], [4].

The most frequently used technique for determination of electron concentration N_e is based on the half-width and shape of the hydrogen Balmer beta ($H_\beta = 486.13$ nm) spectral line.

Electron concentration was estimated by approximate formula by Wiese et al. as

$$N_e = 10^{22} \left(\frac{W_S}{4.7333} \right)^{1.49} \quad [\text{m}^{-3}] \quad (1)$$

where N_e is concentration of electron and W_S is the H_β Stark half width at half maximum – HWHM in 0.1 nm unit. Detail description is in [9], [10], [12].

Unipolar modification of this discharge without ground electrode was used for all measurements.

Result and discussion

The dependence of the rotational temperatures on the distance from end of the nozzle for 5 cm length of nozzle and for rf power 100 W and working gas flow rate 1 slpm are shown in Fig. 3. Same dependence for rf power 125 W is shown in Fig. 4. Negative distance was in nozzle, positive distance was out of nozzle. The rotational temperature is good approximation of gas temperature.

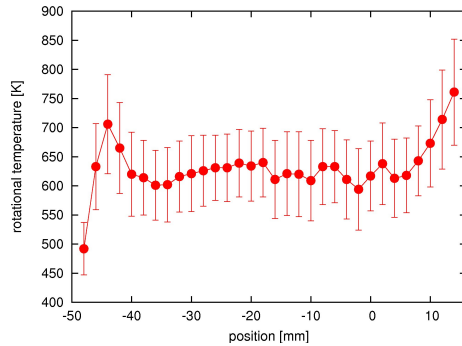


Fig. 3. The rotational temperature from OH, rf power 100 W, working gas (Ar) flow 1 slpm. Negative distance was in nozzle, positive distance was out of nozzle.

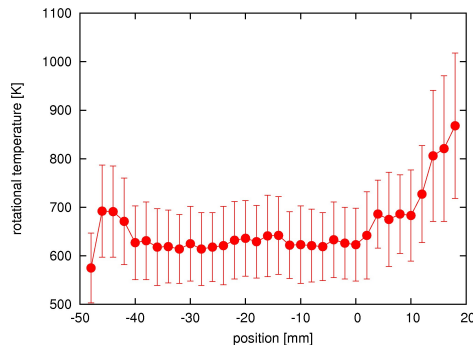


Fig. 4. The rotational temperature from OH, rf power 125 W, working gas (Ar) flow 1 slpm. Negative distance was in nozzle, positive distance was out of nozzle.

The dependence of the concentration of electron on the distance from end of the nozzle for 5 cm length of nozzle and for rf power 100 W and working gas flow rate 1 slpm is shown in Fig. 5. Same dependence for rf power 125 W

is show Fig. 6. Negative distance was in nozzle, positive distance was out of nozzle.

Error of the rotational temperatures were about 10%. The rotational temperatures were approximately same from power electrode (position -50 mm) to the end of the nozzle (position 0 mm). Working gas (argon) was mixtured with air at atmospheric pressure in range from the end of the nozzle (position 0 mm) to end of plasma channel (position $15 \div 20$ mm). Estimated dependence of the rotational temperature on rf power (Figs. 3 and 4) are show too, if the rf power is increase than the rotational temperatures are increase too.

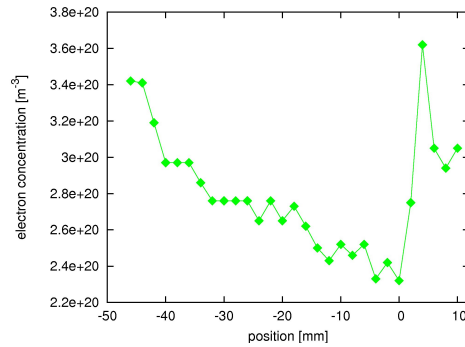


Fig. 5. The concentration of electron calculated from broadening of H_{β} , rf power 100 W; negative distance was in nozzle, positive distance was out of nozzle

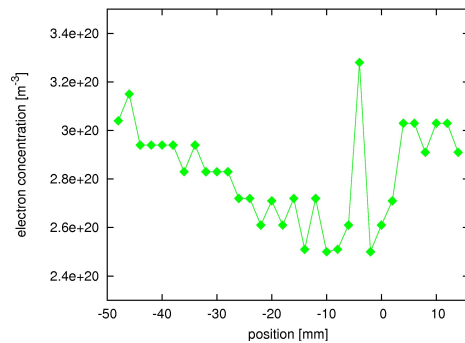


Fig. 6. The concentration of electron calculated from broadening of H_{β} , rf power 125 W; negative distance was in nozzle, positive distance was out of nozzle

The concentration of electron was approximately 10^{20} m^{-3} . Gas temperatures were relatively low (less than 900 K) therefore for first approximation can be neglected resonance and Van der Waals broadening of spectral lines. Estimate error of the concentration is from this first measurements problematic. New measurement and calculation [10] will be done in near future. The increase of the concentration of electron and the rotational temperatures near the nozzle outlet correspond with mixture of argon flow with the surrounding atmospheric gases (nitrogen, oxygen, ...).

The Abel transformation of cylindrical symmetry of discharge was not taken into account for very small diameter of plasma channel (smaller than 1 mm).

Conclusion

In this article results of electron concentration and rotational temperature in discharge generated by plasma pencil at atmospheric pressure were presented. The rotational temperatures in the plasma nozzle are less than 900 K. The concentration of electron in plasma channel was approximately 10^{20} m^{-3} . Main result is that diagnostics of the concentration of electron is possible done for this type of barrier discharge with our spectrometer. New measurement and more accurately calculation will be done in near future.

In this contribution the single nozzle was used, but several nozzles can be applied simultaneously in one device [5], which is more convenient for industrial application.

References

- [1] J. RAHEL, M. SIMOR, M. CERNAK, M. STEFECKA, Y. IMAHORI, M. KANDO: *Hydrophilization of polypropylene nonwoven fabric using surface barrier discharge*. Surf. Coat. Technol, 169-170 (2003), 604–608.
- [2] M. SIRA, D. TRUNEC, P. STAHEL, V. BURSICOVA, Z. NAVRATIL: *Surface modification of polycarbonate in homogeneous atmospheric pressure discharge*. J. Phys. D, 41 (2008), 015205.
- [3] H. R. GRIEM: Principles of plasma spectroscopy. Academic Cambridge Univ. Press, New York 1997.
- [4] LOCHTE-HOLTGREVEN ED.: Plasma Diagnostics. American Institute of Physics, New York 1995.
- [5] M. CADA, Z. HUBICKA, M. SICHÁ, A. CHURPITA, L. JASTRABIK, L. SOUKUP, M. TICHÝ: *Investigation of RF and DC plasma jet system during deposition of highly oriented ZnO thin films*. Surf. Coat. Technol, 174–175 (2003), 627–631.
- [6] P. SLAVICEK, V. BURSICOVA, A. BRABLEC, V. KAPICKA, M. KLIMA: *Deposition of polymer films by rf discharge at atmospheric pressure*. Czech. J. Phys, 54 (2004), C586–C591.

- [7] P. SLAVICEK, M. KLIMA, J. JANCA, A. BRABLEC, J. KADLECOVA, P. SMEKAL: *Diagnostics of rf microdischarge generated at atmospheric pressure*. Czech. J. Phys. B, 56 (2006), B1057–B1061.
- [8] Z. HUBICKA, M. CADA, M. SICHA, A. CHURPITA, P. POKORNY, L. SOUKUP, L. JASTRABIK: *Barrier-torch discharge plasma source for surface treatment technology at atmospheric pressure*. Plasma Sources Sci. Technology, 11 (2002), 195–202.
- [9] W. L. WIESE, D. E. KELLEHER, D. R. PAQUETTE: *Detailed study of the stark broadening of balmer lines in a high-density plasma*. Physycal Review A, 6 (1972), 1132–1153.
- [10] M. IVKOVIC, S. JOVICEVIC, N. KONJEVIC: *Low electron density diagnostics: development of optical emission spectroscopic techniques and some applications to microwave induced plasmas*. Spectrochimica Acta Part B, 59 (2004), 591–605.
- [11] D. E. KELLEHER: *Stark broadening of visible neutral helium lines in a plasma*. J. Quant. Spctrosc. Radiat. Transfer, 25 (1981), 191–220.
- [12] R. ZIKIC, M. A. GIGISOS, M. IVKOVIC, M. A. GONZALES, N. KONJEVIC: *A program for the evaluation of electron number density from experimental hydrogen balmer beta line profiles*. Spectrochimica Acta Part B, 57 (2002), 987–998.

Received May 13, 2010

Molecular structure, hydrophilic character and mechanical properties of diglyme plasma polymer

ROGÉRIO P. MOTA¹, NAZIR M. S. MARINS¹,
MAURICIO A. ALGATTI¹, KONTANTIN G. KOSTOV¹,
ROBERTO Y. HONDA¹, NILSON C. DA CRUZ²,
ELIDIANE C. RANGEL², MILTON E. KAYAMA¹

Abstract. This paper focuses on the hardness, elastic modulus and molecular structure of plasma-polymerized Diglyme films. Plasmas were excited at a fixed pressure of 13.3 Pa, within a stainless steel plasma chamber in a parallel plate electrodes configuration by a RF-power supply operating at 13.56 MHz. RF power was varied from 5 to 40 W. Polymer films hardness and elastic modulus were determined from nanoindentation data. The results showed that hardness and elastic modulus changed from 0.03 to 0.3 GPa and 0.1 to 10 GPa, respectively, when power was varied from 5 to 40 W. These results are in close agreement with the data from FTIR spectroscopy that show a densification of the film structure due the decreasing of C–O–C and C–O bounds with the increasing of RF power. The films' contact angle measurements revealed an increasing from 50° to 63° for RF power varying from 5 to 40 W. Therefore the hydrophilic character of diglyme plasma polymer decreases with the increasing of RF power coupled to plasma.

Key Words. Plasma polymers, diglyme plasmas, nanoindentation, FTIR spectroscopy, contact angle, hardness.

1. Introduction

Plasma polymer processing at low pressure and temperature is essential in many current scientific and technological issues encompassing microelectronics, optical, biomaterial and coating industries [1]–[7]. The main reason is that

¹Universidade Estadual Paulista, Faculdade de Engenharia, Departamento de Física e Química, Av. Ariberto Pereira Cunha 333, CEP: 12516-410, Guaratinguetá, SP, Brazil.

²Universidade Estadual Paulista, Câmpus Experimental de Sorocaba, Av. Três de março 511, CEP: 18087-180, Sorocaba, SP, Brazil.

within such kind of plasmas, the electrons may attain energy in excess of several eV in comparison to the heavy particles present in the discharge. This unusual thermal non-equilibrium state is extremely profitable in molecular fragmentation by electronic impact, giving rise to a very reactive chemistry in a relative cold environment [8]–[12] whose kinetics is not easily controlled. In spite of these characteristics plasma polymerized films with customized properties can be synthesized by this kind of discharges. In the field of biomaterials science and technology, plasma polymerized polyethylene-glycol-dimethyl-ether is an issue that has been keeping the attention of the scientific community due to its non-fouling characteristic [13]–[16]. If appropriate plasma parameters are set such films can be synthesized keeping their molecular structure similar to that of polyethylene oxide-like (PEO-like) films, with the advantage that the former are not soluble in water. The aqueous solubility of PEO makes it less appropriate for many biomaterials applications. In order to set the appropriate experimental parameters that would result in customized film structure of plasma polymerization of PEO-like coatings this paper deals with plasma polymerization of diethylene glycol dimethyl ether (diglyme) for different values of the RF plasma power [3], [9], [17]. The retention of the monomer structure into the films at a fixed pressure and different values of RF plasma power was studied using FTIR spectroscopy. The films hardness and elastic modulus were determined from nanoindentation techniques using a Hysitron TriboIndenter® system and the wetting character of the samples was analyzed by contact angle measurements.

2. Experimental setup and measurements

The glow discharge was generated by a RF power supply operating in the range from 5 to 40 W in $\text{CH}_3\text{O}[\text{CH}_2\text{CH}_2\text{O}]_2\text{CH}_3$ (diglyme) atmosphere at a fixed pressure of 13.3 Pa within a cylindrical stainless steel plasma reactor (210 mm internal diameter and 225 mm long) in parallel plate electrodes configuration. The Fig. 1 shows the experimental setup of deposition system. The pressure inside plasma chamber was monitored by piraniTM (thermocouple) and penningTM (inverse magnetron) gauges. A turbo-molecular pump used for cleaning purposes was coupled to the chamber through a gate valve.

The pressure was pumped down to 1.33×10^{-5} Pa and the chamber was purged several times with argon before running each experiment. In order to minimize the monomer condensation and humidity plasma chamber walls were heated by a temperature-controlled belt. Diglyme monomer was fed into the plasma chamber from a heated stainless steel bottle through a needle valve. Plasma chamber and the bottle were kept at 60 °C and 70 °C, respectively. Diglyme plasmas were excited by a RF power supply operating in 13.56 MHz whose output power could be varied from 0 to 300 W (Tokyo HY-Power model

RF-300TM). The RF power was coupled to the plasma reactor through an appropriate matching network (Tokyo HY-Power model MB-300TM).

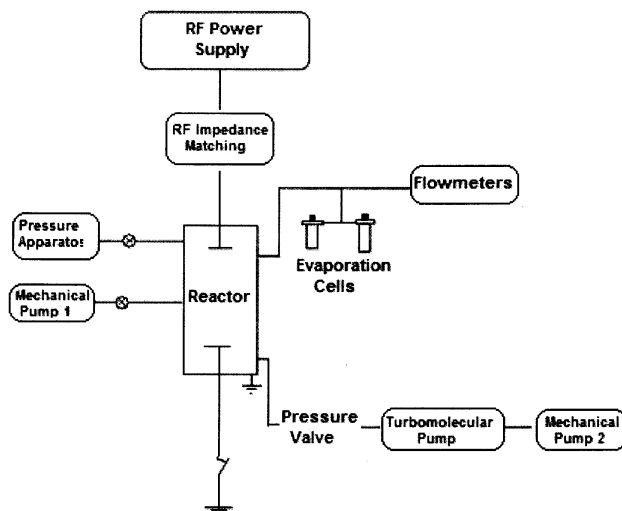


Fig. 1. The diagram of the experimental set up used in the polymer deposition process

Plasma diglyme polymer films were deposited on silicon and quartz substrates during two hours for all RF power conditions. Polymer film thickness was determined through step meter technique using an Alpha Step Tencor 100TM. The typical polymer film thickness varied from 130 nm to 190 nm. Diglyme plasma polymerized films are transparent to visible light and pinhole free. These films resulted from the plasma enhanced chemical vapour deposition and is characterized by a highly crosslinked structure free of islands or grains in which many monomer's functional groups are retained [9].

The FTIR spectra of plasma diglyme films deposited at 13.3 Pa for different values of the RF power was collected by a FTIR spectrometer Jasco 4100TM operating in the spectral range from 4000 cm^{-1} to 400 cm^{-1} . The maximum resolution of the spectrometer is 0.9 cm^{-1} . For FTIR analysis diglyme films were deposited over microscope slides covered by Al films. FTIR spectra were collected in the reflectance operation mode in a dry nitrogen atmosphere. Each spectra resulted from 20 scans in order to reduce the noise of the experimental apparatus. The films hardness measurements were carried out using a Hysitron TriboIndenterTM system provided with a diamond Berkovich indenter and an atomic force-imaging module that allows one to perform indentation with a space accuracy of 50 nm in the horizontal displacement. The nominal

resolution of the indenter's tip displacement during the loading and unloading cycle is of about 2×10^{-4} nm. The load resolution is less than 1 nN. The loading–displacement–curves were obtained in cycles with duration of 15 s. Loading–accommodation–unloading processes compose every indentation cycle that takes 5 s to be completed. The contact angle were performed using a goniometer Ramé-Hart 300™ that allowed measurement of the angle formed between the polymer surface and the water drop with a maximum precision of 0.1° .

3. Results and discussions

Figure 2 shows the FTIR spectra of diglyme plasma polymer films, in the spectral range from 4000 cm^{-1} to 400 cm^{-1} , for different values of the RF power coupled to the plasma chamber. One may distinguish several different absorption bands in these spectra. The spectral range between 3600 cm^{-1} and 3300 cm^{-1} is characterized by OH group's absorption whose low intensity remained approximately constant with the increasing of the RF power.

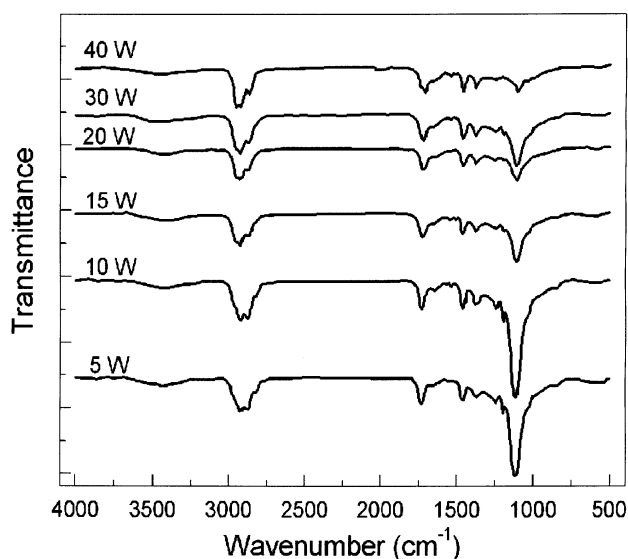


Fig. 2. FTIR spectra of plasma-polymerized diglyme films, for different values of the RF power coupled to the plasma chamber

Although the chemical bond O–H is not present in the monomer structure ($\text{CH}_3\text{O}[\text{CH}_2\text{CH}_2\text{O}]_2\text{CH}_3$), it appears in the polymeric film probably due the fragmentation and recombination processes during the plasma polymerization

process. Two others sources that contribute for the retention of oxygen in Diglyme films are the reactions with residual water vapor inside the plasma chamber and the recombination process of oxygen present in the air with the free radicals at the film's surface, when it is exposed to the atmosphere. The absorption bands at 2900 cm^{-1} and 2960 cm^{-1} are associated to C–H stretching modes in CH_2 and CH_3 groups respectively. The absorptions band between 1650 cm^{-1} and 1750 cm^{-1} is due to C=O stretching. The absorptions showed in the wavenumber range from 1380 cm^{-1} to 1440 cm^{-1} are due to C–H bending modes. The band in the range from 1000 cm^{-1} to 1200 cm^{-1} is associated with C–O–C and C–O stretching modes. Yet the Fig. 2 shows that the same vibrational groups are present in all polymer films deposited at different values of RF power coupled to plasma (i.e. from 5 to 40 W). A quantitative evaluation of the relative (C–O–C, C–O) and C–H bands densities can be performed by the integrated absorption technique, proposed in [18], [19] applied to the bounds at $1000 \div 1200\text{ cm}^{-1}$ and $2900 \div 2960\text{ cm}^{-1}$, respectively.

The accuracy of the data obtained by the technique depends on polymer film thickness measurements and on infrared band area determination. These results are presented in Table 1.

Table 1. Integrated absorptions of diglyme PP measured at $1000 \div 1200\text{ cm}^{-1}$ band and $2900 \div 2960\text{ cm}^{-1}$ band

RF Power [W]	Normalized Integrated Absorption C–O, C–O–C [$1000 \div 1200\text{ cm}^{-1}$]	Normalized Integrated Absorption C–H [$2900 \div 2960\text{ cm}^{-1}$]
5	1.00	0.50
10	0.80	0.55
15	0.77	0.60
20	0.70	0.65
30	0.55	0.80
40	0.50	1.00

It can be seen that C–O–C and C–O bonds decrease from 100% to 50% (relative values) while C–H bond increase from 50% to 100% (relative values) in the range from 5 to 40 W of RF power. These results are in close agreement with the mass spectrometry data presented elsewhere [20]. The increase of the RF power coupled to the discharge enhance the monomer fragmentation processes increasing the number of light chemical species within the discharge. Therefore the high power regime favours the formation of C–H radicals that are attached to the films' structure. From these results one can conclude that the density of hydrogenate groups present in the diglyme plasma polymers tends to increase with the increasing of RF power.

Therefore if one intends to retain the PEO-like structures within the plasma-polymerized diglyme one must operate the plasma reactor at relatively low RF power levels. Figure 3 shows that the hardness of diglyme films increases from 0.03 GPa to 0.3 GPa when the RF power was varied from 5 to 40 W. This behavior of hardness is a strong indicative of the increasing of the polymeric cross-linking which is also corroborated by the FTIR data. The enhance of polymeric cross-linking is a direct effect of the film's surface ion bombardment by particles resulting from molecular fragmentation within the plasma. The increase of RF power causes increasing of the particle's mean energy resulting in much more reactive plasma. This behavior of diglyme plasmas was confirmed by the results from discharge's mass spectrometry published elsewhere [20], which showed that the increase of RF power, at a fixed value of gas pressure, produced intense molecular fragmentation by electronic impact that reduced the number of heavy molecular fragments and increased the light one within the plasma.

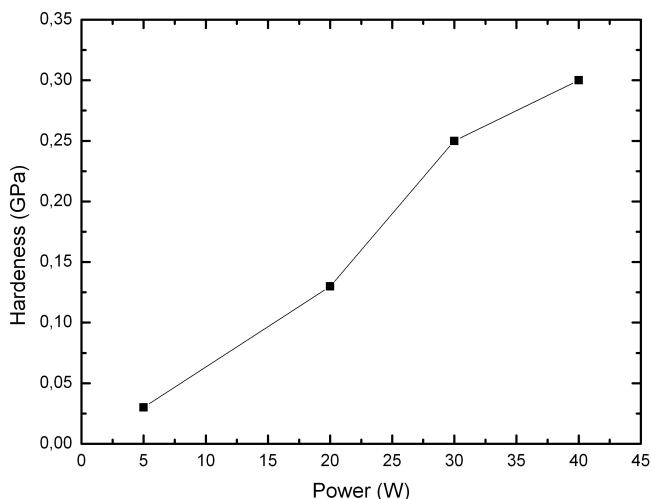


Fig. 3. Plasma-polymerized diglyme films hardness as a function of the RF power coupled to the plasma chamber

Figure 4 shows that the elastic modulus of diglyme films increases from 0.1 GPa to 10 GPa when the RF power was varied from 5 to 40 W. This behavior of the elastic modulus is also a strong indicative of the intense polymeric cross-linking. The increasing of the elastic modulus indicates that these polymer films became more resistant to permanent deformation.

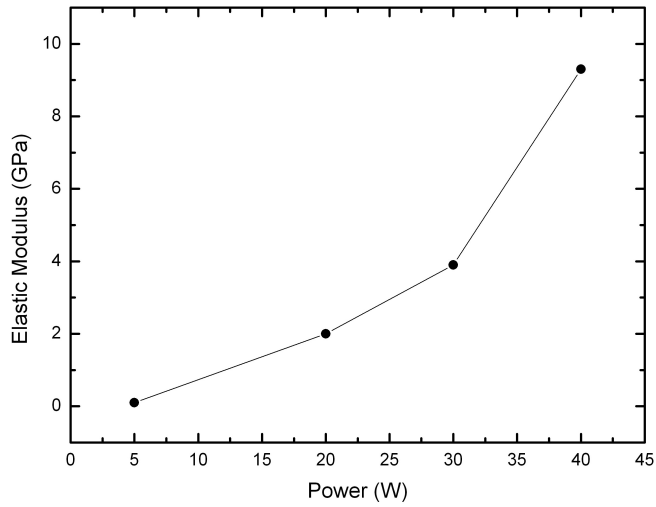


Fig. 4. Plasma-polymerized diglyme film's elastic modulus dependence on RF power coupled to the plasma chamber

Figure 5 shows that the water contact angle of the films increases from 50° to 63° when the RF power was varied from 5 to 40 W, indicating the decrease of sample's hydrophilicity with the increase of RF power. At high RF power the deposition process produces plasma polymer films with highly cross-linked structures, which effectively contributes for the contact angle increasing.

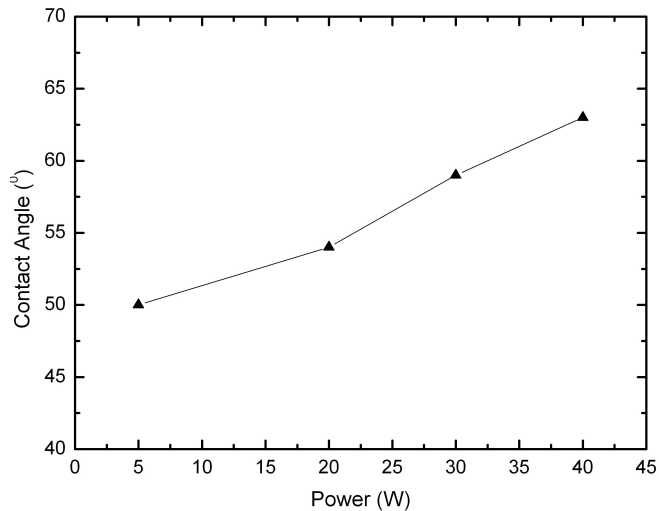


Fig. 5. Plasma-polymerized diglyme films contact angle dependence on RF power coupled to the plasma chamber

On the other hand exposure of plasma polymerized structure to the atmosphere environment can also contribute for the contact angle increasing due the recombination process with oxygen from the air.

4. Conclusions

The present study allows to conclude that if one wants to preserve the monomer's functionalities within the plasma-polymerized films the plasma chamber must be operated at relatively low power levels. Polymer films grown under such conditions are softer than that ones grown under higher RF power levels since in the later the intense ion bombardment of the surface enhances the polymeric cross-linking. Therefore, in principle, customized hard non-fouling diglyme plasma polymerized films may be obtained by monitoring the RF power level coupled to the plasma chamber during the film's growth process. These transparent hydrophilic polymer films with non-fouling properties present promising applications in biomaterials industry.

Acknowledgments

The authors would like to thank FAPESP, FUNDUNESP, CAPES and CNPq for financial support. José Benedito Galharido is acknowledged for technical assistance during the plasma chamber assembling.

References

- [1] J. YANG, J. C. GAO: *MW plasma polymer thin film synthesis using diglyme precursor*. Materials Science and Technology, *24* (2008), 261–265.
- [2] Q. CHENG, K. KOMVOPOULOS: *Synthesis of polyethylene glycol-like films from capacitively coupled plasma of diethylene glycol dimethyl ether monomer*. Journal of Physical Chemistry C, *113* (2009), 213–219.
- [3] H. BIEDERMAN: Plasma polymer films. Imperial College Press, London 2004.
- [4] R. D'AGOSTINO, P. FAVIA, Y. KAWAI, H. IKEGAMI, N. SATO, F. A. KONSARI: Advanced plasma technology. Wiley-VCH, Weinheim 2008.
- [5] P. K. CHU, J. Y. CHEN, L. P. WANG, N. HUANG: *Plasma surface modification of biomaterials*. Materials Science and Engineering: R: Reports, *36* (2002), 143–206.
- [6] A. BOGAERTS, E. NEYTES, R. GIJBELS, J. VAN DER MULLEN: *Gas discharge plasmas and their applications*. Spectrochimica Acta Part B, *57* (2002), 609–658.
- [7] R. D'AGOSTINO, P. FAVIA, C. OEHR, M. R. WEITHEIMER: *Low-temperature plasma processing of materials: post, present and future*. Plasma Process and Polymers, *2* (2005), 7–15.

- [8] R. J. SHUL, S. J. PEARTON: Handbook of advanced plasma processing techniques. Springer Verlag, Berlin 2000.
- [9] H. YASUDA: Plasma polymerization. Academic Press, New York 1985.
- [10] J. R. ROTH: Industrial plasma engineering principles. Taylor & Francis, New York 1995.
- [11] J. R. ROTH: Industrial plasma engineering applications. Taylor & Francis, New York 2002.
- [12] N. INAGAKI: Plasma surface modification and plasma polymerization. CRC Press, Lancaster 1996.
- [13] N. A. ALCANTAR, E. S. AYDIL, J. N. ISRAELACHVILI: *Polyethylene glycol-coated biocompatible surfaces*. Journal of Biomedical Materials Research Part A, 51 (2000), 343–351.
- [14] S. K. HENDRICKS, C. KWOK, M. SHEN, T. A. HORBETT, B. D. RATNER, J. D. BRYERS: *Plasma deposited membranes for controlled release of antibiotic to prevent bacterial adhesion and biofilm formation*. Journal of Biomedical Materials Research Part A, 50 (2000), 160–170.
- [15] E. SARDELLA, R. CRISTINA, G. S. SENESI, R. D 'AGOSTINO, P. FAVIA: *Homogeneous and micro patterned plasma deposition PEO-like coatings for biomedical surfaces*. Plasma Processes and Polymers, 1 (2004), 63–72.
- [16] P. FAVIA, R. P. MOTA, M. VULPIO, R. MARINO, R. D 'AGOSTINO, M. CATALANO: *Plasma deposition of Ag-containing polyethylene oxide-like coatings*. Plasma and Polymers, 5 (2000), 1–4.
- [17] H. BIEDERMAN, D. SLAVINSKÁ: *Plasma polymer films and their future prospects*. Surface & Coatings Technology, 125 (2000), 371–376.
- [18] W. A. LANFORD, M. J. RAND: *The hydrogen content of plasma deposited silicon nitride*. Journal of Applied Physics, 49 (1978), 2473–2477.
- [19] M. A. ALGATTI, R. P. MOTA, R. Y. HONDA, M. E. KAYAMA, K. G. KOSTOV, R. S. FERNANDES, T. C. A. M. AZEVEDO, N. C. CRUZ: *Study of optical properties and molecular structure of plasma polymerized diethylene glycol dimethyl ether*. The European Physical Journal D, 54 (2009), 325–328.
- [20] E. F. ANTUNES, A. R. BIGANSOLLI, M. A. ALGATTI, R. P. MOTA, R. Y. HONDA, J. C. TEIXEIRA, M. E. KAYAMA, E. C. RANGEL, N. C. CRUZ: *Study of the chemical reactions on low pressure RF excited Diglyme plasmas using mass spectrometry and optical spectroscopy*. 15th International Symposium on plasma chemistry (A. Bouchoule, J. M. Pouvesle, A. L. Thomann, J. M. Bauchire, E. Robert). Gremi-CNRS, Orléans 2001, 2317–2322..

Treatment of polyester fabric in atmospheric dielectric barrier discharge operated at low frequencies¹

JAN PÍČHAL^{2, 3}, DANA HOLLÁ², JAN SLÁMA²

Abstract. Due to its environmentally friendly characteristics plasma treatment of polymers happened to be often applied method for improvement of polymer surface properties. Radicals and ions generated in discharge sustaining in proper gas together with its intense ultraviolet radiation are suitable to break molecular bonds and initiate physical and chemical processes in uppermost atomic layers of a material surface. These processes result e.g. in growth of surface hydrophilicity whereas bulk characteristics remain unaffected. Polyester (i.e. polyethylene terephthalate, PES) fibres are one of the most produced and used textile component, unfortunately these fibres are also known with some unwanted properties, e.g. high hydrophobicity, electrostatic charge creation, pilling etc. Earlier we successfully tested application of atmospheric dielectric barrier discharge sustaining in air at atmospheric pressure for PES fibres hydrophilicity improvement. To influence the efficiency of this process, we tried to increase the input energy of the plasma reactor by means of the supply voltage frequency. Correlation of the supply voltage frequency and modification efficiency presented by hydrophilicity changes expressed by means of the area of feathering time evolution (drop test) is described in this paper. Experiments proved that growing reactor input energy/supply voltage frequency shortened necessary modification time.

Key Words. Atmospheric dielectric barrier discharge, fabric, filamentary mode, hydrophilicity, modification, supply voltage frequency.

¹This research has been supported by the Czech Technical University in Prague grant No. SGS10/266/OHK3/3T/13 and project MSM 4644788501.

²Czech Technical University in Prague, Faculty of Electrical Engineering, Department of Physics, Technická 2, 166 27 Praha 6, Czech Republic

³Technical University of Liberec, Faculty of Mechanical Engineering, Department of Material Science, Studentská 2, 461 17 Liberec, Czech Republic

Introduction

Polymer surface properties like wettability and adhesion can be modified without changing polymer bulk properties by use of methods employing low temperature (“cold”) plasma treatment. For survey of these methods see [1].

Probably the easiest way to get the low temperature plasma at atmospheric pressure is the application of an atmospheric dielectric barrier discharge (ADBBD). ADBBDs have proven to be applicable to various purposes; in addition they are also scalable to very large systems. The goal of in this paper described experiments is study of correlation between the reactor input energy/voltage frequency and modification efficiency presented by hydrophilicity changes expressed by means of the area of feathering time evolution (drop test).

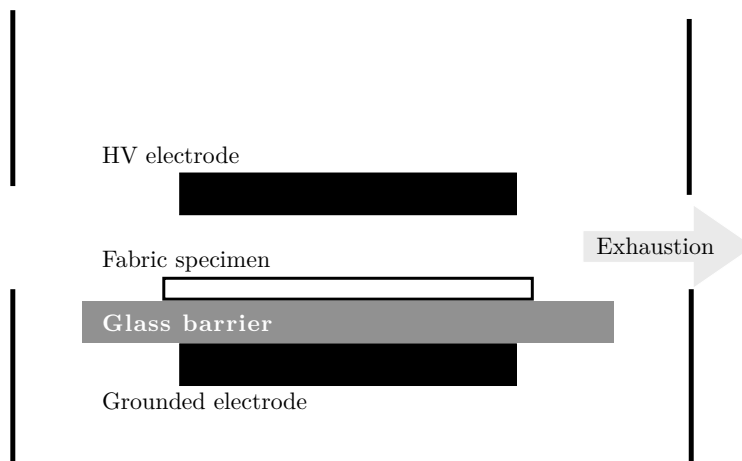


Fig. 1. Cross-section of the reactor

Experimental

For experiments polyester fabric was used. Tested fabric was cut in pieces 100×100 mm (fibre average sectional diameter about $300 \mu\text{m}$, mesh size about $(250 \times 250) \mu\text{m}$, textile thickness about 0.5 mm). Before modification all test samples were properly cleaned. Experimental reactor (Fig. 1) consisted of two plane iron electrodes put into open cylindrical vessel (diameter 153 mm, height 146 mm). Both flat round electrodes were 45 mm in diameter and 10 mm thick. The barrier composed 83×83 mm and 3 mm thick glass table stuck to the higher placed electrode. Distance between electrodes was adjustable and during all

experiments was held at 9 mm. All tests were performed with samples placed on the lower electrode connected to the ground during all experiments.

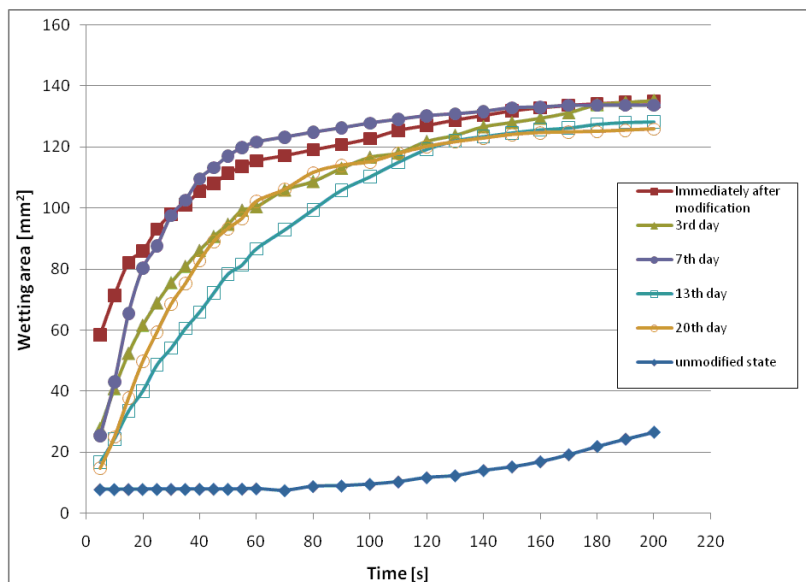


Fig. 2. Hydrophilicity expressed by the area of feathering time evolution, supply voltage 14.7 kV, 50 Hz, modification time 360 s

Hydrophilicity was evaluated by means of the drop test [2]. For better visualization water solution of potassium dichromate ($5 \times 10^{-3} \text{ g } \mu\text{l}^{-1}$) was used as a test liquid. The $20 \mu\text{l}$ of the solution was dropped on the textile sample and the feathering spot size was recorded with a CCD camera. Monitoring was performed in 5 seconds intervals within the first 30 seconds after drop incidence on the fabrics and in 10 seconds intervals afterwards. The total observation time was 200 seconds. The area of the spot in the 60th second after the drop release was used as the standard for the evaluation.

Results and discussion

Tests were carried out in air at room conditions (pressure about 756 torr, temperature about 20°C and humidity about 30%). To held the composition of the atmosphere (air) in reactor constant during the measurements, air from the reactor was continually exhausted with a compressor (air flow speed $0.04 \text{ m}^3 \text{ s}^{-1}$).

ADBD sustained in the filamentary regime: supplied either at [14.7 kV, 50 Hz, modification time 360 s, reactor input energy about 0.5 W] or [7.2 kV,

7 kHz, modification time 8 s, reactor input energy about 40 W]. Supply voltage values were chosen to be maximum permissible values in regard to supply voltage source characteristics and risk of ADBD transition to spark or arc discharge.

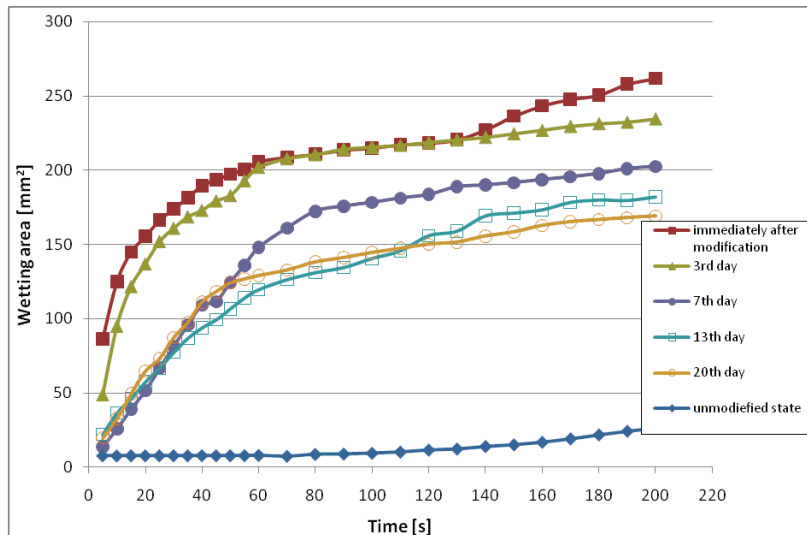


Fig. 3. Hydrophilicity expressed by the area of feathering time evolution, supply voltage 7.2 kV, 7 kHz modification time 8 s

Textile treatment with lower supply voltage frequency (14.7 kV, 50 Hz) resulted in lower modification efficiency (expressed by means of hydrophilicity measurements) and very long treatment times necessary for creation of textile surface changes (Fig. 2). Increase of the supply voltage frequency of about two orders (7.2 kV, 7 kHz) produced reactor input energy increase. It allowed both substantial reduction of the treatment time and more effective modification (Fig. 3).

Aging process of treated fabric surface consists in its hydrophilicity reduction and recovery of its hydrophobicity.

The recovery of hydrophobicity was fastest in the first seven days after treatment in case of 7 kHz supply voltage frequency, when hydrophilicity reduction of individual sheets was about 25 % (Fig. 3). Then it diminished about 40 % and later on remained stable.

There was no distinct aging process development in case of 50 Hz supply voltage frequency (Fig. 2). This result differs slightly from that referred in [3], unfortunately we were not successful in assurance of identical experimental conditions, hence direct comparison is impossible. Modified fibres were stocked in darkness in air at atmospheric pressure and room temperature during aging tests. Duration of modification effect is usually required for a shorter time

period, when some procedures would be performed. Thus there is no need for permanent modification effect and modification effect reduction after some days is considered as admissible.

Conclusion

This paper deals with correlation between the plasma-reactor input energy/voltage frequency and modification efficiency of the polyester textile modification with plasma created in the atmospheric dielectric barrier discharge (ADBD) sustaining in air at atmospheric pressure and ambient temperature and operated in the filamentary mode. Modification process effectivity was tested by means of textile hydrophilicity measurements. For tests two different ADBD supply voltage frequencies were used (50 Hz and 7 kHz).

Increase of the supply voltage frequency of about two orders even with almost 50 % maximum voltage value reduction (7.2 kV, 7 kHz) produced reactor input energy increase. It allowed both substantial reduction of the treatment time and more effective modification.

Modification effect reduction (aging) was fastest in first seven days after modification, then decreased and finally remained stable.

References

- [1] N. DE GEYTER, R. MORENT, C. LEYS, L. GENGEMEBRE, E. PAYEN, S. VLIERBERGHE, E. SCHACHT: *DBD treatment of polyethylene terephthalate: Atmospheric versus medium pressure treatment*. Surface and Coatings Technology, 202 (2008), 3000–3010.
- [2] Y. KLENKO, J. PÍČHAL, L. AUBRECHT: *Atmospheric DBD discharge modification of polyester fabric*. Problems of Atomic Science and Technology, Series Plasma Physics, 12 (2006), 195–197.
- [3] J. PÍČHAL, Y. KLENKO: *ADBD Plasma Surface Treatment of PES Fabric Sheets*. Eur. Phys. J. D, 54 (2009), 271–279.

Received June 26, 2010

Effect of helium plasma immersion ion implantation on plasma-polymerized films

MAURICIO A. ALGATTI¹, ROGÉRIO P. MOTA¹,
REGIANE G. S. BATOCKI¹, DEBORAH C. R. DOS SANTOS¹,
TIAGO J. NICOLETI¹, KONSTANTIN G. KOSTOV¹,
ROBERTO Y. HONDA¹, MILTON E. KAYAMA¹,
PEDRO A. DE P. NASCENTE²

Abstract. This paper presents the effect of helium Plasma Immersion Ion Implantation on surface properties of plasma-polymerized hexamethyldisilazane films. Chemical analysis revealed alterations on atomic composition and molecular structure. These modifications are correlated to refractive index, wettability and etching rate of the samples. Oxygen-containing groups were introduced in the samples and their concentrations are dependent on the process time. The modifications promoted by ion implantation were explained by the increase of crosslinking and unsaturated bond concentration.

Key Words. Plasma-polymerized HMDSN, XPS, wettability, refractive index, etching rate.

1. Introduction

Plasma Immersion Ion Implantation (PIII) is a well established technique in which samples are immersed in a low pressure plasma and are biased by negative high voltage pulses. Positive ions present within the plasma are implanted at normal incidence into all sides of a 3D sample (conformal implantation). The implantation of these energetic ions promotes surface modifications due to changes in materials structure and composition [1], [2]. Because of these features PIII is a widely used technique for improving corrosion resistance of

¹Universidade Estadual Paulista, Faculdade de Engenharia, Departamento de Física e Química, Av. Ariberto Pereira Cunha 333, CEP: 12516-410, Guaratinguetá, SP, Brazil.

²Materials Engineering Department, UFSCar, Rod. Washington Luiz, km 235, São Carlos, CEP 13.565-905, SP - Brazil.

metals and carbon films [3], [4], for increasing biomaterials lifetime [5], [6], for changing surface wettability [7], for increasing the oxidation and abrasion resistance of aerospace devices [8], as well as to improve tribological properties of materials used in many different technological applications [9]. Despite of the broadband applications of PIII there is a lack of studies dealing with the effects of PIII on plasma-polymerized (PP) films. In order to address these issues the present paper reports the study of surface modifications of He PIII on plasma-polymerized hexamethyldisilazane (HMDSN), i.e., $[(\text{CH}_3)_3\text{Si}]_2\text{NH}$, thin films. The choice of this organosilicon compound as a PP precursor is due its low toxicity and the broad band of PP HMDSN applications in many different areas of technology [10], as for instance biocompatible coatings [11], wear-resistant coatings [12], gas barriers [13], gas selective membranes [14], and so on [15].

2. Experimental

Details of the deposition system can be found elsewhere [15]. Briefly, it consists of a stainless-steel cylindrical chamber fitted with two parallel-plate electrodes. The upper electrode is coupled to a radiofrequency (RF) power supply via an impedance matching box, and the grounded lower electrode serves as a substrate holder. PP HMDSN films were deposited by RF discharges excited by a power supply operating at 80 W at 13.56 MHz. The deposition was carried out during 60 min at pressure fixed on 5.3 Pa.

After the deposition, in the same apparatus, films were treated by helium PIII. The discharge was excited by RF power supply operating at 13.56 MHz with the output power of 50 W. The He PIII treatment was carried out at a fixed pressure of 5.3 Pa. During this process, the substrate holder was biased by negative saw-tooth pulses with duration of 5 ms. The amplitude and repetition rate of the pulses were -25 kV and 120 Hz, respectively. The treatment was carried out during 15 min, 30 min, 45 min and 60 min.

In order to evaluate the chemical resistance of PP HMDSN films, PIII treated samples were submitted to etching process in the same system used for deposition and implantation. RF-oxygen plasma was established by a power supply operating at 50 W on 13.56 MHz. Gas pressure was fixed at 5.3 Pa and exposure time was 30 min.

Fourier Transform Infrared (FTIR) spectroscopy was used for the identification of the molecular structure of the samples, using a Perking Elmer FTIR 1600 spectrophotometer from 4000 cm^{-1} to 500 cm^{-1} . X-ray Photoelectron Spectroscopy (XPS) was employed in the investigation of the chemical composition of the film structures, using a Kratos XSAM HS instrument. The spectra were collected using Mg K_α radiation of 1253.6 eV and source power of 30 W. The high-resolution peaks were deconvoluted into their components

using a Gaussian profile, Shirley base and minimum square routine. C 1s peak at 284.8 eV, related to C–C and/or C–H bonds, was taken as bond energy reference.

Film thickness measurements were performed by an Alpha Step 500 Tencor profilometer, and the refractive index was calculated from ultraviolet-visible spectra obtained with a Hitachi U-3501 spectrophotometer.

The wettability of the samples was evaluated by contact angle measurements using a Hamé-Hart 100-00 goniometer. It is known that contact angles (θ) measured between the water drop and the sample surface indicate the hydrophobic ($\theta \geq 90^\circ$) or hydrophilic character ($\theta \leq 90^\circ$) of the samples.

3. Results and discussion

3.1. Molecular and elemental analyses

Fig. 1 depicts IR spectra of PP HMDSN films as a function of PIII treatment time. PP HMDSN film's absorption bands are listed in Table 1.

Table 1. IR absorption bands

Peak position [cm^{-1}]	Band assignment
3400	O–H stretching
3380	N–H stretching
2960	C–H asymmetric stretching in CH_3
2900	C–H symmetric stretching in CH_x ($x = 2, 3$)
2870	C–H symmetric stretching in CH_2
1700–1600	C=C, C=O and N=O stretching
1300	CH_3 asymmetric bending in $\text{Si}-(\text{CH}_3)_x$ ($x = 1, 2, 3$)
1180	N–H bending
1100	CH_2 wagging in $\text{Si}-\text{CH}_2-\text{Si}$
1100–1000	Si–O asymmetric bending in $\text{Si}-\text{O}-\text{Si}$
950	Si–N asymmetric stretching in $\text{Si}-\text{NH}-\text{Si}$
870	Si–H bending
830	CH_3 rocking in $\text{Si}-(\text{CH}_3)_3$
680	Si–H wagging

As it is verified, the main chemical bonds of the as-deposited film are N–H stretching at 3380 cm^{-1} , CH_x stretching at 2960 and 2900 cm^{-1} , CH_3 asymmetric bending in $\text{Si}-(\text{CH}_3)_x$ at 1300 cm^{-1} , CH_2 wagging in $\text{Si}-\text{CH}_2-\text{Si}$ at 1100 cm^{-1} , Si–N asymmetric stretching in $\text{Si}-\text{NH}-\text{Si}$ at 950 cm^{-1} , Si–H bending at 870 cm^{-1} and CH_3 rocking in $\text{Si}-(\text{CH}_3)_3$ at 830 cm^{-1} . The N–H bending located in 1180 cm^{-1} is overlapped by the broad band from 900 to 1300 cm^{-1} .

Besides, Si–O asymmetric bending in Si–O–Si groups (1100 to 1000 cm^{-1}) is present in film's structure because of the post-deposition reactions between free radicals trapped in the structure with oxygen and/or water vapor from the air [9], [10].

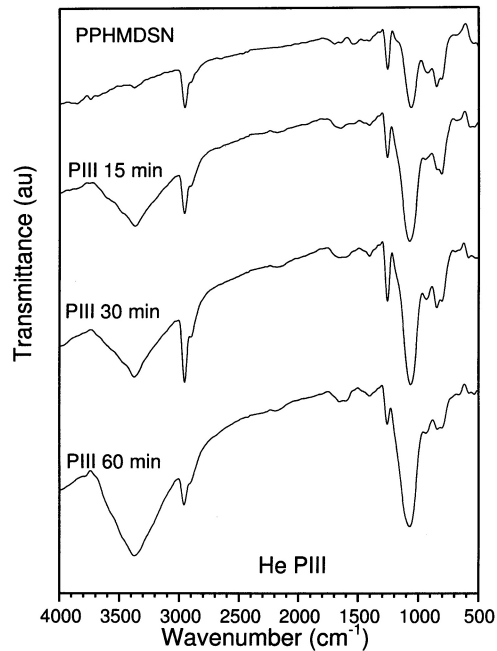


Fig. 1. IR spectra of the PPHMDSN as a function of PIII process time

Spectra of the PP HMDSN modified by helium PIII show practically the same absorption bands as as-deposited film, but their intensities were altered after the treatment. The decrease in CH_3 absorptions at 2960 cm^{-1} and the simultaneous increase in CH_2 absorptions at 1100 cm^{-1} indicates the dehydrogenation of the film structure. The appearance of two new absorption bands located at 3400 cm^{-1} and $1700 \div 1600\text{ cm}^{-1}$ are related to O–H stretching and C=C, C=O and N=O stretching respectively. The increasing of absorption bands associated to O–H stretching and others related to oxygen-containing groups with the increasing of treatment time is attributed to recombination process between free radicals created during the implantation process and atmospheric oxygen [3]. The concentration of oxygen-containing groups is highly dependent on the active free radicals concentration in the film surface, which seems to be dependent on the PIII treatment time. It is known that the collision between an ion and a polymeric material causes electronic excitation or

ionization and displacement of target atoms. Both, electronic and atomic process can result in polymer chain crosslinking and breakage, but the crosslinking predominates in electronic collisions, while the breakage predominates in atomic ones [16]. Chain breakage is pointed as responsible for release of hydrogen atoms and consequently, the creation of dangling bonds. In conclusion, IR analyses confirms hydrogen loss and the recombination of dangling bonds by the appearance of the unsaturated bonds [17], [18]. These changes perceived in all spectra of the modified films are attributed to those simultaneous effects of ion implantation, considering that one of them probably is predominant at a certain process time. It is worth to emphasize that ion implantation promotes surface modifications, and IR analyses were carried out in the film bulk. XPS survey scan revealed the presence of carbon (C), oxygen (O), nitrogen (N) and silicon (Si) in the films. Their atomic concentration is depicted in Fig. 2, as a function of the helium PIII treatment time.

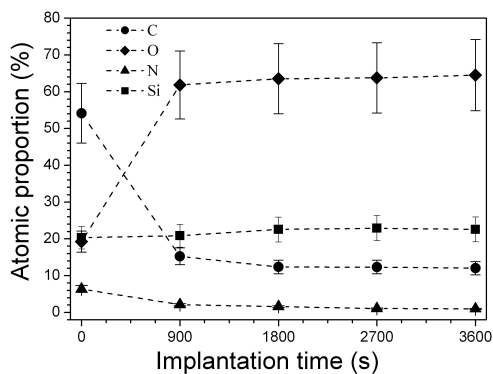


Fig. 2. XPS atomic concentration as a function of PIII process time

As can be seen, O atomic concentration increases from 20% to 60% after the ion implantation, which is interpreted by oxygen incorporation in the film because of free radical recombination. N content is small in the untreated PP HMDSN sample (6%), and it vanished after helium PIII. This is probably due to nitrogen ions that formed volatile chemical compounds which are removed from the plasma by the vacuum pump. Si atomic content is practically constant in all process time, which is confirmed by others authors [19]. Nevertheless, C atomic proportion decreased from 54% to 11% after ion implantation, which may be accounted by polymeric backbone breakage and loss of carbon atoms. It is important to observe that, after 30 min of treatment, C, O and N atomic proportion become constant. Therefore longer time of helium implantation should promote polymeric chain crosslinking. The C 1s high resolution spectra were deconvoluted into three components: the highest peak centered at

284.8 eV related to C–C and/or C–H bonds, a peak at 286.5 eV related to C–O bonds and other peak at 288.5 eV related to C=O bonds.

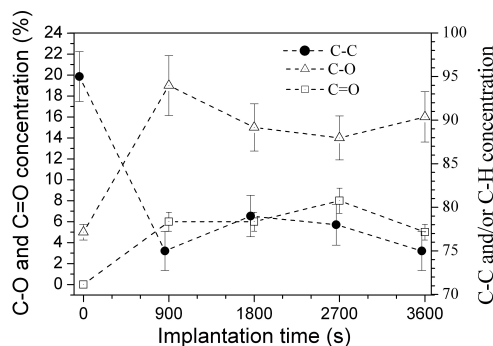


Fig. 3. C–O, C=O and C–C and/or C–H concentration as a function of PIII process time

The deconvoluted peak areas of the functional groups were compared to peak area of C–C and/or C–H bonding and the results are shown in Fig. 3. This figure depicts that untreated film ($t = 0$ s) have no C=O bonds, and these functional groups were introduced after the ion implantation. C=O and C–O concentration rises with increasing of treatment time, while C–C and/or C–H concentration drops. Despite the impossibility of separate identification of C–C and C–H contributions in XPS spectra it is known that C–H bonds were broken after the implantation, as was verified from the IR results. The dehydrogenation of polymeric films with the increasing of He PIII treatment time can be understood by the fact that hydrogen atoms are weakly bonded to the polymeric chain terminations and consequently, they can be easily removed from the solid structure by ionic impact [10].

3.2. Surface properties

Figure 4 shows the thickness measurements of PP HMDSN as-deposited ($t = 0$) and treated by He PIII. As can be seen in this figure, the film thickness decreased from 295 nm to 210 nm after He implantation. This reduction of thickness can be attributed to film's density rise and/or film's sputtering process. The density rise is due to polymeric chains crosslinking processes, and the sputtering occurs by momentum transfer from the ions to the atoms/species at the surface. The results suggest that sputtering process have to be predominant at the beginning of PIII treatment. The subsequent increasing in the number of implanted ions enhances the crosslinking process resulting in film's densification.

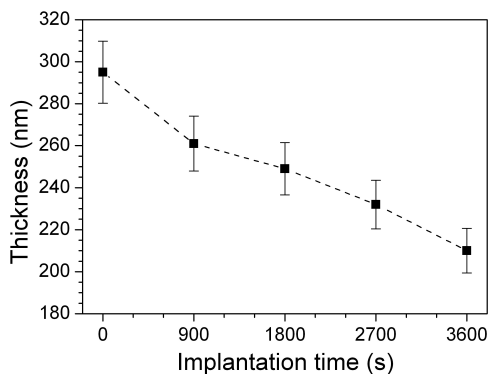


Fig. 4. Thickness of PPHMDSN film as a function of PIII process time

Figure 5 shows the dependence of PP HMDSN film's refractive index on treatment time. The index increased from 1.65 to 1.77 over the considered time range, and this fact is attributed to increase of C=C bond concentration [20]. These bonds were created by recombination of the dangling bonds between carbons belonging to the same chain or recombination between carbon atoms belonging to neighbor chains [16]. Consequently, the rise of refractive index is related to increase of crosslinking and density of the film structure, which is consistent with the thickness decreasing.

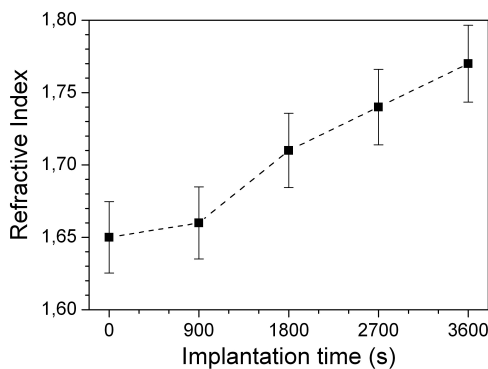


Fig. 5. Refractive index of PPHMDSN film as a function of PIII process time

Figure 6 depicts the contact angle measurements of the PP HMDSN films. The as-deposited PP HMDSN ($t = 0$) presents hydrophobic character with a contact angle around 100° , but this value dropped to 7° immediately after the helium PIII treatment. After 30 days of exposure to atmospheric air the

film's contact angle value stabilized between 45° and 75° according the PIII treatment time. It is known that the stability of a modified surface depends on the chemical structure of the samples, the plasma treatment conditions and the storage environment [10]. These results show that longer treatment time favored the hydrophilic characteristic of polymeric films. This improvement of the wettability of the films is explained by the presence of oxygen-containing groups [7], [9], [18], as verified in the IR and XPS analyses, and improvement of the surface stiffness that avoids molecular rotation that is responsible for polar groups reorientation from surface into the bulk.

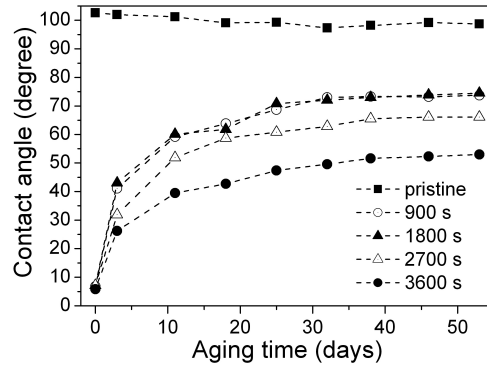


Fig. 6. Aging effect of PPHMDSN contact angle for different PIII process duration

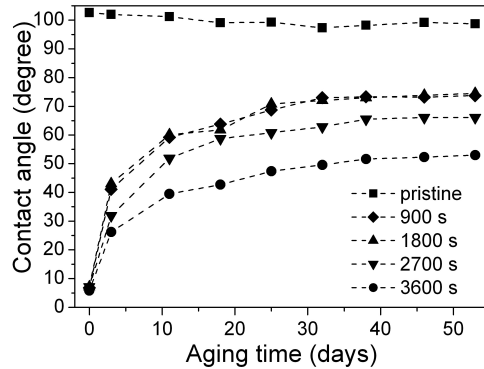


Fig. 7. Etching rate of the PPHMDSN films as a function of PIII process time

Figure 7 depicts the etching rate of the films, which was reduced from 0.55 \AA s^{-1} to 0.32 \AA s^{-1} as the treatment time increased. The etching rate decreasing can be attributed to the increase of polymeric chains crosslinking and to the presence of oxygen atoms in the film structure [21]. Both effects are

responsible for the improvement of the corrosion resistance of He PIII treated PP HMDSN films.

4. Conclusions

Helium PIII promoted surface modifications in the PP HMDSN film. The plasma-polymerized films become hydrophilic, denser and more resistant to etching. Molecular and elemental analyses showed the increment of oxygen-containing groups and unsaturated carbon bonds. These processes are considered to be responsible for film's hydrophilic character. These results show that PIII is a suitable technique for improving surface properties of plasma polymerized films.

Acknowledgements

The authors thank the staff of LAS-INPE (Laboratório Associado de Sensores-Instituto Nacional de Pesquisas Espaciais) for infrared and thickness measurements. FAPESP, CNPq and FUNDUNESP are acknowledged for financial support.

References

- [1] T. BURAKOWSKI, T. WIERZCHON: Surface engineering of metals. CRC Press LLC, Florida 1999.
- [2] M. NASTASI, J. W. MAYER, J. K. HIRVONEN: Ion-solid interactions, fundamentals and applications. Cambridge University Press, Cambridge 1996.
- [3] R. W. Y. POON, J. P. Y. HO, X. Y. LIU, C. Y. CHUNG, P. K. CHU, K. W. K. YEUNG, W. W. LU, K. M. C. CHEUNG: *Improvements of anti-corrosion and mechanical properties of NiTi orthopaedic materials by acetylene, nitrogen and oxygen plasma immersion ion implantation*. Nucl. Instr. and Met. B, 237 (2005), 411–416.
- [4] J. SUI, W. CAI: *Mechanical properties and anti-corrosion behavior of the diamond-like carbon films*. Surface and Coatings Technology, 201 (2006), 1323–1327.
- [5] K. W. K. YEUNG, Y. L. CAHN, K. O. LAM, X. M. LIU, S. L. WU, X. Y. LIU, C. Y. CHUNG, W. W. LU, D. CHAN, K. D. K. LUK, P. K. CHU, K. M. C. CHEUNG: *New plasma surface-treated memory alloys: Towards a new generation of "smart" orthopaedic materials*. Materials Science & Engineering C, 28 (2008), 454–459.
- [6] N. HUANG, P. YANG, Y. X. LENG, J. WANG, H. SUN, J. Y. CHEN, G. J. WAN: *Surface modification of biomaterials by plasma immersion ion implantation*. Surface and Coatings Technology, 186 (2004), 218–226.
- [7] R. K. Y. FU, I. T. L. CHEUNG, Y. F. MEI, C. H. SHEK, G. G. SIU, P. K. CHU, W. M. YANG, Y. X. LENG, Y. X. HUANG, X. B. TIAN, S. Q. YANG: *Surface modification of polymeric materials by plasma immersion ion implantation*. Nuclear Instruments and Methods B, 237 (2005), 417–421.

- [8] I. H. TAN, M. UEDA, R. S. DALLAQUA, J. O. ROSSI, A. F. BELOTO, M. H. TABACNIKS, N. R. DEMARQUETTE, Y. INOUE: *Treatment of polymers by plasma immersion ion implantation for space applications*. Surf. and Coat. Tech., 186 (2004), 234–238.
- [9] A. MATTHEWS, A. LEYLAND, A. WILSON: *Plasma immersion ion implantation as a technique in duplex and hybrid processing*. Vacuum, 68 (2003), 57–64.
- [10] H. BIEDERMAN, Y. OSADA: *Plasma Polymerization Processes*. Elsevier, London 1992.
- [11] C. H. CHEN, M. R. YANG, S. K. WU: *Polymerized hexamethyldisilazane coated on equiatomic TiNi shape memory alloy using DC-pulsed plasma assisted chemical vapor deposition*. Surface and Coatings Technology, 202 (2008), 2709–2714.
- [12] D. PROBST, H. HOCHÉ, Y. ZHOU, R. HAUSER, T. STELZNER, H. SCHEERER, E. BROSEITZ, C. BERGER, R. RIEDEL, H. STAFAST, E. KOKE: *Development of PE-CVD Si/C/N:H films for tribological and corrosive complex-load conditions*. Surface and Coatings Technology, 200 (2005), 355–359.
- [13] G. A. ABBAS, J. A. MACLAUGHLIN, E. H. JONES: *A study of ta-C, a-C:H and Si-a:C:H thin films on polymer substrates as a gas barrier*. Diamond and Related Materials, 13 (2004), 1342–1345.
- [14] P. BANKOVIC, N. R. DEMARQUETTE, M. L. P. DA SILVA: *Obtention of selective membranes for water and hydrophobic liquids by plasma enhanced chemical vapor deposition on porous substrates*. Materials Sci. and Eng. B, 112 (2004), 165–170.
- [15] E. C. RANGEL, P. A. F. SILVA, R. P. MOTA, W. H. SCHREINER, N. C. CRUZ: *Thin polymer films prepared by plasma immersion ion implantation and deposition*. Thin Solid Films, 473 (2005), 259–266.
- [16] H. DONG, T. BELL: *State-of-the-art overview: ion beam surface modification of polymers towards improving tribological properties*. Surface and Coatings Technology, 111 (1999), 29–40.
- [17] E. VASSALO, A. CREMONA, F. GHEZZI, F. DELLERA, L. LAGUARDIA, G. AMBROSONE, U. COSCIA: *Structural and optical properties of amorphous hydrogenated silicon carbonitride films produced by PECVD*. App. Surf. Sci., 252 (2006), 7993–8000.
- [18] A. M. WRÓBEL, M. R. WERTHEIMER, R. D 'AGOSTINO: *Plasma deposition, treatment, and etching of polymers*. Academic Press Inc., San Diego 1990.
- [19] A. KONDYURIN, B. K. GAN, M. M. M. BILEK, K. MIZUNO, D. R. MCKENZIE: *Etching and structural changes of polystyrene films during plasma immersion ion implantation from argon plasma*. Nuclear Instruments and Methods in Physics Research Section, B251 (2006), 413–418.
- [20] E. C. RANGEL, N. C. CRUZ, C. M. LEPIENSKI: *Effect of helium implantation on the properties of plasma polymer films*. Nucl. Instrum. and Met., B191 (2002), 704–707.
- [21] D. C. R. SANTOS, R. C. C. RANGEL, R. P. MOTA, N. C. CRUZ, W. H. SCHREINER, E. C. RANGEL: *Modification of plasma polymer films by ion implantation*. Materials Research, 7 (2004), 493–497.

Effect of shock waves on current-carrying characteristics of HTSC¹

VALERII Y. NIKULIN², LEV I. IVANOV³, GALINA N. MIKHAILOVA⁴, BORIS P. MIKHAILOV³, ALEKSEI V. TROITSKII⁴, LANDYSH K. ANTONOVA³, IRINA V. BOROVITSKAJA³, PAVEL V. GORSHKOV³, ELENA N. PEREGUDOVA², SERGEI V. POKROVSKIJ⁵, IGOR' A. RUDNEV⁵

Abstract. This work presents the results of studying of shock waves effect on properties of composite high temperature superconductor tapes (HTSC). As generator of shock waves the small dense plasma focus installation PF-4 (Lebedev Physical Institute) was used. To realize shock wave action, we used a phenomenon of shock waves generation upon the interaction of a solid state target with high speed cumulative plasma jet generated in plasma focus. The working regime of PF-4 was as follows: the energy stored in the condenser bank is 3.6 kJ; a working gas is argon; pressure of the working gas is 2.5 mbar. This type installation makes possible obtaining of cumulative plasma jets with an ion density of about 10^{18} cm^{-3} . The speed of the plasma jet in the site of the sample location was $1 \div 4 \times 10^7 \text{ cm/s}$. The time of action of the plasma pulse on the sample was about 50 ns. Due to the effect of shock waves significant increasing of the critical current density of composite HTSC tapes was observed. Critical current increasing was about $7 \div 10 \%$ at 77 K, $H = 0$ and about 60 % at strong magnetic fields up to 8 T in commercial sample HTSC tape based on YBCO-123 phase. In case of Bi-2223 tape a critical current enhancement was up to twice at 77 K and $H = 0$ and at high magnetic fields as well that without plasma processing. The reason for such increase in the critical current may be the generation of the additional pinning centers for Abrikosov vortex under the shock wave effect.

¹This research has been supported by the grant of President of the Russian Federation: NSH-3370.2010.2, in part by the Russian Foundation for Basic Research (project nos. 090800430 and 080200759) and by the Grant of the Analytical Departmental Special Program for the “Development of the Scientific Potential of the Higher School” (2.1.1/2479).

²Lebedev Physical Institute of Russian Academy of Sciences, Leninskiy prospekt, 53, 119991, Moscow, Russia

³Baikov Institute of Metallurgy and Material Science of Russian Academy of Sciences, Leninskiy prospekt, 49, 119991 Moscow, Russia

⁴Prokhorov General Physics Institute of Russian Academy of Sciences, Vavilov Str., 38 119991 Moscow, Russia

⁵National Research Nuclear University (MEPhI), Kashirskoe shosse, 31, 115409 Moscow, Russia

Key Words. Composite high temperature superconductor, shock wave, plasma focus, pinning of Abrikosov vortex.

Introduction

This investigation is based on the phenomenon of the formation of point defects vacancies and interstitial atoms (Frenkel pairs) at the front of shock waves upon their passage through metallic and semiconducting materials [1]. In this case, the concentration of the arising vacancies can be several orders greater than the concentration of thermal vacancies present in the investigated material at the selected temperature of the experiment. In 1973, taking into account the effect of the formation of point defects in metallic and semiconducting materials at the front of shock waves, studies were carried out on their action on the temperature of the superconducting transition T_c of niobium based alloys [2], [3]. These studies showed a noticeable effect of the shock waves on T_c . The effect was explained by the acceleration of diffusion processes due to the excess thermodynamically nonequilibrium defects arising upon the passage of shock waves and also by the possible role of arising intrinsic dislocation loops. Subsequently, this approach was confirmed by the formation, upon the passage of shock waves, of an intermetallic compound NbFe at room temperature (under normal conditions, this compound is formed at 2004 °C [4]). These studies give grounds to assume that upon the action of shock waves of large power on HTSC we can also expect substantial changes in the superconducting characteristics both due to the creation of more equilibrium structural and phase states and due to the formation of intrinsic dislocation loops and vacancy pores pinning centers.

In this work, we used, as the samples for the investigation, a commercial tape of HTSC $\text{YBa}_2\text{Cu}_3\text{O}_{7-x}$ produced in the United States.

Experimental

The experiments were performed on the Plasma Focus setup PF-4 (a Tyul'pan complex, FIAN) [5]–[7]. The scheme of the PF-4 setup is shown on Fig. 1. To realize submicrosecond shock wave action, we used the phenomenon of generation of shock waves upon the interaction of a high speed cumulative plasma jet with a solid state target. The working regime was as follows: the energy stored in the condenser storage, 3.6 kJ; working gas, argon; pressure of the working gas, 2.5 mbar. The setup of this type makes it possible to obtain cumulative plasma jets with an ion density of about 10^{18} cm^{-3} . The picture of cumulative plasma jet is shown on Fig. 2. The speed of the plasma jet in the site of the location of the samples was $(1 \div 4) \times 10^7 \text{ cm/s}$. The time of action

of the plasma pulse on the sample was ~ 50 ns. The energy flux of the plasma pulse on the target was from 10^8 to 10^{10} W/cm². The cumulative plasma jet was directed into the unit with the sample, which was a demountable aluminum cuvette with a window in the wall faced to the jet. To eliminate the thermal action of the plasma jet, there was established a protective molybdenum plate. For the uniform transfer of the impact action on the sample plane throughout the entire area of the contact, a vacuum epoxy resin was used, which filled the gap between the molybdenum plate and the sample.

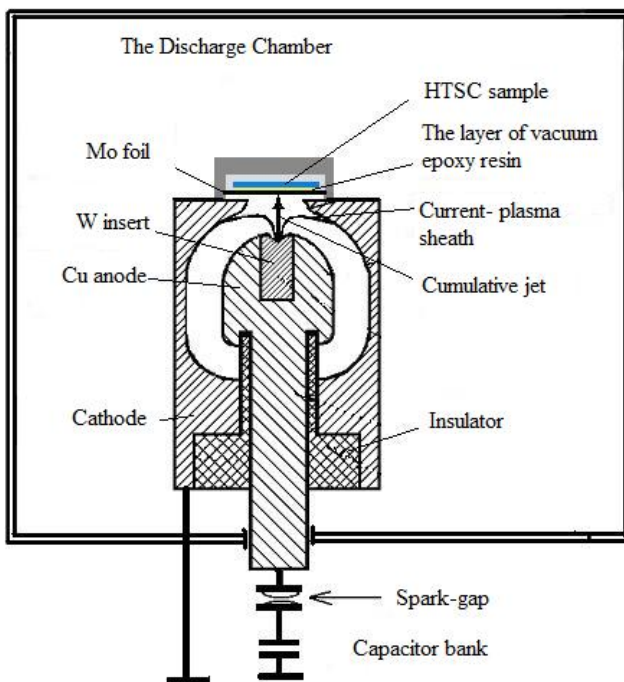


Fig. 1. The scheme of PF-4 setup

The samples were rectilinear pieces of a hermetic composite superconductor in the form of a tape with dimensions of $0.1 \times 4 \times 30$ mm³ (SuperPower Inc., United States) with critical parameters $J_c = 2 \times 10^6$ A/cm² (at $T = 77$ K) and $T_c = 92$ K. The Y-123 tape represents a film of $\text{YBa}_2\text{Cu}_3\text{O}_{7-x}$ on the substrate made of the Hastelloy alloy C276 (Ni–Cr–Mo–Fe–W) with several buffer layers. On the top, the film of the superconductor is covered with a layer of silver 2 μm thick. For the protection from mechanical damage, the hermetization, and the stabilization of the superconductor, the Y-123 tape is covered with a copper layer 20 μm thick [8].

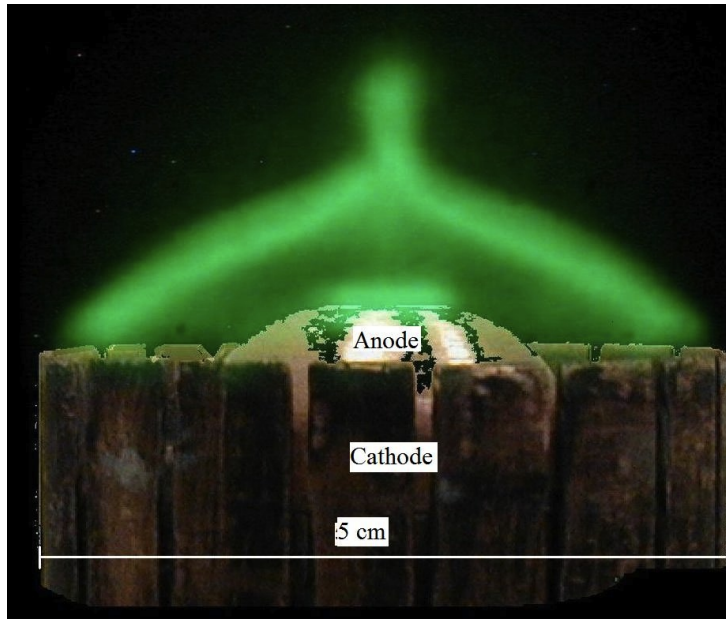


Fig. 2. The cumulative jet in PF-4. The picture was received by MCP convertor with the exposure time 3 ns

Results

The critical current before and after the action of the cumulative plasma jet was determined by the four probe method from the voltage–current characteristics given in Fig. 3. A noticeable increase in the value of the critical current was obtained; J_c increased from 95 to 100 A ($T = 77$ K, $H = 0$).

For investigation of the spatial distribution of the critical current in the HTSC tape after the action of shock waves, the method of scanning Hall magnetometry was employed. The method is based on the fact that the Hall pickup fixes directly the value of the local magnetic field near the surface of the HTSC sample preliminarily magnetized in an external magnetic field. By moving the Hall pickup in two directions, scanning and recording of the magnetic flux over the entire surface is performed. From the thus obtained data, with the aid of the numerical solution of the problem of the inversion of the Biot–Savart law within the Bean model, we can determine the critical current at different points of the sample [9], [10] investigated.

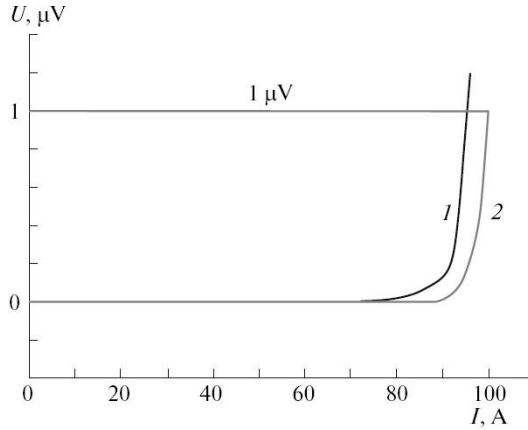


Fig. 3. Current–voltage characteristics of an HTSC tape before and after the action of a cumulative plasma jet ($T = 77\text{ K}$, $H = 0$): (1) initial sample and (2) a sample subjected to the action of a cumulative plasma jet

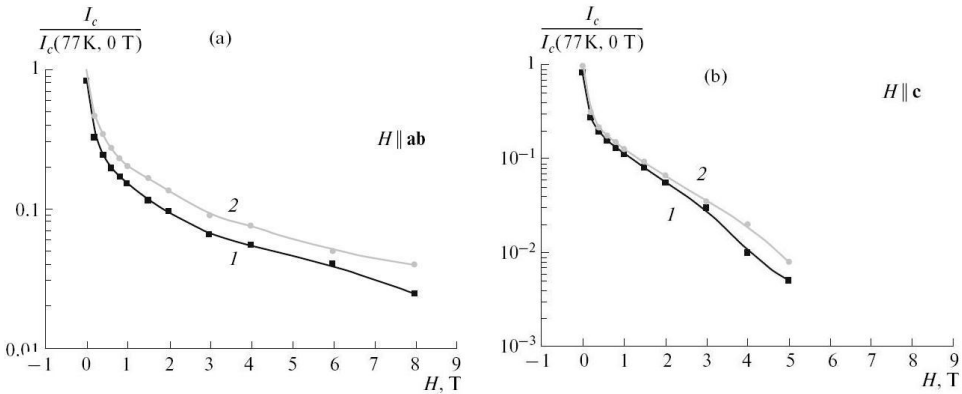


Fig. 4. The dependences of the critical current on the external magnetic field; in the field $H = 8\text{ T}$, an increase in the critical current is approximately 60% in the geometry with $\mathbf{H} \parallel \mathbf{ab}$; the plane \mathbf{ab} of the sample is parallel to the plane of the substrate

The basis of the experimental unit is a semiconductor Hall pickup placed on a two coordinate manipulator. In this work, a Hall transducer with the following characteristics was used: the size of the transducer, $2 \times 1.5 \times 0.6\text{ mm}^3$; the size of the gage zone of the pickup, $0.45 \times 0.15\text{ mm}^2$; the magnetic sensitivity, $64\text{ }\mu\text{V/mT}$. With the aid of the scanning Hall magnetometry, we built the surfaces of the distribution of the captured magnetic field and critical current, which demonstrate an improvement in the current carrying capacity after the

action of the shock wave. For the initial and experimental samples, we measured the dependences of the critical current on the external magnetic field up to 8 T for two orientations of the magnetic field: $\mathbf{H} \parallel \mathbf{ab}$ (Fig. 4a) and $\mathbf{H} \parallel \mathbf{c}$ (Fig. 4b). The plane \mathbf{ab} of the sample is parallel to the plane of the substrate; the axis \mathbf{c} of the sample is perpendicular to the plane \mathbf{ab} . For each orientation, the value of the critical current after the action of the shock wave proved to be greater than in the initial sample. In particular, in the field of 8 T for $\mathbf{H} \parallel \mathbf{ab}$ the increase in the current is approximately 60%.

Conclusions

Thus, it has been established that the action of a pulse of shock wave generated by a high speed cumulative plasma jet can lead to an increase in the critical current of an HTSC tape even in strong magnetic fields up to 8 T. It is assumed that the reason for the increase in the critical current is the generation of pinning centers under the effect of the shock wave.

References

- [1] Z. I. MEZOKH, V. A. YANUSHKEVICH, L. I. IVANOV: *Formation of point defects in Ni under the effect of giant laser pulses*. Fiz. Khim Obrab. Mater., 4 (1971), 163–165.
- [2] I. YA. DEKHTYAR, L. I. IVANOV, N. V. KARLOV, G. P. KUZ'MIN, M. M. NISCHENKO, A. M. PROKHOROV, N. N. RYKALIN, V. A. YANUSHKEVICH: *Effect of laser radiation on the temperature of the superconducting transition of an Nb–Sn alloy*. Pis'ma Zh. Eksp. Teor. Fiz., 18 (4) (1973), 154–156.
- [3] I. YA. DEKHTYAR, L. I. IVANOV, N. V. KARLOV, G. P. KUZ'MIN, M. M. NISCHENKO, A. M. PROKHOROV, N. N. RYKALIN, V. A. YANUSHKEVICH: *Influence of laser irradiation of niobium–base superconducting materials on the nature of changes in the critical temperature*. Kvant. Elektron., 3 (4) (1976), 844–847.
- [4] I. YA. DEKHTYAR, L. I. IVANOV, N. V. KARLOV, YU. N. NIKIFOROV, M. M. NISCHENKO, A. M. PROKHOROV, V. A. YAKUSHKEVICH: *Formation of intermetallic compounds in a Ni–Fe system due to the action of a shock wave produced by laser irradiation*. JETP Letters, 33 (2) (1981), 120–123.
- [5] A. V. OGINOV, V. YA. NIKULIN, A. A. TIKHOMIROV, S. P. ELISEEV: *Laser, X-ray and optical diagnostics on the “Tyulpan” installation*. Czech. J. Phys. B, 56 (2006), 315–323.
- [6] S. P. ELISEEV, V. YA. NIKULIN, A. V. OGINOV, A. A. TIKHOMIROV: *Plasma diagnostics in the optical and X-ray regions on the plasma focus device PF-4 (installation TYULPAN)*. Probl. Atom. Sci. Technol. Ser. Plasma Phys., 12 (6) (2006), 147–149.
- [7] L. I. IVANOV, A. I. DEDYURIN, I. V. BOROVITSKAYA, O. N. KROKHIN, V. Y. NIKULIN, E. N. PEREGUDOVA, A. V. OGINOV, A. A. TIKHOMIROV: *Application of high velocity streams of dense plasma for the creating of high adhesive compounds of chemically noninteracting metals*. Eur. Phys. J D, 54 (2009), 149–152.

- [8] www.superpowerinc.com, Official site of the SuperPower Inc. Co., April 21, 2011.
- [9] A. I. PODLIVAEV, I. A. RUDNEV, S. V. POKROVSKII: *Restoration of distribution of two-dimensional current in superconducting tape along its magnetic field measured with the use of Hall transformers*. Inzh. Fiz., 5 (2007), 18–25.
- [10] S. V. POKROVSKII, I. A. RUDNEV, A. I. PODLIVAEV: *A two-dimensional current mapping in superconducting tapes*. J. Phys. Conf. Ser., 150 (2009), 052211.

Received May 19, 2010

Chemical and structural characterization of fluorinated hydrogenated amorphous carbon films¹

NAZIR M. S. MARINS², ROGÉRIO P. MOTA²,
ROBERTO Y. HONDA², MILTON E. KAYAMA²,
KONSTANTIN G. KOSTOV², MAURICIO A. ALGATTI²,
PEDRO A. P. NASCENTE³, ELIDIANE C. RANGEL⁴

Abstract. Thin films of fluorinated hydrogenated amorphous carbon (a-C:H:F) were synthesized by radiofrequency plasma enhanced chemical vapor deposition on glass and silicon substrates using acetylene, argon, and sulfur hexafluoride mixtures as precursors. The radiofrequency signal was applied to the lower electrode whereas the upper one was grounded. The deposition time was 5 minutes at a pressure of 9.5 Pa and the power varied from 5 to 125 W. Raman spectroscopy and X-ray photoelectron spectroscopy were employed to investigate the molecular structures and chemical compositions of the a-C:H:F films. The Raman spectra indicated that the films had polymer-like structure, for lower power (5 to 25 W), graphitic structure, for intermediate power (50 to 75 W), and higher sp³ hybridization, for higher power (100 and 125 W). The XPS analysis showed the presence of C–C, C–H, C–O, C–CF, C=O, and C–F chemical bonds. The thicknesses of the films were between 55 and 32 nm for RF power varying from 5 to 125 W. The wettability of films revealed that a-C:H:F ones deposited at different conditions were essentially hydrophilic.

Key Words. Fluorinated diamond-like carbon films, sulfur hexafluoride, PECVD, a-C:H:F.

¹The authors would like to thank FAPESP, CNPq, and CAPES for financial support, and José B. Galhardo, for technical assistance during the plasma chamber construction.

²UNESP – Faculty of Engineering of Guaratinguetá, Av. Ariberto Pereira da Cunha, 333, Pedregulho, CEP 12516-410, Guaratinguetá, SP, Brazil

³Federal University of São Carlos, Department of Materials Engineering, Rod. Washington Luiz, km 235, CEP 13565-905 São Carlos, SP, Brazil

⁴UNESP – Experimental Campus of Sorocaba, Av. Três de Março, 511, CEP 18087-180, Sorocaba, SP, Brazil

1. Introduction

Fluorinated hydrogenated amorphous carbon films have attracted considerable interest for practical applications due to a combination of properties such as low surface energy [1], biocompatibility [2], and low friction coefficient [3]. Usually the fluorinated films are obtained using a plasma formed by a mixture of organic compounds such as C_2H_2 and CF_4 , CH_4 and CF_4 [4], or *n*-carbon fluoride and hydrogen. In this work, we have employed a mixture of acetylene, argon, and sulfur hexafluoride in the production of fluorinated films, and have investigated their chemical compositions, structures, and wettabilities.

The fluorination treatment causes changes in the properties of the a-C:H films, such as reduction in the density, variation in the thickness [4]–[6], reduction in the internal stress [7], alteration in the friction coefficient [6], [8], increase in the hydrophobicity [8], [9], decrease in the surface energy [10], and even anti-adherence of bacteria [9]. Sulfur hexafluoride (SF_6) is an inorganic gas whose molecule is formed by one sulfur atom surrounded by six fluoride atoms. It is used mainly in the electrical industry as a dielectric medium and electric arcing suppressor, both in switchgears and screened substation. It has high electronegativity, is chemically inert, and represents less than 1% in the global warming. Thus, the use of SF_6 is viable both economically and environmentally.

Diamond is a material that presents well known properties. In a-C:H films they depend on the quantity of the sp^3 , sp^2 , and sp^1 hybridizations and on the amount of hydrogen on them [11], [12]. These properties vary between the properties of diamond, graphite, and polymers. For instance, the a-C:H mechanical and tribological properties depend on the atomic structure of the material [13].

The fluorination mechanism in the a-C:H films promote the substitution of hydrogen atoms by fluorine atoms in the structural network of this material [14]. This phenomenon was observed by Raman spectroscopy and XPS analyses performed on fluorinated a-C:H films; it was observed an increase in the C–F peak intensity and a decrease in the C–H peak intensity in the spectra [15]. In terms of the deposition process, the hydrogen released from the a-C:H film structural network affected by the high sputtering process, due to the fact that the C–H bond is weaker than the C–F one [16]; however, it is possible that the fluorine atoms are also released if they are weakly bound [17]. The replacement of hydrogen by fluorine in the molecular structure of the a-C:H films causes an increase in the coordination defect amount, due to the fact that the atomic diameter of fluorine is larger than that of hydrogen, and also an increase in the gap, due to the fact that the C–F binding energy (5.4 eV) is larger than the C–C one (3.6 eV) [1], [18].

The incorporation of fluorine in the a-C:H films modifies their chemical bound structure strongly. There are studies reporting that if the amount of

fluorine is higher than 10 at% in the composition of a-C:H films, their D band will become more intense and wider. This increase in the intensity of the D band is due to the formation of aromatic clusters by sp^2 hybridizations [4]. Thus the a-C:H film becomes more graphitic with the presence of high amounts of fluorine in its chemical composition. If the amount of fluorine is higher than 25 %, the luminescent band intensity will increase, associated to a transition between the diamond to a polymeric type structure [19]. The widening of the D band corresponds to changes in the length and angle of the C-C bounds in the hexagonal rings which compress the cluster [20].

The structural network of the fluorinated a-C:H films is formed by ring structures of C-C, C-H, and C-F bounds connected to the C-F₂ group and terminated by the C-F₃ group in a matrix of sp^3 hybridizations [21]. Besides these bounds, it also can occur terminations with the C-F₂ (F₂C=C) group if the fluorine atoms are bound to the olefinic structures of carbon [22]. There are reports in the literature informing that the fluorine atoms have a stronger tendency to bind to sp^3 hybridization instead of sp^2 one [14], [23].

The wettability of the films was analyzed by contact angle measurements using the static drop method [24], which consists to put the sample in contact to a small deionized water volume that forms a drop on the surface.

2. Experimental

The system employed for the deposition of a C:H:F films constitutes of a cylindrical glass reactor, with a diameter of 19 cm and a height of 15 cm, which has circular, plane, and parallel internal electrodes made of stainless steel, with a diameter of 6 cm and spaced by 2 cm.

The a-C:H:F films were deposited using a gas mixture of 30 % acetylene, 65 % argon, and 5 % SF₆, in a total pressure of 9.5 Pa; the radiofrequency (RF) power was varied from 5 to 125 W resulting in a power density from 0.09 W/cm³ to 2.21 W/cm³, and the deposition time was 600 seconds. A 13.56 MHz RF signal was applied to the lower electrode, while the upper one was grounded. The films were deposited onto glass and silicon substrates.

The molecular structures of the films were investigated by Raman spectroscopy using a Renishaw S2000 spectrophotometer with an argon laser operating with a wavelength of 514.5 nm. The spectra ranged between 400 and 2200 cm⁻¹. The spectra were deconvoluted in two bands, D and G, by Gaussian curves. The quantification of the hybridizations of these bands was done by the ratio between the D band intensity and the G band intensity (ID/IG ratio).

The films chemical compositions were analysis by X-ray photoelectron spectroscopy (XPS) performed with a Kratos XSAM HS spectrometer, using non-monochromatized Mg K α radiation (1253.6 eV). The binding energies for all

spectra were determined with respect to the C 1s reference signal (C–H or C–C bands) at 284.8 eV. The Shirley background and Gaussian functions were used for fitting the peaks [25].

The wettability of the samples was analyzed by contact angle measurements using a Ramé-Hart F-300 goniometer. The thicknesses of the films were measured in a Tencor Alpha-Step 500 profilometer.

3. Results and discussion

Figure 1 displays the Raman spectra for the films deposited by PECVD using a gas mixture of 30 % acetylene, 65 % argon, and 5 % SF₆, and power ranging from 5 to 125 W. It can be observed increases in the bandwidth and intensity of the bands with the increase of deposition power, for values higher than 25 W. For the films deposited at 5 and 25 W, it was observed luminescence signals in the spectra, which is an indicative of the polymeric nature of the films [7], [26].

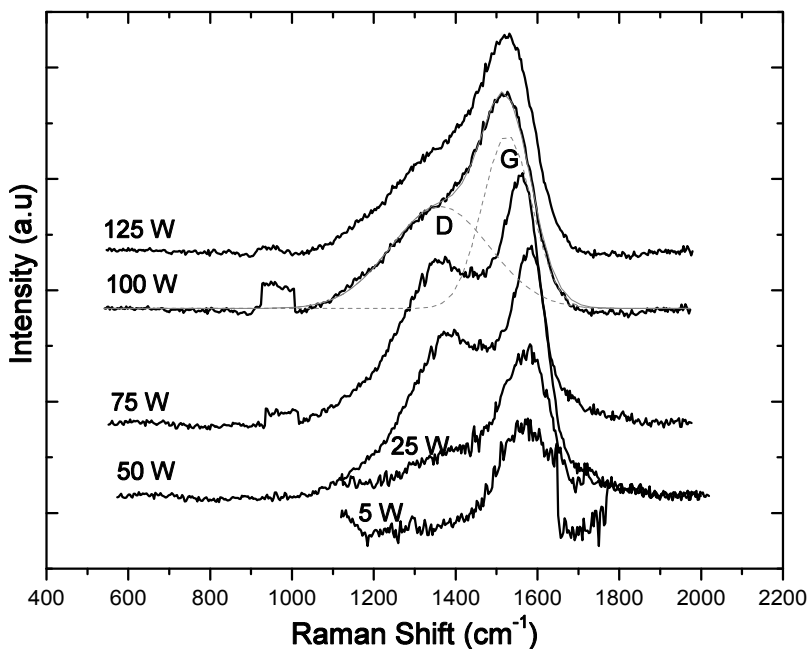


Fig. 1. Raman scattering spectra of the films deposited at different power values

The evaluation of sp² and sp³ contributions in these bands was done by fitting the spectra by two Gaussian curves, after removing the luminescence contribution, using the method proposed by Robertson [13]. The two peaks

are centered at 1360 and 1540 cm^{-1} , characteristic of the D and G bands, respectively. It can be noticed that the G band center (ω_G) shifts towards higher wavenumbers with the increase in power between 5 and 50 W , enhancing the amount of sp^2 hybridizations, and it shifts towards smaller wavenumbers for higher power values (75 , 100 , and 125 W), due to a decrease in the disordered bounds having sp^3 hybridizations. The changes in position, bandwidth, and ID/IG ratios of the bands with the deposition power are shown in Fig. 2.

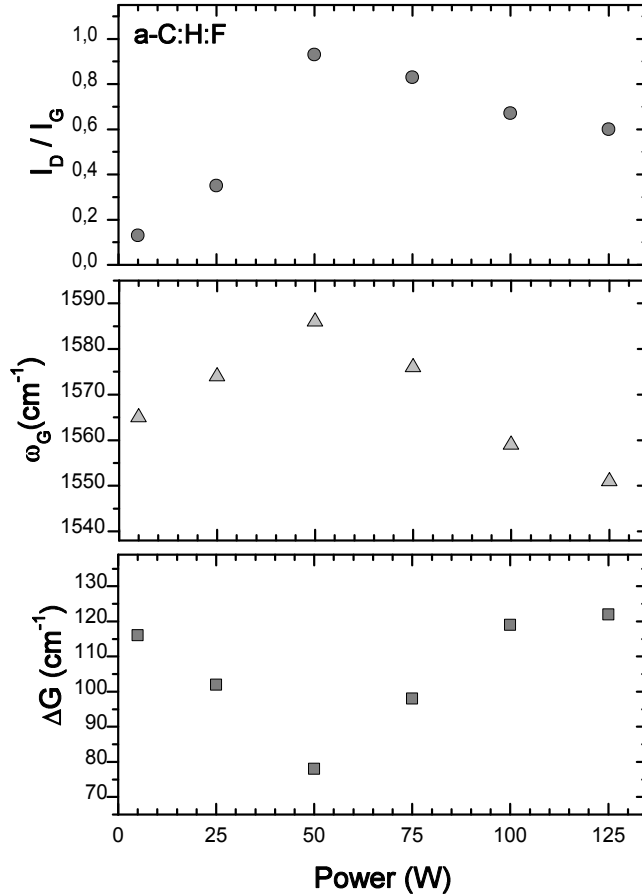


Fig. 2. ID/IG ratios, central positions (ω_G), and G bandwidths (ΔG) of the films deposited at different power values; the resulting power density varied from 0.09 W/cm^3 (5 W) to 2.21 W/cm^3 (125 W)

It can be seen in Fig. 2 that the intensity ratios between the D and G bands (ID/IG ratios) increase with the augment of power for 25 and 50 W , and decrease for higher power values. This indicates a decrease in the sizes of the graphitic centers for the films deposited at power values higher than 50 W .

The G band central position shifts from 1565 to 1585 cm^{-1} for power values between 5 and 50 W, indicating a decrease in the amount of sp^3 hybridizations for this power interval.

The G bandwidth (ΔG) decreases in the power interval between 5 and 50 W, and increases for higher power values. The smallest ΔG value was observed for the film prepared at the plasma of 50 W, indicating a smaller proportion of sp^3 sites compared to the other films. It should be pointed out that for all analyzed parameters, the same tendency of increase and decrease was observed, with the inversion occurring at 50 W.

The implantation model states the formation of sp^3 groups in the structure is favorable under specific conditions of ion bombardment i.e. the energies of the ions that collide with the growing layer. These energies should be high enough for shifting the sp^2 centers, but not promoting fragmentation in the sp^3 centers. The results indicate that the process is more favorable for power values in the range of 75 to 125 W.

From these results it can be inferred that the produced samples are fluorinated hydrogenated amorphous carbon films of different categories. When deposited at a low power plasma (5 and 25 W), the films present polymeric character. For an intermediate power value (50 W), the proportion of sp^2 groups increases, causing the film to be graphitic like [27]. Finally, the films can be classified as amorphous carbon with higher amount of tridimensional bounds when they are deposited in plasma from 75 to 125 W.

Figure 3 shows the behavior of the proportions of C–C and/or C–H (284.8 eV), C–O and/or C–CF (286.5 eV), and C=O and/or C–F (288.5 eV) bounds resulted from the fitting of the C 1s peaks obtained by XPS [28]–[30]. The appearance of carbon atoms bounded to fluorine atoms is due to the removal of hydrogen atoms from C–H groups by means of two different mechanisms. First, the high chemical affinity between hydrogen and fluorine leads to the emission of the bound hydrogen, producing carbon radicals. The fluorine atoms present in the plasma promptly react, satisfying the dangling bounds. Second, the impact of rapid ions gives energy to the structure, causing the emission of hydrogen from C–H groups whose binding energies are weaker than the C–C and C–O binding energies. This process also allows the fluorine atoms to replace a considerable amount of hydrogen atoms during the deposition of the films [26], [31], [32].

Figure 3 also shows that the films have dominant C–C and/or C–H bounds. It can be observed a decrease in the ratio of these bounds with the increase in power up to 50 W, and an increase for higher power values. It is observed for the proportion of C–O and/or C–CF groups an initial increase tendency, with a maximum for 50 W, followed by a decrease for higher power values, indicating that most part of hydrogen was replaced by fluorine and/or oxygen. For all analyzed samples it was detected the presence of C=O and/or C–F bounds,

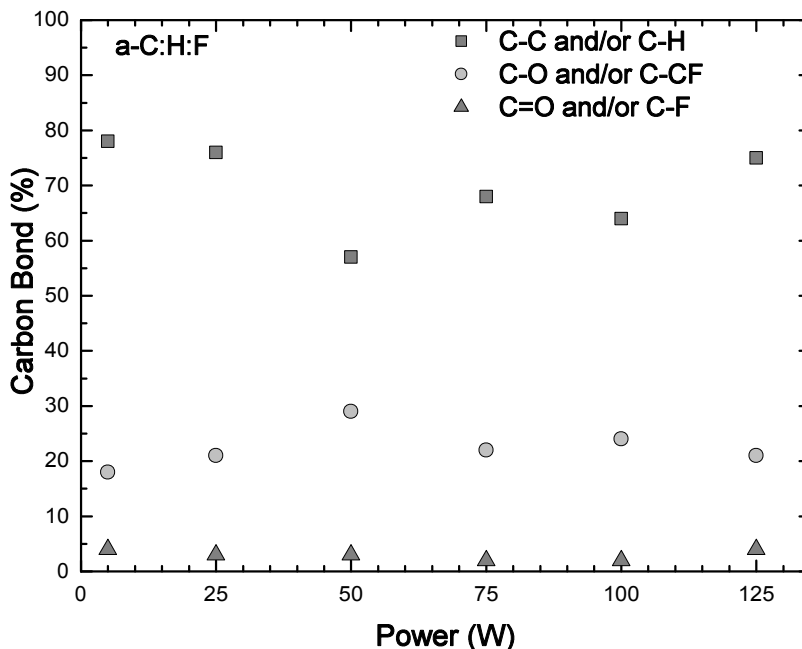


Fig. 3. Proportion of the species present in the a-C:H:F films as a function of the RF deposition power, according to the fitting of the C 1s peak obtained by XPS; the resulting power density varied from 0.09 W/cm^3 (5 W) to 2.21 W/cm^3 (125 W)

in smaller proportions than the C–O and/or C–CF groups, and practically constant with power.

High resolution F 1s spectra obtained by XPS, were fitted to four binding energy components (684.9, 687.4, 688.4, and 689.6 eV). According to Ferrara et al. [33], the lowest value is associated to S–F bounds originated from the fragmentation of SF_6 , and the components at 687.4, 688.4, and 689.6 eV can be attributed to $(-\text{CHFCH}_2-)_n$, $(-\text{CF}_2\text{CH}_2-)_n$, and $(-\text{CF}_2\text{CF}_2-)_n$ groups.

Figure 4 shows the behavior of the proportions of these bounds as function of the power. For the films deposited at 5 and 25 W, fluorine appears bound to carbon and to hydrogen. It was detected fluorine bounded to sulfur in the film prepared at 100 W. For the other films, prevails $(-\text{CHFCH}_2-)_n$ group. The changes in the fluorine amounts in the different functional groups can be attributed to the reactive plasma which contains SF_6 . Several reactions involving free electrons, molecular fragments, and ions having several masses, with different kinetic energies, occur with species provenient from the acetylene. From these reactions, complex structures can be formed, where fluorine atoms replace hydrogen atoms in different proportions in the chains. Different

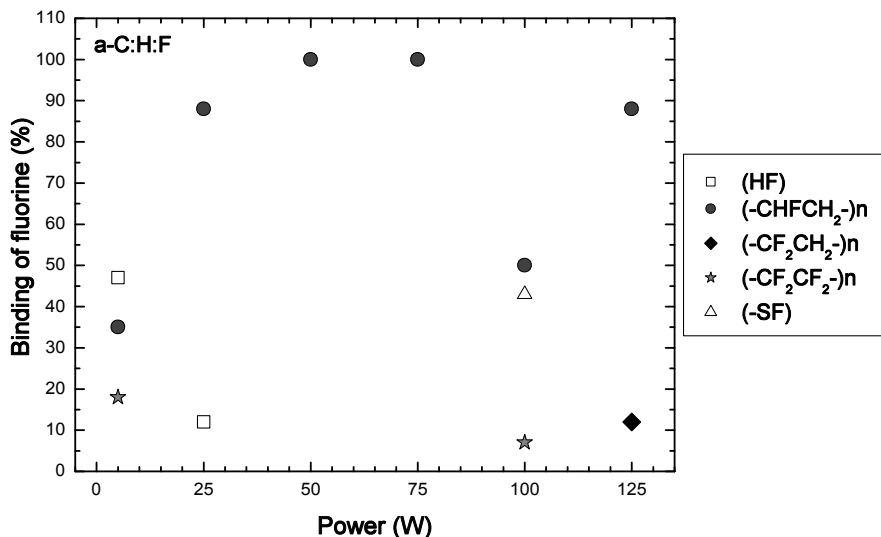


Fig. 4. Proportion of fluorine present in the a-C:H:F films as a function of the deposition power; the resulting power density varied from 0.09 W/cm^3 (5 W) to 2.21 W/cm^3 (125 W)

concentrations of species from the same family can be statistically found at the surface since the plasma is out of the thermodynamic equilibrium.

The atomic concentrations of carbon [C], oxygen [O], fluorine [F], sulfur [S], and silicon [Si] as a function of the deposition power are shown in Fig. 5. Silicon was detected from the substrate. The films are influenced by the recombination of free radicals during the deposition. The residual oxygen and/or water molecules adsorbed on the internal walls of the reactor could also participate. Not all free radicals recombine during the deposition process [34]. Atmospheric oxygen and nitrogen can also be incorporated into the films when they are removed from the reactor.

There is an increase in the atomic concentration of carbon in the films for higher deposition power. The atomic concentration of oxygen follows the inverse tendency low quantity of oxygen was detected for the films prepared at higher power values. Although the degree of ion bombardment enhances for higher power, the proportion of dangling bounds, do not increase proportionally. This tendency is explained by the fact that the energy transferred by the ionic collisions is employed to shift sp^2 hybridization centers, favoring the prevalence of the sp^3 centers which are more stable to the bombardment. Thus,

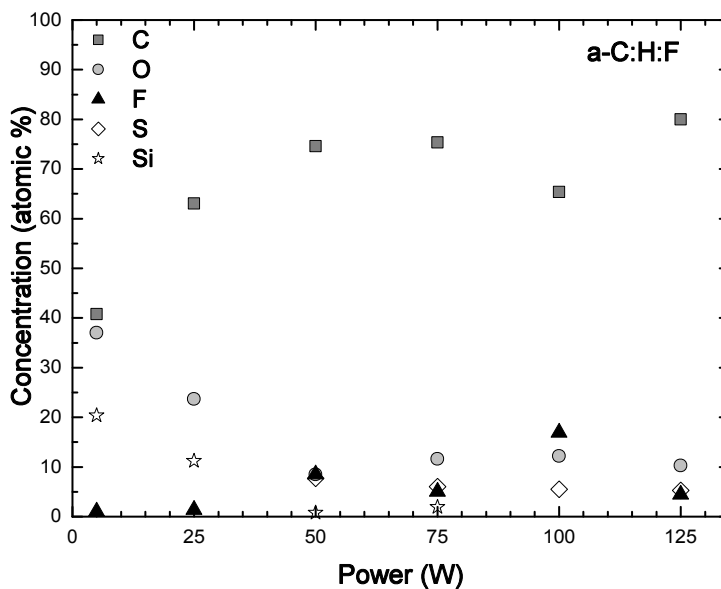


Fig. 5. Relative atomic concentrations of carbon, oxygen, fluorine, sulfur, and silicon in the a-C:H:F films; the resulting power density varied from 0.09 W/cm^3 (5 W) to 2.21 W/cm^3 (125 W)

the proportion of free radicals and, consequently, the amount of oxygen in the film diminish while the proportion of sp^3 sites increases.

The atomic concentration of fluorine in the films remains relatively low, compared to the atomic concentration of carbon, for the entire power interval. One of the reasons for this is the low amount of SF_6 relative to C_2H_2 in the gas mixture. Another reason is the competition among deposition and ablation by the etching of the fluorine atoms. The low concentration of sulfur (less than 10%) detected in the films deposited between 50 and 125 W is related to the low affinity of this species with the others, present in the plasma during the deposition process.

Figure 6 shows the contact angle values as a function of the deposition power. It can be observed that the contact angle did not change too. Thus, the incorporation of fluorine, which was evidenced by XPS, did not occur in a proportion high enough to produce a hydrophobic surface. This effect could be due to fluorinated groups which when singly incorporated in the structure would cause moderate electrostatic forces that would attract the water dipoles. Another possibility would be the constant loss of fluorinated groups from the surface, by the release of these species or by the rotation of the carbonic chain where such groups were bound.

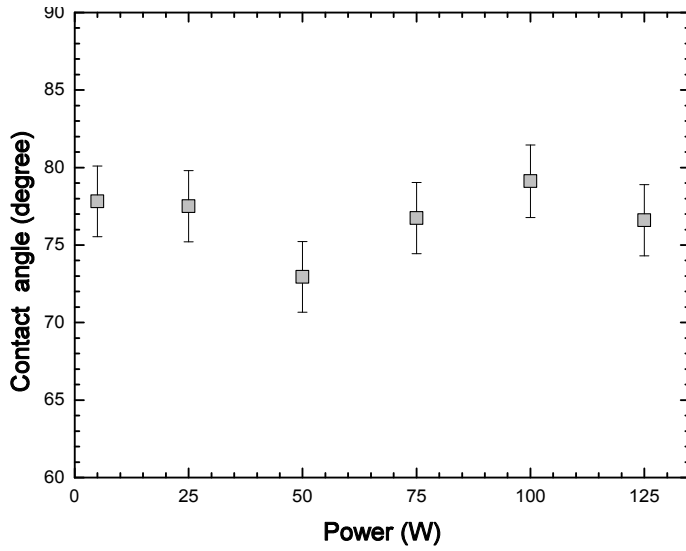


Fig. 6. Contact angle values for the a-C:H:F films as a function of the deposition power. The resulting power density varied from 0.09 W/cm^3 (5 W) to 2.21 W/cm^3 (125 W).

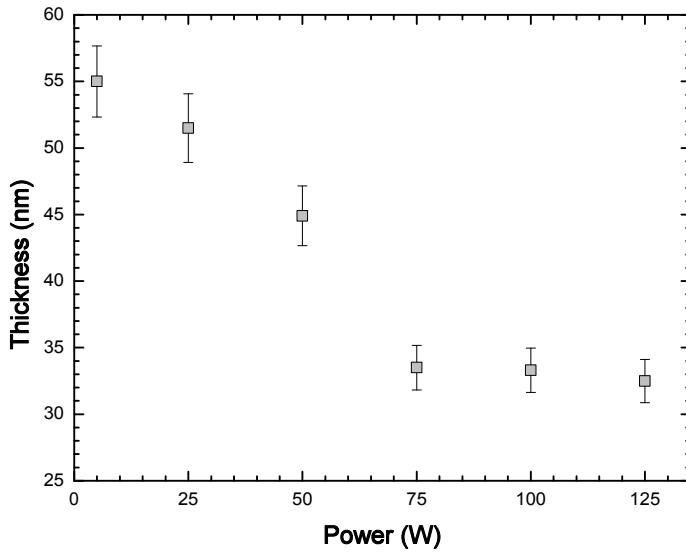


Fig. 7. Thickness of the a-C:H:F films as a function of the deposition power. The resulting power density varied from 0.09 W/cm^3 (5 W) to 2.21 W/cm^3 (125 W).

Figure 7 shows the behavior of the thickness of the films as a function of the deposition power. It can be observed that the thicknesses are very small, and they decrease with the increase of the power. This finding might be attributed to a change in the plasma kinetics, with the increase of the power, the concentration of fluorine ions also increases, due to the intense fragmentation of SF₆. Since these species are highly reactive, there is an increase in the ablation by chemical effects and by heating the substrate, reducing the film growth rate. Similar reduction in the thicknesses of the a-C:H:F films has been reported in the literature [4], [31], [35].

4. Conclusions

This work has shown that the power employed in the deposition of the a-C:H:F films was preponderant to define their molecular structures and chemical compositions. For power values of 5 and 25 W, the materials presented polymeric structures. At 50 W, they presented a graphitic characteristic and in the range 75 to 125 W, the films presented higher proportions of carbon having sp³ hybridizations. The chemical composition of the samples had a predominance of C–C and/or C–H bounds, besides C–O and/or C–CF, and C=O and/or C–F bounds. This reduction in the thickness of the films was due to ablation effects associated mainly to thermal heating during the deposition and etching by SF₆ plasma. In the investigated power range, the surface of the films presented hydrophilic characteristics.

References

- [1] H. YASUDA: Plasma polymerization. Academic Press, New York 1985.
- [2] B. D. RATNER, A. CHILKOTI, G. P. LOPEZ: Plasma deposition, treatment, and etching of polymers. Academic Press, New York 1990.
- [3] Y. MOMOSE, T. TAKADA, S. OKAGAKI: *CF₄ and C₂F₆ plasma fluorination of hydrocarbon and fluorocarbon polymers*. Polymeric Materials Science and Engineering (M. Shen, A. T. Bell). ACS Division of Polymeric Material, Denver 1987, 236–239.
- [4] S. ENDO, T. TATSUMI: *Fluorinated amorphous carbon thin films grown by plasma enhanced chemical vapor deposition for low dielectric constant interlayer dielectrics*. Journal of Applied Physics, 78 (1995), 1370–1372.
- [5] H. YOKOMICHI, T. HAYASHI, A. MASUDA: *Changes in structure and nature of detects by annealing of fluorinated amorphous carbon thin films with low dielectric constant*. Applied Physics Letters, 72 (1998), 2704–2706.
- [6] A. GRILL, V. C. J. PATEL: *Novel low k dielectrics bead on diamond like carbon materials*. Journal Eлектроchemical Soc., 145 (1998), 1649–1653.

- [7] L. G. JACOBSON, D. F. FRANCESCHINI, M. E. H. M. COSTA, F. L. FREIRE JR.: *Structural and mechanical characterization of fluorinated amorphous-carbon films deposited by plasma decomposition of CF_4 - CH_4 gas mixtures*. Journal of Vacuum Science & Technology A, 18 (2000), 2230–2238.
- [8] R. PRIOLI, L. G. JACOBSON, M. E. H. M. COSTA, F. L. FREIRE JR.: *Nanotribological properties of amorphous carbon-fluorine films*. Tribology Letters, 15 (2003), 177–180.
- [9] Z. Q. YAO, Z. Q. YAO, P. YANG, N. HUANG, H. SUN, J. WANG: *Structural, mechanical and hydrophobic properties of fluorine-doped diamond-like carbon films synthesized by plasma immersion ion implantation and deposition (PIII-D)*. Applied Surface Science, 230 (2004), 172–178.
- [10] G. Q. YU, B. K. TAY, Z. SUN, L. K. PAN: *Properties of fluorinated amorphous diamond like carbon films by PECVD*. Applied Surface Science, 219 (2003), 228–237.
- [11] K. WASA: Handbook of sputter deposition techno principles technology and applications. Noyes Publications, New Jersey 1992.
- [12] A. E. BRAUN: *Sputtering targets adapt to new materials and shrinking architectures*. Semiconductor International, 21 (1998), 127–134.
- [13] J. ROBERTSON: *Diamond-like amorphous carbon*. Materials Science and Engineering R (Reports: A), 37 (2002), 129–281.
- [14] R. BUTTER, D. R. WATERMAN, A. H. LETTINGTON, R. T. RAMOS, E. J. FORDHAM: *Production and wetting properties of fluorinated diamond-like carbon coating*. Thin Solid Films, 311 (1997), 107–113.
- [15] R. E. SAH, B. DISCHLER, A. BUBENZERM, P. KODIL: *Amorphous carbon coatings prepared by high rate RF plasma deposition from fluorinated benzenes*. Applied Physics Letters, 46 (1985), 739–741.
- [16] C. VIVENSANG, G. TURBAN, E. ANGER, A. GICQUEL: *Reactive ion etching of diamond and diamond-like carbon films*. Diamond and Related Material, 3 (1994), 645–649.
- [17] J. W. YI, Y. H. LEE, B. FAROUK: *Low dielectric fluorinated amorphous carbon thin films grown from C_6F_6 and Ar plasma*. Thin Solid Films, 374 (2000), 103–108.
- [18] H. YANG, D. J. TWEET, Y. MA, T. NGUYEN: *Deposition of highly crosslinked fluorinated amorphous carbon film and structural evolution during thermal annealing*. Applied Physical Letters, 73 (1998), 1514–1516.
- [19] F. L. FREIRE JR., M. E. H. M. COSTA, L. G. JACOBSON, D. F. FRANCESCHINI: *Film growth and relationship between microstructure and mechanical properties of a-C:F films deposited by PECVD*. Diamond and Related Mater., 10 (2001), 125–131.
- [20] A. C. FERRARI, J. ROBERTSON: *Interpretation of Raman spectra of disordered and amorphous carbon*. Physics Review B, 61 (2000), 14095–14107.
- [21] Y. MA, H. YANG, J. GUO, C. SATHE, A. AGUI, J. NORDGREN: *Structural and electronic properties of low dielectric constant fluorinated amorphous carbon films*. Applied Physics Letters, 72 (1998), 3353–3355.
- [22] X. WANG, H. R. HARRIS, K. BOULDIN, H. TEMKIS, S. GANGOPADHYAY, M. D. STRATHMAN, M. WEST: *Structural properties of fluorinated amorphous carbon films*. Journal of Applied Physics, 87 (2000), 621–623.
- [23] Y. HAMAGAWA, T. TOKAYMA, H. OKAMOTO: *Blue light emission from a-C:H by thin film electroluminescence structure cell*. Journal of Non-Crystalline Solids, 115 (1989), 180–182.

- [24] Z. YAAKOV: *Work of adhesion of a sessile drop to a clean surface*. Journal of Colloid and Interface Science, *213* (1999), 602–605.
- [25] P. A. P. NASCENTE: *Materials characterization by X-Ray photoelectron spectroscopy*. Journal of Molecular Catalysis A: Chemical, *228* (2005), 145–150.
- [26] R. D'AGOSTINO, R. LAMENDOLA, P. FAVIA, A. GIGUEL: *Fluorinated diamond-like carbon films deposited from radio frequency glow discharge in a triode reactor*. Journal of Vacuum Science and Technology A, *12* (1994), 308–313.
- [27] L. F. BONETTI, G. CAPOTE, L. V. SANTOS, E. J. CORAT, V. J. TRAVA-AIROLDI: *Adhesion studies of diamond-like carbon films deposited on Ti_6Al_4V substrate with a silicon interlayer*. Thin Solid Films, *515* (2006), 375–379.
- [28] J. F. MOULDER, W. F. STICKLE, P. E. SOBOL, K. D. BOMBEN: *Handbook of X-Ray photoelectron spectroscopy, a reference book of standard spectra for identification*. Perkin-Elmer Corporation, Eden Prairie 1992.
- [29] Y. B. JIANG, H. X. ZHANG, D. J. CHENG, S. Z. YANG: *Effect of substrate temperature on the deposition of C–N films by pulsed high-temperature C–H–N Plasma CVD*. Thin Solid Films, *360* (2000), 52–55.
- [30] S. TRUSSO, C. VASI, F. NERI: *CN_x thin films grown by pulsed laser deposition: Raman, infrared and X-ray photoelectron spectroscopy study*. Thin Solid Films, *219* (1999), 355–356.
- [31] A. BENDAVID, P. J. MARTIN, L. RANDENIYA, M. S. AMIN: *The properties of fluorine containing diamond-like carbon films prepared by plasma-enhanced chemical vapor deposition*. Diamond & Related Materials, *18* (2009), 66–71.
- [32] S. F. DURRANT, R. P. MOTA, M. A. B. MORAES: *Fluorinated polymer-film from RF plasmas containing benzene and sulfur hexafluorine*. Thin Solid Films, *220* (1992), 295–302.
- [33] A. M FERRARIA, J. D. L SILVA, A. M. B. REGO: *XPS studies of directly fluorinated HDPE: problems and solutions*. Polymer, *44* (2003), 7241–7249.
- [34] H. BIERDERMAN, Y. OSADA: *Plasma Polymerization Process*. Elsevier, Amsterdam 1992.
- [35] H. YOKOMICHI, A. MASUDA: *Effect of sputtering with hydrogen dilution on fluorine concentration of low hydrogen content fluorinated amorphous carbon thin films with low dielectric constant*. Journal of Applied Physics, *86* (1999), 2468–2472.

Received May 16, 2010

Formation of water vapor plasma using a linear DC plasma torch

ANDRIUS TAMOŠIŪNAS¹, PRANAS VALATKEVIČIUS¹,
VIKTORIJA GRIGAITIENĖ¹, VITAS VALINČIUS¹

Abstract. Water vapor plasma formation process has been investigated in the DC arc plasma torch, operating at atmospheric pressure. The torch was designed and tested in Plasma Processing Laboratory of Lithuania Energy Institute for the conversion of biomass and organic waste. Thermal and electrical characteristics have been experimentally established and analyzed employing the theory of modified similarity. It has been found, that the arc voltage slightly drops increasing the arc current. The thermal characteristics of plasma torch decreases with grow of the current strength, while generalized thermal efficiency of plasma source intensity increases. The heat loss through the walls of plasma torch decreases as volume of plasma forming water vapor increases. Generalized operating characteristics helps to control plasma jet parameters during the process of plasma treatment.

Key Words. DC plasma torch, water vapor, atmospheric pressure plasma.

1. Introduction

Recently, a new area of research and development has been started in thermal plasma technology. Plasma torches operating on water vapor provide an alternative to commonly used sources of thermal plasmas based on gas-discharge arcs [1]. The advantages of water vapor plasmas are characterized as following: high enthalpy to enhance reaction kinetics, high chemical reactivity and rapid quenching rate. Because of these advantages, water vapor plasma torch has a wide prospect to be applied to many fields such as biomass and organic waste treatment, synthesis of nanoparticles, chemical vapor deposition and plasma spraying.

Water vapor plasma torches have been investigated and applied in [2], and found as one of the most advanced and commercialized water-stabilized plasma

¹Lithuanian Energy Institute, Plasma Processing Laboratory, Breslaujos g. 3, LT-44403 Kaunas, Lithuania, e-mail: tamosiunas@mail.lei.lt

systems. The commercial version PBR 8 in operation, running with water steam as plasma gas is described in [3].

Water vapor plasma, that produces hydrogen and oxygen at high temperature, are best suited for haloalkanes destruction and decomposition of organic waste and biomass due to economical and chemical reasons. Applications of DC steam plasma generator for decomposition of waste have been reported, for example, PCB (polychlorinated biphenyl) [4], halogenated hydrocarbon [5], hydrocarbon [6], organic waste [7], [8], used tires [9], biomass [10]–[12]. During the decomposition of these organic wastes, mostly tungsten cathode has been used, which should be protected by nitrogen or argon. These protecting gas are not favorable for industrial applications owing to economic reason. Considering the cost reduction, pure-water plasmas without injection of other gases for waste treatment is applied in [5].

Plasma generation system generally requires complex subsystems such as electrical, cooling and supply of gas and water vapor unit. Especially water vapor plasma system requires a sub-equipment such as a heater to prevent condensation of vapor on the walls of the reactor. Thus, efficient plasma generation systems have been required for the industrial application.

Whole plasma process is strongly depend on the plasma torch regime and plasma jet parameters. The main objective of this research is to investigate formation of water vapor plasma by a linear DC plasma torch and to establish thermal and electrical characteristics of constructed experimental equipment. This plasma generation system provides the new incentive for decomposition of biomass and organic waste treatment by thermal plasma gasification. The advantage of water vapor plasma is that it is ecologically clean. Water vapor is a reagent and a heat carrier at once. It's very convenient to use water vapor plasma in plasmachemical reactors for gasification of biomass and organic waste.

2. Experimental setup

The developed water vapor plasma torch with gas-water vapor stabilized electric arc is a DC thermal plasma generator of linear design Fig. 1. The system was operated under atmospheric pressure. The cathode (1) of the torch is made of cooper button and embedded with tungsten-rod to work as electron emitter. The step-formed cooper anode (4) is water-cooled and has a stair-step shape, due to the arc shunting process suppression. The periodic swirling of the electric arc spot has a strong effect on the life-time of the anode. When the shunting amplitude is high, the instability of parameters of the electric arc and gas flow simultaneously increases. To avoid this negative phenomenon and prolong the life-time of the anode, the stair-step anode has been designed.

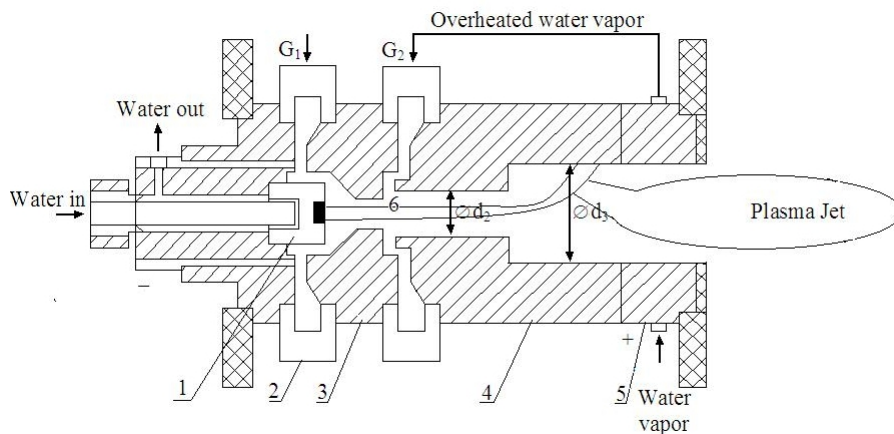


Fig. 1. A scheme of water vapor plasma torch; 1—cathode, 2—insulating rings, 3—neutral section, 4—stair-step anode, 5—superheater, 6—electric arc

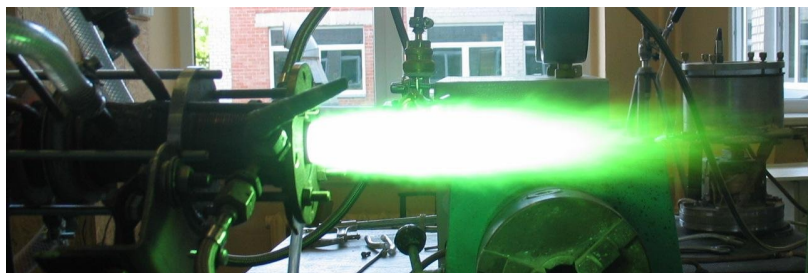


Fig. 2. Water vapor plasma torch in operation

Figure 2 shows an experimental water vapor plasma torch in operation. The DC Ar/water vapor stabilized plasma torch has been employed. The additional system consists of a water steam generator ($1.6 \div 3.1 \times 10^{-3} \text{ kg s}^{-1}$), the argon supply ($5.2 \div 10^{-4} \text{ kg s}^{-1}$), the cooling water supply ($0.1 \times 10^{-3} \text{ kg s}^{-1}$) and a DC power supply. Argon (Ar) was used as shielding gas to protect the cathode from erosion. The amount of the Ar as shielding gas depends on the current value and the type of used main plasma gas. It was in range of $15 \div 24 \%$ of the total mass flow. The basic experimental parameters are given in Table 1. The characteristics of the plasma torch and the parameters of plasma jet were determined from heat conservation calculations while measuring current strength in the column, voltage drop and gas amounts.

Table 1. The experimental parameters of plasma generator and plasma jet

Arc current (A)	139 ÷ 182
Arc voltage (V)	179 ÷ 260
Arc power (kW)	30 ÷ 40
Power loss to the cooling water (kW)	11 ÷ 16
Output power (kW)	16 ÷ 26
Plasma torch efficiency, η	0.51 ÷ 0.7
Argon gas flow rate, G_1 (10^{-4} kg s $^{-1}$)	5.2
Water vapor flow rate, G_2 (10^{-3} kg s $^{-1}$)	1.6 ÷ 3.1
Total mass flow rate, G (10^{-3} kg s $^{-1}$)	2.1 ÷ 3.6
Plasma jet mean temperature at the torch outlet nozzle (K)	3300 ÷ 3500
Plasma jet mean velocity at the torch outlet nozzle (m s $^{-1}$)	210 ÷ 310
Diameter of stair-step anode, d_2 (10^{-3} m)	8
Diameter of stair-step anode, d_3 (10^{-3} m)	14

The water vapor as working gas was tangentially supplied through the blow-holes of insulating rings (Fig. 1, position 2). All parts of plasma torch were water-cooled. Erosion of the electrodes proceeds due to the condensation of water vapor on the walls of the plasma torch. To avoid condensation process, the temperature of the electrodes walls was kept over 373 K.

Before the water vapor flow into the reactor it is overheated by superheater, up to 473 ÷ 573 K temperature. Thus, the higher thermal efficiency of plasma torch is obtained; simultaneously condensation of water vapor is avoided. Water vapor is ionized by electric arc of the plasma torch, i.e. dissociates into ions, atoms, neutrals and electrons. This is very desirable in the gasification of biomass or organic waste, because ionized particles of the water vapor participates in the formation of synthetic gas ($\text{CO} + \text{H}_2$) during the chemical reactions.

3. Results and discussion

3.1. Electrical characteristics of water vapor plasma torch

The electric and thermal characteristics are very important designing and projecting an experimental reactor for thermal plasma gasification of biomass and organic waste.

Static plasma torch voltage–current characteristics (VCC) are descending or remain stable with the current strength increasing (Fig. 3). The electric arc voltage and the power of plasma torch mainly depend on the flow rate of water vapor as working gas. A part of slightly dropping curve appears as a result

of the insignificant influence of the plasma torch channel walls on the electric arc, i.e. tangentially supplied water vapor flow rate has a significant influence on the thickness of the boundary layer. Thus, the diameter of an electric arc column decreases. The part of incident curve appears due to the plasma torch channel walls influence on the characteristics of electric arc, i.e. more and more energy is lost to the channel walls. Thus, the thickness of boundary layer of water vapor gets smaller and the thermal efficiency of water vapor plasma torch decreases either.

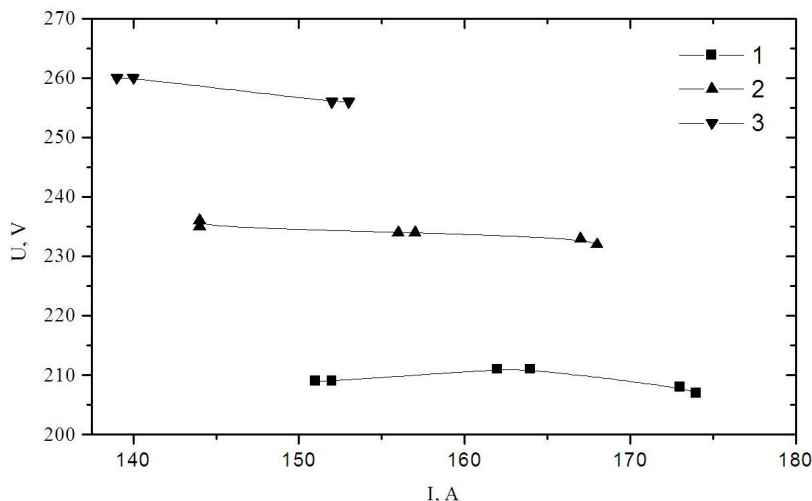


Fig. 3. Voltage–current characteristics of water vapor plasma torch depending on water vapor flow rate, $10^{-3} \text{ kg s}^{-1}$: a – 2.1; b – 3.1; c – 3.6

To ensure a stable work of the water vapor plasma torch rising or steady voltage–current characteristics are desirable. Thus, additional regulating resistors are not required and the thermal efficiency of water vapor plasma torch increases. The water vapor plasma torch works steady than the flow rate of water vapor is in the range of $2.1 \div 3.1 \times 10^{-3} \text{ kg s}^{-1}$ and the current of electric arc varies from 142 through 172 A. Further, the obtained VCC were generalized employing the theory of similarity and described by equation (1).

$$\frac{U d_2}{I} = 3 \times 10^3 \left(\frac{I^2}{G d_2} \right)^{-0.6} \quad (1)$$

where U is voltage (V), d_2 – diameter of anode (m), I – the arc current (A), G – the total mass flow (kg s^{-1}).

A stable work of water vapor plasma torch is required controlling the process and conditions in the thermal plasma gasification of biomass and organic waste.

3.2. Thermal characteristics of water vapor plasma torch

The maximum thermal efficiency of water vapor plasma torch is achieved at the current $I = 140$ A, voltage $U = 260$ V, and the flow rate of water vapor $G_2 = 3.6 \times 10^{-3}$ kg s $^{-1}$, was $\eta = 0.7$. Thermal efficiency of the torch mainly depends on the flow rate of water vapor. The increased thickness of boundary layer of water vapor and voltage improves the thermal efficiency of plasma torch. The increase in current strength and heat loss through the walls of plasma torch reduces thermal efficiency of the torch. It depends on the influence of the declined thickness of boundary layer of the flow. Smaller thickness of boundary layer determines the increase of diameter of the electric arc column.

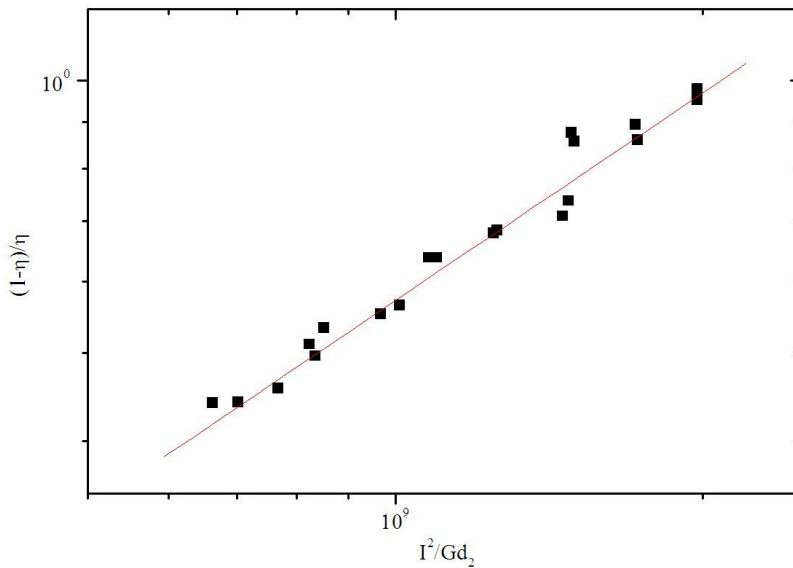


Fig. 4. A general thermal efficiency of plasma torch

The generalized results of plasma torch thermal efficiency (Fig. 4) were estimated using the theory of similarity and are summarized into one equation (2). Any value of plasma torch thermal efficiency may be estimated from this equation. The evaluated results of general thermal efficiency of plasma torch Fig. 4, are taken into account designing water vapor plasma torch for the decomposition of biomass and organic waste.

$$\frac{1-\eta}{\eta} = 1.02 \times 10^{-7} \left(\frac{I^2}{Gd_2} \right)^{0.75} \quad (2)$$

where η is the thermal efficiency, I – the arc current (A), G – the total mass flow (kg s^{-1}), d_2 – the diameter of anode (m).

The knowledge of geometry of water vapor plasma torch and its volt–ampere and thermal characteristics helps to determine the temperature and velocity of the plasma jet at the exhaust nozzle of anode. Thermal and dynamic parameters of plasma jet have the main influence on the effective thermal plasma gasification of biomass and organic waste.

4. Conclusions

The voltage–current characteristics of novel designed water vapor plasma torch are slightly decreasing and are described by equation (1). Generalized thermal characteristics of plasma torch intensity increases and could be characterized by equation (2).

The electrical and thermal characteristics of water vapor plasma torch were carried out to ensure the stable work of the equipment. The obtained results will be useful and necessary projecting a new plasma reactor, designed for the decomposition of biomass and organic waste.

References

- [1] R. JUSKEVICIUS, R. KEZELIS, P. VALATKEVICIUS, A. AMBRAZEVICIUS: *The research on water vapor plasma generator*. Power Engineering, 3 (1999), 51–60.
- [2] M. HRABOVSKY, M. KONRAD, V. KOPECKY, V. SEMBER: *Process and properties of electric arc stabilized by water vortex*. IEEE Transactions on Plasma Science, 25 (1997), 833–839.
- [3] B. GLOCKER, G. NENTWING, E. MESSERSCHMIND: *1–40 kW steam respectively multi gas thermal plasma torch system*. Vacuum, 59 (2000), 35–46.
- [4] S. W. KIM, H. S. PARK, H. J. KIM: *100 kW steam plasma for treatment of PCB's (polychlorinated biphenyl) waste*. Vacuum, 70 (2003), 59–66.
- [5] T. WANATABE, T. TSURU: *Water plasma generation under atmospheric pressure for HFC destruction*. Thin Solid Films, 518 (2009), 924–928.
- [6] A. VAIDYANATHAN, J. MULHOLLAND, J. RYU, M. S. SMITH, L. J. CIRCEO: *Characterization of fuel gas products from the treatment of solid waste streams with a plasma arc torch*. Journal of Environmental Management, 82 (2007), 77–82.
- [7] B. LEMMENS, H. ELSLANDER, I. VANDERREYDT, K. PEYS, L. DIELS, M. OOSTERLINCK, M. JOOS: *Assessment of plasma gasification of high calorific waste streams*. Waste Management, 27 (2007), 1562–1569.
- [8] H. HUANG, L. TANG: *Treatment of organic waste using thermal plasma pyrolysis technology*. Energy Conversion and Management, 48 (2007), 1331–1337.
- [9] J. S. CHANG, B. W. GU, P.C. LOOY, F. Y. CHU, C. J. SIMPSON: *Thermal plasma pyrolysis of used old tires for production of syngas*. Journal of Environmental Science and Health, 31 (1996), 1781–1799.

- [10] G. VAN OOST, M. HRABOVSKY, V. KOPECKY, M. KONRAD, M. HLINA, T. KAVKA: *Pyrolysis/gasification of biomass for synthetic fuel production using a hybrid gas–water stabilized plasma torch*. *Vacuum*, 83 (2009), 209–212.
- [11] G. VAN OOST, M. HRABOVSKY, V. KOPECKY, M. KONRAD, M. HLINA, T. KAVKA, A. CHUMAK, E. BEECKMAN, J. VERSTRAETEN: *Pyrolysis of waste using a hybrid argon–water stabilized torch*. *Vacuum*, 80 (2006), 1132–1137.
- [12] R. KEZELIS, V. MECIUS, V. VALINCIUTE, V. VALINCIUS: *Waste and biomass treatment employing plasma technology*. *Journal of High Temperature Material Processes*, 8 (2004), 273–282.

Received May 17, 2010

Design and realisation of a Thomson spectrometer for laser plasma facilities¹

MARIO MAGGIORE², SALVATORE CAVALLARO^{3,4}, GIUSEPPE A. P. CIRRONE⁴, GIACOMO CUTTONE⁴, LORENZO GIUFFRIDA^{4,5}, FRANCESCO ROMANO⁴, LORENZO TORRISI^{4,5}

Abstract. A research project, LILIA (Laser Induced Light Ion Acceleration), has been funded at INFN (Italian Institute for Nuclear Physics) with the aim to study the mechanisms of charged particles acceleration by high power lasers. In Italy, at LNF — INFN of Frascati, a high power laser (intensity in the range $10^{20} \div 10^{21}$ W cm⁻², 10 Hz repetition rate and high contrast, of the order of 1010, between main pulse and pre-pulse) named FLAME will be operative within 2010. The activities related to this project, along with the FLAME peculiarities, would result in a significant synergy to improve the research on plasma acceleration in Italy. In this frame our group is involved in the design and construction of a spectrometer based on the Thomson's configuration in order to diagnose the ion ejection from the laser-generated plasma. This kind of analyzer allows to get most of information about energy and species of beams produced from a single laser shot. The main goal is to realize a compact system which is both very practical and optimized with regard to the mass and energy resolution of particles obtained by laser-plasma interactions. The preliminary design has to be able to analyze and resolve beams of protons and ions up the total energy of 10 MeV. However, the technical choices adopted in this prototype have to be applied for the final device concerning a challenging spectrograph able to analyze beams of 150 MeV of total energy. An intensive study by means of 3D electromagnetic FEM code and beam dynamics were accomplished out and the results will be shown. The first prototype of the spectrometer is being realized and tested at LNS-INFN of Catania. After the magnetic and electric measurements the device will be calibrated as well as the detectors will be tested with proton and carbon beams delivered by the accelerators operating at LNS-INFN of Catania (Italy) within the expected energy range (0.1 ÷ 10 MeV) and for different charge to mass ratios ($Q = +1 \dots +6$). The results of these tests will be also presented and discussed.

Key Words. Laser accelerated beams, Thomson spectrometer, protontherapy.

¹This work is supported by V INFN Scientific Committee in the framework of the LILIA and Pleaidi Projects

²Laboratori Nazionali di Legnaro of INFN, Padova, (I)

³Physics and Astronomy Department, University of Messina, Messina (I)

⁴Laboratori Nazionali del Sud of INFN, Via S. Sofia 63, 95100, Catania (I)

⁵Department of Physics, University of Messina, Messina (I)

Introduction

A Laser based proton acceleration systems is a promising new technology of accelerating charged particles to energies that might become high enough for therapeutic use in radiation therapy [1]–[3]. Nowadays large and expensive cyclotrons or synchrotrons are used for this task. The mechanism of laser acceleration might potentially reduce the overall costs of proton therapy in cancer treatment with ionizing radiation. The long-term goal of current research is to build a laser based treatment machine that is not much bigger than a conventional photon linac. This would enable the widespread use of the superior properties of protons compared to the conventional X-ray radiation. However, much research needs to be done until a commercial laser accelerated treatment device can be build. Currently, the most important problem is that the achievable energies are not yet high enough for the treatment of patients, but there is hope that this can be achieved soon. Another problem is the energy spectrum of the proton beam. Conventional acceleration machines produce a sharp energy with only little spread therein which gives rise to the sharp Bragg peak in the depth dose curve. Laser accelerated protons, instead, are currently not monoenergetic, showing a Boltzmann-like distribution [4]. Much work is being done to produce sharper energy spectra but it is highly probable that they will never be as sharp as for conventional accelerators. The precise energy spectrum of the final beam is not known yet, but most experiments show exponentially decaying spectra over a wide energy range. We hope that this will change in the future and the possibility to have proton beams with a good level of monochromaticity will be reached.

Inside our group we are principally working in two different directions. Exploiting the experience we have in the detection of the charged particle produced by the laser interaction [5], [6], we are design and developing a Thompson spectrometer able to detect charged particle produced by the laser interaction with the matter. On the other side, making use of the power of the Monte Carlo technique we are designing an electromagnetic selection device to optimize the produced proton beams (in terms of energy spread and divergency) and to study their principal dosimetric characteristics. Monte Carlo simulation will also help us in the final characterization of the Thompson spectrometer.

The traditional protontherapy facility at INFN-LNS

The use of proton beams offers the advantage to improve tumor control, especially for the treatment of small tumors, where it is necessary to obtain a localized dose distribution while sparing the surrounding normal tissues [7]–[9]. The hadrons allow conformation of the dose distribution better than photons or electrons, so the use of these charged particles has developed rapidly in

recent years. There are nearly 20 hadrontherapy facilities worldwide, among them about 10 in Europe. In Italy, the first and actually unique protontherapy facility, named CATANA (Centro di AdroTerapia e Applicazioni Nucleari Avanzate) was built in Catania, at the Istituto Nazionale di Fisica Nucleare-Laboratori Nazionali del Sud (INFN-LNS). Here a 62 MeV proton beam, accelerated by a Superconducting Cyclotron (SC), is used for the treatment of shallow tumors like those of the ocular region. The CATANA project was developed to treat ocular pathologies like uveal melanoma, which is the most frequent eye tumor in adults. Moreover, we treat other less frequent lesions like choroidal hemangioma, conjunctiva melanoma, eyelid tumors and embryonal sarcoma. In the CATANA facility the clinical activity is still ongoing and 200 patients have been treated since March 2002. A global view of the CATANA proton therapy beam line at INFN-LNS is shown in Fig. 1. More details on the beam line are reported in literature [10], [11].

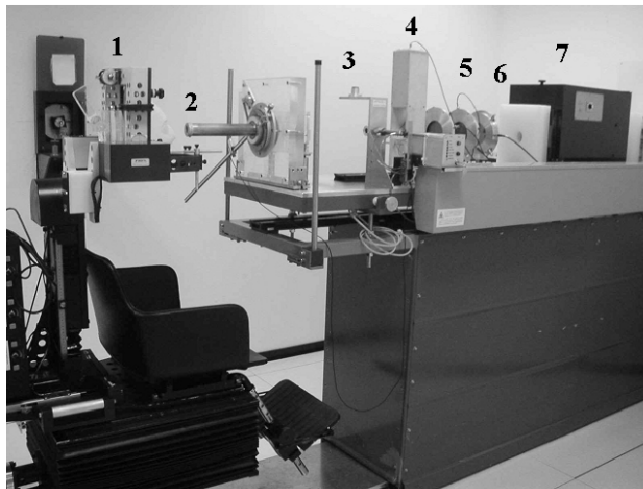


Fig. 1. View of the CATANA beam line; 1—treatment chair for patient immobilization, 2—final collimator, 3—positioning laser, 4—light field simulator, 5—monitor chambers, 6—intermediate collimator, 7—box for the location of modulator wheel and range shifter

Laser driven protons for radiotherapy: advantages and main drawbacks

Today, the vast majority of cancer patients in radiotherapy are treated with conventional therapeutic beams consisting of high-energy electrons and photons. Although therapeutic proton beams were primarily suggested more than 60 years ago [12] and feature an intrinsically advantageous in terms of depth

dose curves characteristic, even modern clinical proton facilities still require large accelerator rings and huge electromagnetic beam steering devices. Due to these circumstances, nowadays, therapeutic proton beams could not represent a serious competition to the conventional, much more practical and less expensive solutions. In the last years, laser-driven proton accelerators were proposed for therapeutic applications [13], [14], as they can potentially provide handy proton sources of reasonable size and reduced costs. For this purpose, ultrashort (i.e. femtosecond scale) laser pulses with peak intensities of the order of $10^{19} \text{ W cm}^{-2}$ are focused on thin hydrogenated solid foils. When incident on the target, this strong em laser field instantaneously ionizes atoms at the target surface and creates an high density plasma. The laser energy is then efficiently absorbed by heating some of the plasma electrons to relativistic energies. Subsequently, a cloud of hot electrons spreads into the quasi-neutral target, overshoots at its edges and forms space-charge regions close to its front and back surfaces. (Note that in this work target-front as well as target-back is always defined relative to the side of laser incidence.) A variety of ions, primarily protons from hydrogenated polymers or from contaminant layers on the target surface [15], [16], are accelerated by the built-up quasi-static electric fields perpendicular to the surface of the foil in the so-called target normal sheath acceleration (TNSA). The most efficient TNSA takes place at the unperturbed rear side of the foil, where the fastest protons can be observed [17]. Peak proton energies around $E_{\text{max}} = 60 \text{ MeV}$ have been achieved so far with laser pulse intensities of the order of $10^{20} \text{ W cm}^{-2}$ [18].

The energy distributions follow only approximately the Boltzmann shape. The laser pulse, in fact, produces ions and the emitted yield is limited by the film thickness and laser spot. The emitted ions contain protons but also a large component of other ions, depending on the target composition. Such ions have high charge state and strong anisotropic distribution. Thus the extractable proton beam should be selected magnetically from such high ions background. Moreover, the proton number is not high, especially if only the high energy component is considered. Thus, repetitive laser pulses on fresh thin film should be used in order to obtain a sufficient average proton current.

In any case, the proton energy is not yet sufficient for therapeutic considerations and it is at the limit also for shallow tumors like eye-melanoma.

However, according to particle-in-cell (PIC) simulations (Malka et al 2004, Schwoerer et al 2006) as well as semi-analytical scaling laws (Fuchs et al 2006) it seems that the new generation of petawatt laser will be able to generate protons with energies suitable for therapeutic applications ($E \leq 250 \text{ MeV}$).

On the other hand, a set of drawbacks must be at moment considered in such kind of beams. The first one is related to the energy distribution of emitted particles. It, in fact, shows a quasi thermal distribution while a mono-energetic beam is required for treatment. Different approach, at different levels (optimization of the target, realization of magnetic devices) have been proposed

to exceed this issue but no final solution as been yet reached. Another drawback is related to the final intensities of the emitted particles that must be sufficiently high to guarantee a treatment in a reasonable time interval.

Thompson Spectrometer Design

A group of researcher at INFN-LNS is actually involved with the design and construction of an innovative spectrometer based on the Thomson's configuration in order to diagnose the ion ejection from the laser-generated plasma and with a maximum energy of 10 AMeV. This kind of analyzer allows to get most of information about energy and species of beams produced from a single laser shot. The particles are deflected by the magnetic and electric fields having the same direction, perpendicular to the trajectory of the incident beams. Therefore, while the electric field deflects charged particle depending on the energy, the magnetic one bends these as a function of the momentum. Neglecting any fringe field effects, the amount of the deflection is given by

$$\theta_{\text{electric}} \approx \frac{qEl}{mv^2}, \quad \theta_{\text{magnetic}} \approx \frac{qBl}{mv}, \quad (1)$$

where B and E are the electric and magnetic fields, l is the length of those fields and m , q , v the particle mass, charge and velocity. If D is the distance from the electromagnetic device and the detector plane such as $D \sim l$ and supposing that the magnetic field deflects on x axis and the electric one on the y , combining the previous relations one gets

$$y = \frac{mE}{qldb^2} x^2. \quad (2)$$

The particles with the same charge-to-mass ratio and different energies are deflected on a parabolic trace in the detector plane, while particles with different charge-to-mass ratio get different parabolas.

The main goal is to realize a compact system which is both very practical and optimized with regard to the mass and energy resolution of particles obtained by laser-plasma interactions. The preliminary design has to be able to analyze and resolve beams of protons and ions up the total energy of 10 MeV. However, the technical choices adopted in this prototype have to be applied for the final device concerning a challenging spectrograph able to analyze beams of 150 MeV of total energy.

The magnetic and electric fields range from few hundreds of gauss to 0.18 T, and few hundreds of volts up to 30 kV in order to cover a wide range of possible setups of the laser-target facility. The conductors are not water cooled since they operate for few minutes at the maximum current density of 4 A mm^{-2} .

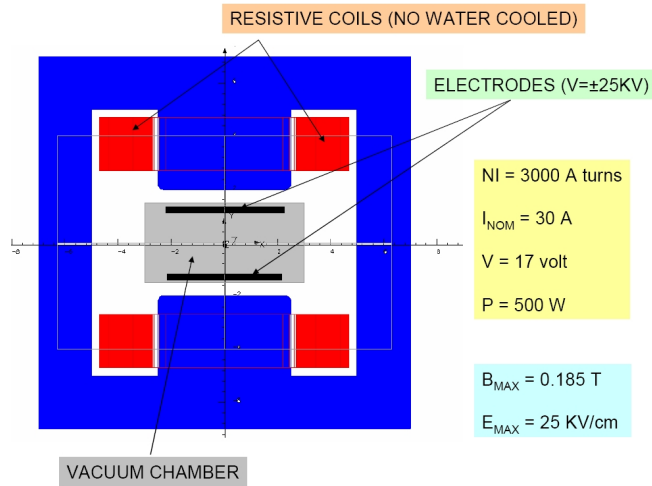


Fig. 3. Front view of the H magnet and positioning of the HV electrodes into the vacuum chamber; dimensions are in cm



Fig. 4. Coils and iron ready to be assembled to form the magnetic part of the spectrometer

Studies have been done concerning the pinholes size and their effects on the performances of the spectrometer. The collimator, indeed, is placed upstream the electromagnet (35 cm from the focal plane) and it gives the angular acceptance ($\sim 10^{-4}$ msr) of the system affecting the effective spatial resolution we will measure on the detector. In order to get a good energy separation (0.5 MeV at 10 MeV) on the detector with a spatial resolution of $100 \mu\text{m}$, it is needed to set the pinhole size to $200 \mu\text{m}$. The main difference about the energy resolution calculated by using a pinhole of $300 \mu\text{m}$ size is shown in Fig. 5.

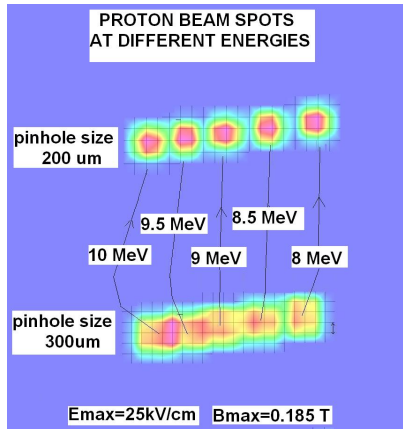


Fig. 5. Simulations of different proton beam delivered through the spectrometer and intercepted on the detector plane; the beam spots at different energies are shown as function of the pinhole size of the collimator placed upstream the magnet; the increasing of the resolving power of the spectrometer in terms of energy, is evident (upper section of the figure) decreasing the collimator aperture to $200\ \mu\text{m}$

The electromagnetic system has been simulated by OPERA 3D and to identify the ion species with a certain charge-to-mass ratio forming a single parabola, a 3-D tracking routine for different ions and energies has been done as shown in Fig. 6.

The choice of the focal plane detector permitting the particles spatial localisation, is a crucial issue in the design and construction of a Thomson-like spectrometer. It must be able to detect particles traversing the magnetic and electric region with a good efficiency and a sufficient spatial resolution. The efficiency is important to permit the detection of also few number of particles coming from the generated plasma. On the other hand, spatial resolution is necessary to achieve the best possible localisation of the incoming ions. More precise is, in fact, the information on the particle position, more accurate results energy resolution power of the device. This is particularly true for the highly energetic particles that are concentrated in the central region of the detector and for which spatial localisation could also result not possible.

We are planning to test and use different detectors for the particle detection. Our first choice has been directed towards the use of the Gafchromic films that have been extensively used by some of the authors of this paper, for the detection of charged particle beams. The Gafchromic shows many advantages in the detection of laser-generated particles: they are not sensible to the visible light (that is an important noise component in a laser-target interaction chamber), they present a good spatial resolution (of the order of $100\ \mu\text{m}$ and

do not need any special development technique. On the opposite side, their use is complicated by the fact that they are off-line detectors (so it is necessary to reopen the chamber after each irradiation) and by their sensibility to the incoming particles.

Gafchromic radiochromic dosimetry films are self-developing film media that have been developed for the measurement of absorbed dose and the mapping of radiation fields. They are largely exploited in the medical physics field for external radiotherapy and brachytherapy but, thanks to their interesting features, they are widely spread used also in different research fields. They consist of radiochromic microcrystalline dispersions on a thin polyester base. Its radiographic sensitivity is based on the solid-state photopolymerization of diacetylene monomer molecules. The colorless nonirradiated radiochromic film responds to ionizing radiations such that its color becomes darker as the total absorbed dose increases. These media can be handled in normal room light, thereby eliminating the cost of darkroom space and of post-exposure processing. Moreover, they are light and flexible and may be cut to any shape or size desired. Individual Gafchromic radiochromic dosimetry film types are available on the market and each of them is optimized for high or low energy photons as well as particle radiation. The degree of darkening is, therefore, proportional to exposure and it can be quantitatively measured with any densitometer, scanner or spectrophotometer. The net optical density is obtained after calibration procedures and by subtracting the background. Gafchromic films are largely used for radiation field measurements thanks to their good spatial resolution ($\leq 100 \mu\text{m}$), which depends also on the system of reading used.

A characterization of different kinds of Gafchromic films for the laser generated charged particle diagnostic is actually in progress in our group and results will be reported in a future paper.

We are also verifying the possibility to use silicon micropixel detector to improve the spatial resolution of the Thomson spectrometer focal plane. A separate investigation is in fact, in progress, to verify the possibility to use the Timepix detector, at least in the central region of the focus plane, where the biggest spatial resolution is requested. The Timepix, that can reach a maximum spatial resolution of the order of $5 \mu\text{m}$, can be used in counting mode and in Time-Over-Threshold mode. This could permit a simultaneous measure of the particles position and their detection time from which and independent energy measure can be extracted.

The spectrometer will be calibrated as well as the detectors will be tested with proton and Carbon beams delivered by the accelerators operating at LNS-INFN of Catania (Italy) within the expected energy range ($0.1 \div 10 \text{ MeV}$) and for different charge to mass ratios ($Q = +1 \dots +6$).

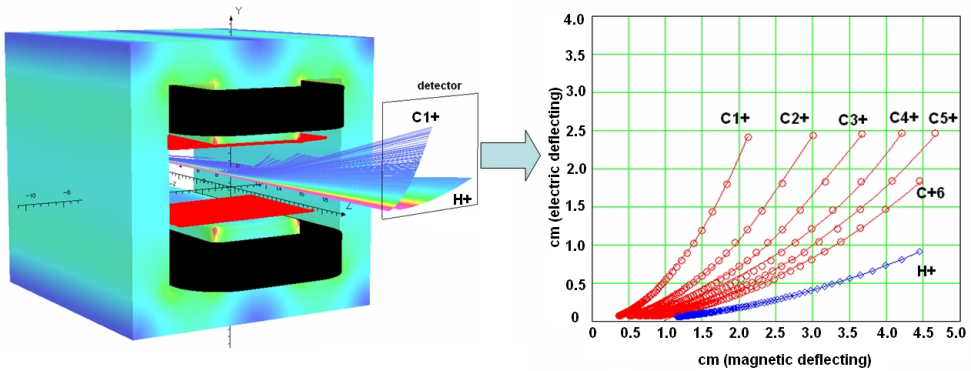


Fig. 6. The simulated trajectories of proton and Carbon ion ($Q = 1+$) ranging from few keV to 10 MeV, are shown in the left side; plot of the expected traces of different Carbon ions on the detector is also shown

Conclusions

Fs-terawatt lasers can be employed to irradiate hydrogenated thin target and to produce high energetic ions potentially useful for radiotherapy. Protons up to 50 MeV and Carbon ions with energy above 100 MeV have been obtained irradiating polyethylene thin films. At the present the ion streams are complex, because contains protons, carbon and other species from the target composition at different charge states. Moreover the energy spectra are approximately Boltzmann shaped and the yields of some species, limited by the film thickness and laser spot, generally are below 10^{16} ions pulse⁻¹. Thus the use of proton and carbon beams extractable from the laser generated plasma need to be studied in terms of mass/charge selection by a suitable magnetic field, in terms of ion energy filtering, in order to provide a near monoenergetic ion beam, and finally in terms of repetitive laser pulses interacting with fresh thin target, in order to generate an ion beam with a near constant output current. Actually these three aspects are under investigations and only after a their improvement the possibility to realize a radiotherapy using laser accelerated ion beam will can really possible. The Thomson parabola represents only one of the different diagnostic techniques useful to investigate about the kind of ions, charge state and energy distributions obtainable from laser-generated plasma, permitting to reach the research goal more fast.

References

- [1] C.-M. MA, I. VELTCHEV, E. FOURKAL, J. S. LI, W. LUO, J. FAN, T. LIN, A. POLLACK: *Development of a laser-driven proton accelerator for cancer therapy*. Laser Physics, *16* (2006), 639–646.
- [2] U. LINZ, J. ALONSO: *What will it take for laser driven proton accelerators to be applied to tumor therapy*. Phys. Rev. ST Accel. Beams, *10* (2007), 094801.
- [3] O. KLIMO, J. PSIKAL, J. LIMPOUCH, V. T. TIKHONCHUK: *Monoenergetic ion beams from ultrathin foils irradiated by ultrahigh-contrast circularly polarized laser pulses*. Phys. Rev. ST Accel. Beams, *11* (2008), 031301.
- [4] L. TORRISI, S. GAMMINO, L. ANDÒ, L. LASKA: *Tantalum ions produced by 1064 nm pulsed laser irradiation*. J. Appl. Phys., *91* (2002), 4685–4692.
- [5] L. TORRISI, S. GAMMINO, L. ANDÒ, L. LASKA, J. KRASA, K. ROHLENA, J. ULLSCHMIED, J. WOLOWSKI, J. BADZIAK, P. PARYS: *Equivalent ion temperature in Ta plasma produced by high energy laser ablation*. J. Appl. Phys., *99* (2006), 083301.
- [6] L. TORRISI, D. MARGARONE, L. LASKA, J. KRASA, A. VELYHAN, M. PFEIFER, J. ULLSCHMIED, L. RYC: *Self-focusing effect in Au-target induced by high power pulsed laser at PALS*. Laser And Particle Beams, *26* (2008), 379–387.
- [7] D. W. MILLER: *A review of proton beam radiation therapy*. Med. Phys., *22* (1995), 92354.
- [8] M. FUSS, L. N. LOREDO, P. A. BLACHARSKI, R. I. GROVE, J. D. SLATER: *Proton radiation therapy for medium and large choroidal melanoma: preservation of the eye and its functionality*. Int. J. Radiat. Oncol. Biol. Phys., *49* (2001), 1053–1059.
- [9] E. S. GRAGOUDAS, M. GOITEIN, L. VERHEY, J. MUNZENREIDER, H. D. SUIT, A. KOEHLER: *Proton beam irradiation: An alternative to enucleation for intraocular melanomas*. Ophthalmology, *87* (1980), 571–581.
- [10] G. A. P. CIRRONE, G. CUTTONE, R. A. LOJACONO, S. LO NIGRO, V. MONGELLI, I. V. PATTI, G. PRIVITERA, L. RAFFAELE, D. RIFUGGIATO, M. G. SABINI, V. SALAMONE, C. SPATOLA, L. M. VALASTRO: *A 62 MeV proton beam for the treatment of ocular melanoma at Laboratori Nazionali del Sud-INFN (CATANIA)*. Nuclear Science Symposium Conference Record, 2003 IEEE, *51* (2004), 860–865.
- [11] C. SPATOLA, G. PRIVITERA, L. RAFFAELE, V. SALAMONE, G. CUTTONE, P. CIRRONE, M. G. SABINI, S. LO NIGRO: *Clinical application of protons beams in the treatment of uveal melanoma: the first therapies carried out in Italy and preliminary results (CATANA project)*. Tumori, *89* (2003), 502–509.
- [12] R. R. WILSON: *Radiological use of fast protons*. Radiology, *47* (1946), 487–491.
- [13] S. BULANOV, V. KHOROSHKOV: *Feasibility of using laser ion accelerators proton therapy*. Plasma Physics Reports, *28* (2002), 493–496.
- [14] E. FOURKAL, B. SHAHINE, M. DING, J. S. LI, T. TAJIMA, C. M. MA: *Particle in cell simulation of laser-accelerated proton beams for radiation therapy*. Medical physics, *29* (2003), 2788–2798.
- [15] S. J. GITOMER, R. D. JONES, F. BEGAY, A. W. EHLER, J. F. KEPHART, R. KRISTAL: *Fast ions and hot electrons in the laser-plasma interaction*. Phys. Fluids, *29* (1986), 2679.
- [16] B. M. HEGELICH, B. J. ALBRIGHT, J. COBBLE, K. FLIPPO, S. LETZRING, M. PAFETT, H. RUHL, J. SCHREIBER, R. K. SCHULZE, J. C. FERNÁNDEZ: *Laser acceleration of quasi-monoenergetic MeV ion beams*. Nature, *439* (2006), 441–444.

- [17] J. FUCHS, Y. SENTOKU, S. KARSCH, J. COBBLE, P. AUDEBERT, A. KEMP, A. NI-KROO, P. ANTICI, E. BRAMBRINK, A. BLAZEVIC, E. M. CAMPBELL, J. C. FERNÁNDEZ, J.-C. GAUTHIER, M. GEISSEL, M. HEGELICH, H. PÉPIN, H. POPESCU, N. RENARD-LEGALLOUDEC, M. ROTH, J. SCHREIBER, R. STEPHENS, T. E. COWAN: *Comparison of laser ion acceleration from the front and rear surfaces of thin foils*. Phys. Rev. Lett., *94* (2005), 045004.
- [18] L. ROBSON, P. T. SIMPSON, R. J. CLARKE, K. W. D. LEDINGHAM, F. LINDAU, O. LUNDH, T. MCCANNY, P. MORA, D. NEELY, C.-G. WAHLSTRÖM, M. ZEPF, P. MCKENNA: *Scaling of proton acceleration driven by petawatt-laser-plasma interactions*. Nat. Phys., *3* (2007), 58–62.

Received June 3, 2010

Nanocrystalline diamond/amorphous composite carbon films prepared by plasma chemical vapor deposition¹

JOZEF HURAN², NIKOLAY I. BALALYKIN³,
GRIGORY D. SHIRKOV³, ALEXANDER P. KOBZEV³,
ALBÍN VALOVIČ²

Abstract. Nanocrystalline diamond/amorphous composite carbon films were deposited by plasma enhanced chemical vapour deposition method. The concentration of species in the films were determined by RBS (Rutherford backscattering spectrometry) and ERD (elastic recoil detection) methods. The RBS results showed the main concentrations of C in the films. The concentration of hydrogen was approximately 20 at.%. Chemical compositions were analyzed by FTIR spectroscopy. IR results showed the presence of C–H specific bonds. Film was used for photocathode application. The original quantum efficiency of prepared photocathode at energy of FH 15.6 mJ was 1.43×10^{-6} %.

Key Words. Plasma deposition, nanocrystalline diamond, amorphous carbon, photocathode.

1. Introduction

Nanocrystalline diamond, ultrananocrystalline diamond or amorphous carbon embedded NCD (NCD/a-C) films, have advantages of having higher surface flatness, high hardness, high wear resistance, high thermal conductivity, low friction coefficient, high electrical resistance, high optical transparency,

¹This research has been supported by the Slovak Research and Development Agency under the contracts APVV-0713-07 and APVV-0459-06 and by the Scientific Grant Agency of the Ministry of Education of the Slovakia and Slovak Academy of Sciences, No. 2/0192/10.

²Institute of Electrical Engineering, Slovak Academy of Sciences, Dúbravská cesta 9, Bratislava, 841 04, Slovakia

³Joint Institute for Nuclear Research, Dubna, 141980, Russia

high electron emission efficiency and excellent chemical inertness. The properties of deposited films are generally characterized by powerful ex-situ techniques that are commonly available, for instance Scanning Electron Microscopy (SEM), Atomic Force Microscopy (AFM), Transmission Electron Microscopy (TEM), Raman spectroscopy or X-ray Diffraction (XRD). Diamond films have been extensively investigated in field electron emission (FEE) [1], [2]. J. E. Yater et al. showed that grains may impede electron transport in diamond films and argued that the reduction of grain sizes is important for diamond film to be used as a cold cathode electron source [3]. This mechanism is actually similar as recently proposed conduction channel model, in which the grain boundary area can act as electron conduction channel in diamond field electron emission. In the electron conduction model, the diamond grain boundary plays the main role, as grain boundaries of diamond film consist of sp^2 phase. The sp^2 -bonded regions are of low electrical resistivity and act as an electron transport path, which facilitates the field electron emission. The plasma was electrically studied by a Langmuir probe in PECVD system [4]. There are several carbon-based photo cathodes, like polycrystalline diamond, hydrogenated amorphous carbon and nanostructured fullerene films. Polycrystalline diamond photocathodes are chemically inert, have a high damage threshold but also a low QE of 10^{-6} . Hydrogenated diamond photocathodes have the highest QE 's of 8×10^{-4} for 213 nm wavelength, but have low damage threshold and become oxidized after irradiation.

In this study, we investigated properties of nanocrystalline diamond/amorphous composite carbon (NCD/a-C) films prepared by plasma enhanced chemical vapour deposition (PECVD) for photocathode application. The properties of films were investigated by RBS, ERD and IR measurement techniques. Property of prepared photocathode was performed by measurement of quantum efficiency.

2. Experiments

The methane was introduced into capacitively coupled plasma reactor through the shower head, which is also an upper electrode with 20 cm diameter. Gas was flown vertically toward the substrate on bottom electrode connected with RF power 100 W and frequency 13.56 MHz. A p-type silicon wafer with resistivity $2 \div 7 \Omega\text{cm}$ and (100) orientation was used as the substrate for the carbon films. Prior to deposition, standard cleaning was used to remove impurities from the silicon surface, and the 5% hydrofluoric acid was used to remove the native oxide on the wafer surface. The wafer was then rinsed in deionized water and dried in nitrogen ambient. The flow rate of CH_4 gas was 40 sccm. The deposition temperature was for sample P1 – 400 °C and P2 – 500 °C. Spectroscopic ellipsometry was used for film thickness measurements

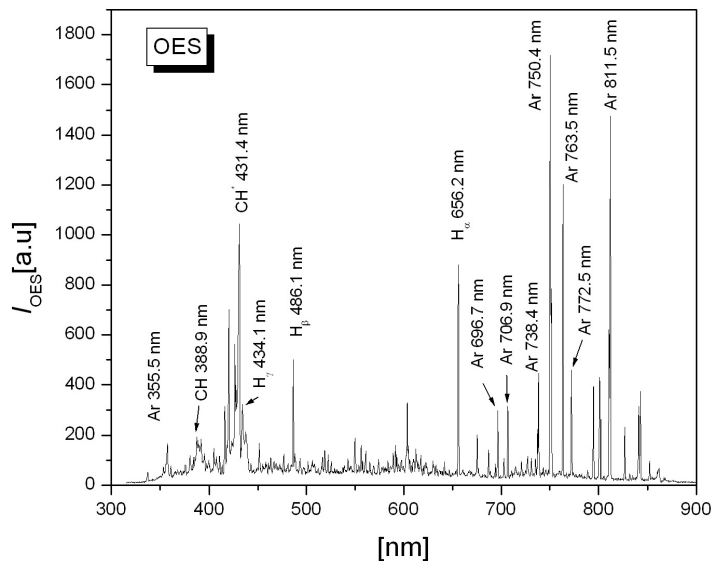


Fig. 1. Optical emission spectrum of CH₄ glow discharge at 10 Pa with small amount of Ar for actinometry method

and results are: for samples P1 – 315 nm and P2 – 325 nm. The concentration of species in the carbon films was determined by Rutherford backscattering spectrometry (RBS). Chemical compositions were analyzed by infrared spectroscopy. The IR spectra were measured from 4000 to 400 cm^{-1} . The hydrogen concentration was determined by the elastic recoil detection (ERD) method. For this purpose the $^4\text{He}^+$ ion beam from a Van de Graaff accelerator at JINR Dubna was applied. The energy of $E = 2.3 \text{ MeV}$ was chosen. The target was tilted at an angle $\alpha = 15^\circ$ with respect to the beam direction and the recoiled protons were measured in forward direction at an angle $\theta_1 (30^\circ)$ by a surface barrier detector. The quantum efficiency (QE) testing of prepared photocathode was performed at JINR. At one side of the cathode test facility vacuum chamber a fused silica window is mounted that transmits UV light. The vacuum condition was 4×10^{-9} mbar. The 15 ns UV laser pulses (quadrupled Nd:YAG laser) are used to illuminate the (NCD/a-C) film as photocathode. Laser spot size 5 mm. During testing, the laser energy was monitored using a calibrated portion of the signal that was picked off from the main beam. To draw the electrons from the cathode a positive voltage was placed on the anode-extractor. This voltage was kept at roughly 5 kV. The photocathode current is measured by using an oscilloscope.

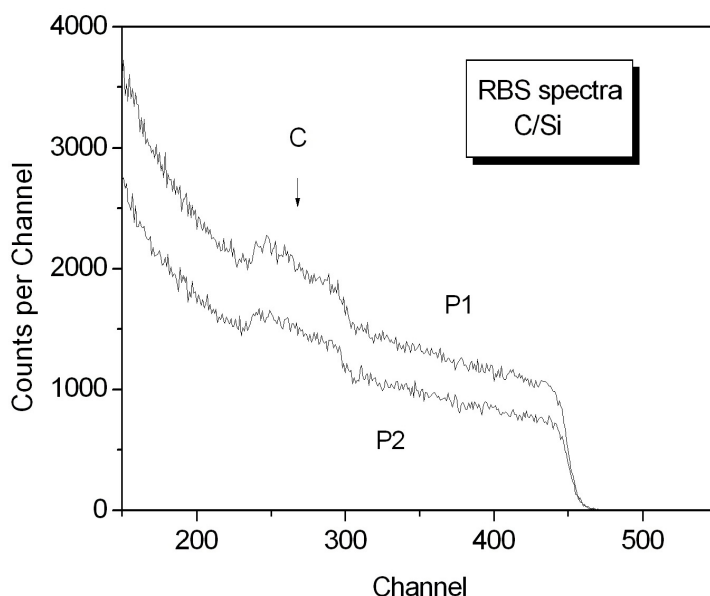


Fig. 2. RBS spectra of (NCD/a-C) films deposited onto a silicon substrate for 2 MeV alpha particles detected at scattering angle of 135° ; the spectra are for samples P1 and P2

3. Results and discussion

An example of plasma optical emission spectrum generated by a CH_4 glow discharge is shown in Fig. 1. By using OES the $\text{CH}(X^2\Pi)$ radical number density using actinometry method and plasma composition are determined.

Figure 2 show RBS spectra of two samples P1 and P2 with different deposition conditions of the deposited carbon films. The (NCD/a-C) films contained C, H and also other species which were under the detection limit of RBS method.

In Fig. 3 are plotted ERD spectra obtained from the deposited layers which contain different amounts of incorporated hydrogen. From ERD measurement, it follows that the concentration of hydrogen in thin films depends on the deposition conditions. ERD analyses made on prepared layers show that amount of incorporated H was decreased from 21 at.% to 17 at.% with increasing of deposition temperature. The values were obtained by computer modeling of measured spectra [5] and compared with the results obtained from the Si reference sample implanted with H. In the case of sample P1 the concentration of hydrogen and carbon are 21 and 75 at.% respectively. The concentrations of H

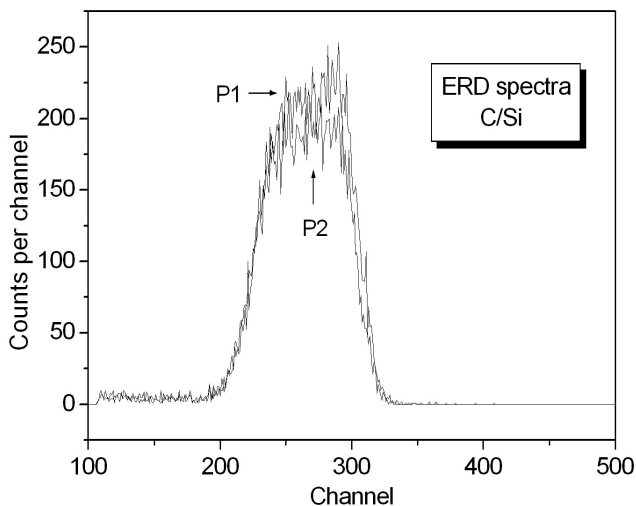


Fig. 3. The ERD spectra of recoiled hydrogen obtained with 2.3 MeV $^4\text{He}^+$; the spectra were measured on (NCD/a-C) films deposited at different temperature

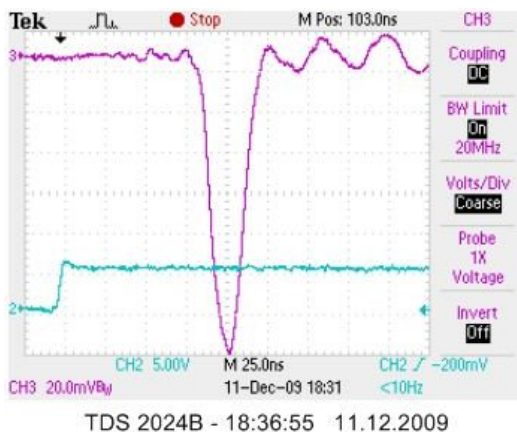


Fig. 4. The (NCD/a-C) photocathode current pulse—red line

and C in sample P2 are 17 and 77 at.% respectively. The FTIR spectra revealed the main absorption region between $1200 \div 1600 \text{ cm}^{-1}$ and $2800 \div 3150 \text{ cm}^{-1}$.

The most important result is that the sp^3 hybridization is stronger in the sample deposited at higher temperatures. At lower wave numbers for the low temperature sample the sp^2 CH olefinic related peak is more pronounced

compared to the high temperature case. For both samples beside the sp^3 bonds sp^2 and graphite like related peaks can be assigned.

The photocathode current is measured by using an oscilloscope as a voltage on resistance $47\ \Omega$, see Fig. 4. QE is defined as ratio of numbers of emitted electrons and injected laser photons. QE in % is expressed with the conventional parameters as $QE [\%] = 123.8 I/\lambda P$, where I is emitted current of the electron beam in mA, λ is wave length of the laser light in nm, P is power of the laser light in Watt. In our case: $I = 3.19$ mA; $\lambda = 266$ nm; $P = 1.04$ MW. The original quantum efficiency at energy of FH 15.6 mJ had been 1.43×10^{-6} %.

4. Conclusion

The RBS results showed that the concentration of C in the films dependent a little on the deposition temperature. The films contain a small amount of oxygen and nitrogen. The concentration of hydrogen dependent on deposition temperature and increases from 17 to 24 at.% with decreasing of deposition temperature. The results presented above demonstrate that 2.3 MeV $^4\text{He}^+$ ERD analyses may be successfully used to measure the hydrogen concentration. FTIR results showed the presence of C–H specific bonds. The original quantum efficiency of prepared photocathode at energy of FH 15.6 mJ was 1.43×10^{-6} %.

References

- [1] X. LU, Q. YANG, C. XIAO, A. HIROSE: *Field electron emission characteristics of chemical vapour deposition diamond films with controlled sp^2 phase concentration*. Thin Solid Films, 516 (2008), 4217–4221.
- [2] P. M. KOINKAR, P. P. PATIL, M. A. MORE, V. N. TONDARE, D. S. JOAG: *Field emission studies of CVD diamond thin films: effect of acid treatment*. Vacuum, 72 (2004), 321–326.
- [3] J. E. YATER, A. SHIH, J. E. BUTLER, P. E. PEHRSSON: *Transmission of low-energy electrons in boron-doped nanocrystalline diamond films*. J. Appl. Phys., 93 (2003), 3082–3089.
- [4] C. CORBELLA, M. C. POLO, G. ONCINS, E. PASCUAL, J. L. ANDÚJAR, E. BERTRAN: *Time-resolved electrical measurement of a pulsed-dc methane discharge used in diamond like carbon films production*. Thin Solid Films, 482 (2005), 172–176.
- [5] <http://www.rzg.mpg.de/~mam/index.html>, Program “SIMRA”, April 2010.

Received May 18, 2010

Investigation of the influence of the discharge chamber ‘loading’ effect on the optical characteristics of resonator type microwave plasmatron

SIARHEI BORDUSAU¹, SIARHEI MADVEIKA¹

Abstract. The investigation data of the influence of the material, quantity and volume of plasma chemical processing objects on plasma formation in a discharge chamber of a microwave plasmatron are presented. The experiments are carried out in a microwave plasmatron with the applicator in the form of a rectangular cavity where resonant volume is partially filled with plasma. The plates of monocrystalline silicon, sital and stainless steel are processing objects. Plasma diagnostics was carried out using such methods as optical emission spectroscopy and registration of integral optical luminosity of microwave discharge. The experimental results indicate that the microwave power magnitude expended on the initiation and maintenance of the discharge depends on the number of silicon plates in the processing zone. This effect can be explained both by a partial absorbing of microwave power plate material which has a high dielectric loss tangent, resonator Q-factor change and conditions of matching a discharge region with a waveguide tract.

Key Words. Plasma, microwave plasmatron, ‘loading’ effect.

Introduction

Recently microwave discharge (the so called microwave plasma) has found wider application in the production of electronic devices. Nonequilibrium plasma of microwave discharge enables plasmochemical processes at low gas temperature, but at higher electrons’ temperature. Such peculiarities of plasma microwave generators as the absence of electrodes, the possibility of using the mode when the load does not affect the operation of microwave plasma generator, highly efficient conversion of industrial frequency current into microwave current stipulate researchers and practitioners close attention to them [1]–[3].

¹Belarusian State University of Informatics and Radioelectronics, Belarus, Minsk;
e-mail: bordusov@bsuir.by.

Thus, the investigation of technological processes of treating materials with microwave discharge as well as the influence of the objects being treated (materials, volume, shape and surface dimensions etc.) on the electric, physical and chemical properties of plasma are of great interest.

Physical-chemical peculiarities of microwave discharges and their difference from direct current and HF-E or HF-H discharges as well as the peculiarities of electromagnetic microwave-range waves interaction with plasma and a solid body do not allow to evaluate univocally the relationships and peculiarities of processes in gas plasma bulk and on the surfaces of the materials under treatment on the base of information about elementary processes in high frequency discharges studied deeper and widely used in modern technology.

Particularly, what concerns the technology of electronic engineering products, the investigation of the influence of the amount and the material of the treated objects placed in the area of plasma formation on the excitation and maintaining of the microwave discharge (the so called 'loading' effect) is of great interest.

Method of experiment

The investigation of the influence of the material, its amount and the volume of the samples placed in the microwave plasmatron discharge chamber on the plasma formation process was carried out using the methods of optical emission spectroscopy and registering integral optical luminosity of microwave discharge.

The choice of investigation methods is explained by the following reasons.

Local electrophysical properties of gas discharge are known to determine the local optical emission capability of elementary plasma volume [4].

In this case, the optical emission intensity of the excited particle I_{X^*} in stationary state may be presented as [5]

$$I_{X^*} = C \cdot k_e \cdot n_e \cdot [X]$$

where

C – constant coefficient;

k_e – constant value of the excitation speed by direct electron impact;

n_e – electron concentration;

$[X]$ – density of particles with lower energy level.

This expression shows that the optical emission intensity of the particle in an excited state depends on the concentration of electrons and the electrons energy distribution function which in their turn are determined by discharge conditions (the energy input to discharge, relationship of electrical field strength to vacuum value and others).

Thus, the intensity of a separate line of optical emission spectrum as well as integral optical luminosity of discharge plasma enable us to judge about the extent of influence of the objects under treatment on the parameters and plasma characteristics (in particular, on the value of microwave power dissipated into microwave discharge).

Plasma discharge was initiated in a cylindric vacuum quartz reactor-tube having the external diameter 200 mm and the length 310 mm placed in the centre of a rectangular resonator with internal dimensions $345 \times 250 \times 380$ mm along the longitudinal sides of the resonator. Microwave energy got into the resonator through the rectangular connection hole placed with its long side along resonant walls parallel to the quartz reactor-tube's axis.

Atmospheric air at the pressure 46 Pa and 106 Pa continuously pumped through the quartz chamber was used as the working gas in the plasmatron chamber.

In the first group, the objects under treatment were varying in number $\varnothing 76$ mm and 0.3 mm thick monocrystalline silicon plates (from 1 to 12 pcs.); in the second group – various number of sitall rectangular plates having the dimension 60×48 mm and 0.6 mm thick; in the third – various number of stainless steel plates (from 1 to 12 pcs.) of $\varnothing 76$ mm and 0.5 mm thick; in the fourth group – monocrystalline silicon plates of $\varnothing 76$ mm of various thickness (0.9 mm; 1.9 mm; 3.9 mm; 7.9 mm; 12.4 mm). The plates were placed along the air inleakage.

Spectral investigation was carried out using a photoelectric system based on SL 40-2-2048 ISA spectrometer. The spectrometer has wide working spectral range ($200 \div 1100$ nm) and a sufficient resolution (0.2 nm). The programme for visual display and spectra registration enables not only detailed comparing up to three spectra simultaneously but registering of temporary dependencies of characteristic elements of emission spectra (atomic lines, molecular bands) during plasmochemical processes as well as working at the algorithm of operative spectrum control.

Photoelectronic multiplexer FEM-112 was used as a sensor for registering plasma integral luminosity. Signals from FEM-112 sensor were fed to ADC PC through an amplifier. Besides, during the experiment, signals of magnetron's anode current and from microwave emission detector were fed to the ADC PC. The experiments were carried out with magnetron working at plasma and active load.

Results and their discussion

The characteristic lines and bands were defined on the base of the registered air discharge spectra data.

Investigating the influence of plasma formation modes on the peculiarities of plasma microwave discharge spectrum components specific character of 'loading' effect while working with silicon plates was identified.

Spectral investigation of O ($\lambda = 777.46$ nm) emission line of microwave discharge in the air in rectangular resonator plasmotron revealed high dependence of their intensity on the number of silicon plates (Fig. 1a) as well as their thickness (Fig. 2).

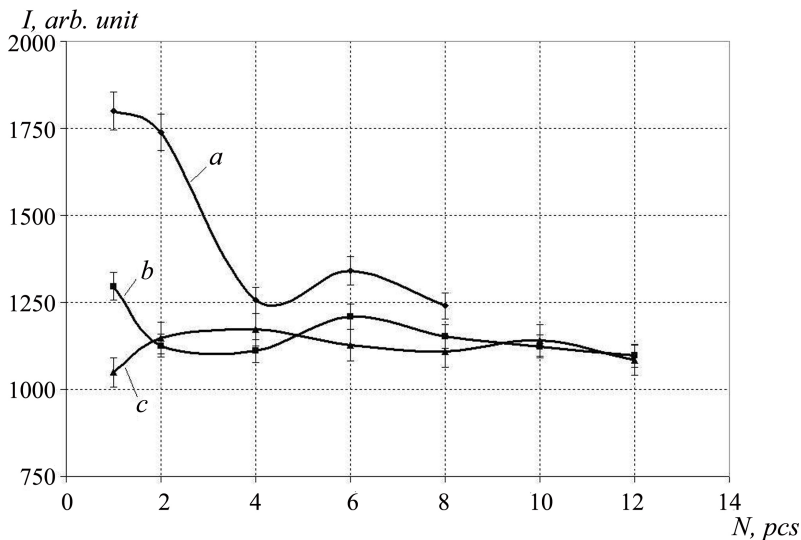


Fig. 1. Character of O ($\lambda = 777.46$ nm) spectrum line of microwave discharge in atmospheric air (46 Pa) depending on the number of monocrystalline silicon plates in the discharge zone: *a* – silicon plates with $\varnothing 76$ mm and 0.3 mm thickness; *b* – silicon plates with the dimensions 60×48 mm and 0.6 mm thickness; *c* – steel plates with $\varnothing 76$ mm and 0.5 mm thickness

Figure 1 shows the data obtained during the experiment with 1–12 monocrystalline silicon plates having the thickness 0.3 mm and the diameter 76 mm placed into the chamber. Figure 2 shows the data obtained during the experiment with silicon monocrystalline plates having the thickness from 0.9 mm till 12.4 mm and the $\varnothing 76$ mm placed into the chamber by one. The experiments were carried out at the pressure 46 Pa in the plasmatron chamber. The same type of dependencies was obtained at the pressure 106 Pa as well.

The emission intensity decrease of line O ($\lambda = 777.46$ nm) dependency (*a*) in Fig. 1 may be explained by a partial absorption of microwave power input into

the area of plasma formation by the material of monocrystalline silicon plates which has high tangent value of dielectric losses [6] and is used as a power absorber in microwave devices [7]. When monocrystalline silicon plates are treated in the plasma of high frequency discharge this effect does not manifest itself because of low absorption of high frequency field power by silicon.

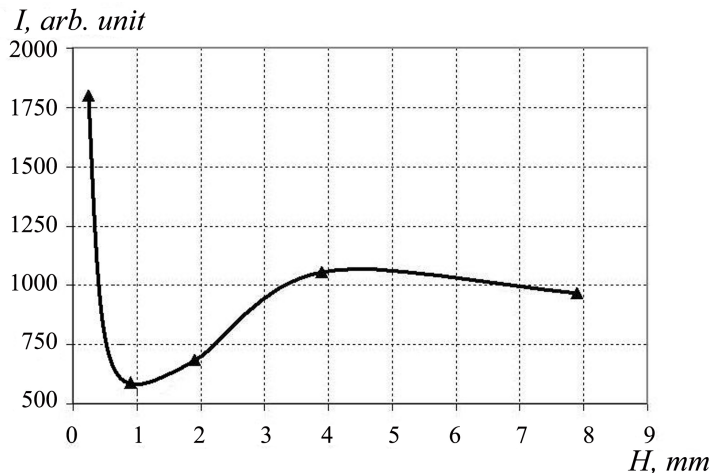


Fig. 2. Character of O ($\lambda = 777.46$ nm) spectrum line of microwave discharge in atmospheric air (46 Pa) depending on the thickness of the monocrystalline silicon plates placed in the discharge zone

It is proved by the behaviour of dependencies (b) and (c) in Fig. 1 obtained for samples not absorbing microwave energy (sital and stainless steel).

Putting into the chamber the materials slightly absorbing microwave energy does not lead to a significant change of spectral lines and bands (Fig. 1b, c). The observed slight changes in their intensity are determined by the loss of microwave discharge plasma particles on the surface of dielectric and metal plates, multiple reflection of microwaves in plasma volume that leads to discharge parameters change, as well as by exchange processes on the surface of 'ionized gas–solid' boundary.

The fact that the prevailing effect causing the decrease of light emission intensity of spectral line in case of microwave plasma is namely the absorption of microwave energy but not the loss of plasma particles on the surface of samples as in high frequency discharge [8], is revealed by the data given in Fig. 2. We explain the deeper collapse on the initial portion of the dependency (Fig. 2) by changed conditions of matching of the discharge area with waveguide when solid objects are put into plasma [9], [10].

It was also found that in certain modes of plasma formation the excess in the number of silicon plates of a certain amount results in discharge instability and

even in its extinction. In our opinion, it happens because of the fact that microwave field in case of presence in plasma volume of materials characterised by high dielectric losses interact with them causing decrease of microwave power input into the discharge.

The experiments on the analysis of the single signals registered with the help of photoelectronic multiplier did not enable establishing the tendency of gas discharge integral optical emission change because of the fact that the form and amplitude of microwave discharge plasma integral optical emission pulses in air atmosphere (as it is shown in Fig. 3) are greatly scattered. The analysis of the experimental data shows that the values of amplitudes of pulses of integral optical glow are scattered within $\pm 20\%$ range of the average signal amplitude.

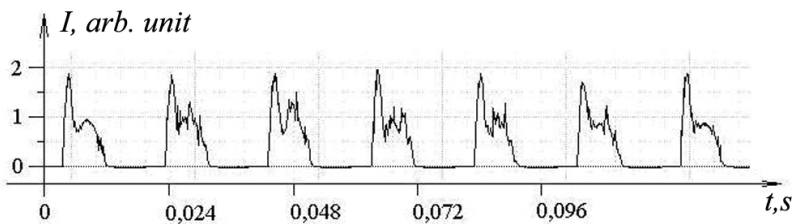


Fig. 3. The shape of microwave discharge plasma optical emission pulses in air atmosphere

Conclusions

The analysis of experimental results enables making the conclusion that during microwave plasma treatment the value of microwave power consumed for maintaining the discharge depends on the number of monocrystalline silicon plates present in the zone of treatment. This effect may be explained by partial absorbing microwave power by the material of the plates having high dielectric loss tangent, resonator Q-factor change and conditions of matching a discharge region with a waveguide tract.

Also it was found out that the increase of the number of silicon plates may lead to high discharge instability and even to its extinction.

References

- [1] S. V. BORDUSOV: Microwave plasma technologies in the production of electronic devices. Bestprint, Minsk 2002.
- [2] <http://iopscience.iop.org/0963-0252/>, Plasma Sources Science and Technology, April 01, 2010.

- [3] <http://jjap.ipap.jp/>, Japanese Journal of Applied Physics, April 01, 2010.
- [4] K. K. NAMITOKOV, P. L. PAKHOMOV, S. N. KHARIN: Emission of gas discharge plasma. Science, Alma-Ata 1984.
- [5] R. D'AGOSTINO, F. CRAMAROSSA, S. DE. BENEDICTIS: *Spectroscopic diagnostics of $CF_4 - O_2$ plasmas during Si and SiO_2 etching processes*. J. Appl. Phys., 52 (1981), 1259–1265.
- [6] E. ABOLTIN: *Semiconductors in the microwave electromagnetic and constant magnetic fields*. News of Latvian Academy of Sciences. Ser. Phis. and Technical Science, 5 (1972), 76–81.
- [7] M. I. BILKO, A. K. TOMASHEWSKI: Measurement of power at microwave frequencies. Radio and Communications, Moscow 1986.
- [8] H. KAWATA, T. SHIBANO, K. MURATA: *The relation between each rate and optical emission intensity in plasma etching*. J. Electrochem., 129 (1982), 1325–1329.
- [9] H. POTTS, J. HUGILL: *Studies of high-pressure, partially ionized plasma generated by 2.45 GHz microwaves*. Plasma Sources Sci. Technol., 9 (2000), 18–24.
- [10] S. I. MADVEYKO, S. V. BORDUSOV, A. P. DOSTANKO: *Investigation the plasma forming conditions in the discharge chamber of microwave plasmatron with resonator type applicator*. (S. A. Astapchik). PhTI National Academy of Sciences of Belarus, Minsk 2009, 56–57.

Received May 16, 2010

Nanocrystalline silicon carbide thin films prepared by plasma enhanced chemical vapor deposition¹

ALBÍN VALOVIČ², JOZEF HURAN², ALEXANDER P. KOBZEV³,
NIKOLAI I. BALALYKIN³, MICHAL KUČERA², ŠTEFAN HAŠČÍK²

Abstract. Nanocrystalline silicon carbide were prepared by PECVD technology in capacitively parallel plate plasma reactor, where both silane and methane were introduced into the plasma reactor. The concentration of species in the SiC films was determined by RBS and ERD. Chemical compositions were analyzed by IR spectroscopy. Film morphology was assessed by AFM. The RBS results showed the main concentrations of Si and C in the films. The concentration of hydrogen was approximately 20 at.%. IR results showed the presence of Si–C, Si–O, Si–N, Si–H, N–H, C–H, C–N specific bonds. Results of I–V measurements before and after samples irradiation by neutrons are presented.

Key Words. Plasma deposition, nanocrystalline silicon carbide, radiation hardness.

1. Introduction

The next generation of electronic devices may benefit from the development of alternatives to silicon and gallium arsenide based devices. The demands of higher power, radiation hardness, operating frequency, temperature and speed are potentially met by silicon carbide with additional attractive properties such as wide band gap, high breakdown field, high electron saturation velocity and physical strength [1]. In addition to high-temperature applications, SiC has potential for use in high-power and high-frequency [2]. However, SiC has several advantages over other wide-band gap semiconductors at the present time

¹This research has been supported by the Slovak Research and Development Agency under the contracts APVV-0713-07 and SK-UA-0011-09 and by the Scientific Grant Agency of the Ministry of Education of the Slovakia and Slovak Academy of Sciences, No. 2/0192/10.

²Institute of Electrical Engineering, Slovak Academy of Sciences, Dúbravská cesta 9, Bratislava, 841 04, Slovakia

³Joint Institute for Nuclear Research, Dubna, 141980, Russia

including commercial availability of substrates, known device processing techniques, and the ability to grow a thermal oxide for use as masks in processing, device passivation layers, and gate dielectrics. Furthermore, SiC can also be used as a thin buffer layer for the growth of diamond films on silicon substrates [3]. For example, a-Si_{1-x}C_x:H was used as a wide window material to enhance the conversion efficiency of amorphous solar cell. The significance of this material follows from the fact that its electrical and optical properties can be controlled by varying the carbon, silicon and hydrogen composition of the film. PECVD technique offers an attractive opportunity to fabricate amorphous hydrogenated N-doped SiC films at intermediate substrate temperatures and it provides high quality films with good adhesion, good coverage of complicated substrate shapes and high deposition rate [4]. Recently, Si-rich a-SiC_x:H films have attracted new attention in the photovoltaic community, since this material has shown excellent electronic surface passivation of c-Si comparable with thermal SiO₂ and low temperature amorphous silicon nitride (a-SiN_x) passivation [5].

In this contribution the attention has been focused to the properties of silicon carbide films prepared by the plasma enhanced chemical vapour deposition (PECVD) of silane SiH₄ and methane CH₄ and is continuation of our work in [6]. The structural properties were investigated by RBS, ERD, IR and XRD measurement techniques. Spectroscopic ellipsometry was used for optical characterization of the film. Electrical characterization was made by I-V measurement technique and radiation hardness was studied by neutron irradiation of samples.

2. Experimental

The silane and methane were introduced into capacitively coupled plasma reactor through the shower head, which is also an upper electrode with 20 cm diameter. Both gases were flown vertically toward the substrate on bottom electrode. A n-type silicon wafer with resistivity $2 \div 7 \Omega\text{cm}$ and (111) orientation was used as the substrate for the silicon carbide films. Prior to deposition, standard cleaning was used to remove impurities from the silicon surface, and the 5% hydrofluoric acid was used to remove the native oxide on the wafer surface. The wafer was then rinsed in deionized water and dried in nitrogen ambient. The flow rates of SiH₄ and CH₄ gases were 10 sccm and 40 sccm, respectively. The deposition temperature was 450 °C. The concentration of species in the SiC films was determined by Rutherford backscattering spectrometry (RBS). Chemical compositions were analyzed by infrared spectroscopy. The IR spectra were measured from 400 to 4000 cm⁻¹. The hydrogen concentration was determined by the elastic recoil detection (ERD) method. For this purpose the ⁴He⁺ ion beam from a Van de Graaff accelerator at JINR Dubna

was applied. The energy of $E = 2.3$ MeV was chosen. For the determination of the hydrogen concentration from the recoiled spectra a computer program has been used. In this program the effects of detector resolution, straggling, and multiple scattering of $^4\text{He}^+$ ions and protons in the target and stopper Al foil are included. These corrections improve essentially the agreement between experimental and simulated spectra. Film morphology was assessed by Atomic Force Microscopy. Irradiation of samples by fast neutrons in IREN facility at JINR Dubna was used for radiation hardness investigation. The thickness, refractive index and optical gap were determined by spectroscopic ellipsometry. For this purpose a SpecEl-200 spectroscopic ellipsometer ($400 \div 900$ nm) manufactured by Micropac, software Scout from Wolfgang Theiss and OJL model [7] was used. The electrical properties of nc-SiC:H films were determined by I-V measurement on diode structures.

3. Results and discussion

We prepared SiC film on Si substrate with thickness $580 \div 593$ nm, refractive index 2.72 and optical band gap $2.18 \div 2.22$ eV. These values were measured by spectroscopic ellipsometry. An example of plasma optical emission spectrum generated by an SiH_4 and CH_4 glow discharge is shown in Fig. 1.

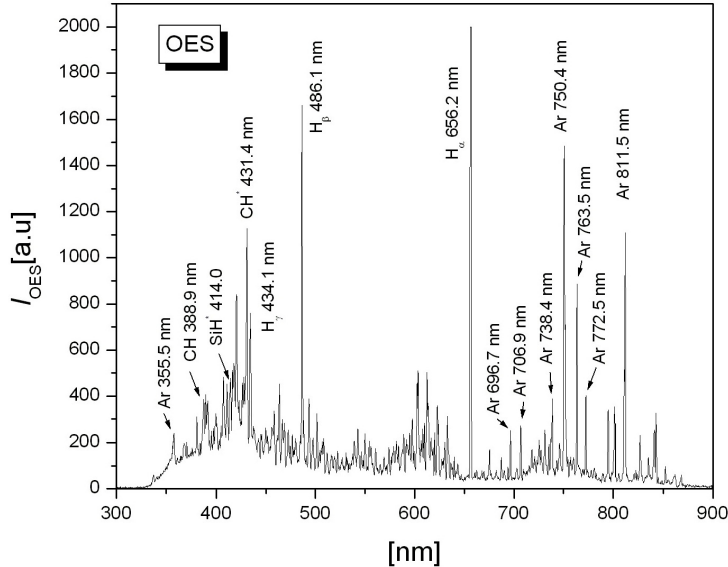


Fig. 1. Optical emission spectrum of SiH_4 and CH_4 glow discharge at 10 Pa with small amount of Ar for actinometry method

When fabricating nc-SiC:H film from SiH_4 and CH_4 , it is known that the $I(\text{CH}^*)$ and $I(\text{SiH}^*)$ ratio, $I(\text{CH}^*)/I(\text{SiH}^*)$, is in a proportional relationship to the ratio of the numbers of carbon and silicon atoms inside the film. The IR spectrum revealed the main absorption region between 400 and 2000 cm^{-1} is shown in Fig. 2. From the spectra we could determine the following vibration frequencies: 520 to 530 and 1090 to 1093 can be related to SiO_2 the higher wavenumber can be also related to Si–N bonds close to Si_3N_4 bonds; 944 to 950 and 1000 to 1005 : they can be roughly related to Si–N bonds from Si_3N_4 ; 1260 to 1265 : they can be related to C–N bonds; 606 to 610 : it can be related to Si–C localised vibration normally found in Si due to C in single crystalline Si. The main phonon or vibration frequency is related to SiC and have the following characteristics determined from the reflection spectra: center position 795 cm^{-1} , width 178 cm^{-1} ; center position 795 cm^{-1} , width 45 cm^{-1} ; center position 804 cm^{-1} , width 42 cm^{-1} . The non stressed phonon position of cubic SiC is 796 cm^{-1} .

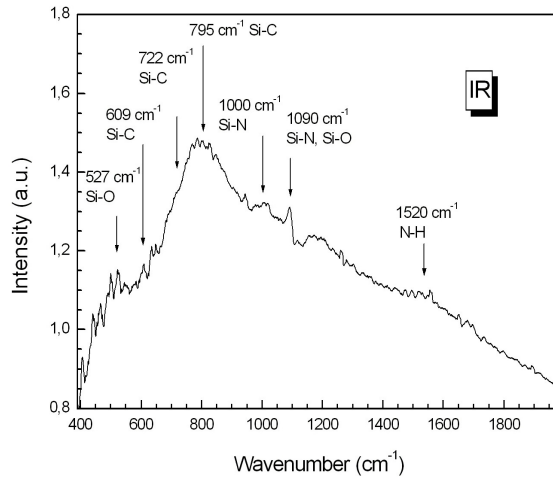


Fig. 2. IR spectrum of SiC films; main absorption region between 400 and 2000 cm^{-1}

In amorphous material a shift to higher values indicate on recrystallisation or nucleation of small crystallites. Figure 3 show RBS spectra of the deposited amorphous silicon carbide film. After modelling, we can show from calculated results the presence of small amounts of oxygen and nitrogen while the concentrations of hydrogen in the SiC film are approximately 20 at.%.

Both of the elements nitrogen and oxygen represent 2–4 at.% in the SiC film. The SiC film contained also other species which were under the detection limit of RBS method. The concentrations of Si and C in the SiC film are 32 and 35 at.% respectively.

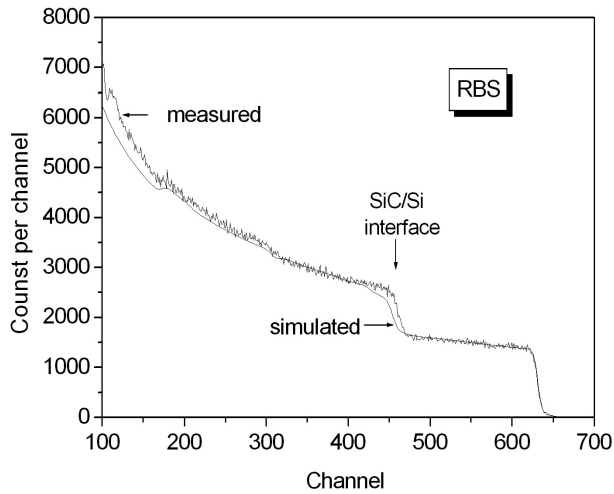


Fig. 3. RBS spectra of SiC film deposited onto a silicon substrate for 2.3 MeV alpha particles detected at scattering angle of 135° ; the spectra are for sample of SiC film with thickness 580–593 nm

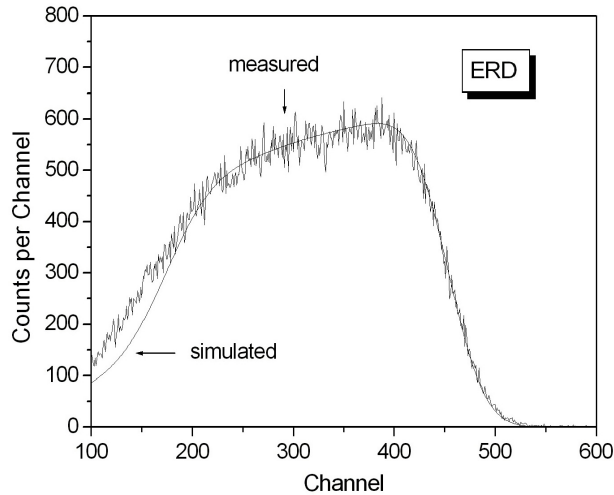


Fig. 4. ERD spectra of recoiled hydrogen obtained with 2.3 MeV $^4\text{He}^+$; the concentration of hydrogen was about 20 at. %

There was no evidence of the substrate mixing into the film. The ERD spectra are shown in Fig. 4. The AFM micrographs of the SiC films prepared by PECVD reveal that the film surface is rather smooth and compact. From the XRD measurement, we can determine only one type of SiC hexagonal polytype.

From I–V characteristics of prepared diode structures Au/SiC/Si/Al before irradiation by neutrons, Fig. 5, we can show, that the conductivity of the SiC layer prepared at 450 °C for sample is very small about 10^{-12} S for reverse current before irradiation. From I–V characteristics of structure Au/SiC/Si/Al for all Schottky contacts we observed dispersion in characteristics that is due to the inhomogeneity of SiC film parameters. At higher voltages, the current is limited by the series resistance due to ohmic contact and the bulk resistance of SiC layer. In Fig. 6 we can see I–V characteristics for diode structure Au/SiC/Si/Al after irradiation by neutrons with fluence of 5×10^{11} cm $^{-2}$. From measured I–V characteristics we can see difference before and after irradiation. It can be explained by the degradation of interface between top contact and film surface-increasing density of interface state. Change of forward current can be explained by change of bulk film properties after neutron irradiation.

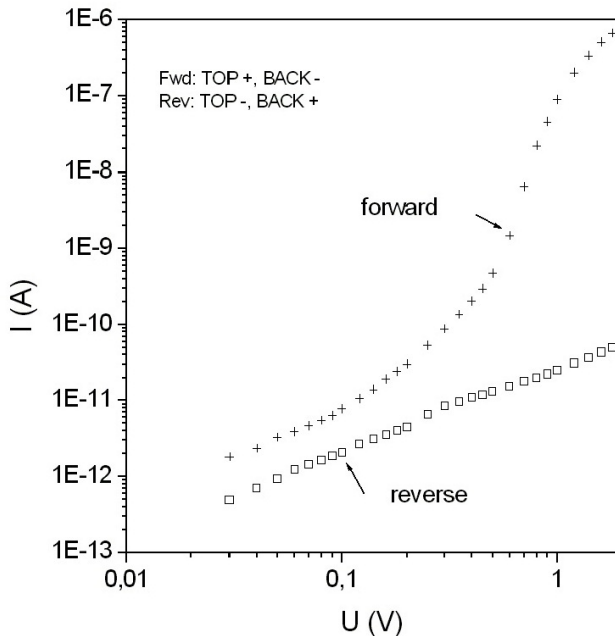


Fig. 5. I–V characteristics for diode structures Au/SiC/Si/Al with Au top contacts ($d = 1.2$ mm) on SiC film before irradiation by neutrons with fluence of 5×10^{11} cm $^{-2}$

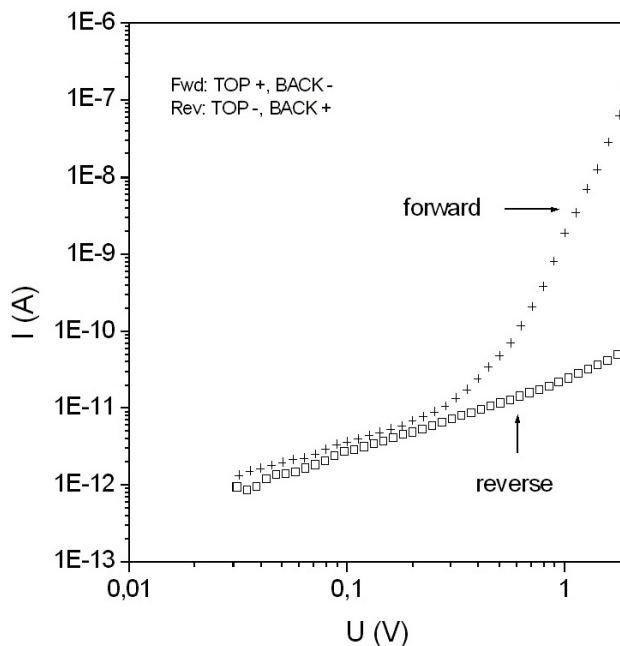


Fig. 6. I-V characteristics for diode structure Au/SiC/Si/Al with Au top contacts ($d = 1.2 \text{ } \mu\text{m}$) on SiC film after irradiation by neutrons with fluence of $5 \times 10^{11} \text{ cm}^{-2}$

4. Conclusion

We have investigated the structural and electrical properties of nc-SiC films prepared by plasma enhanced chemical vapor deposition at $450 \text{ }^\circ\text{C}$. The RBS results showed that the concentrations of Si and C in the films are practically the same. The concentration of hydrogen was determined by the ERD method and the value is approximately 20 at.%. The films contain a small amount of oxygen and nitrogen. IR results showed the presence of Si-C, Si-N, Si-H, C-H and Si-O bonds. From measured I-V characteristics we can see difference before and after irradiation at forward and reverse currents for diode structure.

References

- [1] H. MORKOC, S. STRITE, G. B. GAO, M. E. LIN, B. SVERDLOV, M. BURNS: *Large-band gap SiC, III-V nitride, and II-VI ZnSe-based semiconductor device technologies*. J. Appl. Phys., 76 (1994), 1363-1394.

- [2] H. ZHANG, Z. XU: *Structural and optical properties of four-hexagonal polytype nanocrystalline silicon carbide films deposited by plasma enhanced chemical vapour deposition technique*. Thin Solid Films, 446 (2004), 99–105.
- [3] E. G. WANG: *A model for buffer layer formed on silicon during HFCVD diamond growth*. Physica B, 185 (1993), 85–89.
- [4] H. COLDER, P. MARIE, L. PICHON, R. RIZK: *Hydrogenated nanocrystalline silicon carbide: fabrication, properties and heterostructure device application*. Phys. Stat. Sol. C, 1 (2004), 269–273.
- [5] M. VETTER, C. VOZ, R. FERRE, I. MARTIN, A. ORPELLA, J. PUIGDOLLERS, J. ANDREU, R. ALCUBILA: *Electronic properties of intrinsic and doped amorphous silicon carbide films*. Thin Solid Films, 511–512 (2006), 290–294.
- [6] J. HURAN, I. HOTOVY, J. PEZOLTD, N. I. BALALYKIN, A. P. KOBZEV: *Effect of deposition temperature on the properties of silicon carbide thin films*. Thin Solid Films, 515 (2006), 651–653.
- [7] S. K. O'LEARY, S. R. JOHNSON, P. K. LIM: *The relationship between the distribution of electronic states and the optical absorption spectrum of an amorphous semiconductor: An empirical analysis*. J. Appl. Phys., 82 (1997), 3334–3340.

Received May 18, 2010

Influence of deposition rate on optical properties of silicon-oxide thin films

DMITRIY A. GOLOSOV¹, SERGEY M. ZAVATSKIY¹,
SERGEY N. MELNIKOV¹, ZHU CHANG²,
MI GAOYUAN²

Abstract. The paper is focused on studying silicon oxide thin films deposited by the method of reactive ion-beam sputtering (RIBS) of Si targets in the environment of Ar/O₂ gas mixture without heating the substrates. The concentration of O₂ in the producer gas mixture varied from 0 up to 100 % under the total pressure of 0.01 ÷ 0.04 Pa in the chamber. The substrates were placed at a distance of 19 ÷ 24 cm from the target surface. The films were deposited at a rate of 0.1 ÷ 0.6 nm/s to reach the thickness of 0.15 ÷ 0.35 μm. The refractive index n , extinction coefficient k , and stoichiometric index were determined as functions of the oxygen concentration in Ar/O₂ gas mixture and deposition rate. Silicon oxide films characterized by the refractive index $n = 1.48$ and extinction coefficient less than 10^{-5} on the wavelength 0.63 μm were deposited with the RIBS method. The analysis of the IR transmission spectrum proved that all the deposited films did have oxygen deficiency and, judging by the position of the main absorption peak, the stoichiometric index of silicon oxide did not exceed 1.8. The dependence between IR adsorption peak position and refractive index of silicon oxide were established. It was found out that an increase in the deposition rate results in the growth of the refractive index and extinction coefficient of the film due to incomplete oxidation of silicon and formation of suboxides. In case when the deposition rate was more than 0.3 nm/s, even if sputtering was performed in pure oxygen atmosphere, the minimal value of refractive index had been more than 1.5.

Key Words. Silicon oxide, reactive ion-beam sputtering, optical constant, deposition rate.

¹Belarusian State University of Informatics and Radioelectronics, 6, P. Brovka, Minsk, 220013, Belarus, phone: +375-017-2-93-80-79; e-mail: svad@bsuir.by

²Xi'an Technological University, 4, Jinhua Road, Xi'an, 710032, China; e-mail: gdzhuchang@163.com

Introduction

For an extended period of time the silica films have been employed for production of multilayer optical filters and interference mirrors [1]. Traditionally high quality silica films are deposited on glass substrates by either electron-beam evaporation (EBE) or ion-assisted EBE (IAEBE) methods at high substrate temperatures (up to 300 °C) [2].

However in the recent years the demands for the processes that provide for deposition of component and multicomponent coatings on large-sized substrates including on flexible substrates, have sharply risen. The development of flexible electronics opens up new possibilities in applications of flat panel displays, solar cells, RFID tags, low cost sensors and other disposable electronics devices [3]. Aluminum foil or polymers are used as materials for flexible substrates. Due to a very low thermal stability of substrates, the temperature during the film deposition must not exceed 80 ÷ 120 °C (and must be preserved at a level of 70 ÷ 80 °C).

Silicon oxide films seem to be a good candidate to be used as barrier layer when transparent conducting oxides are deposited onto flexible polymer substrates. Barrier layers prevent interaction and degradation of the TCO layer. At the same time the barrier layer may be a center for crystallization to ensure polycrystalline structure of TCO without heating the substrate. Apart from that the application of the barrier layer permits to improve the plasticity and adhesion of the TCO film to the substrate, and optical properties of TCO owing to interference effects in the structure. For this purpose SiO₂ layers should have a low extinction coefficient, the refractive index constant process-to-process, high electrical resistance, adhesion to the substrate, a very flat surface, and flexibility.

All the above has caused an intense interest of the scientific community to the reactive sputtering (RS) methods [4]. The RS technologies enable forming films without heating the substrate and provide for the deposited multilayer optical structure improved adhesion characteristic. Absence of the substrate heating of make it possible to deposit films onto different types of substrates, including polymers. Excellent controllability of the ion sputtering process helps reaching the required optical parameters of layers with high accuracy, which is extremely important when depositing multilayer optical structures.

Earlier the authors have studied the optical characteristics of SiO₂ layers deposited by reactive ion-bema and reactive magnetron sputtering methods [5]–[7]. The RIBS method was proved to have good perspectives in what concerns forming of SiO₂ barrier layers. However the issue of how to increase the efficiency of the RIBS method through raising the deposition rate is still undecided.

Therefore the objective of this paper was to establish how the deposition rate can influence the optical characteristics of the silicon oxide layers in order

to determine choose appropriate process parameters for the reactive ion-beam sputtering for the purposes of industrial deposition of SiO_2 onto flexible polymer substrates.

1. Experimental

The schematic of the experimental facility for deposition of silicon oxide films by reactive ion-beam sputtering is shown in Fig. 1. The experimental facility was constructed on the basis of a vacuum unit Z-1200. The vacuum chamber of the experimental facility was equipped with a sputtering ion source (SIS) and a clearing ion source (CIS) based on the hall-current accelerator. One of the ion sources was used for ion cleaning of substrate surface, and the other one — for sputtering of the target material.

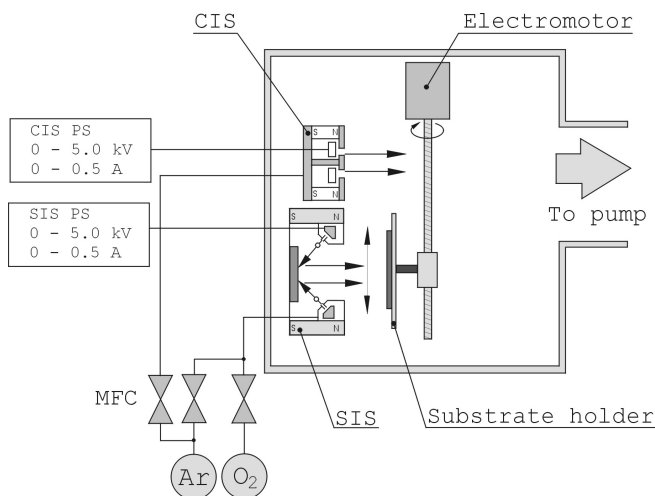


Fig. 1. The experimental facility schematics for RIBS deposition of silicon oxide films: CIS—clear ion source, SIS—sputtering ion source, PS—power supply unit; MFC—mass flow controller

Two-sided polished single-crystalline silicon Si (100) and optical glass BK7 were used as substrates. The substrates were placed on a removable substrate holder that made it possible to bring the substrates to the working zone of all kinds of ion-plasma sources. Ion cleaning of the substrates had been carried out before the deposition was started. The vacuum chamber was pumped down to the base pressure of 3×10^{-3} Pa. Ar was fed into the CIS up to the working pressure of 2.0×10^{-2} Pa. The cleaning time, ion energy, and discharge current in all the experiments were constant and equal to 3 min, 500 eV, 70 mA accordingly.

Silicon oxide films were deposited by the method of reactive ion-beam sputtering. Sputtering of a single-crystalline Si target having \varnothing 80 mm in diameter and 10 mm thick was performed by Ar^+/O_2^+ ions with the energy of $1000 \div 1300$ eV, generated by SIS. The flow of Ar/O_2 producer gases in the sputtering ion source was controlled with the mass flow controllers RRG-1. During the experiments the O_2 content in the producer gas mixture varied from 0 up to 100% under the overall pressure of $0.02 \div 0.04$ Pa in the chamber. The deposition time during all the experiments was constant and equal to 10 min. The film deposition rate was altered by changing the target-substrate distance and discharge current within $19 \div 24$ cm, and the SIS discharge current $100 \div 170$ mA. Depending on the deposition rate the film thickness varied within $150 \div 350$ nm.

The film thickness, dispersions of the refractive index and extinction coefficient in the $300 \div 1600$ nm wavelength were determined by the ellipsometry technique using the spectroscopic ellipsometer M2000UI, under 75° in the light angle. IR transmission spectra in the $400 \div 1400$ cm^{-1} range were determined by the FTIR spectrometer Vertex 70 Bruker Optik GmbH.

2. Results and discussion

The properties of silicon oxide films deposited by method of silicon target RIBS were studied. Dependences of the optical characteristic (n , k) of silicon-oxide films on the deposition rate and O_2 concentration in the Ar/O_2 gas mixture were obtained. Figures 2 and 3 illustrate the dispersion of the refractive index and extinction coefficient of the silicon oxide films deposited by the RIBS method.

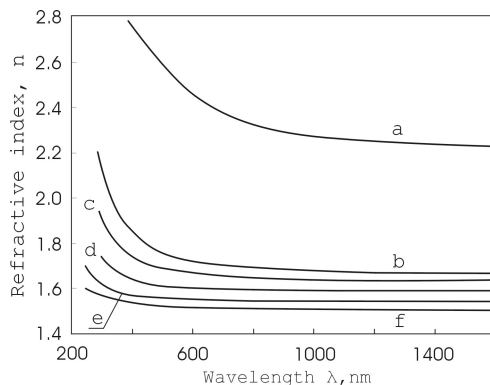


Fig. 2. Dispersion of the refractive index of silicon oxide films deposited by RIBS with different oxygen concentrations in the Ar/O_2 working gas mixture: a—46%, b—63%, c—73%, d—84%, e—91%, f—100%

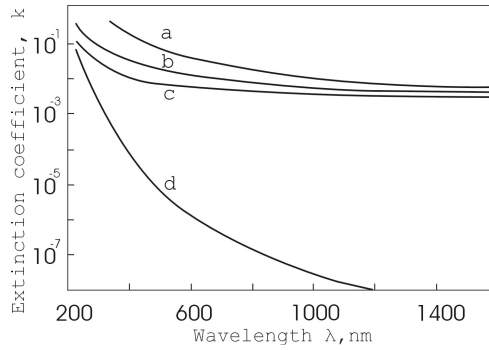


Fig. 3. Dispersion of the extinction coefficient of silicon oxide films deposited by RIBS with different oxygen concentrations in the Ar/O₂ working gas mixture: a—46 %, b—63 %, c—73 %, d—84 %

The films were deposited under the following process condition: the discharge voltage of SIS 4.5 kV, the discharge current 150 mA, and the deposition time 10 min. While changing the O₂ flow rate, we chose the Ar flow rate based on the requirement to maintain the discharge current constant. At the same time the average deposition rate was 0.6 nm/s.

Figure 4 shows the refractive index and extinction coefficient as functions of the wavelength 0.63 μm as functions of oxygen concentration in Ar/O₂ working gas mixture. The silicon oxide films with refractive index between $n = 1.52 \div 1.6$ and extinction coefficient less than 10^{-5} were deposited by the method of reactive ion-beam sputtering of a Si target. With the O₂ concentration greater than 84 %, the extinction coefficient was not recorded by the ellipsometer, for it had been lower than the susceptibility threshold of the instrument, which was 10^{-5} . The optical-quality silicon oxide films were deposited under the oxygen

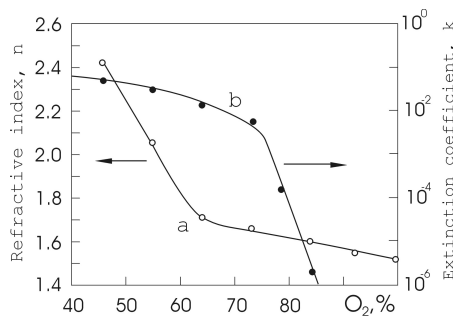


Fig. 4. Refractive index (curve a) and extinction coefficient (curve b) on a wavelength 0.63 μm of silicon oxide films deposited by RIBS method as a function of oxygen concentration in Ar/O₂ working gas mixture

concentration greater than 80% in the producer gas mixture. The refractive index was apt to decrease even at 100% of the O₂ concentration. It is worth mentioning that the method of RIBS with the deposition rate of 0.6 nm/s did not yield films with the refractive index close to that of fused silica ($n \approx 1.46$).

IR transmission spectra of samples were measured to estimate the stoichiometry of the deposited films. Figure 5a shows the IR transmission spectra of the silicon-oxide films deposited by RIBS at various O₂ concentrations in the producer gas mixture (the deposition rate of 0.6 nm/s).

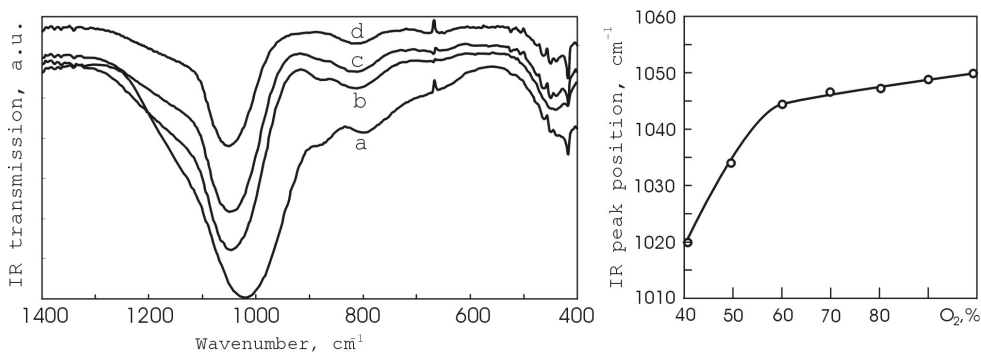


Fig. 5. IR transmission spectrums of silicon oxide thin films deposited by RIBS with different oxygen concentrations in the Ar/O₂ working gas mixture: a—40%, b—60%, c—80%, d—100% (a); the IR main absorption peak position as a function of the oxygen concentration in the Ar/O₂ working gas mixture (b)

In the range of $400 \div 1400 \text{ cm}^{-1}$ the silicon-oxide films were characterized by a typical absorption band with its maximum in the vicinity of 1100 cm^{-1} , corresponding to the valence symmetric vibration; and the absorption band in the vicinity of 450 cm^{-1} , corresponding to the deformation vibration of SiO₂. As the O₂ concentration was increasing the position of the main absorption peak maximum shifted to a high-frequency region from 1020 cm^{-1} to 1053 cm^{-1} (Fig. 5b). However the peak position, characteristic of vitreous quartz ($\sim 1085 \text{ cm}^{-1}$) was not reached even at 100% of the O₂ concentration. Since the displacement of the peak in the region with a greater wave-number was caused by a bond shortening [8], it may be assumed that the deposited films are a mixture of silicon oxides having different structures and a great number of broken bonds. The proportion of different structural entities of oxides defined the stoichiometry of the deposited films. The displacement of the absorption peak was caused by the oxygen deficiency [9], and the stoichiometric index of the deposited films did not exceed 1.8 [10].

The features of film deposition under lower sputtering rates were studied in order to increase the stoichiometric index of SiO₂ films. While doing so it was assumed that decreasing the silicon deposition rate would result in an increase of the exposure time of the reactive gas with silicon on the condensation

surface. The film deposition rate was changed through varying the substrate–target distance and the discharge current of the sputtering ion source. The substrate–target distance was varied within $19 \div 24$ cm, and the discharge current $100 \div 170$ mA. The curves of the refractive index for SiO₂ films as a function of the O₂ percentage in the producer gas mixture under various deposition rates are plotted in Fig. 6.

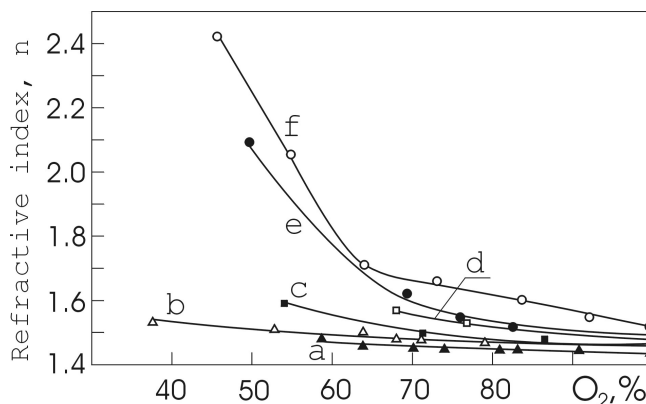


Fig. 6. Refractive index on a wavelength $0.63 \mu\text{m}$ of silicon oxide films as a function of the oxygen concentration in the Ar/O₂ working gas mixture at different deposition rate: a— 0.11 nm/s , b— 0.15 nm/s , c— 0.2 nm/s , d— 0.3 nm/s , e— 0.45 nm/s , f— 0.6 nm/s

The refractive index (ref. Fig. 7) was observed to drop down under continuous flow of the reactive gas and reducing deposition rate. When the deposition rate exceeds the value of 0.3 nm/s the refractive index for the deposited SiO₂ films did not drop below 1.5 even when the deposition was performed in the pure oxygen atmosphere. With the deposition rates below 0.2 nm/s and $50 \div 100\%$ of O₂ concentration in the gas mixture the refractive index practically showed no dependence on the reactive gas flow and was within $1.47 \div 1.5$. However when the O₂ flow was reduced the absorption coefficient was observed to grow up to 10^{-2} .

All the film samples obtained under diversified deposition rates were analyzed by the FRIT spectroscopy. It was established that regardless of the deposition process parameters the refractive index of the deposited layers had a direct relation to the IR absorption peak position (ref. Fig. 8). Thus judging by the IR absorption peak position the refractive index of the deposited SiO₂ layers can be estimated with a great extent of accuracy.

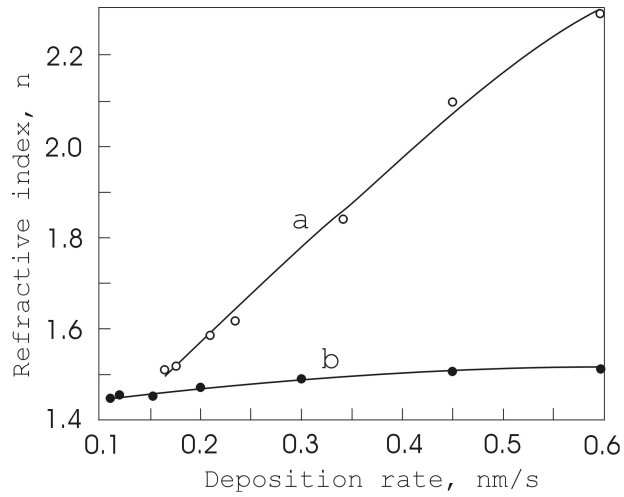


Fig. 7. Refractive index on a wavelength $0.63 \mu\text{m}$ of silicon oxide films as a function of the deposition rate at different oxygen concentration in the Ar/O₂ working gas mixture: a—50 % O₂, b—100 % O₂

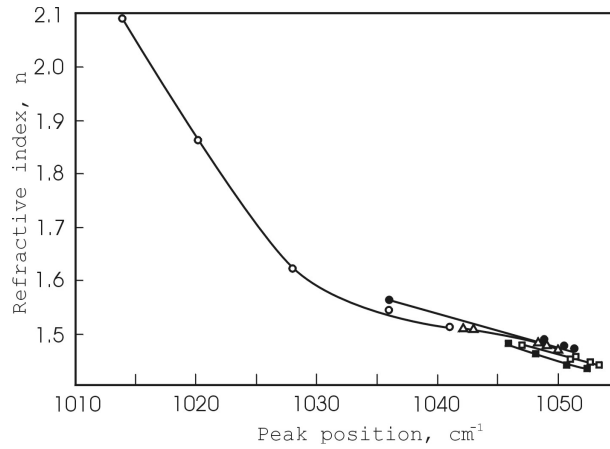


Fig. 8. Interdependence between refractive index and the main IR absorption peak position of silicon oxide films deposited at different deposition rate

Conclusion

The process of deposition of thin silicon-oxide films by the method of reactive ion-beam sputtering of a silicon target in the environment a mixture of the producer gas without heating the substrate was studied. The dependences of the refractive index n and the absorption coefficient k on the oxygen percentage in the Ar/O₂ producer gas mixture and the deposition rate were established.

Silicon oxide films characterized by the refractive index of $n = 1.47$ and absorption coefficient below 10^{-5} at the wavelength of $0.63 \mu\text{m}$ were obtained by the RIBS method. It was proved that an increase in the deposition rate results in the growth of the refractive index and the absorption coefficient owing to incomplete oxidation of the silicon and formation of sub-oxides. With the deposition rates over 0.3 nm/s the minimal value of the deposition rate was more than 1.5 even if the deposition had been performed in pure oxygen environment. The refractive index can be reduced through decreasing the deposition rate and/or increasing the oxygen concentration in the Ar/O₂ producer gas mixture.

Analysis of the IR transmission spectra proved, that all the deposited films have oxygen deficiency and, judging by the position of the main absorption peak, the stoichiometric index of the silicon oxide does not exceed 1.8. It has been also proved that there is a relation between the position of the IR absorption peak and the silicon refractive index.

References

- [1] P. J. MARTIN: *Review. Ion-based methods for optical thin film deposition*. J. Mater. Sci., 21 (1986), 1–25.
- [2] W. HEITMANN: *Reactive evaporation in ionized gases*. Appl. Opt., 10 (1971), 2414–2418.
- [3] *Flexible Display (Report)*. DisplaySearch, an NPD Group Company, 2006.
- [4] M. VARASI, C. MISIANO, L. LASAPONARA: *Deposition of optical thin films by ion-beam sputtering*. Thin Solid Films, 117 (1984), 163–172.
- [5] D. A. GOLOSOV, S. M. ZAVATSKIY, A. P. DOSTANKO, ZHU CHANG, JUNQI XI: *Optical properties of a silicon oxide thin films deposited by reactive magnetron sputtering method*. VI. International Conference Plasma physics and plasma technology: Contributed papers. Minsk 2009, 535–538.
- [6] D. A. GOLOSOV, S. M. ZAVATSKIY, A. P. DOSTANKO: *Properties of silicon oxide films deposited by methods of ion-beam and reactive ion-beam sputtering*. IV. International Conference Modern methods and technologies material formation and processing: Contributed papers. Minsk 2009, 81–86.
- [7] ZHU CHANG, MI GAOYUAN, A. P. DOSTANKO, D. A. GOLOSOV, S. M. ZAVATSKIY: *Comparison of reactive magnetron and reactive ion-beam sputtering methods for deposition of silicon oxide thin films*. Surface Technology, 31 (2010), 855–859.

- [8] F. GIUSTINO, A. PASQUARELLO: *Infrared spectra at surfaces and interfaces from first principles: evolution of the spectra across the Si(100)-SiO₂*. InterfacePhys. Rev. Lett., 95 (2005), 7402–7405.
- [9] N. TOMOZEIU, J. J. VAN HAPERT, E. E. VAN FAASSEN, W. ARNOLDBIK, A. M. VREDENBERG, F. H. P. M. HABRAKEN: *Structural properties of α -SiO_x layers deposited by reactive sputtering technique*. J. Optoel. and Advanced Mater., 4 (2002), 513–521.
- [10] N. TOMOZEIU: *SiO_x thin films deposited by r.f. magnetron reactive sputtering: structural properties designed by deposition conditions*. J. Optoel. and Advanced Mater., 8 (2006), 769–775.

Received May 19, 2010

Plasma spheroidization process of refractory metal powders¹

MARCIN LIS², MIECZYŚLAW WOCH²

Abstract. Because of the need to use spherical powders in many powder metallurgy technologies an investigation was carried out into spheroidization process of the powders of tungsten, molybdenum and rhenium obtained by plasma spraying technique. An effect of electrical parameters of the plasma arc (current, voltage), powder morphology, grain size and feeding rate, as well as of plasma stream temperature on powder spheroidization process was investigated. In the paper results of morphology examination and of the analysis of powder particles size distribution for the studied metals have been presented in dependence on starting powder characteristics and on atomization process parameters. Optimal process parameters ensuring maximum yield of spherical powder fraction were chosen for each studied metal. Taking tungsten as an example it was demonstrated that the plasma spraying technique leads to the increase in metal's chemical purity.

Key Words. Plasma technology, powder metallurgy, spheroidization, high-melting metals.

1. Introduction

The plasma technologies have become widely used in powder metallurgy for preparation of anticorrosive coatings, thermal barrier coatings and hardening layers by means of plasma spraying technique. They are also applied for synthesis or thermal decomposition of various bulk and powder materials. One of the areas of their application is transformation of the powders aimed at changing dimensions, morphology or shape of powder particles, e.g. to the spherical form. The spherical powders are suitable for many applications due to their high flowability, which is beneficial in fabrication of high-volume powder products since it influences the rate and homogeneity of filling the die during pressing [1]. The spherical shape of particles is also of great importance in

¹This work has been supported by the Ministry of Science and Higher Education under the Targeted Project No PBZ-MNiSW-3/3/2006.

²Institute of Non-ferrous Metals, Gliwice, Poland

case of powders and pastes used for soldering because it ensures homogeneous flowability of that powder or paste during the soldering process [2]. Spherical powders are also applied in jet moulding processes, where spherical shape of particles facilitates formation of a uniform mixture with the binding agent. Good flowability of spherical powders used in the processes of thermal spraying and surfacing enables uniform supply of the powder from the feeder to the plasma flame thus ensuring uniform thickness of the formed coating. Moreover, the coatings obtained by spherical powder spraying are characterised by higher density and better microstructure compared to the coatings prepared with the use of powders irregular in shape [3]. The possibility of getting powders with a uniform, spherical shape from the plasma spraying process depends on the type of the material, its melting temperature, morphology and grain size, type of plasma-generating gas and current–voltage characteristics of the plasma arc, as well as on powder feeding rate. This paper presents results from an investigation into an effect of these plasma spraying process parameters on spheroidization of high-melting metal powders of tungsten, molybdenum and rhenium.

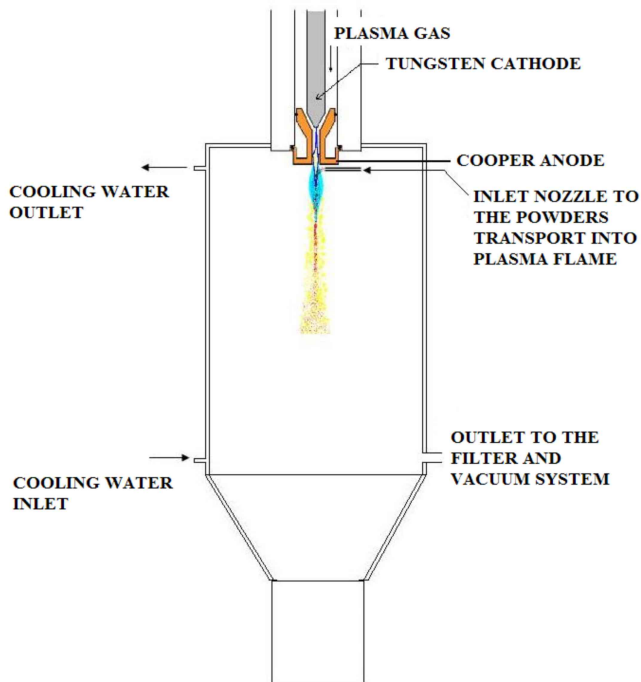


Fig. 1. Diagram of the reaction column used for conducting plasma spraying process

2. Material

For the plasma spraying process commercially available powders of tungsten and molybdenum were used, whereas the powder of rhenium was prepared by the reduction of ammonium perrhenate in hydrogen. The applied powders are characterized by the grains with developed surface and inhomogeneous shape and size distribution, which is illustrated by the specification given in Table 1 and microstructure images from the X-ray microanalyzer JXA-8230 (Fig. 2). Chemical purity of the powders was checked by X-ray method using the characteristic Co $K\alpha$ radiation. It was found that diffraction patterns of the powders of molybdenum and rhenium contained only the diffraction lines for these metals, whereas in case of tungsten weak lines from the $\text{Fe}_2(\text{WO}_4)_3 \times 10.7\text{H}_2\text{O}$ phase were observed, besides the lines characteristic for this element (Fig. 5).

Table 1. Properties of the powders before plasma spraying

Metal	Theoretical density [g cm ⁻³]	Measured density [g cm ⁻³]	Specific surface area [m ² g ⁻¹]	Average particle size (median) [μm]
W	19.25	18.31	0.312	5.50
Mo	10.28	9.79	0.2541	17.01
Re	21.02	20.19	0.7414	52.56

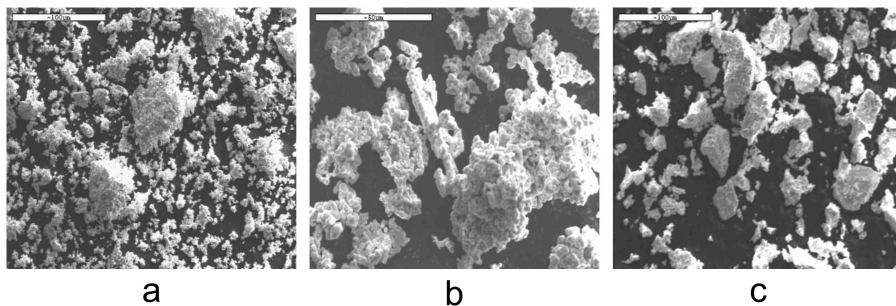


Fig. 2. Powder particles morphology: a—W, magn. 400 \times ; b—Mo, magn. 1000 \times ; c—Re, magn. 400 \times

The following starting materials, based on the selected powders, were prepared in order to check their suitability for spheroidization:

W1 – commercial powder of tungsten with an average grain diameter of 5.5 μm ,
 W2 – granulated tungsten powder with 2% addition of an organic binder (polyvinyl alcohol), 20 ÷ 40 μm in grain size,

M – molybdenum powder about 17 μm in grain size,
 R1 – rhenium powder fraction, 71 \div 315 μm in grain size,
 R2 – rhenium powder fraction, 71 \div 150 μm in grain size.

3. Results and discussion

Parameters of the process of powder melting and spraying were selected with an account of melting temperature of a specific metal, specifications of the starting powder, and technological parameters of the plasma system installation used. The results from spheroidization process are presented below separately for each metal.

Tungsten

Parameters of tungsten powder spheroidization process are given in Table 2, and images of the obtained powders are shown in Fig. 3. As it can be seen in Fig. 4, in case of the powder W1 the results from powder spheroidization process were not successful – the content of non-spherical phase was considerable. Because of small grain size of this powder it exhibited low flowability so that it was non-uniformly fed to the plasma stream zone. Plugging of a powder feed nozzle was observed, which could not be eliminated by the change in a flow rate of the carrier gas (samples W1.1 and W1.2). A slight increase in spherical fraction content was obtained for the sample W1.3 subjected to spraying at higher hydrogen content in a plasma gas (16.7%), and consequently at higher plasma temperature.

Table 2. Parameters of tungsten powder spheroidization process

Test No.	DC Current [A]	Voltage [V]	Hydrogen content in plasma gas [%]	Carrier gas flow [$\text{l} \cdot \text{min}^{-1}$]
W1.1	500	53	7.5	5
W1.2	500	53	7.5	10
W1.3	500	66	16.7	5
W2.2	750	51	5.8	4
W2.3	500	83	15.8	4

As a result of granulation of the W1 powder the W2 powder was obtained, which was characterised by greater size of particles and clearly improved flowability, which had beneficial effect on powder spheroidization, particularly at higher plasma temperature obtained by the increase of hydrogen content in a

plasma gas to 15.8%. It is seen in the images of the W2.2 powder particles, shown in Fig. 4, that the spherical fraction is predominant. This observation was confirmed by the results from measurements of an average specific surface area given in Table 3, which is the smallest for the W2.2 powder. Additional beneficial effect of the process of melting and spraying of the tungsten particles was the improved chemical purity of the powder. As it can be seen in the diffraction patterns shown in Fig. 5, the weak diffraction lines from the iron tungstate phase disappear after powder spheroidization. This effect was also confirmed by J. S. O'Dell and others in the case of Mo and Mo–Re spheroidization [4].

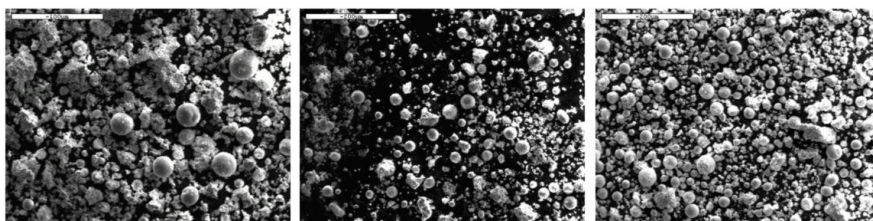


Fig. 3. Morphology of the W1 tungsten powder particles obtained at the spraying conditions specified in Table 3 (samples W1.1, W1.2, W1.3); magnification 200×

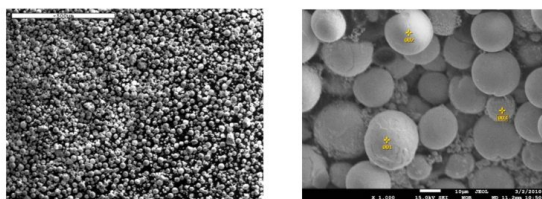


Fig. 4. Morphology of tungsten powder particles (sample W2.2) after plasma spraying, magnification 100× (left) and 1000× (right)

Table 3. Specific surface of tungsten powders after plasma spraying

Sample	W1.1	W1.2	W1.3	W2.1	W2.2
Specific surface [m ² · g ⁻¹]	0.2102	0.2440	0.1742	0.1750	0.1338

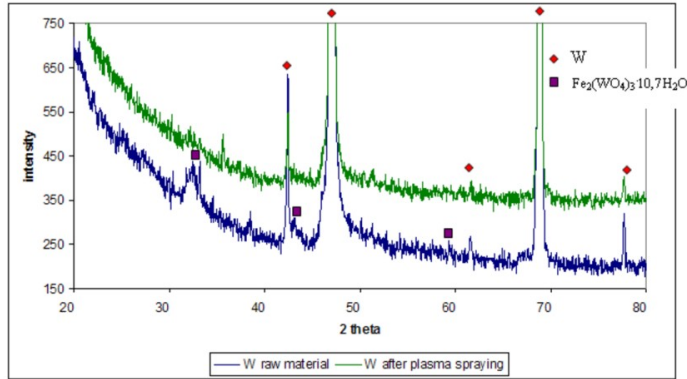


Fig. 5. X-ray diffraction patterns for the starting tungsten powder and the W2 powder after spraying process

Molybdenum

The commercial powder of molybdenum exhibited good flowability and there were no problems with supplying it to the plasma stream. The main objective of the tests carried out was the selection of optimal powder feeding rate and suitable current–voltage parameters ensuring required efficiency of the spheroidization process. These parameters for particular tests are summarised in Table 4.

Table 4. Parameters of molybdenum powder spheroidization process

Test No.	DC Current [A]	Voltage [V]	Hydrogen content in plasma gas [%]	Carrier gas flow [$l \cdot \text{min}^{-1}$]
M1	500	50	7.1	6
M2	500	60	14.5	6
M3	500	80	15.8	4

The best powder properties were obtained from the test M2, since the fabricated powder had the highest density of $9.4182 \text{ g} \cdot \text{cm}^{-3}$ and the smallest specific surface area of $0.0746 \text{ m}^2 \cdot \text{g}^{-1}$. Parameters of the M2 test appeared to be optimal from the point of view of spheroidization of the applied molybdenum powder, which was confirmed by the morphology of the particles after spraying, shown in Fig. 6b. It was initially expected that conducting the process at the highest hydrogen content of 15.8% (test M3), and consequently at higher temperature should result in higher efficiency of spheroidization and

in better physical and technological properties of the powder. However, the results from this test did not confirm these expectations: the powder exhibited greater inhomogeneity of particle sizes (Fig. 6c), a fraction of non-spherical fine particles was observed, and the specific surface area was greater reaching $0.0947 \text{ m}^2 \cdot \text{g}^{-1}$. Besides, the X-ray phase analysis made for this powder revealed the presence of weak diffraction lines of the MoO_2 molybdenum oxide, which were not observed in case of the powders obtained from the tests M1 and M2.

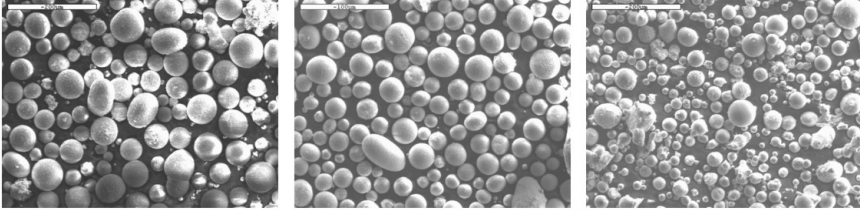


Fig. 6. Morphology of molybdenum powder particles obtained from the tests: a—M1, b—M2, c—M3

Rhenium

The rhenium powder fabricated under this work by the reduction of ammonium perrhenate in hydrogen was separated by screen analysis into fractions R1 and R2. Parameters of the plasma spraying process are given in Table 5.

Table 5. Parameters of rhenium powder spheroidization process

Test No.	DC Current [A]	Voltage [V]	Hydrogen content in plasma gas [%]	Carrier gas flow [$\text{l} \cdot \text{min}^{-1}$]
R1.1	500	66	14.3	2
R1.2	500	66	14.3	4
R1.3	500	66	14.3	8
R2.1	500	59	9.1	4
R2.2	500	66	14.3	4

The R1 powder was sprayed with different powder feeding rates at the same current–voltage parameters. Morphology of the obtained powders, which is shown in Fig. 7, indicates that the carrier gas flow rates of $21 \cdot \text{min}^{-1}$ and $81 \cdot \text{min}^{-1}$ are not suitable. However, the spheroidization process was clearly seen during the test R1.2 at the rate of $41 \cdot \text{min}^{-1}$. At this rate of carrier gas flow the powder gets to the plasma stream core.

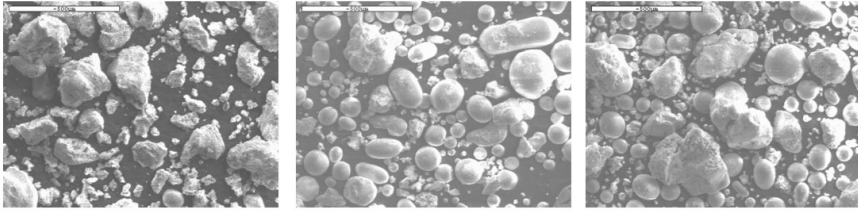


Fig. 7. Morphology of rhenium powders, sample R1 after spheroidization in the tests R1.1 (left), R1.2 (centre), and R1.3 (right); magnification 100x

In case of the powder R2, narrowing of the grain size distribution at the same parameters of the spraying process as those used in test R1.2 improves the spheroidization effect, which is illustrated in Fig. 8b.

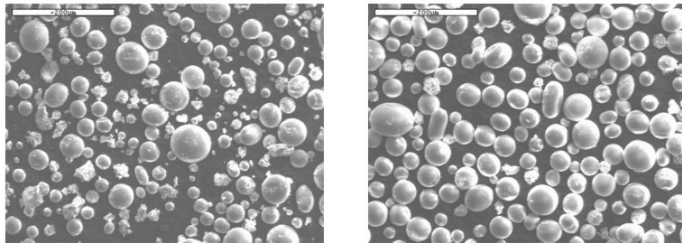


Fig. 8. Morphology of rhenium particles from the R2 powder obtained from the tests: a—R2.1, b—R2.2

Comparison of the morphology of powders obtained from tests R2.1 and R2.2, shown in Fig. 7, indicates that an optimal hydrogen content in the plasma gas should be at the level of 14%, since the decrease of this content in the test R2.1 gave worse results of spheroidization. As the quantitative measure of spheroidization process efficiency an average specific surface area of the powders after spraying was taken, which correlates with the conclusions from analysis of morphology images of powder particles. The results from measurements carried out are given in Table 6, indicating that the least specific surface area had the powder obtained from the test R2.2.

Table 6. Specific surface of rhenium powders after plasma spraying

Test	R1.1	R2.2	R1.3	R2.1	R2.2
Specific surface [$\text{m}^2 \cdot \text{g}^{-1}$]	0.3105	0.1313	0.2113	0.0625	0.0262

4. Conclusions

This investigation showed that plasma spheroidization of high-melting metals such as tungsten, molybdenum and rhenium depends on many factors. The first group of these factors includes the type of powder and its grain size distribution, and the rate with which it is fed to the plasma stream. The second group are process parameters influencing the shape, dimensions and temperature of the plasma stream. To this group belong the current and voltage supplied to the torch, and composition of argon-hydrogen mixture of a plasma gas. Even small deviation from optimal parameters can result in considerable changes in spheroidization degree. Therefore, production of spherical powders from the metals studied herein should be preceded by the choice of suitable starting powders and the choice of optimal process parameters.

References

- [1] Z. GRONOSTAJSKI: Badania stosowane w zaawansowanych procesach kształtowania plastycznego. Oficyna wydawnicza Politechniki Wrocławskiej, Wrocław 2003.
- [2] H. HACKIEWICZ, K. BUKAT: Lutowanie bezołowiowe. Wydawnictwo BTC, Legionowo 2008.
- [3] M. BOULOS: *Plasma power can make better powders*. Metal Powder Report, 59 (2004), 16–21.
- [4] J. S. O'DELL, E. C. SCHOFIELD, R. HICKMAN, T. N. MCKECHNIE, C. POWER: *Powder Alloying and Spheroidization*. Proceedings of PM² Tec Conference, Chicago 2004, <http://www.plasmapros.com/pas.pdf>

Received May 5, 2010

Action of an Ar–N₂ plasma on browning of sherry Fino wine¹

ROCIO RINCÓN², CRISTINA YUBERO², MARIA D. CALZADA²,
LOURDES MOYANO³, LUIS ZEA³

Abstract. The preliminary result of using the afterglow of an Ar–N₂ (2.8%) surface wave discharge generated at atmospheric pressure on sherry Fino wine sample is presented. After two years of storage, the colour of the sample treated was analyzed by absorbance measurement at 420 nm showing that plasma keeps the characteristic pale yellow colour of Fino wine. Besides this important result, the generation and the emission of excited molecular in a metaestable state $N_2(B^3\Pi_g \rightarrow A^3\Sigma_u^+)$ had been studied.

Key Words. Ar, N₂, surface wave discharge, atmospheric pressure, sherry Fino wine, CIELab parameters.

Introduction

All food and dairy products deteriorate at some rate or other in a manner that depends on food type, composition, formulation, packaging and storage regime. When preservation fails the consequences range broadly. At the one extreme, deterioration provokes undesirable effects in food, such as loss of colour or flavour. At the other extreme, the most serious forms of deterioration are those associated with the presence or multiplication of microorganisms. In order to avoid the main effects of deterioration, food industry has developed new techniques, the most of them act by inhibiting microbial growth, others inactivating microorganisms and others removing O₂ in vacuum or modified atmosphere packages [1].

¹This research has been supported by the Ministry of Science and Innovation (Spain) and FEDER Funds within the framework of the project no. ENE2008-01015/FTN.

²Grupo de Espectroscopía de Plasmas, Edificio Einstein (C-2), planta baja, Campus de Rabanales, Universidad de Córdoba, 14071 Córdoba, Spain

³Grupo de Viticultura y Enología. Campus de Rabanales. 14071 Córdoba (Spain)

For instance, wine industry is used to change atmosphere in bottle of wine. Typical air atmosphere is replaced by nitrogen gas so as to avoid oxidative processes. Nevertheless, this industry is looking for new techniques in order to elude the browning of sherry Fino wine over storage. In this paper the action of a surface-wave sustained discharge at atmospheric pressure over sherry Fino wine is studied.

In the last years, plasmas operated at atmospheric pressure have been the object of increased attention due to their potential and current use in various application such as excitation for elemental analysis [2] and more recently sterilization of medical instruments [3], which consists in destroying or eliminating all forms of life, specially microorganisms [3]–[5]. This application had been widely studied [4]–[14], the mayor issue of plasma sterilization is the respective roles of ultraviolet photons and reactive species, like excited molecules in a metastable state, from the plasma [3].

In this work, a preliminary study has been carried out on the generation of the molecules $N_2(A^3\Sigma_u^+)$ species in an Ar– N_2 SWD at atmospheric pressure to assess its application in sherry Fino wine.

Experimental device

The plasma was created in a quartz tube with one of its end opened to the atmosphere. The inner and outer diameters of the discharge tube were 4 and 6 mm, respectively. Several gas mixtures of high purity (99.999%) Ar and N_2 were used as plasma gases. The total Ar flow was equal to 3.5 slm and 0.1 slm for N_2 .

The microwave (2.45 GHz) power used to create and maintain the discharge was supplied in a continuous mode by a SAIREM generator (GMP 03K/M) and coupled to the plasma by means of a surfatron device (Fig. 1)[15]. A stub system was also used in order to ensure that the reflected power was less than 2% of the incident power. The power value was always the same and equal to 200 W.

At the end of the plasma, a post-discharge (or afterglow) was also observed. The plasma and the post-discharge lengths were different for each one of the gas mixture used to generate the plasma. In this research, the radiation emitted by the plasma was recorded by an optical fiber and directed to the entrance of a Jobin–Yvon monochromator (1000M, Czerny–Turner type) with 1 m of focal length and a holographic diffraction grating of 2400 lines/mm. A CCD camera was used as radiation detector (Symphony CCD-1024x256-OPEN-STE).

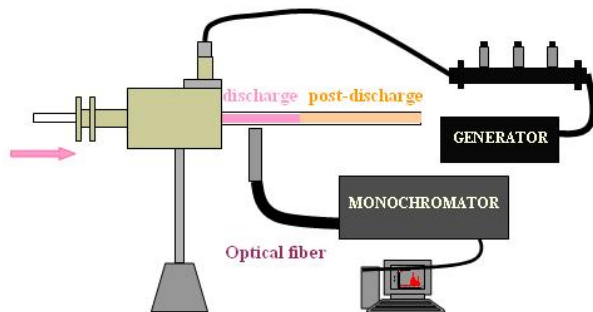


Fig. 1. Schematic drawing of the experimental device used in the laboratory experiments

Treatment of sherry Fino wine samples

The experimental device used in the treatment of the sherry Fino wine samples was the shown one in Fig. 1, but arranged vertically. The quartz tube protruded 11.5 cm from the surfatron and the distance between the end of the tube and the sample of wine was approximately 1 cm.

Four samples of 23 ml each one of sherry Fino wine from “Los Raigones” winery, Córdoba (Spain), were treated. The first sample was considered as the control one just to be able to compare and contrast the effect of different treatments (gas and plasma). A flowing of gas mixture with Ar (3.5 slm) and N₂ with (0.1 slm) was applied to the second sample (Fig. 2a). The postdischarge of pure Ar (3.5 slm) and Ar–N₂ (2.8 %) plasmas were applied to the third and the fourth samples. In these last two cases, the wine samples were refrigerated placing them in ice-water container in order to avoid their heating during their treatment (Figs. 2b and c). In all cases, the treatment time was over 5 seconds. Next, the samples were kept, for two years, in an airtight tube and stored in a dark environment where the temperature was lower than 20 °C.

One important property of Fino wines, which are obtained by biological aging, is their pale yellow colour. It should be pointed out that this type of wine does not brown under flor yeasts, preserving its pale color with slight oscillations for years. This has traditionally been ascribed to the flor yeasts that grow on its surface making difficult the diffusion of atmospheric oxygen across the flor film and protecting wine from it. This type of wine is a delicate product because its trends to browning after bottling. As far as others organoleptic qualities such as smell or flavour are concerned no analysis of them have been done, focusing on colour quality.

The external aspect of the samples is shown in Fig. 3. As it can be observed, the sample which shows less browning is that treated with a postdischarge of Ar-N₂ (2.8%).

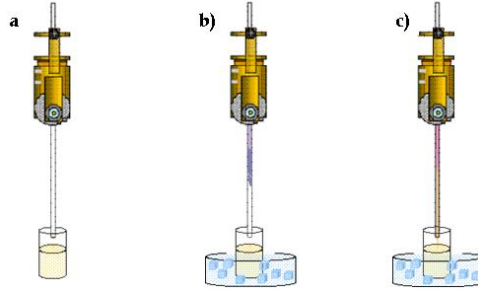


Fig. 2. Schematic drawing of the procedure used in the treatment of the samples with a) Ar-N₂ (2.8%) gas, b) Ar postdischarge and c) Ar-N₂ (2.8%) postdischarge

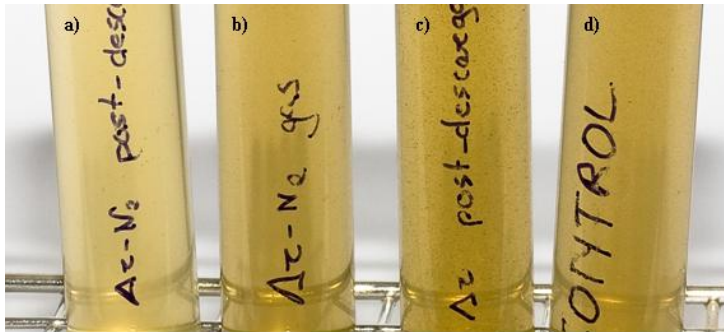


Fig. 3. Aspect of the samples after two years storage treated with a) Ar-N₂ (2.8%) postdischarge, b) Ar-N₂ (2.8%) gas, c) Ar postdischarge and d) the control one

In addition to a direct observation of the sample, other analysis were carried out in order to know what of the treatments utilized, gas or plasma, increased the resistance of Fino wines to browning.

Particular chromatic parameters for the samples were obtained from direct spectrophotometric measurements. These ones were carried out on a path-length of 10 mm using a Perkin Elmer Lambda 25 spectrophotometer. Color analyses were carried out following International Commission on Illumination recommendations (C.I.E., 2004), and using the visible spectrum obtained from 380 to 780 nm. In this work, the following CIELab uniform space colorimetric

parameters have been considered: a^* and b^* (chromatic coordinates representing red–green and yellow–blue axis respectively), rectangular coordinates L_{ab}^* (black–white component, lightness), and the cylindrical coordinates C_{ab}^* (chroma or saturation), and h_{ab} (hue angle). These parameters were measured using as references the CIE 1964 Standard Observer (10° visual field) and the CIE standard illuminant D_{65} . Besides, the absorbance at 420 nm can be also used as a measure of wine browning [16], [17]. Table 1 shows the CIELab parameters a^* (red/green coordinate), b^* (yellow/blue coordinate), lightness (L_{ab}^*), chroma (C_{ab}^*) and hue (h_{ab}) and the absorbances at 420, 520 and 620 nm, for the control Fino wine and for the Fino wines subjected to Ar–N₂ (2.8 %) gas and postdischarges of Ar and Ar–N₂ (2.8 %) plasmas.

Table 1. CIELab parameters

Chromatic characteristics	Control	Ar–N ₂ (2.8 %) gas	Ar postdischarge	Ar–N ₂ (2.8 %) postdischarge
a^*	1.96 ± 0.02	2.30 ± 0.01	3.26 ± 0.02	-0.36 ± 0.01
b^*	31.30 ± 0.02	31.2 ± 0.02	34.90 ± 0.01	24.10 ± 0.02
L_{ab}^*	82.40 ± 0.03	81.90 ± 0.04	78.60 ± 0.02	90.10 ± 0.04
C_{ab}^*	31.4 ± 0.1	31.30 ± 0.02	35.00 ± 0.03	24.10 ± 0.02
h_{ab}	86.4 ± 0.4	85.80 ± 0.03	84.70 ± 0.03	90.80 ± 0.04
$A_{420 \text{ nm}}$	0.70 ± 0.01	0.70 ± 0.01	0.83 ± 0.02	0.46 ± 0.01
$A_{520 \text{ nm}}$	0.26 ± 0.02	0.27 ± 0.01	0.32 ± 0.01	0.14 ± 0.01
$A_{620 \text{ nm}}$	0.13 ± 0.01	0.16 ± 0.02	0.17 ± 0.02	0.07 ± 0.02

Related to the absorbance, the results show a high values in A420 for the control Fino wine and for the wines subjected to Ar–N₂ (2.8 %) gas and Ar postdischarge, which reached values above than 0.70 au. However, the Fino wine with Ar–N₂ (2.8 %) postdischarge treatment showed the lowest values near to 0.46 au. It is corresponding to a decrease of 65 % with respect to control wine. The absorbance at 520 nm, which is a measure of brown–red color, and at 620 nm (blue), exhibited the same trend that the observed for 420 nm.

As can be seen from Table 1, CIELab coordinates a^* and b^* decreased in the Fino wine with Plasma Ar–N₂ (2.8 %) treatment. Chroma (C_{ab}^*) measures the contribution of a^* and b^* to the color of wine, indicating values close to 50 saturated colors [18]. C_{ab}^* also was lower in the wine subjected to above mentioned treatment, and with substantial differences respect to the control wine and with the rest Fino wines. Both, lightness (L_{ab}^*) range from 0 (black) to 100 (white), and hue (h_{ab}), defined as the arctan(b^*/a^*), slightly increased in the Fino wine subjected to postdischarge Ar–N₂ (2.8 %) plasma.

These previous results show that the exposure of wine to the Ar–N₂ (2.8%) postdischarge could be used as a technique to increasing the resistance of the Fino wines to browning.

Active species in the postdischarge of Ar–N₂ (2.8%) plasma

From these preliminary results the mechanisms induced by the species and radiation of the postdischarge on the resistance increase of the Fino wine to browning can not be known. However, in a first approximation, it is possible to know that are the active species in the Ar–N₂ (2.8%) postdischarge which could be capable of acting on the samples.

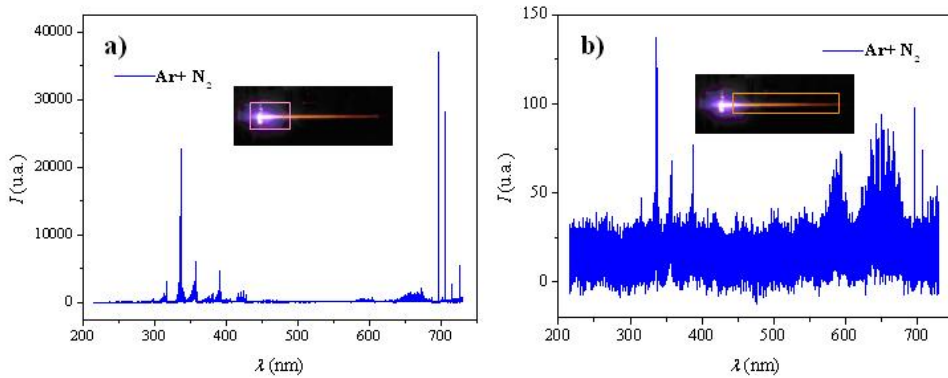


Fig. 4. Emission of $N_2(A^3\Sigma_u^+)$ in a) the discharge and b) the postdischarge of a mixture of Ar–N₂ (2.8%)

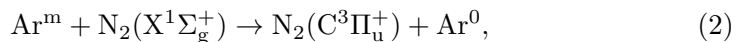
Spectra registered from the discharge and postdischarge for Ar–N₂ (2.8%) are shown in Figs. 4a and b. In these figures, emission of the excited metastable species $N_2(A^3\Sigma_u^+)$ are observed and pointing out that this metastable species is dominant in the postdischarge region.

$N_2(A^3\Sigma_u^+)$ metastable molecules are generated from de-excitation of $N_2(B^3\Pi_g)$ state by reaction [19]–[21]



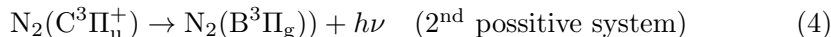
and two channels can be considered for the formation of $N_2(B^3\Pi_g)$ in a plasmas generated with a mixture of Ar and N₂.

In this plasma type, some reactions between Ar and N₂ are energetically favourable. Particularly, Penning excitation (2) and charge transfer (3) [22]





Next reaction (2), molecules at $\text{N}_2(\text{B}^3\Pi_g)$ state are obtained from de-excitation of $\text{N}_2(\text{C}^3\Pi_u^+)$ state (4)



and $\text{N}_2(\text{A}^3\Sigma_u^+)$ molecules are generated from (1).

Considering reaction (3), collisions of nitrogen molecular ions in the ground state $\text{N}_2^+(\text{X}^2\Sigma_g^+)$ with electrons lead to produce nitrogen atoms (5). $\text{N}_2(\text{B}^3\Pi_g)$ molecules are obtained from third body recombination process (6) in which the nitrogen atoms participate. Finally $\text{N}_2(\text{A}^3\Sigma_u^+)$ molecules are generated from reaction (1)



In surface wave discharges at atmospheric pressure, the transport of nitrogen metastable molecules ($\text{N}_2(\text{A}^3\Sigma_u^+)$) toward the postdischarge is possible using a large flow for the carrier Ar gas (3.5 slm) [20], [23].

References

- [1] G. W. GOULD: *Biodeterioration of foods and an overview of preservation in the food and dairy industries*. International Biodeterioration and Biodegradation, 36 (1995), 267–277.
- [2] F. SUN, R. E. STURGEON: *Furnace atomization plasma emission spectrometry with He/Ar mixed gas plasmas*. Spectrochimica Acta B, 54 (1999), 2121–2141.
- [3] M. MOISAN, J. BARBEAU, M. C. CREVIER, J. PELLETIER, N. PHILIP, B. SAOUDI: *Plasma sterilization. Methods and mechanisms*. Pure Appl. Chem., 74 (2002), 349–358.
- [4] N. PHILIP, B. SAOUDI, M. C. CREVIER, M. MOISAN, J. BARBEAU, J. PELLETIER: *The respective roles of UV photons and oxygen atoms in plasma sterilization at reduced gas pressure: the case of $\text{N}_2\text{-O}_2$ mixtures*. IEEE Transactions on Plasma Science, 30 (2002), 1429–1436.
- [5] M. K. BOUDAM, M. MOISAN, B. SAOUDI, C. POPOVICI, N. GHERARDI, F. MASSINES: *Bacterial spore inactivation by atmospheric-pressure plasmas in the presence or absence of UV photons as obtained with the same gas mixture*. Journal of Physics D: Applied Physics, 39 (2006), 3494–3507.
- [6] M. LAROSSI: *Low temperature plasma-based sterilization: overview and state-of-the-art*. Plasma Processes and Polymers, 2 (2005), 391–400.
- [7] M. LAROSSI: *Nonthermal decontamination of biological media by atmospheric-pressure plasmas: review, analysis and prospects*. IEEE Transactions on Plasma Science, 30 (2002), 1409–1415.

- [8] M. LAROUBI, F. LEIPOLS: *Evaluation of the roles of reactivities, heat, and UV radiation in the inactivation of bacterial cells by air plasmas at atmospheric pressure*. International Journal of Mass Spectrometry, 233 (2004), 81–86.
- [9] T. AKITSUA, H. OHKAWA, M. TSUJI, H. KIMURA, M. KOGOMA: *Plasma sterilization using glow discharge at atmospheric pressure*. Surface and Coatings Technology, 193 (2005), 29–34.
- [10] B. J. PARK, D. H. LEE, J. C. PARK, I. S. LEE, K. Y. LEE, S. O. HYUN, M. S. CHUN, K. H. CHUNG: *Sterilization using a microwave-induced argon plasma system at atmospheric pressure*. Physics of Plasmas, 10 (2003), 4539–4544.
- [11] K. LEE, B. J. PARK, D. LEE, I. S. LEE, S. O. HYUN, K. H. CHUNG, J. C. PARK: *Sterilization of Escherichia coli and MRSA using microwave-induced argon plasma at atmospheric pressure*. Surface and Coatings Technology, 193 (2005), 35–38.
- [12] M. HEISE, W. NEFF, O. FRANKEN, P. MURANYI, J. WUNDERLICH: *Sterilization of polymer foils with dielectric barrier discharges at atmospheric pressure*. Plasmas Polymers, 9 (2004), 23–33.
- [13] A. I. KUZMICHEV, I. A. SOLOSHENKO, V. V. TSIOLKO, V. I. KRZYZHANOVSKY, V. Y. BAZHENOV, I. L. MIKHNO, V. A. KHOMICH: *Features of sterilization by different types of atmospheric pressure discharges*. Proceedings International Symposium on High Pressure, Low Temperature Plasma Chemistry HAKONE VII, Greifswald 2000, 402–406.
- [14] J. POLLAK, M. MOISAN, D. KÉROACK, M. K. BOUDAM: *Low-temperature low-damage sterilization based on UV radiation through plasma immersion*. Journal of Physics D: Applied Physics, 41 (2008), 1–14.
- [15] M. MOISAN, P. LEPRINCE, C. BEAUNDRY, E. BLOYET: *Perfectionnements apportés aux dispositifs d'excitation par des ondes HF d'une colonne de gaz enfermée dans un enveloppe*, Brevet France (1974).
- [16] M. FABIOS, A. LOPEZ-TOLEDANO, M. MAYEN, J. MERIDA, M. MEDINA: *Phenolic compounds and browning in sherry wines subjected to oxidative and biological ageing*. J. Agric. Food Chem., 48 (2000), 2155–2159.
- [17] J. A. MORENO: *Influencia del tipo de envejecimiento sobre el perfil aromático de vinos generosos andaluces*, Ph.D. Thesis. Universidad de Córdoba (Spain). 2005.
- [18] R. GIL-MUÑOZ, E. GÓMEZ-PLAZA, A. MARTÍNEZ, J. LÓPEZ-ROCA: *Evolution of the CIELAB and other spectrophotometric parameters during wine fermentation. Influence of some pre and postfermentative factors*. Food Res. Int., 30 (1997), 699–705.
- [19] A. RICARD: *The production of active plasma species for surface treatments*. Journal of Physics D: Applied Physics, 30 (1997), 2261–2269.
- [20] G. CALLEDE, J. DESCHANPS, J. L. GODART, A. RICARD: *Active nitrogen atoms in an atmospheric pressure flowing Ar-N₂ microwave discharge*. Journal of Physics D: Applied Physics, 24 (1991), 909–914.
- [21] A. RICARD, H. MALVOS, S. BORDELEAU, J. HUBERT: *Production of active species in common flowing post-discharge of Ar-N₂ plasma and an Ar-H₂-CH₄ plasma*. Journal of Physics D: Applied Physics, 27 (1994), 504–508.
- [22] E. TATAROVA, F. M. DIAS, J. HENRIQUES, C. M. FERREIRA: *Large-scale Ar and N₂-Ar microwave plasma sources*. Journal of Physics D: Applied Physics, 39 (2006), 2747–2753.

- [23] A. RICARD, J. TÉTREULT, J. HUBERT: *Nitrogen atom recombination in high pressure Ar-N₂ flowing post-discharges*. *Journal of Physics B: Atomic, Molecular and Optical Physics*, *24* (1991), 1115–1123.

Received May 10, 2010

Express method determination of the gas pressure optimal for microwave chemical materials processing

SIARHEI BORDUSAU¹, ANATOLII DOSTANKO¹,
SIARHEI MADVEIKA¹

Abstract. A method of rapid determination of gas pressure value which provides the most favorable conditions for microwave plasma chemical processing at low vacuum is developed. The method is based on the characteristic property of microwave plasma materials processing which consists in pulsation nature of microwave discharge. The method is based on the experimentally established dependence of delay period duration of the microwave discharge start with respect to the start of microwave energy generation on plasma forming gas pressure value. This dependence has an extreme character. The determination method of the desired gas pressure value in a plasmatron discharge chamber and instrumentation for its realization are stated. The technological experiment data illustrate the reliability of the obtained results are given. The data are presented by the examples of plasma chemical removal of photoresist films and monocrystalline silicon etching.

Key Words. Gas pressure, microwave plasma, materials processing.

Introduction

One of the biggest issues that must be decided on in the design process of plasma chemical processing of materials is the choice of plasma-forming modes and conditions (microwave power magnitude, pressure and type of gas, pumping rate of gaseous media, etc.). This task is rather complicated because in many cases plasma processing requirements (in particular, material removal) such as etching rate and uniformity on a substrate, anisotropy, selectivity, etc., are mutually exclusive.

It is known [1] that for each process of plasma chemical interaction of ionized media with solid surface there is a definite optimum combination of discharge

¹Belarusian State University of Informatics and Radioelectronics, Belarus, Minsk;
e-mail: bordusov@bsuir.by

conditions which ensure maximum speed of plasma chemical interaction between plasma particles and material surface layer. The current selecting process of plasma-forming parameters is time-consuming and laborious since it is carried out with the method of pilot selection combining different processing modes and the following evaluation of quantitative and qualitative indicators of plasma effect on the material.

One of the main parameters of the process of microwave plasma chemical etching and material cleaning is the pressure in the discharge area. At the same time dependence of plasma chemical etching rate on pressure is extreme by nature [2]. The existing maximum can be accounted for the fact that at low pressures the number of active plasma particles is small and their flow on the material surface decreases with the pressure decrease. The particle flow on the surface also decreases with increasing pressure due to the difficulties in plasma-forming process and the increase in rate of disappearance of active etching particles in the volume because of the recombination processes, conditioned by the frequency increase in their collisions among themselves as well as by the loss on the walls of a discharge chamber. One of the main tasks of technological process designing and optimization is to determine the pressure of plasma-forming mixture which will provide the maximum rate of plasma material processing.

The common methods of contact and noncontact plasma diagnostics do not allow to determine the optimal rate modes of pressure which implement microwave plasma chemical processes [3], [4]. For instance the probe method of plasma parameter measurement and control provides the information on the electronic or ionic discharge component which enlarge monotonically with the increasing pressure. Spectral diagnostic method and some others also do not demonstrates the presence of peaks of values while changing the gas pressure.

Experimental results and discussions

One of the peculiarities of microwave vacuum plasma processing of materials is that nowadays microwave generators with a simplified scheme of continuous-wave magnetron powered with the unfiltered rectified voltage of industrial frequency is used in experimental, research and industrial equipment as a microwave power source. Such a scheme of magnetron power supply (for example M-105, M-112 and etc. with a working characteristics: pulse mode generation of microwave energy, output power 700 W, anode voltage 4.0 kV, microwave frequency 2450 MHz) presupposes quasi-continuous mode of their work resulting in a pulsating nature of the generated microwave power delivered to the load from generator device. This, in its turn, leads to a pulsating mode of microwave discharge excited in the discharge area of microwave plasmatron. In this case gas discharge is excited under definite for these discharge conditions

breakdown threshold intensity of electrical field and goes out with the field intensity decrease below a certain value [5]. It was experimentally established [6] that delay duration of the microwave discharge start with respect to the start of microwave energy generation (Fig. 1) depends on gas pressure and has an extreme character.

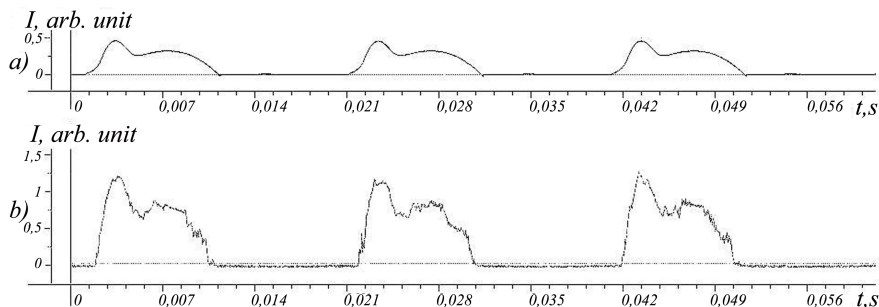


Fig. 1. Oscillograms of pulses: of anode magnetron current (a) and optical signal of plasma glow (b): microwave power – 700 W; pressure in the discharge chamber – 70 Pa; gas – O₂

The comparative analysis of technological experiments and the research results of microwave plasma forming conditions made it possible to identify the correlation between the maximum rate of microwave plasma chemical material removal and the delay time of the microwave breakdown in gas discharge volume under certain discharge conditions. The variable (adjustable) parameter in this case is the pressure in the microwave plasmatron discharge area.

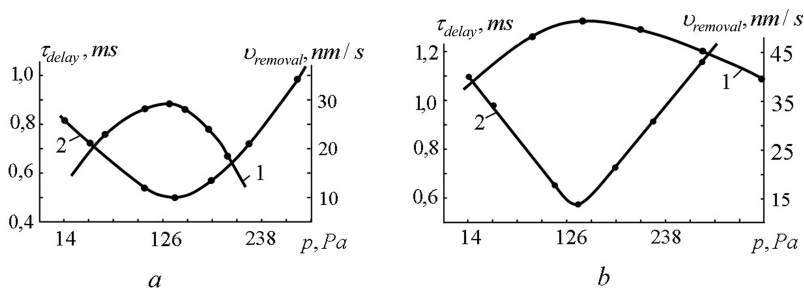


Fig. 2. Dependences of time delay of microwave discharge excitation and material removal rate on the pressure of plasma-forming gas during the processing of monocrystalline silicon in CF₄ (a) and photoresist films in O₂ (b): 1 – removal rate; 2 – delay time

As an example, Fig. 2 shows the experimentally obtained dependence of etching rate of monocrystalline silicon in microwave discharge in the atmosphere of CF₄ and time delay of microwave breakdown on gas pressure.

The similar dependence for the process of photoresist coating removal from the surface of silicon wafers in the atmosphere O_2 is demonstrated. The research results served as a basis of the developed rapid method for determining the optimum pressure for the processes of microwave plasma chemical material removal under low vacuum conditions.

The technique consists in the fact that on the basis of a comparative analysis of the temporal characteristics of optical pulsed signal of microwave discharge and the pulsed signal of magnetron anode current during changing a gas pressure in the range of $100 \div 200$ Pa, the gas pressure at which the delay period duration of the microwave discharge start with respect to the start of microwave energy generation is minimum is evaluated. Under this pressure maximum rate of plasma chemical material removal from the solid surface is provided.

The block diagram of hardware implementation of the developed express method of determining the optimal gas pressure for microwave plasma chemical material removal is given in Fig. 3.

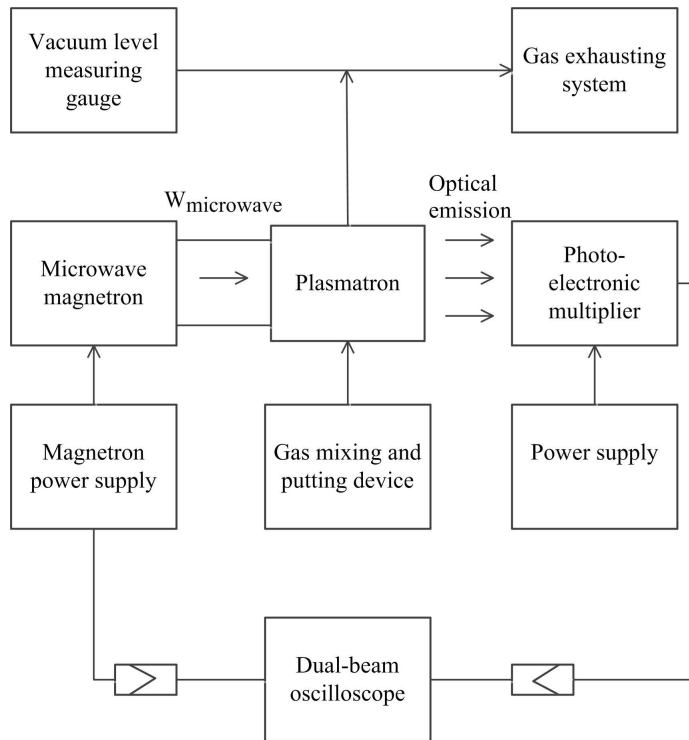


Fig. 3. Block diagram of hardware implementation of the developed express method of determining the optimal gas pressure for microwave plasma chemical material removal from the solid surface

The plasmatron is a rectangular resonator with a horizontally placed quartz reactor in diameter 200 mm and 350 mm long.

Signals from the magnetron and photo-electronic multiplier are transmitted to the dual-beam oscilloscope working in the synchronous start-up mode of both traces.

Shifting of the working pressure in the discharge chamber is regulated by the gas flow supplied to the plasma-forming chamber. In the process of pressure shifting time intervals of discharge excitation delays relatively to the start of microwave energy generation supplied to the plasmatron is determined. The pressure at which this interval is minimum is set as well. At such pressure the processes of microwave plasma chemical material removal from the solid surface will proceed with maximum rate.

Conclusions

The method developed was tested and showed a high degree of results consistency with the technological experiments on monocrystalline silicon etching in CF_4 , as well as with the photoresist films aching in the atmosphere of O_2 . This reduces the duration and complexity of the procedure of the desired pressure determining.

References

- [1] A. P. DOSTANKO, S. P. KUNDAS, S. V. BORDUSOV: Plasma processes in electronic engineering production. FUAinform, Minsk 2000.
- [2] B. S. DANILIN, V. Y. KIREEV: Application of low-temperature plasma for materials cleaning and etching. Energoatomizdat, Moscow 1987.
- [3] V. K. JIVOTOV, V. D. FRIDMAN, V. D. RUSANOV: Diagnostic of nonequilibrium chemically active plasma. Energoatomizdat, Moscow 1985.
- [4] Y. A. IVANOV, Y. A. LEBEDEV, L. S. POLAK: Methods of contact diagnostic in nonequilibrium plasma chemistry. Science, Moscow 1981.
- [5] A. MAC-DONALD: Microwave breakdown in gases. Mir, Moscow 1969.
- [6] S. V. BORDUSOV: *Stability of microwave discharge in the plasmatron with a ring-type waveguide applicator*. Journal of Applied Spectroscopy, 69 (2002), 109–112.

Received May 16, 2010

The software-operated generator of high-voltage pulses for plasma technological application

DMITRII GODUN¹, SIARHEI BORDUSAU¹, ANATOLII DOSTANKO¹

Abstract. The paper describes the design and functional peculiarities of the software-operated generator of high-voltage pulses for plasma technological processes. It considers the problems connected with the creation of the microprocessor equipment configuration capable to reproduce high-voltage pulses of both positive and negative polarity. The software-operated generator consists of the analog–digital stabilized pulse converter and the digital modulator of the power pulses. The generator of high-voltage pulses provides the following output parameters: the stabilized output voltage is in the range from 600 to 1200 V with the fixed step of 20 V; the value of the pulse output current is not less than 4 A; the interval of the deviation of the power pulse frequency is in the range from 5 to 45 kHz; the pulse ratio is 2–10. The application of the microprocessor system of pulse high-voltage key control enables the generator to work in two regimes: forming a series of constant pulses and forming single pulses with the regulated width and pause. The time of determining the current overload does not exceed 55 nanoseconds. The time of the protective switching-off of the high-voltage pulse converter does not exceed 1 microsecond.

Key Words. Software-operated, generator, high voltage, plasma.

Introduction

To carry out plasma processes of vacuum treatment such as ion nitriding, cathode sputtering, application of hollow-cathode discharge and to form plasma glow discharge, technological systems should contain a generator of high-voltage negative polarity pulses with wide facilities to control the characteristics of power pulses.

The researches into the output parameters of power pulse sources show that while carrying out plasma technological processes in the low-pressure environment, the software-operated generator of high-voltage pulses with a combined

¹Belarusian State University of Informatics and Radioelectronics, Belarus, Minsk,
e-mail: bordusov@bsuir.by

control analog–digital system is an optimum configuration of a power source intended for glow discharge excitation [1]. The application of the analog–digital method to control pulse power elements allows to combine a high-speed analog control system of power switch modules, covered by a negative feedback on the current and voltage, with the digital system of threshold regulation [2].

Main part

The block diagram of the developed software-operated generator of high-voltage pulses is shown in Fig. 1.

The software-operated generator consists of a digital power pulse modulator and analog–digital step-up stabilized pulse converter which power cascade is made isolated from the primary network. The implementation of this solution allows applying the software-operated generator in gas-discharge power supply systems of both positive and negative polarity.

The software-operated generator of high-voltage pulses has been developed with the view of connection to a three-phase four-wire industrial network. After turning on the software-operated generator, mains voltage is straightened by the three-phase diode bridge and arrives at the input of the power factor corrector. The system of smooth start is applied in order to carry out a smooth charge of the primary power circuit capacities and to start the generator of pulse-duration modulation. The reduction of the influence of transient processes in the power converting device is achieved by a smooth increase in the width of working pulses. The generator of pulse-duration modulation forms signals controlling IGBT drivers which, in their turn, provide the parameters of a pulse sequence necessary to control the power bridge converter. The driver control system provides quite abrupt trajectories of switching IGBT power devices, and it also galvanically separates the generator of pulse-duration modulation from the power converter.

The power converter is realized according to the full bridge scheme which advantage is the absence of the overvoltage on key IGBT elements. The function of the power converter is to switch diagonals of the transistor bridge on the frequency of transformation through the primary winding of the step-up transformer. In this case the transformation frequency is 20 kHz. The high-voltage rectifier and LC filter transform the variable voltage, received on the secondary winding of the transformer, into the direct-current voltage. In view of the big output power, the output cascade of the increasing pulse converter is made of two modules of 2.5 kW each one. The practical application of this technical solution increases the output power, reduces the influence of the temperature component on power transistors and transformers.

The circuit of the negative feedback on the voltage, integrated with the digital microprocessor system, has been inserted into the control system to obtain the stabilized output voltage in the whole range of loadings. The proportional change of the voltage mismatch is achieved by changing the division factor on the input of the negative feedback block on the voltage with the help of the digital potentiometer controlled by the microprocessor. The three-wire support-regulated stabilizer has been used as a precision voltage sensor of loading. Its stabilization voltage changes depending on what size of the voltage amplitude is delivered to the operating input. The generator of pulse-duration modulation corrects the width of control pulses, and the system tends to the established value while the mismatch voltage tends to zero. The output voltage either increases or decreases. The speed of the negative feedback reaction determines the level of output pulsations not only in the established condition, but also at the moment when the output voltage amplitude changes.

The digital threshold control of the negative feedback system on the voltage allows to regulate and stabilize the target voltage amplitude in the range from 600 to 1200 V with the 20 V step.

During the research of the output parameters of the pulse converter after the connection of the gas-discharge system it has been discovered that a high level of the clutter influencing the analog–digital transformation of signals, and a quite low speed of transformation of the voltage into a code and of processing the result bring about the increased pulsation of the output voltage. The circuit of the negative feedback on the current is provided in the generator design, which in view of plasma loading is quite an essential constructive element. The application of the high-speed optodecoder with the switching time up to 75 nanoseconds provides the advantage on speed of analog current protection systems over digital ones.

The current protection of the step-up pulse converter is executed in the form of a trigger scheme and is intended for the operate current of 4 A with the protective switching-off time not exceeding 1 μ s. The analog systems of the analysis of the pulse power supply output characteristics, constructed on comparators and operational amplifiers, have quite a high speed of acceptance of the operating solutions to influence on a power part. The basis of the applied current protection device is the high-speed analog comparator which compares the amplitude values of the basic signal with the voltage taken from the resistive divider in the bottom shoulder of which there is a current sensor. While comparing the amplitude values of two signals on the inputs of the comparator, the output condition of the comparator is switched and through the optical device of data transmission the current protection device stops the operation of the generator of pulse-duration modulation.

The application of the pulse control structure has allowed creating the power supply source with good weight and dimension parameters and the increased value of the efficiency coefficient up to 86 %.

The formation of the high-voltage pulse voltage is made by the block of data processing under the control of the digital software. The microprocessor generator of pulse-duration modulation reproduces pulses in the frequency interval from 5 to 45 kHz, with the possibility to change the porosity value from 2 to 10, and controls the IGBT driver. The driver system strengthens the signal up to the level of opening the complex power breaker module. Working in the key mode the power module commutates the constant voltage with the amplitude of 1200 V. The device is covered by the circuit of the negative feedback on the current and, after the pulse current exceeds more than 4 A, the driver system corrects the width of power module control pulse. The device functions as a temporal current stabilizer. The limitation of the output pulse current value to 4 A is necessary to extend the time intervals of the actuation of the current protection device of the high-voltage pulse converter, as well as to eliminate uncontrollable throws of the pulse current when the system carries out stabilization within a short period of time and restores to a working condition.

The application of the microprocessor control system of the pulse high-voltage key allows to generate not only constant pulse sequence, but also to obtain the high-voltage single pulses combined in the packages with the software-operated width of the pulse and pause.

Operating the generator manually or with the help of software makes it possible to use it as a separate unit for the generation of the unipolar high-voltage pulses as well as a part of a technological device with the possibility to carry out diagnostics, regulation and indication of working parameters, which directly refer to the functioning of the technological gas-discharge system.

To obtain the maximal conditions of the electric parameters concordance of the given technological equipment and gas-discharge system, an operated inductive-compensatory block has been installed in the break of the power circuit.

Conclusions

The software-operated generator of unipolar high-voltage pulses has been worked out and tested on plasma loading in the form of the glow discharge of the pulsing current.

Using the analog–digital control system has allowed to transform the electric energy of the power network into the type necessary for the specialized technological process flow complying with the required standards on the protection of the power cascades of the pulse high-frequency converter.

The application of the power coefficient corrector in the structure of the increasing pulse converter has made it possible to obtain more powerful output cascades with smaller influence of the pulse clutter on the power network.

The application of the pulse-duration control of the output power breaker, covered by the negative return circuit on the current, is the feature of the construction of the modulator-shaper of electric output signals. The period of reaction to overload does not exceed 55 nanoseconds which provides a steady functioning of the software-operated generator of high-voltage pulses on the plasma loading.

References

- [1] D. V. GODUN, A. P. DOSTANKO, S. V. BORDUSOV: *Stabilization and regulation of value of an output voltage of a high-voltage sources for forming gas-discharge devices with the combined analogue-digital method of transformation*. Modern methods and technologies of creation and processing of materials(S. A. Astapchik). PhTI National Academy of Sciences of Belarus, Minsk 2008, 233–235.
- [2] D. V. GODUN, A. P. DOSTANKO: *The program-operated generator of rectangular impulses for a technological gas-discharge devices*. Problems of designing and manufacture of electronics(G. Grozberg). PSU, Novopolotsk 2008, 3–6.

Received May 16, 2010

Modeling of plasma-assisted coal dust ignition and combustion

ALIA S. ASKAROVA¹, VLADIMIR E. MESSERLE²,
ALEXANDR O. NAGIBIN¹, ALEXANDR B. USTIMENKO³

Abstract. Combustion of pulverized coal flame was numerically simulated. The results of three-dimensional calculations of the processes of conventional and plasma activated combustion of coal in furnaces are discussed. Computer code CINAR ICE was verified at coal combustion in experimental furnace of 3MW thermal power equipped with plasma-fuel system. Operation of the furnace in traditional mode of coal combustion and with its plasma activation was investigated. Also this paper presents the results of numerical simulation of the plasma thermochemical enhancement of coal for ignition and combustion in a furnace of power boiler. Influence of plasma activation of combustion onto thermotechnical characteristics of the flame, decrease of unburned carbon and nitrogen oxides concentrations at the furnace exit was discovered.

Key Words. Plasma-fuel system, coal, combustion, simulation.

Introduction

Reorientation of the fuel balance of thermal power plants (TPP) from gaseous and liquid fuels to the solid ones is a worldwide tendency. Pulverized coal TPP share in the electricity production is growing up permanently and now it is about 60 % in the USA, 80 % in Kazakhstan and 87 % in China [1]. That is why increase of solid fuels use efficiency is one of the actual issues of modern thermal physics. But it is unachievable without detail study of the pulverized coal flame combustion in furnaces of TPP.

To increase efficiency of solid fuels utilization, to decrease fuel oil and natural gas flow rate, and dangerous emissions at TPP plasma technology of coal ignition was developed. It is based on electro-thermo-chemical preparation of

¹Kazakhstan National University, Physical Department, Almaty, Kazakhstan.

²Combustion Problems Institute, Almaty, Kazakhstan.

³Research Department of Plasmotechnics, Research Institute of Experimental and Theoretical Physics, Almaty, Kazakhstan.

fuel to burning (ETCPF) [2]. ETCPF is realized with the aid of plasma-fuel systems (PFS). In this technology pulverized coal is replaced traditionally used for the boiler start up and pulverized coal flame stabilization fuel oil or natural gas. Part of coal/air mixture is fed into the PFS where plasma-flame, having a locally high concentration of energy, induces coal gasification and partial oxidation of char carbon (Fig. 1). The resulting coal/air mixture is deficient in oxygen, the carbon being mainly oxidized to carbon monoxide. As a result, a highly reactive mixture of combustible gases (at a temperature of about 1300 K) and partially oxidized char particles are obtained at the exit of the PFS. On entry to the furnace, this combustible mixture is easily ignited. This allows prompt ignition and much enhanced flame stability of the main portion of the coal flame which is not directly treated by plasma.

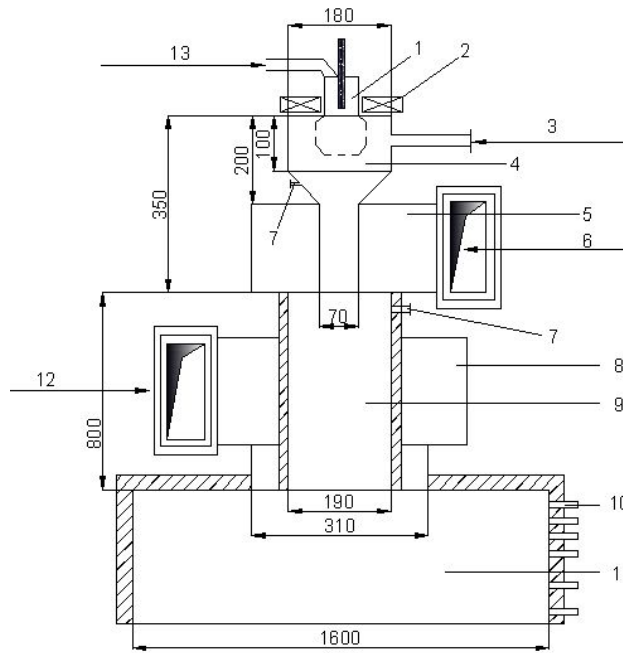


Fig. 1. Layout drawing of plasma-fuel system and experimental furnace: 1 – plasmatron, 2 – electromagnetic coil, 3 – air/coal mixture, 4 – ETCPF chamber, 5 – air/coal mixture scroll, 6 – air/coal mixture, 7 – window for temperature measuring and gas sampling, 8 – secondary air scroll, 9 – central tube of the burner, 10 – windows for temperature measuring and gas and coke residue sampling, 11 – furnace, 12 – secondary air, 13 – plasma forming air

Detailed mathematical modeling is required for enhancement and dissemination of the plasma technology of coal ignition. Lack of detailed experimental

data on plasma ignition of coals and combined their burning with the highly reactive two-component fuel complicates the development of mathematical and physical models. To develop such models knowledge of the main characteristics of ETCPF and combustion processes, temperature fields, velocities and concentrations of gaseous and condensed components, is required.

To understand physical mechanism of ETCPF and combustion more completely, and to verify CINAR ICE software code, investigations of coal incineration in the equipped with PFS experimental furnace of 3 MW thermal power have been fulfilled. Two computer codes were used for that. The first one was 1D code PLASMA-COAL. It describes two-phase chemically reactive flow in a plasma-chamber with an internal source of heat (plasma flame). The second is 3D code CINAR ICE. It operates with real geometry of a furnace. PLASMA-COAL code has been verified using experimental data on plasma gasification and ETCPF [3]–[6]. It was used for plasma-fuel system computation, and data to enable 3D numerical simulation of coal combustion in the furnace equipped with PFS were collected. CINAR ICE code was used for computation of coal co-combustion with highly reactive two-component fuel in the furnace. The code has been verified for 3D simulation of traditional furnace processes [7]–[9]. However, to use this code for computation of the equipped with PFS furnaces verification was required.

1. Calculation method and results of experimental furnace study

CINAR ICE code (Cinar Integrated CFD Environment) [2], [7]–[9] was designed to provide computational solutions of industrial problems, especially those related to two-phase combustion. It solves the governing time-averaged Eulerian equations for the gas phase mixture combined with Lagrangian tracking of the particles [7], [12]–[14] and simulates devolatilisation, volatiles combustion (fast diffusion combustion), char combustion and the turbulence (k - ε model). “Fast chemistry kinetics” model of chemical reactions is used in the code. The kinetic model is based on the conception of multi-fraction mixtures burning [12]. Radiative heat transfer is represented by six-flow model of particles radiation and reemission [13]. The Control Volume method is used for discretization of the initial equations. SIMPLE [12] algorithm is used for calculation of pressure field.

To verify CINAR ICE code two regimes of experimental furnace were selected. The first one was conventional coal combustion and the second regime was combustion of plasma activated coal. Plasma activation of coal combustion was provided with plasma flame of 36 kW power. Parameters of two-component

high reactive fuel produced in PFS (Fig. 1) were calculated using PLASMA-COAL computer code. These parameters were used as initial data for PFS equipped experimental furnace 3D simulation.

Mathematical model of ETCPF describes two-phase (coal particles and gas-oxidiser) chemical reacting flow with an internal heat source (electric arc or plasma). Generally coal particles and gas are admitted into the PFS at ambient temperatures. Particle-to-particle, gas-to-particle transfer and gas-to-plasma heat-mass transfers are considered. Heat and momentum transfer between the flow and the PFS wall have been calculated. The average size of the coal particles was taken as a constant and equal to the particle mineral skeleton size. In other words the particle was not resized at conversion. The particles were spherical and the temperature gradients within the particle are negligible. Also, some chemical transformations of fuel were considered. They are as follows: formation of primary volatile products from coal, conversion of evolved volatile products in the gas phase and char carbon gasification reactions. Coal composition was presented in the model by its organic and mineral parts. Organic mass of coal was specified by the set of the functional groups (CO, CO₂, CH₄, H₂O, C₆H₆) and carbon. An entrained flow reactor was considered and plug flow was assumed. Resulting set of ordinary differential equations includes equations for species concentrations (chemical kinetics equations) in conjunction with equations for gas and particle velocities and temperatures, respectively. Energy contribution from plasmas had been found empirically [3] and included into the energy equation as a distribution of internal heat source. Also the model was distinguished by its detailed description of the kinetics of the chemical reactions mentioned above [10]. Kinetic scheme consists of 116 chemical reactions. Temperature dependence of rate constants is governed by the Arrhenius equation. In [2], [3], [5], [11] the model was presented in detail.

The swirl burner was mounted axial on the furnace top (Fig. 1). Ekibastuz bituminous coal of 45.2% ash content, 14.7% devolatilization, 1.3% humidity and 15960 kJ/kg heat value was incinerated in the experimental furnace [4]. Grinding of coal gave the average particle size of 60 microns. PLASMA-COAL computer code has been used for calculation of ETCPF in the volume of PFS of 1.15 m length. The following initial parameters were used for calculations: plasmatron power was 36 kW, initial temperature of pulverized coal (coal/air mixture) was 300 °C, coal and air consumption through PFS were 410 and 600 kg/h correspondingly. The air is composed of nitrogen (79 vol.%) and oxygen (21 vol.%) and neither carbon dioxide nor noble gas were taken in consideration.

As a result of calculations temperature distribution (Fig. 2), gas and particles velocities (Fig. 3), gas-phase components concentrations (Fig. 4), gasification degree and carbon concentrations in coke residue (Fig. 5) were found. Gas and coal particles temperatures (Fig. 2) increase along the PFS. The heat exchange between plasma source and gas-phase is prevailing at the initial section

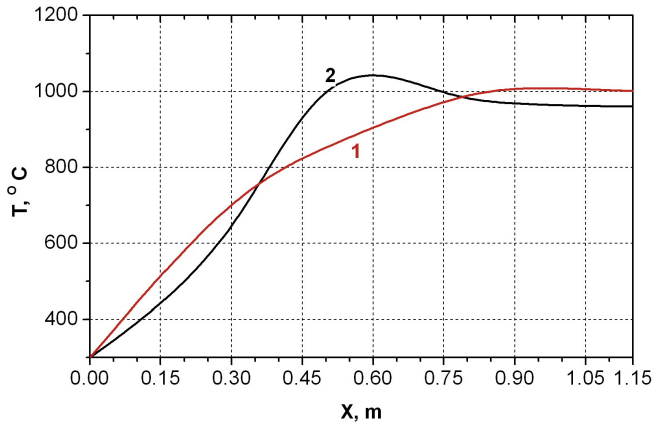


Fig. 2. Gas (1) and particles (2) temperatures along the PFS

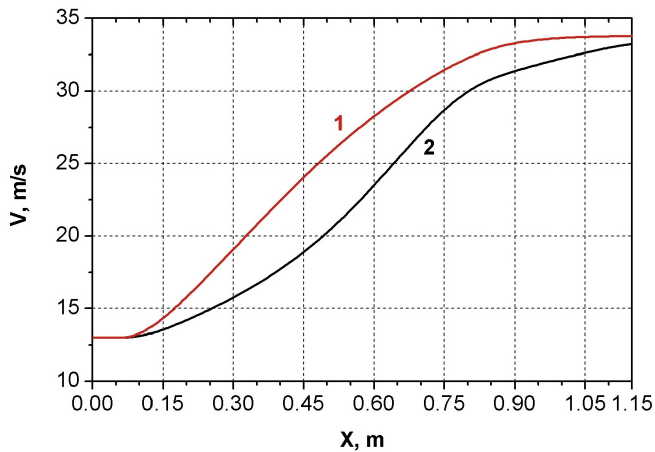


Fig. 3. Gas (1) and particles (2) velocities along the PFS

($0 < X < 0.35$ m). Coal particles are heated from gas and their temperature increase up to 1121 °C at the section $0.35 \leq X < 0.8$ m due to carbon oxidation and corresponding out of heat. It exceeds the gas temperature by 264 °C. As a result of that inversion of temperature curves is observed at the section. Gas temperature reaches maximum at 1015 °C ($X = 0.9$ m) and goes down to the outlet of PFS ($T = 1002$ °C). Gas temperature is 41 degrees higher than

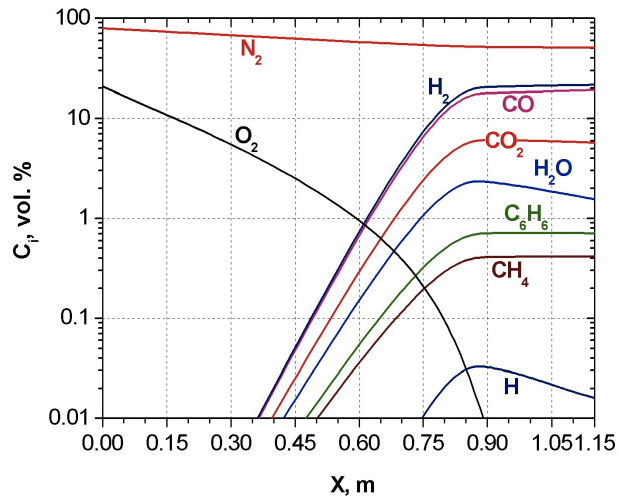


Fig. 4. Gas phase components concentrations along the PFS

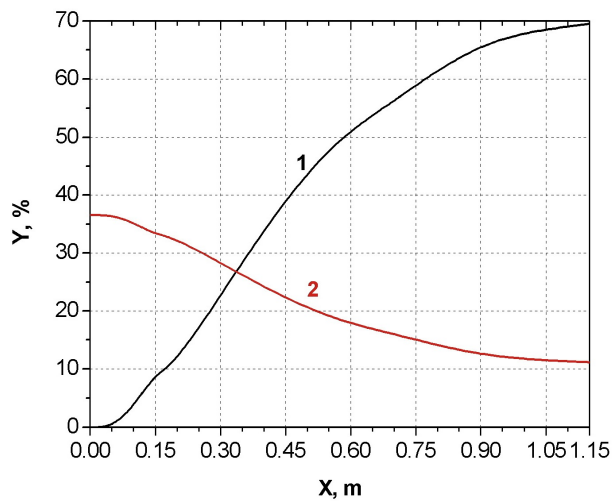


Fig. 5. Gasification degree (1) and carbon concentration (2) in coke residue along the PFS

particles temperature, that is related to heat-emission from the particles to the wall of PFS.

Equal at the PFS inlet velocities of gas and particles (Fig. 3) increase with the length achieving their maxima of 33.8 and 33.2 m/s at the PFS exit accordingly. Meanwhile gas velocity is higher one of particles along the full PFS.

Note velocity of the flow at the exit of PFS is considerably higher for traditional pulverized coal burner.

With coal particles heating it is observed devolatilization and carbon gasification (Fig. 4, Fig. 5). Concentration of combustible components (CO , H_2 , H , CH_4 , C_6H_6) increases along the PFS and reaches its maximum of 41.8% at the PFS outlet. Oxidants concentration (CO_2 , H_2O , O_2) does not exceed 7.3% at the PFS outlet. The nitrogen concentration (N_2) decreases along the PFS from 79% to 50.8% at the outlet. The carbon concentration in the coke residue decreases, and carbon gasification degree (Fig. 6) increases along the PFS and achieves 69.5% at the outlet. The two-component fuel with afore-said characteristics is intensively ignited mixing with the secondary air flow in the furnace volume. Calorific value of the coke residue was amounted to 7200 kJ/kg.

Integral characteristics of ETCPF at the PFS exit are gathered in Table 1. They were taken as initial data for numerical simulation of ETCPF combustion in the experimental furnace using CINAR ICE software code. Secondary air flow rate was 2322 kg/h. The furnace height was 7.5 m. Computing origin was the furnace top. The x , y , z grid size was, respectively: $56 \times 56 \times 60$.

Table 1. Characteristics of ETCPF at the PFS exit

Content of gas phase, (vol. % & kg/h)						
H_2	CO	CH_4	C_6H_6	CO_2	H_2O	N_2
21.6	19.2	0.4	0.7	5.8	1.6	50.8
14.0	174.2	2.2	18.0	82.2	9.1	462.0
Gas temperature, $^{\circ}\text{C}$			Particles temperature, $^{\circ}\text{C}$		Velocity of the flow, m/s	
1002			961		33.8	
Ash, kg/h			Char carbon, kg/h			
185.3			68.4			

The calculations results are shown in Figs. 6–10. Figure 6 visually demonstrates the difference between temperature fields for two operational regimes of the furnace. The traditional mode flame, with maximum temperature of 1580°C , generates the common flame body with the temperature 1300 to 1580°C . The PFS impact appears as transformation of high reactive two-component flame shape, decrease of the flame length and increase of temperature maximum up to 2015°C . That can be explained by earlier ignition and more complete burning-out of ETCPF.

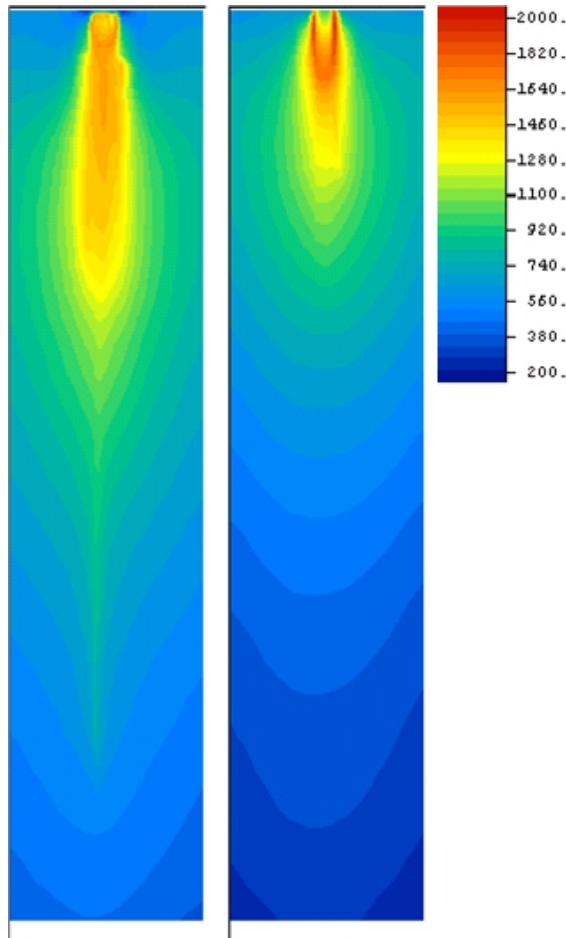


Fig. 6. Temperature fields along the furnace height in the central section for conventional (on the left hand side) and plasma supported (on the right hand side) regimes

2. Comparison of Numerical and Experimental Data

Experimental and numerical temperatures dependences on the furnace height (Fig. 7) are similar. The curves have typical maxima at the distance of 0.5 m from the top of the furnace. The maximal temperature level for conventional mode of the furnace operation at the distance $H < 0.13$ m is higher than one for plasma activated fuel combustion. This difference is up to 164 degrees ($0.025 < H < 0.13$ m). It can be explained by more intensive radiation

from coal particles having higher concentration and total surface when the furnace operation is in conventional mode in comparison with plasma activated regime of coal combustion. When PFS operates electro-thermo-chemically prepared fuel (two component high reactive fuel) is gone from it to the furnace. The fuel contains combustible gas and particles of coke residue which mass do not exceed 30% of the initial coal mass. That brings to triple decrease of radiative particles total surface. In section $0.13 \leq H < 0.6$ m temperature at plasma activated regime is higher than one for conventional mode of the furnace operation. The maximum difference reaches 260 degrees at height 0.4 m. The maximum combustion temperature of plasma activated fuel at the experiment was 200 degrees higher one for conventional mode. Experimental temperature maximum was at the furnace height of 0.67 m. Higher temperature of the flame of plasma activated fuel can be explained by more complete burnout of the fuel. Sharp decrease of oxygen and increase of carbon dioxide concentrations at the section $H < 0.67$ m (Fig. 8) confirm this statement. Unburned carbon concentration in the exit of the furnace ($H = 7.5$ m) is 3 times less when the furnace operates in plasma assisted mode in comparison with conventional mode of the furnace. Also PFS improves ecological characteristics of coal incineration. Figure 9 demonstrates double decrease of nitrogen oxides at the furnace exit.

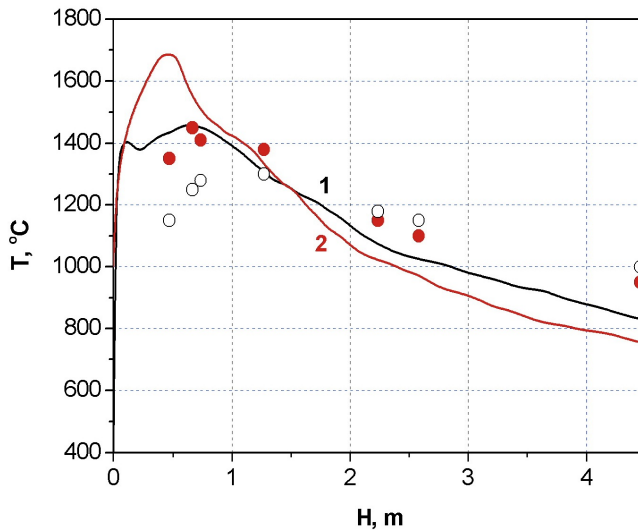


Fig. 7. Furnace height distribution of the combustion materials maximal temperature: 1 – conventional incineration of coal, 2 – incineration of coal in the furnace with PFS; ●, ○ – experimental data on coal incineration in the furnace with PFS and without PFS correspondingly [4]

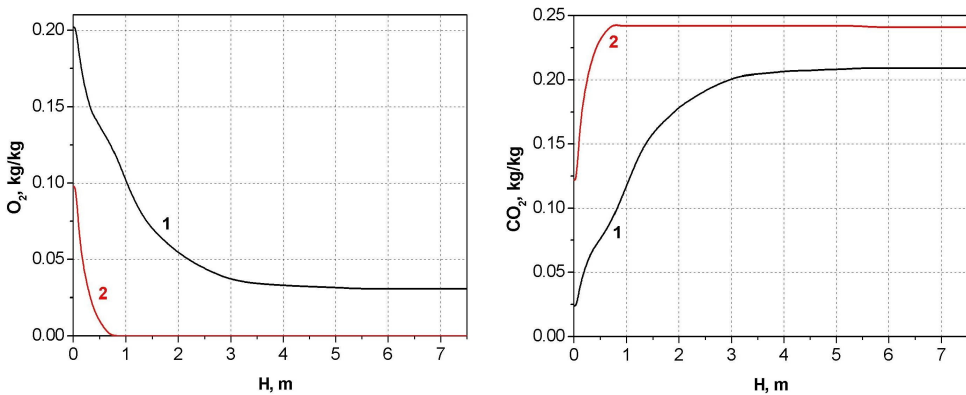


Fig. 8. Furnace height distribution of oxygen (left) and carbon (right) dioxide mean concentration: 1 – conventional incineration of coal, 2 – incineration of coal in the furnace with PFS

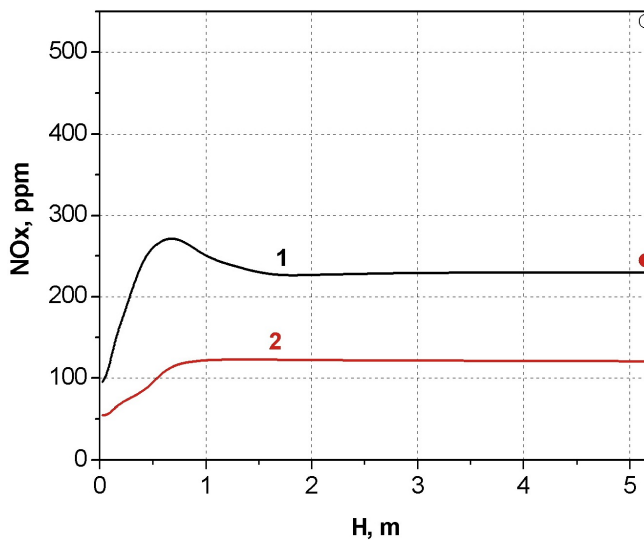


Fig. 9. Furnace height distribution of NOx mean concentration: 1 – conventional incineration of coal, 2 – incineration of coal in the furnace with PFS; ●, ○ – experimental data on coal incineration in the furnace with PFS and without it correspondingly [6]

Thus, the experimental data [4] were used for verification of CINAR ICE computer code. Figures 7 and 9 confirms the qualitative agreement between calculated and experimental data. Divergence of experimental and calculated values of temperature of combustion products does not exceed 20% along the full height of the furnace. The divergence explains by imperfection of the “fast

chemistry” scheme of fuel combustion used by CINAR ICE program. The concentration of unburned carbon was measured at the exit of the experimental furnace. Also divergence of the experimental and calculated values does not exceed 20 %. In experiments unburned carbon was found as 3.1 and 1.8 % for traditional and plasma activated mode correspondingly. Computed figures were 3.72 and 1.42 % accordingly for these two modes. Concentration of nitrogen oxides at the furnace exit is significantly lower for ETCPF combustion than for conventional mode of coal combustion. However, essential quantitative difference of experimental and calculated values of NO_x concentrations (52–54 %) shows that CINAR ICE kinetic scheme of NO_x formation is in need of revision.

3. Computation of PFS and Full-Scale Boiler’s Furnace

The fulfilled verification of CINAR ICE code for plasma assisted coal combustion in the experimental furnace of 3 MW power confirmed legitimacy of the used codes complex (PLASMA-COAL and CINAR ICE) for simulation of the furnaces equipped with PFS. Thus in this part the numerical study was performed for a power-generating boiler with a steam productivity of 420 t/h. The boiler’s furnace (Fig. 10) is equipped with 6 swirl burners arranged in two layers, three burners each, on faced wall of the furnace. As it is seen from the figure three PFS are installed instead of two burners of the lower layer and one of the upper layer. Low-rank Ekibastuz bituminous coal of 40 % ash content, 24 % devolatilization, 5 % humidity and 16700 kJ/kg heat value was incinerated in the furnace. The coal grinding fineness was $R_{90} = 15\%$. All the calculations were performed in accordance to the aforementioned technique.

PLASMA-COAL computer code has been used for calculation of ETCPF in the volume of PFS of 3.687 m length and 0.46 m diameter. The following initial parameters were used for calculations: plasmatron power was 200 kW, initial temperature of pulverized coal (coal/air mixture) was 90 °C, coal and air consumptions through PFS were 6000 and 8955 kg/h correspondingly.

The results of numerical simulation by the PLASMA-COAL code are summarized in Table 2. Heat value of the coke residue was 6165 kJ/kg. These data obtained for the PFS exit were taken as initial parameters for 3-D computation of the furnace of a power-generating boiler equipped with PFS. This computation was performed using CINAR ICE code to demonstrate advantages of plasma aided coal combustion technology.

Initial parameters for calculations of the furnace (Fig. 10) in different operational regimes were the following: temperature of the secondary air was 280 °C, coal productivity of the burner was 12000 kg/h and primary air flow rate through the burner was 17900 kg/h. Secondary air flow rate to the boiler

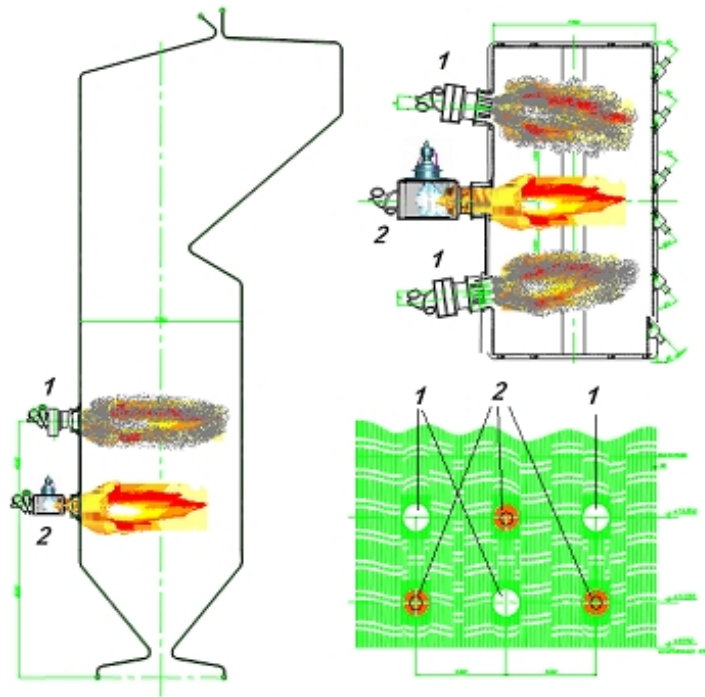


Fig. 10. Scheme of the furnace of the industrial 420 t/h steam productivity boiler in Almaty TPP-2 (Kazakhstan) retrofitted with PFS: 1 – standard pulverized coal swirl burner, 2 – PFS

Table 2. Characteristics of ETCPF at the PFS exit

Content of gas phase, (vol. % & kg/h)							
H ₂	CO	CH ₄	C ₆ H ₆	CO ₂	H ₂ O	N ₂	O ₂
1.05	7.75	0.3	0.77	15.6	3.55	70.84	0.15
7.272	751.4	16.75	207	2378	220.5	6870	16.49
Gas temperature, °C			Particles temperature, °C			Velocity of the flow, m/s	
1025			1025			48.2	
Ash, kg/h			Char carbon, kg/h				
1518			261				

was 446412 kg/h. Averaged size of the coal particles was 60 micron. The furnace size is as follows: 27 m height, 7.7 m depth and 14.5 m width. The x, y, z grid size was, respectively: $106 \times 38 \times 104$.

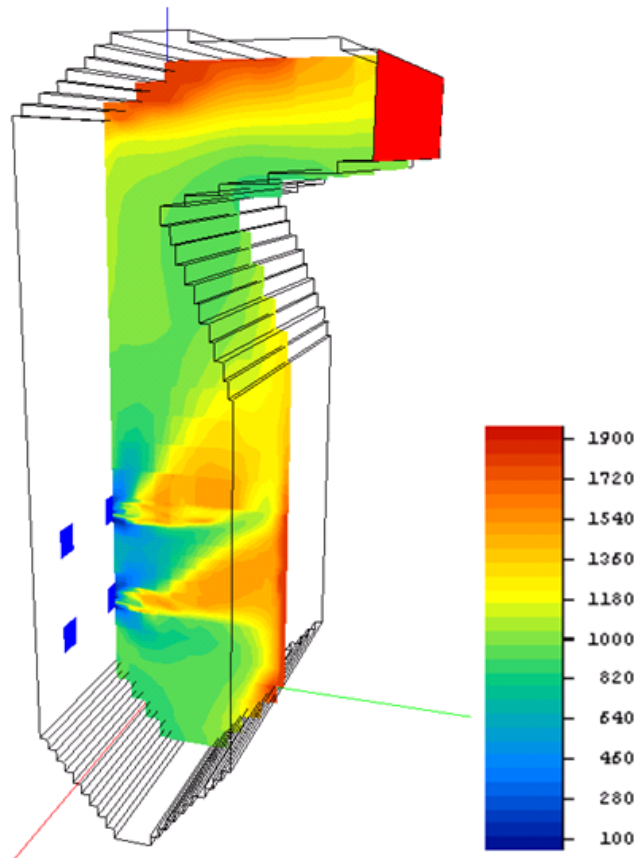


Fig. 11. Temperature field along the furnace height in the mean cross-sectional plane of the furnace when it works in conventional mode of coal combustion

The model predictions are presented in the following figures which show results for the plasma-activated coal combustion in comparison with conventional coal combustion. Figures 11 and 12 show temperature fields along the furnace height in the mean cross-sectional plane for two regimes of the furnace operation, traditional (Fig. 11) and plasma activated coal combustion (Fig. 12). The figures visually demonstrate the difference between the temperature fields for the two modes of coal combustion. When the coal combustion is in conventional mode, six symmetric pulverized coal flames are formed. Maximum temperature of these flames is 1852°C . In Fig. 12 one can see PFS influence on the shape of the ETCPF flame and its maximal temperature. In the presented plane PFS is upwardly. High temperature body of the flame moves closer to the PFS exit and upper in the furnace. Its maximal temperature is 1588°C .

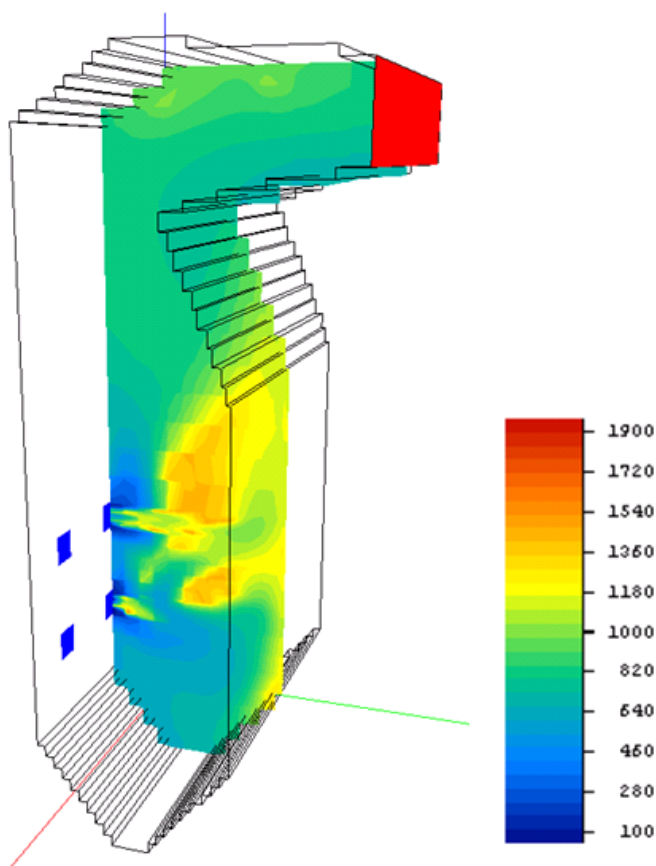


Fig. 12. Temperature field along the furnace height in the mean cross-sectional plane of the furnace when it works in plasma-assisted mode of coal combustion using 3 PFS

Averaged temperature curves (Fig. 13) have their maxima. At conventional mode of coal combustion the first maximum ($H = 3$ m) is generated by overheating of the furnace back wall by the pulverized fuel flame. The second maximum is above the level of the burners of the lower layer due to common forming of the flame body and observed moving is a result of natural convection. At plasma activated mode of coal combustion the first maximum is observed above the lower layer of the PFS. The maxima at $15 \div 17$ m of the furnace are the results of the completing of the flame body forming for the both modes. Averaged temperatures in the furnace operated in conventional mode are higher one for the furnace operated in plasma assisted regime using PFS. Exception is the furnace area from 7 to 11 m, for which the temperature is increased due to plasma activation of the fuel combustion. The difference

achieves 350 degrees at the furnace exit. The reason of this is more intensive radiation of coal particles which have higher concentration and total reacting surface when the furnace operates in conventional mode in comparison with plasma assisted coal combustion (Fig. 11). When PFS operates two component fuel of combustible gas and particles of coke residue enters the furnace. Mass of the coke does not exceed 30% of the initial coal mass. That decreases total surface of the radiative particles. Due to plasma activation of pulverized coal flame the process of combustion is intensified, the fuel is burnt out quicker and at the furnace exit temperature decreases.

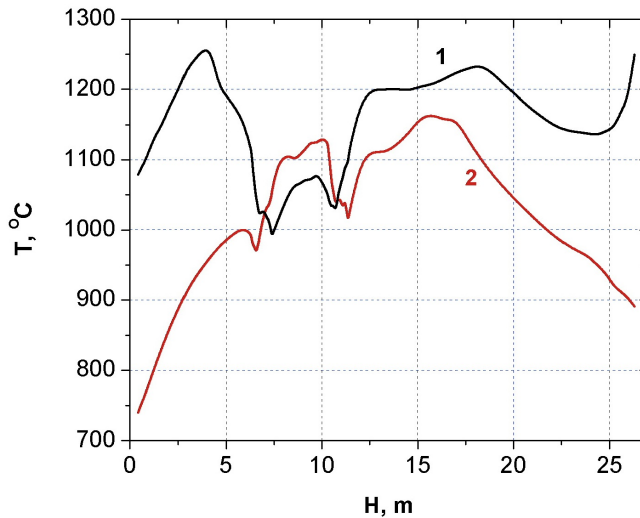


Fig. 13. Mean temperature (T) along the furnace height (H):
1 – conventional incineration of coal, 2 – incineration of coal when
3 PFS operate

Table 3 gives a comparison of the two predicted cases, conventional and plasma activated coal combustion. Plasma activation of coal combustion 26% decreases temperature of flue gas and more than 34% decreases nitrogen oxides concentration. At the furnace exit when three PFS operate concentration of unburned carbon is 16% less one when the furnace works in traditional mode of coal combustion. This is confirmed by decrease of O₂ concentration (17%) and corresponding increase of CO₂ concentration (14%).

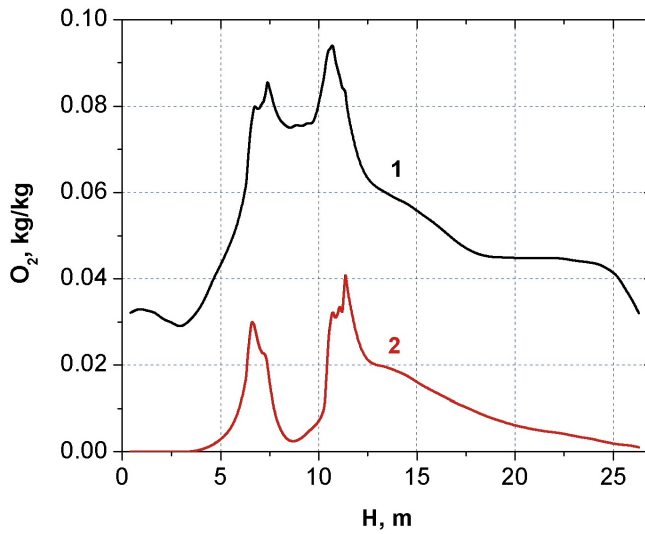


Fig. 14. O₂ mean concentration along the furnace height (H):
 1 – conventional incineration of coal, 2 – incineration of coal when
 3 PFS operate

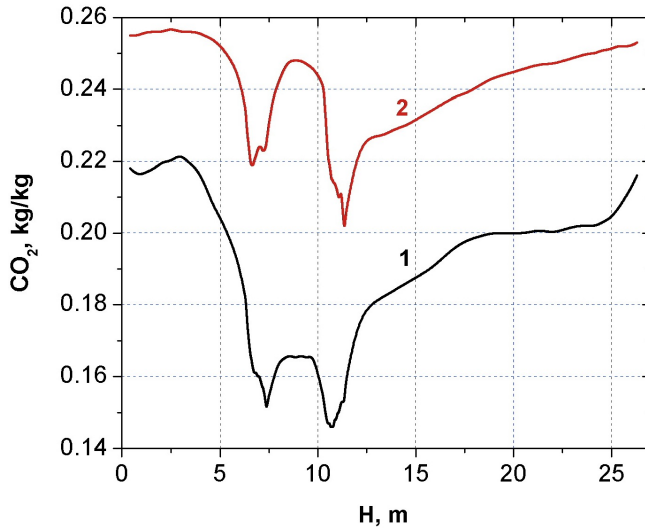


Fig. 15. CO₂ mean concentration along the furnace height (H):
 1 – conventional incineration of coal, 2 – incineration of coal when
 3 PFS operate

Table 3. Characteristics of flue gas at the outlet of the furnace

	Conventional combustion	Plasma activated combustion
T, °C	1280	950
NO _x , ppm	239	157
CO ₂ , kg/kg	0.22	0.25
O ₂ , kg/kg	2.9×10^{-2}	0.1×10^{-2}
C, kg/kg	751.4	16.75

Conclusions

To investigate the processes of coal combustion including plasma assisted one complex of two software codes (PLASMA-COAL and CINAR ICE) was used. The fulfilled verification of CINAR ICE code for plasma assisted coal combustion in the experimental furnace of 3 MW power confirmed legitimacy of the used codes complex for simulation of the furnaces equipped with PFS. These codes application allowed investigating the processes of coal plasma assisted combustion. Plasma activation of coal combustion increases efficiency of its incineration decreasing unburned carbon and nitrogen oxides concentrations. Evidently decrease of unburned carbon and NO_x concentrations at the furnace exit means improving of ecology-economic indexes of TPP. On the base of the presented numerical research renovation of the furnace of 420 t/h steam productivity boiler is scheduled.

References

- [1] E. I. KARPENKO, YU. E. KARPENKO, V. E. MESSERLE, A. B. USTIMENKO: *Using plasma-fuel systems at eurasian coal-fired thermal power stations*. Thermal Engineering, 56 (2009), 456–461.
- [2] M. A. GOROKHOVSKI, Z. JANKOSKI, F. C. LOCKWOOD, E. I. KARPENKO, V. E. MESSERLE, A. B. USTIMENKO: *Enhancement of pulverized coal combustion by plasma technology*. Combustion Science and Technology, 179 (2007), 2065–2090.
- [3] R. A. KALINENKO, A. P. KUZNETSOV, A. A. LEVITSKY, V. E. MESSERLE, YU. A. MIROKHIN, L. S. POLAK, Z. B. SAKIPOV, A. B. USTIMENKO: *Pulverized coal plasma gasification*. Plasma Chemistry & Plasma Processing, 13 (1993), 141–167.
- [4] Z. B. SAKIPOV, V. E. MESSERLE, SH. SH. IBRAEV: *Electrothermochemical preparation of coal to burning*. (in Russian), Almaty: “Nauka”, 1993, 259 p.
- [5] M. GOROKHOVSKI, E. I. KARPENKO, F. C. LOCKWOOD, V. E. MESSERLE, B. G. TRUSOV, A. B. USTIMENKO: *Plasma technologies for solid fuels: experiment and theory*. Journal of the Energy Institute, 78 (2005), 157–171.

- [6] Z. JANKOSKI, F. C. LOCKWOOD, V. E. MESSERLE, E. I. KARPENKO, A. B. USTIMENKO: *Modelling of plasma pre-treatment of powdered coal for combustion*. Thermophysics and Aeromechanics, 11 (2004), 461–474.
- [7] F. C. LOCKWOOD, A. P. SALOOJA, A. A. SYED: *A prediction method for coal-fired furnaces*. Combustion and Flame, 38 (1980), 1–15.
- [8] F. C. LOCKWOOD, T. MAHMUD, M. A. YEHIA: *Simulation of pulverised coal test furnace performance*. Fuel, 77 (1998), 1329–1337.
- [9] F. C. LOCKWOOD, T. MAHMUD: *The prediction of swirl burner pulverised coal flames*. Symposium (International) on Combustion, 22 (1989), 165–173.
- [10] A. S. ASKAROVA, E. I. KARPENKO, Y. I. LAVRISHCHEVA, V. E. MESSERLE, A. B. USTIMENKO: *Plasma-supported coal combustion in boiler furnace*. IEEE Trans. Plasma Sci., 35 (2007), 1607–1616.
- [11] I. B. MATVEEV, V. E. MESSERLE, A. B. USTIMENKO: *Plasma gasification of coal in different oxidants*. IEEE Trans. Plasma Sci., 36 (2008), 2947–2954.
- [12] B. E. LAUNDER, D. B. SPALDING: *The numerical computation of turbulent flows*. Comput. Meth in Appl. Mech. And Eng., 3 (1974), 269–289.
- [13] F. C. LOCKWOOD, N. G. SHAN: *Evaluation of an efficient radiation flux model for furnace prediction procedures*. Sixth Int. Heat Transfer Conference, 6 (1978), 33–42.
- [14] F. C. LOCKWOOD, N. G. SHAN: *A new radiation solution method for incorporation in general combustion prediction procedures*. Symposium (International) on Combustion, 18 (1981), 1405–1414.

Received May 17, 2010

Plasma treatment of silicon surface by DCSBD¹

DANA SKÁCELOVÁ², PAVEL ŠTAHEL², MARTIN HANIČINEC²,
MIRKO ČERNÁK^{2,3}

Abstract. This paper focuses on the plasma treatment of crystalline Si (100) surface. The plasma was generated by Diffuse Coplanar Surface Barrier Discharge (DCSBD) at atmospheric pressure using ambient atmosphere. Surface free energy of silicon was investigated by contact angle measurement and surface morphology was studied by Atomic force microscope. Plasma treatment increases the surface wettability and AFM measurements showed that the plasma influences also the surface roughness.

Key Words. Silicon surface, plasma treatment, DBD, coplanar discharge, contact angle measurement, AFM.

Introduction

Silicon is the second most common element on Earth. Except for the silicon as an essential element in biology, it has also many industrial uses. Silicon is the most widely used material by the production of semiconductors in the current microelectronics, photovoltaic applications, integrated circuits etc [1]. Due to its great importance in the industry, it is probably the most investigated material.

Unfortunately, most of the production processes include manufacturing operations that are not fully environmentally friendly, especially chemical etching, cleaning, chemical modification or coating of surfaces [2]. During several last decades it was found, either accidentally or intentionally, that the plasma could

¹This research has been supported by the research intent MSM:0021622411 funding by the Ministry of Education of the Czech Republic and by the contract KAN101630651 by Grant Agency of Academy of Science of Czech Republic.

²Department of Physical Electronics, Faculty of Science, Masaryk University, Kotlářská 2, 611 37, Brno, Czech Republic

³Department of Experimental Physics, Faculty of Mathematics, Physics and Informatics, Comenius University, Mlynská dolina F2, 842 48, Bratislava, Slovak Republic

provide a good ecologically solution to environmentally friendly processes and products. Presently, it is possible by means of plasma cleaning, activation and coating of surfaces, hydrophobization or hydrophilization of surfaces or plasma polymerization [3], [4].

In this paper we examine, by means of contact angle measurement and atomic force microscope (AFM), the influence of the plasma on the silicon surface and the following surface modification. The knowledge of the wetting behaviour, surface energy and roughness could enable to optimize the plasma cleaning and activation parameters. Furthermore, the good and uniform wettability of surfaces plays an important role in all wet chemical processes.

It was found that plasma treatment increases the surface wettability. Furthermore, the ageing effect of the treated surface was studied because it was found that effect of plasma is not stable. As the plasma treated sample is exposed to an ambient air, the treated surface evolves into less hydrophilic. The surface roughness depends on the plasma treatment duration and it was possible to create by plasma conditions the surface roughness from units to hundreds of nm.

Experimental setup

As a plasma source was used the special construction of dielectric barrier discharge, the so called Diffuse Coplanar Surface Barrier Discharge (DCSBD) (Fig. 1) [5]. This type of discharge produces the large area of thin layer of atmospheric non – isothermal low temperature plasma on the surface of dielectric barrier. The dielectric barrier is made of Al_2O_3 ceramics with embended metallic electrodes.

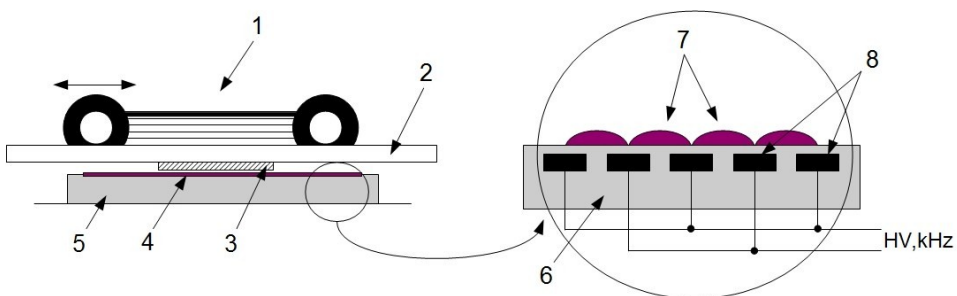


Fig. 1. Laboratory DCSBD reactor with detail of the discharge electrode system cross section: 1 – sample holder, 2 – rail, 3 – sample, 4 – plasma layer, 5 – DCSBD electrode, 6 – Al_2O_3 dielectric, 7 – plasma, 8 – electrodes with HV

Treated samples were placed on the movable holder that moves the sample over the plasma layer. Treatment velocity and the distance between the sample surface and the ceramics plate were adjustable.

The n-type, (100) oriented, monocrystalline polished silicon wafers, doped with antimony were used in our experiment. Before plasma treatment all samples were cleaned by isopropyl alcohol and then immersed in 1% HF solution at room temperature for 45s for native oxide removal [7]. The treatment has been carried out in ambient air at the discharge power 300 W, treatment time 2.4s and the distance between the sample surface and ceramics plate was 0.3 mm. Contact angle measurements were realised by Surface Energy Evaluation (SEE) System. For calculation of surface free energy Van-Oss-Chaudbury-Good method was used and distilled water, glycerol and diiodomethane were used as the measuring liquids [6].

Results and discussion

In Fig. 2 results of the contact angle measurements are shown. It stands to reason that plasma treatment makes the silicon surface hydrophilic. Contact angle of water drop was about 80° before plasma treatment. Plasma treatment decreases contact angle up to less than 10° , depending on conditions.

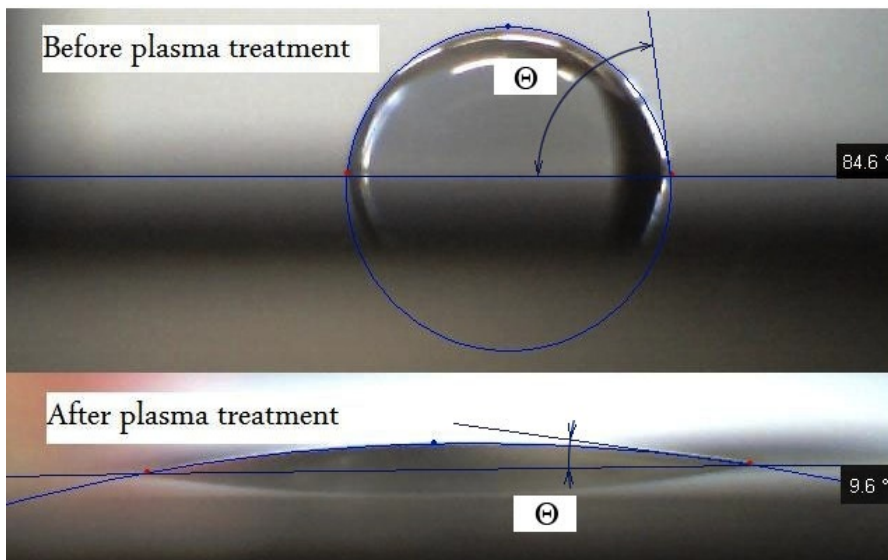


Fig. 2. The fitted water drop on the silicon surface before and after plasma treatment; before plasma treatment, water contact angle was 84° , in comparison with less than 10° after plasma treatment

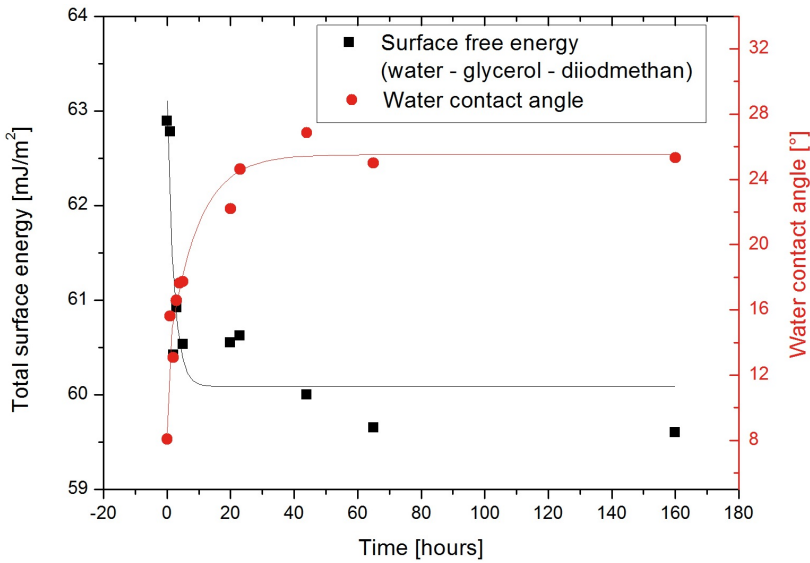


Fig. 3. Ageing effect of the treated silicon surface; a change of contact angle of water and, related to it, surface free energy of treated Si surface during the storage time

Figure 3 shows that the effect of plasma treatment is not stable over time. When the treated surface is exposed to a surrounding ambient the contact angle increases, wettability decreases. This effect can be explained by the contamination of impurities and organic compounds from an ambient air [7], [8].

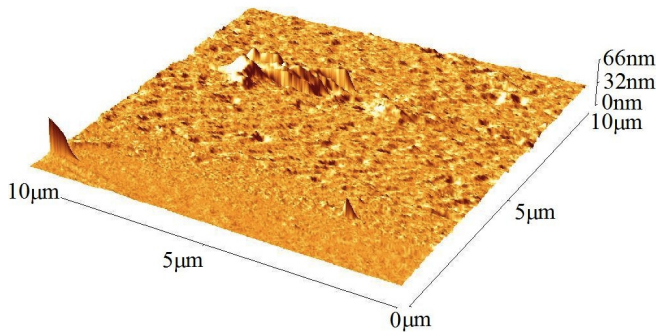


Fig. 4. AFM image of the typical polished silicon surface

Results of AFM measurements are shown in Figs. 4 and 5. Figures represent the AFM images of the silicon surface untreated, plasma treated for 1 s and plasma treated for 60 s. It is evident that RMS roughness depends on the plasma treatment duration. The longer treatment duration caused the greater

roughness of the silicon surface. The typical RMS roughness value of clean polished untreated silicon surface is 2.23 nm. The RMS roughness of 1 s treated surface was 19.6 nm and 60 s treated sample was 32.0 nm. Values of the RMS roughness are shown in the Table 1.

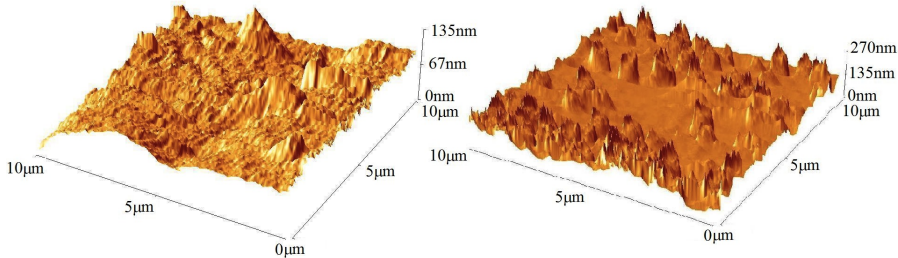


Fig. 5. AFM images of plasma treated silicon surface; the left one was treated for 1 s, the right one for 60 s

Table 1. Comparison of RMS roughnesses untreated and plasma treated samples

Treatment time [s]	0	1	60
RMS roughness [nm]	2.23	19.6	32.0

Conclusion

In this work the influence of plasma to polished silicon wafer surface was investigated. The plasma treatment of silicon surface by DCSBD led to an increase of wettability nevertheless this change is not permanent. The treated surface exposed to an ambient atmosphere became less hydrophilic within a few hours, the so called ageing effect. Furthermore the plasma treatment can change the roughness of the surface. The longer duration of plasma treatment, the greater roughness of silicon surface.

References

- [1] P. SIFFERT, E. F. KRIMMEL: *Silicon: evolution and future of a technology*. Springer-Verlag, Berlin, Heidelberg, New York 2004.
- [2] U. GANGOPADHYAY, S. K. DHUNGEL, A. K. MONDAL, H. SAHA, J. YI: *Novel low – cost approach for removal of surface contamination before texturization of commercial monocrystalline silicon solar cells*. *Solar Energy Materials and Solar Cells*, 91 (2008), 1147–1151.

- [3] A. BUČEK, T. HOMOLA, M. ARANYOSIOVÁ, D. VELIČ, T. PLECENIK, J. HAVEL, P. ŠTAHEL, A. ZAHORANOVÁ: *Atmospheric pressure non-equilibrium plasma treatment of glass surface*. *Chemické listy*, 102 (2008), 1459–1462.
- [4] L. ČERNÁKOVÁ, R. SZABOVÁ, M. WOLFOVÁ, A. BUČEK, M. ČERNÁK: *Surface modification of polypropylene nonwoven after plasma activation at atmospheric pressure*. *FIBRES & TEXTILES in Eastern Europe*, 15 (2007), 121–123.
- [5] <http://gimmel.ip.fmph.uniba.sk/treaters/>, Surface modification of nonwoven fabrics by atmospheric pressure plasma in continuous regime, April 20, 2011.
- [6] M. ZENKIEWICZ: *Methods for the calculation of surface free energy of solids*. *Journal of Achievements in Materials and Manufacturing Engineering*, 24 (2007), 137–145.
- [7] X. G. ZHANG: *Electrochemistry of silicon surface and its oxide*. Kluwer Academic Publisher, New York 2003.
- [8] G. F. CEROFOLINI, L. MEDA: *Chemistry at silicon crystalline surface*. *Applied Surface Science*, 89 (1995), 351–360.

Received May 10, 2010

Application of pulsed plasma streams for surface modification of constructional materials¹

OLEG BYRKA², ANDRIY BANDURA², IGOR GARKUSHA²,
VALERIY TARAN², VADIM MAKHLAI², VLADIMIR TERESHIN²

Abstract. Recent experimental studies on plasma surface interactions resulting in surface modification of different constructional materials and deposited coatings by pulsed plasma streams are presented. In particular, changes of physical and mechanical properties of hafnium, zirconium based alloys and Hastelloy under the influence of pulsed plasma streams treatment is discussed. Materials surface morphology, structure and thickness of modified layer, which is formed under the plasma processing have been investigated. It is shown that modified layer resistant to etching with homogeneous structure and thickness up to 20 μm is formed as a result of plasma treatment. Experiments revealed the positive influence of alloying by Nb on zirconium behaviour at high heat loads and particle bombardment. X-ray diffraction analysis of investigated materials shows halo appearance for small angles indicating quasi-amorphous structure of modified surface layer. Plasma processing resulted in development of nano- and submicron cellular structures in surface layer of Hastelloy N samples. Ordered cellular structures form specific morphology with average cell size of about 200 nm. Decreasing grain size and amorphous transformations are found to be important for improvement of corrosion properties of this material.

Key Words. Pulsed plasma streams, modified surface layer, coating, hafnium, zirconium, Hastelloy N.

¹This work has been supported by CNCP program within the STCU project “Pulsed plasma treatment”. The authors would like to thank V. Gasilin and A. Timoshenko for PVD coatings depositions and their assistance in the performed experiments.

²Institute of Plasma Physics of the National Science Center “Kharkov Institute of Physics and Technology”, 61108 Kharkov, Akademicheskaya Str. 1, Ukraine

1. Introduction

Surface processing with pulsed plasma streams of different gases is found to be effective tool for modification of surface layers of different materials [1]–[4]. In particular, exposures with pulsed powerful plasma streams result in hardening their surfaces and increasing the wear resistance of industrial steels [5], [6]. Fast heating and melting of treated surface, considerable temperature gradients ($\sim 10^6$ K/cm) arising in surface layer of material under the pulsed plasma impact contribute to high speed diffusion of plasma stream ions into the depth of the modified layer, during the liquid stage, phase changes in the surface layer, and formation of the fine-grained or quasi-amorphous structures under the following fast resolidification. The cooling speed of $\sim 10^6 \div 10^7$ K/s is achieved in this case due to the contact of thin melt layer ($h_{\text{melt}} \sim 10 \div 50 \mu\text{m}$) with massive bulk of the sample.

Plasma can also be considered as a source of alloying elements to be introduced into modified layer structure. That is why nitrogen is preferentially used for pulsed plasma processing of different steels. Another possibility of alloying under the pulsed plasma processing is mixing of previously deposited thin ($h_{\text{coat}} < h_{\text{melt}}$) coatings of different predetermined composition with the substrate in result of powerful plasma impact.

Results of pulsed plasma stream treatment for different kinds of steels are presented in [7], [8]. In this paper, construction materials tests with pulsed high heat loads are described. Features of surface modification for constructional materials, relevant to nuclear power systems, and different deposited coatings by pulsed plasma streams are presented. In particular, mitigation of brittle damage and possibility of improvement of physical and mechanical properties of hafnium, zirconium based alloys and Hastelloy under the influence of pulsed plasma streams treatment is discussed.

2. Experimental equipment and diagnostics

Experiments on material samples treatment with powerful pulsed plasma streams were carried out with use of pulsed plasma accelerator (PPA) [1], [2]. Scheme of the device is presented in Fig. 1. The PPA stand consists of coaxial set of electrodes with anode diameter of 14 cm and cathode diameter of 5 cm and vacuum chamber of 120 cm in length and 100 cm in diameter. The power supply system is condenser banks with stored energy of 60 kJ (for 35 kV). The amplitude of a discharge current is ~ 400 kA, plasma stream duration is $3 \div 6 \mu\text{s}$. The pulsed plasma accelerator generates plasma streams with ion energy up to 2 keV, plasma density $(2 \div 20) \times 10^{14} \text{ cm}^{-3}$, average specific power of about 10 MW/cm^2 and plasma energy density varied in the range of $(5 \div 40) \text{ J/cm}^2$. Nitrogen, helium, hydrogen and different mixtures can be used as working

gases. The regime of plasma treatment could be chosen with variation of both accelerator discharge voltage and the distance of the exposed samples from the PPA output.

High quality coatings of Mo and W were previously deposited using planar rectangular ECR plasma source with a multipolar magnetic field [9]. The working frequency of ECR source and HF power are 2.45 GHz and 300 W, respectively. The ultimate pressure in the vacuum chamber was about 2×10^{-5} Torr. The working pressure (2×10^{-3} Torr) was defined by variation of the working gas (Ar) flow and the pumping speed. The plasma parameters close to surface of processed target were as follows: electron density up to 10^{11} cm $^{-3}$, electron temperature ~ 12 eV, ion current density to the grounded substrate ~ 3.5 mA/cm 2 .

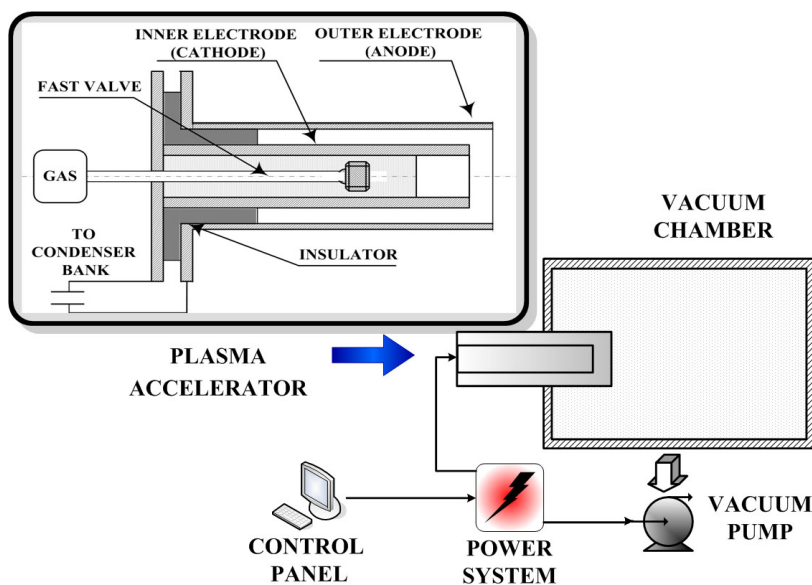


Fig. 1. Scheme of PPA device

TiN, TiC, Cr, Cr, CrN and other coatings were deposited to the samples surfaces by PVD method in “Bulat” installation [10].

For plasma parameters measurements a wide range of diagnostics was used: calorimetry, electric and magnetic probes, piezo-detectors etc. X-ray diffraction (XRD) has been used to study the microstructural evolution of exposed targets. θ - 2θ scans were performed using a monochromatic $K\alpha$ line of Cu anode radiation. The analysis of diffraction peaks intensity, profiles and angular positions was applied to evaluate texture, coherent scattering zone size, macrostrain and lattice parameters. Surface observations with optical microscopy and SEM were performed also.

3. Experimental results

3.1. Hafnium behavior and main damage mechanisms under pulsed plasma loads

Initial analysis of hafnium samples surfaces has shown rather developed structure with traces of preliminary mechanical processing with some cavities having typical size of $5\ \mu\text{m}$. After plasma streams treatment essential changes of surface morphology occur. It was observed that material surface is smoothed in result of surface layer melting and resolidification and roughness parameters are decreased. Distinguished boundary of grains as result of plasma ions bombardment and some isolated intergranular cracks due to the thermal stresses are observed. However it should be noted that cracks do not form the complete network. Another feature of cracks formation (Fig. 2) is cracks are formed in points of grains confluence as well as at the boundary separate grains. The crack length does not exceed $200\ \mu\text{m}$ and the width is not more than $2\ \mu\text{m}$.

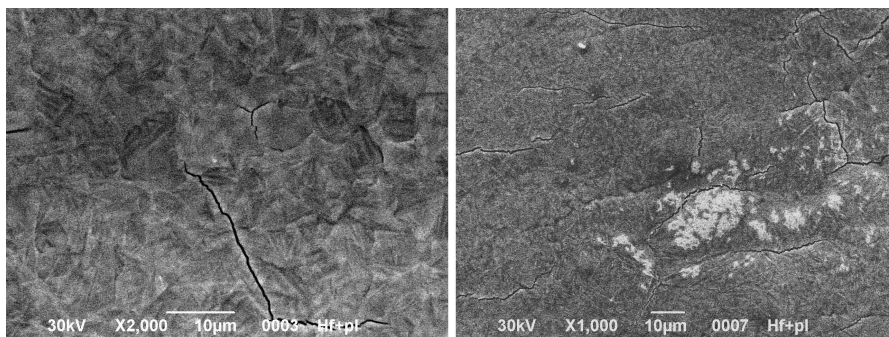


Fig. 2. SEM micrograph of hafnium surface

3.2. Plasma treatment of zirconium based alloys

Plasma treatment of two types of samples Zr and Zr+1 % Nb was carried out. Size of samples was $20 \times 20 \times 2\ \text{mm}$, preliminary sample surface preparation and regimes of exposures (5 pulses of $5\ \mu\text{s}$ duration with deposited energy density of $28 \div 30\ \text{J}/\text{cm}^2$) were the same in both cases.

Irradiation of pure zirconium samples resulted in formation of molten layer on the processing surface. In result of plasma treatment separate grain boundaries became visible due to sputtering process by plasma ions. Grain size achieves $20 \div 25\ \mu\text{m}$. Separate short cracks along the grains are formed on the irradiated surface. It should be noted that swelling of grain boundaries is initiated by cracks as it is shown in Fig. 3. This process may initiate material

delamination in surface layer. As consequence of surface morphology changes roughness increasing up to 30 % is measured.

According to X-ray analysis after Zi treatment with nitrogen plasma stream, no other phases except zirconium are found on the exposed surface (Fig. 4). Halo area is registered in the spectrum within the range of $15 \div 20$ degrees of 2θ angles, with a maximum at $2\theta \approx (17 \div 18)^\circ$. On the base of analysis performed for diffraction lines profiles an asymmetry in line shape for smaller 2θ angles was identified. Such asymmetry may be attributed to the nitrogen penetration (as working gas for these exposures) into the molten material layer. Performed analysis has shown that the coherent-scattering region (CSR) size i.e. the minimum dimension of crystallites in the perpendicular to the exposed surface direction near the halo is equal to $\approx (15 \div 50) \text{ \AA}$. Typical CSR parameters of virgin samples are within $(1500 \div 2000) \text{ \AA}$. Thus, from the X-ray measurements one possible to conclude that modified layer of several microns in the thickness that has nanocrystalline structure is formed on the irradiated surface.

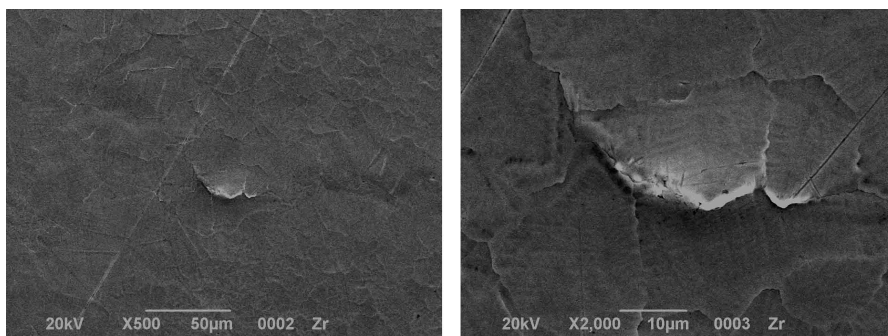


Fig. 3. SEM micrographs of zirconium surface after plasma treatment

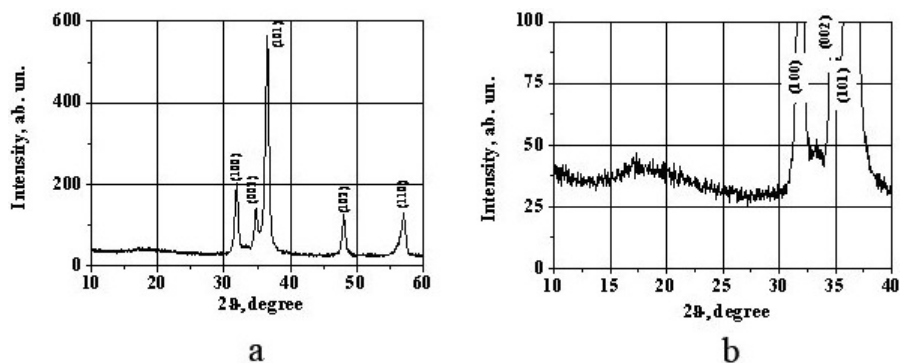


Fig. 4. X-ray analysis results; a) spectrum on the processing zirconium surface sample, b) halo area on the X-ray spectrum

The surface morphology of zirconium–niobium alloy samples (Zr + 1 % Nb) after the pulsed plasma treatment significantly differs from pure zirconium one (Fig. 5). Origination of a homogeneous resolidified fine grained layer does not accompanied by surface cracking. It can be considered as important advantage of this alloy in power engineering from the point of view it response to the pulsed heat loads. The improved material properties of this alloy can be explained by decreased brittleness caused by Nb 1 % alloy addition.

There are clearly visible boundaries of separate material grains appeared after plasma treatment. Grain size does not exceed 10 μm , being in $2 \div 2.5$ times less than for pure Zr samples. The surface roughness did not change significantly. On the base of XRD analysis only presence of zirconium phase was identified.

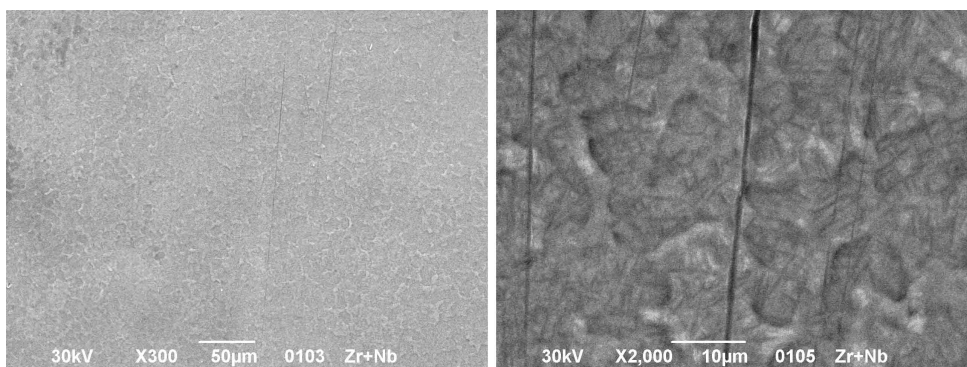


Fig. 5. SEM micrographs of zirconium surface based alloys (Zr + 1 % Nb) with different magnification

3.3. Surface modification of Hastelloy N under the pulsed plasma processing

The primary function of Hastelloy and other nickel alloys is effective survival under high-temperature, high-stress conditions in moderate corrosive and/or erosive conditions, where usual and less expensive iron-based alloys (steels) would fail. The applications of Hastelloy include the pressure vessels of some power reactors and pipes, valves in chemical industry etc. The predominant alloying element in Hastelloy N is nickel. Other alloying dopes are Mo, Cr, Fe, Si, Mn of varying percentage.

As a result of pulsed plasma treatment modified surface layer with essentially changed structure has been formed in Hastelloy samples. Besides typical “large-scale” grain structures with grain size up to $50 \div 100 \mu\text{m}$, which is seen in Fig. 6a, higher magnification reveals fine cellular structure inside the grains with submicron- and nano-dimension, as shown in Fig. 6b. Appearance of fine

cellular structure is attributed to powerful pulsed plasma impact with high-speed heating and cooling in non-equilibrium conditions with high temperature gradients in surface layer. It should be noted that no cracks or visual defects are arisen in the course of plasma treatment. These ordered cellular surface structures are primary oriented along the direction of surface machining, which was previously applied for sample surface preparation. Average cell dimensions are in the range of $200 \div 500$ nm.

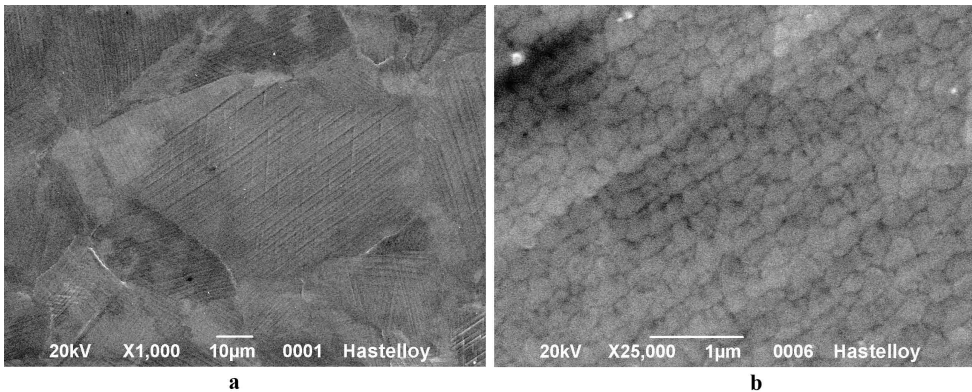


Fig. 6. SEM micrographs of Hastelloy N surface after plasma treatment

Investigations of Hastelloy sample cross-cuts revealed that modified layer with the thickness of $5 \div 10$ μm is formed on the alloy surface. Figure 7 shows cross-sections of Hastelloy samples before (a) and after plasma treatment (b) respectively. Surface roughness is decreased in result of plasma treatment. The fine-grained modified layer has uniform structure resistant to etching. Large grains typical for virgin structure are seen below the modified layer.

In experiments on Hastelloy treatment with electron beams [11], similar surface structure refinement was described. It is attributed to short-pulse quenching effect, when grains could not be formed during fast re-solidification of the molten surface layer. Decreasing grain size and amorphous transformations are found to be important for improvement of corrosion properties of this material in the liquid lead environment [11]. In our case plasma treatment has clear advantage related with combined influence of the heat load and particle bombardment, which can drive chemical transformation in surface layer. Modified layer thickness is higher for plasma pulses applied and, what is more important, the surface roughness is essentially smaller for plasma treatment because of the difference in energy transfer to the surface (volumetric heating mechanism with maximal temperature in some depth for high-energy electron beam exposures and surface heating by low-energy ions for pulsed plasma treatment).

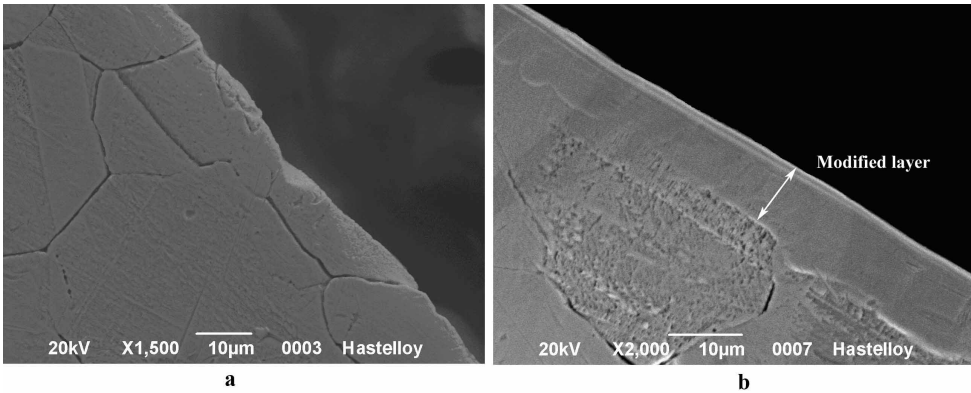


Fig. 7. Cross-sections of Hastelloy samples before (a) and after (b) plasma treatment

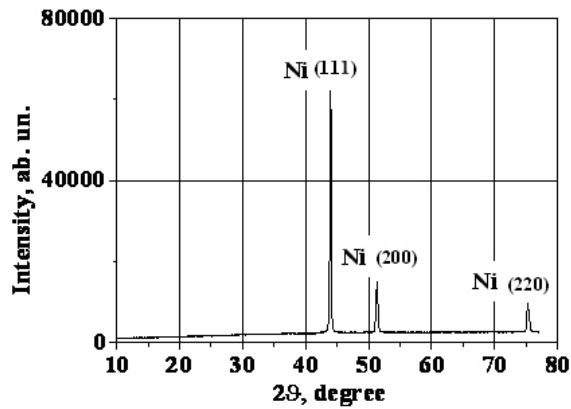


Fig. 8. X-ray spectrum of treated Hastelloy N sample

XRD results for the irradiated surface are presented in Fig. 8. Typically XRD technique is able to detect only the phase of the dominating element (nickel) for this alloy. Based on these results size of coherent-scattering region (CSR) was estimated. For the diffraction peaks of Ni (111) and Ni (220) CSR it achieved 480 Å and 340 Å correspondingly. The penetration depth of X-rays for these peaks is in the range of (7 ÷ 12) µm. This is in rather good agreement with the results of modified layer thickness measurements in irradiated sample cross-sections. Since the penetration depth of X-rays may exceed the modified layer thickness and diffraction peaks intensity in the studied range is almost extreme, the halo is not clearly identified in X-ray spectra.

3.4. Alloying of surface layers by mixing of coatings with substrate under the plasma treatment

Modification of thin ($0.5 \div 2 \mu\text{m}$) PVD coatings of MoN, C+W, TiN, TiC, Cr, Cr+CrN and other with the pulsed plasma processing is investigated for varied parameters of impacting nitrogen plasma stream. It is shown that pulsed plasma treatment results in essential improvement of physical and mechanical properties of exposed materials.

The performed experiments have shown that pulsed plasma treatment leads to improvement of physical and mechanical properties of exposed cast iron and steel materials. These materials were used as substrate for coating deposition in consecutive studies. Essential increase of microhardness in result of pulsed plasma treatment was achieved for both cases: exposures of samples with and without previously deposited coatings. Comparative studies of tribology characteristics of the modified layers with different coatings are performed.

Table 1. Results of tribological tests; (*) – transport and sticking of indenter material to the sample

Type of sample	Indentor wear 10^{-4} g	Sample wear 10^{-4} g	Friction coefficient $p = 1 \text{ kN}$	Microhardness kg/mm^2	
				area of contact	outside of contact
initial	26.5	2.5	0.084	893	785
5 pulses (nitrogen, $28 \text{ J}/\text{cm}^2$)	32.0	4.0	0.088	1013	1013
Cr + 5 pulses (nitrogen, $28 \text{ J}/\text{cm}^2$)	24.0	3.0	0.074	1100	1630
Cr + CrN	57.0	0	0.076	962(*)	1420
TiN	655.5	5.5	0.085	695(*)	25.75
MoN	25.5	4.5	0.080	1100	1079
TiC	79.0	2.0	0.084	550(*)	2232
C+W	23	1.0	0.084	1100(*)	2232

Table 1 shows the results of wear resistance tests for the samples subjected to coating deposition and pulsed plasma exposures in different combinations. It should be noted that smallest friction coefficient (from 1.5 to 3 times decrease) is measured in wear resistance tests for samples with previously deposited Cr and CrN coatings, especially for those treated with powerful plasma pulses. Increasing wear resistance is achieved for samples with coatings TiC, C+W, Cr+CrN and Cr with subsequent pulsed plasma treatment. It is interesting to note that TiN coatings without following pulsed plasma processing demonstrate the worst result due to essentially increased indenter wear, which is

accompanied by transport and sticking of indenter material to the sample during the friction.

Experiments with different steels and cast iron reveal possibility for essential improvement of wear resistance in the course of applied combination of coatings deposition with pulsed plasma processing. Alloying of surface layer in result of the coating–substrate mixing in liquid stage allows achievement of desirable chemical composition in surface layers being most loaded in all machine components. In particular, combined plasma processing is found to be prospective for modification of piston rings and other machine parts operating in conditions of bearing or dry friction.

4. Conclusions

Influence of pulsed plasma streams processing on the surface morphology and physical properties of constructional materials relevant to nuclear power engineering, such as hafnium, zirconium based alloys and Hastelloy N is investigated.

In particular, materials tests against high heat loads, estimations of main damage mechanisms and cracking development under the short-pulse powerful plasma impacts have been performed. XRD of investigated Hf and Zr based materials shows halo appearance for small angles indicating quasi-amorphous structure of modified surface layer. It is concluded that alloying of Zr with 1% Nb significantly contributes to the material response to the pulsed high heat loads and intense particle bombardment. The obtained results of plasma tests can be interpreted as important advantage of this alloy in power engineering from the point of view improved material properties. Prospects of this alloy are related with the decreased brittleness which allows complete mitigation of surface cracking in thermal stress conditions. Plasma processing resulted in development of nano- and submicron cellular structures in surface layer of Hastelloy N samples. It is caused by fast heating and melting of treated surface, considerable temperature gradients ($\sim 10^6$ K/cm) arising in surface layer of material under the pulsed plasma impact. Ordered cellular structures form specific morphology with average cell size of about 200 nm. Decreasing grain size and amorphous transformations are important for improvement of corrosion properties of this material.

Features of surface layers alloying from gas and metallic plasma as well as previously deposited coating mixing with the steel substrate in liquid phase are investigated also. In particular, modification of thin ($0.5 \div 2 \mu\text{m}$) PVD coatings of MoN, C+W, TiN, TiC, Cr, Cr+CrN and others in result of pulsed plasma processing are analyzed. Alloying of surface layer in result of the coating–substrate mixing allows achievement of desirable chemical composition in surface layers being most loaded in all machine components. Thus, combined

plasma processing is found to be prospective for modification of piston rings and other machine parts operating in conditions of bearing or dry friction. Increasing wear resistance is achieved for samples with coatings TiC, C+W, Cr+CrN and Cr with subsequent pulsed plasma treatment.

References

- [1] O. V. BYRKA, V. V. CHEBOTAREV, N. T. DEREPOVSKI, I. E. GARKUSHA, G. MÜLLER, G. SCHUMACHER, N. S. POLTAVTSEV, V. I. TERESHIN: *Properties of modified surface layers of industrial steels samples processed by pulsed plasma streams*. Vacuum, 58 (2000), 195–201.
- [2] A. N. BANDURA, A. M. BOVDA, O. V. BYRKA, I. G. BROWN, V. V. CHEBOTAREV, I. E. GARKUSHA, A. S. TORTIKA, V. I. TERESHIN: *Pulsed plasma accelerators of different gas ions for surface modification*. Review of sci. inst., 73 (2002), 831–833.
- [3] V. V. UGLOV, N. N. CHERENDA, V. M. ANISHCHIK, A. K. STALMASHONAK, V. M. ASTASHYNSKI, A. A. MISHCHUK: *Formation of alloying layers in a carbon steel by compression plasma flows*. Vacuum, 81 (2007), 1341–1344.
- [4] V. TERESHIN, A. BANDURA, O. BYRKA, V. CHEBOTAREV, I. GARKUSHA, O. SHVETS, V. TARAN: *Coating deposition and surface modification under combined plasma processing*. Vacuum, 73 (2004), 555–560.
- [5] A. N. BANDURA, O. V. BYRKA, V. V. CHEBOTAREV, I. E. GARKUSHA, O. M. SHVETS, V. S. TARAN, V. I. TERESHIN: *Surface modification and coatings deposition under plasma streams processing*. Advances in App. Plasma Sci., 4 (2003), 265–270.
- [6] J. PIEKOSZEWSKI, J. LANGNER: *High intensity pulsed ion beams in material processing: equipment and applications*. Nuclear Instruments and Methods in Physics Research Sec. B: Beam Interactions with Materials and Atoms, 53 (1991), 148–160.
- [7] B. A. KALIN, V. L. YAKUSHIN, V. I. VASILIEV, S. S. TSEREVITINOV: *Use of high temperature pulsed plasma fluxes in modification of metal materials*. Surface and Coatings Technology, 96 (1997), 110–116.
- [8] V. M. ANISHCHIK, V. V. UGLOV, V. V. ASTASHYNSKI, V. M. ASTASHYNSKI, S. I. ANANIN, E. A. KOSTYUKEVICH, A. M. KUZMITSKI, N. T. KVASOV, A. L. DANILYUK, I. N. RUMIANCEVA: *Compressive plasma flows interaction with steel surface: structure and mechanical properties of modified layer*. Vacuum, 70 (2003), 269–274.
- [9] I. E. GARKUSHA, A. N. BANDURA, O. V. BYRKA, V. V. CHEBOTAREV, V. D. FEDORCHENKO, V. A. MAKHLAJ, A. V. MEDVEDEV, V. I. TERESHIN: *Features of materials alloying under exposures to pulsed plasma streams*. European Physical Journal D, 54 (2009), 185–188.
- [10] V. V. GASILIN, YU. N. NEZOVIBAT'KO, G. S. POKLIPACH, O. M. SHVETS, V. S. TARAN, V. I. TERESHIN, A. I. TIMOSHENKO: *Filtred arc plasma discharge for coating deposition under HF biasing of samples*. Journal of IAPS, 13 (2005), 87–92.
- [11] G. MÜLLER, G. SCHUMACHER, F. ZIMMERMANN: *Investigation on oxygen controlled liquid lead corrosion of surface treated steels*. J. of Nuclear Mat., 278 (2000), 85–95.

Plasma technologies in building industry

GENNADIY G. VOLOKITIN¹, NELLY K. SKRIPNIKOVA¹,
ANDREY A. NIKIFOROV¹, OLEG G. VOLOKITIN¹

Abstract. Electro arc plasma is widely used in different technology processes of producing new building materials in building industry. The plasma technique and technologies – one of those fields of building industry where interests of manufacture and applied researches most connected with fundamental science. It is impossible to create effectively working plasma generators and plasma technologies in building industry, without understanding and description of the physical processes occurring at interaction of plasma with a solid body in thermal low-temperature plasma.

Key Words. Electric arc, building materials and industry, low-temperature plasma.

Plasma generators with the pressed out, taken out arc

The first stage in plasma generators producing is working out plasma generator with pressed out, taken out arc, intended for processing small building products (a brick, a tile, etc.) for the purpose of reception on their surface protectively-decorative coverings. By working out of a design of the generator, factors which negatively affected on service life of plasma generators [1], and its constructive lacks were taken into account.

Taking into account all these factors, the design of the generator with the taken out spent graphite electrode Fig. 1 has been developed [2].

Installation technical characteristics:

- Power consumption: 60–120 kW
- Productivity: 4 million piece of a brick per year
- Gas: Nitrogen

¹Tomsk state university of architecture and building, Solyanaya sq. 2, Tomsk, Russia; e-mail: vgg-tomsk@mail.ru, nks2003@mail.ru, aan@sibmal.com, volokitin.oleg@mail.ru

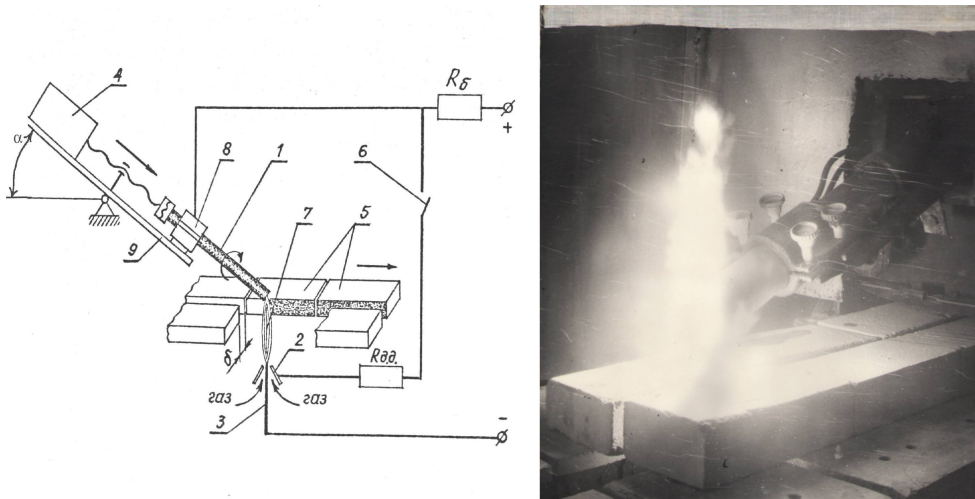


Fig. 1. Generator of plasma for processing building products (brick) with the spent anode: 1 – graphite anode; 2 – form-building nozzle; 3 – cathode; 4 – electric drive; 5 – processed products; 6 – contour of inclusion; 6 – switch an arc “on duty”; 7 – plasma cord; 8 – water cooled wire

The plasma generator for processing big building products

Creation of technology of plasma processing big building products (concrete and gas-concrete plates, panels, blocks, etc.) is rather actual idea. It has demanded working out of plasma generators allowing to process a wide strip of surface for one pass. On Fig. 2 the plasma generator with electromagnetic transport of an arc is presented [3].

The principle of work of the generator is based on electromagnetic moving of the arc discharge on a processed surface of a building product.

On the basis of the developed plasma generators, technologies on creation of protectively-decorative coverings at the enterprises of building industry are realized:

- the plasma technology of processing of a silicate brick is realized at the enterprises of Lipetsk, Ufa, Tomsk, Volgograd, Surgut, v. Masljanino (Novosibirsk region);
- the automated plasma installation “Hermes-010” intended for processing big building products (Tomsk).

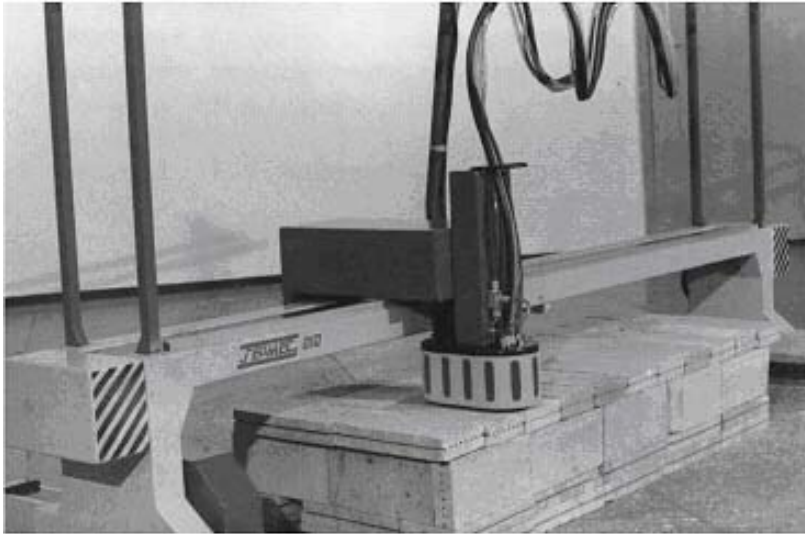


Fig. 2. The plasma generator with electromagnetic transport of an arc

Working out of the technology of a mineral fiber production in plasma reactor

The established efficiency of use of plasma technologies has planned prospects of development of new directions in building industry, one of which – producing mineral fiber in plasma rotating reactor. On Fig. 3 the scheme of experimental installation intended for melt producing from refractory silicate materials [4] is presented.

The principle of work of installation is based on interaction high temperature streams of plasma 5 with powdery refractory silicate material. As a result, heating of dispersion particles with the melt 6 formation is carried out. Formed melt goes in rotating reactor 8 where under action centrifugal forces, breaking from its walls it is extended in fibers. Melt at heats possesses electro conductivity, the current of the arc discharge of plasma generator proceeds on melt volume, simultaneously providing Joule melt heating.

Technology of glass-making furnace restoration

The process of glass founding includes high temperature, about 1600 °C. As a result furnace walls are worn out with dint of complex geometric form. Because of this aggressive influence on the walls, glass-making furnace can not be

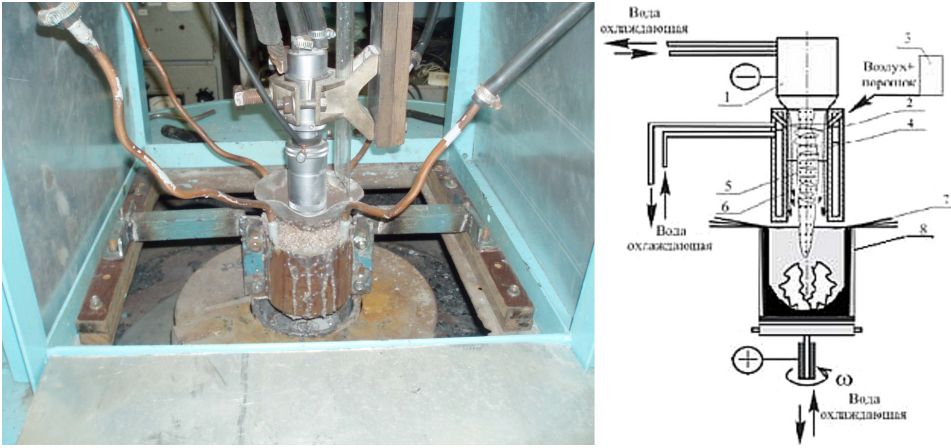


Fig. 3. The scheme of experimental installation for reception of a mineral fiber: 1 – cathode unit; 2 – thermal energy concentrator; 3 – a portioning device for raw materials giving; 4 – protecting layer; 5 – plasma arc; 6 – melt; 7 – mineral fibers; 8 – the rotating reactor

used in right conditions and walls tearing can lead to emergency situation with the staff health harm. Using plasma technology of walls restoration allows repairing furnace without its stripping. Technology is based on low-temperature plasma influence on a restoring surface. It allows restoring surface to initial condition. Power consumption is 35–50 kW/h. As a raw material use charge, received by crushing fire-resistant bars (fraction 5–10 mm) of the same structure as repaired.

Figure 4 shows process of brick restoring. The process is carried out in the way level-by-level melting: on the restoring surface 1 by the stream of low-temperature plasma (plasma generator 5) forming bath melt and add to this zone fire-assistant charge 7, then heat to the temperature of melt creating. This technology is realized in the city of Moscow, Tulun, Angero-Sudgensk, Akuticha (Altay region) and provides high economical effect.

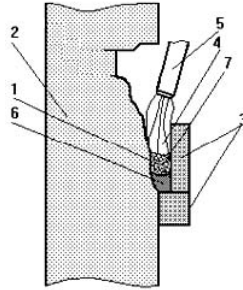


Fig. 4. Technology scheme: 1 – restoring surface; 2 – fire resistant bar; 3 – graphite planking; 4 – forming module; 5 – plasma generator; 6 – melt; 7 – fire-assistant charge

References

- [1] L. D. KISELEVSKY, V. D. SHIMANOVICH, A. K. SHIPAJ: A.c. 88076 USSR. *The device for high-temperature processing surfaces of dielectric materials*, 1981.
- [2] G. G. VOLOKITIN, V. D. SHIMANOVICH, A. I. ZOLOTOVSKY: A.c. 845342 USSR. *The device for arc materials processing*.
- [3] G. G. VOLOKITIN, A. V. PETROV, V. D. SHIMANOVICH: A.c. 749355. *The Plasma generator for materials processing*, 1980.
- [4] O. G. VOLOKITIN, E. V. GAJSLER, A. A. NIKIFOROV, N. K. SKRIPNIKOVA: The Patent of the Russian Federation No. 2355651 *Installation for reception mineral melt with plasma heating*, 2009.

Received May 7, 2010

Interaction of low-energy hydrogen plasma with polycrystalline aluminium

ALEXANDER A. SAVITSKY¹, ALEXANDER L. ZAITSEV²

Abstract. Theoretical and experimental research of hydrogen plasma interactions with a surface of polycrystalline aluminium is presented. The Density Functional Theory (DFT) is used for potential energy calculation of molecular and atomic hydrogen interaction with an aluminium (100) surface. It was found, that atomic hydrogen adsorption onto aluminium surface is irreversible one with energy release of the order of 3 eV, while molecular hydrogen adsorption is physical one only. The formation of chemisorbed layer require to overcoming the energy barrier of 0.45 eV. By the means of scanning electron and atomic force microscopy and mass-spectrometry, the surface and composition of low molecular weight compounds desorbed from Al, treated by low-energy plasma, were studied. It was shown, that energy of hydrogen plasma is a main factor determining features of formation Al nanostructure. The increasing of energy of plasma up to 1 keV is accompanied by growth of a roughness and occurrence of intense peaks of hydrogen and hydrides desorption at temperatures close to those of Al melting. At low energy of plasma and low concentration of atomic hydrogen the latter interacts with an Al surface and nanograin boundaries, where the silicon concentrates.

Key Words. Plasma, hydrogen, aluminium, density functional theory, scanning electron microscopy, atomic force microscopy, thermodesorption, mass-spectrometry.

1. Introduction

Hydrogen low-energy plasma is widely used in quantum electronics for synthesis of specific surface structures (nanowires, quantum dots, two-dimensional periodic structures and so on), as well as for purification and modification of metals' and semiconductors' surface by various substances [1]–[3]. Some aspects of hydrogen interaction with materials used in electronics till now are not clear and require further investigations. In the paper we present results of

¹Belarusian State University, 4 Nezavisimosti av., 220050 Minsk, Republic of Belarus

²A.V.Luikov Heat and Mass Transfer Institute National Academy of Sciences of Belarus, 15 P. Brovki st., 220072 Minsk, Republic of Belarus

theoretical study of atomic and molecular hydrogen interaction with ideal aluminium (100) surface and experimental investigation of low-energy hydrogen plasma interaction with a polycrystalline aluminium.

2. Theoretical and experimental techniques

The theoretical calculations of the potential energy for molecular and atomic hydrogen interaction with (100) f.c.c. aluminium (100) surface are done within the framework of DFT [4] (thanks to ABINIT (v.5.0.1) package [5]). The code allows calculating the total energy of molecular-crystal system in the ground state and makes structural optimization (to find well converged atomic position) in two type of exchange-correlation functional approximation (LDA, GGA), taking into account electronic interaction with metal ions core that fitted by norm conserving pseudopotentials [6]. The calculations are performed according to a technique given in [7].

Experiments are carried out with the use of hydrogen plasma at energy of 1 and 1000 eV. The aluminium of 10 microns thickness foil manufactured by “Rusal-Sayansk foil” was used for plasma treatment. The atomic composition of a metal foil was investigated by X-ray fluorescence analysis (Al – 98.26, Si – 0.81, Fe – 0.90 mass. %, Cr, Ni, Cu, Mg – rest). Hydrogen plasma was excited by a microwave radiation. Measurement of a stream density of molecular and atomic hydrogen, that is equal to $1 \times 10^{18} \text{ cm}^{-2} \cdot \text{s}^{-1}$, carried out by constant pressure method. The atomic hydrogen stream density, that is equal to $8 \times 10^{15} \text{ cm}^{-2} \cdot \text{s}^{-1}$, is determined on vanadium targets under the fixed parameters of leaking and microwave radiation energy. Atomic force and scanning electron microcopies are used for analysis of Al surface, treated by low-energy plasma. Thermodesorption and mass-spectrometry are used for the quantitative and qualitative composition of interaction products investigation.

3. Results and discussion

Theoretical calculations have allowed establishing the principal difference in the nature of molecular hydrogen, from the one hand, and atomic hydrogen, from the other hand, interaction with aluminium surface and, consequently, in the potential energy magnitude. Figure 1 shows, that atomic hydrogen chemisorbed by Al (100) surface exothermally with energy of 2.9 eV. Atomic hydrogen diffusion into surface layer requires overcoming the energy barrier of the order of 0.5 eV. From potential energy curves one can see, that most stable states inside the Al bulk are octahedral hollows, and the H jumps between noted hollows is possible at high energies. One can conclude that depending on plasma energy hydrogen atoms can permeate into the bulk and form the

stable nonstoichiometric hydrides, or freely move through a surface and surface layers of Al, and chemically react with impurities chemically.

Molecular hydrogen, having energy smaller than 0.45 eV, does not react chemically with the surface, but can exist on the surface in unstable state of physical adsorption, having the energy of 10 times lower than the activation barrier of chemisorption. The chemisorption state is energetically favorable, but it can be implemented on the surface only. The energy barrier of 1 eV hampers diffusion of partially dissociated hydrogen molecule into Al bulk. At the energy values sufficient for diffusion hydrogen molecules dissociate and occupy tetrahedral sites in a surface layer, so the octahedral position contrary to atomic hydrogen case are not energetically favorable.

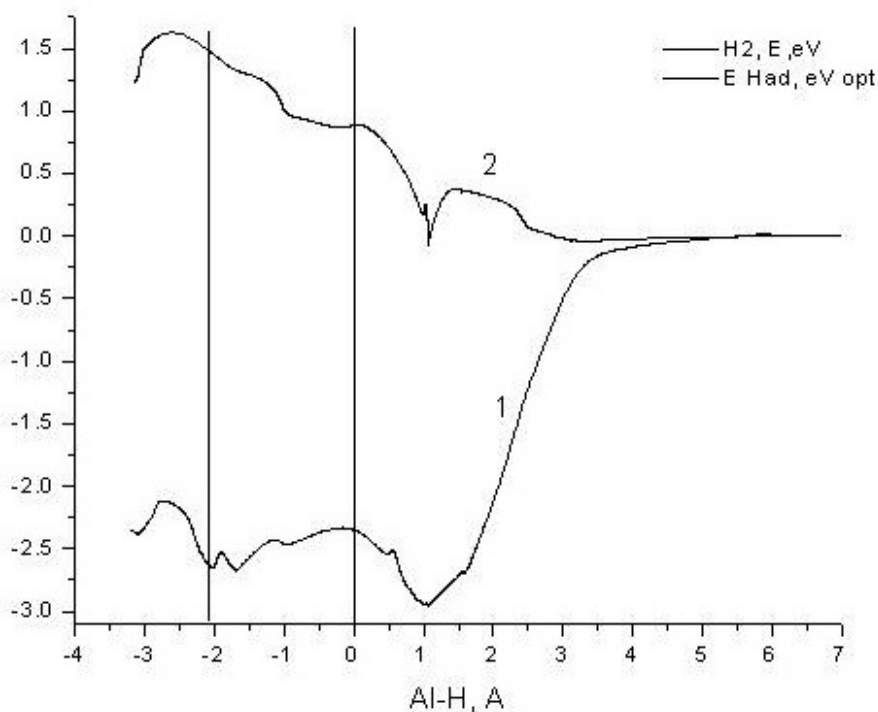


Fig. 1. Dependence of potential energy of atomic (1) and molecular (2) hydrogen with an aluminium (100) surface on the distance from surface; vertical lines on the figure show a positions of f.c.c. Al atomic layers

Results of quantum simulation show, that at interaction of low-energy H-plasma with Al surface uncertainty of relative concentration of atomic and molecular hydrogen occurs. So at TSD data analysis it is necessary to take into account the energy of various adsorption positions, that define the temperature of peaks in desorption spectra.

Let's address to experimental results. TSD spectra after aluminium foil treatment by low-energy H-plasma ($E = 1$ eV) are shown on Fig. 2. For comparison the TSD spectra of initial Al and after ionic etching by H-plasma having the energy of 1 keV are shown. Spectra of untreated foil up to temperatures of the order of 500°C exhibit a negligible yield of thermodesorption products. The TSD spectra of Al exhibit small peaks at 80 , 150 , 280 , 380 and 470°C , having intensities not exceeding $0,013$ Pa/mg. At the temperatures close to Al melting point two peaks of volatile compound release are noted (at 600 and 670°C) that, as follows from mass spectrum, are caused by the yield of ions having $m/z = 28$, 44 , that can be attributed to CO , CO_2 and SiO .

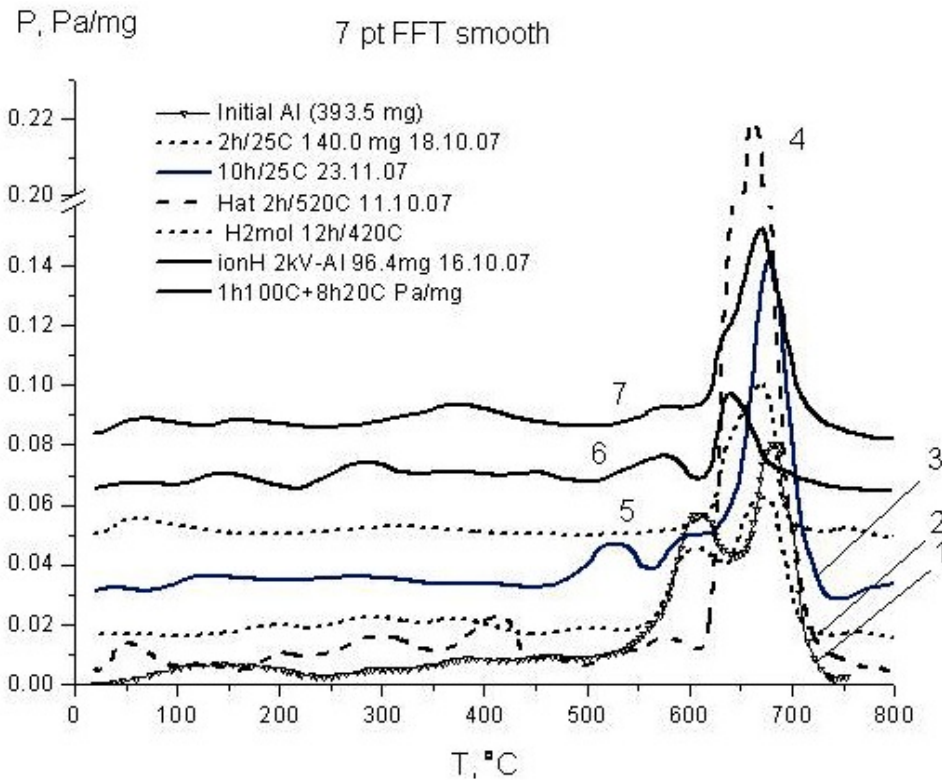


Fig. 2. TSD spectra of volatile compounds released from the Al bulk in dependence on time, energy of H-plasma and heating temperature; 1 - initial Al; 2 - treatment at $T = 20^\circ\text{C}$, $t = 120$ min; 3 - $T = 20^\circ\text{C}$, $t = 600$ min; 4 - $T = 520^\circ\text{C}$, $t = 120$ min; 5 - $T = 420^\circ\text{C}$, $t = 720$ min; 6 - $T = 20^\circ\text{C}$, $t = 90$ min; 7 - $T = 100^\circ\text{C}$, $t = 90$ min + $T = 20^\circ\text{C}$, $t = 480$ min; 1 - 5, 7 - $E = 1$ eV; 6 - $E = 1$ keV

The comparative analysis of TSD spectra shows, that exposition and temperature of Al foil imply essentially on the quantitative and qualitative composition of low molecular weight products released in the temperature range

of $20 \div 800$ °C. TSD spectra of Al foils (Fig. 2 curves 4, 5), treated by plasma at temperatures $400 \div 550$ °C, slightly differ from each other. In comparison with initial Al TSD spectra, one can see that the desorption product composition changes: the peak at 600 °C caused by volatile compounds of silicon that included in Al bulk in forms of α -solid solution and aluminosilicide [8] disappears.

Ambient temperatures of Al the plasma treatment results in decrease of high-temperature peaks intensity. The increasing of treatment duration leads to disappearance of the peak at 600 °C. TSD spectra has small peaks at 180 , 290 and 380 °C. With increasing of exposure up to 10 hours small peaks ($0.004 \div 0.006$ Pa/mg) at 50 , 135 , 230 , 300 , 380 °C and intense peak at 530 °C registered. This data show, that hydrogen interacts mainly with dopant elements, dissolved in aluminium. As a result of this interaction, the volatile substances of silanes, silanols and other more complex aluminium–silicon compounds are desorbed in vacuum under a pressure of 40 to 50 Pa.

Plasma treatment of Al during $10 \div 12$ hours, at 420 and 520 °C results in formation of peak at 55 °C, its intensity increases with temperature from 0.007 (420 °C) to 0.01 Pa/mg (520 °C). At $T = 250 \div 400$ °C the wide area of low intensity (0.002 Pa/mg) volatile compounds yield is formed in TSD spectra. The increase of volatile compounds yield with separation of wide area on two peaks at 300 and 410 °C it is found out (at 520 °C).

The treatment by high-energy plasma leads to complicated TSD spectra, having low intensity desorption peaks, that testify the chemical interaction between hydrogen and the foil surface with removing of reaction products under vacuum condition.

The chemical composition of volatile products of desorption analyzed by mass-spectrometry. The analysis takes into account the degradation of individual molecules on the fragment ions. The table shows chemical composition of volatile compounds released from Al after treatment by H-plasma in accordance with the curve 7 presented in Fig. 2 (100 °C, $t = 90$ min and 20 °C, $t = 480$ min).

In the temperature range of $20 \div 160$ °C the desorption products from the initial Al and the same, treated by H-plasma, contain water and carbon dioxide. The content of ions with $m/z = 44$ (CO_2 , SiO , AlOH and SiCH_4) attains up to 22%. The growth of temperature leads to increase of ions having $m/z = 28$ concentration, attributed to CO and AlH . Starting from $T = 330$ °C concentration of ions having $m/z = 2$, 28 and 44 , corresponds to hydrogen and carbon oxides in initial Al foil and to more complex products for Al, which treated by hydrogen plasma, increases. In the temperatures up to $420 \div 520$ °C the content of molecular hydrogen and ions with $m/z = 40$, 44 , corresponding to Si and Al oxy-hydrides, in thermodesorption products of Al after plasma treatment, grows. TSD peaks at temperatures close to Al melting point are formed by the ions having $m/z = 2$, 18 , 28 and 44 , that attributed to H_2 , H_2O , CO , CO_2 , SiO and, probably, to AlCH , SiCH_4 , and AlOH . More exact analysis of

mass-spectrometry data, unfortunately, is impossible due to use of a spectrometer having low resolution. However, the results obtained show that low-energy H-plasma interacts actively with aluminium and dopant constituents.

Table 1. Chemical composition and yield of desorption products from initial Al (in numerator) and treated by H-plasma (denominator) at various temperatures

T (° C)	Ionic current (%)					
	$m/z = 2$ H ₂	$m/z = 18$ H ₂ O	$m/z = 28$ CO, Si, AlH	$m/z = 32$ SiH ₄	$m/z = 40$ SiC AlCH	$m/z = 44$ CO ₂ , SiO SiH ₄ , AlOH
160	0/0	60.5/59.5	0/0	0/0	0/0	5.7/21.8
260	2.5/2.3	41.6/1.5	0.4 /93.5	0/0	0.3/2.9	2.9/1.4
330	0.6/0.5	20.9/8.4	20.9/68.0	0/0	0/0.95	12.5/9.5
420	0.2/2.7	2.0/8.9	59.2/59.9	0/0	0.1/0.3	10.7/12.5
520	0.3/5.4	1.8/1.0	61.8/64.7	0/0.5	0.7/1.3	14.1/8.2
570	1.9/11.3	0.8/0	63.4/70.5	0.3/1.3	0.1/0.3	13.4/5.0
630	3.3/7.5	0/4.1	63.6/75.1	0.2/1.0	0.3/0.5	11.0/4.2

4. Structure of an aluminium foil surface

AFM and SEM analyses of Al surface structure before and after H-plasma treatment show that at ambient temperature the plasma action on Al within 1 hour results in decrease of Al surface roughness and increase of phase inhomogeneity of a surface (Fig. 3). Initial Al surface has polycrystalline structure having the grain size not exceeding of 200 nm; after an exposure in H-plasma the fine surface polycrystalline structure the grain size of 50 ÷ 70 nm is formed. The more distinct manifestation of Al nanostructure, in the latter case, shows that the hydrogen interacts primary with silicon that concentrates on grain boundaries.

At an Al treatment within of 10 hours, lead to formation of pits, extended sites having non-regular shape and grid of microcracks appearance, which testifies the primary etching of grain boundaries. AFM data reveal elliptic shape of grains having size up to 50 ÷ 70 nm and height up to 5 nm. Investigation in phase contrast regime shows, that the chemical composition of the grains is non-uniform one.

The surfaces of aluminium, after H-plasma treatment at 520 °C for 2 hours, are shown in Fig. 5. The foil surface is etched by plasma with formation of deep pits and extended sites having non-regular form. Agglomerations of fine cubic particles having the size up to 50 nm also are found on the surface.

From the optical microphoto of Al surface treated by plasma, having the energy of 1 keV, shown on a Fig. 6, one can conclude, that the increase of H-plasma energy leads to destruction of surface with high roughness topography formation. Hence, if H-plasma energy exceeds the diffusion barrier, then surface layers will be removed owing to phase transition of Al to gaseous state by means of formation of the alumo-silicon hydride volatile compounds.

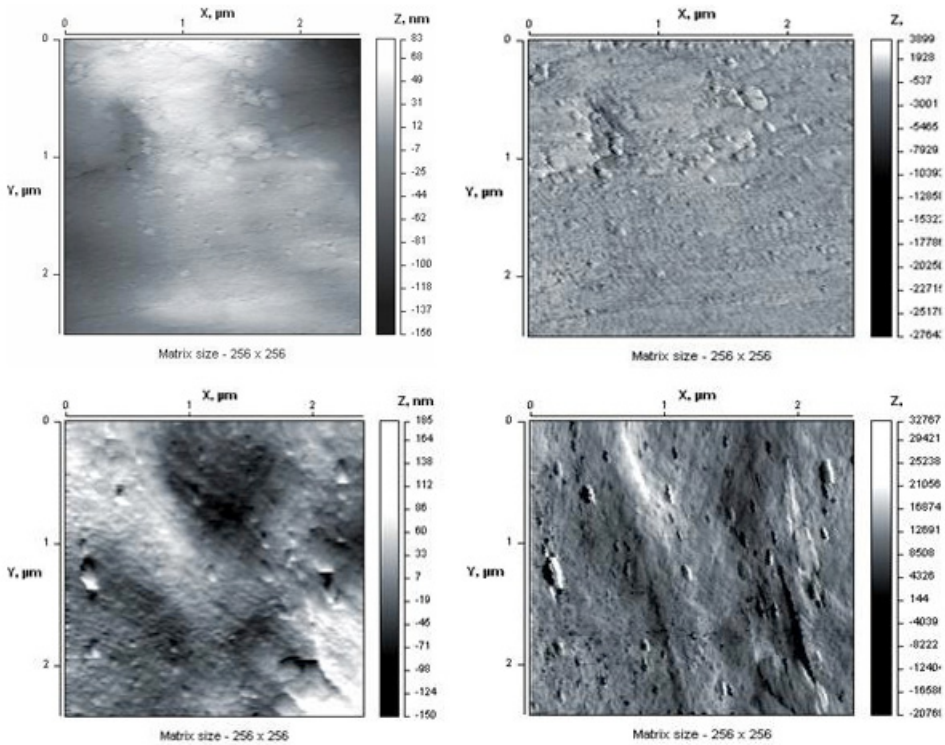


Fig. 3. AFM image of aluminium foil surfaces before and after H-plasma treatment at 20°C within 1 h: a), c) surface topography; b), d) image of console torsion AFM oscillations; a), b) AFM the plotting before; c), d) after treatment

The data obtained allow interpreting the H-plasma interaction with Al as follows. At ambient temperatures the chemical reduction and cleaning of surface layers are the main constituents of the interaction of molecular hydrogen with an aluminium foil. Hydrogen reacts primarily with dopant components, in particular with silicon. This process changes the surface phase composition and facilitates hydrogen diffusions in the aluminium bulk and cleans off impurities. The prolongation of the treatment promotes more complete cleaning of Al surface and, probably, the bulk, from silicon, but simultaneously can be

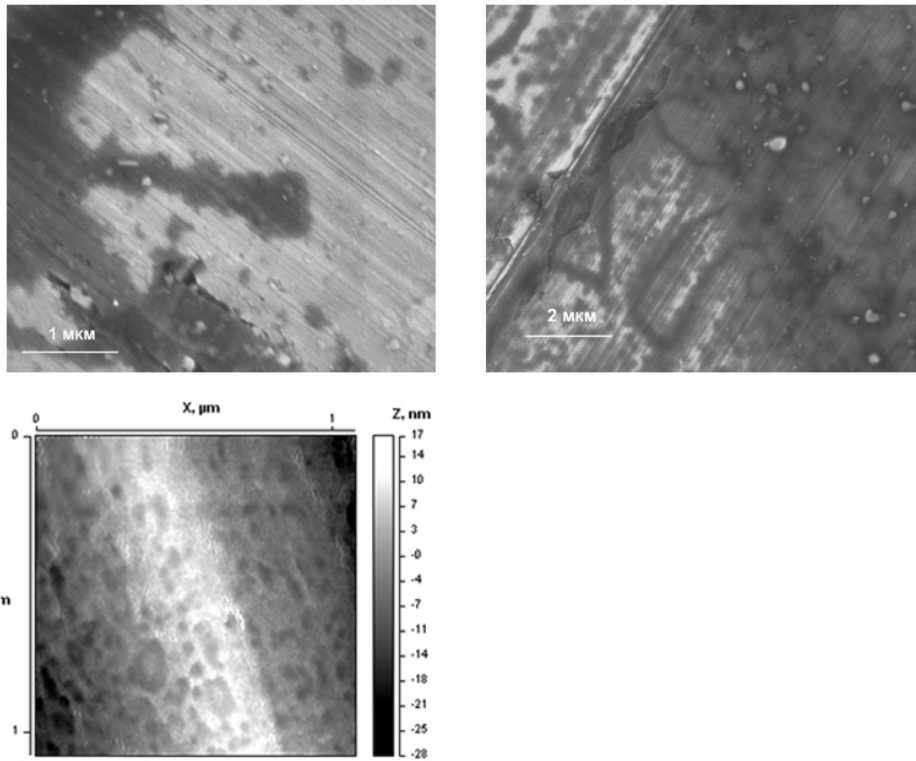


Fig. 4. SEM (a, b) and AFM (c) images of Al surface before and after 1 eV H-plasma treatment within of 10 h at ambient temperature; a) initial surface, b), c) after treatment

accompanied by storage of the hydrogen, water and other products of chemical reactions, based on Al and Si, that can be desorbed at a wide range of temperatures. Desorption of the hydrogen, captured by Al foil, begins in the temperature range of $300 \div 400^\circ\text{C}$. These data shows, that the hydrogen is accumulated primarily in local sites, having silicon excess concentration.

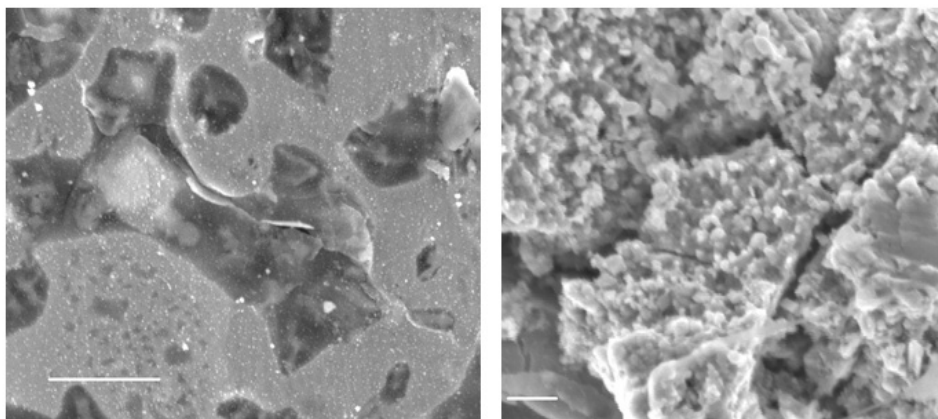


Fig. 5. An Al-foil surface after hydrogen treatment within 2 hours at 520 °C. a) the deep pores on Al surface; b) agglomerations of nanoparticles having the size of $50 \div 100$ nm. A scale is 200 nanometers.

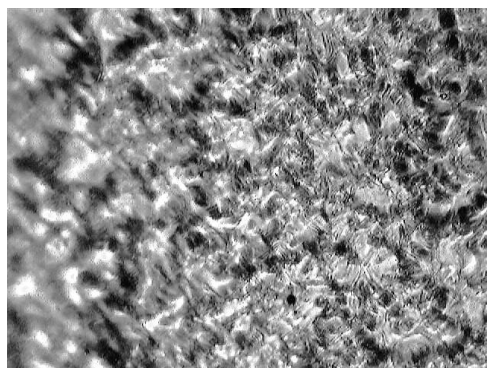


Fig. 6. Optical photo of Al foil surface treated by H-plasma, having the energy of 1 keV during 1.5 hours. The photo area is 250×200 microns²

5. Summary

DFT calculations show, that atomic hydrogen interacts with aluminium with energy yield of the order of 3 eV. Contrary, molecular hydrogen reaction with Al surface is accompanied with the energy absorption of 0.45 eV. Under of low-energy (1 eV) hydrogen plasma action the nanostructure of surface is changed with formation of nanograins of size not exceeding 100 nm. The experiments

performed under the Al heating, allow establishing the growth of an Al surface roughness and occurrence of intense desorption peaks of hydrogen and more complex products of interaction. The obtained data confirm that the energy of hydrogen plasma is a main factor, determines the hydrogen interaction with Al metal. At low energies and low concentration of atomic hydrogen, the molecular hydrogen interacts with nanograin boundaries that contain high silicon content, with subsequent desorption of the volatile compounds such as hydrides, oxides and aluminosilicon oxyhydroxides.

References

- [1] S. J. PEARTON, J. W. CORBETT, M. STAVOLA: *Hydrogen in crystalline semiconductors*. Springer, Berlin, Heidelberg, New York 1992.
- [2] F. SHIMURA: *Oxygen in silicon*. Academic Press, New York 1994.
- [3] M. R. BAKLANOV, D. G. SHAMIRYAN, ZS. TÖKEI, G. P. BEYER, T. CONARD, S. VANHAELEMEERSCH, K. MAEX: *Characterization of Cu surface cleaning by hydrogen plasma*. *J. Vac. Sci. Technol.*, 19 (2001), 1201–1211.
- [4] W. KOHN: *Electronic structure of matter – wave function and density functional*. The Nobel lectures on chemistry, 172 (1998), 336–348.
- [5] X. GONZE, J.-M. BEUKEN, R. CARACAS, F. DETRAUX, M. FUCHS, G.-M. RIGNANESE, L. SINDIC, M. VERSTRAETE, G. ZERAH, F. JOLLET, M. TORRENT, A. ROY, M. MIKAMI, PH. GHOSEZ, J.-Y. RATY, D. C. ALLAN: *First Principal computation of material properties the ABINIT software project*. *Comput. Mater. Sci.*, 25 (2002), 478–495.
- [6] N. TROULLIER, J. L. MARTINS: *Efficient pseudopotentials for plane-wave calculations*. *Phys. Rev. B*, 43 (1991), 1993–2006.
- [7] A. L. ZAJTSEV, YU. M. PLESKACHEVSKY, S. A CHIZHIK: *Energetics of adsorption and diffusion of hydrogen molecule in (001) slab of nanocrystallin aluminium*. *IFZ* (in Russian), 81 (2008), 157–164.
- [8] I. G. EROSHENKOVA, V. G. OLENICHEVA, L. A. PETROV, N. V. AGEEVA (ED.): *Phase diagrams of metal systems* (in Russian). VINITI, Moscow 1976.

Received May 27, 2010

Study of thin SiO_x film deposition by DBD at the atmospheric pressure¹

YULIYA KLENKO², JAN PÍCHAL^{2,3}

Abstract. Our contribution takes a step towards the transfer of the well proven plasma enhanced chemical vapour deposition (PE CVD) method into the atmospheric pressure region and discusses possible application of DBD sustaining in argon with admixture of hexamethyldisiloxane (HMDSO) and oxygen for deposition of SiO_x thin films. Films were deposited on polystyrene substrates. The relations between thin film parameters and deposition process conditions were studied. Our research focused on influence of surface morphology and chemical composition in dependence on working parameters. We concentrated on connection between concentration of the organosilicon reagent transported by the argon flow into the discharge region, concentration of the oxygen in the discharge atmosphere and surface properties of SiO_x thin films. Deposited samples were studied by means of the atomic force microscopy (AFM) scans and surface energy evaluation. In contrast to undeposited polystyrene substrate (CA values about 75°), contact angle values of SiO_x thin films were in the range between $11 \div 25^\circ$. The chemical compound was studied by X-ray photoelectron spectroscopy (XPS). XPS tests of SiO_x thin films were performed on unsputtered and ion sputtered surfaces and detected important difference between chemical composition of uttermost layers of films and their bulk composition.

Key Words. Plasma enhanced chemical vapour deposition, silicon dioxide, atmospheric plasma deposition, dielectric barrier discharge.

1. Introduction

In recent years much attention has been paid to atmospheric gas discharges plasma, e.g. dielectric barrier discharge (DBD). In the last years some papers described application of this type of discharge in the thin film deposition by PECVD – plasma enhanced chemical vapour deposition. The use of PECVD

¹This research has been supported by the Czech Technical University in Prague grant No. SGS10/266/OHK3/3T/13 and project MPO FI-IM/065

²Czech Technical University in Prague, Faculty of Electrical Engineering, Technická 2, 166 27 Prague, Czech Republic

³Technical University of Liberec, Faculty of Mechanical Engineering, Department of Material Science, Studentská 2, 461 17 Liberec, Czech Republic

processes is preferred, since the deposition costs can be considerably lower than in the other methods. For more detailed description of PECVD principles see [1], [2]. PECVD methods allow preparation of layers with a wide range of properties, but practical usability of this method applying atmospheric DBD (ADBBD) is still subject of the study. DBD plasma reactor developed for thin film deposition process and operation at atmospheric pressure and near room temperatures and its use for silicon dioxide plasma enhanced chemical deposition on polymeric substrates are described in the paper.

2. Experimental part

The films were prepared using ADBBD in the HMDSO/Ar/O₂ gas mixture. Experiments were carried out in a Plexiglas discharge reactor with dimensions (90 × 79 × 41) mm (Fig. 1). The discharge sustained between two brass electrodes (45 × 8 × 18) mm and (40 × 17 × 18) mm respectively. The greater, grounded, electrode was covered by the glass plate (70 × 46 × 1) mm. Discharge gap was set to 6 mm.

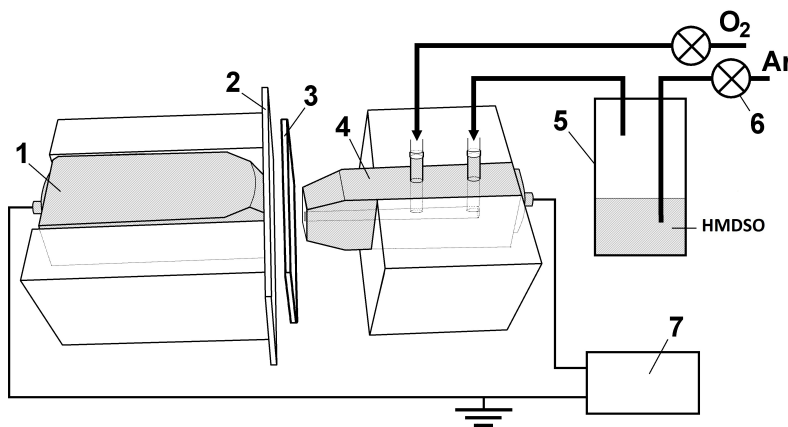


Fig. 1. Experimental set-up: 1 – HV electrode, 2 – dielectric barrier, 3 – substrate, 4 – ground electrode, 5 – evaporator, 6 – mass flow controller, 7 – HV power supply

The single molecular precursor hexamethyldisiloxane (HMDSO, C₆H₁₈O₂Si, 98% purity), was used as a source of silica. It was heated, evaporated and mixed with argon and transported in the HV electrode cavity where it was mixed with O₂. Then gas mixture feed was implemented through the hole in the electrode (diameter 3 mm) into the discharge space.

The main parameters of the deposition process are presented in Table 1. Gas flow rates were adjusted by means of the mass flow controllers. Thin film

Table 1. Deposition parameters used in experiments

Ar gas flow rate (Q_{Ar})	0.5 slm; 1.0 slm
TTIP fraction in Ar	0.54% (for $Q_{Ar} = 0.5$ slm) 0.40% (for $Q_{Ar} = 1.0$ slm)
Reaction gas flow rate (O_2)	0.5 ÷ 2.5 slm
Distance between electrodes	6 mm
Bubbler temperature	23 °C
Deposition time (t)	10 min
Substrate	polystyrene (PS)
Supplied voltage	30 ÷ 35 kV

deposition was run on polymer substrate. Deposition time duration was 10 minutes for all experiments.

Surface morphology of the SiO_x layers deposited on polymer substrates was studied by the atomic force microscopy (AFM, Quesant, Q-Scope) using 10 μ m scans recorded in contact mode with silicon cantilever. Thin film aging was studied by water contact angle (CA) test (with distilled water drops' size about 0.5 μ l). CA was measured by a sessile drop technique when constant time (30 s) passed after dropping of water. CA value has been estimated from five independent measurements.

The film thickness was determined with the surfometer (Planer Industrial, SF 200) and scratch test.

Chemical composition of the SiO_x thin films was analyzed by X-ray photoelectron spectroscopy performed with Omicron Nanotechnology system incorporating Al K_{α} radiation (1486.7 eV) and operating at 15 kV, 5.2 mA. The pressure in the chamber was maintained at 2×10^{-10} mbar. Spectra were acquired at the take-off angle of 85° relatively to the sample surface and all binding energies were given in reference to carbon line (C 1s) at 285.0 eV.

Electrical characteristics of the ADBD were measured with the LeCroy LT264 oscilloscope equipped with HV probe Tektronix P6015A used for sampling of voltage on DBD between reactor electrodes (for characteristic time behavior of AP DBD electric current $i(t)$ and voltage $u(t)$ see Fig. 1). Discharge current $i(t)$ was determined by a voltage drop on the 1 Ω resistor. A single measurement contained 250000 samples taken in the 60 ms time span.

Film deposition was performed with discharge power about 350 mW [at (14.5 ÷ 15.5) kV, 50 Hz].

Experiments were carried out in air atmosphere at room temperature (20 ÷ 22) °C.

ADBD was operated in the filamentary regime when a large number of spike-like current pulses with nanosecond duration randomly appeared during half

cycle of the applied voltage [3]. Figure 2 depicts the typical current–voltage waveform of the ADBD in air. Numerous peaks in the current waveforms indicate filamentary character of discharge, where $i(t)$ reaches at some moments $10 \div 15$ mA. As clearly shown in presented characteristics, under standard conditions, the maximum value of the current was about 1 mA and the voltage was about 15 kV.

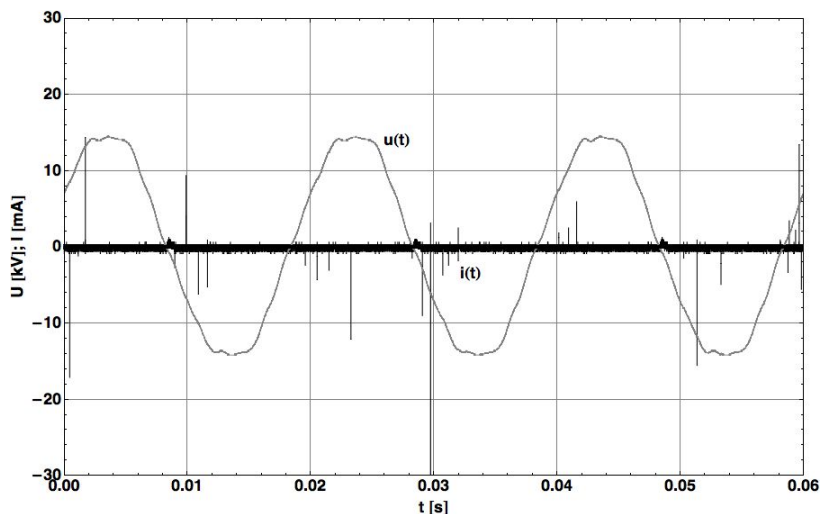


Fig. 2. Time dependence of current i and voltage u of ADBD in air (discharge power about 350 mW)

3. Results and discussion

The thickness of all deposited films was low, about 130 nm. More precise film thickness detection was excluded due to softness of the substrate and low thickness of films.

Surface morphology of deposited films as a function of Ar/HMDSO and O_2 flow rates was investigated by AFM. Figs. 3a, b and 4a, b show selected AFM images.

Figure 3a corresponds to the sample prepared at optimized deposition conditions (0.4% HMDSO in argon flow of 1 slm and oxygen flow of 0.5 slm), when surface with the lowest roughness (about 10 nm) was created. Though, this surface had not been fully “smooth”. The sample showed small sporadic “spikes” in the smooth and clean areas. Probably, these “spikes” were created due to condensation of precursor vapours near the sample surface and subsequently these during condensation created “particles” were transferred by the gas flow to the substrate.

Addition of oxygen into working gas mixture amplified the filamentary character of the discharge and increased of surface nonhomogeneity of the film (Fig. 3b).

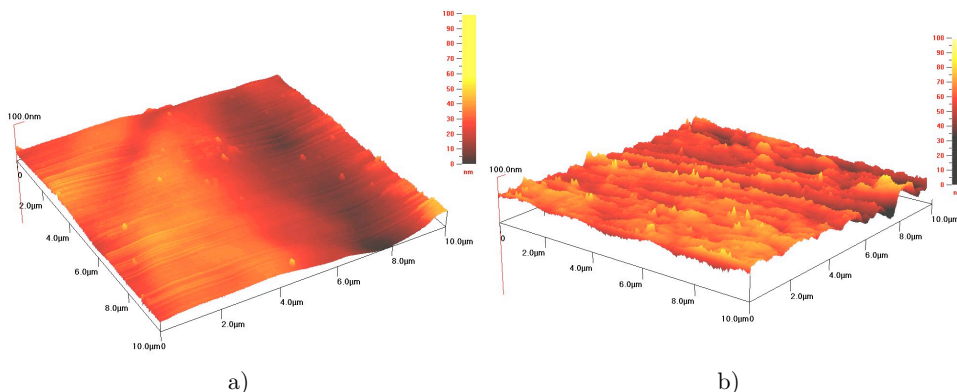


Fig. 3. AFM images of SiO_x -like films deposited by ADBD, scanned area $(10 \times 10) \mu\text{m}$
 a) $Q_{\text{Ar}/\text{TTIP}} = 1 \text{ slm}$, $Q_{\text{O}_2} = 0.5 \text{ slm}$, $d = 6 \text{ mm}$, b) $Q_{\text{Ar}/\text{TTIP}} = 0.5 \text{ slm}$, $Q_{\text{O}_2} = 2.0 \text{ slm}$

Rapid reduction of argon flow rate to 0.5 slm with synchronous increase of precursor concentration up to 0.54 % resulted in rough multi-peak surface creation (Fig. 4a, b). The growth of oxygen content in the discharge atmosphere led to extensive agglomeration of “peaks” on the surface (Fig. 3b). These nonhomogeneities were probably related with existence of $\text{Si}-(\text{CH}_x)_y$ groups in the film. $\text{Si}-(\text{CH}_x)_y$ groups might cause film density decrease and might be connected with porosity of films [4].

Static contact angle measurements of SiO_x thin films deposited in Ar/O_2 mixtures were used for film aging studies. Measurements were performed over the whole area of films and results were averaged for every substrate. In contrast to undeposited polystyrene substrate, with typical contact angle values about 75° , contact angle values of substrates with films were in the range between $11 \div 25^\circ$ immediately after deposition process and reached only 45° after 28 days.

The influence of working gas composition on thin SiO_x film wettability was investigated, too. All samples (deposited in different gas mixtures) of SiO_x thin films exhibited almost the same behaviour of wettability changes. From the curves presented in Fig. 5a, b it follows that rapid change of the films’ wettability occurred during first 7 days.

Then wettability of films seemed to be almost constant and only small hydrophilicity decrease was observed. Its existence might be related with chemical contamination of films from ambient environment. All samples were stocked in darkness in air at room temperature during test period.

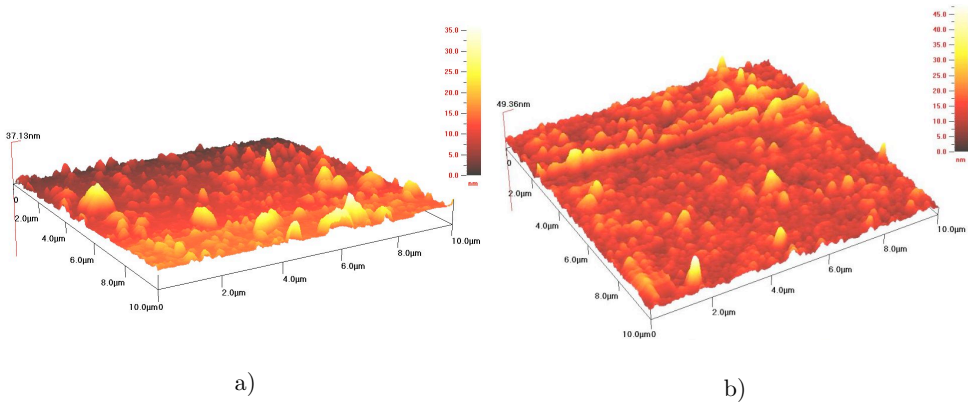


Fig. 4. AFM images of SiO_x films deposited by AP DBD (scanned area (10 × 10) μm)
 a) $Q_{Ar/TTIP} = 0.5 \text{ slm}$, $Q_{O_2} = 1 \text{ slm}$; b) $Q_{Ar/TTIP} = 0.5 \text{ slm}$, $Q_{O_2} = 2.5 \text{ slm}$

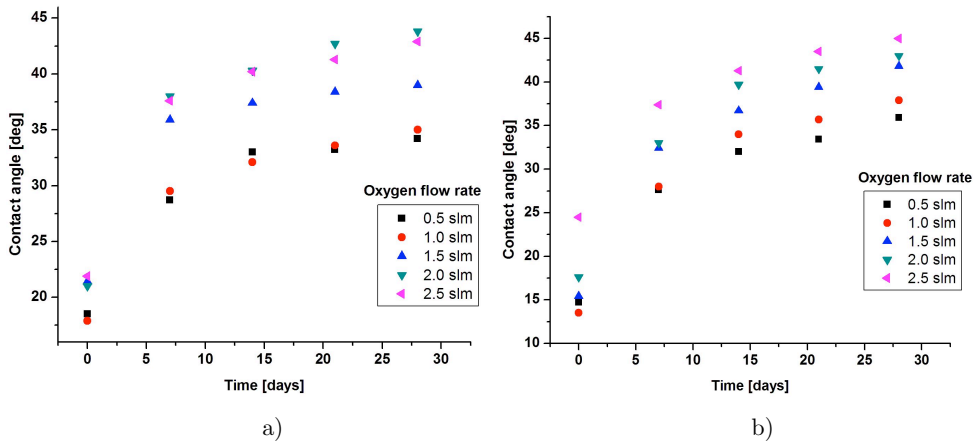


Fig. 5. Thin film aging: variation of contact angle with time for different oxygen flow rates: $d = 6 \text{ mm}$, $t = 10 \text{ min}$, a) $Q_{Ar/TTIP} = 1 \text{ slm}$, b) $Q_{Ar/TTIP} = 0.5 \text{ slm}$

Chemical composition of the deposited SiO_x films has been studied with XPS to obtain information about relative amounts of O, C and Si at the film surfaces. XPS analyses were performed with and without film surface cleaning. Cleaning consisted in 5 minutes sputtering of film surface with Ar ions. This procedure was necessary for removal of contaminants from ambient air contained in uttermost layers of the film.

Table 2. SiO_x films chemical composition: a) unspattered film, b) film sputtering with Ar ions

Flow rate, Ar/TTIP	slm O ₂	Sample No.	C (at.%)		O (at.%)		Si (at.%)	
			a	b	a	b	a	b
1.0	0.5	Si42	18.6	5.0	53.9	61.2	27.5	33.8
0.5	0.5	Si49	22.5	2.6	50.8	61.3	26.7	36.1
0.5	1.5	Si57	18.7	2.8	54.6	61.3	26.7	33.9
1.0	2.0	Si62	23.3	5.8	51.0	58.4	24.2	35.8

Elemental composition of SiO_x films on the PS substrate before and after sputtering shows Table 2. Initial concentrations of elements indicate high presence of carbon on the surface. Several nm of uttermost part of the surface of this sample contained even 23.3 at.% of carbon. However, carbon concentration in this region quickly decreased to 5% after 5 minutes argon ions sputtering. XPS analysis after sputtering revealed together with relatively low carbon content also high content of silica and oxygen in the film (Fig. 6).

Unspattered samples exhibit ratio of Si and O content percentages very close to 1:2. After argon ions sputtering the O/Si ratio was approximately 1.8 and deficit of oxygen in reactor atmosphere essential for SiO₂ creation was obvious [5]. Si atomic concentration in sputtered films had not exceeded 36.1%. Chemical composition data acquired from our sputtered films are conformable with data recently published for ADBD deposition by other scientific team [6], [7]. XPS analysis also confirmed that growth of oxygen content in the gas mixture cannot totally eliminate carbon from the deposited film. Similar results in case of residual carbon content in deposited film were discussed also in [6], [8].

Results in the Tab. 2 have shown that the chemical composition of the samples is almost the same for different gas mixtures. It indicates that oxygen or Ar/TTIP flow rates changes would not influence chemical composition of the film, but only its surface morphology.

High resolution of Si 2p and C 1s spectra of SiO_x thin films are presented in Fig. 6. The binding energy scales were referenced to the C 1s peak at 285 eV. Asymmetric of high resolution scans peak indicates the presence of C–O (286.6 eV), O–C=O (289.2 eV), C=O (287.8 eV), Si–C (283 eV) bonds.

Main peak was observed around 103.3 eV and corresponds to oxide/SiC interface region that is usually found in region (100 ÷ 103.3) eV. SiO₂ and SiC are referred to 103.3 eV and 100 eV, respectively. In the silica oxide/carbide region, the Si 2p core-level shifts attributed to SiO_x, when *x* was less than 2, were observed. Assuming validity of the bonding model [9], deconvolution of the XPS curves led to five chemical states, corresponding to Si⁰, Si¹⁺, Si²⁺, Si³⁺ and Si⁴⁺.

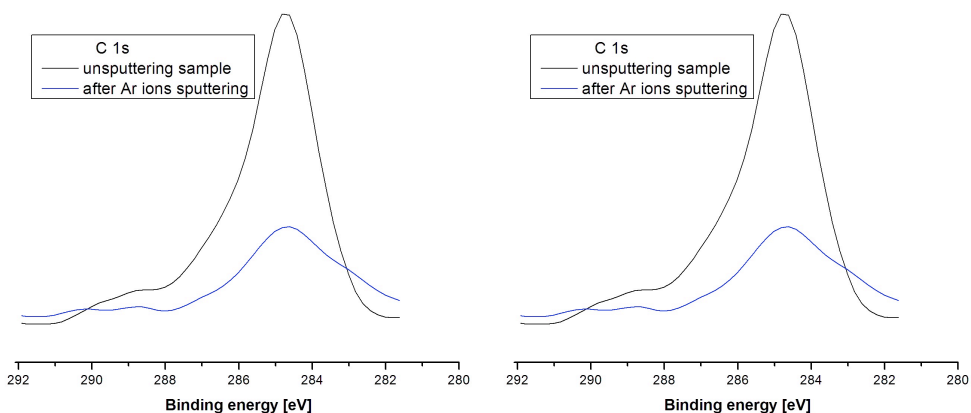


Fig. 6. High resolution scans of C 1s, and Si 2p peak of SiO_x film, (sample Si42)

As it follows from XPS results the presence of carbon atoms in unspattered samples was mainly due to the technological procedure used for thin film deposition (i.e. deposition at atmospheric pressure is also related with film surface contamination with particles of ambient air).

4. Summary

Presented paper describes results of deposition of SiO_x thin films on the polymer substrates in the DBD reactor at atmospheric pressure. The deposition was performed at different flow rates of reagent gases.

Hydrophilicity of deposited thin films and their aging were evaluated with contact angle test. Hydrophilicity of samples with deposited SiO_x films significantly differed from that of clear PS substrates.

The influence of gas flow rates on the surface topography were also studied by atomic force microscopy. Results show diverse morphology in dependence on Ar/HMDSO/ O_2 ratio.

Chemical composition of deposited films was tested with XPS. These analyses were performed with and without film surface cleaning by sputtering with Ar ions. This procedure was necessary for removal of contaminants from ambient air contained in uttermost layers of the film. It was ascertained important contamination of the film surface uttermost part with carbon atoms from the atmosphere.

References

- [1] M. RONDANINI, S. CEREDA, F. MONTALENTI, L. MIGLIO, C. CAVALLOTTI: *A multiscale model of the plasma assisted deposition of crystalline silicon*. Surface and Coatings Technology, 201 (2007), 8863–8867.
- [2] M. RONDANINI, C. CAVALLOTTI, D. RICCI, D. CHRASTINA, G. ISELLA, T. MOISEEV, H. VON KÄNEL: *An experimental and theoretical investigation of a magnetically confined dc plasma discharge*. J. Appl. Phys., 104 (2008), 013304.
- [3] U. KOGELSCHATZ: *Fundamentals and applications of dielectric – barrier discharges*. Proc. of Int. Symp. On High Pressure Low Temperature Plasma Chemistry, HAKONE VII(H. E. Wagner). Ernst-Moritz-Arndt Univ., Greifswald, Germany 2000, V 1(2).
- [4] A. MILELLA, M. CREATORE, M. A. BLAUW, M. C. M. VAN DE SANDEN: *Remote plasma deposited silicon dioxide-like film densification by means of RF substrate biasing: film chemistry and morphology*. Plasma Process. Polym., 4 (2007), 621–628.
- [5] Z. H. LIU, N. M. D. BROWN: *XPS characterization of mica surfaces processed using a radio-frequency (rf) argon plasma*. J. Phys. D: Appl. Phys., 31 (1998), 1771–1781.
- [6] S. STAROSTIN, E. ALDEA, H. DE VRIES, M. CREATORE, M. C. M. VAN DE SANDEN: *Atmospheric pressure deposition of silica-like films on polymer in APG discharge*. Institute of Plasma Physics AS CR, v.v.i., Prague 2007, 749–752.
- [7] S. STAROSTIN, E. ALDEA, H. DE VRIES, M. CREATORE, M. C. M. VAN DE SANDEN: *Application of atmospheric pressure glow discharge (APGD) for deposition of thin silica-like films on polymeric webs*. Plasma Process. Polym., 4 (2007), S440–S444.
- [8] F. MASSINES, N. GHERARDI, A. FORNELLI, S. MARTIN: *A new approach to SiO₂ deposit using a N₂-SiH₄-N₂O glow dielectric barrier discharge at atmospheric pressure*. Surf. & Coat. Technology, 200 (2005), 1855–1861.
- [9] C. TENDERO, C. TIXIER, P. TRISTANT, J. DESMAISON, P. LEPRINCE: *Atmospheric pressure plasmas: a review*. Spectrochimica Acta, Part B, 61 (2006), 2–30.

Received June 10, 2010

Plasma flow in different gliding discharge reactor configurations¹

JAN SLÁMA², JAN PÍCHAL^{2,3}, RADEK PROCHÁZKA²

Abstract. One possibility of plasma-chemical decomposition and modification of gases and aerosols is employment of gliding discharge sustaining in proper atmosphere. Crucial step in the gliding discharge reactor design is the selection of proper form of electrodes and their mutual position. We investigated connection between form of electrodes and shape of the plasma flow. Experiments were performed in air at atmospheric pressure. For identification of the most reactive plasma region in the flow, plasma was investigated by means of its visible spectral lines. There were tested three basic configurations of wire electrodes representing their limit forms (low-divergent, circular, high-divergent) and recognized ionized regions of the flow. Results can be used in decision making about shaping of the gliding discharge reactor ionized gas region, especially in case when both volume and surface treatment is needed.

Key Words. Gliding arc, spectral analysis, form of electrodes, plasma reactor, plasma flow.

Introduction

In last decades there have appeared many technological applications of the gliding discharge as “an auto-oscillating phenomenon developing between at least two electrodes that are immersed in a laminar or turbulent gas flow” [1]. Most of these applications take advantage of favourable characteristics of gliding discharge plasma, but also impose requirements on gliding discharge properties, e.g. shape of the plasma flow in the reactor. This paper deals with connection of plasma flow shape and form of electrodes.

¹This research has been supported by the Czech Technical University in Prague grant No. SGS10/266/OHK3/3T/13 and project MPO FI-IM5/065.

²Faculty of Electrical Engineering, Czech Technical University in Prague, Technická 2, 166 27 Prague, Czech Republic

³Faculty of Mechanical Engineering, Department of Material Science, Technical University of Liberec, Studentská 2, 461 17 Liberec, Czech Republic

Experimental

Experimental apparatus (Fig. 1) consisted of reactor containing nozzle and electrodes and gas distribution (compressor, reduction valve and flowmeter). Electrodes were made from copper wire of diameter 1 mm and powered with high voltage power source (50 Hz, 8 kV). The interelectrode distance in the area of initial discharge breakdown was held at 3 mm (“ignition region length”). The average input volume flow was about 20 slm.

Experiments were performed in air at atmospheric pressure 101 kPa, temperature about 21 °C and humidity about 30 %.

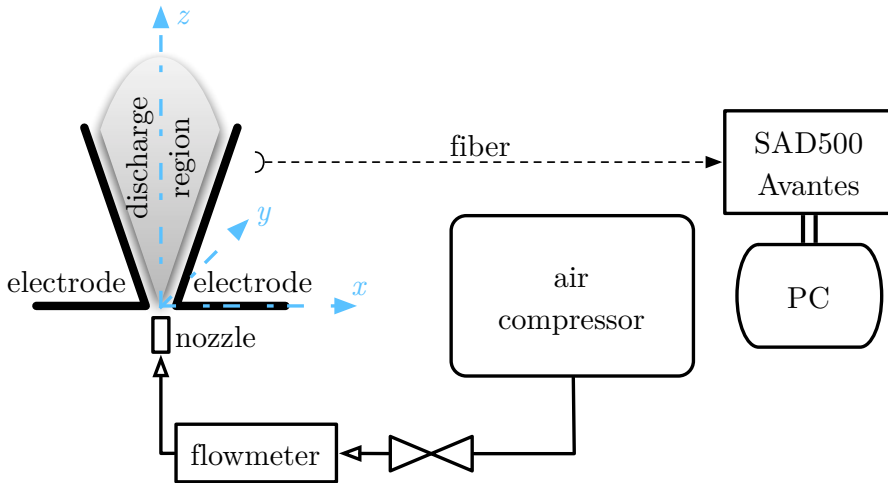


Fig. 1. Apparatus scheme

There were tested three basic forms of wire electrodes: “low-divergent” – (a), “circular” – (b) and “high-divergent” – (c) (Fig. 2). Low-divergent configuration consisted of two straight electrodes of length 130 mm, circular configuration was created by two ring-shaped electrodes of radius $r = 22$ mm and high-divergent configuration was represented by two triangle-shaped electrodes forming right angle. The low-divergent and high-divergent configurations represent limit shapes of electrodes.

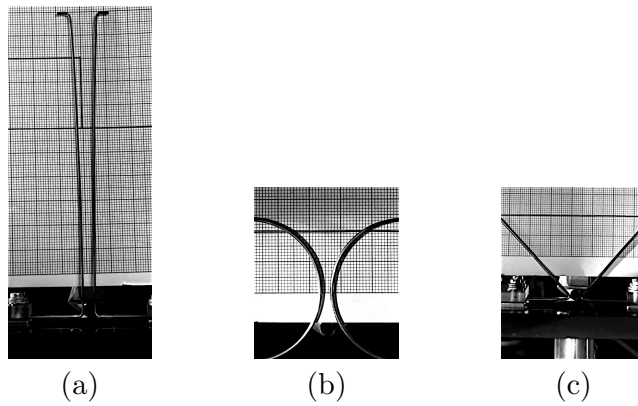


Fig. 2. Electrode configurations; (a) – low-divergent, (b) – circular, (c) – high-divergent

Reference photos were taken with the “Nikon D90” digital photo camera and the “AF-S Nikkor 18–200 mm” objective. Photos (Fig. 3) were exposed with shutter speed 1 s, aperture $f/13$ and by CMOS chip sensitivity ISO 160 for circular and high-divergent configuration, ISO 200 for low-divergent respectively.

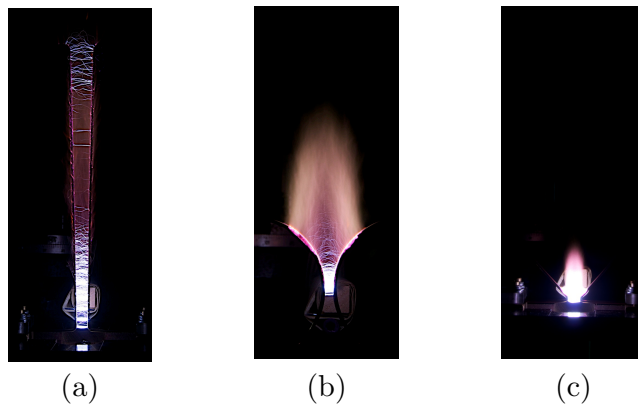


Fig. 3. Plasma flows; (a) – low-divergent, (b) – circular, (c) – high-divergent

The air streamed upwards into the reactor (Fig. 1). Initial discharge breakdown region ignition area was at its bottom during all experiments (Fig. 3).

Spectra

Values of plasma flow visible spectral lines intensities indicate existence of ionized regions in the flow. Spectra were measured by “OceanOptics SAD 500, Avantes” fiber optic spectrometer. Sensor was placed perpendicular to the plasma flow z -axis (Fig. 1) and spectral intensity values were taken along this axis in the whole discharge region. To prevent random measurement errors 7 measurements of spectral intensity were performed in each position.

Spectral range was divided into 2048 values equal to the wavelength range $\lambda \in (190.35; 861.41)$ [nm]. The resolution of the spectrometer was 0.328 nm. Each intensity value plotted in graphs on Figs. 4, 5 and 6 is a mean value of 7 measurements.

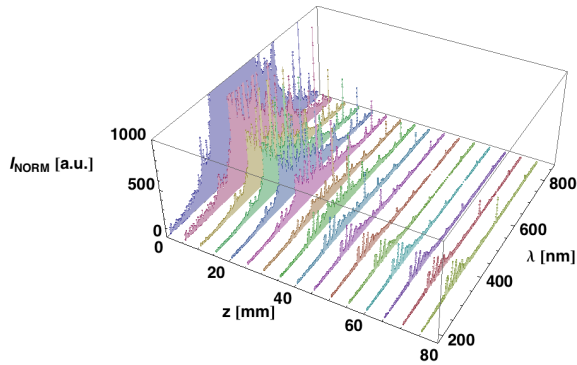


Fig. 4. Spectra for low-divergent electrode configuration

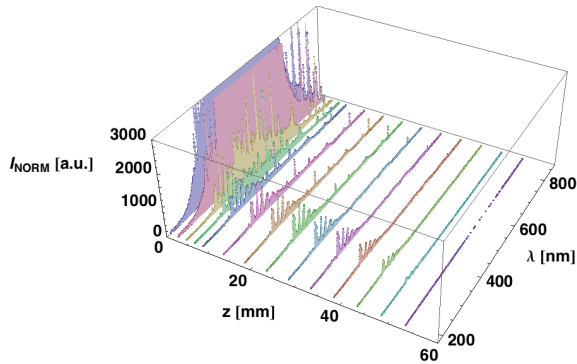


Fig. 5. Spectra for circular electrode configuration

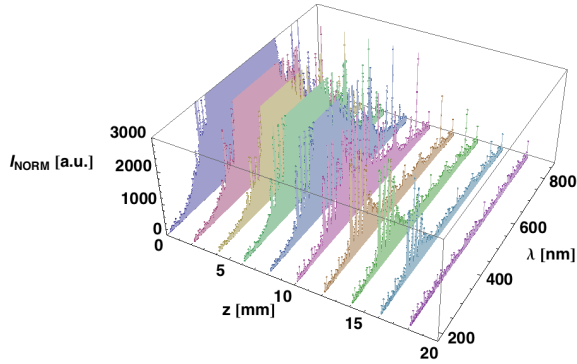


Fig. 6. Spectra for high-divergent electrode configuration

Results and Discussion

We identified the most intensive lines

$$\begin{aligned}
 \lambda_A &= 463.061 \text{ nm: N III; } 2s2p(^3P^\circ)4p - 2s2p(^3P^\circ)5s, \\
 \lambda_B &= 463.885 \text{ nm: O II; } 2s^22p^2(^3P)3s - 2s^22p^2(^3P)3p, \\
 \lambda_C &= 500.113 \text{ nm: N II; } 2s^22p(^2P^\circ)3p - 2s^22p(^2P^\circ)3d, \\
 \lambda_D &= 567.602 \text{ nm: N II; } 2s^22p(^2P^\circ)3s - 2s^22p(^2P^\circ)3p.
 \end{aligned} \tag{1}$$

by means of the NIST database [2]. In addition we found spectral line band $\lambda_E \sim 390 \text{ nm}$ (higher energetic UV spectra range) pertaining to the first negative system of N_2^+ and the second positive system of N_2 in all three measured spectra.

There is connection between observed spectral intensity peaks and plasma particles excitation. Intensity values distribution indicates shape of the plasma region. The most excited part of the plasma flow can be assigned in the vicinity of the ignition region in all tested electrode configurations (Figs. 3, 7, 8 and 9).

In the low-divergent configuration plasma region extended to the end of the electrodes (Figs. 4 and 7).

In circular configuration the dimension of plasma region outside of electrodes was approximately equal to the electrode radius (Fig. 5).

In the high-divergent configuration plasma region outreached the top of the electrodes for about 20 mm and analysis of spectral line intensity curves indicates sharp transition between ionized and neutral part of the flow.

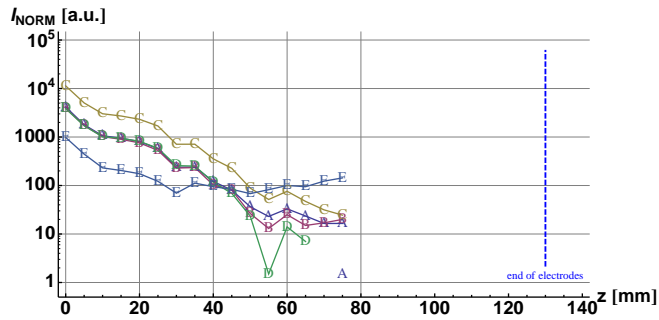


Fig. 7. Low-divergent configuration: spectral lines intensities (λ_A , λ_B , λ_C , λ_D peaks and λ_E band) in dependence on position along z -axis.

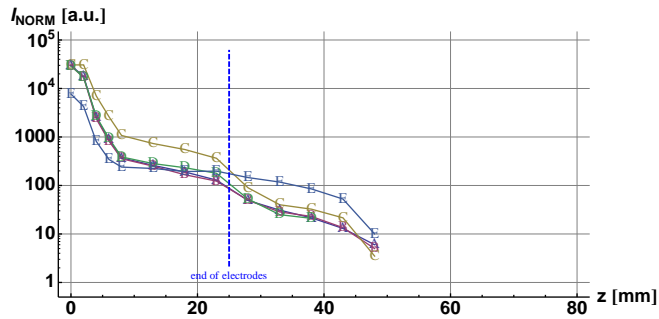


Fig. 8. Circular configuration: spectral lines intensities (λ_A , λ_B , λ_C , λ_D peaks and λ_E band) in dependence on position along z -axis.

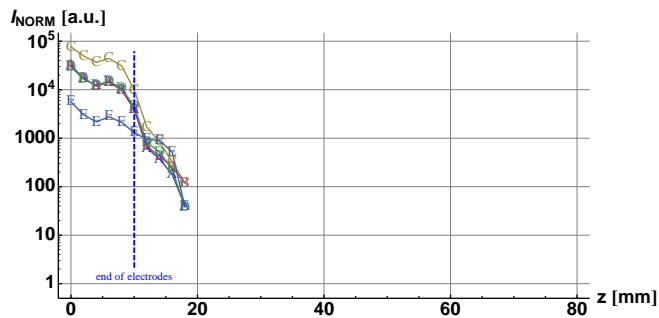


Fig. 9. High-divergent configuration: spectral lines intensities (λ_A , λ_B , λ_C , λ_D peaks and λ_E band) in dependence on position along z -axis.

Results of spectral measurements correspond to plasma flow photos, too. We can see that plasma flow existence was fully limited to the interelectrode space in case of low-divergent configuration. Decay of the ionized column began in the first third of the interelectrode space (Fig. 3a). In both circular and high-divergent configurations plasma filled the whole interelectrode region and reached beyond ends of electrodes (Figs. 3b, c).

Combination of these three electrode configurations together with proper selection of discharge characteristics might allow shaping of the ionized gas flow for every specific application of the gliding discharge reactor.

Summary

We studied connection between some elementary electrode forms and corresponding plasma flow shapes in the gliding discharge reactor. Experiments were performed in air at atmospheric pressure and room temperature. For identification of the most reactive plasma region in the flow, plasma was investigated by means of its visible spectral lines.

There were tested three basic configurations of wire electrodes representing limit forms of electrodes and recognized ionized regions in the flow. Our results can be used in decision making about shaping of the gliding discharge reactor ionized gas region, especially in case when both volume and surface treatment is needed, e.g. for gas decomposition might be suitable the low-divergent configuration, for surface treatment seems to be more suitable the circular configuration, etc.

References

- [1] Z. BO, J. H. YAN, X. D. LI, Y. CHI, B. CHÉRON, K. F. CEN: *The Dependence of Gliding Arc Gas Discharge Characteristics on Reactor Geometrical Configuration*. Plasma Chem Plasma Process, 27 (2007), 691–700.
- [2] http://physics.nist.gov/PhysRefData/ASD/lines_form.html, NIST, 1st April 2010.

Received June 14, 2010

Limiting parameter values for switch-on and switch-off shocks in ideal MHD

PETER DELMONT¹, RONY KEPPENS^{1–3}

Abstract. We investigate under which parameter regimes the MHD Rankine–Hugoniot conditions, which describe discontinuous solutions to the MHD equations, allow for switch-on and switch-off shock solutions. We derive limiting values which agree with the literature and show how we can visualize these limits in the parameter space spanned by Alfvén Mach number and plasma beta. We show that the superposition of a switch-on and a switch-off shock is also an MHD shock, such that the magnetic field is aligned with the shock normal.

Key Words. MHD, shocks, Rankine-Hugoniot.

Introduction

The dynamical behaviour of plasmas is often described by the equations of ideal magnetohydrodynamics (MHD). Whereas the stationary Euler equations only have the isotropic sound speed as a characteristic speed, the stationary MHD system has three highly anisotropical characteristic speeds: the slow magnetosonic speed, the Alfvén speed and the fast magnetosonic speed, which makes the MHD system much more rich and complex.

The MHD system is highly nonlinear and allows for large-amplitude waves. In the wave steepening limit, these solutions become discontinuous. The mathematical description of MHD discontinuities is given by the *Rankine–Hugoniot* (RH) jump conditions. The MHD discontinuities can be classified in (i) *linear discontinuities* and (ii) *MHD shocks*. This does not imply that all solutions to the RH jump conditions are physically admissible.

¹Centre for Plasma Astrophysics, K.U.Leuven, Belgium

²Astronomical Institute, Utrecht University, The Netherlands

³FOM institute for Plasma Physics Rijnhuizen, Nieuwegein, The Netherlands

The Alfvén speed plays a central role in ideal MHD, and MHD shocks can connect sub-Alfvénic flow to super-Alfvénic flow. These solutions to the RH conditions are called *intermediate shocks*.

The existence of these intermediate shocks is still under debate. Let us first summarize the main arguments against the existence of intermediate shocks. Landau & Lifschitz [14] performed a classical stability analysis and showed that intermediate shocks are unstable with respect to small perturbations. Also Falle & Komissarov [8] reject the existence of intermediate shocks. They argue that wave steepening would lead to compound waves instead of intermediate shocks. Most intermediate shocks cross even more than one characteristic speed. On the other hand, Coppi [3] countered some of these objections by noticing that the ideal MHD system is not strictly hyperbolic. Wu [19], De Sterck et al. [7], Delmont & Keppens [6] and many other authors have found intermediate shocks in numerical simulations. Amongst other observers, Chao et al. [2] and Feng & Wang [9] claim to have observed intermediate shocks in respectively Voyager 2 and Voyager 1 data.

An alternative manner to connect a sub-Alfvénic state to a super-Alfvénic state would be by a compound wave. These compound waves can consist of a slow shock which travels with its maximal propagation speed and a rarefaction fan directly attached to it. Brio & Wu [1] detected those compound waves in numerical simulations which have become classical test problems for numerical codes. Another type of compound signal consists of a slow shock layer, immediately followed by a rotational discontinuity (Whang et al. [18]).

Recently, Goedbloed [11] classified the MHD shocks by rewriting the RH equations in the de Hoffmann–Teller frame (de Hoffmann & Teller [12]) introducing the existence of a distinct time reversal duality between entropy-allowed and entropy-forbidden solutions. Delmont & Keppens [5] revisited the classical RH conditions and augment these results in terms of the commonly exploited shock parameters in any shock frame. We found parameter ranges for intermediate shocks. These parameter ranges can be interesting to study the behavior of an intermediate shock, e.g. if one performs a numerical simulation involving intermediate shocks (as in e.g. Delmont & Keppens [6]).

In this paper we summarize the findings of that paper, and focus on the switch-on and switch-off solutions to the RH jump conditions in greater depth. A switch-on shock can be seen as the transition between a fast and an intermediate shock, while a switch-off shock is the transition case between an intermediate and a slow shock. These switch-on and switch-off shocks are proved to be stable with respect to small perturbations (theoretically by Todd [17] and numerically by Chu & Taussig [4]).

Solving the Rankine–Hugoniot conditions

Governing equations

The set-up of our problem is the following. Given is a known state \mathbf{u}_k , connected to an unknown state \mathbf{u}_u by a stationary MHD shock. We will show that there exist at most three real possibilities for the value of \mathbf{u}_u . As mentioned above, discontinuous solutions to the ideal MHD equations should satisfy the RH jump conditions. Defining the flux term $\mathbf{F} = (\rho v_n, \rho v_n^2 + p + B_t^2/2, \rho v_n v_t - B_n B_t, v_n(\gamma/(\gamma - 1)p + \rho(v_n^2 + v_t^2)/2 + B_n^2) - B_n B_t v_t, v_n B_t - v_t B_n, B_n)$, in any frame where the shock is stationary (including the de Hoffmann–Teller frame), the MHD RH conditions become

$$\mathbf{F}_u = \mathbf{F}_k. \quad (1)$$

Index ‘n’ refers to the direction of the shock normal, and index ‘t’ refers to the tangential vector components in the plane spanned up by \mathbf{B}_u and \mathbf{B}_k . Further, ρ is the mass density, \mathbf{v} is the velocity, p the thermal pressure and \mathbf{B} the magnetic field. The ratio of specific heats, γ , is considered a constant parameter, as we will assume an ideal gas equation of state. For a derivation of these well-known expressions, we refer to De Hoffmann & Teller [12]; Jeffrey & Taniuti [13]; Liberman & Velikhovich [16], Goedbloed & Poedts [10]. Since MHD shocks are essentially 2-D, the system is reduced to a 6×6 -system.

We introduce the parameters plasma beta

$$\beta \equiv \frac{2p}{B_n^2 + B_t^2}, \quad (2)$$

inclination to the shock normal

$$\theta \equiv \frac{B_t}{B_n}, \quad (3)$$

and the Alfvén Mach number

$$M \equiv \sqrt{\frac{\rho v_n^2}{B_n^2}}. \quad (4)$$

It is possible to recover the primitive variables from these parameters (see e.g. Delmont & Keppens [5]). We note $\mathbf{u}_u = (M_u, \theta_u, \beta_u)$, and $\mathbf{u}_k = (M, \theta, \beta)$, where we have dropped the index ‘k’.

Now, define

$$\xi \equiv ((M^2 - 1)\theta, 2M^2 + \beta(1 + \theta^2) + \theta^2, (\gamma/(\gamma - 1)\beta + M^2)(1 + \theta^2)M^2).$$

We showed in [5] that the stationary MHD RH system can be reduced to a 3×3 -system, namely

$$\xi_u = \xi_k. \quad (5)$$

MHD shock types: classical 1–2–3–4 classification

Whereas in HD, a certain state can only be sub- or supersonic, ideal MHD has three highly anisotropic characteristic speeds: the slow magnetosonic speed v_s , the normal Alfvén speed a_n and the fast magnetosonic speed v_f . The full set of MHD equations is hyperbolic, but non-strictly hyperbolic: $0 \leq v_s \leq a_n \leq v_f$. These three characteristic speeds divide states into four categories. Superfast states ($|v_n| > v_f$) are called 1-states, subfast states ($a_n < |v_n| < v_f$) are 2-states and superslow ($v_s < |v_n| < a_n$) and subslow ($|v_n| < v_s$) states are respectively called 3-states and 4-states. A shock is said to be of *shock type* $i \rightarrow j$ if it connect an upstream i -state to a downstream j -state. It is well-known (see e.g. Libermann & Velikhovich [16]) that once the shock type and one state is given, if a solution exists, it must be unique.

We call a shock admissible if it satisfies the second law of thermodynamics: entropy should increase during the passage of a shock, and admissible versus inadmissible shocks can be related through the time duality principle from Goedbloed [11]. When the upstream state is of type i and the downstream state is of type j , then the shock type is $i \rightarrow j$. Furthermore, in terms of these shock types, the admissibility condition translates as $i < j$.

Switch-on & switch-off shocks

Assume now that $\xi_{1,k} = 0$. This means that the known state is exactly Alfvénic in the stationary shock frame ($M = 1$) or that the magnetic field of this state is aligned with the shock normal ($\theta = 0$). Suppose the state \mathbf{u}_k is connected through an MHD shock to an unknown state \mathbf{u}_u . Then $\xi_{1,u}$ should also vanish. Therefore, solutions which are characterized by $\xi_1 = 0$ can be classified as follows:

- $1 \rightarrow 4$ shocks with $\theta_u = \theta_k = 0$. Although these shocks connect a sub- to a super-Alfvénic state, they are stable. We will refer to this shock as an HD-shock.
- $2 = 3 \rightarrow 2 = 3$ rotational waves. These solutions are linear discontinuities. They satisfy $\theta_u = -\theta_k$, such that the magnetic field flips around the shock normal.
- $1 \rightarrow 2 = 3$ shocks are called *switch-on* shocks. The upstream magnetic field is aligned with the shock normal, and the downstream is exactly Alfvénic.

- $2 = 3 \rightarrow 4$ shocks are called *switch-off* shocks. The downstream magnetic field is aligned with the shock normal, and the downstream is exactly Alfvénic.

General solution

Given is a state \mathbf{u}_k in the stationary shock frame. Solving the RH conditions leads to the following unknown state \mathbf{u}_u :

$$\begin{aligned} M_u &= \sqrt{\frac{(M^2 - 1)\theta + \psi}{\psi}}, \\ \beta_u &= \frac{((\gamma - 1)((\theta - \psi)^2 + (1 + \theta^2)\beta) - 4M^2)(M^2 - 1) + 2M^2(\psi\theta + \psi^2)}{(M^2 - 1)(\gamma + 1)(1 + \psi^2)}, \\ \theta_u &= \psi, \end{aligned} \quad (6)$$

where ψ satisfies the cubic equation

$$C(\psi) \equiv \psi^3 + \tau_2\psi^2 + \tau_1\psi + \tau_0 = 0, \quad (7)$$

with its coefficients given by

$$\begin{aligned} \tau_2 &= -\theta((\gamma - 1)(M^2 - 1) - M^2), \\ \tau_1 &= (M^2 - 1)((\gamma - 1)(M^2 - 1) + \gamma(\beta(\theta^2 + 1) + \theta^2) - 2), \\ \tau_0 &= -(\gamma + 1)\theta(M^2 - 1)^2. \end{aligned} \quad (8)$$

Note that this only holds when $M \neq 1$. Let us now consider the 2 singular cases: $\theta = 0$ and $M = 1$.

In the specific case, where $\theta = 0$, one HD solution, and potentially also two switch-on or switch-off solutions, exist. Those two solutions are essentially the same, except for the sign of θ_u . The HD shock solution is given by

$$(M_u, \theta_u, \beta_u) = \left(\sqrt{\frac{(\gamma - 1)M^2 + \gamma\beta_1}{\gamma + 1}}, 0, \frac{4M^2 - (\gamma - 1)\beta}{\gamma + 1} \right), \quad (9)$$

while the two switch-on or switch-off solutions are given by

$$\begin{aligned} M_u &= 1, \\ \beta_u &= \frac{1 - 2M^2 - \beta}{(\gamma - 1)M^4 + \gamma(\beta - 2)M^2 - \gamma(\beta - 1)} - 1, \\ \theta_u &= \pm \sqrt{((\gamma\beta - 2) - (\gamma - 1)(M^2 - 1))(M^2 - 1)}. \end{aligned} \quad (10)$$

Finally, we consider the irregular case where $M = 1$. In this case a rotational solution $((M_u, \theta_u, \beta_u) = (M, -\theta, \beta))$ and both a switch-on and a switch-off solution exist, where $\mathbf{u}_u(\mathbf{u}_k)$ is the inverse function of the switch-on and switch-off solutions described above, namely

$$\begin{aligned} M_u &= \sqrt{\frac{\sqrt{A} \pm 2\gamma(\beta + 1)(\theta^2 + 1)}{2(\gamma + 1)}}, \\ \beta_u &= \beta(1 + \theta^2) + \theta^2 - 2(M_u^2 - 1), \\ \theta_u &= 0, \end{aligned} \tag{11}$$

where

$$A = 2\gamma^2\beta\theta^2 + \gamma^2\beta^2 + 2\gamma^2\beta^2\theta^2 + \gamma^2\beta^2\theta^4 + 2\gamma^2\beta\theta^4 + \gamma^2\theta^4 - 4\gamma\beta - 4\gamma\beta\theta^2 + 4 + 4\theta^2.$$

As we will show later on, these switch-on and switch-off unknown states, can also be connected through a stationary HD shock.

Results

Restrictions to the existence of switch-on and switch-off shocks

As mentioned earlier, solving the RH conditions reduces to solving a cubic equation. Therefore, there are always one or three real solutions. Lax [15] has shown that when only one real solution exists, it must be a $1 \rightarrow 2$ or a $3 \rightarrow 4$ solution. It is well-known that the cubic C has three real solutions if and only if

$$\Omega \equiv 27\tau_0^2 + 4\tau_1^3 + 4\tau_2^2\tau_0 - \tau_2^2\tau_1^2 - 18\tau_2\tau_1\tau_0 < 0. \tag{12}$$

On the other hand, when $\Omega > 0$, there is only one non-trivial solution. In the transition case where $\Omega = 0$, there exist two distinct non trivial solutions.

Since both τ_0 and τ_1 have $(M^2 - 1)$ as a factor, $M^2 - 1 = 0$ implies that $\Omega = 0$. Therefore, there are two distinct solutions with $\theta_u \neq \theta$.

On the other hand, when $\theta = 0$, we have that

$$\Omega = 1728(M^2 - 1)^3((\gamma - 1)M^2 + \gamma(\beta - 1) - 1)^3. \tag{13}$$

This implies that switch-on shocks can only exist when

$$1 < M < \sqrt{\frac{\gamma(1 - \beta) + 1}{\gamma - 1}}, \tag{14}$$

and switch-off shocks can only exist when

$$\sqrt{\frac{\gamma(1-\beta)+1}{\gamma-1}} < M < 1. \tag{15}$$

This restriction is only valid when $\frac{\gamma(1-\beta)+1}{\gamma-1} > 0$, i.e. when $\beta < (\gamma+1)/\gamma$. These results agree with the literature (see e.g. De Sterck et al. [7]).

Another non-trivial requirement is that β_u should be positive. For the switch-on and switch-off shocks, this requirement reduces to

$$\frac{1-2M^2-\beta}{(\gamma-1)M^4+\gamma(\beta-2)M^2-\gamma(\beta-1)} > 1, \tag{16}$$

which is satisfied whenever

$$0 < \beta < \frac{(\gamma-1)M^4-2\gamma M^2+(\gamma-1)}{\gamma M^2-\gamma+1}. \tag{17}$$

A mathematical solution to the HD shocks always exists, the only requirement here is the positive β requirement, which now reduces to

$$0 < \beta < \frac{4}{\gamma-1}M^2.$$

For $\gamma = 5/3$, all these observations are summarized in Fig. 1.

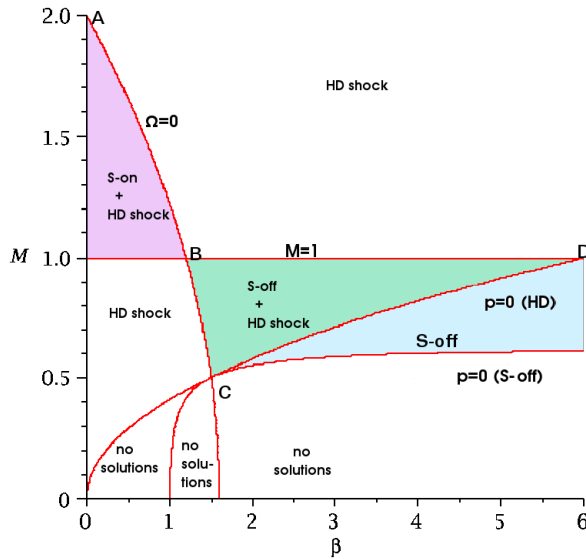


Fig. 1. Shown is the $\theta = 0$ plane of the (M, θ, β) parameter space; the color coding refers to different regions where certain shock types are possible

Limiting values for switch-on and switch-off shocks

We will now use Fig. 1 to derive limiting values for switch-on and switch-off shocks.

- *Point A.* The maximum Mach number at which switch-on shocks can be found is reached in point *A* (see Fig. 1). Filling out $\beta = 0$ in $\Omega = 0$, and solving for M , leads us to conclude that the maximum Mach number for switch-on shocks equals $\sqrt{(\gamma + 1)/(\gamma - 1)}$.
- *Point B.* Note that the coordinates of point *B* are given by $(\beta, M) = (2/\gamma, 1)$. This can be found by filling out $M = 1$ in $\Omega = 0$. Note that at $\beta = 2/\gamma$, also the transition between magnetically and thermally dominated plasmas takes place.
- *Point C.* We can still derive a minimum value of the Alfvénic Mach number for the existence of switch-off shocks. Therefore we need to find the M coordinate of point *C* in Fig. 1. We solve the system

$$\begin{aligned} \frac{(\gamma - 1)M^4 - 2\gamma M^2 + (\gamma - 1)}{\gamma M^2 - \gamma + 1} &= \beta. \\ (\gamma - 1)M^2 + \gamma(\beta - 1) - 1 &= 0. \end{aligned} \tag{18}$$

The solution to this eq. is $(M, \theta) = \left(\sqrt{(\gamma - 1)/(\gamma + 1)}, 4/(\gamma + 1)\right)$. Therefore switch-off shocks can only exist when $M > \sqrt{(\gamma - 1)/(\gamma + 1)}$.

- *Point D.* Filling out $M = 1$ in $\beta_u = 0$, gives the coordinates of point *D*. The solution is $(M, \theta) = (1, 4/(\gamma - 1))$. Therefore the maximum plasma- β at which switch-off shocks can occur is $4/(\gamma - 1)$.

We summarize these findings in Table 1.

Table 1. Limiting values for the plasma- β and the Alfvénic Mach number.

parameter	Switch-on	Switch-off	Switch-on ($\gamma = 5/3$)	Switch-off ($\gamma = 5/3$)
M_{\min}	1	$\sqrt{(\gamma - 1)/(\gamma + 1)}$	1	0.5
M_{\max}	$\sqrt{(\gamma + 1)/(\gamma - 1)}$	1	2	1
β_{\min}	0	$2/\gamma$	0	1.2
β_{\max}	$2/\gamma$	$4/\gamma - 1$	1.2	6

HD shock as superposition of switch-on and switch-off shock

The RH conditions are equivalent to equations $\xi_u = \xi_k$, which express the existence of three shock invariants. Therefore two states can be connected through the stationary RH conditions if and only if they have the same value for the expression $\xi_1 \equiv (M^2 - 1)\theta$, $\xi_2 \equiv 2M^2 + \beta(1 + \theta^2) + \theta^2$ and $\xi_3 \equiv (\gamma/(\gamma - 1)\beta + M^2)(1 + \theta^2)M^2$. Denoting the relation “state A can be connected to state B through the stationary RH conditions” as $A \mapsto_{\text{RH}} B$, this relation \mapsto_{RH} is an equivalence. Indeed:

- \mapsto_{RH} is reflexive: $A \mapsto_{\text{RH}} A$. Every state can be connected to itself through the stationary RH conditions.
- \mapsto_{RH} is symmetric: $A \mapsto_{\text{RH}} B \Rightarrow B \mapsto_{\text{RH}} A$. If state A can be connected to state B through the stationary RH conditions, then also state B can be connected to state A by these conditions. Of course only one of these connections satisfies the entropy condition.
- \mapsto_{RH} is transitive: $A \mapsto_{\text{RH}} B \wedge B \mapsto_{\text{RH}} C \Rightarrow A \mapsto_{\text{RH}} C$. Indeed: if $A \mapsto_{\text{RH}} B$, then $\xi_i(A) = \xi_i(B)$, and if $B \mapsto_{\text{RH}} C$, then $\xi_i(B) = \xi_i(C)$. Hence $A \mapsto_{\text{RH}} B \wedge B \mapsto_{\text{RH}} C$ implies $\xi_i(A) = \xi_i(B) = \xi_i(C)$, which means that $A \mapsto_{\text{RH}} C$.

Therefore, an HD shock with $\Omega < 0$, can be seen as the superposition of a switch-on and a switch-off shock, since in that case, the equivalence class, containing the up- and downstream states of the HD shocks, also contains two exactly Alfvénic states.

Conclusion

We have derived limiting values of the plasma parameters at which the Rankine–Hugoniot jump conditions allow for switch-on and switch-off shocks. We have shown that the superposition of a switch-on and a switch-off shock leads to an HD shock.

References

- [1] M. BRIO, C. C. WU: *An upwind differencing scheme for the equations of ideal magnetohydrodynamics*. J. Comp. Phys., 75 (1988), 400–422.
- [2] J. K. CHAO, L. H. LYU, B. H. WU, A. J. LAZARUS, T. S. CHANG, R. P. LEPPING: *Observation of an intermediate shock in interplanetary space*. J. Geophys. Res., 98 (1993), 17443–17450.
- [3] P. S. COPPI, R. D. BLANDFORD, C. F. KENNEL: *On the existence and stability of intermediate shocks*. ESA SP-285, 1 (1989), 381–384.

- [4] C. K. CHU, R. T. TAUSSIG: *Numerical experiments of magnetohydrodynamic shocks and the stability of switch-on shocks*. Phys. Fluids, *10* (1967), 249–256.
- [5] P. DELMONT, R. KEPPENS: *Parameter regimes for slow, intermediate and fast MHD shocks*. J. Plasma. Phys., *77* (2010), 207–229.
- [6] P. DELMONT, R. KEPPENS: *Shock refraction in ideal MHD*. Journal of Physics: Conference Series (2010), accepted.
- [7] H. DE STERCK, B. C. LOW, S. POEDTS: *Complex magnetohydrodynamic bow shock topology in field-aligned low- β flow around a perfectly conducting cylinder*. Phys. of Plasmas, *11* (1998), 4015–4027.
- [8] S. A. E. G. FALLE, S. S. KOMISSAROV: *On the existence of intermediate shocks*. Mon. Not. R. Astron. Soc., *123* (1997), 265–277.
- [9] H. FENG, J. M. WANG: *Observations of a $2 \rightarrow 3$ type interplanetary intermediate shock*. Solar Phys., *247* (2008), 195–201.
- [10] H. GOEDBLOED, S. POEDTS: *Principles of magnetohydrodynamics with applications to laboratory and astrophysical plasmas*. Cambridge University Press, Cambridge 2004.
- [11] J. P. GOEDBLOED: *Time reversal duality of magnetohydrodynamical shocks*. Phys. Plasmas, *15* (2008), 062101.
- [12] F. DE HOFFMANN, E. TELLER: *Magneto-hydrodynamic shocks*. Phys. Rev., *80* (1950), 692–703.
- [13] A. JEFFREY, T. TANIUTI: *Nonlinear wave propagation*. Academic Press, New York 1964.
- [14] L. D. LANDAU, E. M. LIFSCHITZ: *Fluid mechanics*. Pergamon press, Oxford 1959.
- [15] P. D. LAX: *Hyperbolic system of conservation laws II*. Comm. Pure Appl. Math., *10* (1957), 537–566.
- [16] M. A. LIBERMAN, A. L. VELIKHOVICH: *Physics of shock waves in gases and plasmas*. Springer, Berlin 1986.
- [17] L. TODD: *Evolution of switch-on and switch-off shocks in a gas of finite electrical conductivity*. J. Fluid Mech., *24* (1965), 597–608.
- [18] Y. C. WHANG, J. ZHOU, R. P. LEPPING, A. SZABO, D. FAIRFIELD, S. KUKOBUN, K. W. OGILVIE, R. FITZENREITER: *Double discontinuity: A compound structure of slow shock and rotational discontinuity*. J. Geophys. Res., *103* (1998), 6513–6520.
- [19] C. C. WU: *On MHD intermediate shocks*. Geophys. Res. Lett., *14* (1987), 668–671.

Received May 14, 2010

Effect of magnetic field on jeans instability of quantum dusty plasma: application in white dwarf star¹

RAMPRASAD P. PRAJAPATI², RAJENDRA K. CHHAJLANI³

Abstract. In the present paper, we study the modified Jeans instability of magnetized quantum dusty plasma and formation of white dwarf star. The basic equations for such magnetized homogeneous plasma are constructed and the general dispersion relation is obtained using the normal mode analysis. The electrons and ions are assumed to be inertia less while dust grains to be mobile. The effect of magnetic field, dust temperature and quantum correction is studied on the growth rate of Jeans instability for white dwarf star formation. We find that the Jeans criterion of instability is modified due to the quantum Bohm potential and dust temperature but it is unaffected by the presence of magnetic field. The growth rate of Jeans instability is determined for white dwarf star taking the numerical parameters in the interior zone. We find that magnetic field and quantum corrections both have stabilizing role on the growth rate of Jeans instability.

Key Words. Star formation, quantum dusty plasma, jeans instability, magnetic field.

1. Introduction

The condensation of dusty plasma into a crystalline state through gravitational collapsing is an interesting phenomenon of astrophysics. This causes the formation of planetary nebula, stars, galaxies and other astrophysical objects. The Jeans gravitational instability of plasma plays crucial role in the formation of these suggested objects. The formation of white dwarf star and neutron star are mainly due to the gravitational collapsing process of dusty plasma at extremely low temperature. At such temperature the system passes

¹The authors are thankful to Prof. S. K. Ghosh, HOD, S. S. in Physics for his constant encouragements.

²Institute for Plasma Research, Bhat, Gandhinagar-382428, India;
e-mail: prajapati_iter@yahoo.co.in

³School of Studies in Physics, Vikram University Ujjain-456010, M.P., India

through quantum corrections and this dense cooled plasma is called the quantum dusty plasma. It is seen from the recent spectral studies the dust is the most prominent component in the astrophysical plasma. Jeans [1] has first given the fundamental idea of the fragmentation of interstellar matter and discussed the gravitational instability. Recently, many authors [2]–[5] have investigated the Jeans instability of dusty plasma including various assumptions and different parameters. Prajapati et al. [6] have also studied the problem of Jeans instability in the spiral arms of galaxies taking the corresponding values of the parameters.

Along with this in recent time the study of waves and instabilities in dusty plasma is become more important due to their large applications. The dust temperature is one of the important parameter which gives the information about the dust-particle interactions. Mamun [7] has investigated the effect of dust temperature and non thermal fast ions on gravitational instability of self-gravitating magnetized dusty plasma. Gill and Kour [8] have considered the effect of non thermal distribution and dust temperature on non linear dust acoustic solitary waves. Wang and Ticos [9] have found that dust is the versatile matter for high temperature diagnostics. Williams and Thomas have measured the kinetic dust temperature of weakly coupled dusty plasma. Thus it is interesting to incorporate the effect of dust temperature parameter in the present study.

The above studies [2]–[6] deal with the phenomena that the de Broglie wavelength of the charged dust grains is much smaller than the dimension of the system. But at extremely low temperature when plasma is cooled then the de Broglie wavelength of the charged dust grains could be of the order of dimension of the system. In such conditions, the ultra cold dense plasma is treated as Fermi or quantum plasma. This type of medium exists in the interior of white dwarf star, atmosphere of neutron star and in planetary nebula. The typical range of magnetic field in white dwarf star varies between $100 \div 200$ T which play important role in condensation of cold plasma through gravitational collapsing process. It is well known that every astrophysical object has influence of gravitational force thus it may be a subject of interest to study Jeans instability of the considered system in such parametric regimes. In order to study the effect of self-gravitation in many astrophysical objects Shukla and Stenflo [11] have investigated the Jeans instability in quantum dusty plasma and found that the Jeans stability criterion is modified due to the quantum corrections. They did not consider the effect of magnetic field in their study. Masood et al. [12] have presented a quantum hydrodynamic (QHD) model for multi-component quantum magnetoplasma with Jeans term. In this case they have considered the quantum statistical effects of electrons and ions but they did not consider the effect of quantum Bohm potential for dust grains and finite dust temperature effect. The problem of Jeans instability of quantum

dusty plasma in the presence of the ambient magnetic field is discussed by Salmullah et al. [13]. In this case they have also considered the effect of quantum Bohm potential for dust grains. Lundin et al. [14] have investigated the modified Jeans instability for magnetized quantum MHD plasma including electron spin effect. Ren et al. [15] have explored the effect of electrical resistivity and magnetic field on the Jeans instability of quantum MHD plasma.

Along with this, in recent years the importance of magnetic field in dusty interstellar gas dynamics has been recognized by many researchers. In the ISM large amount of energy is injected by the stars which lead to the formation of shock waves. But when these shock waves weaken, they become large amplitude hydromagnetic Alfvén waves. In this direction, Hennebelle and Parault [16] have investigated dynamical condensation process in a magnetized and thermally conducting medium and stressed their importance on thermal condensation modes with magnetic field. Falceta-Goncalves et al. [17] showed that magnetic field plays an important role in the stability of ISM molecular clouds. Colle and Raga [18] have studied the effects of the magnetic field on the H_α emission from astrophysical jets. These studies make an interest about the contribution of magnetic field in the quantum dusty plasma that leads to many important phenomena during condensation of astrophysical dusty objects.

In the present paper, our aim is to study effect of magnetic field and dust temperature on the Jeans instability of quantum dusty plasma and the formation of white dwarf star. The dust grains are assumed so massive that they experience quantum Bohm potential. We also wish to see how the fundamental Jeans criterions of instability get modify due to the presence of magnetic field, dust temperature and quantum corrections for the considered system.

2. Formulation of the problem

We assume three species quantum plasma having electrons and ions as inertia less and mobile massive charged dust grains. The formation of white dwarf star is mainly due to the gravitational condensation of quantum plasma with these considered dust grains. The magnetic field is assumed in z -direction (i.e. $\mathbf{B} = B\mathbf{z}$, where \mathbf{z} is unit vector along z -direction). In equilibrium at extremely low temperature the plasma behaves like Fermi gas and passes through the quantum corrections. The above quantum plasma is characterized by the following quasineutrality condition

$$e n_{e0} = e n_{i0} + q_d n_{d0} \quad (1)$$

where q_d and n_{j0} are the dust charge and unperturbed number density of electrons, ions and dust grains respectively.

In present case the contribution of self-gravitational force of electrons and ions are not considered because they are assumed to be inertia less. We also assume that on a dust time scale the electrons and ions are aligned along the magnetic field. Thus in the presence of an electrostatic field $\mathbf{E} = -\nabla\varphi$ (where φ is the electrostatic potential), the electron and ion momentum equations can be written as

$$0 = e n_e \nabla\varphi - \nabla p_e + \frac{\hbar^2}{4m_e} \nabla \left(\frac{\nabla^2 \sqrt{n_e}}{\sqrt{n_e}} \right), \quad (2)$$

and

$$0 = -e n_i \nabla\varphi - \nabla p_i + \frac{\hbar^2}{4m_i} \nabla \left(\frac{\nabla^2 \sqrt{n_i}}{\sqrt{n_i}} \right). \quad (3)$$

For the dynamics of the charged dust grains we write the dust momentum equation including finite dust temperature and Bohm potential term. In general the heavy dust grains do not experience the effect of Bohm potential and their trajectories are unaffected by the quantum corrections. But the dust grains of lighter mass of the order of proton mass ($m_d \approx m_p$) passes through the necessary quantum corrections. In the present case we are dealing with the problem having dust grains of mass ($m_d \approx 5m_p$). In case of Salimullah et al. [13] they have also considered the effect of quantum Bohm potential for dust grains. The dust temperature term is assumed to be classical which is unaffected by the presence of quantum statistical effects. Thus the momentum transfer equation for the dynamics of such dust grain is given by

$$m_d n_d \frac{dv_d}{dt} = \varepsilon e Z_d n_d \nabla\varphi + \frac{\varepsilon e Z_d n_d}{c} (v_d \times B) - m_d n_d \nabla\psi + \frac{\hbar^2}{4m_d} \nabla \left(\frac{\nabla^2 \sqrt{n_d}}{\sqrt{n_d}} \right) - \frac{5}{3} \frac{\sigma_d}{n_d^{1/3}} \nabla n_d, \quad (4)$$

where $\varepsilon = \pm 1$ for positive and negative dust grain respectively.

The continuity equation, Poisson equation for electrostatic and gravitational potential are given by respectively

$$\frac{\partial n_j}{\partial t} + \nabla \cdot (n_j v_j) = 0, \quad (5)$$

$$\nabla^2 \varphi = 4\pi e (n_e + \varepsilon Z_d n_d - n_i), \quad (6)$$

and

$$\nabla^2 \psi = 4\pi G m_d n_d, \quad (7)$$

where v_j , n_j , ψ , φ , m_d , $\sigma_d (= T_d/q_d T_i)$, e and c denote velocity of j^{th} species (electron, ion and dust), density of j^{th} species, gravitational potential, electrostatic potential, dust mass, dust temperature, electronic charge and speed of sound respectively.

3. Dispersion relation and discussions

Let us assume that all the perturbed quantities vary as $\exp(ikr - i\omega t)$, where ω is frequency of harmonic disturbances in the entire media and $k = k_x \hat{x} + k_z \hat{z}$ is the wavenumber. From equations (2)–(7) we obtain the following equations by employing the plane wave analysis:

$$n_{e1} = \frac{e\varphi_1 n_{e0}}{m_e f_e}, \quad (8)$$

$$n_{i1} = \frac{-e\varphi_1 n_{i0}}{m_i f_i}, \quad (9)$$

$$-i\omega v_{d1} = \frac{ik\varepsilon eZ_d}{m_d} \varphi_1 + v_{d1} \times \Omega_{cd} - ik\psi_1 - \frac{\hbar^2 k^2}{4m_d^2 n_{d0}} ikn_{d1} - \frac{5}{3} ik\sigma_d n_{d1}, \quad (10)$$

where $f_{e,i} = V_{Fe,i}^2(1 + \gamma_{e,i})$, $V_{Fe,i} = \sqrt{2k_B T_{Fe,i}/m_{e,i}}$ are Fermi velocities of electrons and ions and $\gamma_{e,i} = \hbar^2 k^2 / 4m_{e,i}^2 V_{Fe,i}^2$. $\Omega_{cd} = eZ_d B / m_d c$ is dust Larmor frequency. v_{d1} , φ_1 , ψ_1 and n_{d1} are perturbation in dust velocity, electrostatic potential, gravitational potential and dust density respectively.

Similarly equation (5) for dust grains and equations (6) and (7) can be written as

$$\omega \frac{n_{d1}}{n_{d0}} = k \cdot v_{d1}, \quad (11)$$

$$-k^2 \varphi_1 = 4\pi e(n_{e1} + \varepsilon Z_d n_{d1} - n_{i1}), \quad (12)$$

and

$$-k^2 \psi_1 = \frac{\omega_J^2}{n_{d0}} n_{d1}, \quad (13)$$

where $\omega_J^2 = 4\pi G m_d n_{d0}$ is the square of the Jeans dust frequency.

Taking the divergence of equation (10) and using equations (11) and (13), then we get the expression for perturbed dust density as

$$n_{d1} = \frac{-k^2 \varepsilon e Z_d n_{d0} \varphi_1}{m_d \left(\omega^2 + \omega_J^2 - i\omega \Omega_{cd} - \frac{\hbar^2 k^4}{4m_d^2 n_{d0}} - \frac{5}{3} k^2 \sigma_d n_{d0} \right)}. \quad (14)$$

On substituting equations (8), (9) and (14) in equation (12) we obtain the following dispersion relation

$$1 + \frac{\omega_{pe}^2}{f_e k^2} + \frac{\omega_{pi}^2}{f_i k^2} - \frac{\omega_{pd}^2}{\left(\omega^2 + \omega_J^2 - i\omega \Omega_{cd} - \frac{\hbar^2 k^4}{4m_d^2 n_{d0}} - \frac{5}{3} k^2 \sigma_d n_{d0} \right)} = 0, \quad (15)$$

where $\omega_{pe,i}^2 = 4\pi e^2 n_{e0,i0} / m_{e,i}$ is the square of electron and ion plasma frequency and $\omega_{pd}^2 = 4\pi e^2 Z_d^2 n_{d0} / m_d$ is the square of the dust plasma frequency.

Equation (15) represents the dispersion relation of Jeans instability of magnetized quantum dusty plasma including finite dust temperature and Bohm potential term experienced by the dust grains. We find that magnetic field, dust temperature and Bohm potential terms significantly modify the dispersion relation.

Limiting cases

3.1. $\Omega_{cd} = 0, \omega_J \neq 0$

For the case of self-gravitating un-magnetized quantum plasma we obtain the following dispersion relation including the quantum statistical effects, Bohm potential and finite dust temperature as

$$1 + \frac{\omega_{pe}^2}{f_e k^2} + \frac{\omega_{pi}^2}{f_i k^2} - \frac{\omega_{pd}^2}{\left(\omega^2 + \omega_J^2 - \frac{\hbar^2 k^4}{4m_d^2 n_{d0}} - \frac{5}{3} k^2 \sigma_d n_{d0}\right)} = 0. \quad (16)$$

On comparing equation (16) with equation (17) of Masood et al. [12], we find that the present dispersion relation is modified due to the presence of quantum Bohm potential and dust temperature term.

The roots of equation (16) can be written as

$$1 + \frac{\omega_{pe}^2}{f_e k^2} + \frac{\omega_{pi}^2}{f_i k^2} - \frac{\omega_{pd}^2}{\left(\omega^2 + \omega_J^2 - \frac{\hbar^2 k^4}{4m_d^2 n_{d0}} - \frac{5}{3} k^2 \sigma_d n_{d0}\right)} = 0 \quad (17)$$

where $s = (1 + \omega_{pe}^2 / f_e k^2 + \omega_{pi}^2 / f_i k^2)$ is the quantum statistical parameter.

The system will be unstable if the below condition is satisfied i.e.

$$\frac{\omega_{pd}^2}{s} + \frac{\hbar^2 k^4}{4m_d^2 n_{d0}} + \frac{5}{3} k^2 \sigma_d n_{d0} - \omega_J^2 < 0. \quad (18)$$

It is clear that the condition of Jeans instability is modified due to the quantum statistical effect, Bohm potential and finite dust temperature effect.

3.2. $\Omega_{cd} = 0, \omega_J = 0$

In the case of non-gravitating un-magnetized quantum plasma we obtain the following dispersion relation

$$1 + \frac{\omega_{pe}^2}{f_e k^2} + \frac{\omega_{pi}^2}{f_i k^2} - \frac{\omega_{pd}^2}{\left(\omega^2 - \frac{\hbar^2 k^4}{4m_d^2 n_{d0}} - \frac{5}{3} k^2 \sigma_d n_{d0}\right)} = 0. \quad (19)$$

Equation (19) represents the dispersion relation with quantum statistical effects, Bohm potential and dust temperature term. It is the modified results than that of Masood et al. [12].

3.3. $\omega_{pe, pi} = 0$, $\Omega_{cd} \neq 0$ and $\omega_J \neq 0$

In the case when the quantum statistical effects of electrons and ions are neglected we obtain the following dispersion relation by putting $i\omega = \sigma$

$$\sigma^2 + \sigma \Omega_{cd} + \frac{\hbar^2 k^4}{4m_d^2 n_{d0}} + \frac{5}{3} k^2 \sigma_d n_{d0} + \omega_{pd}^2 - 4\pi G m_d n_{d0} = 0. \quad (20)$$

Equation (20) shows the dispersion relation for Jeans instability of quantum dusty magnetized plasma including the effects of dust temperature and quantum Bohm potential. The modified condition of Jeans instability is given by

$$\left(\frac{\hbar^2 k^4}{4m_d^2 n_{d0}} + \frac{5}{3} k^2 \sigma_d n_{d0} + \omega_{pd}^2 \right) < 4\pi G m_d n_{d0}. \quad (21)$$

The critical Jeans mass can be obtained by the following expression

$$M_J = \frac{4}{3} \pi \lambda_J^3 n_{d0} = \left[\frac{\pi K_B T}{G \mu m_p} \right]^{3/2} \frac{1}{n_{d0}^{1/2}}. \quad (22)$$

From condition (21) it is obvious that the magnetic field does not affect the condition of Jeans instability. The Jeans criterion is modified due to the presence of quantum Bohm potential, dust temperature and dust plasma frequency. If we ignore the effects of quantum Bohm potential and dust temperature then we obtain the classical Jeans criterion of instability $\omega_{pd}^2 < 4\pi G m_d n_{d0}$ for dusty plasma.

In order to discuss the formation of white dwarf star we calculate the growth rate of Jeans instability taking the arbitrary numerical parameters in the interior of white dwarf star. We write the dispersion relation (20) in dimensionless form using some dimensionless parameter as

$$\sigma^{*2} + \sigma^* \Omega^* + \frac{Q^*}{n_{d0}^*} k^{*4} + \frac{5}{3} k^{*2} \delta^* n_{d0}^* + \omega_{pd}^{*2} - 1 = 0, \quad (23)$$

where the following dimensionless parameters have been used

$$\begin{aligned} \sigma^* &= \frac{\sigma}{\sqrt{4\pi G m_d n_{d0}}}, & \Omega^* &= \frac{\Omega_{cd}}{\sqrt{4\pi G m_d n_{d0}}}, \\ n_{d0}^* &= \frac{n_{d0}}{\sqrt{4\pi G m_d n_{d0}}}, & k^* &= \frac{k}{\sqrt{4\pi G m_d n_{d0}}}, \\ \delta^* &= \frac{\sigma_d}{\sqrt{4\pi G m_d n_{d0}}}, & \omega_{pd}^* &= \frac{\omega_{pd}}{\sqrt{4\pi G m_d n_{d0}}}, \\ Q^* &= \frac{\hbar^2}{4m_d^2 \sqrt{4\pi G m_d n_{d0}}}. \end{aligned} \quad (24)$$

In Figs. 1–3 we have plotted the dimensionless growth rate of Jeans instability (σ^*) against the dimensionless wavenumber (k^*) for various values of quantum correction parameter (Q^*), dust temperature (δ^*) and magnetic field (Ω^*) respectively.

From Fig. 1 it is clear that presence of quantum correction stabilizes the growth rate of Jeans instability. The curve is also plotted for the case of classical magnetized plasma taking $Q^* = 0.0$. It is also clear that the peak value remains constant for each value of Q^* . This result play important role in the formation of dense white dwarf star.

In Fig. 2 we have shown the effect of dust temperature on the growth rate of Jeans instability. The similar feature is also observed for the dust temperature parameter. We find that the growth rate of Jeans instability decreases due to increase in dust temperature. Hence dust temperature stabilizes the growth rate of Jeans instability. The peak value of growth rate in this case also does not depend upon dust temperature parameter.

In Fig. 3 the effect of magnetic field in terms of dust cyclotron frequency is observed. We find that magnetic field stabilizes the growth rate of Jeans instability. The peak value of growth rate is maximum for the case of unmagnetized quantum plasma. Thus quantum corrections, dust temperature and magnetic field all have stabilizing influence on the growth rate if Jeans instability.

These results play crucial role in the formation of cold dense white dwarf star and neutron star.

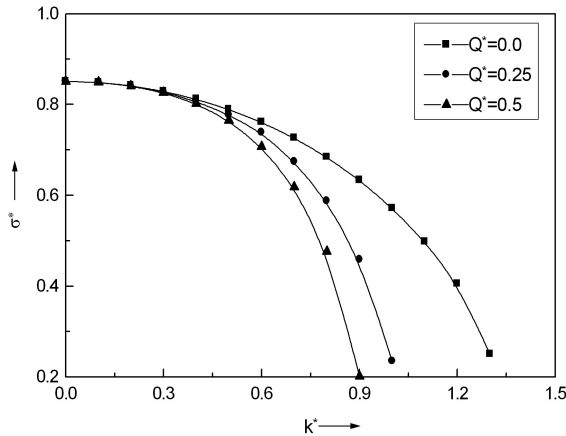


Fig. 1. The growth rate of Jeans instability versus wavenumber for different values of quantum correction parameter; the constant values of the parameters are taken as $\Omega^* = 0.25$, $n_{d0}^* = 0.7$, $\delta^* = 0.4$ and $\omega_{pd}^* = 0.25$ respectively

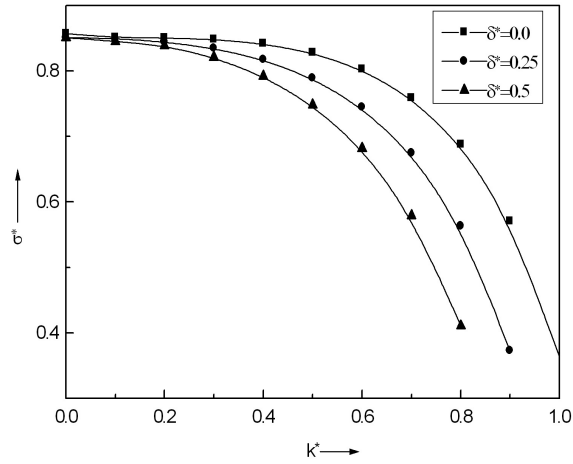


Fig. 2. The growth rate of Jeans instability versus wavenumber for different values of dust temperature parameter; the constant values of the parameters are taken as $\Omega^* = 0.25$, $n_{d0}^* = 0.7$, $Q^* = 0.5$ and $\omega_{pd}^* = 0.25$ respectively

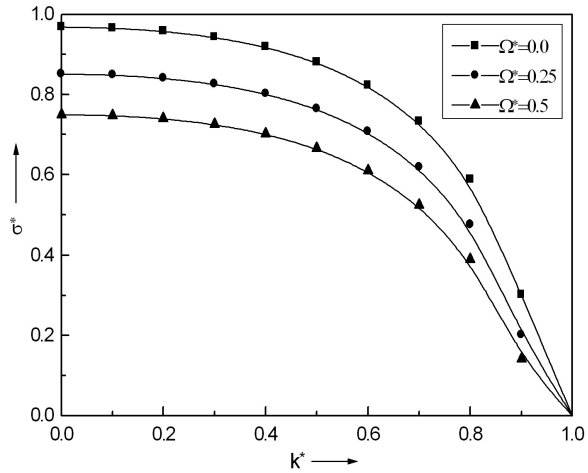


Fig. 3. The growth rate of Jeans instability versus wavenumber for different values of dust cyclotron frequency (magnetic field); the constant values of the parameters are taken as $\delta^* = 0.4$, $n_{d0}^* = 0.7$, $Q^* = 0.5$ and $\omega_{pd}^* = 0.25$ respectively

4. Concluding remarks

We have investigated the effects of magnetic field, finite dust temperature and quantum Bohm potential for dust grains on the multi-component self-gravitating quantum dusty plasma. The limiting cases for Jeans instability including dust temperature and quantum Bohm potential are discussed. We found that in all the cases Jeans criterion of instability is satisfied and it is modified due to the combined effects of quantum Bohm potential and dust temperature. The presence of magnetic field has no influence on the Jeans criterion of instability. From the curves we conclude that magnetic field, dust temperature and quantum corrections all have stabilizing influence on the growth rate of Jeans instability. These parameters play an important role in the condensation of magnetized cloud of white dwarf star via the gravitational collapsing process.

References

- [1] J. H. JEANS: *The stability of a spherical nebula*. Phil. Trans. Roy. Soc. London, *A199* (1902), 1–53.
- [2] F. VERHEEST, P. K. SHUKLA, G. JACOBS, V. V. YAROSHENKO: *Jeans instability in partially ionized self-gravitating dusty plasmas*. Phys. Rev. E, *68* (2003), 1–4.
- [3] R. P. PRAJAPATI, R. K. CHHAJLANI: *Effect of dust temperature on radiative condensation instability of self-gravitating magnetized dusty plasma*. Phys. Scr., *81* (2010), 045501.
- [4] N. L. TSINTSADZE, R. CHAUDHARY, H. A. SHAH, G. MURTAZA: *Jeans instability in a magneto-radiative dusty plasma*. J. Plasma Phys., *74* (2008), 847–853.
- [5] R. P. PRAJAPATI, A. K. PARIHAR, R. K. CHHAJLANI: *Self-gravitational instability of rotating anisotropic heat-conducting plasma*. Phys. Plasmas, *15* (2008), 012107.
- [6] R. P. PRAJAPATI, G. D. SONI, R. K. CHHAJLANI: *Self-gravitating rotating anisotropic pressure plasma in presence of Hall current and electrical resistivity using generalized polytropic laws*. Phys. Plasmas, *15* (2008), 062108.
- [7] A. MAMUN: *Effects of dust temperature and fast ions on gravitational instability in a self-gravitating magnetized dusty plasma*. Phys. Plasmas, *5* (1998), 3542–3546.
- [8] T. S. GILL, H. KOUR: *Effect of nonthermal ion distribution and dust temperature on nonlinear dust acoustic solitary waves*. Pramana-J Physics, *55* (2000), 855–859.
- [9] Z. WANG, C. M. TICOS: *Dust as a versatile matter for high temperature plasma diagnostic*. Rev. Sci. Instrum, *79* (2008), 10F333.
- [10] J. D. WILLIAMS, E. THOMAS: *Measurement of the kinetic dust temperature of a weakly coupled dusty plasma*. Plasma Science IEEE, *35* (2007), 303–308.
- [11] P. K. SHUKLA, L. STENFLO: *Jeans instabilities in quantum dusty plasmas*. Phys. Letters A, *355* (2006), 378–380.
- [12] W. MASOOD, M. SALLIMULLAH, H. A. SHAH: *A quantum hydrodynamic model for multicomponent quantum magnetoplasma with Jeans term*. Phys. Letters A, *372* (2008), 6757–6760.

- [13] M. SALIMULLAH, M. JAMIL, H. A. SHAH, G. MURTAZA: *Jeans instability in a quantum dusty magnetoplasma*. Phys. Plasmas, 16 (2009), 014502.
- [14] J. LUNDIN, M. MARKLUND, G. BRODIN: *Modified Jeans instability criteria for magnetized systems*. Phys. Plasmas, 15 (2008), 072116.
- [15] H. REN, Z. WU, J. CAO, P. K. CHU: *Jeans instability in quantum magnetoplasma with resistive effects*. Phys. Plasmas, 16 (2009), 072101.
- [16] P. HENNEBELLE, M. PERAULT: *Dynamical condensation in a magnetized and thermally bistable flow Application to interstellar cirrus*. Astronomy & Astrophysics, 359 (2000), 1124–1138.
- [17] D. FALCETA-GONCALVES, M. C. DE JULI, V. JATENCO-PEREIRA: *Dusty molecular cloud collapse in the presence of Alfvén waves*. Astrophys. J., 597 (2003), 970–974.
- [18] F. DE COLLE, A. RAGA: *Effects of the magnetic field on the H α emission from jets*. Astrophys. & Space Sci., 293 (2004), 173–180.

Received May 6, 2010

Dust ion acoustic shock waves in dusty plasmas

HASSAN ALINEJAD¹, MOHAMMAD A. MOHAMMADI²

Abstract. A Theoretical investigation of the one-dimensional dynamics of nonlinear electrostatic dust ion-acoustic waves in an un-magnetized dusty plasma consisting of warm ions, charge fluctuating stationary dust grains and trapped electrons has been made by the reductive perturbation technique. The basic features of dust ion-acoustic shock waves are studied by deriving the modified Kortewg–de Vries–Burgers-like equation. It is shown that the special patterns of nonlinear electrostatic waves are significantly modified by the presence of trapped electron component and dust charge fluctuations. In particular, the dust charge fluctuation is a source of dissipation, and is also responsible for the formation of the dust ion-acoustic shock waves. Furthermore, a stronger nonlinearity in comparison to the isothermal electron is found which is due to the effect of non-isothermal electrons which follows the vortex-like electron distribution. The results of the present work should help us in understanding the localized electrostatic disturbances in space and laboratory dusty plasmas.

Key Words. Shock waves, trapped electrons.

Theoretical model and numerical results

Shukla and Silin [1] were the first theoretically shown the existence of low frequency dust ion-acoustic (DIA) waves, whose speed is much larger (smaller) than the ion (electron) thermal speed, and a frequency much higher than the dusty plasma frequency, in a three component dusty plasma containing electrons, ions and negatively charged stationary dust. The existence of the DIA wave has been confirmed by the laboratory experiment [2]. On the other hand dust ion acoustic shock waves in dusty plasma have received a great deal of attention [3], [4]. Most of the studies up to now are restricted to the theoretical investigations on shock dynamics in a dusty plasma with isothermal electrons

¹Department of Basic Science, Babol University of Technology, Babol 47148-71167, Iran, e-mail: alinejad@nit.ac.ir

²Faculty of physics, Tabriz University, Tabriz, Iran

in the frame work of the Boltzmann distribution function. Of particular interest is the case that electrons interact with the DIA wave potential during its evolution, and therefore can be trapped in the wave potential. In this case, the isothermally distributed electrons often change toward trapped electron distributions. Owing to the presence of trapped particles, dusty plasmas are characterized by new, modified properties and conditions for the existence of the DIA shock waves.

In this paper, we consider a one-dimensional, collisionless and unmagnetized dusty plasma consisting of ion fluid, trapped as well as free electrons, and charge fluctuating immobile dust particles. The nonlinear dynamics of DIA waves, whose phase speed is much smaller (larger) than the electron (ion) thermal speed, propagating in such a dusty plasma system is governed by

$$\frac{\partial n_i}{\partial t} + \frac{\partial}{\partial x} (n_i u_i) = 0, \quad (1)$$

$$\frac{\partial u_i}{\partial t} + u_i \frac{\partial u_i}{\partial x} + \frac{\partial \varphi}{\partial x} = -\frac{\sigma}{n_i}, \quad (2)$$

$$\frac{\partial^2 \varphi}{\partial x^2} = \mu n_e - n_i + (1 - \mu) Z_d, \quad (3)$$

where n_i is the ion number density normalized by its equilibrium value n_{i0} , u_i is the ion fluid speed normalized to the ion acoustic speed $C_i = (\kappa T_{\text{ef}}/m_i)^{1/2}$, φ is the electrostatic wave potential normalized to $\kappa T_{\text{ef}}/e$, and Z_d is the number of electrons residing onto the dust grain surface normalized by its equilibrium value Z_{d0} . Here κ is the Boltzmann's constant, T_{ef} is the constant temperature of the free electrons, m_i is the ion mass and $\mu = n_{e0}/n_{i0}$ is the population of the background free electrons. The time and space variables are given in the units of the ion plasma period $\omega_{\text{pi}}^{-1} = (\varepsilon_0 m_i/n_{i0} e^2)^{1/2}$ and the Debye length $\lambda_{\text{De}} = (\varepsilon_0 \kappa T_{\text{ef}}/n_{i0} e^2)^{1/2}$, respectively.

To model the electron distribution in the presence of trapped particles, we employ the vortex-like electron distribution which solves the electron Vlasov equation. Thus, the electron number density n_e can be expressed as

$$n_e = \text{erfc}(\sqrt{\beta} \varphi) e^\varphi + \frac{e^{\beta \varphi}}{\sqrt{\beta}}, \quad (4)$$

where $\beta = T_{\text{ef}}/T_{\text{et}}$ is the trapping parameter describing the temperature of the trapped electrons. Equation (4) shows that electrons could interact nonlinearly with the low-frequency DIA potential during its evolution, and can be trapped in the wave potential. It should be noted here that if we neglect the resonant effects, n_e is reduced to the Boltzmann distribution function.

We note that the dust grain is charged by the plasma currents at the grain surface. It means that Z_d is not constant but varies with space and time.

We also consider a situation in which the charging current originates from the collections of electrons and ions hitting the grain surface. Accordingly, the variable dust charge $q_d = -eZ_d$ is determined by

$$\frac{dq_d}{dt} = I_e + I_i, \tag{5}$$

where I_e and I_i are, respectively, the average microscopic electron and ion currents entering the dust grains. We consider a more general situation in which ions have some finite streaming speed. For such a situation the ion and electron current have the following expression.

$$I_i = \pi r_d^2 e \left(\frac{8T_i}{\pi m_i} \right)^{\frac{1}{2}} n_i \left[F_1 + F_2 \frac{e^2 Z_d}{r_d T_i} \right],$$

$$I_e = -\gamma \left[\left(1 - \frac{1y}{\beta^2} + \left(1 - \frac{1}{\beta} \right) (\varphi - \alpha Z_d) \right) \exp(\alpha\beta) + \exp(\beta(\varphi - \alpha Z_d)) \right], \tag{6}$$

where $\gamma = \sqrt{8\pi} r_d^2 n_{d0} \lambda_{De} \sqrt{m_i/m_e} \mu e^{-\alpha\beta}$, $\alpha = Z_{d0} e^2 / \kappa T_e r_d$, $L = -\alpha/\sigma$, $F_1(u_0) = \sqrt{\pi}/4u_0(1 + 2u_0^2) \operatorname{erf}(u_0) + \frac{1}{2} \exp(-u_0^2)$ and $F_2(u_0) = \sqrt{\pi}/2u_0 \operatorname{erf}(u_0)$. Here r_d is the radius of the dust grains which are assumed to be spherical. Now, substituting (6) into (5), the normalized form of the charging equation is expressed as

$$\frac{\partial Z_d}{\partial t} = -\gamma \left[\left(1 - \frac{1}{\beta^2} + \left(1 - \frac{1}{\beta} \right) (\varphi - \alpha Z_d) \right) \exp(\alpha\beta) + \exp(\beta(\varphi - \alpha Z_d)) \right] -$$

$$-\pi r_d^2 e \left(\frac{8T_i}{\pi m_i} \right)^{\frac{1}{2}} n_i \left[F_1 + F_2 \frac{e^2 Z_d}{r_d T_i} \right], \tag{7}$$

We now derive a dynamical equation for the nonlinear propagation of the DIA waves from the basic equations by using the reductive perturbation technique. In this case the independent variables are stretched as

$$\xi = \varepsilon^{1/2} (x - v_0 t), \quad \tau = \varepsilon t, \tag{8}$$

where ε is a small dimensionless parameter measuring the weakness of the dispersion and nonlinearity, and v_0 is the wave speed normalized by C_i . To derive the required governing equation, we also expand the perturbed quantities n_i , u_i , φ and Z_d asymptotically about their equilibrium values in powers of ε including $\varepsilon^{3/2}$:

$$n_i = 1 + \varepsilon n_i^{(1)} + \varepsilon^{3/2} n_i^{(2)} + \dots, \tag{9}$$

$$\varphi = \varepsilon \varphi^{(1)} + \varepsilon^{3/2} \varphi^{(2)} + \dots, \tag{10}$$

$$u_i = u_{i0} + \varepsilon u_i^{(1)} + \varepsilon^{3/2} u_i^{(2)} + \dots, \tag{11}$$

$$Z_d = 1 + \varepsilon Z_d^{(1)} + \varepsilon^{3/2} Z_d^{(2)} + \dots, \tag{12}$$

and develop equations in various powers of ε . Substituting (8) and (9)–(12) into (1)–(7) and comparing the various order in ε , we obtain in the lowest order

$$\omega_0 n_i^{(1)} = u_i^{(1)}, \quad (13)$$

$$\omega_0 u_i^{(1)} = \varphi^{(1)} + \sigma n_i^{(1)}, \quad (14)$$

$$\mu \varphi^{(1)} - n_i^{(1)} + (1 - \mu) Z_d^{(1)} = 0, \quad (15)$$

$$\gamma_1 \varphi^{(1)} + \gamma_2 Z_d^{(1)} - \gamma_3 n_i^{(1)} = 0, \quad (16)$$

where $\omega_0 = v_0 - u_{i0}$, $\gamma_1 = \gamma(1 - 1/\beta + \beta \exp(-\alpha))$, $\gamma_2 = L_2 F_2 L - \alpha \gamma(1 + \beta)$ and $\gamma_3 = L_2(F_1 - F_2 L)$. Now, using the lowest order equations (13)–(16), we obtain the following linear dispersion relation

$$\omega_0^2 = \sigma - \frac{1 - (1 - \mu)\gamma_3/\gamma_2}{\mu - (1 - \mu)\gamma_1/\gamma_2}. \quad (17)$$

Now, to the next higher order in ε , the basic equations provide us with a set of coupled equations for the second order perturbed quantities, which finally yield

$$\partial_\tau \varphi^{(1)} + A \varphi^{(1)1/2} \partial_\xi \varphi^{(1)} = B \partial_\xi^2 \varphi^{(1)}, \quad (18)$$

where the nonlinear coefficient $A = -2(1 - \beta)/\sqrt{\pi} \alpha_1$ and the dissipation coefficient $B = \alpha_2/\alpha_1$ in which

$$\alpha_1 = \frac{2\omega_0}{\omega_0^2 - \sigma} \left[\frac{\gamma_1}{\gamma_2} (1 - \mu) - \mu \right], \quad (19)$$

$$\alpha_2 = \frac{v_0}{\gamma_2} (1 - \mu). \quad (20)$$

Equation (18) is a modified Burgers equation which includes the effects of the vortex-like electron distribution and dust charge fluctuation. It is clear that the dust charge fluctuation is a source of dissipation, and is also responsible for the formation of the dust ion-acoustic shock waves. Moreover, a stronger nonlinearity in comparison to the isothermal electron is found which is due to the effect of trapped electrons. For a frame moving with a speed U_0 , the stationary localized solution of the modified Burger equation is

$$\varphi = \varphi_m (1 + \tanh(\chi/\lambda))^2,$$

where $\varphi_m = (3U_0/4A)^2$ and $\lambda = 4B/U_0$ are, respectively, the height and thickness of the shock waves. It is obvious that this type of shock solution arises due to the combined effects of nonlinear term (containing A) which

arises due to the trapped electrons, and the dissipative term (containing B) which arises due to the dust charge fluctuation.

To have some numerical appreciations of this work, we have numerically analyzed the shock height and the shock thickness. We have chosen the parameters corresponding to laboratory dusty plasma [5], viz, $n_{d0} = 10^5$, $T_e = 0.1$ eV, $Z_d = 10^3$ and $r_d = 5 \mu\text{m}$, which corresponds to $\alpha = 1.44$. The main results of the investigation in Figs. 1–6 are the following:

1) In Figs. 1–3, we observe that the DIA shock structures exist only with positive ($\varphi > 0$) in the plasma system under consideration.

2) The shock structures depend sensitively on the trapping parameter β . It is shown from 1 and 4 that the amplitude (width) of the shock waves increases (decreases) with increasing the trapping parameter.

3) The hight (thickness) of these shock structures increases (decreases) with the increase of μ (ratio of the equilibrium electron to ion number density) and σ (ratio of the ion and electron temperature).

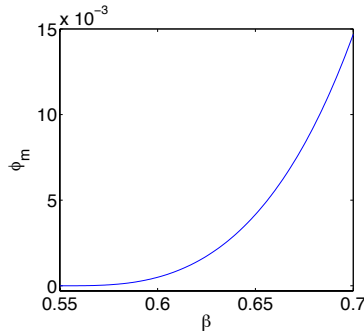


Fig. 1. Variation of the amplitude φ_m of the DIA shock waves with β .

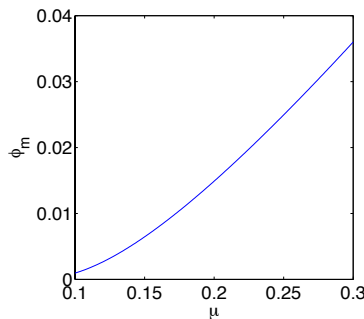


Fig. 2. Variation of the amplitude of the DIA shock waves with μ .

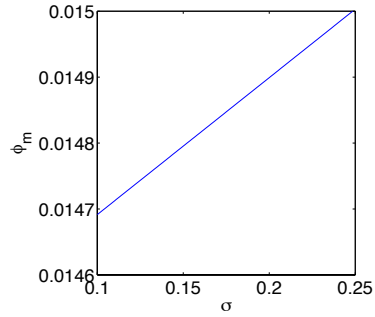


Fig. 3. Variation of the amplitude of the DIA shock waves with σ .

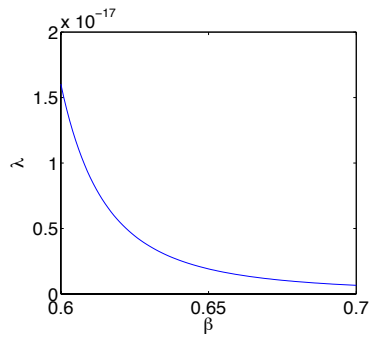


Fig. 4. Showing the variation of the width λ of the shock waves with β .

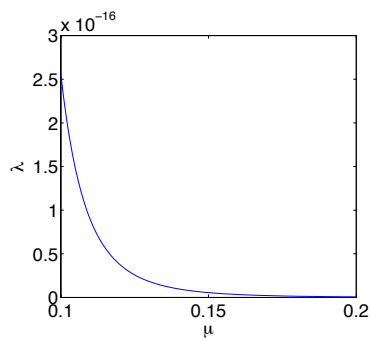


Fig. 5. Showing the variation of the width λ of the shock waves with μ .

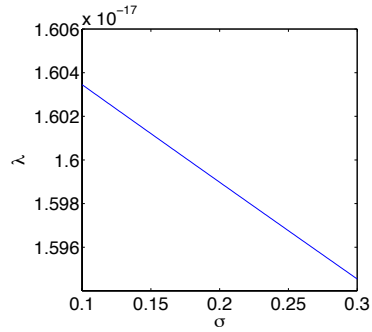


Fig. 6. Showing the variation of the width λ of the shock waves with σ .

References

- [1] P. K. SHUKLA, V. P. SILIN: *Dust ion-acoustic wave*. Phys. Scr., 45 (1992), 508–511.
- [2] Y. NAKAMURA, H. BAILUNG, P. K. SHUKLA: *Observation of ion-acoustic shocks in a dusty plasma*. Phys. Rev. Lett., 83 (1999), 1602–1605.
- [3] P. K. SHUKLA, A. A. MAMUN: *Introduction to dusty plasma physics*. Institute of physics publishing Ltd., Bristol 2002.
- [4] A. A. MAMUN, R. A. CAIRNS, P. K. SHUKLA: *Dust negative ion acoustic shock waves in a dusty multi-ion plasma*. Phys. Lett. A, 373 (2009), 2355–2359.
- [5] R. L. MERLINE, A. BARKEN, C. THAMSON, N. D'ANGELO: *Laboratory studies of waves and instabilities in dusty plasmas*. Phys. Plasmas, 5 (1998), 1607–1615.

Received May 13, 2010

Determination of gas temperature from van der Waals broadening of atomic spectral lines in atmospheric pressure argon–neon microwave plasmas¹

JOSÉ MUÑOZ², MILAN S. DIMITRIJEVIĆ³, MARÍA D. CALZADA²

Abstract. The use of the van der Waals broadening to measure the gas temperature in an atmospheric pressure Ar–Ne surface–wave discharge (1200 ÷ 1400 K) is studied comparing the obtained results with those given by the OH radical and extended to Ne proportions up to 99%. A good agreement is found between both techniques. Influence of the electron density through Stark broadening on the calculation of gas temperature is found to be negligible under our experimental conditions. Spectral line Ar I 425.9 nm is found to be the best choice for this purpose and the influence of the neon neutral has been found to be critical for evaluating gas temperature.

Key Words. Van der Waals broadening, Ar, Ne, microwave plasma, atmospheric pressure.

Introduction

In the last decades, a common characteristic of many of the applications of atmospheric pressure plasmas [1], [2] is that they use a gas mixture. In order to understand the processes taking place during these applications, it is necessary to know the kinetics of the discharge, which depends on the plasma parameters such as densities and temperatures. However, when more than one kind of gas is present the complexity of experimental determination of plasma

¹This research has been supported by the Ministry of Science and Technology (Spain) within the framework of the project no. ENE2005-00314 and FEDER Funds, and by the Ministry of Science of Serbia through the project 146001.

²Grupo de Espectroscopía de Plasmas, Edificio Einstein (C-2), planta baja, Campus de Rabanales, Universidad de Córdoba, 14071 Córdoba, Spain

³Astronomical Observatory, Volgina 7, 11060 Belgrade 38, Serbia

parameters by spectroscopic techniques increases due to the influence of the different types of perturbers in the plasma gas, which have influence on the spectral line profiles used.

Research on van der Waals broadening, which has its origin on the dipolar interaction between an excited atom (the emitter) and the dipole induced by it over a neutral perturbing atom in the ground state, is a very important issue in recent spectroscopy studies [3] since the values of this parameter can be easily related by means of the Lindholm–Foley theory to that of the gas temperature (T_g), being the knowledge of the later determining on the heavy particle kinetics.

In the present work, the use of the van der Waals broadening of atomic argon lines to determine the T_g in an atmospheric pressure Ar–Ne microwave plasma, taking into account both argon and neon atoms as perturbers, has been analyzed. The values of the gas temperature inferred from this broadening have been compared to those obtained from the spectra emitted by the OH molecular species in the discharges.

Experimental

Figure 1 shows the plasma source and the optical detection and data acquisition systems for emission spectroscopy measurements. Microwave power was provided to the plasma by a SAIREM 12 kT/t microwave generator of 2000 W maximum power in continuous mode. The discharge was contained in quartz tubes of 1.5 and 2.5 mm inner and outer radii, respectively. Several gas mixtures of high purity (99.999 %) Ar and Ne were used as plasma gases keeping the same total flow equal to 0.5 slm (standard litre per minute).

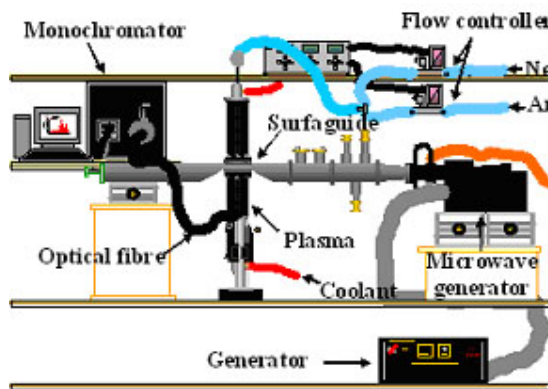


Fig. 1. Experimental Setup

An optical fiber was used to pick up the light emitted from the discharge at and drive it to the entrance slit of a 1 m monochromator (Jobin-Yvon Horiba 1000 M) previously calibrated and equipped with a 2400 grooves/mm holographic grating. In each measure, spectrums from OH radicals (306 ÷ 312 nm) were taken, as well as those of some Ar I lines. Moreover, the H_β line from the Balmer series was registered for electron density measurement. Both OH radicals and hydrogen atoms were present as impurities in the plasma gas. A Hamamatsu R928P photomultiplier (spectral interval of 200 ÷ 750 nm) was used as detector for Ar I and H_β lines, while a symphony CCD was the detector used for OH radical spectra.

Results and discussion

In atmospheric pressure plasmas spectral lines can be considered Voigt profiles stemming from the convolution of Lorentzian and Gaussian profiles originated by the different effects affecting the line shape. In our case the line profiles were deconvoluted using a commercial software (Microcal Origin Peak Fitting) to separate the Gaussian and Lorentzian broadening of the profiles. The Lorentzian width can be considered as the sum of the Stark and the van der Waals broadening under our experimental conditions. The Stark broadening of these lines was estimated using the expression given by Griem [4] for the electron density, calculated for different Ar–Ne mixtures from the H_β line using the data from [5]. In Table 1, the values of the 425.9 and 603.2 nm Lorentzian width and the Stark broadening for the studied Ar–Ne mixtures are shown. One observes that w_S is typically one order lower than w_L for both lines. Then, the assumption that w_L can be attributed mainly to the van der Waals broadening does not induce a significant error in the calculation of T_g .

Table 1. Lorentzian and Stark widths of the Ar atomic lines considered in this work for several Ne concentrations

[Ne] (%)	425.9 nm w_L ($\times 10^{-2}$ nm)	425.9 nm w_S ($\times 10^{-2}$ nm)	603.2 nm w_L ($\times 10^{-2}$ nm)	603.2 nm w_S ($\times 10^{-2}$ nm)
0	0.91	0.03	3.13	0.30
10	0.92	0.03	2.96	0.29
30	0.81	0.03	2.60	0.26
50	0.78	0.02	2.36	0.24
70	0.71	0.02	1.92	0.19
90	0.60	0.02	1.42	0.17

According to the theory, (see e.g.: expression (25) in [3]), the van der Waals broadening (w_W) of the Ar atomic lines considered in this work can be expressed as

$$w_W(425.9 \text{ nm}) = \chi_{\text{Ar}} \frac{1.479}{T_g^{0.7}} + \chi_{\text{Ne}} \frac{0.932}{T_g^{0.7}}, \quad (1)$$

$$w_W(603.2 \text{ nm}) = \chi_{\text{Ar}} \frac{4.217}{T_g^{0.7}} + \chi_{\text{Ne}} \frac{0.932}{T_g^{0.7}} \quad (2)$$

being χ_{Ar} and χ_{Ne} the volume fractions of the constituting gases (Ar and Ne) within the discharge. For a more detailed description of the theory, the reading of reference [3] is suggested.

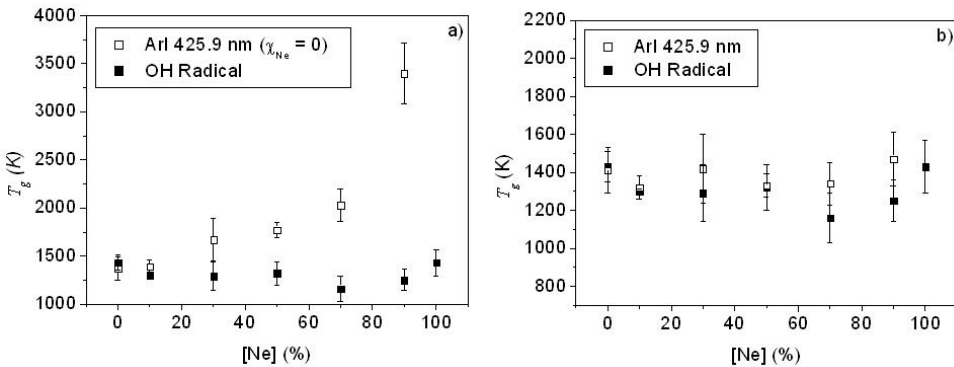


Fig. 2. Gas temperature calculated with the van der Waals broadening of the 425.9 nm Ar atomic line a) neglecting and b) considering the influence of Ne neutral perturbers; gas temperature calculated with the OH radical is provided for comparison purposes.

Figures 2 and 3 show the values of T_g obtained using the expressions above. There, T_g values are obtained using the van der Waals broadening of Ar atomic lines considering (Figs. 2a and 3a) and neglecting (Figs. 2b and 3b) the influence of Ne neutral perturbers and are compared with those obtained using the rovibrational band (306 ÷ 312 nm) of the OH species existing in the discharge as impurities. From these figures it can be seen that it is necessary to take into account the influence of Ne neutral perturbers, especially at high Ne concentrations. It is also important to note that the first point in the figures above corresponds to the conditions of a pure Ar discharge under similar conditions to those used in [3], for which a good agreement is found ($T_g = 1400$ K).

In the case of the 603.2 nm Ar atomic line it can be seen that even considering this influence of the Ne perturbers, there are some important differences for Ne concentrations above 50%. One of the possible causes for this difference can be found in [6], where it was stated that for nd–4p transitions of argon the theoretical description of the pressure broadening using a Lennard–Jones or

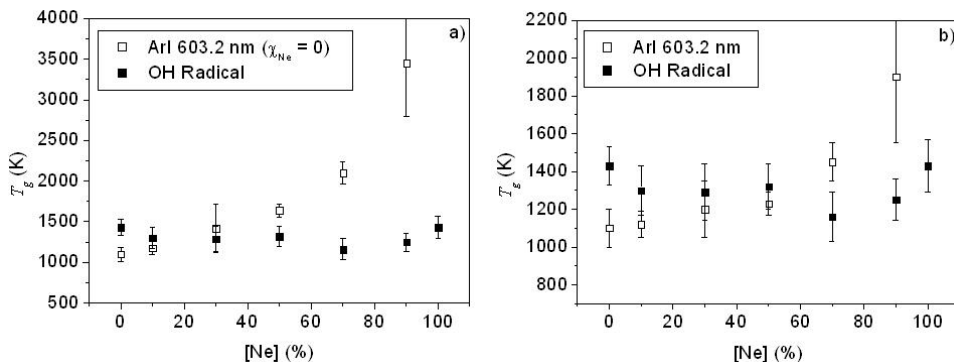


Fig. 3. Gas temperature calculated with the van der Waals broadening of the 603.2 nm ArI atomic line a) neglecting and b) considering the influence of Ne neutral perturbers; gas temperature calculated with the OH radical is provided for comparison purposes

van der Waals potential was adequate for Ar–Ar interactions, while the theoretical predictions in the case of Ar–He or Ar–Ne interactions failed. However, it must be noticed that in their case the experimental results were overestimated respect to the theoretical predictions while in our case an overestimation of the van der Waals broadening will lead to an underestimation of gas temperature.

Conclusions

The use of the van der Waals broadening of ArI lines (425.9 and 603.2 nm) emitted by an atmospheric pressure discharge has been studied. In general, a good agreement between the results obtained using this method and those obtained from other spectroscopic methods (OH rovibrational spectra) is obtained, particularly for the 425.9 nm line. The influence of the collisions of argon excited atoms with ground state neutral atoms has been shown to be critical for the use of the van der Waals broadening for gas temperature determination purposes.

References

- [1] A. MONTASER: *Inductively Coupled Plasma Mass Spectrometry*. Wiley-VCH, New York 1998.
- [2] K. JANKOWSKI, A. JANKOWSKA: *Spectroscopic diagnostics for evaluation of the analytical potential of argon+helium microwave-induced plasma with solution nebulization*. *Journal of Analytical Atomic Spectrometry*, 22 (2007), 1076–1082.

- [3] C. YUBERO, M. S. DIMITRIJEVIĆ, M. C. GARCÍA, M. D. CALZADA: *Using the van der Waals broadening of the spectral atomic lines to measure the gas temperature of an argon microwave plasma at atmospheric pressure*. Spectrochimica Acta B, 62 (2007), 169–176.
- [4] R. GRIEM: Spectral line broadening by plasmas.. Academic Press, London 1964.
- [5] M. A. GIGOSOS, V. CARDEÑOSO: *New plasma diagnosis tables of hydrogen Stark broadening including ion dynamics*. Journal of Physics B, 29 (1996), 4795–4838.
- [6] J. WOLNIKOWSKI, A. BIELSKI, R. X. TRAWINSKI, J. SZUDY: *Interpretation of low-pressure broadening and shift in the Argon spectrum*. Phy. Scr., 47 (1993), 186–191.

Received May 17, 2010

Magneto-active laser and astrophysical plasmas¹

VADIM S. BELYAEV², ANATOLY P. MATAFONOV²

Abstract. The similarity of laser relativistic plasmas to astrophysical plasmas has been investigated in frames of magnetic hydrodynamics. The similarity criteria of these physical objects was determined. The results of experimental investigations of number of processes of vortex magnetic hydrodynamics in the plasmas produced by action on solid target of laser radiation intensity $\sim 3 \times 10^{18} \text{ W/cm}^2$ have been presented. It has shown that in the magnetic field generation conditions there are direct effective mechanism of vortical energy of electrons transformation in the energy of their translatory motion. Formation of such structure so much connected with it super strong quasi-stationary magnetic fields generation have also relativistic character. It has been shown that the lifetime of such structures may be more (> 100 times) then laser pulse duration. The obtained results indicate its possibilities and perspective for thermonuclear research. The presented results of experiments at $3 \times 10^{18} \text{ W/cm}^2$ intensity favour the obtained theoretical conclusions. It is established that magneto-hydrodynamic processes in laser produced plasma realized in the conditions of huge magnetic fields on micro scale are similar of magneto-hydrodynamic processes observed in weak magnetic fields on cosmic scale.

Key Words. Laser relativistic plasmas, laboratory astrophysics, superstrong magnetic fields.

Introduction

Main peculiarities that determine properties of relativistic laser plasmas are:

1. **Electrons interacting with a field of electromagnetic wave can be considered as free particles.** The potential well of an each atom is deformed very strong under the condition of above-barrier ionization, so that the energy level of the ground state is higher than the maximum

¹Work was financially supported by RFBR (projects 08-02-00435, 09-02-00041, 09-08-13629, 10-02-01095, 10-08-00752).

²Central Research Institute of Machine Building, 4 Pionerskaya St., 141070, Korolev, Russia

value of the potential. As a result, an electron becomes unbound, and it can be considered as a free particle.

2. **Free electrons in relativistic laser plasmas interact only with an electromagnetic wave.** Such interaction is characteristic for electromagnetic radiation of relativistic intensity when electrons fast, in time there is less than phase of a wave gain a velocity, close to a velocity of light. The mean free path of such electrons is great, so for electrons with an energy 2 MeV ($J = 3.5 \times 10^{19} \text{ W/cm}^2$) this path is equal for aluminium of 3.7 mm. It is possible to consider that such electrons do not interact with substance if thickness of a target is less than path of their run. Interaction with an electromagnetic field of laser radiation for such electrons predominates above processes of scattering.
3. **The conservation laws and motion integrals are valid also in the range of relativistic laser intensities.** The role of the motion integrals and conservation laws increases with the laser intensity. It is explained by increasing of uncertainty in laser action, i.e. in parameters of temporal and spatial structure of focusing radiation, in particular, in phase of light wave. In this case only an application of the conservation laws (motion integrals) can describe main processes of laser–matter interaction.

1. Spatial structure of the quasi-stationary magnetic field in laser plasmas

The liquid model has been successfully used in plasma physics as well as in nuclear and atomic theory for long. In hydrodynamics, all motions are classified into potential and vortical ones. It can be shown that the general motion of liquid can be decomposed to rotation and potential motion. The tangential break can be considered as a vortical motion example. Decomposing, the tangential break transforms to vortical turbulent motion. This can be realized with a laser plasma at a target–vacuum or a plasma–vacuum interface, or on a smaller atomic scale.

Following [1], the magnetic hydrodynamic equation which stems from the combined Ohm's law for plasma and associates \mathbf{B} and \mathbf{V} can be written as

$$\frac{\partial \mathbf{B}}{\partial t} + \mathbf{B}(\nabla \cdot \mathbf{V}) - (\mathbf{B} \cdot \nabla)\mathbf{V} + (\mathbf{V} \cdot \nabla)\mathbf{B} = \frac{c^2}{4\pi\sigma} \nabla^2 \mathbf{B}, \quad (1)$$

where electroconductivity σ is expressed via density n and mean (effective) collision rate v_{eff} as

$$\sigma = \frac{ne^2}{mv_{\text{eff}}} = \frac{1}{4\pi} \frac{\omega_{\text{pe}}^2}{v_{\text{eff}}}. \quad (2)$$

Consider the case of magnetic field quick rise when the inertial terms comprising the velocity in (1) can be neglected. It corresponds to the case of small values of magnetic Reynolds number

$$Re_m = \frac{4\pi\sigma l_c v_c}{c^2} \ll 1, \quad (3)$$

where l_c and v_c – size and velocity characteristic for the case.

Physically, it means that the matter motion has no considerable effect on the magnetic field. In this case equation (1) is reduced to the diffusion equation

$$\frac{\partial \mathbf{B}}{\partial t} = \frac{c^2 v_{\text{eff}}}{\omega_{pe}^2} \nabla^2 \mathbf{B}. \quad (4)$$

The case of large Re_m values means approach to perfectly conducting liquid, implying physically that the magnetic field lines are transported with the moving liquid, hence can be treated as “frozen-in”. However, the criterion $Re_m \gg 1$ cannot be considered as a magnetic hydrodynamic applicability criterion [2]. As an example, high-conductivity liquid can be taken which, though satisfying the condition, has magnetic field so weak that it makes no effect on the motion. Magnetic hydrodynamics is applicable when a sufficiently strong magnetic field is present in a liquid. This requirement is met with the Lundquist criterion

$$L = \frac{\sigma B_c l_c}{n^{1/2} c^2} \gg 1. \quad (5)$$

Note that the condition (5) is met quite well for the space plasma. Therefore, the superdense plasma produced by action of high-level ultrashort laser radiation on a target adequately reproduces the space plasma conditions and can model the physical processes going on space scales [3].

It should be noted that the Lundquist criterion is determined by the product $B_c l_c$ which has a dimension of the vector potential. In the case of electromagnetic radiation this quantity is proportional to the value of the vector potential. It is possible to say that the Lundquist criterion is the criterion of similarity for processes with the same value of the vector potential at other similar conditions. This fact allows us to generalize processes in laser plasma taking place in micro scale to much large scales, up to cosmic distances. It is important the correctness of the opposite modeling of large scale phenomena by processes which occur in spot of laser radiation, i.e. in laser plasma. Thus, the above circumstance results in importance and practical great value of investigations of atomic and nuclear processes in laser relativistic plasma.

Thus, it was found that under the conditions of applicability of magneto-hydrodynamics, at large values of magnetic Reynolds number in laser plasma, and under the conditions of applicability of London’s equation, vortex electron

structures are produced; their properties are identical to properties of vortexes in classical hydrodynamics.

The condition $Re_m \gg 1$ corresponds to the case, when magnetic force lines move together with the particles of vortex structure; they can be considered as “freezing” lines. Analogous phenomena occur at large astrophysical scales. According to [4], if plasma eruption takes place on the Sun (this is a cloud of hot gas with the infinite conductivity), then the magnetic field moves together with plasma and is ejected from the Sun into the interplanetary space. Due to the stability of such magnetized vortex matter they can overcome large distances and produce, in particular, magnetic thunderstorms on the Earth.

Intense investigations devoted to the determination of the value and spatial configuration of quasi-static magnetic fields in various regimes of the target irradiation are carried out during last eight years. Mechanisms of generation of these magnetic fields and of their influence upon plasma parameters are developed. The magnetic field is considered as quasi-static one when it varies slowly during one period of the laser pulse.

Quasi-static magnetic fields with the magnetic displacement of the order of $10^7 \div 10^8$ G are of a great importance due to problem of the laser fusion, since these fields can be used as magnetic traps for thermal insulation of nuclear fuel from the walls of the set. These magnetic fields are produced in plasma near its critical surface where laser frequency coincides with the plasma frequency. Super-intense quasi-static magnetic field was measured on the laser facility “Vulcan” (Great Britain) in 2002. The laser wavelength was $1.05 \mu\text{m}$, the maximum pulse intensity in the focus was of $9 \times 10^{19} \text{ W/cm}^2$, and the pulse duration was about of one picosecond. Laser beam was focused on the surface of the thin (about of $0.1 \div 1 \text{ mm}$) solid target. The measured quasi-static magnetic field was about of 3.4×10^8 G. This value is nearly of the oscillating magnetic field of the laser pulse.

2. Vortex potential character of magnetic field generated in laser plasma

The motion of plasma matter together with the transport processes of charged particles in laser plasma result in correlation between problems of dynamics of laser plasma and problems of mechanics of continuous medium. This correlation of electromagnetic and hydrodynamic phenomena is investigated by methods of the magnetohydrodynamics under the conditions of decisive role of super-intense magnetic fields generated in laser plasma.

The magnetohydrodynamics allows us to describe processes of generation of such fields, their transformations and related transport processes.

The real vortexes in mechanics of continuous medium are described well using three Helmholtz theorems [4].

The first theorem determines the strength of the vortex tube,

$$\boldsymbol{\Omega} = \text{rot } \mathbf{V}, \quad (6)$$

and states that the strength of the vortex tube is the same along the tube, and it is of characteristic for a given tube.

The field lines along the direction of the vector $\boldsymbol{\Omega}$ are called the vortex lines; their density in a given region is proportional to the value of $\boldsymbol{\Omega}$. The vortex tube is produced from vortex lines that go through all points of closed curve (which is not a vortex line itself) [4].

The second Helmholtz theorem is expressed by continuity equation, and it follows directly from the continuity of the field strength $\boldsymbol{\Omega}$ and conservation law for the strength of vortex tubes. From the physical point of view, it means that vortex tubes cannot begin and finish inside the medium; these vortex tubes can be closed curves, or they can begin and finish on the borders of the moving medium, or they can go to infinity for unlimited media.

The potential vortex presents good description of the observed vortex. Uniform rotation is unfit for description of the observed vortex. The velocity inside the observed vortex is high and outside of it is small, while the inverse statement is valid for the case of the uniform rotation. Oppositely, the potential vortex gives the good description of the observed vortex. It is determined by expressions

$$V_r = 0, \quad V_g = \boldsymbol{\Omega} \cdot \frac{S}{2\pi r}, \quad (7)$$

or in Cartesian coordinates

$$\mathbf{V} = \frac{\boldsymbol{\Omega} S}{2\pi r}. \quad (8)$$

The third Helmholtz theorem is expressed by the formula

$$\frac{\partial \boldsymbol{\Omega}}{\partial t} + \text{rot} [\boldsymbol{\Omega} \times \mathbf{V}] = 0. \quad (9)$$

H. Helmholtz described this theorem by words: vortex lines are moving together with the liquid. This means that the vortex contains the same particles for any time instance. The example of such a vortex is the smoking ring produced by a smoker. The smoking ring is the torus from the vortex lines. According to Eq. (6) these vortex lines describe also the velocity circulation. Since according to the third Helmholtz theorem vortex lines of $\boldsymbol{\Omega}$ are transferred together with the liquid, then they move forward with the velocity \mathbf{V} , i.e. along the direction which puts right screw with $\boldsymbol{\Omega}$. Velocity of the vortex is

$$\frac{d\mathbf{r}}{dt} = \frac{\mathbf{W} \times \boldsymbol{\Omega}}{\Omega^2}. \quad (10)$$

When $W = v^2/r$, $\Omega = v/r$, and $\mathbf{W} \perp \boldsymbol{\Omega}$, one obtains

$$\frac{d\mathbf{r}}{dt} = \mathbf{v}. \quad (11)$$

The mechanics of continuous medium considers dynamics and stability of vortex flows in liquids (gases). When the liquid is viscous, or the motion does not satisfy the condition of barotropy $p = p(\rho)$, or the external mass forces are not potential, or the continuity of velocity fields is violated, vortices in liquid can appear and disappear [4]. It follows from the Maxwell equations and the equation which connects magnetic field with the motion of a matter.

$$\text{rot}(\mathbf{v} \times \mathbf{B}) + \frac{c^2}{4\pi\sigma} \Delta \mathbf{B} - \frac{\partial \mathbf{B}}{\partial t} = 0 \quad (12)$$

The parameter $c^2/4\pi\sigma$ has the dimension of the coefficient of kinematic viscosity; it is called the coefficient of magnetic viscosity

$$\nu_m = \frac{c^2}{4\pi\sigma}. \quad (13)$$

The dimensionless parameter VL/ν_m (L is the typical length) is called the magnetic Reynolds number

$$Re_m = \frac{VL}{\nu_m}. \quad (14)$$

When the Reynolds number is small, the first term in Eq. (12) is negligibly small in comparison with the second term; then Eq. (12) becomes the diffusion equation

$$\Delta \mathbf{B} = \frac{1}{D} \frac{\partial \mathbf{B}}{\partial t}, \quad (15)$$

where the diffusion coefficient D is equal to the coefficient of magnetic viscosity, Eq. (13). The estimation of various terms in Eq. (12) is made by the method of estimations in magnetohydrodynamics based on the typical values of the velocity V_c , magnetic field B_c and linear dimensions of the considered phenomenon l_c :

$$|\text{rot}(\mathbf{v} \times \mathbf{B})| = \frac{V_c B_c}{l_c}, \quad (16)$$

$$|\Delta \mathbf{B}| = \frac{B_c}{l_c^2}. \quad (17)$$

This method of estimation for terms in differential equation based on substitution of differentiation over coordinates by dividing by a typical length, is very useful and is applied often in practice. However, as it mentioned in [2], this method is very rough and it can be used sometimes with great caution.

In the case of large value of the magnetic Reynolds number the Eq. (12) reduces to the form

$$\frac{\partial \omega_c}{\partial t} + \text{rot}(\omega_c \times v) = 0. \tag{18}$$

It is identical to Eq. (9) which determines the vortex in a liquid according to the third Helmholtz theorem about vortexes, with the substitution Ω by the quantity $\omega_c = eB/mc$ that is the cyclotron frequency for electron rotation in magnetic field.

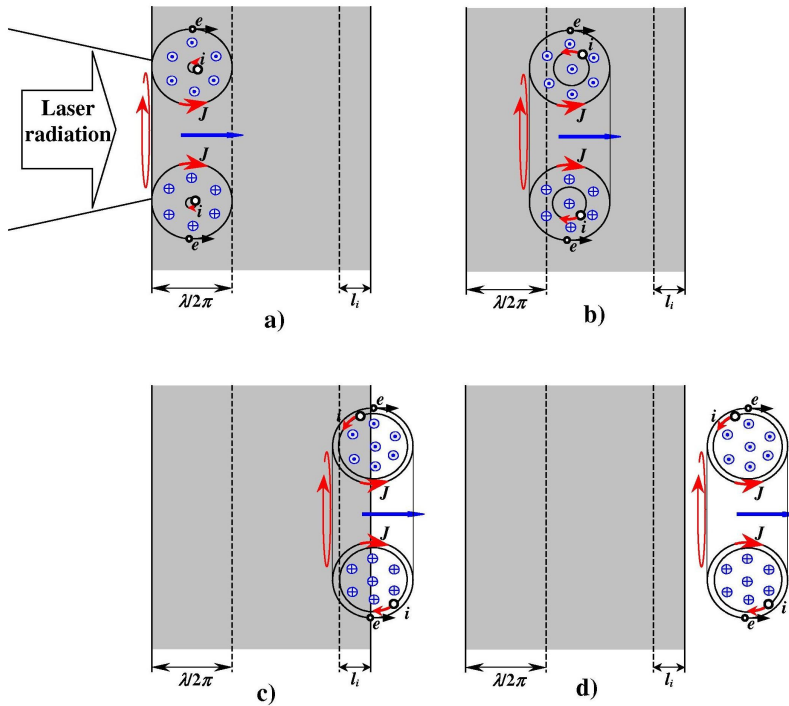


Fig. 1. Stages of evolution of laser plasma; a) I-st stage – vortex electron structure is produced in anomaly skin-layer in order to carry magnetic field; b) II-nd stage – ions are involved in vortex motion, they are decelerated in target with loss and acquire of new ions by vortex structure; c) ions are not disappeared due to their deceleration in a layer which is less than absorption length in a matter; d) propagation of quasi-neutral potential plasma vortex in a space

The condition $Re_m \gg 1$ corresponds to the case, when magnetic force lines move together with the particles of vortex structure; they can be considered as “freezing” lines. Analogous phenomena occur at large astrophysical scales. According to [4], if plasma eruption takes place on the Sun (this is a cloud of hot gas with the infinite conductivity), then the magnetic field moves together

with plasma and is ejected from the Sun into the interplanetary space. Due to the stability of such magnetized vortex matter they can overcome large distances and produce, in particular, magnetic thunderstorms on the Earth.

Let us estimate the velocity of the considered electron vortexes. The equation

$$\mathbf{E} = -\frac{\mathbf{v}}{c} \times \mathbf{B} \quad (19)$$

is valid in a medium with the infinite conductivity which moves with the velocity \mathbf{v} in the reference system of the observer. The expression for the velocity coincides with the velocity of electric drift of a charged particle in electric and magnetic fields which are perpendicular to each other.

Let us remark one peculiarity. The ion velocity and the ion free path are small in the process of ion motion. Ions are decelerated in a target; then new ions take their place, and finally the whole vortex structure occurs on the rear side of the target. If l_i is the depth for ion deceleration, the last ions propagate together with electrons producing quasi-neutral potential plasma vortex (see Fig. 1).

The drift motion does not produce the electric current and charge separation, since particles with positive and negative charge drift in the same direction with the same velocity. Thus, drift produces motion of neutral plasma. Plasma magnetization results in small divergence of these flows. It is explained by a stability of vortex quasi-neutral structures as quasi-particles (or mesostructures according to classification in plasmadynamics). Some recent publications report about experimental confirmation of generation of magnetized toroidal plasma structures. Ring-shaped proton flows with small divergence were observed [6], [7]. The magnetic field of about 100 MG has been measured by direct spectral method on large distance (several hundreds of microns) from the target surface [9].

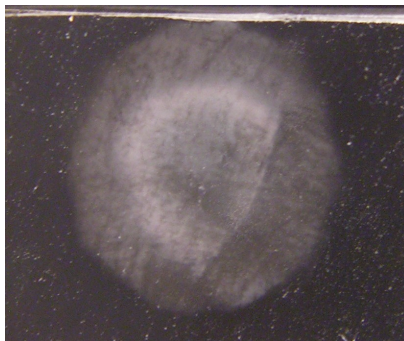


Fig. 2. The photo of the track detector CR-39 covered by 11 mm Al filter; detector CR-39 shows the tracks of protons with energies $E_p > 0.8 \text{ MeV}$ and $\varphi_{1/2} \approx 14^\circ$ (cone half angle)

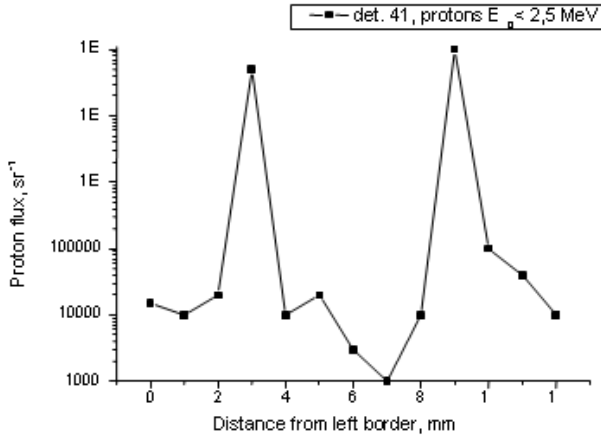


Fig. 3. The proton distribution inside the spot for detector with $11 \mu\text{m}$ Al ($E_p > 0.8$ MeV); protons with energy $E < 2,5$ MeV; target Cu 25 m

Our experiments at the peak laser intensity of $3 \times 10^{18} \text{ W/cm}^2$ allows us to observe on the rear side of thin ($30 \mu\text{m}$) titanium target clear ring-shaped structures by the proton detector CR-39 placed on a distance of 20 mm. Photo of ring-shaped proton structure is presented in Fig. 2, and proton distributions with the energy of 2.5 MeV are presented in Fig. 3. The divergence of the proton beam is $\varphi_{1/2} \approx 14^\circ$ [9].

Let us make the conclusions from the above consideration. Super-intense intensity of laser radiation and its ultra-short duration result in effective collisionless mechanism of direct transfer of momentum and angular momentum from electromagnetic radiation to charged particles – electrons and atomic ions. The plasma evolution contains strongly pronounced two stages. During the first stage the toroidal electron structure is produced on the depth of anomaly skin-layer. This is potential vortex determining spatial structure of electromagnetic quasi-stationary fields generated in laser plasmas. The requirement of relativistic invariance results in drift of these fields and electrons with the same velocity. Their collisionless motion occurs due to transfer of momentum of electromagnetic field produced in plasma. Ions and electrons together form quasi-neutral toroidal structure – magnetized plasma which moves with constant velocity as the whole. This velocity is equal to velocity of the electric drift. The drift velocity can increase significantly under condition of development of pinch-effect up to relativistic values. Respectively, not only electron velocity, but also the velocity of heavy positively charged atomic ions can increase up to relativistic values [10].

3. Values, lifetimes and increment of magnetic fields generated in plasmas

Equations describing quasi-stationary magnetic fields which are generated in laser plasmas can be derived from the conservation law for generalized momentum

$$\bar{\mathbf{P}} = m\bar{\mathbf{v}}\gamma - \frac{e}{c}\bar{\mathbf{A}}. \quad (20)$$

Here $\bar{\mathbf{A}}$ is the vector-potential of an electromagnetic wave.

Here we present the quantitative estimates of the values, stability and lifetimes of magnetic fields based on above considered qualitative analysis of electron vortex structures in plasma. From law for generalized momentum (20) accepting $\bar{\mathbf{P}} = 0$ — next equation for the density of current generated in plasma $\bar{\mathbf{j}} = n_e e\bar{\mathbf{v}}\gamma$ follows

$$\bar{\mathbf{j}} = -\frac{n_e e^2}{mc}\bar{\mathbf{A}}, \quad (21)$$

which is known as Londons' equation — the basic equation of an electrodynamics of superconductivity [11]. Londons' equation, it is possible to show, immediately follows from a requirement of interaction of electrons only with an electromagnetic wave. Londons' equation (21) states equality of vectors of an electric current j , induced in plasma and a vector of potential $\bar{\mathbf{A}}$ describing an electromagnetic wave, acting on electrons. The equality of these two vectors means equality of their various derivatives, and also identity of their fields. The rotational field of vector potential $\bar{\mathbf{A}}$ is transformed at interaction with electrons to a rotational current $\bar{\mathbf{j}}$.

Occurrence in description of laser relativistic plasma Londons' equation as a corollary of a law of conservation of momentum stipulates a series of its unique properties, first of all generation of quasistationary superstrong magnetic fields.

Avoiding the occupied term of “superconductivity” where Londons' equation plays a key role, for laser relativistic plasma in which Londons' equation also is fulfilled, use the term “Londons' medium” [12]. Effectiveness of transformation of a laser energy of the electromagnetic wave described by a vector potential $\bar{\mathbf{A}}$, in electronic structure with currents $\bar{\mathbf{j}}$ is determined by an integral of an energy of interaction of these physical quantities:

$$U_{\text{int}} = \frac{1}{c} \int \bar{\mathbf{A}}\bar{\mathbf{j}} \, dy. \quad (22)$$

In case of Londons' plasmas, i.e. realizations of a requirement (21) equalities (proportionality) of magnitudes and this integral has maximum value and can be noted in the form of

$$U_{\text{int}} = \frac{1}{c} \frac{ne^2}{mc} \int A^2 \, d\nu = \frac{4\pi ne^2}{m\omega^2} \int \frac{B^2}{4\pi} \, d\nu, \quad (23)$$

or $U_{\text{int}} = (\omega_{\text{pe}}/\omega)^2 \varepsilon_{\text{laz}}$, where $\omega_{\text{pe}} = \sqrt{4\pi n e^2/m}$ — an electron plasma frequency, ε_{laz} — an energy of laser radiation.

The equality of an energy of laser radiation of an energy of current structure or energy of the magnetic field generated in plasma, is reached under condition of

$$\omega_{\text{pe}} = \omega, \quad (24)$$

which is a condition of optimum transmission of a laser energy in an energy of a magnetic field generated in plasma. In the case of laser wavelength of $\lambda = 10^{-4}$ cm the optimal electron number density determining ω_{pe} , is equal to $n = 10^{21}$, cm^{-3} . This is the number density of the vortex structure producing the magnetic field.

Taking into account high efficiency of transformation of laser energy into the energy of the magnetic field, we can estimate the maximum value of the magnetic field generated in plasma from the condition

$$\frac{B_{\text{max}}}{8\pi} = \frac{J}{c}. \quad (25)$$

Hence,

$$B_{\text{max}} \cong 93 \sqrt{\frac{J}{10^{18}}}, \quad (26)$$

where B_{max} is given in MG, and the laser intensity J is given in W/cm^2 . In [13] experimental confirmation of Eq. (26) is contained.

Now we consider the estimate for the increment of the magnetic field. The equation for ionization process is of the general form

$$\frac{dj}{dt} = \omega_i, \quad (27)$$

where ω_i is the ionization rate.

Taking into account that the current \mathbf{j} is proportional to the vector potential \mathbf{A} (London's equation) and the relation $\mathbf{B} = \text{rot } \mathbf{A}$ we can transform this relation into the equation

$$\frac{dB}{dt} = \omega_i B. \quad (28)$$

It follows from this equation that the increment of the magnetic field is equal to the ionization rate and

$$B = B_0 \exp(\omega_i t). \quad (29)$$

The ionization rate is larger than the plasma frequency, as a rule, by one–two decimal orders. Therefore according to Eq. (28) the magnetic field increases faster than, for example, in the case of the Weibel instability [14].

Let's estimate a lifetime of the considered magnetic fields generated in laser plasma. This time can be obtained as time T of transient with a modification of an energy ε of system of common type as it is made in Lyapunov's theory [15]

$$\frac{1}{\varepsilon} \frac{d\varepsilon}{dt} = \frac{2}{T}, \quad (30)$$

where $d\varepsilon/dt \cong \Delta\varepsilon/\Delta t$ — a velocity of a modification of an energy. From here lifetime T is determined as

$$T = 2 \frac{\varepsilon}{\Delta\varepsilon} \Delta t.$$

The modification of an energy $\Delta\varepsilon$ for electronic rotational structure with a magnetic field can be presented in the form of $\Delta\varepsilon = \Delta\varepsilon_{\text{field}} + \Delta\varepsilon_{\text{rad}}$, where $\Delta\varepsilon_{\text{field}}$ — losses of an energy of a magnetic field, $\Delta\varepsilon_{\text{rad}}$ — losses of an energy due to radiation losses. It is possible to show, as $\Delta\varepsilon_{\text{field}} \gg \Delta\varepsilon_{\text{rad}}$ and $\Delta\varepsilon \approx \Delta\varepsilon_{\text{field}}$. Time Δt for which happens losses of an energy $\Delta\varepsilon$, it is possible to estimate as the characteristic time of anomalous Bohm's diffusions as fastest process of a drift of particles from area of a magnetic field $\Delta t = \lambda^2/D$, where λ — a wave length of radiation (the characteristic scale of process), $D \approx 1 \text{ m}^2/\text{s}$ — coefficient of Bohm's diffusion [9].

Let's suppose, according to the previous deductions an energy of the laser radiation, an equal energy of a generated magnetic field, we shall take $\lambda = 10^{-4} \text{ cm}$ and an estimate $\Delta\varepsilon/\varepsilon$ for small group of monoenergetic electrons of description of the experiments [10], equal $\Delta\varepsilon/\varepsilon \approx 10\%$. We shall gain a lifetime of magnetic field $T = 20 \text{ ps}$. This time does not depend on duration of laser action and can exceed it on one-two order. For this reason the superstrong magnetic fields generated in laser plasma, term quasistationary.

The obtained theoretical results are in good agreement with results of our recent experiments.

4. Experimental results

Results of experimental investigations:

- **Laser facility “Neodymium”.** Its power is of 10 TW, the radiation intensity is up to $3 \times 10^{18} \text{ W/cm}^2$, the pulse duration is 1.5 ps, the wavelength is 1.055 m. The facility is provided with a complex for measurements and control of parameters of laser radiation and diagnostic of atomic and nuclear processes in laser plasmas (parameters of X-ray, γ -radiation, yields of neutrons and charged particles) [10].
- **Generation of super-strong magnetic fields.** We suggested and checked experimentally the direct spectral method for measurements of values of super-strong magnetic fields generated in laser plasmas.

This method is based on the observation of resonance interaction between the Landau levels in magnetic field and energy levels of plasma ions. The value of the magnetic field is of about 40 MG at the laser intensity of 2×10^{17} W/cm² and of about 60 MG at the laser intensity of 3×10^{17} W/cm². The approach for control of generation of super-strong magnetic fields in laser plasmas has been checked using the method of interferometry of chirped laser pulses [8].

- **The effective temperature and the directed motion of fast atomic ions in laser picosecond plasmas.** Results are based on the measurements of the Doppler spectra of fluorine hydrogenlike ions (the target is the plates from fluoride plastics with the thickness of 200 μ m). The important peculiarity of the energy distribution of fast ions is their slow decreasing up to the energy of 1.4 MeV at the laser intensity of 2×10^{18} W/cm²; the effective temperature of fast ions is of the order of 350 keV. The directed motion of fast ions inside the target has been observed using red shift of the Doppler profile of the $L_{\gamma\alpha}$ line [16].
- **Generation of MeV-energy γ -quanta.** The photo-nuclear reactions ${}^9\text{Be}(\gamma, n)2\alpha$ with the threshold energy of 1.67 MeV as well as ${}^{18}\text{Ta}(\gamma, n){}^{180}\text{Ta}$ with the threshold energy of 7.56 MeV have been used for investigation of generation of MeV-energy γ -quanta. Accordingly, we observed the generation of 10^8 γ -quanta with the energy higher than 1.67 MeV, and 10^3 γ -quanta with the energy higher than 7.56 MeV [17].
- **The neutron-less fusion reaction ${}^{11}\text{B}(\text{p}, \alpha)2\alpha$.** For the first time the yield of alpha-particles in neutron-less fusion reaction ${}^{11}\text{B} + \text{p}$ in laser plasmas has been observed. The yield of α -particles was of 10^3 particles per laser pulse. We found also the energy spectrum of α -particles which contains the maxima at the energies of $3 \div 4$ MeV and $6 \div 10$ MeV. We did not observe neutrons at simultaneous registration [18].
- **Investigation of the fusion reactions based on the perspective nuclear fuels DD, D^6Li , D^3He , H^7Li .** Results are presented for detailed investigation of the fusion reaction $\text{D}(\text{d}, \text{n}){}^3\text{He}$ in laser picosecond plasmas. Both solid targets ($\rho \approx 1$ g/cm³) $(\text{CD}_2)_\text{n}$, BeD, TiD, and foam targets ($\rho = 0.01 \div 0.05$ g/cm³) $(\text{CD}_2)_\text{n}$ had been used. We measured the dependence of the neutron yield on the p- or s-polarization of laser radiation and on the laser contrast in various temporal ranges between 1 ps and 10 ns. The perspective fusion reactions ${}^6\text{Li}(\text{d}, \alpha){}^4\text{He}$, ${}^3\text{He}(\text{d}, \text{p}){}^4\text{He}$, and ${}^7\text{Li}(\text{p}, \alpha){}^4\text{He}$ were investigated in our experiments [19]. We measured the energy spectra of α -particles and protons, containing the peaks: 1) at the energy of 11 MeV for the fusion reaction ${}^6\text{Li}(\text{d}, \alpha){}^4\text{He}$, 2) at the energy of 9 MeV for the fusion reaction

${}^7\text{Li}(\text{p}, \alpha){}^4\text{He}$, 3) at the proton energy of 3.7 MeV for the fusion reaction ${}^3\text{He}(\text{d}, \text{p}){}^4\text{He}$, and 4) at the proton energy of 14.7 MeV for the fusion reaction ${}^3\text{He}(\text{d}, \text{p}){}^4\text{He}$ [19].

- **Generation of fast protons.** The nuclear exchange reaction ${}^7\text{Li}(\text{p}, \text{n}){}^7\text{Be}$ with the threshold energy of 1.88 MeV has been used for investigation of generation of fast protons. It was shown that of about 10^8 fast protons are produced in laser plasma with the energy higher than the threshold energy [10], [20].
- **Investigation of energy spectra of fast protons.** It follows from obtained energy spectra that the proton beams observed by CR-39 detectors which are placed behind the target exceed significantly the proton beams observed before the target (i.e. irradiated oppositely the laser beam). The maximum proton beam with the energy in the range of $0.8 \div 2.5$ MeV was of 10^9 per one steradian and per one shot of laser pulse. The anisotropy in the proton yield disappears at the decreasing of the laser intensity up to 5×10^{17} W/cm²; the protons beam diminished up to 10^3 per steradian [10].
- **Investigation of spatial and angular distribution of fast protons.** We considered the targets from Ti and Cu foils with the thickness of 25 and 30 μm . It was shown that the divergence angle for protons ejected forward normal to the rear side of the target is $\varphi_{1/2} = 26^\circ$ for Ti foil, and $\varphi_{1/2} = 14^\circ$ for Cu foil. The ring structures can be seen on CR-39 detectors; they are produced by proton beams with the energy less than 2.5 MeV. Protons with the energy higher than 2.5 MeV present narrow collimated beam with the divergence angle of $\varphi_{1/2} = 3^\circ$. Inside this narrow collimated beam with the divergence angle $\varphi_{1/2} = 3^\circ$ we observed well collimated proton beams with the divergence angle of $\varphi_{1/2} = 0.1^\circ \div 0.3^\circ$.

References

- [1] N. KRALL, A. TRIVELPIECE: Principles of plasma physics. McGraw-Hill, New York 1973.
- [2] H. ALFVEN, C.-G. FALTHAMMAR: Cosmical electrodynamics. Clarendon Press, Oxford 1963.
- [3] L. P. PERATT: Physics of the Plasma Universe. Springer-Verlag, New York 1992.
- [4] L. I. SEDOV: All-over environment mechanics. Science, Moscow 1983.
- [5] V. S. BELIAEV, V. N. MICHAILOV: *Quantum plasma: criteria, anomalous diffusion, antireflection in a magnetic field*. Laser Physics, 11 (2001), 12–27.

- [6] T. NAKAMURA, K. MIMA: *Magnetic-dipole vortex generation by propagation of ultraintense and ultrashort laser pulses in moderate-density plasmas*. Physical Review Letters, *100* (2008), 205006.
- [7] E. L. CLARK, K. KRUSHELNICK, M. ZEPF, F. N. BEG, M. TATARAKIS, A. MACHACEK, M. I. K. SANTALA, I. WATTS, P. A. NORREYS, A. E. DANGOR: *Energetic heavy-ion and proton generation from ultraintense laser-plasma interactions with solids*. Physical Review Letters, *85* (2000), 1654–1657.
- [8] V. S. BELYAEV, V. I. VINOGRADOV, A. S. KURILOV, A. P. MATAFONOV, V. S. LISITSA, V. P. GAVRILENKO, A. YA. FAENOV, T. A. PIKUZ, I. YU. SKOBELEV, A. I. MAGUNOV, S. A. PIKUZ JR.: *Plasma satellites of X-ray lines of ions in a picosecond laser plasma*. Journal of Experimental and Theoretical Physics, *126* (2004), 819–833.
- [9] V. S. BELYAEV, V. I. VINOGRADOV, A. P. MATAFONOV: *Relativistic magneto-active laser plasmas*. 35th EPS Conference on Plasma Phys.(P. Lalouis, S. Moustazis). ECA Vol.32D, Hersonissos, Greece 2008, P-1.120.
- [10] V. S. BELYAEV, A. YA. FAENOV, A. I. MAGUNOV, A. P. MATAFONOV, T. A. PIKUZ, S. A. PIKUZ JR., I. YU. SKOBELEV, V. I. VINOGRADOV: *Directed inward beams of ions in laser produced plasma*. Journal De Physique IV France, *133* (2006), 525–530.
- [11] D. UMSTADTER: *Relativistic laser–plasma interactions*. Journal of Physics D: Applied Physics, *36* (2003), R151–R165.
- [12] A. V. GORDEEV, T. A. LOSSEVA: *Localization of magnetized electrons in current filaments as a fundamental cause of coulomb explosion*. Plasma Physics Reports, *31* (2005), 26–46.
- [13] V. S. BELYAEV: *Mechanism of high-energy electron production in a laser plasma*. Quantum Electronics, *34* (2004), 41–56.
- [14] A. I. AREFYEV, V. S. BELYAEV, G. FERRANTE, M. ZARCONI, V. P. SILIN, S. A. URYUPIN: *Generation of magnetic field under atomic tunnel ionization*. Laser Physics, *10* (2000), 594–605.
- [15] P. M. DERUSSO, R. J. ROY, C. M. CLOSE: *State variables for engineers*. John Wiley & Sons, New York–London–Sydney 1970.
- [16] V. S. BELYAEV, V. I. VINOGRADOV, A. P. MATAFONOV, V. P. KRAINOV, V. S. LISITSA, A. YA. FAENOV, T. A. PIKUZ, I. YU. SKOBELEV, A. I. MAGUNOV, S. A. PIKUZ JR., V. P. ANDRIANOV, G. N. IGNATIEV, YU. I. KOZHUNOV, O. B. KOZLOV, A. M. CHEKMAREV: *Effective temperature and the directional motion of fast ions in a picosecond laser plasma*. Letters to Journal of Experimental and Theoretical Physics, *81* (2005), 616–620.
- [17] V. S. BELYAEV, V. I. VINOGRADOV, A. P. MATAFONOV, V. P. KRAINOV, V. S. LISITSA, V. P. ANDRIANOV, G. N. IGNATYEV, YU. A. MERKUL'EV, V. S. BUSHUEV, A. I. GROMOV: *Generation of MeV photons and protons in laser picosecond plasmas*. Physica of Atomic Nuclei, *71* (2008), 443–453.
- [18] V. S. BELYAEV, A. P. MATAFONOV, V. I. VINOGRADOV, V. P. KRAINOV, V. S. LISITSA, A. S. ROUSSETSKI, G. N. IGNATYEV, V. P. ANDRIANOV: *Observation of neutronless fusion reactions in picosecond laser plasmas*. Physical Review E, *72* (2005), 026406.

- [19] V. S. BELYAEV, V. I. VINOGRADOV, A. P. MATAFONOV, S. M. RYBAKOV, V. P. KRAINOV, V. S. LISITSA, V. P. ANDRIANOV, G. N. IGNATIEV, V. S. BUSHUEV, A. I. GROMOV, A. S. RUSSETSKY, V. A. DRAVIN: *Excitation of promising nuclear fusion reactions in picosecond laser plasmas*. Physics of Atomic Nuclei, 72 (2009), 1077–1098.
- [20] V. S. BELYAEV, V. P. KRAINOV, V. S. LISITSA, A. P. MATAFONOV: *Generation of fast charged particles and superstrong magnetic fields in the interaction of ultrashort high-intensity laser pulses with solid targets*. Physics – Uspekhi, 51 (2008), 793–814.

Received May 19, 2010

Developing the numerical model for studying laser-compression of magnetized plasmas¹

VIKTOR V. KUZENOV², SERGEI V. RYZHKOV²

Abstract. The magneto-inertial (hybrid) approach to nuclear fusion is considered. Numerical simulation of radiation magneto-gas dynamic processes in the interaction of laser beams with a dense magnetized plasma (target) is created. A new quasi-monotone numerical method and model for laser driven implosion of magnetized target (laser driven magneto-inertial fusion) is proposed. Distinctive features of this problem are the presence of initial seed field (the imposed pulse magnetic field) and compression of a magnetic flux by laser beams (laser driver). The task for plasma formation and laser induced compression of magnetized target is formulated. Detailed numerical models of laser-driven magnetic flux compression and the pulsed high-temperature processes in two dimensions are developed.

Key Words. Magneto-inertial fusion, radiation magneto-gas dynamic processes, external magnetic field, radiative transport, kinetic equations.

Introduction

Magneto-inertial fusion (MIF) [1], [2], [3] represents evolution of traditional inertial confinement fusion with elements of magnetic confinement fusion, i.e. the concept with plasma of high density ($n \geq 10^{25} \text{ m}^{-3}$) in ultrahigh magnetic fields ($B \geq 100 \text{ T}$). High-convergence uniform implosion and properly synchronized laser beams (laser intensity $\geq 10^{20} \text{ W/m}^2$) are assumed. Presence of a magnetic field reduces the heat conductivity and plasma should be at thermonuclear temperatures for only microseconds. Magneto-inertial approach has two main advantages compare to inertial confinement fusion (ICF) and magnetic confinement fusion (MCF): magnetic insulation + dense plasma

¹This work is supported by Ministry of Education and Science of the Russian Federation Task Programme RNPVSh (2009-2011), RFBR grant No. 09-08-00137-a and RFBR (Russia) – Consortium EINSTEIN (Italy) project No. 09-08-92422-KE.

²Bauman Moscow State Technical University, Department of Thermal Physics. Russia

at modest requirement for confinement time and driver energy than in MCF and ICF.

Table 1 consists of main parameters of plasma confinement fusion concepts. Second and third columns show the particle and energy confinement. Plasma density together with the energy confinement time represent $n\tau$ parameter of the fusion plasma, that can be calculated easily for MIF $n\tau_E \geq 10^{20} \text{ s/m}^3$. Typical areal mass density or the density-radius product ρR is presented in the last column. Should be noted, that ρR depends on the drive mechanism, e.g. for plasma liner (plasma jet driver) it will be less than for laser system.

Table 1. Scope of main plasma confinement concepts for controlled fusion

Concept	Particle	Energy	Plasma density	Time τ_E	ρR [kg/m ²]
ICF	Inertial	Inertial	$\sim 10^5 \text{ kg/m}^3$	$\sim 10 \text{ ps}$	~ 10
MIF	Inertial	Magnetic	$\sim 1 \text{ kg/m}^3$	$\sim 100 \text{ ns}$	0.01-1
MCF	Magnetic	Magnetic	$\sim 10^{21} \text{ m}^{-3}$	$\sim 1 \text{ s}$	—

An embedded magnetic field is compressed along with the target plasma to achieve magnetic insulation. Plasmoid target envisaged is compact toroid having closed magnetic flux surfaces, such as field reversed configuration (FRC) or spheromak, or target with open field area, such as a mirror trap [4] or cusp [5]. Current drive in a dense plasma using lasers beams may also be used to create seed fields and preheat fuel in the target plasma [6].

Interaction of high energy laser pulses with a magnetized target presents symmetrical implosion of the magnetic field configuration by laser beams [7]. The pre-seeded initial magnetic field can be generated by two high-current loops (see Fig. 1). Typical ICF target may be used for laser driven magneto-inertial fusion (LDMIF) with pre-seeded (initial) magnetic field. The apparatus for generating a seed magnetic field of the order of $10 \div 15 \text{ T}$ has been developed and tested successfully [8].

The implosion scheme is following: the spherical target (plasma of magnetic field configuration) compressed under laser beams. An imploding target traps and amplifies a pre-seeded magnetic flux. The distribution of the electromagnetic field in space at a late stage of compression is close to quasi-spherical (due to frozen fields in the plasma and the spherical nature of the compression). In this case, end losses of particles are negligible compared with the number of particles inside the irradiated target. We design the simulations to be relevant to the geometries of cylindrical and spherical targets – Nonstationary Instruments and Codes for fusion Applications (NICA).

Numerical simulation model, which is presented in the paper and intended for interpretation of available experimental data, and also for prediction various characteristics of the interaction, is constructed on the basis of the equations of multi-species two-temperature radiative gasdynamics in view of electromagnetic fields and turbulence of plasma. Radiation transfer is considered within the framework of multi-group approach. System of equations of the two-temperature radiation magnetogasdynamics (RMGD) are supplemented with the equations describing processes of heating of plasma under action of laser radiation. It consists from quasi two dimensional equation of heat conductivity in moving system of coordinates in perpendicular direction to surface of the target. The system of the equations also contains kinetic equations for particles in fusion reaction.

It is known, that there are a lot of different physical processes under interaction of intense ($10^{18} \div 10^{20}$ W/m²) laser beam with target plasma. Burning plasma parameters can be produced when the laser-target interaction conditions approach the magneto-inertial fusion requirements.

This work is devoted to the simulation of laser beams interaction with an axisymmetric dense plasma. For this reason the numerical model of the process is based on the multi-component radiative gas dynamics with turbulence model. The radiation transfer is taking into account in multi-group diffusive approach. The main distinguish of this proposed model is the presence of the externally applied magnetic field.

The goal of the investigation is complex numerical research and optimization of the pulsed high-temperature processes in a dense magnetized plasma (target). Distinctive feature of this problem is the presence of initial seed fields (the imposed external pulse magnetic field) and compression of a magnetic flux by laser beams (laser driver).

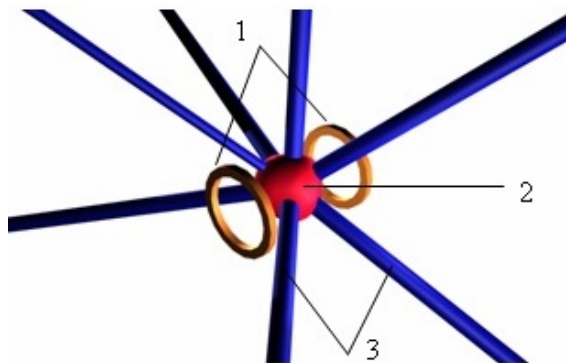


Fig. 1. Scheme of quasi-spherical implosion of target with pre-seeded magnetic field by high energy laser pulses (laser driven magneto-inertial fusion): 1—magnetic coils, 2—target, 3—laser beams

The configuration of pre-seeded magnetic field used in the experiments [4] is close to solenoid-like, which is far from optimal because of large particle losses from the solenoid ends. We propose to use the cusp configuration of the pre-seeded magnetic field [5]. The cusp configuration (see Fig. 2) provides better confinement of the fast charged particles than the configuration used in [4], [8]. It also provides implosion that close to spherical. Like in the experiments the pre-seeded magnetic can be easily generated by two oppositely directed high-current loops.

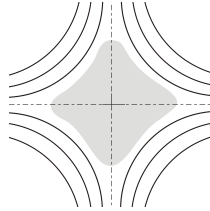


Fig. 2. Initial configuration of magnetic field in the target

Government equations

To describe the hole class of fluxes the equations should be converted to dimensionless form, using following values: characteristic size L and characteristic time t . Let us introduce following designations for dimensionless values [9]: $t = V_* \bar{t} / L_*$, $\xi = \bar{\xi} / L_*$, $\eta = \bar{\eta} / L_*$, $V_\xi = \bar{V}_\xi / L_*$, $V_\eta = \bar{V}_\eta / L_*$, $u = \bar{u} / V_*$, $v = \bar{v} / V_*$, $T = \bar{T} / T_*$, $e = \bar{e} / e_*$, $\rho = \bar{\rho} / \rho_*$, $P = \bar{P} / P_*$, $\mu_\Sigma = \bar{\mu}_\Sigma / \mu_*$, $\lambda_\Sigma = \bar{\lambda}_\Sigma / \lambda_*$, $\gamma = C_{p*} / C_{V*}$, $q = \bar{q} / q_*$, $\omega = \bar{\omega} / \omega_*$, $B = \bar{B} / B_*$, $E = \bar{E} / E_*$. We use additional algebraic connectivity between characteristic quantities $t_* = L_* / V_*$, $e_* = C_{V*} T_* = V_*^2$, $P_* = \rho_* V_*^2$, $q_* = P_* V_*$, $E_* = B_*$ and in this case the Euler's number $Eu = P_* / \rho V_*^2$ and temperature factor $\Theta = V_*^2 / e_*$ have simplified forms $Eu = 1$, $\Theta = 1$. The ionization energy of the “average ion” may be approximated by [10]

$$I(Z_i) = 13.8 \left[\frac{Z_i^3}{3} + \frac{Z_i^2}{2} + \frac{Z_i}{6} \right] / (0.85 + 0.15 Z_i^{2/3}), \text{ [eV]}$$

where Z is the nucleus charge. In the numerical calculations of the nonequilibrium plasma composition under conditions of high temperatures is justified, because distribution in different degrees of ionization is sufficiently narrow. Fractional-rational form of the function $I(z)$ is an adequate to rigid method for integrating the equations of which allow to calculate the nonequilibrium

plasma [11]. Of course, one can use other models for transport coefficients and $I(z)$ [12], which will be discussed in later papers.

The plasma dynamic processes in laser-induced plasma may be described in the framework of system of two-temperature, single-fluid, viscous, radiation plasma dynamics equations. In dimensionless form they are

$$\begin{aligned}
\frac{\partial \rho}{\partial t} + \frac{d\xi}{dt} \frac{\partial \rho}{\partial \xi} + \frac{d\eta}{dt} \frac{\partial \rho}{\partial \eta} + \frac{1}{J} \frac{\partial(J\rho V_\xi)}{\partial \xi} + \frac{1}{J} \frac{\partial(J\rho V_\eta)}{\partial \eta} &= -\alpha \frac{\rho u}{r}, \\
\frac{\partial \rho u}{\partial t} + \frac{d\xi}{dt} \frac{\partial \rho u}{\partial \xi} + \frac{d\eta}{dt} \frac{\partial \rho u}{\partial \eta} + \frac{1}{J} \frac{\partial(J\rho u V_\xi)}{\partial \xi} + \frac{1}{J} \frac{\partial(J\rho u V_\eta)}{\partial \eta} &= \\
&= -\xi_r \frac{\partial P}{\partial \xi} - \eta_r \frac{\partial P}{\partial \eta} - \alpha \frac{\rho u^2}{r} + \frac{S_r}{Re} + \frac{L_*}{c} [\mathbf{j} \times \mathbf{B}]_r, \\
\frac{\partial \rho v}{\partial t} + \frac{d\xi}{dt} \frac{\partial \rho v}{\partial \xi} + \frac{d\eta}{dt} \frac{\partial \rho v}{\partial \eta} + \frac{1}{J} \frac{\partial(J\rho v V_\xi)}{\partial \xi} + \frac{1}{J} \frac{\partial(J\rho v V_\eta)}{\partial \eta} &= \\
&= -\xi_z \frac{\partial P}{\partial \xi} - \eta_z \frac{\partial P}{\partial \eta} - \alpha \frac{\rho u v}{r} + \frac{S_z}{Re} + \frac{L_*}{c} [\mathbf{j} \times \mathbf{B}]_z, \\
\frac{\partial \rho e}{\partial t} + \frac{d\xi}{dt} \frac{\partial \rho e}{\partial \xi} + \frac{d\eta}{dt} \frac{\partial \rho e}{\partial \eta} + \frac{1}{J} \frac{\partial(J\rho e V_\xi + J \sum q_{i\xi})}{\partial \xi} + \frac{1}{J} \frac{\partial(J\rho e V_\eta + J \sum q_{i\eta})}{\partial \eta} &= \\
&= -\frac{P}{J} \left\{ \frac{\partial(JV_\xi)}{\partial \xi} + \frac{\partial(JV_\eta)}{\partial \eta} \right\} - \alpha \frac{P u}{r} - \alpha \frac{\rho e u}{r} + \frac{S_e}{Re} + \frac{L_*}{V_*} (\mathbf{j} \mathbf{E}), \\
S_e &= \frac{(\mu_\Sigma^\perp + \mu_\Sigma^\parallel)}{2} D + \frac{\gamma}{Pr} \operatorname{div} \left(\sum_k [\lambda_{k,\Sigma}^{\perp,\parallel} \operatorname{grad} T_k] \right) + \frac{Re t_*}{(\rho_* e_*)} Q_L + \frac{Re t_*}{(\rho_* e_*)} Q_{\text{Fus}}, \\
\frac{\partial \rho e_i}{\partial t} + \frac{d\xi}{dt} \frac{\partial \rho e_i}{\partial \xi} + \frac{d\eta}{dt} \frac{\partial \rho e_i}{\partial \eta} + \frac{1}{J} \frac{\partial(J\rho e_i V_\xi)}{\partial \xi} + \frac{1}{J} \frac{\partial(J\rho e_i V_\eta)}{\partial \eta} &= \\
&= -\frac{P_i}{J} \left\{ \frac{\partial(JV_\xi)}{\partial \xi} + \frac{\partial(JV_\eta)}{\partial \eta} \right\} - \alpha \frac{P_i u}{r} - \alpha \frac{\rho e_i u}{r} + Q_{\text{ei}} + Q_{\text{Fus}}, \\
[\mathbf{j} \times \mathbf{B}]_r &= j_\varphi B_z, [\mathbf{j} \times \mathbf{B}]_z = -j_\varphi B_r, (\mathbf{j} \mathbf{E}) = j_\varphi E_\varphi, \tag{1}
\end{aligned}$$

where $k = (e, i)$ are indexes, corresponding to electrons and ions, S_e is the volume power flux due to friction work $D(\mu_\Sigma^\perp + \mu_\Sigma^\parallel)/2$ (D is the dissipative function), thermal conduction processes $\operatorname{div}(\sum[\lambda_{k,\Sigma}^{\perp,\parallel} \operatorname{grad} T_k]) \approx \operatorname{div}(\lambda_{e,\Sigma}^{\perp,\parallel} \operatorname{grad} T_e)$ and energy-release Q_L , induced by the laser beam interaction with the target plasma, energy released in fusion reactions Q_{Fus} . $Re = L_* \rho_* V_* / \mu_*$ is a Reynolds number and $Pr = \mu_* c_{p*} / \lambda_*$ is a Prandtl number. The variables S_r, S_z corresponds to the viscous forces in a flux. They represent the sum of works of liquid friction, thermoconductive heat fluxes and plasma heating by laser radiation.

External magnetic fields

The equation of plasma magnetic field generation \mathbf{B} is

$$\frac{\partial \mathbf{B}}{\partial t} = \text{rot}[\mathbf{V} \times \mathbf{B}] - \frac{c^2 t_*}{4\pi L_*^2} \text{rot} \left(\frac{\text{rot} \mathbf{B}}{\sigma} \right), \quad \mathbf{j} = \sigma \left(\mathbf{E} + \frac{V_*}{c} [\mathbf{V} \times \mathbf{B}] \right), \quad (2)$$

where σ is the electrical conductivity coefficient, \mathbf{E} is the intensity of electric field, \mathbf{V} is the plasma velocity.

A dynamic equation for magnetic field \mathbf{B} may be written in a simplified form taken into consideration the grid space:

$$\begin{aligned} \frac{\partial B_r}{\partial t} + \frac{d\xi}{dt} \frac{\partial B_r}{\partial \xi} + \frac{d\eta}{dt} \frac{\partial B_r}{\partial \eta} &= \frac{\partial(uB_z)}{\partial z} - \frac{\partial(vB_r)}{\partial z} + \\ &+ \frac{c^2 t_*}{4\pi L_*^2} \left\{ \frac{\partial}{\partial z} \left(\frac{1}{\sigma_{\parallel}} \frac{\partial B_r}{\partial z} \right) - \frac{\partial}{\partial z} \left(\frac{1}{\sigma_{\parallel}} \frac{\partial B_z}{\partial r} \right) \right\}, \\ \frac{\partial B_z}{\partial t} + \frac{d\xi}{dt} \frac{\partial B_z}{\partial \xi} + \frac{d\eta}{dt} \frac{\partial B_z}{\partial \eta} &= -\frac{\partial r(uB_z)}{r\partial r} + \frac{\partial r(vB_r)}{r\partial r} + \\ &+ \frac{c^2 t_*}{4\pi L_*^2} \left\{ \frac{\partial}{r\partial z} \left(\frac{1}{\sigma_{\parallel}} \frac{\partial B_z}{\partial r} \right) - \frac{\partial}{r\partial r} \left(\frac{r}{\sigma_{\parallel}} \frac{\partial B_r}{\partial z} \right) \right\}, \\ j_{\varphi} &= \sigma_{\parallel} \left(E_{\varphi} + \frac{V_*}{c} [\mathbf{V} \times \mathbf{B}]_{\varphi} \right), \quad [\mathbf{V} \times \mathbf{B}]_{\varphi} = -uB_z + vB_r, \\ j_r &\equiv 0, \quad j_z \equiv 0, \quad B_{\varphi} \equiv 0, \quad V_{\varphi} \equiv 0. \end{aligned} \quad (3)$$

Derivatives $\partial f/\partial r$, $\partial f/\partial z$ (where f is some function) in the curvilinear coordinate system (ξ, η) simplified:

$$\begin{aligned} \left(\frac{\partial f}{\partial r} \right)_z &= \frac{1}{J} \left\{ \frac{\partial [fD(z, \xi)/D(\eta, \xi)]}{\partial \xi} + \frac{\partial [fD(z, \eta)/D(\eta, \xi)]}{\partial \eta} \right\}, \\ \left(\frac{\partial f}{\partial z} \right)_r &= -\frac{1}{J} \left\{ \frac{\partial [fD(r, \xi)/D(\eta, \xi)]}{\partial \xi} + \frac{\partial [fD(r, \eta)/D(\eta, \xi)]}{\partial \eta} \right\}. \end{aligned}$$

Dynamics of the electromagnetic field in the (ξ, η) coordinate system:

$$\begin{aligned} \frac{\partial B_r}{\partial t} + \frac{d\xi}{dt} \frac{\partial B_r}{\partial \xi} + \frac{d\eta}{dt} \frac{\partial B_r}{\partial \eta} &= \\ &= -\frac{1}{J} \left\{ \frac{\partial [(uB_z - vB_r)D(r, \xi)/D(\eta, \xi)]}{\partial \xi} + \frac{\partial [(uB_z - vB_r)D(r, \eta)/D(\eta, \xi)]}{\partial \eta} \right\} + \end{aligned}$$

$$\begin{aligned}
& + \frac{c^2 t_*}{4\pi L_*^2} \frac{1}{J} \frac{\partial}{\partial \xi} \left[\left(\frac{\partial [B_r D(r, \xi)/D(\eta, \xi)]}{J\sigma_{\parallel} \partial \xi} + \frac{\partial [B_r D(r, \eta)/D(\eta, \xi)]}{J\sigma_{\parallel} \partial \eta} \right) \frac{D(r, \xi)}{D(\eta, \xi)} \right] + \\
& + \frac{c^2 t_*}{4\pi L_*^2} \frac{1}{J} \frac{\partial}{\partial \eta} \left[\left(\frac{\partial [B_r D(r, \xi)/D(\eta, \xi)]}{J\sigma_{\parallel} \partial \xi} + \frac{\partial [B_r D(r, \eta)/D(\eta, \xi)]}{J\sigma_{\parallel} \partial \eta} \right) \frac{D(r, \eta)}{D(\eta, \xi)} \right] + \\
& + \frac{c^2 t_*}{4\pi L_*^2} \frac{1}{J} \frac{\partial}{\partial \xi} \left[\left(\frac{\partial [B_z D(z, \xi)/D(\eta, \xi)]}{J\sigma_{\parallel} \partial \xi} + \frac{\partial [B_z D(z, \eta)/D(\eta, \xi)]}{J\sigma_{\parallel} \partial \eta} \right) \frac{D(z, \xi)}{D(\eta, \xi)} \right] + \\
& + \frac{c^2 t_*}{4\pi L_*^2} \frac{1}{J} \frac{\partial}{\partial \eta} \left[\left(\frac{\partial [B_z D(z, \xi)/D(\eta, \xi)]}{J\sigma_{\parallel} \partial \xi} + \frac{\partial [B_z D(z, \eta)/D(\eta, \xi)]}{J\sigma_{\parallel} \partial \eta} \right) \frac{D(z, \eta)}{D(\eta, \xi)} \right]. \\
\frac{\partial B_z}{\partial t} + \frac{d\xi}{dt} \frac{\partial B_z}{\partial \xi} + \frac{d\eta}{dt} \frac{\partial B_z}{\partial \eta} = \\
= \frac{1}{rJ} \left\{ \frac{\partial [r(vB_r - uB_z)D(z, \xi)/D(\eta, \xi)]}{\partial \xi} + \frac{\partial [r(vB_r - uB_z)D(z, \eta)/D(\eta, \xi)]}{\partial \eta} \right\} + \\
+ \frac{c^2 t_*}{4\pi L_*^2} \frac{1}{rJ} \frac{\partial}{\partial \xi} \left[\left(\frac{r\partial [B_z D(z, \xi)/D(\eta, \xi)]}{J\sigma_{\parallel} \partial \xi} + \frac{r\partial [B_z D(z, \eta)/D(\eta, \xi)]}{J\sigma_{\parallel} \partial \eta} \right) \frac{D(z, \xi)}{D(\eta, \xi)} \right] + \\
+ \frac{c^2 t_*}{4\pi L_*^2} \frac{1}{rJ} \frac{\partial}{\partial \eta} \left[\left(\frac{r\partial [B_z D(z, \xi)/D(\eta, \xi)]}{J\sigma_{\parallel} \partial \xi} + \frac{r\partial [B_z D(z, \eta)/D(\eta, \xi)]}{J\sigma_{\parallel} \partial \eta} \right) \frac{D(z, \eta)}{D(\eta, \xi)} \right] + \\
+ \frac{c^2 t_*}{4\pi L_*^2} \frac{1}{rJ} \frac{\partial}{\partial \xi} \left[\left(\frac{r\partial [B_r D(r, \xi)/D(\eta, \xi)]}{J\sigma_{\parallel} \partial \xi} + \frac{r\partial [B_r D(r, \eta)/D(\eta, \xi)]}{J\sigma_{\parallel} \partial \eta} \right) \frac{D(z, \xi)}{D(\eta, \xi)} \right] + \\
+ \frac{c^2 t_*}{4\pi L_*^2} \frac{1}{rJ} \frac{\partial}{\partial \eta} \left[\left(\frac{r\partial [B_r D(r, \xi)/D(\eta, \xi)]}{J\sigma_{\parallel} \partial \xi} + \frac{r\partial [B_r D(r, \eta)/D(\eta, \xi)]}{J\sigma_{\parallel} \partial \eta} \right) \frac{D(z, \eta)}{D(\eta, \xi)} \right].
\end{aligned}$$

Radiation heat transfer

It is known, that plasma dynamical processes are strongly affected by irradiation, if laser plasma temperature achieve 1 eV. In that case the gas dynamic fields of thermo physical variables may be calculated only with taking into account the radiation fields. In this work the radiation transfer equation is used in the form of multi-group diffusive approach.

$$\begin{aligned}
\frac{1}{J} \frac{\partial (Jq_{i\xi})}{\partial \xi} + \frac{1}{J} \frac{\partial (Jq_{i\eta})}{\partial \eta} + \chi_i c U_i &= 4\chi_i \sigma_i T^4, \\
\frac{c}{3} \frac{\partial U_i}{\partial \xi} + \chi_i q_{i\xi} &= 0, \\
\frac{c}{3} \frac{\partial U_i}{\partial \eta} + \chi_i q_{i\eta} &= 0,
\end{aligned} \tag{4}$$

where $U_i(y, z, t)$ is the radiation power density in i -th spectral group, χ_i is the spectral absorption coefficient. Besides of the method mentioned above, the discrete ordinates method (MDO) has been used in the work, which gets an opportunity to solve the radiation transfer equation on tetrahedral non-structured mesh [13]. Modified alternatively triangular three-layered iterative scheme is applied for the solution of radiation transport equations, where the time step selected via conjugate directions method.

One can use the mechanism of collisional absorption, the opposite to electron bremsstrahlung process under conditions of local thermodynamic equilibrium (LTE), to define the plasma absorption coefficient for laser radiation

$$\chi_\omega = \frac{4.97gZ_in_in_e}{n_c^2\lambda^2(kT_e)^{3/2}} \frac{1}{\sqrt{1 - n_e/n_c}}, \quad [\text{cm}^{-1}]$$

where λ is the laser radiation wavelength [μm], n_e, n_i are the electron and ion densities correspondingly [cm^{-3}], kT_e is the electron temperature [keV], g is the Gaunt factor, $n_c = 10^{21}\lambda^{-2}$ is the critical electron density [cm^{-3}].

Turbulence model and equations

The turbulent viscous coefficient $\mu_\Sigma^{\perp, \parallel}$ is calculated by using of the Bussinesk hypothesis, when effective viscous is $\mu_\Sigma^{\perp, \parallel} = \mu_m^{\perp, \parallel} + \mu_t$, where $\mu_m^{\perp, \parallel}$ is a molecular viscosity coefficient and μ_t is a turbulent one, determined from $q-\omega$ turbulence model. The equations of $q-\omega$ turbulence model in curvilinear coordinates (ξ, η) are:

$$\begin{aligned} \frac{\partial \rho q}{\partial t} + \frac{d\xi}{dt} \frac{\partial \rho q}{\partial \xi} + \frac{d\eta}{dt} \frac{\partial \rho q}{\partial \eta} + \frac{1}{J} \frac{\partial (J\rho V_\xi q)}{\partial \xi} + \frac{1}{J} \frac{\partial (J\rho V_\eta q)}{\partial \eta} + \alpha \frac{\rho q u}{r} = \\ = S_q + \frac{\rho q}{2\omega} \left(C_\mu f D - \frac{2}{3} \omega \operatorname{div} \mathbf{V} - \omega^2 \right), \\ \frac{\partial \rho \omega}{\partial t} + \frac{d\xi}{dt} \frac{\partial \rho \omega}{\partial \xi} + \frac{d\eta}{dt} \frac{\partial \rho \omega}{\partial \eta} + \frac{1}{J} \frac{\partial (J\rho V_\xi \omega)}{\partial \xi} + \frac{1}{J} \frac{\partial (J\rho V_\eta \omega)}{\partial \eta} + \alpha \frac{\rho \omega u}{r} = \\ = S_\omega + \rho \left(C_1 (C_\mu D - \frac{2}{3} \omega \operatorname{div} \mathbf{V}) - C_2 \omega^2 \right), \\ S_q = \frac{1}{J} \frac{\partial \{ J(\mu_{\Sigma q}^\perp \xi_r^2 + \mu_{\Sigma q}^\parallel \xi_z^2) q_\xi + J(\mu_{\Sigma q}^\perp \xi_r \eta_r + \mu_{\Sigma q}^\parallel \xi_z \eta_z) q_\eta \}}{\partial \xi} + \\ + \frac{1}{J} \frac{\partial \{ J(\mu_{\Sigma q}^\perp \eta_r \xi_r + \mu_{\Sigma q}^\parallel \eta_z \xi_z) q_\xi + (J(\mu_{\Sigma q}^\perp \eta_r^2 + \mu_{\Sigma q}^\parallel \eta_z^2) q_\eta \}}{\partial \eta} + \\ + \alpha \frac{\mu_{\Sigma q}^\perp}{r} \left\{ \xi_r \frac{\partial q}{\partial \xi} + \eta_r \frac{\partial q}{\partial \eta} \right\}, \end{aligned}$$

$$\begin{aligned}
S_\omega = & \frac{1}{J} \frac{\partial \left\{ J(\mu_{\Sigma\omega}^\perp \xi_r^2 + \mu_{\Sigma\omega}^\parallel \xi_z^2) \omega_\xi + J(\mu_{\Sigma\omega}^\perp \xi_r \eta_r + \mu_{\Sigma\omega}^\parallel \xi_z \eta_z) \omega_\eta \right\}}{\partial \xi} + \\
& + \frac{1}{J} \frac{\partial \left\{ J(\mu_{\Sigma\omega}^\perp \eta_r \xi_r + \mu_{\Sigma\omega}^\parallel \eta_z \xi_z) \omega_\xi + (J(\mu_{\Sigma\omega}^\perp \eta_r^2 + \mu_{\Sigma\omega}^\parallel \eta_z^2) \omega_\eta) \right\}}{\partial \eta} + \\
& + \alpha \frac{\mu_{\Sigma\omega}^\perp}{r} \left\{ \xi_r \frac{\partial \omega}{\partial \xi} + \eta_r \frac{\partial \omega}{\partial \eta} \right\}, \\
\mu_{\Sigma q}^{\perp, \parallel} = & \mu_m^{\perp, \parallel} + \mu_t, \quad \mu_{\Sigma\omega}^{\perp, \parallel} = \mu_m^{\perp, \parallel} + 1.3\mu_t, \quad \mu_t = C_\mu f(n) \rho \frac{q^2}{\omega}, \\
C_1 = & 0.045 + 0.405f(n), \quad C_2 = 0.92, \quad C_\mu = 0.09, \\
f(n) = & 1 - \exp\left(-0.0065 \frac{\rho q n}{\mu_m^{\perp, \parallel}}\right), \tag{5}
\end{aligned}$$

where q is a pseudo velocity, w is a pseudo vortex, $f(n)$ is a wall function for correct flux parameters evaluation in laminar sub-layer near a solid streamline surface and n is the normal distance from the given point to the nearest surface.

Under supposition of molecular Prandtl number is $Pr = 0.72$ and turbulent one is $Pr_t = \mu_t c_p / \lambda_t = 0.9$ it is possible to determine the corresponding turbulent heat conductivity coefficient as $\lambda_{e, \Sigma}^{\perp, \parallel} = \lambda_{\perp, \parallel}^e + c_p \mu_t^{\perp, \parallel} / Pr_t$.

We use the simple model for the fusion fuel burning process, assuming that all neutrons would be lost from the plasma, the fuel mass is constant and fusion products and high-energy particles will be trapped by the higher magnetic field. The variation of particles number in the fusion reaction is described by kinetic equations [11]

$$\begin{aligned}
\frac{\partial N_D}{\partial t} + \frac{d\xi}{dt} \frac{\partial N_D}{\partial \xi} + \frac{d\eta}{dt} \frac{\partial N_D}{\partial \eta} + \frac{1}{J} \frac{\partial (J N_D V_{D, \xi})}{\partial \xi} + \frac{1}{J} \frac{\partial (J N_D V_{D, \eta})}{\partial \eta} + \alpha \frac{N_D u}{r} &= F_D, \\
F_D &= -F_1 - 2F_2 - 2F_3 - F_4, \\
\frac{\partial N_T}{\partial t} + \frac{d\xi}{dt} \frac{\partial N_T}{\partial \xi} + \frac{d\eta}{dt} \frac{\partial N_T}{\partial \eta} + \frac{1}{J} \frac{\partial (J N_T V_{T, \xi})}{\partial \xi} + \frac{1}{J} \frac{\partial (J N_T V_{T, \eta})}{\partial \eta} + \alpha \frac{N_T u}{r} &= F_T, \\
F_T &= -F_1 + F_2, \\
\frac{\partial N_\alpha}{\partial t} + \frac{d\xi}{dt} \frac{\partial N_\alpha}{\partial \xi} + \frac{d\eta}{dt} \frac{\partial N_\alpha}{\partial \eta} + \frac{1}{J} \frac{\partial (J N_\alpha V_{\alpha, \xi})}{\partial \xi} + \frac{1}{J} \frac{\partial (J N_\alpha V_{\alpha, \eta})}{\partial \eta} + \alpha \frac{N_\alpha u}{r} &= F_\alpha, \\
F_\alpha &= F_1 + F_4, \\
\frac{\partial N_{3\text{He}}}{\partial t} + \frac{d\xi}{dt} \frac{\partial N_{3\text{He}}}{\partial \xi} + \frac{d\eta}{dt} \frac{\partial N_{3\text{He}}}{\partial \eta} + \frac{1}{J} \frac{\partial (J N_{3\text{He}} V_{3\text{He}, \xi})}{\partial \xi} + \\
& + \frac{1}{J} \frac{\partial (J N_{3\text{He}} V_{3\text{He}, \eta})}{\partial \eta} + \alpha \frac{N_{3\text{He}} u}{r} = F_{3\text{He}}, \\
F_{3\text{He}} &= F_3 - F_4,
\end{aligned}$$

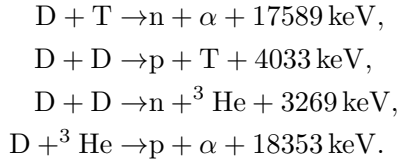
$$\frac{\partial N_p}{\partial t} + \frac{d\xi}{dt} \frac{\partial N_p}{\partial \xi} + \frac{d\eta}{dt} \frac{\partial N_p}{\partial \eta} + \frac{1}{J} \frac{\partial(JN_p V_{p,\xi})}{\partial \xi} + \frac{1}{J} \frac{\partial(JN_p V_{p,\eta})}{\partial \eta} + \alpha \frac{N_p u}{r} = F_p,$$

$$F_p = F_2 + F_4,$$

$$F_1 = \langle \sigma v \rangle_1 n_D n_T, \quad F_2 = 0.5 \langle \sigma v \rangle_2 n_D^2,$$

$$F_3 = 0.5 \langle \sigma v \rangle_3 n_D^2, \quad F_4 = \langle \sigma v \rangle_4 n_D n_{3He}. \tag{6}$$

Numbers 1, 2, 3 and 4 correspond to reactions



Numerical algorithm

Non-stationary two dimensional radiation magneto-gas dynamic model is developed by authors. The numerical solution is based on splitting method in terms of physical processes and spatial directions. The calculations of thermodynamic $e(T, r)$, $P(T, r)$ and optical $\chi(T, r)$ media parameters occur with the aid of computer system ASTEROID, developed by S. Surzhikov [14].

Solve this equations system (1)–(6) by the method of fractional steps using the splitting on physical processes. “Hyperbolic” (frictionless) part of the equations system (1)–(6) is solved by using the explicit integro-interpolation method and boundary conditions on the 1st fractional time step. This is the gasdynamic (convective part of Navier–Stokes equations, magnetic field dynamics \mathbf{B} , q - ω model of Coacly) phase of numerical simulation. The “viscous” part of Navier–Stokes equations are approximated explicitly. The calculated codes have been developed use multi-blocks, multi-grids technology on non orthogonal, structured grids. Nonlinear quasi-monotone compact difference scheme, that allows to get seventh order of accuracy in spatially smooth solution [15] is applied.

The second fractional time step – implicit method with a boundary condition attachment tool is used, for solution of the “parabolic” (viscous) part of the equations system (1)–(5). Calculation of second partial derivatives in the finite – differences equations system (1)–(5) based on the developed finite – differences quasi-monotone compact seventh-order scheme.

For the third stage of the splitting (laser radiation absorption) differentiation operator has the form

$$\frac{\partial \rho e}{\partial t} = \frac{t_*}{\rho_* e_*} Q_L,$$

$$Q_L = \chi_\omega(z) P_L(t) \exp\left(\frac{-z^n}{R_L^n}\right) \exp\left[-\int \chi_\omega(x, r=0) dx\right] \frac{1}{\pi R_L^2}.$$

We create an end-to-end simulation for laser absorption. We assumed that full absorption of laser radiation takes place in the point of critical laser plasma density.

On the fourth splitting phase, that corresponds to the electron thermal conductivity of the plasma, consider the following equation:

$$\frac{\partial \rho e_e}{\partial t} = \frac{\gamma}{Pr Re} \operatorname{div} \left(\lambda_{e,\Sigma}^{\perp,\parallel} \operatorname{grad} T_e \right),$$

or

$$\begin{aligned} \frac{3}{2} n_e k \frac{\partial T_e}{\partial t} = & \frac{1}{J} \partial \left\{ \frac{J(\lambda_{e,\Sigma}^{\perp} \xi_r^2 + \lambda_{e,\Sigma}^{\parallel} \xi_z^2) T_{e,\xi} + J(\lambda_{e,\Sigma}^{\perp} \xi_r \eta_r + \lambda_{e,\Sigma}^{\parallel} \xi_z \eta_z) T_{e,\eta}}{\partial \xi} \right\} + \\ & + \frac{1}{J} \partial \left\{ \frac{J(\lambda_{e,\Sigma}^{\perp} \xi_r \eta_r + \lambda_{e,\Sigma}^{\parallel} \xi_z \eta_z) T_{e,\xi} + J(\lambda_{e,\Sigma}^{\perp} \eta_r^2 + \lambda_{e,\Sigma}^{\parallel} \eta_z^2) T_{e,\eta}}{\partial \eta} \right\} + \\ & + \alpha \frac{\lambda_{e,\Sigma}^{\perp}}{r} \left\{ \xi_r \frac{\partial T_e}{\partial \xi} + \eta_r \frac{\partial T_e}{\partial \eta} \right\}. \end{aligned}$$

To solve this equation most efficiently use implicit finite-difference schemes. A more detailed description of the mathematical model and numerical method is given in the authors preprint [11]. Model of “full absorption of laser radiation at the critical density” is quite rough and demanding changes [16]–[18]. But for the initial calculations of interaction of laser beams of high energy pulses with a plasma target located in the seed magnetic field in the opinion of the authors is justified. Because it can correctly estimate the marginal parameters of thermonuclear magnetized laser plasmas.

Conclusion

The mathematical model of magnetized plasma-laser beams of high energy pulses has been developed. It is based on radiation plasma dynamics equations in arbitrary curvilinear coordinates. A new quasi-monotone numerical method for laser driven magneto-inertial fusion (MIF) is created, which can help solve single-fluid, two-temperature equations of motion with contributions from diffusion, convection, heat conduction in cylindrical or spherical geometries. Electromagnetic processes are described by the Maxwell–Ohm equations in plasma with final conductivity. The transport coefficients in the given system of the equations taking into account magnetized laser plasma. Fusion reactions D–T, D–D (two branches) and D–³He are included in the model. External magnetic fields are taken into account.

Non-stationary two dimensional radiation magneto-gas dynamics model is developed by authors. The model is based on splitting method in terms of physical processes and spatial directions, that in spatially smooth solution allows to get seventh order of accuracy. Modified alternatively triangular three-layered iterative scheme is applied for the solution of radiation transport equations, where the time step selected via conjugate directions method.

Two-dimensional radiative gas dynamics NICA (Nonstationary Instruments and Codes for fusion and nonelectric Applications) for the simulation of MIF radiation magneto gas dynamic problems is proposed. New program takes into account radiation transport in multi-group diffusion approach and gas dynamics according to an improved Lagrangian difference scheme. Mathematical method developed here may be applied for both impact fast ignition and uniform compression calculations [19]–[21].

References

- [1] S. G. ALIKHANOV, V. P. BAKHTIN, A. G. ES'KOV, R. K. KURTMULLAEV, V. N. SEMENOV, E. F. STRIZHOV, N. P. KOZLOV, V. I. KHVESYUK, A. V. YAMINSKIJ: *Three-dimensional plasma compression in a Z-pinch liner system – transport and compression of a compact torus by a quasi-spherical liner*. Proc. of the 9th Int. Conf. on Plasma Physics and Controlled Nuclear Fusion Research, 3 (IAEA, Vienna, 1983), 319. IAEA-CN-41/W3.
- [2] A. HASEGAWA, H. DAIDO, M. FUJITA, K. MIMA, M. MURAKAMI, S. NAKAI, K. NISHIHARA, K. TERAI, C. YAMANAKA: *Magnetically insulated inertial fusion: a new approach to controlled thermonuclear fusion*. Phys. Rev. Lett., 56 (1986), 139–142.
- [3] Y. C. F. THIO: *Status of the U. S. program in magneto-inertial fusion*. Journal of Physics: Conference Series, 112 (2008), 042084.
- [4] O. V. GOTCHEV, N. W. JANG, J. P. KNAUER, M. D. BARBERO, R. BETTI, C. K. LI, R. D. PETRASSO: *Magneto-inertial approach to direct-drive laser fusion*. Journal of Fusion Energy, 27 (2008), 25–31.

- [5] I. YU. KOSTYUKOV, S. V. RYZHKOV: *Magneto-inertial fusion with laser compression of magnetized spherical target*. Russian Applied Physics (Prikladnaya Fizika), 1 (2011), 65–72.
- [6] S. A. SLUTZ, M. C. HERRMANN, R. A. VESEY, A. B. SEFKOW, D. B. SINARS, D. C. ROVANG, K. J. PETERSON, M. E. CUNEO: *Pulsed-power-driven cylindrical liner implosions of laser preheated fuel magnetized with an axial field*. Phys. Plasmas, 17 (2010), 056303.
- [7] S. V. RYZHKOV: *The behavior of a magnetized plasma under the action of laser with high pulse energy*. Problems of atomic science and technology. Series “Plasma Electronics and New Methods of Acceleration”, 7 (2010), 105–110.
- [8] O. V. GOTCHEV, P. Y. CHANG, J. P. KNAUER, D. D. MEYERHOFER, O. POLOMAROV, J. FRENJE, C. K. LI, M. J.-E. MANUEL, R. D. PETRASSO, J. R. RYGG, F. H. SÉGUIN, R. BETTI: *Laser-driven magnetic-flux compression in high-energy-density plasmas*. Phys. Rev. Lett., 103 (2008), 215004.
- [9] V. V. KUZENOV: *The choice of numeric algorithm for the laser plume simulation* Contributed Papers VI Int. Conf. on Plasma Physics and Plasma Technology, National Academy of Sciences of Belarus, Minsk, 2009, 67–70.
- [10] V. A. GASILOV, A. S. CHUVATIN, A. YU. KRUKOVSKII, E. L. KARTASHEVA, O. G. OLKHOVSKAYA, A. S. BOLDAREV, D. S. TARASOV, N. V. SEROVA, S. V. D’YACHENKO, O. V. FRYAZINOV: *A program package “Razryad”: modeling of plasma acceleration in pulsed-power systems*. Matem. Mod., 15, 9 (2003), 107–124.
- [11] V. V. KUZENOV, S. V. RYZHKOV: *A mathematical model of the interaction of high pulse energy laser with dense plasma target with initial seed magnetic field*. Preprint IPMech RAS (in Russian), 942 (2010), 1–56.
- [12] www.t4.lanl.gov/opacity/sesame.html, SESAME Format Tables, April 3, 2010.
- [13] S. T. SURZHIKOV, V. V. KUZENOV, A. S. PETRUSEV: *Radiation gas dynamics of aluminium laser plume in air*. AIAA 2008–1108, 1–8.
- [14] S. T. SURZHIKOV: *Computing system for solving radiative gasdynamic problems of entry and re-entry space vehicles*. First International Workshop on Radiation of High Temperature Gases in Atmospheric Entry(B. Warmbein). ESA SP-533, Lisbon 2003, 111–118.
- [15] O. M. BELOTSERKOVSKII, YU. M. DAVYDOV: *The method of large particles in gas dynamics*. Computer experiments. Nauka, Moskva 1982.
- [16] P. MORA: *Theoretical model of absorption of laser light by a plasma*. Phys. Fluids, 25 (1982), 1051–1056.
- [17] D. BATANI, H. STABILE, A. RAVASIO, G. LUCCHINI, F. STRATI, T. DESAI, J. ULLSCHMIED, E. KROUSKY, J. SKALA, L. JUHA, B. KRALIKOVA, M. PFEIFER, CH. KADLEC, T. MOCEK, A. PRÄG, H. NISHIMURA Y. OCHI: *Ablation pressure scaling at short laser wavelength*. Phys. Rev. E, 68 (2003), 067403.
- [18] C. GARBAN-LABAUNE, E. FABRE, C. E. MAX, R. FABBRO, F. AMIRANOFF, J. VIRMONT, M. WEINFELD, A. MICHARD: *Effect of laser wavelength and pulse duration on laser-light absorption and back reflection*. Phys. Rev. Letters, 48 (1982), 1018–1021.
- [19] M. G. HAINES, K. KRUSHELNICK, R. J. KINGHAM, A. R. BELL, A. E. DANGOR, M. S. WEI, A. GOPAL, M. TATAKARIS, F. N. BEG, P. A. NORREYS, R. G. EVANS, E. L. CLARK, R. J. CLARK: *Fast ignition studies and magnetic field generation*. 20th IAEA Fusion Energy Conference Proceedings, Vilamoura, 2004. Paper IF/P7-27.

- [20] M. MURAKAMI, H. NAGATOMO, H. AZECHI, F. OGANDO, M. PERLADO, S. ELIEZER: *Innovative ignition scheme for ICF-impact fast ignition*. Nuclear Fusion, 46 (2006), 99–103.
- [21] H. AZECHI, T. SAKAIYA, T. WATARI, M. KARASIK, H. SAITO, K. OHTANI, K. TAKEDA, H. HOSODA, H. SHIRAGA, M. NAKAI, K. SHIGEMORI, S. FUJIOKA, M. MURAKAMI, H. NAGATOMO, T. JOHZAKI, J. GARDNER, D. G. COLOMBANT, J. W. BATES, A. L. VELIKOVICH, Y. AGLITSKIY, J. WEAVER, S. OBENSCHAIN, S. ELIEZER, R. KODAMA, T. NORIMATSU, H. FUJITA, K. MIMA: *Experimental evidence of impact ignition: 100-fold increase of neutron yield by impactor collision*. Phys. Rev. Letters, 102 (2009), 235002.

Received May 16, 2010

Application of alternating electric field for excitation of surface cyclotron O-modes

ANASTASIIA GIRKA¹, VOLODYMYR GIRKA¹, IVAN PAVLENKO¹

Abstract. Properties of electromagnetic surface O-modes propagating across an external magnetic field along planar boundary of plasma filled waveguide at electron cyclotron frequency are studied in this paper. Theoretical research into the surface cyclotron O-modes is carried out using kinetic description for the plasma particles affected both by constant magnetic field and alternating electric field. Fields of these O-modes are described by Maxwell equations. Nonlinear boundary condition has been applied to derive equation that describes excitation of surface cyclotron O-modes. Values of their growth rates are examined analytically and numerically. Electrodynamical model of gas discharge sustained by the O-modes is proposed. Estimation of uniform plasma volume sustained by propagation of these modes coincides with result obtained experimentally.

Key Words. Surface cyclotron O-modes, parametrical instability, gas discharge.

1. Introduction

Propagation of bulk cyclotron waves are well-known physical phenomenon and their application is very important in such branches as nuclear fusion, plasma physics and radiophysics. Under the laboratory conditions propagation of eigen surface waves (SW), that are located nearby plasma boundary becomes possible. During the last decade dispersion properties of SW are intensively being investigated both theoretically and experimentally [1] due to their advantages in sustaining gas discharges as compared with the case of bulk waves' utilization. SW properties are integrally determined by different waveguides' parameters as arrangement of the construction elements, external constant magnetic field \mathbf{B}_0 and alternating electric field $\mathbf{E}_0(t)$, plasmas' density and temperature profiles, etc.

¹Kharkiv National University, Svobody sq. 4, Kharkiv, 61077 Ukraine;
e-mail: v.girka@gmail.com, nasturtsia@i.ua

Surface cyclotron O-modes (SCOM) were found [2] to propagate along plane plasma–dielectric interface, when an external constant magnetic field is parallel to the plasma boundary and penetration depth of the modes is approximately equal to their wavelength. In this case the SCOM frequencies decrease when wave number grows, their damping is determined by both collisional (interaction between plasma particles) and kinetical (interaction between particles and plasma interface) mechanisms. Experimentally SCOM at electron cyclotron frequency have been studied in a mirror machine during gas discharge [3]. There it was proved possibility of these waves to sustain gas discharge in chamber and special investigations have been conducted to prove that these waves' field was characterized by surface type spatial distribution.

Mathematical simplicity as well as the significant role of the hydrodynamic instabilities are the main reasons for the wide application of the magneto-hydrodynamic description for analytical study of the waves' propagation in plasmas. But there is no opportunity in the frame of magneto-hydrodynamics to study electromagnetic perturbations at harmonics of cyclotron frequencies, they can be correctly studied only by the kinetic description [4]. The theory of SCOM is supplemented here by the way of considering two components of the modes' wave vector and taking into the consideration effect of external alternating electric field when solving Vlasov–Boltzmann kinetic equation.

2. Basic equations

Let's consider planar plasma boundary restricted on the plane $x = 0$ by vacuum. An external constant magnetic field \mathbf{B}_0 is applied parallelly to the plasma surface along z direction. Plasma space is supposed to be uniform in the z direction (it means $\frac{\partial}{\partial z} = 0$). An external alternating electric field $\mathbf{E}_0 \sin(\omega_0 t)$ is oriented perpendicular to z axis (ω_0 is frequency of the electric field). The plasma particles motion is described by Vlasov–Boltzmann kinetic equation with Maxwellian nonperturbed plasma particles distribution function. The assumption of weak plasma thermal motion (or weak plasma spatial dispersion $|\mathbf{k}_\perp \rho_\alpha| \ll 1$, here $\mathbf{k}_\perp = \mathbf{k}_1 + \mathbf{k}_2$ is the wave vector, ρ_α is Larmor radius of the plasma particles, $\alpha = e$ for electrons, $\alpha = i$ for ions, $\rho_\alpha = v_{T\alpha}/|\omega_\alpha|$, $v_{T\alpha}$ and ω_α are thermal velocity and cyclotron frequency of the plasma particles) is applied. To describe the SCOM electromagnetic field we used Maxwell equations.

The problem is studied by the method of Fourier transform, doing that dependence of the SCOM field on the y coordinate and time t is chosen in the form $E, H \propto f(x) \exp(i \cdot k_2 y - i \cdot \omega t)$, where k_2 and ω are the frequency and the wave vector of the SCOM along plasma interface, respectively. The set of Maxwell equations can be divided into two independent systems. One of them describes the SCOM with components H_x, H_y, E_z . Application Fourier transform allows one to derive equations for Fourier coefficients of the SCOM

field (H_1 , H_2 , E_3 , respectively) in the plasma region. As far as the SCOM damping connected with interaction between plasma particles and its boundary is out of scope of the paper then Fourier coefficient of electric current density can be represented in the following form $j_3 = \sigma_{33}E_3$. Here component of the plasma conductivity σ_{33} tensor is equal to

$$\sigma_{33} = \frac{i}{4\pi} \sum_{\alpha} \sum_{s=-\infty}^{\infty} \sum_{m=-\infty}^{\infty} \sum_{l=-\infty}^{\infty} \frac{\Omega_{\alpha}^2 I_n(k_{\perp}^2 \rho_{\alpha}^2 / 2) J_m(b) J_{m-l}(b)}{(\omega - s\omega_{\alpha} + \omega_0(n+m)) \exp(k_{\perp}^2 \rho_{\alpha}^2 / 2)}, \quad (1)$$

where Ω_{α} is the plasma frequency, $J_n(z)$ and $I_m(x)$ are the first order and modified Bessel functions, respectively [5],

$$b = \frac{k_{\perp} E_0 e_{\alpha}}{m_{\alpha} (\omega_{\alpha}^2 - \omega_0^2)} = \frac{\sqrt{2y_{\alpha}} E_0 e_{\alpha}}{m_{\alpha} (\omega_{\alpha}^2 - \omega_0^2) \rho_{\alpha}} = \sqrt{2y_{\alpha}} b_{\alpha},$$

b_{α} is amplitude of plasma particles oscillation affected by external alternating electric field normalized by Larmor radius, $y_{\alpha} = k_{\perp}^2 \rho_{\alpha}^2 / 2$.

Then in order to obtain equation determined the SCOM excitation one can apply the following boundary conditions for the waves' fields: first, continuity of the tangential electric field on the plasma–dielectric boundary; second, discontinuity of the tangential component of the SCOM magnetic field on the plasma–dielectric boundary. The second condition has nonlinear form and is determined by presence of the following sums: $\sum_{m=-\infty}^{\infty} \sum_{l=-\infty}^{\infty} J_m(b) J_{m-l}(b)$ in expression for the σ_{33} that describe nonlinear electric current on the plasma boundary affected by external alternating electric field.

From analysis of expression (1) one can make conclusion that the problem can't be studied analytically for arbitrary number of cyclotron harmonic. Thus let's consider the case of SCOM at the main electron cyclotron harmonic. To formulate explicit form of the nonlinear boundary condition one can apply assumption on weak spatial dispersion of the plasma that allows one to utilize asymptotic expressions of Bessel functions when their arguments are less than unit. Then nonlinear boundary condition for electric current density on the plasma interface has the following form

$$H_y^{(pl)}(0) = -i \frac{k_2}{k} E_z(0) + \frac{4\pi}{c} \int_{+0}^{-0} j_z dx. \quad (2)$$

Value of j_z can be calculated using expression for its Fourier coefficient $j_3(k_1) = \sigma_{33}E_3(k_1)$ by the aid of theory of residues. Result of calculation the integral in the right hand side of expression (2) under the applied assumptions can be written in the form

$$\int_{+0}^{-0} j_z dx \approx \frac{i\Omega_e^2}{4\pi} \sum_{m=-\infty}^{\infty} \sum_{l \neq 0, l=-\infty}^{\infty} \frac{y_e(gq_0\rho_e/2)^{|m|+|m-l|}}{2k_2 m!(m-l)! \omega_{n+m}} \times \left[1 + \frac{\omega_{n+m}^2 q_0^2 \rho_e^2 / 2}{\omega_{n+m}^2 - \omega_e^2} \right] \left[1 + \frac{\omega_n^2 \Omega_e^2 \rho_e^2 / 2}{c^2(\omega_n^2 - \omega_e^2)} \right]^{-1}, \quad (3)$$

where q_0 is the root of the equation $\Delta(k_1 = q_0) = 0$ located in upper complex semiplane,

$$k_1^2 + k_2^2 - \omega_n^2 \varepsilon_3 c^{-3} + \frac{\omega_n^2 \Omega_e^2 k_1^2 \rho_e^2}{2c^2 \omega_n^2 - \omega_e^2} = \Delta(k_1),$$

$\varepsilon_3 = 1 - (\Omega_e^2 + \Omega_i^2 \omega_n^{-2})$ is the component of dielectric permeability tensor in the approach of cold plasma, $\omega_n = \omega + n\omega_0$, $\omega_{n+m} = \omega + (n+m)\omega_0$, $g = b_e$. Using reverse Fourier transform for expression $E_3(k_1)$ one can find the set of equations that determine growth rate of SCOM excitation:

$$E_z^{(n)}(0)\lambda^{(n)} + F^{(n,l)} E_z^{(n+l)}(0) = 0. \quad (4)$$

Here

$$\lambda^{(n)} = \sqrt{\left[1 + \frac{\omega_n^2 \Omega_e^2 \rho_e^2}{2c^2(\omega_n^2 - \omega_e^2)} \right]^2 - \frac{\omega_n^2 \varepsilon_3}{c^2 k_2^2} \left[1 + \frac{\omega_n^2 \Omega_e^2 \rho_e^2}{2c^2(\omega_n^2 - \omega_e^2)} \right] - 1}, \quad (5)$$

$$F^{(n,l)} = \sum_{m,l \neq 0} \frac{(gq_0\rho_e/2)^{|m|+|m-l|} \Omega_e^2 \omega_n}{c^2 q_0^2 m!(m-l)! \omega_{n+l}} \times \left[1 + \frac{\omega_{n+m}^2 q_0^2 \rho_e^2 / 2}{\omega_{n+m}^2 - \omega_e^2} \right] \left[1 + \frac{\omega_n^2 \Omega_e^2 \rho_e^2 / 2}{c^2(\omega_n^2 - \omega_e^2)} \right]^{-1} \quad (6)$$

where limits of sums $\sum_{m,l \neq 0}$ are the same as it is indicated in expression (3), equating function $\lambda^{(n)} = \lambda^{(n)}(\omega_n, k_2)$ to zero one can obtain dispersion relation of the SCOM with frequency ω_n . To simplify the further consideration let's consider the case that just meaning ω is eigen frequency of the SCOM, thus there is only one dispersion equation: $\lambda^{(0)}(\omega) = 0$ and all other functions $\lambda^{(n \neq 0)}(\omega) \neq 0$.

3. Results of the SCOM excitation analysis

For accurate answer on question about effect of external alternating electric field on excitation of SCOM one can solve infinite set of equations (4), but for approximate analysis of their instability it will be enough to consider the following shortened set of equations

$$\begin{aligned} \lambda^{(-1)} E_z^{(-1)}(0) + F^{(-1,+1)} E_z^{(0)}(0) + F^{(-1,+2)} E_z^{(1)}(0) &= 0, \\ F^{(0,-1)} E_z^{(-1)}(0) + \lambda^{(0)} E_z^{(0)}(0) + F^{(0,+1)} E_z^{(1)}(0) &= 0, \\ F^{(+1,-1)} E_z^{(-1)}(0) + F^{(+1,-2)} E_z^{(0)}(0) + \lambda^{(+1)} E_z^{(+1)}(0) &= 0. \end{aligned} \quad (7)$$

Set of equations (7) has solution if determinant formed with coefficients nearby fields $E_z^{(m)}(0)$ is equal to zero. Under the condition of parametrical resonance: $\omega = |\omega_e| + \Delta_T + \gamma$, here Δ_T is the SCOM frequency shift from accurate meaning of cyclotron resonance. Then one can obtain a cubic equation for parameter γ that allows one to estimate growth rate of the SCOM instability affected by external alternating electric field. Approximate value of $\text{Im}(\gamma)$ is as follows

$$\text{Im}(\gamma) \approx \frac{0.2|\omega_e|gk_2^4\rho_e^2c^2}{\Omega_e^2}. \quad (8)$$

Results of numerical solving set of equations (7) are represented on Fig. 1 for $\omega_0|\omega_e|^{-1} = 1.2$. Numbers 1, 2, 3, 4 relate to the cases: $\Omega_e^2\omega_e^{-2} = 10, 10, 50, 10$; plasma beta 0.4, 0.4, 0.4, 0.2; $g = 0.9, 0.8, 0.9, 0.9$. The SCOM growth rates' values increase with decreasing plasma density and with increasing amplitude of external alternating electric field and plasmas' beta.

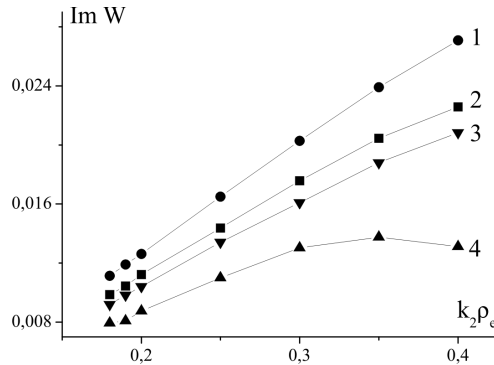


Fig. 1. Dependence of the SCOM growth rate $\text{Im}(\omega/|\omega_e|)$ on the $k_2 \rho_e$

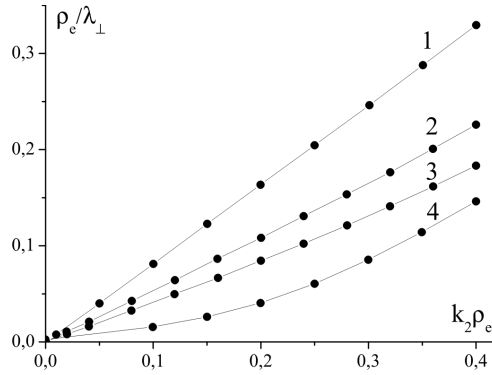


Fig. 2. The SCOM penetration depth λ_\perp as a function of the $k_2\rho_c$

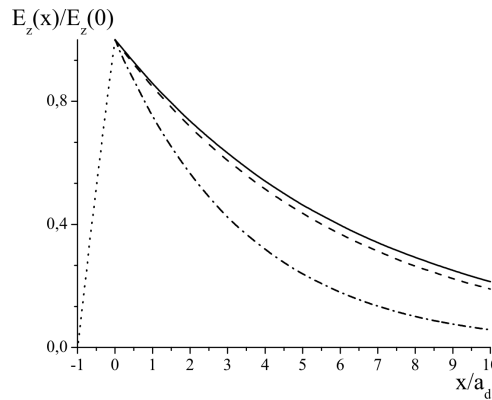


Fig. 3. Spatial distribution of the SCOM electric field

4. Power Balance Equation

At present time, the main field of SWs' technological application is gas discharge. Simple electrodynamic model of plasma sustained by SCOM propagation can be developed [1] by construction of their power balance equation. At the stationary stage of the gas discharge where SCOM is utilized as operating mode, all quantity of SCOM power flow is determined by their quantity, which is absorbed by produced plasma. There are two main mechanisms of the power absorption: collisional absorption connected with Ohmic plasma heating Q_{col} and kinetic absorption of the SCOM power Q_{kin} connected with interaction between plasma particles and plasma surface. Using Fourier method one

can find out expressions for the SCOM fields and derive the following power balance equation [2]

$$\frac{dS_y}{dy} = -Q_{\text{col}} - Q_{\text{kin}}, \quad (9)$$

where

$$Q_{\text{col}} \approx \frac{\nu_e k_2 \delta^4 H_y^2(0)}{4\pi\rho_\alpha^3 (1 + k_2^2 \delta^2) \text{ch}^3(a_d k_2) \text{sh}(a_d k_2)},$$

$$\varphi = 1 + \frac{\omega^2 \rho_e^2 \delta^{-2}}{\omega^2 - \omega_e^2},$$

$$\delta = c\Omega_e^{-1},$$

$$Q_{\text{kin}} \approx \frac{\nu_{T_\alpha} \Omega_\alpha^2 H_y^2(0)}{6\pi^{3/2} \omega^2 \text{cth}^2(a_d k_2)},$$

$$\frac{S_y(x)}{H_x^2(0)} = \frac{-k_2 \omega \exp\left(-2x \sqrt{k_2^2 - k^2 \varepsilon_3 \varphi^{-1}}\right)}{8\pi\varphi(k_2^2 \varphi - k^2 \varepsilon_3)} \text{th}^2(k_2 a_d).$$

Applying generator with frequency 2.45 GHz, $B_0 = 857$ G, in discharge chamber with wall thickness $a_d = 1$ mm one can obtain plasma density $n_{\text{pl}} \approx 5 \times 10^{11} \text{ cm}^{-3}$ with $T_e \approx 1$ [2]. Discharge length can be calculated from (9). Numerical analysis proves that penetration depth λ_\perp is about wave length for different values of the plasma thickness a_N (see Fig. 2). Here $\Omega_e^2 = 10^3 \omega_e^2$, $\beta_e = 1$, $a_d = \rho_e$. Numbers 1, 2, 3 and 4 relate to the cases: $a_N = \rho_e$, $3\rho_e$, $10\rho_e$ and semi-bounded plasma, respectively) and the main part of the SCOM power is located in plasma region (see Fig. 3). Here solid, dashed and chain lines relate to the cases $\Omega_e^2 \omega_e^{-2} = 3.0$; 2.0 and 1.0, respectively). Thus for SCOM with $\lambda_\perp \approx 4$ cm discharge length is equal approximately 50 cm as it was obtained experimentally in [3].

5. Conclusions

We carried out the research into excitation of SCOM affected by alternating electric field using the Maxwell equations for the SCOM field and kinetic Vlasov–Boltzmann equation for plasma particles. The results presented concern the SCOM propagating at the main harmonic of electron cyclotron frequency, but there is no principal restriction for studying the cases of high cyclotron harmonics. Simple analytical expression for the SCOM growth rate is found in the limiting case of weak spatial dispersion of plasma particles ($k_\perp \rho_\alpha \ll 1$).

SCOM can be used as for our mind in some plasma technologies. It is known that surface waves are applied for cleaning solids interfaces and it was experimentally determined that the SW have in this process advantages over

bulk waves. Experimental results [1] suggest that an external steady magnetic field facilitates the plasma production and makes the discharge longer. SW are widely used for studying the physical properties of solids and for various radiotechnical purposes as well. As far as the SCOM frequency depends upon the physical characteristics of the dielectric coating on the metal interface, one can apply these modes for the technical control of such coating. Analyzing the SCOM frequency value one can estimate the thickness of the dielectric layer or value of its dielectric constant.

References

- [1] YU. M. ALIEV, H. SCHLUTER, A. SHIVAROVA: *Guided-wave-produced plasmas*. Springer, New York 2000.
- [2] V. O. GIRKA, A. V. KLYZHKA: *Surface cyclotron O-modes in planar waveguides of finite width with dielectric sheaths and transverse nonuniformity of plasma concentration*. *Plasma Sources Science and Technology*, 17 (2008), 025015.
- [3] A. GANGULI, M. K. AKHTAR, R. D. TAREY: *Investigation of microwave plasmas produced in a mirror machine using ordinary-mode polarization*. *Plasma Sources Science and Technology*, 8 (1999), 519–529.
- [4] N. A. KROLL, A. W. TRIVELPIECE: *Principles of plasma physics* McGraw-Hill., New York 1973.
- [5] M. ABRAMOWITZ, I. A. STEGUN: *Handbook of Mathematical Functions with formulas, graphs and mathematical tables*. National Bureau of Standards Applied Mathematics Series 55, New York 1964.

Received May 1, 2010

Impact of electrons and ions on micron-sized dust particulates in plasma: realisation in particle and hybrid computer models¹

PETR BARTOŠ²

Abstract. This contribution deals with the numerical realisation of the interaction of charged particles with micron sized powder particulates immersed into low-temperature plasma. We focus our attention on the possible realisation of this interaction in computer models based on the particle modelling technique in both the purely particle models and the hybrid computer simulations.

Three algorithms for the detection of particles impinging the surface of powder particulate are presented and their advantages and drawbacks are discussed.

In the contribution there are continuously presented the results of computer simulations performed for powder particles with diameters 10, 20, 30, 60, 120 and 250 μm .

Key Words. Computer simulations, plasma, powder particles, interaction of particles.

1. Introduction

Computer simulations are powerful and relatively cheap instrument used for the study of various processes in physics. Computer simulations also found their place in disciplines involved interaction of plasma with micron-sized particulates – they allow to study the creation and growth of dust species, the processes associated with the electrical charging of the surface, temperature-dependent processes, influence of the dust presence on plasma parameters etc. Results obtained by this basic research are afterwards used in many technological processes like deposition of thin films or surface modification of power particulates [1].

¹This research has been supported by the grant project GAČR 202/09/P140.

²University of South Bohemia, Pedagogical Faculty, Department of Physics, Jeronýmova 10, 371 15 České Budějovice, Czech Republic

Scientist aimed by the development of computer models enabling the plasma–solid interactions developed many algorithms that can be roughly divided into three main groups – particle, fluid and hybrid approaches [2], [3]. In this paper the particle and hybrid methods will be considered.

At the beginning of every simulation several parameters have to be determined. One of the most important parameters is the time-step length that is used for numerical realisation of the particle movement. The value is determined on the bases of an analysis of the problem that imposes (usually contradictory) requirements. In dusty plasma physics three main factors should be considered:

- the mean free path,
- performance of the computer on which the calculation will be implemented,
- the size of dust particulates.

The first two items are frequently discussed in the literature [4]. For example, in computer simulations of low-temperature argon plasma at pressure 133 Pa the time step length for electrons is usually 1×10^{-11} s, for heavier and therefore slower ions the time step length is 1×10^{-8} s [5]. Increasing of computer performance and the usage of multi-thread simulations allow to decrease the time step length. The requirements on the time step length given by the diameter of the powder particulate will be the scope of our following considerations.

The collision of species with the surface of large-scale solid object can be determined easily – the particle is considered to hit the surface, when its new position on the end of the time step is located in the area corresponding to the solid object. For small objects, where the distance covered by the specie during one time step is comparable with the characteristic distance of the object or shorter, the decision about the collision occurrence may not be evaluated correctly. The situation is presented in Fig. 1. Although the particulate position at the end of the time step is located outside the solid object, the trajectory covered during the given time step can go through the solid object (in our case through the powder particulate). The species should be considered as captured, but (according to the procedure described above) the particulate will be considered as free in real.

This situation does not occur only in simulations of dusty plasma, but it can also occur in many other models – for example in interaction of plasma with finely broken surface [6].

If the decreasing of the time step is not possible enabling the performance of the calculation, the decision about the collision between the electron or ion should be done by an more precise algorithm. Unfortunately, these algorithms

are much more time consuming, that can make the calculation unfeasible. The question is, when such algorithms have to be used.

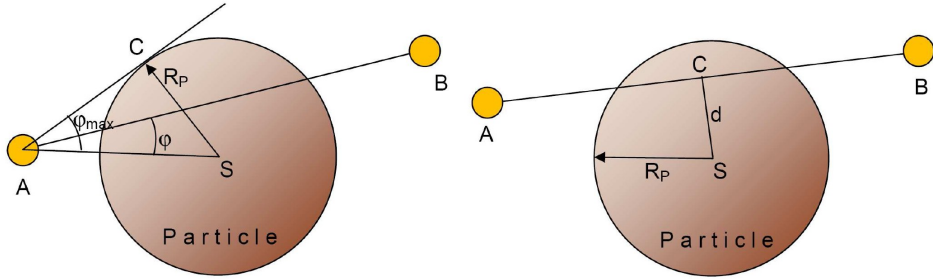


Fig. 1. Sketch of the situation (algorithm B – left, algorithm C – right)

2. Description of algorithms

The movement of particulates in the working area was realized by Euler algorithm. In all performed calculations the presence of the electric field was neglected in order to obtain results that will be minimally influenced by other effects. The collision between the species and particulate was evaluated according to the following algorithms.

2.1. Algorithm A

This algorithm is the simplest one. It is fast but also imprecise under several conditions. The particle is considered to be captured on the surface, when its distance from the center of powder particle is lower than the radius i.e. $|BS| \leq R_P$.

2.2. Algorithm B

The sketch of the situation is in Fig. 1. The particle position on the beginning of the time step is in point A and during the time step it moves to the new position – point B. The radius of the powder species is denoted R_P , the angle between vectors AS and AB is denoted φ . Symbol φ_{\max} denotes the angle between the tangent to the surface of the particulate and the abscissa AS. The collision arrive when $\varphi \leq \varphi_{\max}$ and concurrently the Point B is located inside the powder species and $|AC| \leq |AB|$. The algorithm scheme is presented in Fig. 2. The algorithm was used for the studies presented in [7].

This algorithm is precise and all the particles that trajectory come through the powder particulate are correctly detected.

2.3. Algorithm C

This algorithm is based on the calculation of the distance of the trajectory from the center of the particulate (see Fig. 1). The condition for the impact of the particle on the surface is fulfilled, when the point C (intersection of the plane given by normal vector AB and passing by point S) is between points A and B or when the point B is inside the powder specie (see algorithm in Fig. 2).

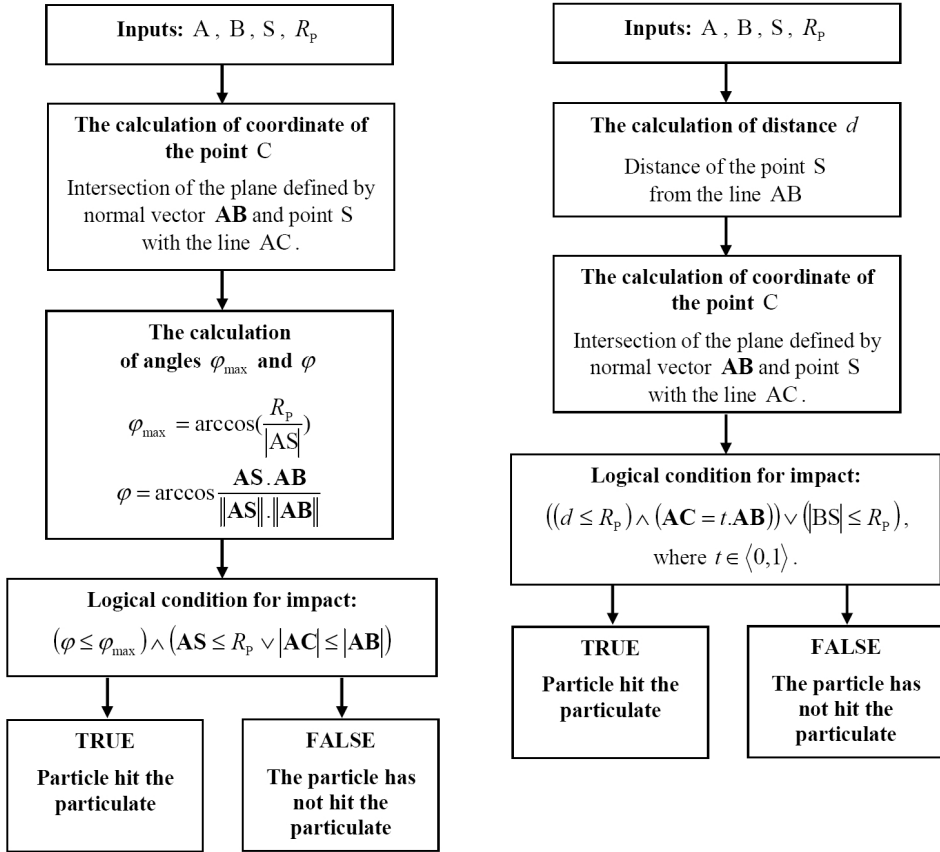


Fig. 2. Algorithms B (left) and C

3. Results and discussion

Both algorithms B and C are able to determine precisely whether the particle hits the surface of the powder specie. On the other hand, these algorithms are much more time consuming – the imprecise algorithm A is approximately twenty-times faster. The number of errors of the algorithm A (i.e. situations, when the particle should be captured by it was not) was tested for micron-sized dust particulates with radiuses 5, 10, 15, 30, 60 and 125 μm . The most simplest models were used – monoenergetic particles were considered (the trajectory that the particle moves in one time step is constant) and the influence of the electric field was neglected. The results of the test are presented in Fig. 3.

As we expected, the number of errors decrease with the increasing radius of the particulate and with increasing trajectory covered by the particle during one time step. For very small particulates with diameter of several micrometers the time step length should be chosen cautiously and the distance covered during one time step should not exceed 1×10^{-6} m.

In real plasma the velocities of particles are not constant but they take values from a given interval and they have a given energy distribution. Therefore, the particulates with different velocities cover in one time step various trajectories and, according to results presented in Fig. 3, they are captured by the powder specie with various probability. This leads to the deformation of the energy distribution function as presented in Fig. 4. The data were obtained by an easy particle simulation: the particles were moving in a box, in that center the powder particulate was placed (radius 30 μm , $\Delta t = 1 \times 10^{-10}$ s).

At the end of the simulation various number of particles remained in the working area. Whereas the algorithm A captured circa 33 percent, the precise algorithm B captured almost 64 percent of all particles. This significant difference influents for example the concentration of charged species in the vicinity of the powder particulate.

The non-physical changes in energy distribution function have impact on further physical quantities that depend on it. For example in hybrid models the energy distribution function is used for the calculation of coefficient of mobility and diffusion coefficient, reaction rates for various collisions etc [8]. Consequently, the usage of such values in the parts of the hybrid calculation can lead to the inaccurate estimation of the distribution of electric potential and concentrations of charged particulates in plasma.

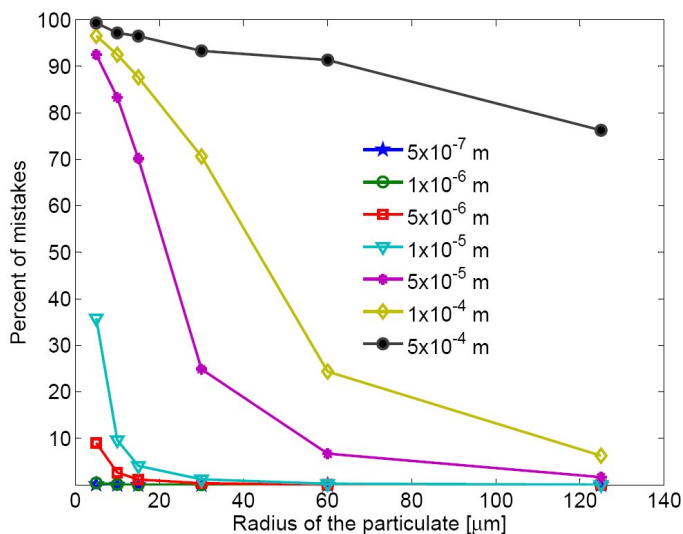


Fig. 3. The dependence of the number of errors on the particle radius and the distance covered by the specie during one time step

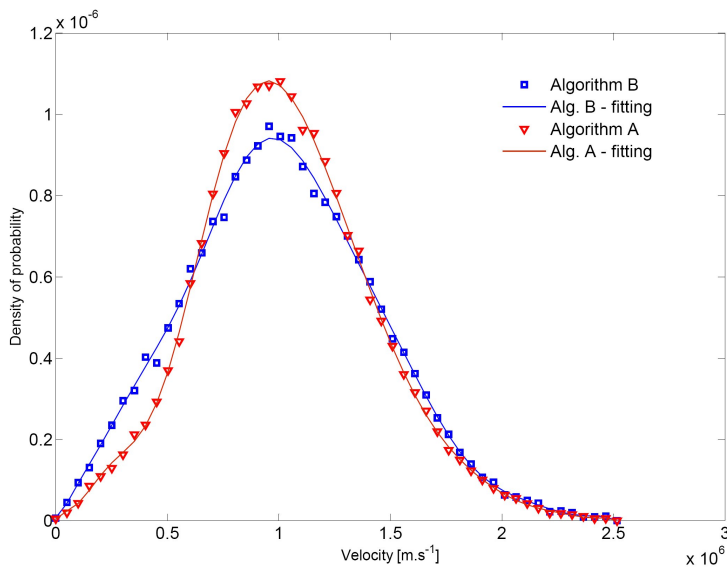


Fig. 4. Energy distribution function obtained by the calculation with algorithms A and B

4. Conclusion

It can be concluded that:

- the algorithm A is about twenty times faster than the precise algorithms B and C,
- algorithm A is practically unusable for computer simulation of the interaction of electrons and ions with very small powder particulates because of high number of numerical errors,
- the usage of the algorithm A leads to the deformation of energy distribution function that has not a physical reason.

References

- [1] A. BOGAERTS, K. DE BLEECKER, V. GEORGIEVA, I. KOLEV, M. MADANI, E. NEYTS: *Computer simulations for processing plasmas*. Plasma Processes and Polymers, 3 (2006), 110–119.
- [2] A. BOGAERTS, E. BULTINCK, M. ECKERT, V. GEORGIEVA, M. MAO, E. NEYTS, L. SCHWAEDERLÉ: *Computer modeling of plasmas and plasma–surface interactions*. Plasma Processes and Polymers, 6 (2009), 295–307.
- [3] A. LIPATOV: *The hybrid multiscale simulation technology*. Springer, Berlin 2002.
- [4] R. HRACH, P. JELÍNEK, J. ŠIMEK, O. BAŘINA, M. VICHER: *Self-consistent particle modelling of plasma-solid interaction: influence of substrate geometry*. Czech. J. Phys. Suppl. C, 54 (2005), 671–675.
- [5] P. JELÍNEK, R. HRACH: *One-dimensional hybrid model of plasma-solid interaction in argon plasma at higher pressures*. Journal of Physics, Conference series 63 (2007), 012010.
- [6] R. HRACH, P. BARTOŠ, V. HRACHOVÁ: *Computational study of plasma-surface interaction in plasma-assisted technologies*. European Physical Journal D, 54 (2009), 417–423.
- [7] P. BARTOŠ, R. HRACH, P. JELÍNEK: *Multidimensional fluid-particle modelling technique in low-temperature argon plasma at low pressure*. Vacuum, 82 (2) (2008), 220–223.
- [8] P. BARTOŠ, R. HRACH, P. JELÍNEK: *Computer simulations of probe measurements in argon plasma: effects of finite dimensions of the probe*. Contrib. Plasma Phys. 48, 5–7 (2008), 406–411.

Received May 17, 2010

Contents

<i>Topical issue containing selected papers presented at the 24th Symposium on Plasma Physics and Technology</i>	T1–T2
Yuri Akishev, Gregory Aponin, Anton Balakirev, Mikhail Grushin, Vladimir Karalnik, Alexander Petryakov, Nikolay Trushkin: Spatial-temporal behavior of individual microdischarges in dielectric barrier discharge	T3–T14
Tomaž Gyergyek, Jernej Kovačič, Milan Čerček: Transitions between space charge limited and temperature limited emission of electrons from a planar collector immersed in a plasma that contains an electron beam	T15–T29
Radomír Pánek, Milan Aftanas, Petra Bílková, Petr Bohm, Josef Havlíček, Jan Horáček, Martin Hron, Filip Janky, Diana Naydenkova, Jan Stockel, Jakub Urban, Vladimír Weinzettl, Jaromír Zajac, František Žáček, the COMPASS team: First results of the COMPASS tokamak	T31–T42
Charles Klett, Sylvain Touchard, Arlette Vega, Michael Redolfi, Xavier Duten, Khaled Hassouni: An experimental and modelling study of acetaldehyde oxidation by an atmospheric non-thermal plasma discharge	T43–T55
Luca Antonelli, Dimitri Batani, Andrea Patria, Orlando Ciriocosta, Carlo A. Cecchetti, Petra Koester, Luca Labate, Antonio Giulietti, Leonida A. Gizzi, Alessandro Moretti, Maria Richetta, Lorenzo Giuffrida, Lorenzo Torrasi, Michaela Kozlová, Jaroslav Nejdil, Magda Sawicka, Daniele Margarone, Bedřich Rus, Guy Schurtz, Xavier Ribeyre, Marion Lafon, Chris Spindloe, Tim O’Dell: Laser–plasma coupling in the shock-ignition intensity regime	T57–T69

Pavlina Ivanova, Tsviatko Popov, Miglena Dimitrova, Evgenia Benova, Todor Bogdanov, Jan Stöckel, Reunard Dejarnac: Precise evaluation of the plasma potential in COMPASS tokamak diverter area	T71–T83
Iwona Wodniak, Krzysztof Drozdowicz, Jan Dankowski, Barbara Gabańska, Andrzej Igielski, Arkadiusz Kurowski, Barbara Marczevska, Tomasz Nowak, Urszula Woźnicka: Diamond detectors for diagnostic of fast alpha particles escaping from the tokamak plasma . .	T84–T92
Diana Naydenkova, Vladimír Weinzettl, Jan Stöckel, David Šesták, Filip Janky: The optical system for visible plasma radiation measurements in the COMPASS tokamak – design and testing	T93–T100
Natalya A. Krutko, Oleg A. Lavrent'ev, Volodymyr A. Maslov, V. P. Oboznyj: Plasma accumulation and confinement in a multislit electromagnetic trap “Jupiter F”	T101–T106
Katarzyna Jakubowska, Monika Kubkowska, Elzbieta Skladnik-Sadowska, Karol Malinowski, Marian Paduch, Marek Jan Sadowski, Marek Scholz, Marina Ladygina: Optical spectroscopy of plasma beam interaction with tungsten target and temporal characteristic of spectral line emission in PF-1000	T107–T112
Anna Marchenko, Igor Garkusha, Vladimir Chebotarev, Marina Ladygina, Yuriy Petrov, Dmitriy Solyakov, Vladimir Tereshin, Valerij Staltsov, Ahmed Hassanein, Elzbieta Skladnik-Sadowska: Features of plasma focus formation in different operation modes of gas-discharge magnetoplasma compressor	T113–T122
Veronika Picková, Libor Švéda, Ondřej Klimo, Adam Darebníček, Michal Drahokoupil: Measuring the EUV pulse shape of the fs laser	T123–T133
Yuriy V. Korobkin, Victor L. Paperny, Igor V. Romanov, Andrei V. Brantov, Aleksandr A. Rupasov, Andrey S. Shikanov: Production of multiple charged and high energy ions by moderate energy laser facilities	T134–T144
Lorenzo Torrisi, Lorenzo Giuffrida: Post-acceleration of ions produced by laser-generated plasma	T145–T156
Mohammad A. Mohammadi, Samad Sobhanian, Masomeh Kiantaj: Effect of gas type on pinch current and soft X-ray emission in Sahand plasma focus	T157–T164
Oldřich Renner, Eduard Krouský, Richard Liska, Michal Šmíd, Olivier Larroche, Elisabeth Dalimier: Ion collisions and deceleration in laser-produced plasma-jet interaction with walls	T165–T174

Alireza Paknezhad, Davoud Dorrnian: Brillouin back scattering in vertically magnetized plasmas	T175–T182
Jan Pšikal, Jiří Limpouch, Ondřej Klimo, Vladimir Tikhonchuk: Generation of high energy electrons and ion acceleration in small structured targets	T183–T188
Lorenzo Torrisi, Francesco Caridi, Anna M. Visco, Nino Campo: Effect of filler amount in the welding of plastics induced by visible laser irradiation	T189–T198
Hendrik Bahre, Volker Schulz-von der Gathen, Hartmut Lange, Rüdiger Foest: Emission of vacuum ultraviolet radiation by a micro atmospheric pressure plasma jet operated in helium–oxygen mixtures into ambient air	T199–T206
Dana Skácelová, Pavel Slavíček: Diagnostics of plasma at atmospheric pressure by optical emission spectroscopy using broadening of lines	T207–T213
Rogério P. Mota, Nazir M. S. Marins, Mauricio A. Algatti, Konstantin G. Kostov, Roberto Y. Honda, Nilson C. da Cruz, Elidiane C. Rangel, Milton E. Kayama: Molecular structure, hydrophilic character and mechanical properties of diglyme plasma polymer	T214–T222
Jan Píchal, Dana Hollá, Jan Sláma: Treatment of polyester fabric in atmospheric dielectric barrier discharge operated at low frequencies	T223–T227
Mauricio A. Algatti, Rogério P. Mota, Regiane G. S. Batocki, Deborah C. R. dos Santos, Tiago J. Nicoleti, Konstantin G. Kostov, Roberto Y. Honda, Milton E. Kayama, Pedro A. de P. Nascente: Effect of helium plasma immersion ion implantation on plasma-polymerized films	T228–T237
Valerii Y. Nikulin, Lev I. Ivanov, Galina N. Mikhailova, Boris P. Mikhailov, Aleksei V. Troitskii, Landysh K. Antonova, Irina V. Borovitskaja, Pavel V. Gorshkov, Elena N. Peregudova, Sergei V. Pokrovskij, Igor' A. Rudnev: Effect of shock waves on current-carrying characteristics of HTSC	T238–T244
Nazir M. S. Marins, Rogério P. Mota, Roberto Y. Honda, Milton E. Kayama, Konstantin G. Kostov, Mauricio A. Algatti, Pedro A. P. Nascente, Elidiane C. Rangel: Chemical and Structural Characterization of Fluorinated Hydrogenated Amorphous Carbon Films	T245–T257
Andrius Tamošiūnas, Pranas Valatkevičius, Viktorija Grigaitienė, Vitas Valinčius: Formation of water vapor plasma using a linear DC plasma torch	T258–T265

Mario Maggiore, Salvatore Cavallaro, Giuseppe A. P. Cirrone, Giacomo Cuttone, Lorenzo Giuffrida, Francesco Romano, Lorenzo Torrisi: Design and realisation of a Thomson spectrometer for laser plasma facilities	T266–T277
Jozef Huran, Nikolay I. Balalykin, Grigory D. Shirkov, Alexander P. Kobzev, Albín Valovič: Nanocrystalline diamond/amorphous composite carbon films prepared by plasma chemical vapor deposition	T278–T283
Siarhei Bordusau, Siarhei Madveika: Investigation of the influence of the discharge chamber ‘loading’ effect on the optical characteristics of resonator type microwave plasmatron	T284–T290
Albín Valovič, Jozef Huran, Alexander P. Kobzev, Nikolai I. Balalykin, Michal Kučera, Štefan Haščík: Nanocrystalline silicon carbide thin films prepared by plasma enhanced chemical vapor deposition	T291–T298
Dmitriy A. Golosov, Sergey M. Zavatskiy, Sergey N. Melnikov, Zhu Chang, Mi Gaoyuan: Influence of deposition rate on optical properties of silicon-oxide thin films	T299–T308
Marcin Lis, Mieczysław Woch: Plasma spheroidization process of refractory metal powders	T309–T317
Rocio Rincón, Cristina Yubero, Maria D. Calzada, Lourdes Moyano, Luis Zea: Action of an Ar–N ₂ plasma on browning of sherry Fino wine	T318–T326
Siarhei Bordusau, Anatolii Dostanko, Siarhei Madveika: Express method determination of the gas pressure optimal for microwave chemical materials processing	T327–T331
Dmitrii Godun, Siarhei Bordusau, Anatolii Dostanko: The software-operated generator of high-voltage pulses for plasma technological application	T332–T337
Alia S. Askarova, Vladimir E. Messerle, Alexandr O. Nagibin, Alexandr B. Ustimenko: Modeling of plasma-assisted coal dust ignition and combustion	T338–T355
Dana Skácelová, Pavel Štáhel, Martin Haničinec, Mirko Černák: Plasma treatment of silicon surface by DCSBD	T356–T361
Oleg Byrka, Andriy Bandura, Igor Garkusha, Valeriy Taran, Vadim Makhlai, Vladimir Tereshin: Application of pulsed plasma streams for surface modification of constructional materials	T362–T372

Gennadiy G. Volokitin, Nelly K. Skripnikova, Andrey A. Nikiforov, Oleg G. Volokitin: Plasma technologies in building industry . . .	T373–T377
Alexander A. Savitsky, Alexander L. Zaitsev: Interaction of low- energy hydrogen plasma with polycrystalline aluminium	T378–T387
Yuliya Klenko, Jan Píchal: Study of thin SiO _x film deposition by DBD at the atmospheric pressure	T388–T396
Jan Sláma, Jan Píchal, Radek Procházka: Plasma flow in different gliding discharge reactor configurations	T397–T403
Peter Delmont, Rony Keppens: Limiting parameter values for switch- on and switch-off shocks in ideal MHD	T404–T413
Ramprasad P. Prajapati, Rajendra K. Chhajlani: Effect of magnetic field on jeans instability of quantum dusty plasma: application in white dwarf star	T414–T424
Hassan Alinejad, Mohammad A. Mohammadi: Dust ion acoustic shock waves in dusty plasmas	T425–T431
José Muñoz, Milan S. Dimitrijević, María D. Calzada: Determination of gas temperature from van der Waals broadening of atomic spec- tral lines in atmospheric pressure argon–neon microwave plasmas	T432–T437
Vadim S. Belyaev, Anatoly P. Matafonov: Magneto-active laser and astrophysical plasmas	T438–T453
Viktor V. Kuzenov, Sergei V. Ryzhkov: Developing the numerical model for studying laser-compression of magnetized plasmas . . .	T454–T467
Anastasiia Girka, Volodymyr Girka, Ivan Pavlenko: Application of al- ternating electric field for excitation of surface cyclotron O-modes	T468–T475
Petr Bartoš: Impact of electrons and ions on micron-sized dust par- ticulates in plasma: realisation in particle and hybrid computer models	T476–T482